

UNCLASSIFIED

AD 264687

DEFENSE DOCUMENTATION CENTER

FOR

SCIENTIFIC AND TECHNICAL INFORMATION

CAMERON STATION, ALEXANDRIA, VIRGINIA



UNCLASSIFIED

REPRODUCED FROM
BEST AVAILABLE COPY

NOTICE: When government or other drawings, specifications or other data are used for any purpose other than in connection with a definitely related government procurement operation, the U. S. Government thereby incurs no responsibility, nor any obligation whatsoever; and the fact that the Government may have formulated, furnished, or in any way supplied the said drawings, specifications, or other data is not to be regarded by implication or otherwise as in any manner licensing the holder or any other person or corporation, or conveying any rights or permission to manufacture, use or sell any patented invention that may in any way be related thereto.

**REFERENCE
COPY**

WADD TECHNICAL REPORT 59-22
VOLUME I

30 Dec 59

SKL

AERODYNAMIC AND STRUCTURAL ANALYSES OF RADOME SHELLS

VOLUME I. AERODYNAMIC ANALYSIS

BY

MARTIN H. BLOOM
DENNIS EISEN
MELVIN EPSTEIN
LAWRENCE GALOWIN
ANDREW G. HAMMITT
ERNEST D. KENNEDY
FRANK LANE
DANIEL E. MAGNUS
ALFRED A. MARINO
HAROLD S. PERGAMENT

GENERAL APPLIED SCIENCE LABORATORIES, INC.

FEBRUARY 1961

WRIGHT AIR DEVELOPMENT DIVISION

264687

FOREWORD

This report (which is divided into two volumes) was prepared by the General Applied Science Laboratories, Inc., Westbury, New York, and represents the completion of work performed under Contract No. AF 33 (616)-3956, entitled "Monocoque Radome Stress Study." The contract was documented under Task 41538 of Project 4152, "Radome Technology and Components." The contract efforts were accomplished under the cognizance of the Electronic Technology Laboratory, Wright Air Development Division (formerly Wright Air Development Center), with the technical work directed by James Dickinson and Lt. M. P. Davis, Jr., in turn as task engineers. The period covered by the contract was 8 January 1957 to 16 January 1960.

The material presented in Volumes I and II has appeared in Scientific Reports Nos. 1 through 17 which were prepared by GASL under this contract. The authors of the various parts in this final report have also prepared the corresponding scientific reports.

The Director of Aerodynamic Research for GASL is Dr. Antonio Ferri and the Director of Structural Analysis is Dr. Lee Arnold. The project engineers were Mr. Robert W. Byrne and Dr. Simon Slutsky.

Harold S. Pergament
Simon Slutsky

ABSTRACT

An analysis of the aerodynamic and stress problems encountered in the design of radome shells is presented.

Volume I discusses the aerodynamics with special emphasis on the calculation and reduction of heat transfer to the radome. Results are shown for Mach numbers up to 7 and altitudes to 150,000 feet. A chapter on shock layer ionization is also included in which the flow field about a typical radome configuration is studied for Mach numbers of 15 and 20 at altitudes of 150,000 and 200,000 feet.

In Volume II, the structural analysis is presented for axisymmetric radomes treating both homogeneous isotropic construction and sandwich construction. A description is given of numerical and programming techniques employed in the IBM 704 digital program prepared for homogeneous isotropic cones and ogives, including the central boom configuration for the truncated conical radome. An analysis is presented of thermal stresses in closed spherical shells of arbitrary thickness using the exact mathematical formulation of the theory of elasticity, thereby giving us a means of eventual evaluation of the thermal stresses at the stagnation point region of a radome with a rounded nose of small thickness to radius ratio. A discussion is also presented for the truncation error growth of the heat conduction programs to be used for the thermal loadings on the radomes.

PUBLICATION REVIEW

The publication of this report does not constitute approval by the Air Force of the findings or conclusions contained herein. It is published only for the exchange and stimulation of ideas

FOR THE COMMANDER:



W.S. HEAVER
Colonel, USAF
Chief, Reconnaissance Laboratory

TABLE OF CONTENTS

Foreword	ii
Abstract	iii
Introduction	1

VOLUME I - AERODYNAMIC ANALYSIS

Chapter I - METHODS OF DETERMINING HEAT TRANSFER	3
Part A General Discussion of Aerodynamic Problems	3
Part B Method of Calculating Pressure Distributions of Various Nose Shapes at Zero Angle of Attack in the Range of Mach Numbers from 0.9 to 7.0. --by Ernest D. Kennedy	18
Part C Methods of Calculating the Pressure Distribution on Various Nose Shapes at Small Angle of Attack in the Range of Mach Numbers from 0.9 to 7.0 --by Ernest D. Kennedy	75
Part D Calculation of Heat Transfer to Radome-Shaped Bodies. --by Martin H. Bloom and Melvin Epstein	105
Part E Charts and Equations for the Determination of Aerodynamic Heat Transfer to Radome-Shaped Bodies. --by Harold S. Pergament and Melvin Epstein	185
Chapter II - COOLING TECHNIQUES FOR RADOMES	254
Part A General Discussion of Cooling Problems	254

Table of Contents (Continued)

Part B	Radome Cooling Analysis	263
a.	Transpiration Cooling. --by Melvin Epstein	263
b.	Convective Cooling. --by Alfred A. Marino	299
c.	Cooling Effects of Localized Mass Addition. --by Martin H. Bloom	376
d.	Comparison of Transpiration, Convection and Film Cooling --by M. H. Bloom, A. A. Marino, M. Epstein	399
Part C	The Effect of Upstream Transpiration Cooling on the Compressible, Turbulent Boundary Layer.	406
a.	Analytical Investigation --by Harold S. Pergament	406
b.	Applications of Analytical Results --by Harold S. Pergament	463
Part D	Effect of Upstream Transpiration Cooling in Laminar Flow on the Downstream Wall Temperature over the Surface of a Cone. --by L. Galowin	486
Part E	Effects of the Separated Region of the Heat Transfer and Flow about a Chin Radome Configuration. --by A. G. Hammitt	524
Part F	An Investigation of the Use of a Spike in Front of a Radome to Reduce the Tempera- ture. --by A. G. Hammitt	551

Table of Contents (Continued)

Chapter III - SHOCK LAYER IONIZATION	590
Part A General Discussion of Ionization Problems	590
Part B An Approximate Method for the Calculation of the Shock Shape and Flow Field Properties about Long Blunted Cones at Hypersonic Speeds. --by Aerodynamic Department, General Applied Science Laboratories, Inc.	593

VOLUME II - STRUCTURAL ANALYSIS

Chapter IV	
Part A Structural Analysis of Homogeneous Axisymmetric Radome Shells under Mechanical, Thermal and Inertial Loading. --by Frank Lane	659
Part B Truncation Error Growth in Explicit Difference Schemes for Numerical Solutions of Heat Conduction Equations. --by Frank Lane	725
Part C Thermal Stresses in Spherical Shells of Arbitrary Thickness under Arbitrary Axisymmetric Temperature Distributions. --by Dennis Eisen and Frank Lane	751
Part D Digital Programs for the Structural Analyses of Homogeneous Conical and Ogival Shells under Mechanical and Thermal Loading. --by Daniel E. Magnus and Dennis Eisen	770
Part E Analysis of Sandwich Shells --by Frank Lane	846

INTRODUCTION

The purpose of this report is to investigate and evaluate the aerodynamic and stress problems encountered in the design of radome shells.

In Volume I, the aerodynamic analysis is presented. Three areas of interest are discussed; these are: (1) methods of determining heat transfer, (2) cooling techniques, and (3) the effects of ionization in the shock layer.

The importance of calculating the heat transfer rate is twofold: first, it serves as input to the heat conduction equation (which must be solved in order to determine the temperature distribution through the shell), and second, the design of a cooling system depends upon a knowledge of the heat flux into the uncooled body.

In the chapter on cooling techniques, a variety of schemes has been investigated. Among these are mass injection through slots and porous materials, and the use of a spike in front of the body to reduce the surface temperature. It should be pointed out that although the methods considered here are applicable to flight at very high Mach numbers (approximately 20), the emphasis has been on flight up to Mach 7 and 150,000 feet.

If the flow field about a body is ionized, the problem of signal attenuation becomes important and the properties of the ionized flow (or plasma sheath) must be determined. In Chapter III, the flow about a typical radome configuration is studied for free stream Mach numbers of 15 and 20 at altitudes of 150,000 and 200,000 feet.

Manuscript released by authors on 15 January 1960 for publication as a WADD Technical Report.

In Volume II, the structural analysis is presented for axisymmetric radomes treating both homogeneous isotropic construction and sandwich construction. A description is given of numerical and programming techniques employed in the IBM 704 digital program prepared for homogeneous isotropic cones and ogives, including the central boom configuration for the truncated conical radome. An analysis is presented of thermal stresses in closed spherical shells of arbitrary thickness using the exact mathematical formulation of the theory of elasticity, thereby giving us a means of eventual evaluation of the thermal stresses at the stagnation point region of a radome with a rounded nose of small thickness to radius ratio. A discussion is also presented for the truncation error growth of the heat conduction programs to be used for the thermal loadings on the radomes.

AERODYNAMIC AND STRUCTURAL ANALYSES OF RADOME SHELLS

VOLUME I

AERODYNAMIC ANALYSIS

CHAPTER I

METHODS OF DETERMINING HEAT TRANSFER

PART A

GENERAL DISCUSSION OF AERODYNAMIC PROBLEMS

A. GENERAL DISCUSSION OF AERODYNAMIC PROBLEMS *

Aerodynamic information required for the structural design of radomes consists primarily of pressure distributions and heat inputs to the surface. Surface shear stresses may also be important for erosion studies.

The external pressures form the basis of the mechanical loads, being supplemented by the internal pressures, inertia loads due to acceleration, and transient loads due to winds or blasts. The external pressure distribution is also part of the basic information required for estimating heat inputs. In this regard Prandtl's well-known boundary layer concept is recalled. According to this concept the explicit effects of transport properties, i. e., viscosity, conductivity and diffusion, are confined to a thin boundary layer near the surface under "usual" conditions. For present purposes, it is sufficient to remark that "usual" conditions involve Reynolds numbers which are not very low, radii of curvature which are much larger than the boundary layer thickness and continuum or near-continuum behavior of the air (Reference 1). The lower bound of the Reynolds number is of particular interest in the tip region of sharp or slightly blunted bodies in hypersonic flow (References 2 and 3), where low Reynolds numbers are associated with low densities and small tip dimensions rather than with low velocities. It appears that the distinction between viscous and inviscid flow regimes is

* Most of the material in this part has been taken from GASL Scientific Report No. 6 by Dr. Martin H. Bloom.

applicable at much lower Reynolds numbers than was originally expected. However, consideration must be given even to the minute bluntness of supposedly sharp tips when slender bodies are studied.

Using the Prandtl concept, the flow properties such as pressure and velocity outside the boundary layer may be determined theoretically or experimentally by neglecting the explicit presence of transport properties, and in a first approximation the displacement effect of the boundary layer. Because of the approximately parallel nature of the boundary layer flow, the pressure variation along surface-normals within the layer is negligible and the local inviscid pressure is transmitted to the surface unchanged. If the boundary layer displacement due to mass defect becomes significant, it may be treated as an alteration of the effective body shape and an iteration procedure used to determine the changed inviscid flow properties.

The known inviscid flow properties are used as boundary conditions for the determination of the boundary layer transport phenomena, such as the heat flux.

It is advisable here to point out two effects which are encountered in hypersonic flow around thin (two-dimensional) and slender (three-dimensional) bodies. The first concerns the fact that in the tip region measured pressures may be higher than those expected on the basis of conventional analysis; on wedges and cones they may be as much as 70 or 80% higher. This has been explained to some extent by recognizing that all sharp tips are somewhat blunt and must be so treated under certain hypersonic conditions. Moreover, it is

seen that rapid boundary layer growth leads to a further effective blunting of the tip. This blunting engenders detachment of the bow shock and increased tip pressures. The zone of influence of the induced pressure-rise decays rather sharply on non-slender bodies and decreases with increases in the initial angle. It will not be important in the radome noses of interest here, but may be important in future cases. Tests in helium at Mach 16 to 18 (Reference 4) have indicated virtually no pressure difference from the classical inviscid value on a 10° half-angle cone, whereas a 5° half-angle cone showed a 20% rise.

A second effect attributable to severe boundary layer thickening concerns the changes in flow properties along the downstream surfaces of slender bodies and the increased importance of the transverse body curvature. For example, multiples of the usual skin friction values have been estimated on such surfaces under high altitude conditions (Reference 2). Although this factor will not affect the radome surfaces under consideration here, it may be of significance for radomes on lateral surfaces.

More generally we see that nose-radome shapes which are suitable from an optical standpoint are relatively well-behaved from the standpoint of aerodynamic analysis. Shapes of interest consist of pointed or blunted bodies of revolution with length-to-diameter ratios on the order of 1 to 5. Concavities, abrupt changes in curvature, and departures from axial symmetry are usually absent. The pressures generally decrease monotonically from a maximum value at the stagnation point, i. e., "favorable" pressure

gradients exist, and boundary layer separation is not encountered. In fact, on common sharp-nosed shapes such as tangent ogives with attached shocks at zero incidence, the pressure decreases almost linearly in the streamwise direction (Reference 6).

In the portion of an axially symmetric or two-dimensional flow field which is purely supersonic, as is the case for most sharp nose-radomes at moderate supersonic Mach numbers, a powerful tool, the method of characteristics (Reference 7), is available for a very accurate calculation of the inviscid flow properties. However, this method involves a rather unwieldy step-by-step numerical procedure and cannot be used directly for true three-dimensional problems. As a result, numerous approximate methods have been developed, each having advantages and disadvantages in various flight regimes and for various body shapes. Furthermore, the advent of very high speeds has made necessary the use of noses which are blunt to some extent in order to provide cooling relief in the body and a decrease in the heat flux rates into the body. It has been found that a degree of blunting can be applied to a body of revolution without necessarily increasing the drag (Reference 8). This blunting results in detachment of the bow shock and in the formation of a subsonic region of flow in the stagnation region. For spherical bluntness the subsonic region extends approximately to the point $\theta = 50^\circ$, where θ is the angle between the flight direction and the local surface tangent. Only recently have relatively precise methods emerged for the calculation of such flow (References 2, 9 and 10). At present they are being extended to the

case of non-zero angle of attack and are being utilized to treat flat and even concave noses. Prior to this, semi-empirical procedures were used to treat the detached-shock flow field; one such method, the "modified Newtonian" method for estimating pressures (Reference 11) is cited here because of its degree of success under a variety of conditions, and its simplicity. It may be expressed in the form

$$(p-p_f)/(p_s-p_f) = \sin^2 \theta \quad (1)$$

where

p = local pressure

p_f = undisturbed ambient pressure

p_s = maximum pressure on the body, say the stagnation pressure behind a normal shock wave

θ = local flow deflection angle; the angle between the flight direction and the local surface tangent

This formula provides a good idea of the pressure distributions on blunt bodies for Mach numbers above 2 at zero and non-zero angles of attack (Reference 12) although its accuracy is diminished for $\theta < 40^\circ$. It can also be used to some extent on sharp-nosed bodies (Reference 6).

The importance of convenience for engineering calculations has been implied in the foregoing discussion and parts C and D give recommended procedures for the calculation of pressure distributions on a number of different body shapes, for both zero and small angles of attack.

It may be pointed out here that in many circumstances the pressure distributions over noses must be known with greater accuracy for the computation of heat transfer rates than for the evaluation of structural loads. This is particularly true in the stagnation regime of blunt bodies where the heat flux is proportional to the square root of the velocity gradient, which in turn is proportional to the pressure gradient.

Once the pressure distribution over a body is known the inviscid velocity distribution can usually be determined readily by well-known relations of fluid mechanics.

Heat Transfer

The range of flight conditions for which a radome must operate is well-known, and the effect of large heat transfer rates, developed in this flight regime, on the structural design is now familiar. A discussion of astronomical radome problems has been given by Behrens (Reference 5).

Bloom, several years ago, prepared a detailed compilation of heat transfer formulas and data to be used in aeronautical applications (Reference 15). This has been brought up to date in a monograph which appears in AGARDograph 28 (Reference 16). Recommended design procedures for nose-radome applications have been set forth in parts D and E of this section.

It may be noted that References 15 and 16 contain extensive bibliographies. In fact, Reference 16 lists 19 surveys and bibliographies

concerning aerodynamic heat transfer. Also given in Reference 16 is a brief description of the various modern types of heat transfer test facilities now in use or anticipated.

Several points are of particular interest for nose-radome applications. It is recognized that there are several modes of energy transfer: Conduction, diffusion and radiation. Forced convection denotes mechanically-enforced fluid motion which permits the transport properties to act more readily. The nature of the boundary layer flow, i. e., whether it is laminar or turbulent is of extreme importance since the skin friction and heat transfer values in the two cases are quite different. At present, our inability to predict with reliability the conditions for the onset of turbulence forms the weak link in our chain of engineering estimates. Low speed flow over smooth plates have remained laminar at local Reynolds numbers up to 3 to 5 million. A criterion which has been used on blunt bodies is that laminar flow can be expected in the stagnation region at least up to the point where the local Reynolds number based on the momentum thickness (a boundary layer parameter indicating momentum defect) as a reference length, does not exceed 150. It has been found also that the acceleration or deceleration of the body may have a strong influence on triggering the transition from laminar to turbulent flow. Extensive reviews of transition information have been given in References 18 and 19. For design purposes, estimates based on completely laminar and completely turbulent flow may be made. A transition point or region can be chosen on the basis of a reasonable guess, preferably based on data taken

under similar circumstances.

The actual formulas used for predicting heat rates are given in parts D and E of this section. Some of the ideas behind the procedures recommended for radome surfaces will be discussed now.

On sharp-nosed bodies with attached shocks, it will be found that the pressure variations are relatively small. Therefore, heat rates can be given with a good approximation by evaluating locally what will be termed a "flat plate" formula, that is, one derived under zero pressure gradient conditions. This procedure is suitable for both laminar and turbulent flows. A numerical coefficient must be adjusted to take into account the approximate conical nature of the flow near the tip. Conical heat rates are larger than the corresponding two-dimensional values by a factor of $\sqrt{3}$ in laminar flow and by about 1.15 in turbulent flow.

On blunt bodies above Mach 2 or 3 a very convenient formula for laminar flow developed by Lees (References 20 and 21) can be used. This gives the ratio of heat flux at a point along the body to the stagnation point value. For engineering purposes, the stagnation point value can be represented for air by the following simple relation which is valid even at hypersonic speeds where the effects of air dissociation are taken into account.

$$q_0 = 2.2(\rho_f/r_0)^{1/2} u_f^3 \left(1 - \frac{h_w}{h_{sf}}\right) \quad (2)$$

where

q_0 = heat flux (Btu/ft²-sec)

ρ_f = ambient density (slugs/ft³)

r_0 = radius of curvature at the stagnation point (ft)

u_f = flight speed (ft/sec)

h_w/h_{sf} = ratio of enthalpy at the surface to the stagnation
enthalpy of flight (for hypersonic conditions $h_{sf} \approx u_f^2/2$
and the ratio is negligible)

For flat-faced bodies the value given in Equation (2) must be modified by multiplying it by the square root of the ratio of the actual velocity gradient to the spherical-nose stagnation value. Again it is pointed out that the explicit influence of dissociation on the stagnation point heat transfer rate is a secondary one, and need not appear in the preliminary estimates.

In laminar flow over blunt bodies, the maximum heat flux occurs in the stagnation region and drops off drastically as the flow accelerates over the body. If the flow becomes turbulent, the heat flux increases considerably outside the stagnation region (the flow in the stagnation region is expected to remain laminar because of the low velocity and small boundary layer thickness there) and may rise to as much as 2 or 3 times the stagnation value as the flow accelerates to sonic velocity. The peak turbulent heating occurs in the neighborhood of the sonic region.

In turbulent flow over blunt bodies, when the flow density at the surface is high relative to the local inviscid density, it has been determined by experiments (Reference 22) that the heat flux data is represented well by a

local evaluation of a "flat plate" formula. Since the density ratio is inversely proportional to the corresponding ratio of surface temperature to local inviscid temperature, the temperature ratio will be small. This is the case in hypersonic flow. Actually, it appears that the flat plate relation applies even when the temperature ratio is as large as 0.5, which may be the case in low supersonic flow. This represents an important simplification of the turbulent convective heat transfer problem. The charts presented later in this section make use of this.

It should be pointed out that the effects of radiation heat transfer from a high temperature surface can serve to alleviate strongly the net heat flux to the surface. The radiation heat loss is proportional to the fourth power of the surface temperature according to well-known relations.

The effect of radiant heat transfer to the surface from ionized gases in the boundary layer or the ionosphere has received attention lately (References 21, 23, 24 and 25). For ballistic missiles and trajectories decaying from a circular satellite orbit the stagnation-region equilibrium radiative heat rates are quite small. However, for vertical reentry at initial velocities on the order of 35,000 ft/sec the radiation heat transfer may become large and even dominate the convective heat rate. It may be noted that the radiative heat rate is approximately proportional to the 12th power of the flight velocity, the $3/2$ power of the ambient density and the first power of the nose radius.

For computing heat rates to blunt bodies of revolution at angles of attack an engineering approach has been suggested in part D according to a procedure used at the General Electric Company's Missile and Space Vehicle Department. More rigorous procedures have been recently developed for this case (Reference 26) based on the assumption that for well-behaved bodies (whose curvatures in tangent planes are not large) the boundary layer characteristics can be computed in a two-dimensional fashion along planes normal to the surface and passing through the inviscid streamlines. Additional work concerning blunt body pressure distributions and heat transfer at zero and non-zero angle may be found in References 13 and 14.

A word can be said of transient effects such as those generated by blast waves. It can be suggested that in this case a series of instantaneous steady states can be considered over the entire body with only the ambient conditions changing with time. That is, the explicit effects of the time variations can be neglected in a first approximation and a quasi-steady approach used. Confidence in this procedure is engendered, for example, by the rapid adjustment of low fields to steady conditions in shock tubes where testing flow durations are on the order of a millisecond and steady flows are achieved on small models in times on the order of microseconds.

Estimates of mechanical loads and heat rates under extreme non-continuum conditions, that is, in the free-molecule regime, which exist at very high altitudes can be made with reasonable confidence. These are discussed, for example, in References 27 and 28.

REFERENCES

1. Goldstein, S., Editor, Modern Developments in Fluid Dynamics, Oxford University Press, V. I, p. 116, 1938.
2. Lees, L., Recent Developments in Hypersonic Flow. Jet Propulsion, November 1957, p. 1182.
3. Hammitt, A.C. and Bogdenoff, S.M.: Hypersonic Studies of the Leading Edge Effect on the Flow Over a Flat Plate. Jet Propulsion, V. 26, No. 4, April 1956, p. 241.
4. Erickson, W.D.: Study of Pressure Distributions on Simple Sharp-Nosed Models at Mach Numbers from 16 to 18 in Helium Flow. NACA TN 4113, October 1957.
5. Behrens, F.H.: Astronautical Program Influences on Radome Development Planning. WADC, Presented at the OSU-WADC Radome Symposium, Columbus, Ohio, June 1958.
6. Ehret, D.M.: Accuracy of Approximate Methods for Predicting Pressures on Pointed Nonlifting Bodies in Supersonic Flow. NACA TN 2764, August 1952.
7. Ferri, A.: Elements of Aerodynamics of Supersonic Flows. Macmillan Company, New York, 1949.
8. Eggers, A.J., Jr.: Performance of Long-Range Hypervelocity Vehicles. Jet Propulsion, November 1957.
9. Van Dyke, M.D.: The Supersonic Blunt-Body Problem -- Review and Extension. Institute of Aeronautical Sciences Preprint 801, Jan. 1958.
10. Vaglio-Laurin, R.: Theoretical Investigation of the Flow Field Around Blunt-Nosed Bodies in Supersonic Flight. General Applied Science Laboratories, Inc., Technical Report No. 54, February 1958.
11. Lees, L.: Hypersonic Flow. Fifth International Aeronautical Conference, Los Angeles, Calif. (I. A. S. Fairchild Reprint) 1955.
12. Bryant, W.T. and Machell, R.M.: An Experimental Investigation of Flow over Blunt-Nosed Cones at a Mach Number of 5.8. Journal of Aeronautical Sciences, V. 23, No. 11, p. 1054, November 1956.

13. Ferri, A.: A review of Some Recent Developments in Hypersonic Flow. Polytechnic Institute of Brooklyn, PIBAL Report No. 426, ASTIA Doc. No. 155 822, September 1958.
14. Zakkay, V.: Pressure and Laminar Heat Transfer Results in Three-Dimensional Hypersonic Flow. Polytechnic Institute of Brooklyn, WADC TN 58-182, ASTIA AD 155 679, September 1958.
15. Bloom, M.H.: Thermal Conditions Associated with Aircraft in Flight, WADC TR 55-169, March 1956.
16. Bloom, M.H.: External Sources of Heat (in Aeronautics), Monograph in AGARDograph 28 - High Temperature Effects in Aircraft Structures. N.J.Hoff, Editor, Pergamon Press, 1958.
17. Ferri, A. and Libby, P.A.: A New technique for Investigating Heat Transfer and Surface Phenomena under Hypersonic Flow Conditions. Journal of Aeronautical Sciences, V. 24, No. 6, June 1957.
18. Smith, A.M.O. and Gamberoni, N.: Transition, Pressure Gradient and Stability Theory. Douglas Aircraft Co., Inc. Report ES 26388, August 31, 1956.
19. Probstein, R. F. and Lin, C.C.: A Study of the Transition to Turbulence of the Laminar Boundary Layer at Supersonic Speeds. Institute of Aeronautical Sciences Preprint No. 596, January 1956.
20. Lees, L.: Laminar Heat Transfer over Blunt-Nosed Bodies at Hypersonic Flight Speeds. Jet Propulsion, V. 26, No. 4, p. 259, April 1956.
21. Lees, L.: Recovery Dynamics -- Heat Transfer at Hypersonic Speeds in a Planetary Atmosphere. Univ. of California, Space Technology Lecture 6A, February 1958.
22. Libby, P.A. and Cresci, R.: Evaluation of Several Hypersonic Turbulent Heat Transfer Analyses by Comparison with Experimental Data, Polytechnic Institute of Brooklyn, WADC TN 57-72, ASTIA AD 118 093, July 1957.
23. Heck, J., Kivel, B. and Wentink, T.: Emmissivity of High Temperature Air, Heat Transfer and Fluid Mechanics Institute, Stanford University Press, Stanford, California, p. 279, 1957.
24. Gazely, C., Jr. and Masson, D.J.: Recovery of Circum-Lunar Instrument Carrier, Eighth International Astronautical Congress, Barcelona, Spain, Report No. 488-57, p. 1-22, 6-12, October 1957.

25. Meyerott, R.E.: Radiation Heat Transfer to Hypersonic Vehicles. Third AGARD Combustion and Propulsion Panel Colloquium, Palermo, Sicily, March 1958.
26. Vaglio-Laurin, R.: Laminar Heat Transfer on Blunt-Nosed Bodies in Three-Dimensional Hypersonic Flow. WADC Technical Note 58-147, ASTIA Document No. AD 155 588, May 1958.
27. Patterson, G.N.: Molecular Approach to Problems of High-Altitude, High-Speed Flight. AGARD Report No. 134, July 1957.
28. Schaaf, S.A., Rarefied Gas Dynamics. Applied Mechanics Review, Vol. 9, No. 10, p. 413, 1956.

CHAPTER I - PART B

METHOD OF CALCULATING PRESSURE DISTRIBUTIONS OF
VARIOUS NOSE SHAPES AT ZERO ANGLE OF ATTACK IN THE
RANGE OF MACH NUMBERS FROM 0.9 TO 7.0

by Ernest D. Kennedy

TABLE OF CONTENTS

	<u>Title</u>	<u>Page</u>
	Summary	20
1	Introduction	21
2	Symbols	22
3	Outline of the Methods of Calculation	24
	a. Shock Expansion Method	24
	b. Newtonian Flow Theory	25
	c. von Karman-Moore Linearized Theory	25
	d. Lighthill Slender Body Theory	26
	e. Hypersonic and Supersonic Similarity Rules	26
4	Calculation of Pressure In Supersonic and Hyper- sonic Ranges On:	28
	a. Tangent Ogives	28
	b. Cones	29
	c. Ellipsoids of Revolution	29
	d. Paraboloids of Revolution	31
5	Transonic Range	32
6	Conclusions	35
	References	36
	Appendix A	41
	Appendix B	43
	Appendix C	47

**B. METHOD OF CALCULATING PRESSURE DISTRIBUTIONS OF
VARIOUS NOSE SHAPES AT ZERO ANGLE OF ATTACK IN THE
RANGE OF MACH NUMBERS FROM 0.9 to 7.0**

SUMMARY

Methods are given for calculating pressures on noses of various shapes in the range of Mach number from transonic to $M = 7$ at zero angle of attack. The nose shapes considered are cones, tangent ogives, ellipsoids and paraboloids of revolution. The method of characteristics is not considered since its higher accuracy is not warranted for the purpose of this study. The methods decided upon are the shock expansion method, the modified Newtonian method, the von Karman-Moore linearized theory and the Lighthill slender body theory. The regions of applicability of each method, established by comparison with either characteristics calculations or experimental data, are given. The above methods will give the pressure on any body in the given range with a relatively small amount of calculation.

1. INTRODUCTION

The purpose of this study was to determine methods of calculating pressures on various nose shapes in the transonic, supersonic and hypersonic regimes. The shapes considered were cones, tangent ogives, ellipsoids and paraboloids of revolution at angles of attack from 0 to 45° in the Mach number range from 0.9 to 7 and fineness ratios from 0.5 to 10.0. The results for zero angle of attack are reported herein. The method of characteristics was not considered since there are alternate methods available which, although less accurate in certain ranges, entail much less computational effort.

The range of Mach numbers, fineness ratios and body shapes is sufficiently wide to prevent any single method being used. However, most of the required results may be obtained from the modified Newtonian theory, the shock expansion method, the linearized supersonic theory of von Karman and Moore and the slender body theory of Lighthill. Good use can be made of the hypersonic, supersonic and transonic similarity rules to reduce calculations for certain bodies. The accuracy of the various methods is ascertained by comparison with the characteristics theory or experimental data.

2. SYMBOLS

P static pressure

L/D fineness ratio (the ratio of the nose length to its base diameter)

M_0 Mach number

$K = \frac{M_0}{L/D}$ hypersonic similarity parameter

γ ratio of specific heats

$q = \frac{\gamma}{2} M_0^2 P$ dynamic pressure

$\Delta P = P_1 - P_0$

C_p Pressure coefficient = $\Delta P/q_0$

Θ slope of the body

U velocity

ϕ velocity potential

S cross-sectional area

$B = \sqrt{M_0^2 - 1}$

\ln natural logarithm

$F(C_p) = C_p(L/D)^2 - \frac{S''(x)}{\pi} \left(\frac{L}{D}\right)^2 \ln(L/D)^2$, the transonic pressure parameter

$K_T = B^2 \left(\frac{L}{D}\right)^2$, transonic similarity parameter.

$B = \sqrt{M_0^2 - 1} \quad M > 1$

$\sqrt{1 - M_0^2} \quad M < 1$

γ = Prandtl-Meyer angle

P_T Stagnation pressure

Subscripts

o free stream

L local

2D two-dimensional

max maximum

s refers to conditions at the tip of the body immediately behind the shock

Superscripts

i $\frac{d}{dx}$

n $\frac{d^2}{dx^2}$

3. OUTLINE OF THE METHODS OF CALCULATION

a. Shock Expansion Method

This method is based on the observation that in certain cases, the Mach number and pressure on the surface of a body of revolution can be calculated as though the flow downstream of the nose shock were two-dimensional. The method requires that the nose shock be attached. In Ref. 1 it is shown by comparison with characteristics calculations that this method yields good accuracy for ogives for a value of the hypersonic similarity parameter (i. e., the ratio of free stream Mach number to fineness ratio) above unity. The actual calculation procedure is as follows: The Mach number and pressure at the tip behind the shock are taken as on a cone of the same angle as the initial slope of the body. A Prandtl-Meyer expansion is then assumed over the nose shape which gives the pressure distribution immediately from the local slope.

Zienkiewicz (Ref. 2) has extended this concept to values of the hypersonic similarity parameter of 0.4 for tangent ogives. He noted that for these lower values, the actual pressure, $P_L - P_S$, although not the two-dimensional value, was a constant fraction of the two-dimensional pressure, $P_{2DL} - P_S$, over the length of the body. Figure 1, reproduced from Ref. 2, gives values of these constants for $0.4 < K \leq 1$ and $1.5 < M_0 < 3.5$.

b. Newtonian Flow Theory

This theory assumes that the flow is turned parallel to the body at the surface of the body rather than by means of a shock wave. With this assumption, the pressure coefficient varies only with the local flow deflection and is given by $C_p = 2 \sin^2 \Theta$. However, for a blunt body, the pressure coefficient at a stagnation point ($\Theta = 90^\circ$) is determined by the free stream Mach number only and approaches the value of 2 given by the Newtonian theory only for infinite Mach number and when real gas effects are considered.

Accordingly, the above expression for pressure coefficient is modified to give the correct value at the stagnation point and is rewritten $C_p = C_{p \max} \sin^2 \Theta$, where $C_{p \max}$ is the stagnation point pressure coefficient and is given in Figure 2 as a function of free stream Mach number. This expression has been shown in Refs. 15, 16, 18 and 19 to yield good results for blunt bodies for Mach numbers above about 2. It should be noted that this method will not give results for a surface negatively inclined to the free stream.

c. von Karman-Moore Linearized Theory

This method, given in Ref. 3, replaces a slender body of revolution with sources and sinks, their strengths being determined by the body shape. A discussion may be found in many references, for example

Ref. 4. The required equations are given in Appendix A.

d. Lighthill Slender Body Theory

This method, advanced in Ref. 7, relates the pressure distribution to the variation of cross-sectional area and the slope of the body. A detailed description of the method is given in Ref. 20. Although developed for pointed bodies, the theory can be shown to give reasonable results for blunt bodies far from the stagnation point. Equations are developed in Appendix B which may be applied to paraboloids and ellipsoids of revolution.

e. Hypersonic and Supersonic Similarity Rules

It was shown by Tsien (Ref. 5) that slender affine bodies having the same value of the parameter $\frac{M_0}{L/D}$, (the so-called hypersonic similarity parameter) have the same distribution of pressure. This concept was extended to the low supersonic range by van Dyke (Ref. 21) who replaced M_0 by $\sqrt{M_0^2 - 1}$ in the similarity parameter to get a rule valid for any Mach number above the transonic range. The van Dyke similarity parameter, (or supersonic similarity parameter), of course, reduces to that given by Tsien for high Mach numbers. It should be noted that the pressure distributions are similar when expressed as $\frac{\Delta P}{P_0}$ or $\frac{P}{P_0}$ but are not similar in terms of C_p .

The region of applicability of this rule for cones and ogives was investigated in Ref. 6 by comparing pressure distributions as calculated

by the method of characteristics. It was concluded that the rule applied for $\frac{L}{D} \geq 2$ and $M \geq 1.5$ for both shapes. Ogives do not transform affinely, but the discrepancy is evidently insufficient to significantly affect the result in the range considered.

4. CALCULATION OF PRESSURE IN SUPERSONIC AND
HYPERSONIC RANGES ON:

a. Tangent Ogives

Figure 3 shows the range of interest of fineness ratio and Mach number. The shock detachment line and the region of applicability of the hypersonic similarity rule are also shown.

The following procedures may be used to calculate the pressure distribution with good accuracy:

1. For attached shock and $K \geq 1$, the shock expansion method as previously outlined should be used.
2. For $0.4 \leq K \leq 1$, the pressure calculated by the shock expansion method must be multiplied by the factors in Figure 1. If the body lies outside the range shown in Figure 1, the pressure on an affinely related body inside the range can be calculated and the similarity rule applied.
3. In the range of $K < 0.4$ to the transonic range, the von Karman-Moore theory can be used. Application of the similarity rule gives the pressure on a family of bodies for each calculation.
4. For $L/D = 0.5$, the tangent ogive becomes a hemisphere and can be handled with the modified Newtonian theory.

These four methods cover the entire range except the region between $L/D = 0.5$ and $L/D = 2.0$ where none of the methods are accept-

able. However, this region is sufficiently narrow that the pressures may be interpolated with a fair degree of confidence.

Figure 3 also shows bodies for which pressure distributions (either experimental or calculated from the method of characteristics) are available in the literature. With these data available, a good deal of the required range can be covered immediately with the similarity rule.

b. Cones

Figure 4 shows that the entire range (with the exception of the transonic) is available immediately from the cone tables (Refs. 22 or 23). The validity of these tables has been, of course, firmly established.

c. Ellipsoids of Revolution

There are unfortunately no similarity rules available for blunt nosed bodies such as ellipsoids. Such a rule, if it did exist, could not be valid near the stagnation point, but it might be hoped to correlate pressures far from the nose (say downstream of the sonic point) by such a method. However, the experimental data which are available (Figure 5) are insufficient to establish such a rule.

The Newtonian concept, modified to satisfy the stagnation point pressure, has been used successfully to calculate the pressure distribution on a variety of blunt bodies above a Mach number of about 2. For Mach numbers lower than 2 there is no method available which is valid every-

where, but a reasonable estimate may be made using the slender body theory of Lighthill (Ref. 7). This method relates the pressure distribution on a slender body to the variation of cross-sectional area and the slope of the body. The derivation of the expression for pressure coefficient for ellipsoids of revolution is given in Appendix B. The predicted pressure distributions using this expression are compared with experimental data in Figures 6-9 for various combinations of Mach number and fineness ratio. The theory is, of course, invalid in the region of the stagnation point (an infinite pressure is predicted at this point). However, the actual stagnation point pressure is known from the free stream Mach number. The figures show that for fineness ratios as low as 3, the slender body theory is within a few percent of the test points over the last 80% of the nose. However, for a fineness ratio of 2, the errors are much larger - approximately 25 percent at the shoulder at $M_0 = 1.8$ and 13 percent for $M_0 = 1.4$.

It seems then that for L/D greater than about 3, the pressure distribution on ellipsoids of revolution may be calculated by the slender body theory for the rear 80% of the length and then fairing this curve to the known value at the stagnation point.

These two methods cover the range of interest except the region below $M = 2$ and below $L/D = 3.0$. However, in this range, several

sets of experimental data are available (Refs. 8 and 9). These data are sufficiently close to each other or to regions where the analyses apply so that the pressure on any body may be interpolated with some degree of confidence.

d. Paraboloids of Revolution

No experimental data were found for paraboloids of revolution. However, the Newtonian flow concept may be used above Mach number 2 with reasonable assurance of accuracy in view of its success with other blunt bodies. For the low Mach number range, it is inferred, by analogy with the ellipsoid case, that the slender body theory can be used for $L/D > 3$ by fairing the calculated curve to the stagnation point pressure. The slender body expression for pressure coefficient on paraboloids of revolution is derived in Appendix B.

5. TRANSONIC RANGE

There is no analytical method available for determining the pressure distribution on bodies of revolution in the transonic speed range. This complication arises because differential equation of motion cannot be linearized and thus far the nonlinear equation has not been solved. However, similarity rules have been discovered in this speed range and hence a single set of experimental data may be applied to a family of affine bodies within the range of applicability of the rule.

The transonic similarity rule for axially symmetric bodies has been developed by Oswatitsch and Berndt (Reference 28). They show that for slender bodies having the same value of the parameter $\frac{1}{2} (1 - M^2) (L/D)^2$, the quantity $F(C_p) = C_p \left(\frac{L}{D} \right)^2 - \frac{S''(x)}{\pi} \left(\frac{L}{D} \right)^2 \ln \left(\frac{L}{D} \right)^2$ has the same value at corresponding points on the two bodies. Hence, one set of experimental data can be used for a family of bodies.

A search of the literature revealed comparatively few data for the bodies of interest in the transonic speed range. Figures 11, 12, and 13 show these data points for cones, ogives and ellipsoids of revolution respectively. No data were found for paraboloids of revolution. Figure 12 includes some data on bodies other than ogives, but sufficiently similar to the ogival shape to be included.

These data have been used to derive curves of the parameter $K_T = (1 - M^2) (L/D)^2$ against $F(C_p)$ for various streamwise locations for ellipsoids and ogives. The similarity rule was not applied to the cone data shown in Figure 11 since these cones are sufficiently blunt to violate the assumptions under which the rule was developed. (It is assumed that the velocity perturbation is much smaller than the free stream velocity.) The same argument applies, of course, to ellipsoids of revolution in the vicinity of the stagnation point where the velocity perturbation is exactly equal to the free stream velocity. Figures 14, 15 and 16 give the parameter $F(C_p)$ at the 25, 50 and 100% stations respectively for ellipsoids of revolution based on the experimental data of Figure 13. The pressure at the nose depends only on the free stream Mach number and is given in Figure 2. Figures 17, 18 and 19 give $F(C_p)$ for ogives at the 10, 50 and 100% stations respectively. The considerable scatter of the data for both bodies is characteristic of wind tunnel measurements in this speed range since it is very difficult to avoid the wall interference effects. There is the further complication that in transonic or subsonic flow the shape of the rear portion of the body affects the flow over the forward part and all of the bodies tested did not have similar shapes aft of the maximum thickness. In spite of the scatter, reasonable curves can be passed through the data points. In view of the fact that for slender bodies an error in $F(C_p)$ gives

a much smaller error in C_p , the faired curves will yield reasonable results. In most cases, there is some degree of symmetry about $K_T = 0$ (i. e., $M_0 = 1$) which would be suspected on physical grounds since for slightly supersonic free stream Mach numbers a nearly normal shock will stand upstream of the body with the result that the Mach number approaching the body is slightly subsonic. The pressure distribution on the body is that corresponding to the subsonic Mach number.

In summary, the method of calculating the pressure distribution on a given body at a particular Mach number is to calculate the parameter $(1 - M_0^2)(L/D)^2$ and read the values of $F(C_p)$ at each station from the appropriate curves. The value of $S^*(x)$ can be calculated from the equations in Table I and hence $F(C_p)$ gives C_p . Since the perturbation velocities are assumed small in the derivation, the above method should not be used for fineness ratios below about 3 or in the region near stagnation points.

Since in the low supersonic range there are few data for ellipsoids of revolution, the theory of Appendix C has been used to derive the curve of $F(C_p)$.

6. CONCLUSIONS

Methods have been given which can be used to calculate the pressure distribution on cones, ogives, ellipsoids and paraboloids at zero angle of attack quickly and with good accuracy. The Mach number range from the transonic to Mach number 7 has been covered. Pressures for conical shapes are available immediately from the cone tables. Pressure on tangent ogives can be calculated from the shock expansion method, the von Karman-Moore theory and the Newtonian theory. Use of the similarity rules can save a good deal of calculation if families of bodies are to be considered. For the ellipsoids and paraboloids, most of the required results can be calculated with the Newtonian and slender body theories. Neither method gives accurate results in the low Mach number and small fineness ratio range.

In the transonic range, the transonic similarity rule can be used to extend available experimental data over most of the required range. The rule cannot be used for low fineness ratios or in the region of stagnation points.

REFERENCES

1. Eggers, A. J., Jr. and Savin, Raymond C. - Approximate Methods for Calculating the Flow about Non-Lifting Bodies of Revolution at High Supersonic Airspeeds - NACA TN 2579, December 1951
2. Zienkiewicz, H. K. - A Method for calculating Pressure Distributions on Circular Arc Ogives at Zero Incidence at Supersonic Speeds Using the Prandtl-Meyer Flow Relations - Great Britain ARC CP 114
3. von Karman, T. and Moore, N. B. - Resistance of Slender Bodies Moving with Supersonic Velocities - ASME Transactions 54 (1932)
4. Ferri, A. - Elements of Aerodynamics of Supersonic Flows - MacMillan 1949
5. Tsien, H. S. - Similarity Laws of Hypersonic Flows - Journal of Mathematics and Physics, 25 (1946)
6. Ehret, D. M., Rossow, V. J. and Stevens, J. I. - An Analysis of the Applicability of the Hypersonic Similarity Law to the Study of Flows about Bodies of Revolution at Zero Angle of Attack - NACA TN 2250, December 1950
7. Lighthill, N. J. - Supersonic Flow Past Bodies of Revolution - RM ARC No. 2003

8. Holder, D. W. and Chinneck, A. - The Flow Past Elliptic-Nosed Cylinders and Bodies of Revolution in Supersonic Airstreams - Aeronautical Quarterly, Vol. IV, February 1954
9. Wright, R. H. and Ward, V. G. - NACA Transonic Wind-Tunnel Test Sections - NACA Report 1231, 1955
10. Moskowitz, B. and Maslen, S. H. - Experimental Pressure Distributions Over Two Wing Body Combinations at Mach Number 1.9 - NACA RM E50J09, February 1951
11. Savin, R. C. - Application of the Generalized Shock-Expansion Method to Inclined Bodies of Revolution Traveling at High Supersonic Airspeeds - NACA TN 3349, April 1955
12. Perkins, E. W. and Kuehn, D. M. - Comparison of Experimental and Theoretical Distributions of Lift on a Slender Inclined Body of Revolution at $M = 2$ - NACA TN 3715, May 1956
13. Perkins, E. W. and Jorgensen, L. H. - Comparison of Experimental and Theoretical Normal Force Distributions (Including Reynolds Number Effects) on an Ogive Cylinder Body at Mach Number 1.98 - NACA TN 3716, May 1956
14. Rossow, V. J. - Applicability of the Hypersonic Similarity Rule to Pressure Distributions which Include the Effects of Rotation for Bodies of Revolution at Zero Angle of Attack - NACA TN 2399

15. Oliver, R. E. - An Experimental Investigation of the Flow Over Simple Blunt Bodies at a Nominal Mach Number of 5.8 - GALCIT Memo No. 26
16. Crawford, D. H. and McCauley, W. D. - Investigation of the Laminar Aerodynamic Heat-Transfer Characteristics of a Hemisphere Cylinder in the Langley 11-Inch Hypersonic Tunnel at a Mach Number of 6.8 - NACA TN 3706, July 1956
17. Bach - Drickverteilungsmessungen on Geschossmodellen. Deutsche Luftfahrtforschung, Untersuchungen und Mitteilungen No. 6057, 1945
18. Stine, H. A. and Wanlass, K. - Theoretical and Experimental Investigation of Aerodynamic Heating and Isothermal Heat Transfer Parameters on a Hemispherical Nose with Laminar Boundary Layer at Supersonic Mach Numbers - NACA TN 3344, December 1954
19. Winkler, E. M. and Danberg, J. E. - Heat Transfer Characteristics of a Hemisphere Cylinder at Hypersonic Mach Numbers - IAS Preprint No. 622, January 1956
20. Ward, G. N. - Linearized Theory of Steady High Speed Flow - Cambridge University Press 1955
21. van Dyke, M. D. - The Combined Supersonic-Hypersonic Similarity Rule - Journal of the Aeronautical Sciences, Vol 18, No. 7, July 1951

22. Ames Research Staff - Equations, Tables and Charts for Compressible Flow - NACA Report 1135, 1953
23. Massachusetts Institute of Technology - Tables of Supersonic Flow Around Cones - Department of Electrical Engineering Technical Report No. 1, Cambridge, Massachusetts, 1947
24. Erdmann - Druckverteilungsmessung am A4V1P im Bereich der Unter und Überschallgeschwindigkeit. Archiv. Nr. 66/100 g.Kdos. Aerodynamisches Institut. Ausfertigung. Peenemunde, den 27, XI, 1942
25. Robinson, H. L. - Pressures and Associated Aerodynamic and Load Characteristics for Two Bodies of Revolution at Transonic Speeds - NACA RM L53L28a, March 1954
26. Danforth, E. C. B. and Johnston, J. F. - Pressure Distribution over a Sharp Nose Body of Revolution at Transonic Speeds by the NACA Wing Flow Method - NACA RM L7K12, March 1948
27. Oswatitsch, K. and Keune, F. - The flow Around Bodies of Revolution at Mach Number 1 - Proc. of the Conference on High Speed Aeronautics, Polytechnic Institute of Brooklyn, January 1955
28. Oswatitsch, K. and Berndt, S. B. - Aerodynamic Similarity at Axisymmetric Transonic Flow Around Slender Bodies - Royal Institute of Technology, Stockholm KTH Aero TN 15, May 1950.

29. Thompson, J. R. - Measurements of the Drag and Pressure Distribution Throughout Transition from Subsonic to Supersonic Speeds - NACA RM L9J27, January 1950
30. Cole, R. I. - Pressure Distributions on Bodies of Revolution at Subsonic and Transonic Speeds - NACA RM L52D30, July 1952
31. Hallissy, J. M., Jr. - Pressure Measurements on a Body of Revolution in the Langley 16-Foot Transonic Tunnel and a Comparison with Free Fall Data - NACA RM L51L07a, March 1952
32. Matthews, C. W. - Pressure Distributions over a Wing-Fuselage Model at Mach Numbers of 0.4 to 0.99 and at 1.2 - NACA L8H06, November 1948
33. Boltz, F. W. and Beam, B. J. - The Effects of Compressibility on the Pressures on a Body of Revolution and on the Aerodynamic Characteristics of a Wing Nacelle Combination Consisting of the Body of Revolution Mounted on a Swept-Back Wing - NACA RM A50E09, July 1950
34. Matthews, C. W. - A Comparison of the Experimental Subsonic Pressure Distributions about Several Bodies of Revolution with Pressure Distributions Computed by Means of the Linearized Theory - NACA Report 1155, 1953
35. Solomon, George E. - Transonic Flow Past Cone Cylinders - NACA Report 1242, 1955.

APPENDIX A

von Karman-Moore Theory

The method replaces a sharp nosed body by a series of frustra of cones and the pressure calculated by a step by step procedure. The pressure on the initial segment can be calculated from the equation

$$C_p = -\frac{2u}{U_0} - \left(\frac{v}{U_0}\right)^2 \quad (1)$$

where u is the streamwise perturbation velocity and for a cone is given by (Reference 4)

$$\frac{u}{U_0} = -\frac{A_1}{U_0} \cosh^{-1} \frac{\cot \Theta_2}{B} \quad (2)$$

and v is the perturbation velocity normal to the free stream and is given by

$$\frac{v}{U_0} = \frac{A_1}{U_0} B \sqrt{\frac{\cot^2 \Theta_2}{B^2} - 1} \quad (3)$$

A_1 is a constant given by

$$\frac{A_1}{U_0} = \frac{\tan \Theta_2}{\sqrt{\cot^2 \Theta_2 - B^2} + \tan \Theta_2 \cosh^{-1} \frac{\cot \Theta_2}{B}} \quad (4)$$

For the subsequent segments, the perturbation velocities are given by

$$\frac{u_n}{U_0} = \sum_{i=1}^n \frac{A_i}{U_0} \left(\cosh^{-1} \frac{X_n - E_i}{B r_n} - \cosh^{-1} \frac{X_n - E_{i-1}}{B r_n} \right) \quad (5)$$

and

$$\frac{v_n}{U_0} = -B \sum_{i=1}^n \frac{A_i}{U_0} \left[\sqrt{\left(\frac{x_n - \xi_i}{Br_n} \right)^2 - 1} - \sqrt{\left(\frac{x_n - \xi_{i-1}}{Br_n} \right)^2 - 1} \right] \quad (6)$$

where x and r are the body coordinates parallel and perpendicular to the free stream and ξ_n is the coordinate of the n^{th} source and is related to x_n by the relation

$$\xi_n = x_n - Br_n \quad (7)$$

With A_1/U_0 known, Equations 5 and 6 will give $\frac{u_2}{U_0}$ and $\frac{v_2}{U_0}$ in terms of the unknown constant A_2/U_0 . Since the flow must be tangent to the

body, we have the condition $\frac{v_2}{U_0 + u_2} = \left(\frac{dr}{dx} \right)_2$

and since the slope is known, Equation 8 can be solved for A_2/U_0 and

hence $\frac{u_2}{U_0}$, $\frac{v_2}{U_0}$ and C_{p2} can be calculated. Proceeding in a similar fashion the value of each $\frac{A_i}{U_0}$ in turn can be determined from the previous $\frac{A_i}{U_0}$'s and the tangency condition. The accuracy of the method depends, of course,

on the number of segments into which the body is split. Appendix B gives

a method whereby for certain bodies, the pressure coefficient can be

given directly and this method should be used when the integrals involved

can be evaluated. This is not the case for tangent ogives. The von Karman-

Moore method is discussed more fully in Reference 4.

APPENDIX B

Calculation of Pressure Distribution on Ellipsoids and Paraboloids of Revolution

We consider the slender body shown in Figure 10 in supersonic flow. The velocity potential for such a body is derived in Ref. 20 and is given by:

$$\varphi = -\frac{U_0}{2\pi} \int_0^{x-\beta r} \frac{S'(\xi) d\xi}{\sqrt{(x-\xi)^2 - \beta^2 r^2}} \quad (1)$$

where x , r and s are defined in the figure.

Equation (1) yields upon differentiation

$$\begin{aligned} \frac{\partial \varphi}{\partial x} &= -\frac{U_0}{2\pi} \left[\frac{S'(0)}{\sqrt{x^2 - \beta^2 r^2}} + \int_0^{x-\beta r} \frac{S''(\xi) d\xi}{\sqrt{(x-\xi)^2 - \beta^2 r^2}} \right] \\ &= -\frac{U_0}{2\pi} \left[\frac{S'(0)}{\sqrt{x^2 - \beta^2 r^2}} + \int_0^{x-\beta r} \frac{[S''(\xi) - S''(x)] d\xi}{\sqrt{(x-\xi)^2 - \beta^2 r^2}} + \int_0^{x-\beta r} \frac{S''(x) d\xi}{\sqrt{(x-\xi)^2 - \beta^2 r^2}} \right] \\ &= -\frac{U_0}{2\pi} \left[\frac{S'(0)}{\sqrt{x^2 - \beta^2 r^2}} + S''(x) \ln \frac{x}{\beta r} (1 + \sqrt{1 - \beta^2 r^2/x^2}) + \int_0^{x-\beta r} \frac{[S''(\xi) - S''(x)] d\xi}{\sqrt{(x-\xi)^2 - \beta^2 r^2}} \right] \quad (2) \end{aligned}$$

A. Paraboloid

For a paraboloid of revolution with the tip at the origin and axis in the direction of positive x , $r^2 = \frac{D^2}{4L} x$, $S'(x) = \frac{D^2}{4L}$ and $S''(x) = 0$

Equation (2) then reduces to

$$\frac{\partial \psi}{\partial x} = -\frac{U_0 D^2}{8L} \frac{1}{\sqrt{x^2 - \beta^2 r^2}} \quad (3)$$

also,

$$\frac{1}{U_0} \frac{\partial \psi}{\partial r} = r' = \frac{D}{4L} \frac{1}{\sqrt{x/L}} \quad (4)$$

The expression for the pressure coefficient is given by

$$C_p = -\frac{2}{U_0} \frac{\partial \psi}{\partial x} - \left[\frac{1}{U_0} \frac{\partial \psi}{\partial r} \right]^2 \quad (5)$$

Substituting (3) and (4) in (5) gives

$$C_p = \frac{D^2}{4L^2} \left[\frac{1}{\sqrt{\left(\frac{x}{L}\right)^2 - \frac{D^2}{4L^2} \frac{x}{L}}} - \frac{1}{4 \frac{x}{L}} \right] \quad (6)$$

For large L/D , Equation (6) gives the surface pressure as

$$C_p = \frac{3}{16} \frac{D^2}{L^2} \frac{1}{x/L} \quad (7)$$

B. Ellipsoids

For an ellipsoid of revolution with the nose at $\frac{x}{L} = 0$

$$\frac{r^2}{L^2} = \frac{D^2}{4L^2} \left[1 - \left(\frac{x}{L} - 1 \right)^2 \right]$$

$$S'(x) = -\frac{\pi D^2}{2L} \left(\frac{x}{L} - 1 \right) \text{ and } S''(x) = -\frac{\pi D^2}{2L^2}$$

Equation (2) reduces to

$$\frac{\partial \phi}{\partial x} = -\frac{U_0}{4} \frac{D^2}{L^2} \left[\frac{1}{\sqrt{\left(\frac{x}{L}\right)^2 - \beta^2 \frac{r^2}{L^2}}} - \ln \frac{x}{\beta r} \left(1 + \sqrt{1 - \beta^2 \frac{r^2}{x^2}} \right) \right] \quad (8)$$

and

$$\frac{1}{U_0} \frac{\partial \phi}{\partial r} = -\frac{D}{2L} \frac{(x/L - 1)}{\sqrt{1 - (x/L - 1)^2}} \quad (9)$$

and hence

$$C_p = \frac{D^2}{2L^2} \left[\frac{1}{\sqrt{\left(\frac{x}{L}\right)^2 - \beta^2 \frac{r^2}{L^2}}} - \ln \frac{x}{\beta r} \left(1 + \sqrt{1 - \beta^2 \frac{r^2}{x^2}} \right) - \frac{1}{2} \frac{(x/L - 1)^2}{1 - (x/L - 1)^2} \right] \quad (10)$$

which becomes, on the body surface for large L/D

$$C_p = \frac{D^2}{2L^2} \left[\frac{1}{x/L} - \frac{1}{2} \frac{(x/L - 1)^2}{1 - (x/L - 1)^2} - \ln \frac{2x}{\beta r} \right] \quad (11)$$

TABLE I

Quantities Needed in Slender Body Theory

<u>Body</u>	<u>Slope</u>	<u>$S''(x)$</u>
Cone	$D/2L$	$\frac{\pi}{2} \frac{D^2}{L^2}$
Tangent Ogive	$-(x/L - 1)$ $\sqrt{\frac{4(L/D)^2 + 1}{4L/D} - (x/L - 1)^2}$	$\frac{2\pi}{R^2 - x^2} \left[x^2 - R^2 + R^2 \left(\frac{R - D/2}{\sqrt{R^2 - x^2}} \right) \right]$
Ellipsoid	$-\frac{D}{2L} \frac{(x/L - 1)}{\sqrt{1 - (x/L - 1)^2}}$	$-\frac{\pi}{2} \frac{D^2}{L^2}$
Paraboloid	$\frac{D}{4L} \sqrt{\frac{L}{x}}$	0

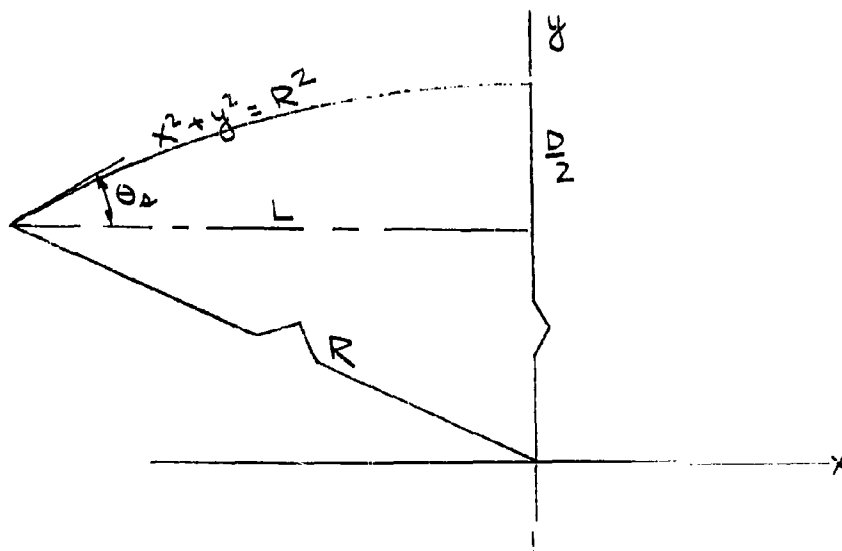
where for tangent ogives, R is the radius of the describing arc and is

given by $R = D \left[\frac{L^2}{D^2} + \frac{1}{4} \right]$

APPENDIX C

a. Shock Expansion Method

As an illustration of this method, the pressure distribution on a tangent ogive of fineness ratio 8 at a Mach number 4 will be calculated. Referring to Figure 3, this combination lies in the region of application of the modified shock expansion method, but outside the range of values of the parameter λ given in Figure 1. The pressure must therefore be calculated on an affine body for which λ is available. Since $K = \frac{M}{L/D} = 0.5$, we arbitrarily choose the related combination $L/D = 6$, $M = 3$ which has the same value of K and for which λ ($\lambda = .81$) is known. The starting point is to determine the pressure at the nose immediately behind the shock. The meridian section of an ogive, being a circular arc, has the equation $x^2 + y^2 = R^2$ in the coordinate system shown and hence $\frac{dy}{dx} = \tan \Theta = -x/y$



$$\text{or } \tan \Theta = \frac{-x}{\sqrt{R^2 - x^2}} = \frac{-x/L}{\sqrt{\frac{R^2}{L^2} - \frac{x^2}{L^2}}}$$

$$\text{where } \frac{R}{L} = \frac{L}{D} + \frac{.25}{L/D}$$

For this case, $L/D = 6$ and hence $\frac{R}{L} = 6.043$

$$\text{and } \tan \Theta = \frac{-x L}{\sqrt{36.52 - (x L)^2}}$$

At the nose, $x = -L$, $\tan \Theta = .1678$ and $\Theta = 9.52^\circ$

The pressure coefficient and Mach number on the surface can now be found from the conical shock tables (Charts 6 and 7 respectively of Reference 22) using the free stream Mach number and the initial inclination.

This yields $C_{p_s} = 0.08$ and $M_s = 2.73$. Since $C_{p_s} = \frac{P_s - P_0}{q_0}$ we have

$$\frac{P_s - P_0}{P_0} = C_{p_s} \left(\frac{q_0}{P_0} \right) = C_{p_s} \frac{\gamma}{2} M_0^2 = 0.504$$

$$\frac{P_s}{P_0} = 1.504$$

In order to calculate the pressure on the rest of the shape, we treat the flow as two-dimensional and hence the flow parameters at any point can be related to those at the nose by means of the difference in inclination of the surface between the two points. The procedure is as follows:

From the tables in Reference 22 take the Prandtl-Meyer angle (ν) and the parameter P/P_T corresponding to the Mach number M_s . At any other position add to the Prandtl-Meyer angle at the nose, the difference in inclination between the tangent to the body at the nose point and the tangent at the point. This gives a new value of the Prandtl-Meyer angle which gives the value of M and P/P_T at the point. The stagnation pressure P_T is constant so the ratio of the two P/P_T 's gives the ratio of the surface pressures. The pressure difference $\frac{P_L - P_s}{P_s}$ may then be formed and the factor λ applied to get the actual pressure difference referred to the nose pressure. The ratio P_s/P_o being known, it is then possible to write the pressure difference as $\frac{P_L - P_o}{P_o}$ or $\frac{P_L - P_o}{q_o}$. These operations are illustrated in Table II.

b. Newtonian Theory

The expression for the pressure coefficient assuming a Newtonian flow is ~~very simple~~ and requires knowledge only of the slope of the body. The pressure distribution on a sphere^{sc} Mach number 7 will be used as an illustration.

For a sphere with center at the origin, the slope is given by

$$\tan \Theta = -x/y$$

where $x^2 + y^2 = R^2$. The Newtonian expression for pressure coefficient is

$$C_p = C_{pmax} \sin^2 \Theta$$

$$\text{Since } \tan \Theta = -\frac{x}{y} = \frac{-x}{\sqrt{12} x^2},$$

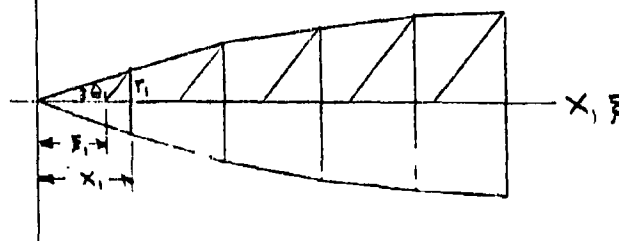
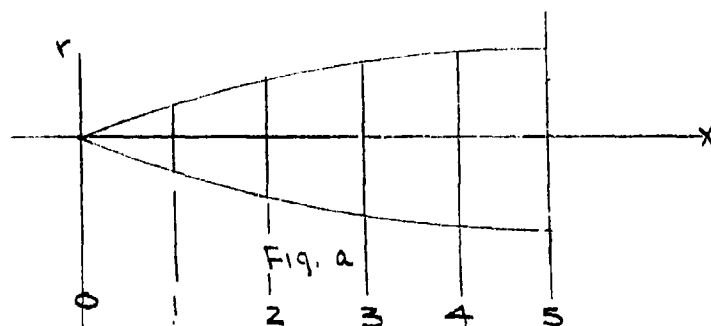
$$\sin^2 \Theta = \frac{x^2}{R^2}$$

$$\text{and } \frac{C_p}{C_{p\max}} = \frac{x^2}{R^2}$$

For $M = 7$, $C_{p\max} = 1.827$ (Figure 2) and $C_p = 1.827 \frac{x^2}{R^2}$

c. von Karman-Moore Theory

As an illustration of this method the pressure distribution on a tangent ogive of fineness ratio 10 at Mach number 2 will be shown.



$$\begin{array}{ll} x_0 = 0 & r_0 = 0 \\ x_1 = .2 & r_1 = .018 \\ x_2 = .4 & r_2 = .032 \end{array}$$

$$\begin{array}{ll} \bar{x}_0 = 0 & \tan \theta_1 = .09 \\ \bar{x}_1 = .169 & \tan \theta_2 = .07 \\ \bar{x}_2 = .345 & \end{array}$$

The body is arbitrarily divided into 5 segments as shown in Figure (a) and the body shape replaced by straight lines joining the end points of each interval. We omit the calculation of the local slopes and show only the modified shape in Figure (b) where the original body is replaced by a series of frusta of cones. The first segment is a 5.16° cone and the pressure is calculated from Equations 1, 2, 3, and 4 of Appendix A.

$$\frac{A_1}{U_0} = \frac{\tan 5.16^\circ}{\sqrt{\cot^2 5.16^\circ - 3} + \tan 5.16^\circ \cosh^{-1} \frac{\cot 5.16^\circ}{\sqrt{3}}} = 0.00843$$

and hence

$$\frac{u_1}{U_0} = -0.00843 \cosh^{-1} \frac{\cot 5.16^\circ}{\sqrt{3}} = -0.0214$$

$$\text{and } \frac{v_1}{U_0} = 0.00843 \sqrt{3} \sqrt{\frac{\cot^2 5.16^\circ}{3} - 1} = 0.0921$$

$$\therefore C_{p1} = 2(0.0214) - (0.0921)^2 = 0.0343$$

We now use Equations 5 and 6 of Appendix A to determine the pressure on the second segment.

$$\frac{u_2}{U_0} = \frac{A_1}{U_0} \left[\cosh^{-1} \frac{x_2 - x_1}{Br_2} - \cosh^{-1} \frac{x_2 - x_0}{Br_2} \right] + \frac{A_2}{U_0} \left[\cosh^{-1} \frac{x_2 - x_2}{Br_2} - \cosh^{-1} \frac{x_2 - x_1}{Br_2} \right]$$

$$\frac{u_2}{U_0} = -R \left\{ \frac{1}{U_0} \left[\sqrt{\left(\frac{x_2 - \bar{x}_1}{Rr_1} \right)^2 - 1} - \sqrt{\left(\frac{x_2 - \bar{x}_2}{Rr_2} \right)^2 - 1} \right] + \frac{A_2}{U_0} \left[\sqrt{\left(\frac{x_2 - \bar{x}_1}{Rr_1} \right)^2 - 1} - \sqrt{\left(\frac{x_2 - \bar{x}_2}{Rr_2} \right)^2 - 1} \right] \right\}$$

$$\frac{x_2 - \bar{x}_1}{Rr_1} = 7.21$$

$$\sqrt{\left(\frac{x_2 - \bar{x}_1}{Rr_1} \right)^2 - 1} = 7.15$$

$$\frac{x_2 - \bar{x}_2}{Rr_2} = 2.76$$

$$\sqrt{\left(\frac{x_2 - \bar{x}_2}{Rr_2} \right)^2 - 1} = 2.57$$

$$\frac{x_2 - \bar{x}_3}{Rr_3} = 1$$

$$\sqrt{\left(\frac{x_2 - \bar{x}_3}{Rr_3} \right)^2 - 1} = 0$$

$$\frac{u_2}{U_0} = -0.0745 \left(\cosh^{-1} 2.76 - \cosh^{-1} 7.21 \right) + \frac{A_2}{U_0} \left(\cosh^{-1} 1 - \cosh^{-1} 2.76 \right)$$

$$= -1.074 A_2/U_0 - 0.0095$$

$$\frac{u_2}{U_0} = -\sqrt{3} \left\{ -0.0745 (2.57 - 7.15) + \frac{A_2}{U_0} (0 - 2.57) \right\}$$

$$= 1.45 A_2/U_0 + 0.007$$

$$\frac{A_2/U_0}{1 + 1.45/U_0} = \frac{1.45 A_2/U_0 + 0.007}{-0.992 - 1.074 A_2/U_0}$$

$$\text{or } A_2/U_0 = 0.0036$$

$$\therefore \frac{u_2}{U_0} = -0.0103, \quad \frac{u_2}{U_0} = -0.0095$$

$$\therefore C_{P2} = 2 \left[(0.0103)^2 - (-0.0095)^2 \right] = 0.0153$$

The same procedure is followed for the 3rd, 4th and 5th segments.

d. Lighthill Slender Body Theory

The expressions for pressure coefficient on paraboloids and ellipsoids of revolution are given by Equations 7 and 11 respectively of Appendix B. Since these expressions involve only the streamwise coordinate, a sample calculation is not deemed necessary.

e. Transonic Method

Figures 18 and 19 give the expression $F(C_p) = C_p \left(\frac{L}{D}\right)^2 - \frac{S''(x)}{\pi} \left(\frac{L}{D}\right)^2 \ln \left(\frac{L}{D}\right)^2$ in terms of $K_T = (1 - M_o^2) (L/D)^2$ for tangent ogives and Figures 14, 15, and 16 are similar curves for ellipsoids of revolution. As an illustration of this method the pressure on each of the shapes will be calculated for fineness ratio 6 and Mach number 0.9.

1. Ogive

In this case, $K_T = (1 - 0.9^2) 6^2 = 6.85$. Corresponding to $K = 6.85$, Figures 17, 18, and 19 give the value of $F(C_p)$ at 10, 50 and 100% of the nose length. Using the equation shown in Table I the values of $S''(x)$ can be calculated. The values of C_p then follow from the values of $F(C_p)$

x/L	$F(C_p)$	$\frac{S''(x)}{\pi}$	C_p
0.1	-1.95	4.0415	0.0945
0.5	-0.17	-.0072	-0.0306
1.0	41.77	-.0275	-0.0495

2. Ellipsoids of Revolution

The above procedure is repeated using Figures 14, 15, and 16 for ellipsoids of revolution. Table 1 gives $S^* = \frac{-\pi D^2}{2 L^2}$ for these shapes.

Therefore, we have

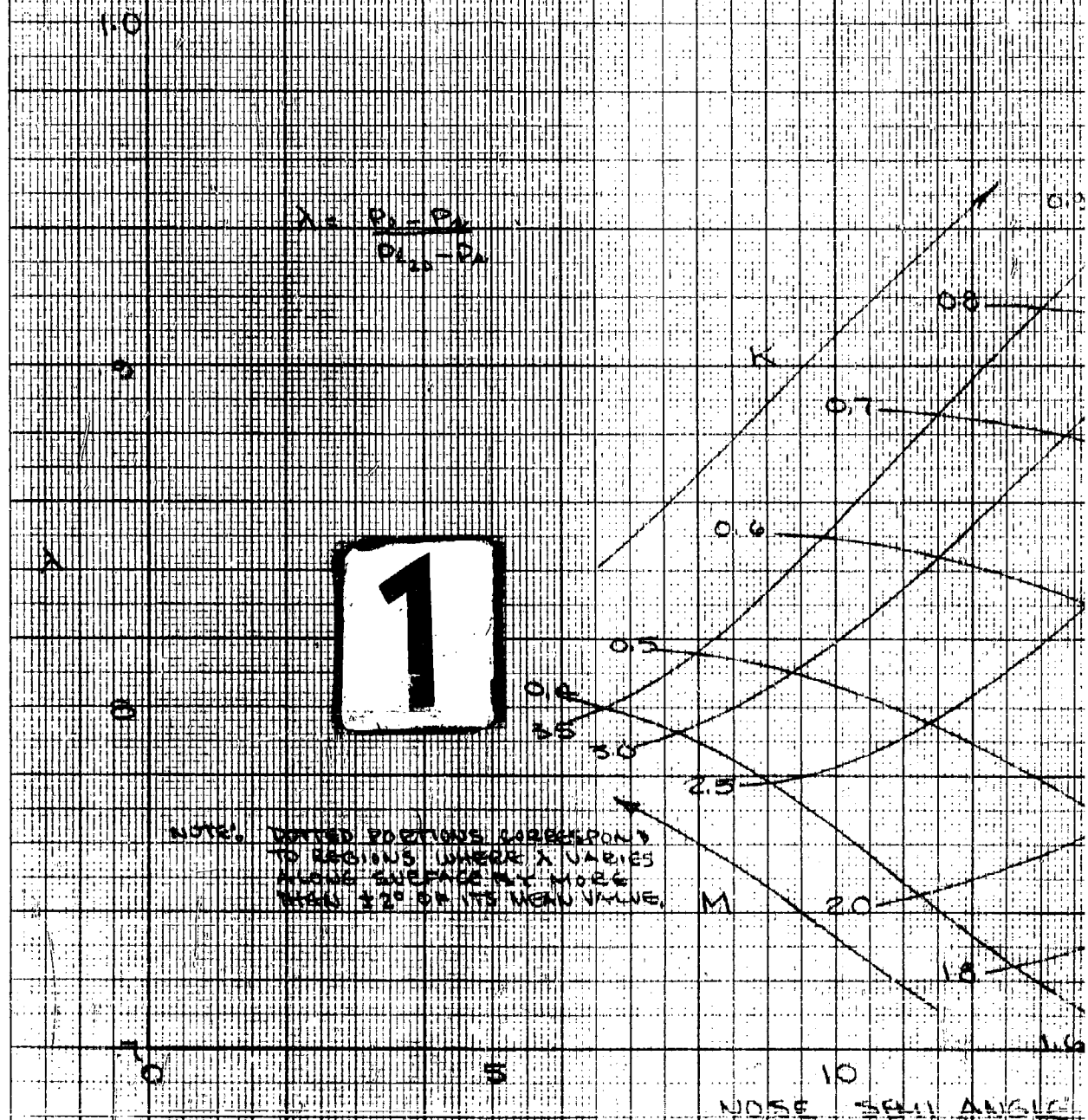
x/L	$F(C_p)$	$\frac{S^*(x)}{\pi}$	C_p
.25	+ .84	- 1/72	- .0205
.50	+ .64	- 1/72	- .032
1.0	+ .33	- 1/72	- .033

The value of the pressure coefficient at the stagnation point ($x/L = 0$) is given in Figure 2.

TABLE II

①	②	③	④	⑤	⑥	⑦	⑧	⑨	⑩	⑪	⑫
x/L	θ	Δy	γ_L	M_L	P/P_L	$\frac{P_{2D}}{P_3}$	$\frac{P_{2D}-P_3}{P_3}$	$\frac{P_L-P_3}{P_3}$	P_L/P_3	P_L/P_0	$\frac{\Delta P}{P_0}$
		9.52-②	44.27+③	REF	22 →	⑥/④①	⑦-1	.81③	1+③	1.504⑩	⑪-1
-1.0	9.52	0	44.27	2.730	0.0410	1.000	0	0	1.000	1.504	.504
-0.8	7.62	1.90	46.17	2.820	0.0357	.871	-.129	-.104	.896	1.347	.347
-0.6	5.70	3.82	48.09	2.915	0.0310	.756	-.244	-.198	.802	1.206	.206
-0.4	3.80	5.72	50.00	3.012	0.0266	.649	-.351	-.284	.716	1.077	.077
-0.2	1.90	7.62	51.89	3.113	0.0230	.561	-.439	-.355	.645	.970	-.030
0	0	9.52	53.79	3.217	0.0197	.481	-.519	-.420	.580	.872	-.128

VARIATION OF λ WITH NOSE θ AND HYPERSONIC SIMILARITY K



WITH NOSE SEMI ANGLE, MACH NUMBER IS
SIMILARITY PARAMETER FOR TRANSLAT GIVES

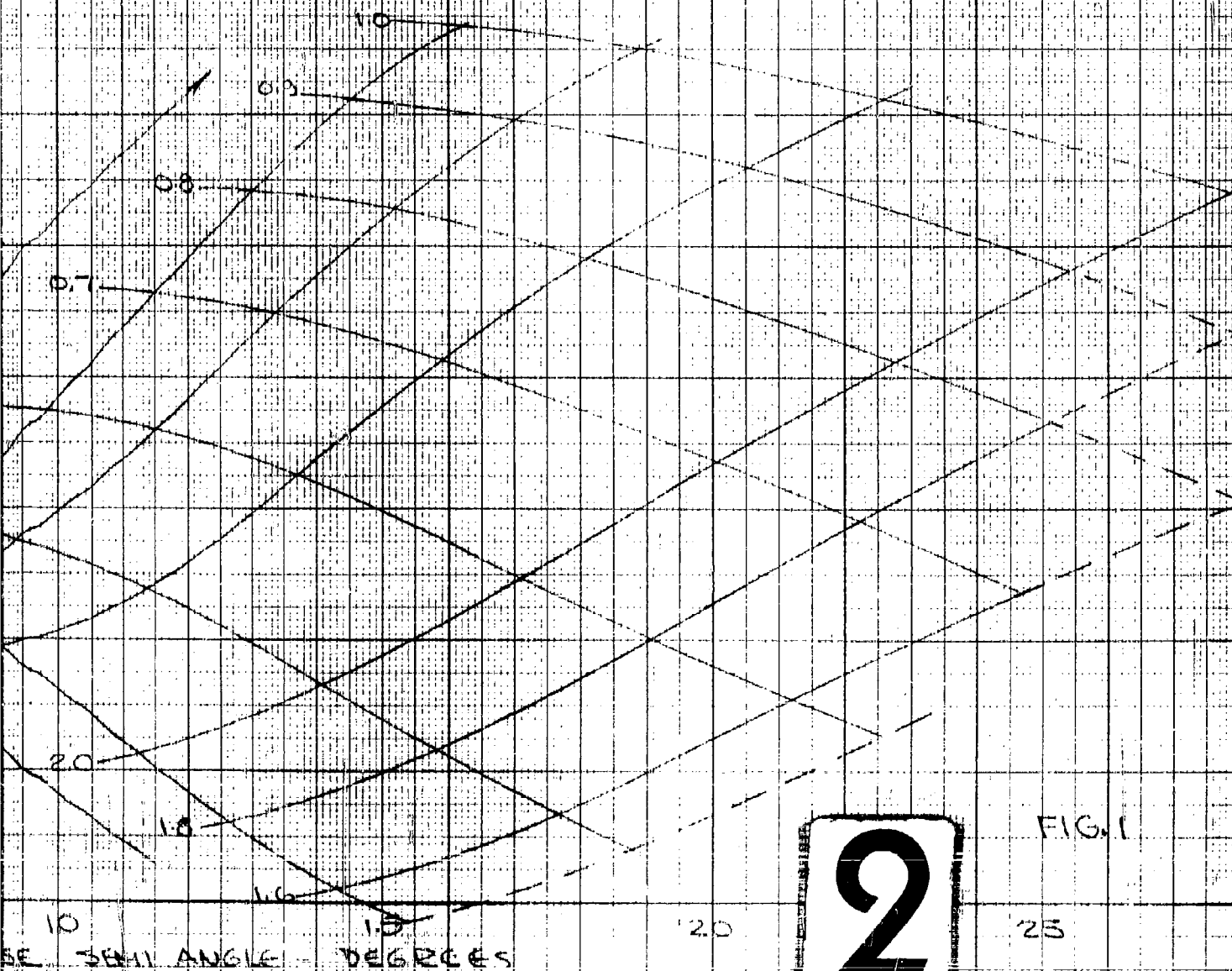
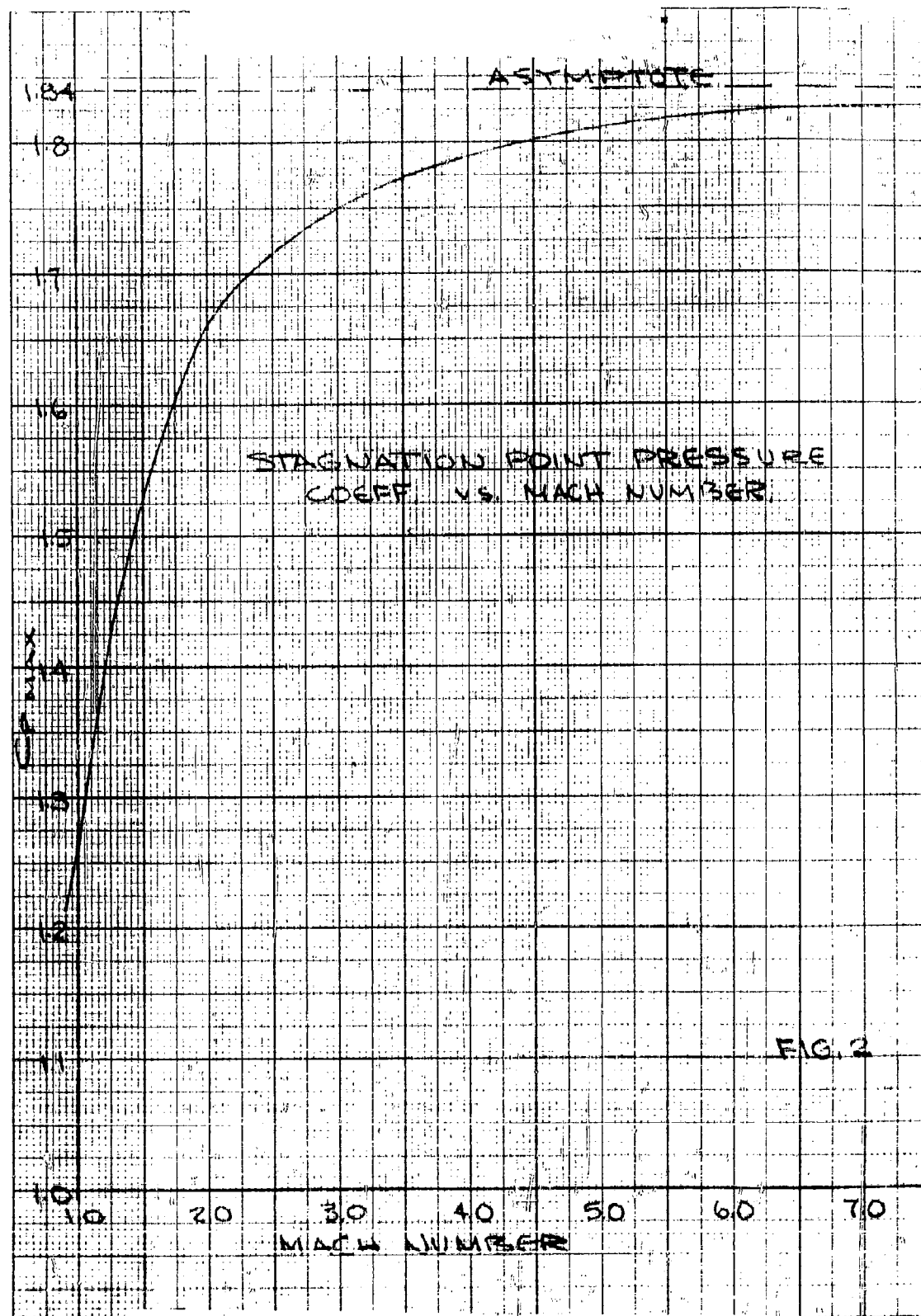
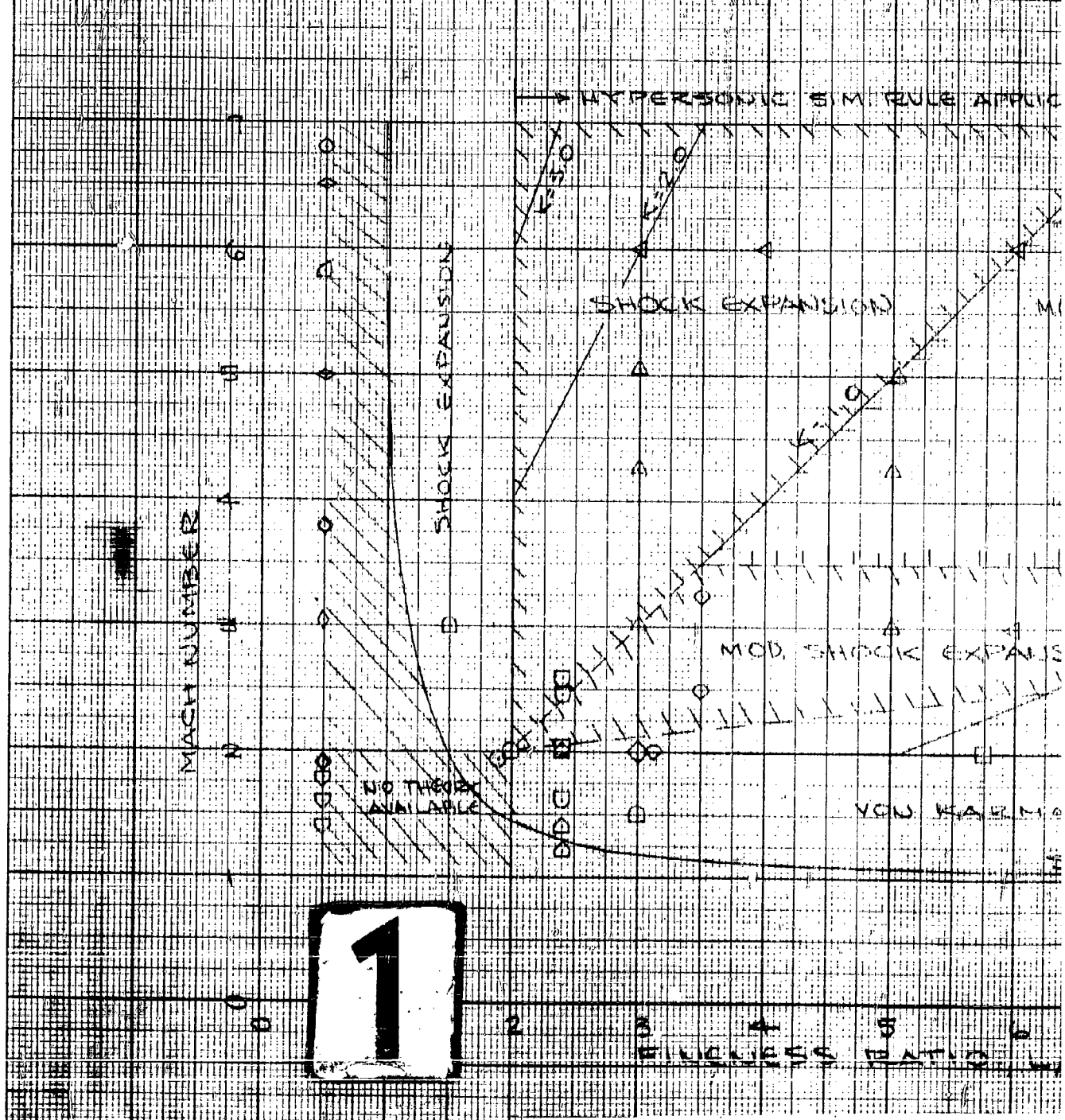


FIG. 1



REGIONS OF APPLICABILITY OF VARIOUS CALCULATING PRESSURES ON TANGENT FLAT PLATE



APPLICABILITY OF VARIOUS METHODS OF PRESSURE ON TANGENT OVES

W/D

ONIC S.M. RULE APPLICABLE

EXPANSION

MOD. SHOCK EXPANSION
+ S.M. RULE

MOD. SHOCK EXPANSION

NON KARNAN - MOORE
THEORY

NON KARNAN - MOORE THEORY

SHOCK DETACHMENT LINE

EXP. DATA OR
CHAR. SOLUTIONS

REF. 10

11

12

13

14

15

16

17

18

19

20

21

22

23

24

25

26

27

28

29

30

31

32

33

34

35

36

37

38

39

40

41

42

43

44

45

46

47

48

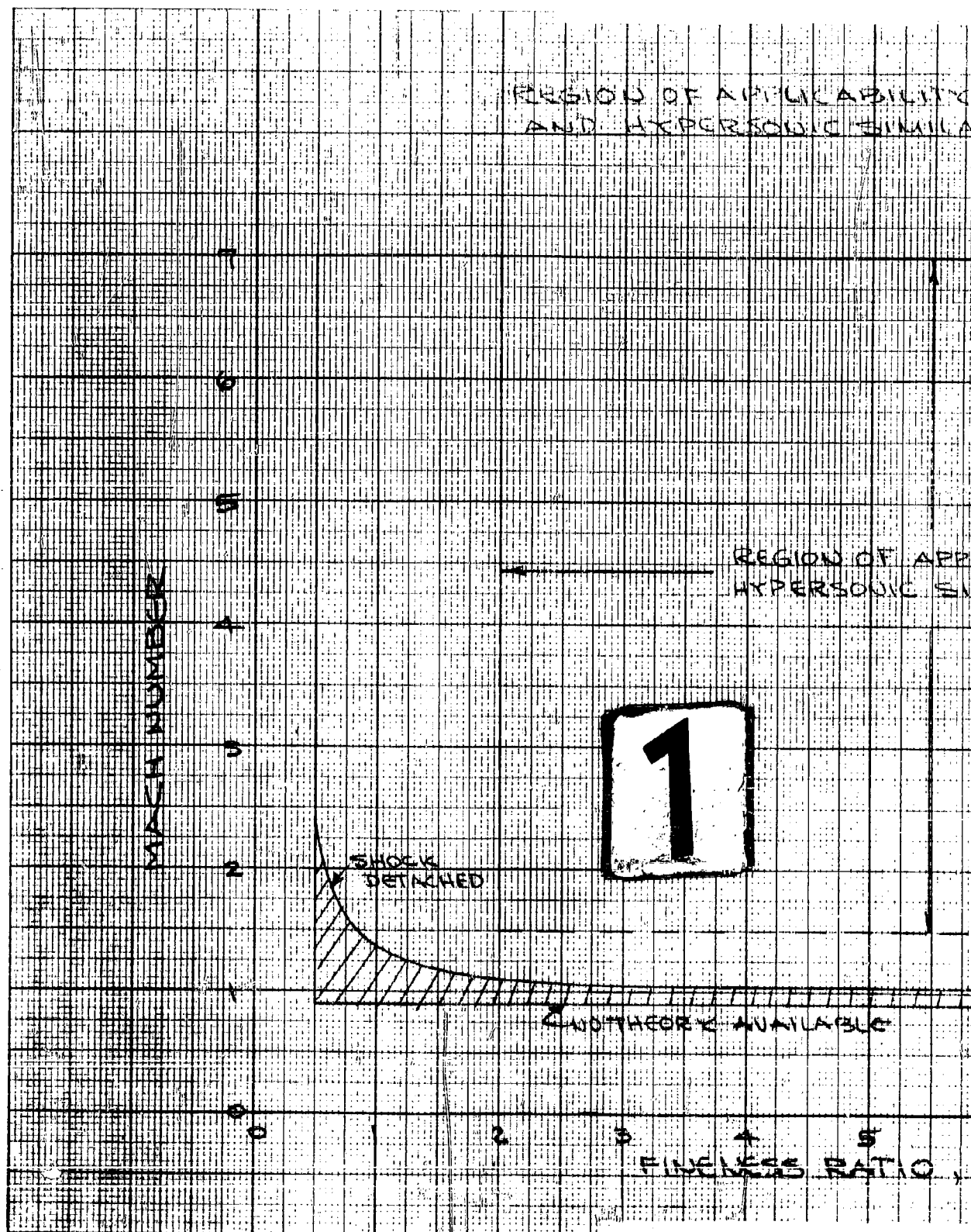
49

50

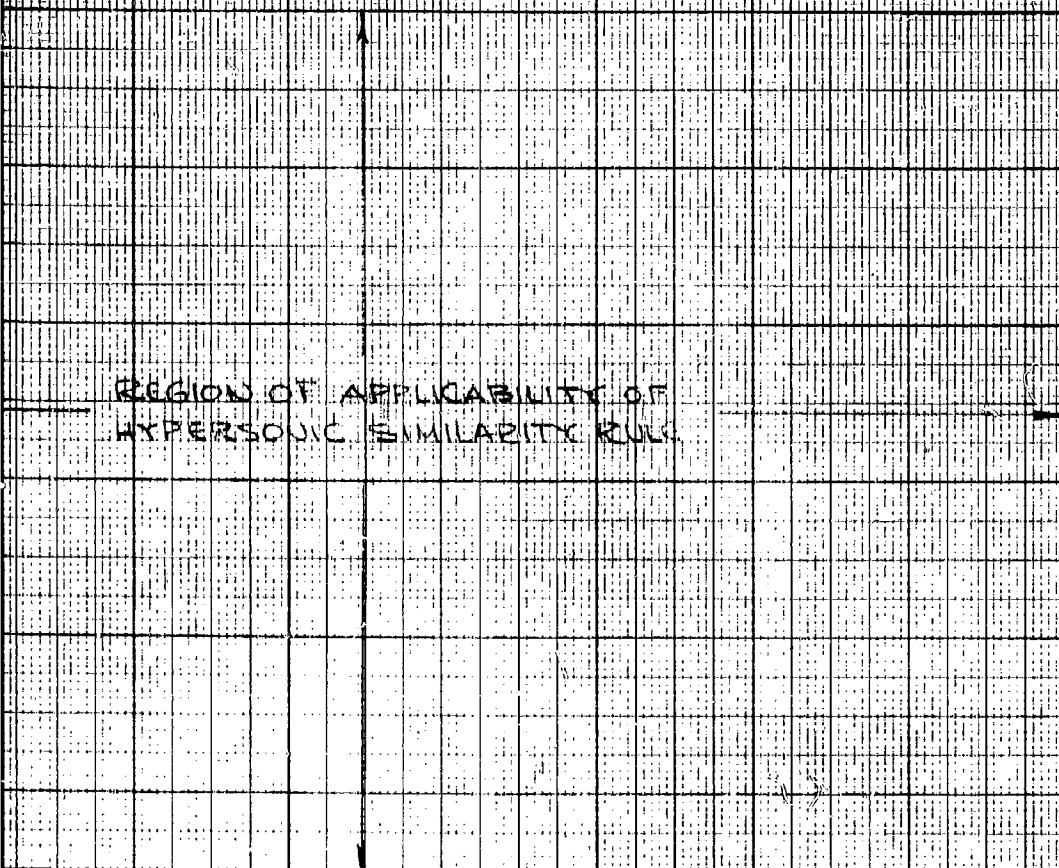
2

FIG. 3

W/D



REGION OF APPLICABILITY OF CONICAL SHOCK THEORY
AND HYPERSONIC SIMILARITY RULE FOR CONES



2

DATA AVAILABLE

FINENESS RATIO, L/D

FIG. 4

REGIONS OF APPLICABILITY CALCULATING PRESSURES

WADD

MODIFIED NEWTONIAN T

1

BLEND

FINENESS RATIO

OF APPLICABILITY OF VARIOUS METHODS OF FINDING PRESSURES ON ELLIPSOIDS OF REVOLUTION

1000

EXP. DATA

O REF. 8

Δ " 8

◇ " 16

◇ " 19

◇ " 15

◇ " 16

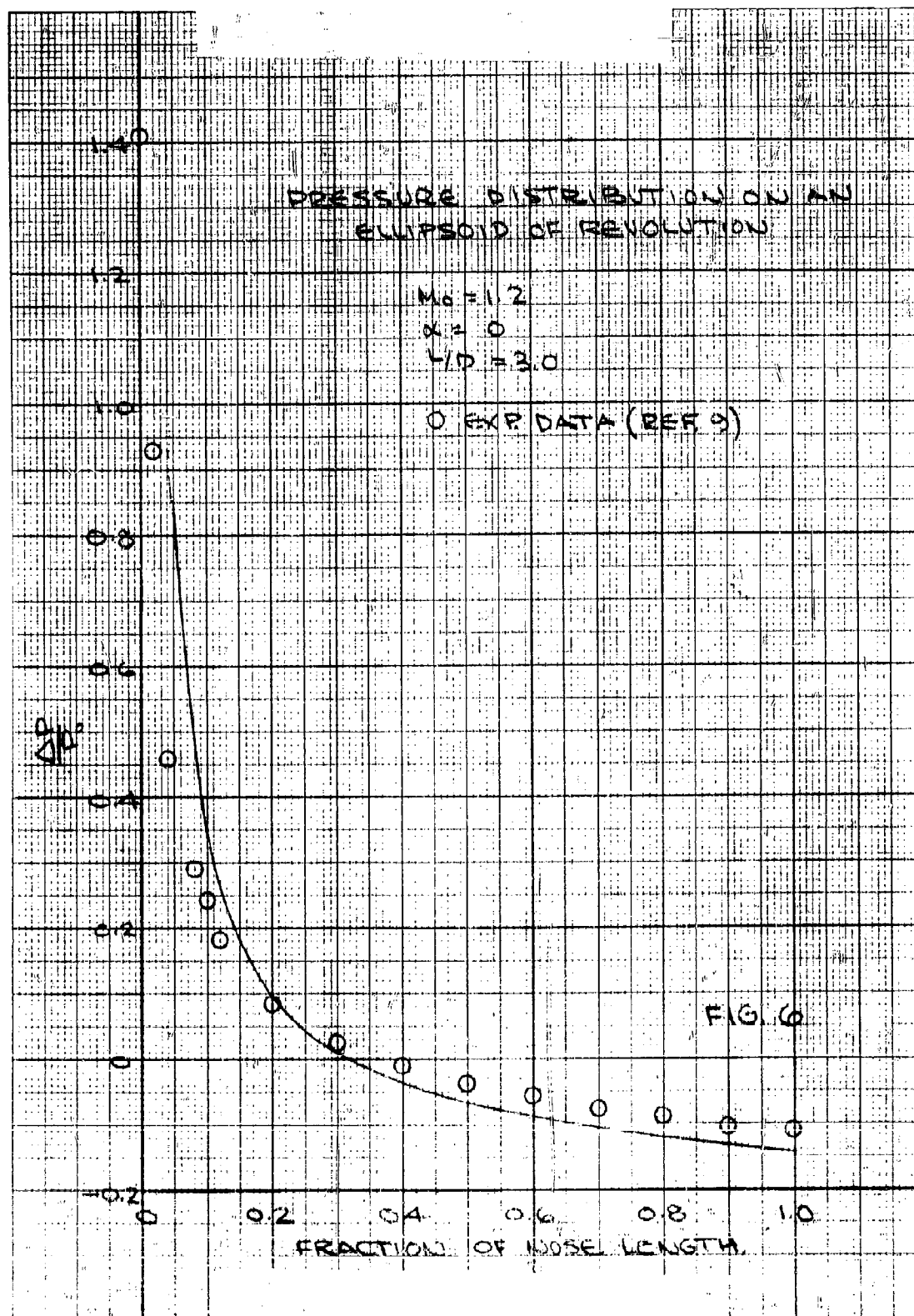
FIELD NEWTONIAN THEORY

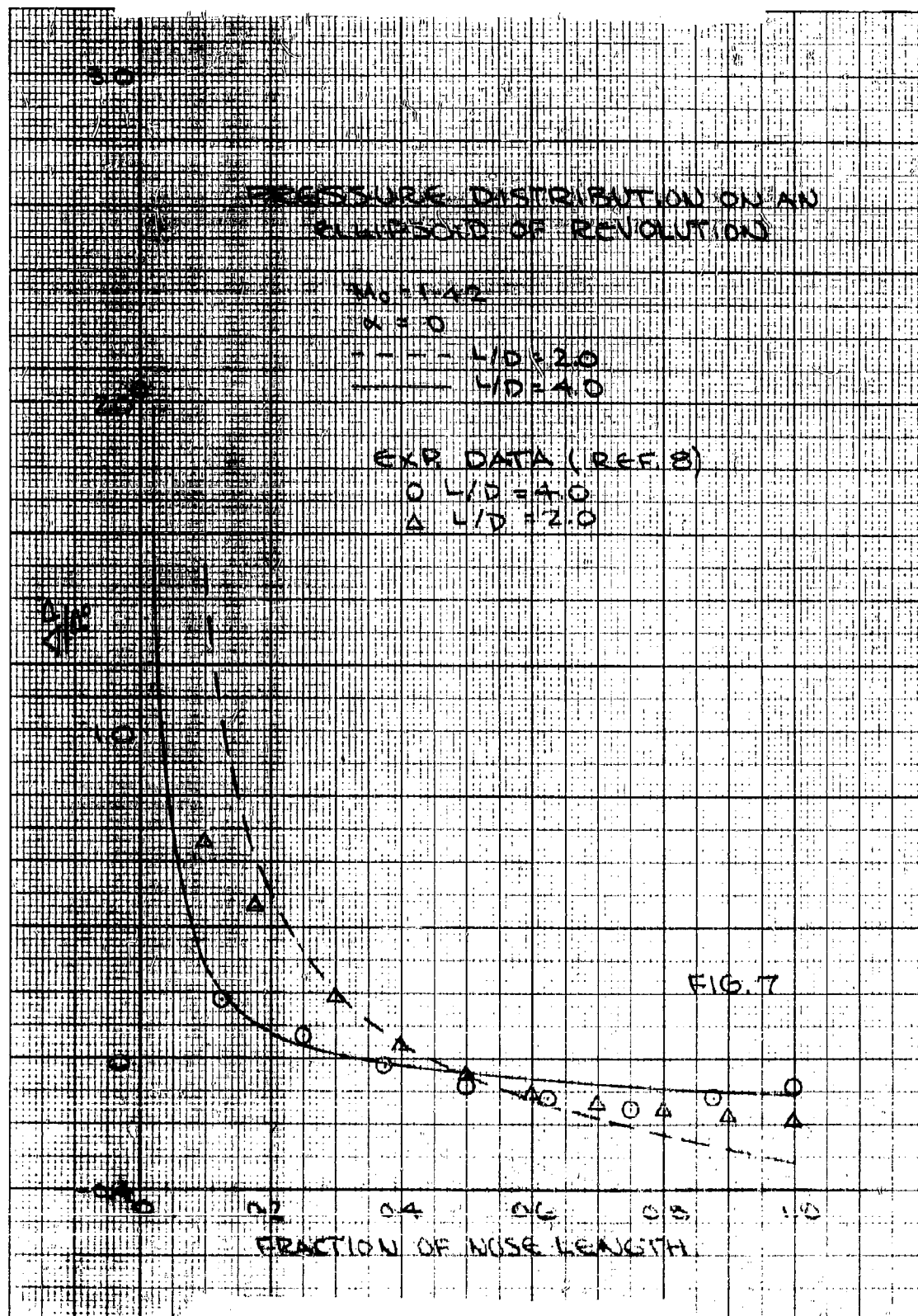
2

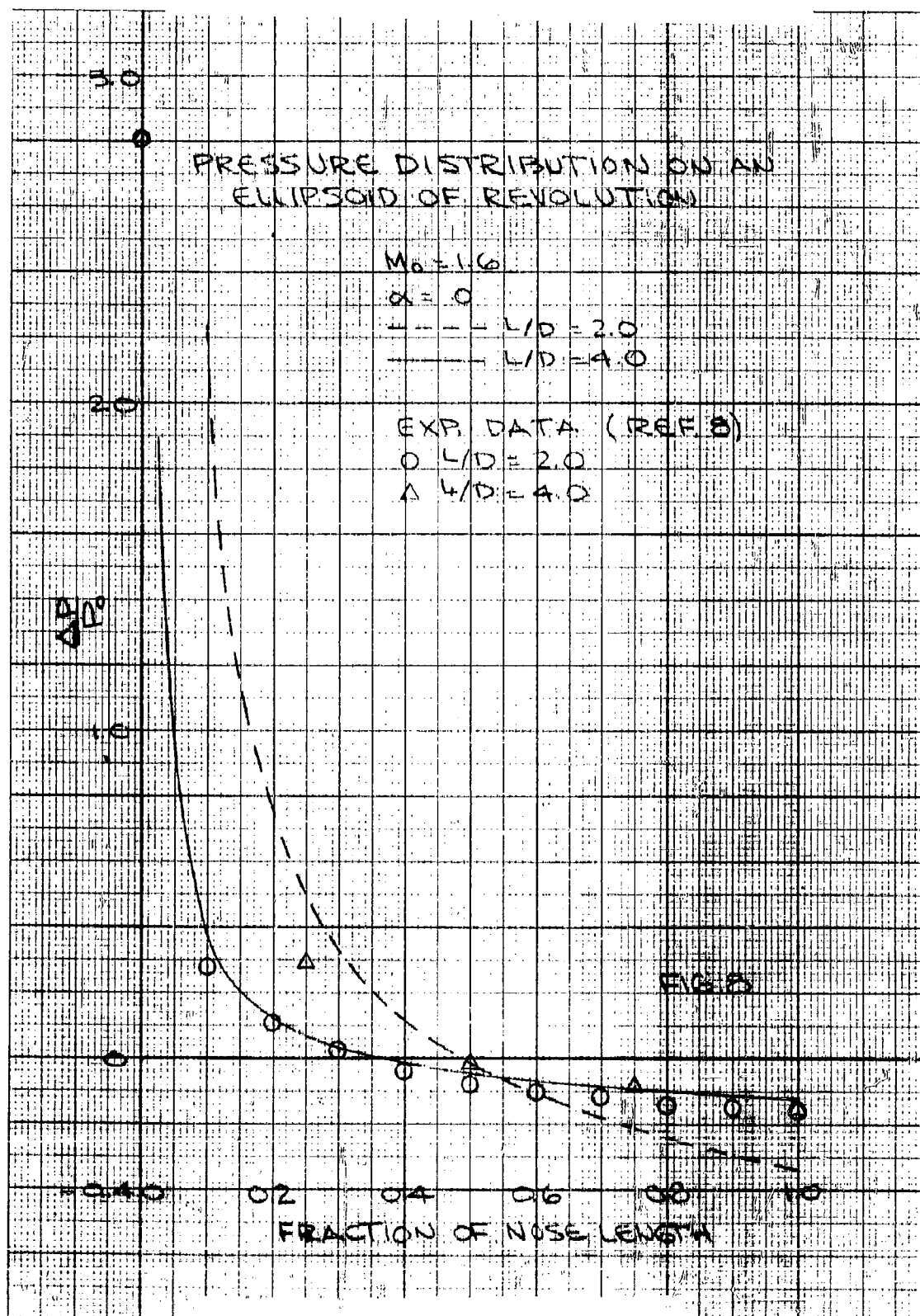
SLENDER BODY THEORY

40 50 60 70 80 90 100
 RADIUS RATIO

FIG. 5







PRESSURE DISTRIBUTION ON AN ELLIPSOID OF REVOLUTION

$M_0 = 11.8$

$\alpha = 0$

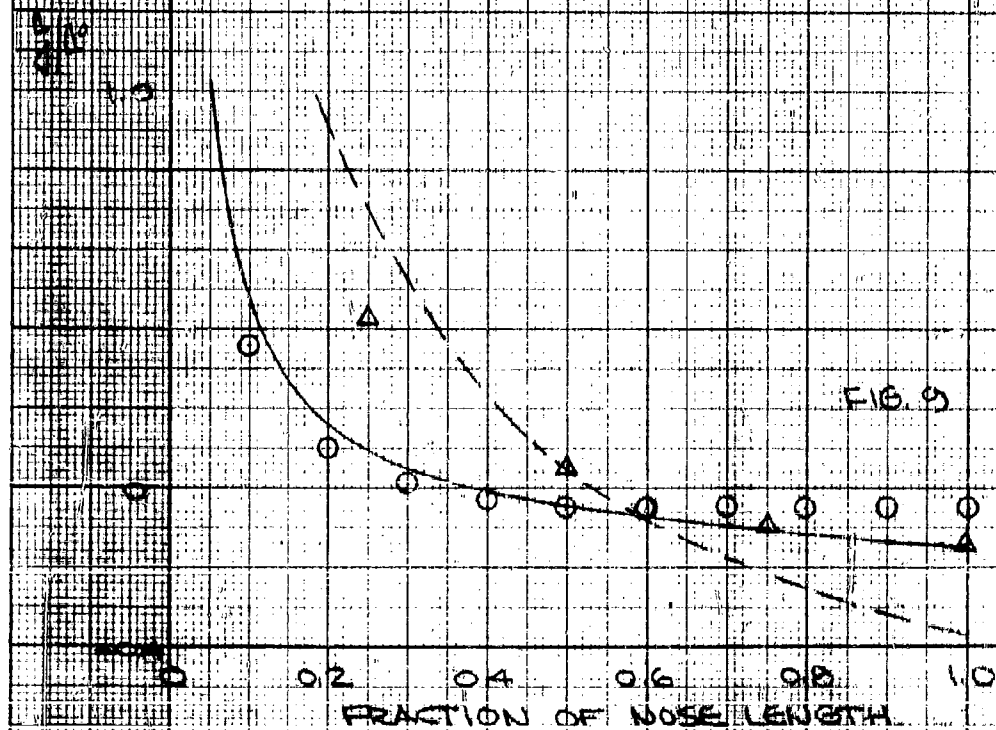
--- $L/D = 2.0$

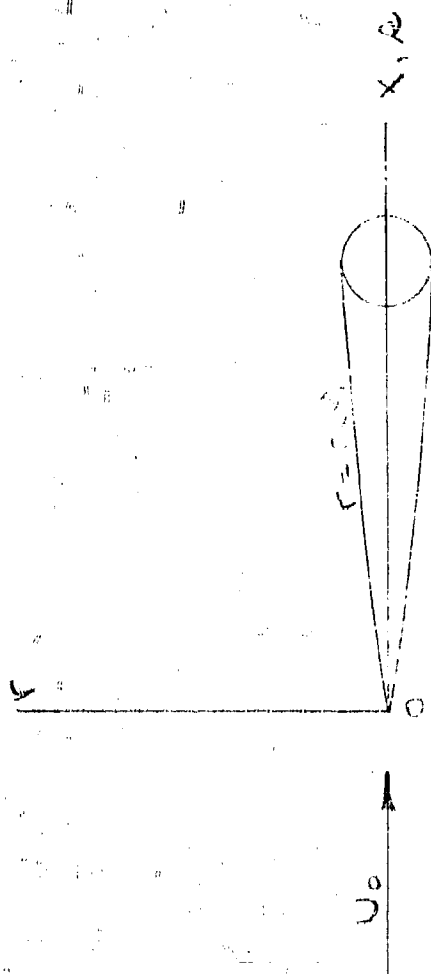
— $L/D = 4.0$

EXP. DATA (REF. 3)

○ $L/D = 4.0$

△ $L/D = 2.0$





x AND y ARE COORDINATES OF POINT ON BODY
 r IS COORDINATE OF POINT

NOMENCLATURE FOR SLENDER BODY THEORY

FIG. 10

RANGE OF EXPERIMENTAL DATA FOR CONICAL NOSE SHAPES

REF. 35

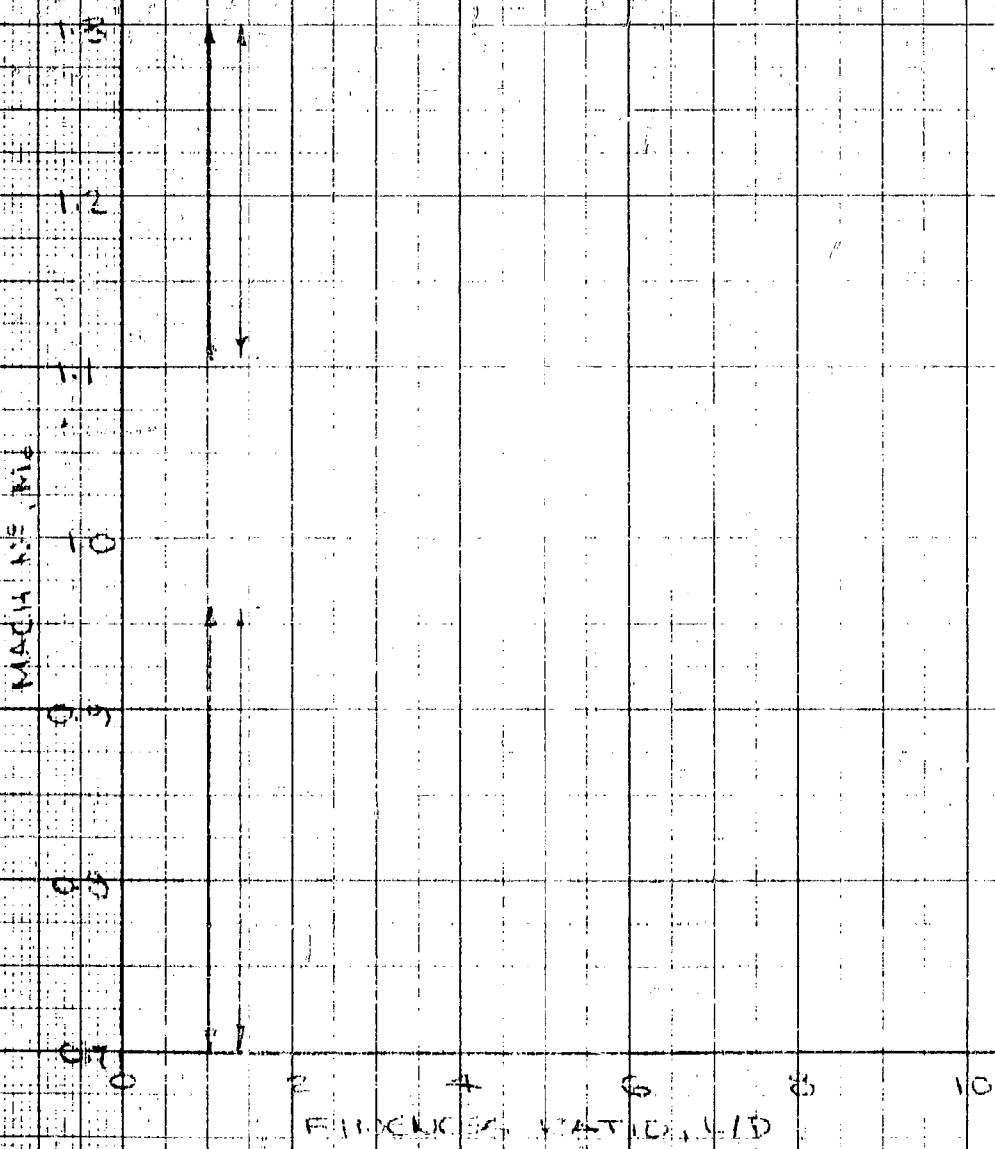


FIG. 11

SUMMARY OF EXPERIMENTAL PRESSURE DISTRIBUTIONS ON TANGENT OGIVES

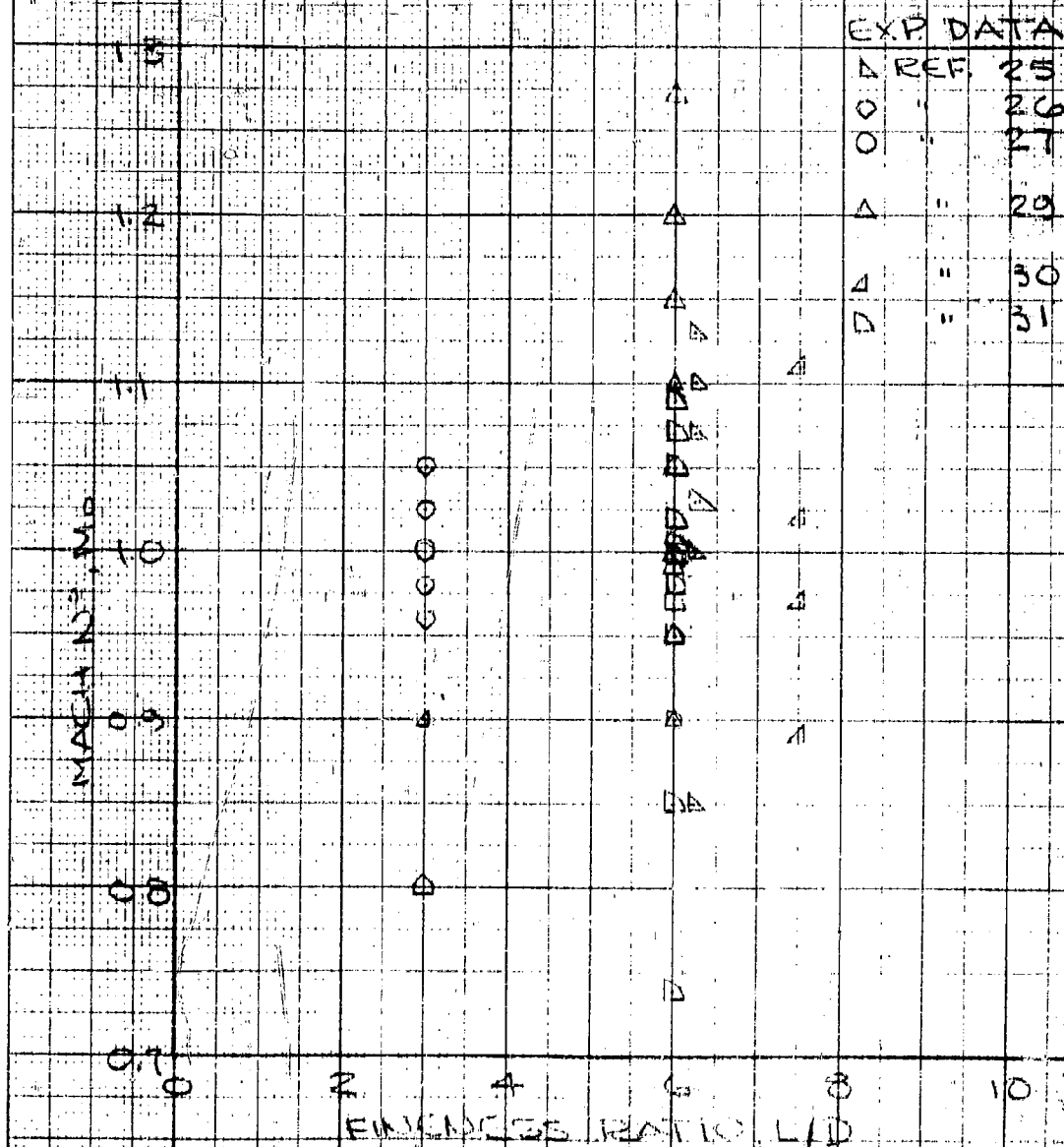


FIG 12

SUMMARY OF EXPERIMENTAL PRESSURE DISTRIBUTIONS ON ELLIPSOIDS OF REVOLUTION

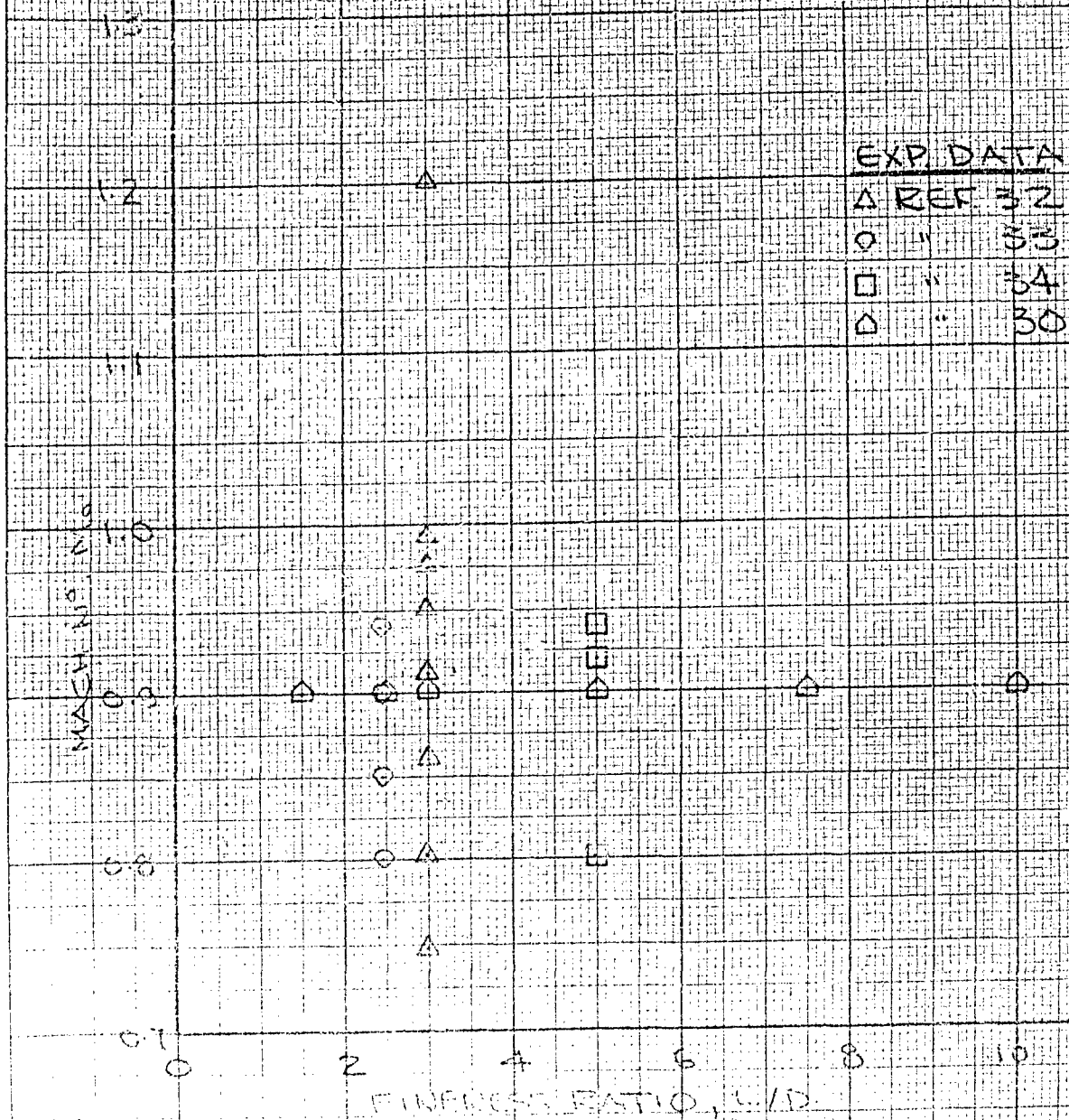


FIG 13

SUMMARY OF EXPERIMENTAL PRESSURE DISTRIBUTIONS ON ELLIPSOIDS OF REVOLUTION

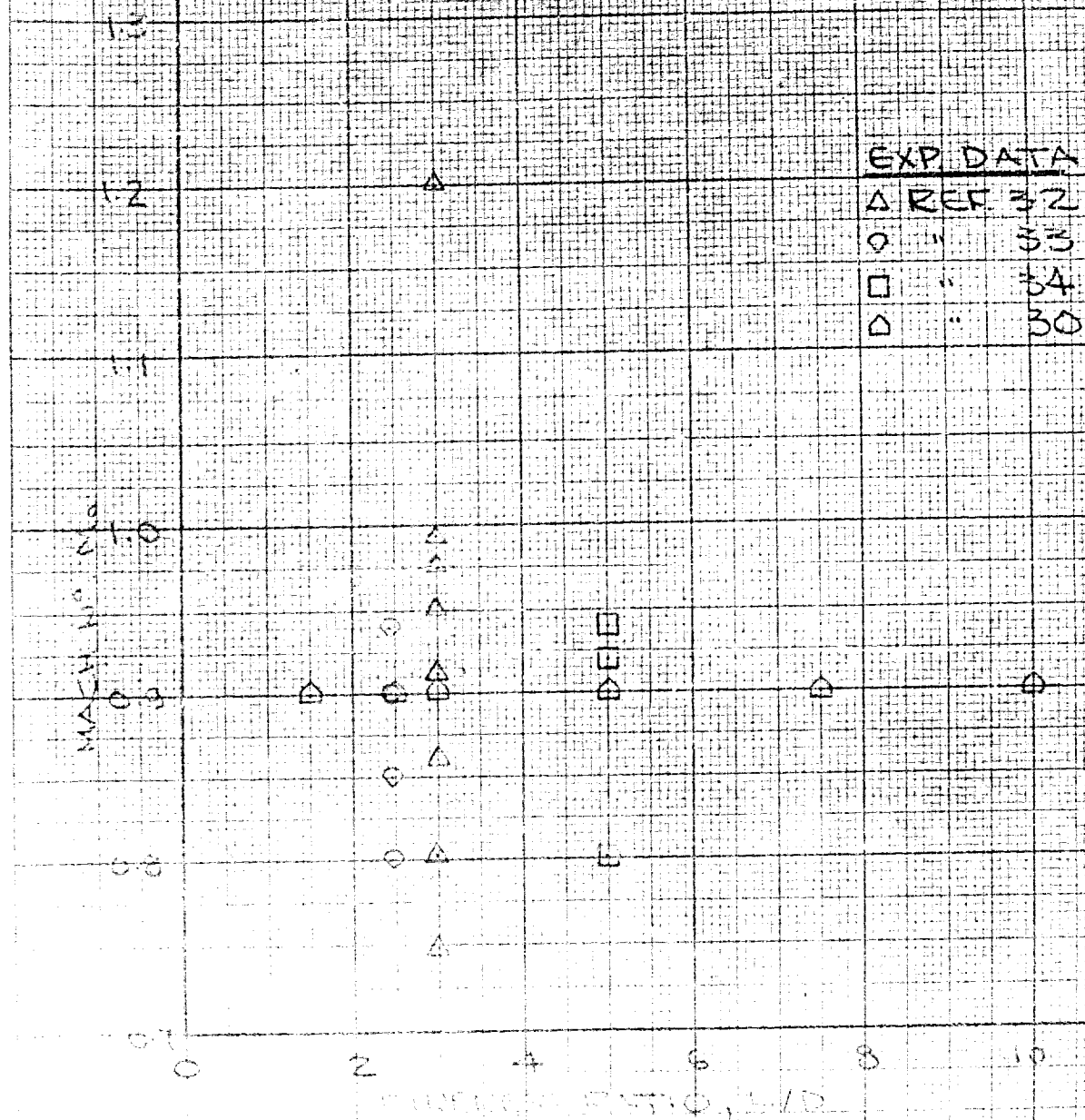


FIG 13

TRANSONIC SIMILARITY PARAMETER FOR ANALYSIS OF REVOLUTION

$K/M = 0.25$

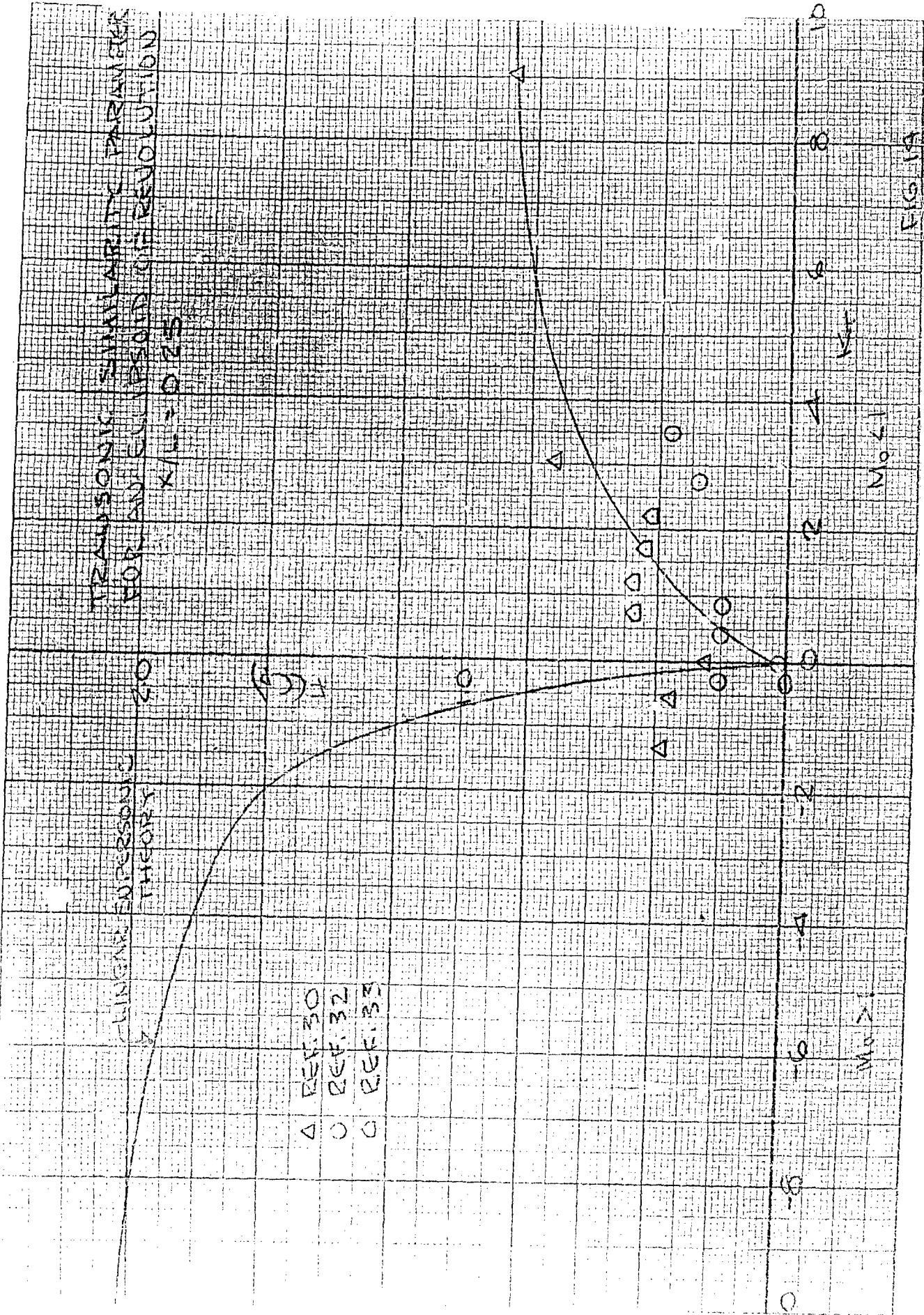
CLINICAL SUPERSONIC
THEORY

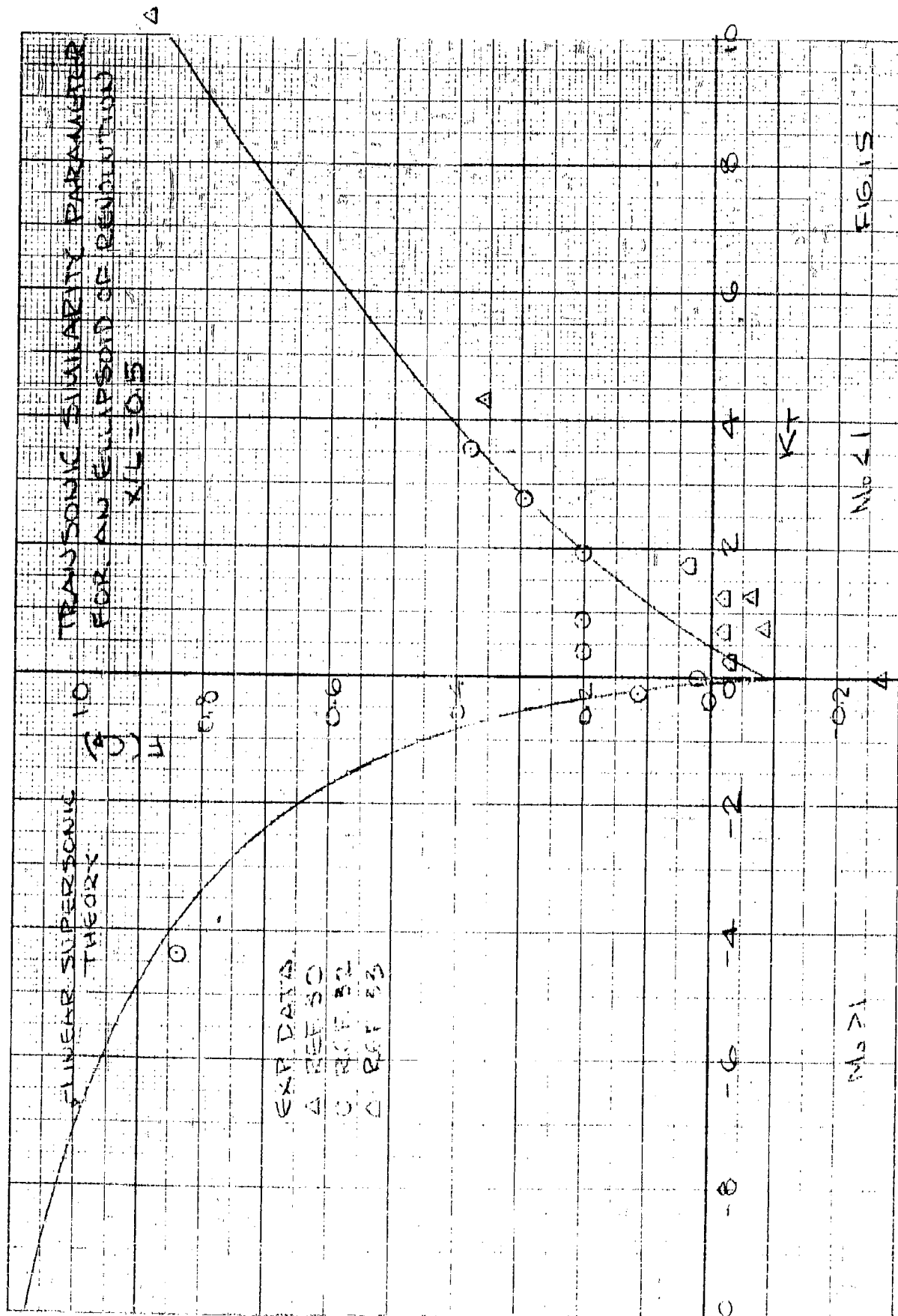
- △ REF. 30
- REF. 32
- REF. 33

(A)

$M_0 < 1$

FIG. 14





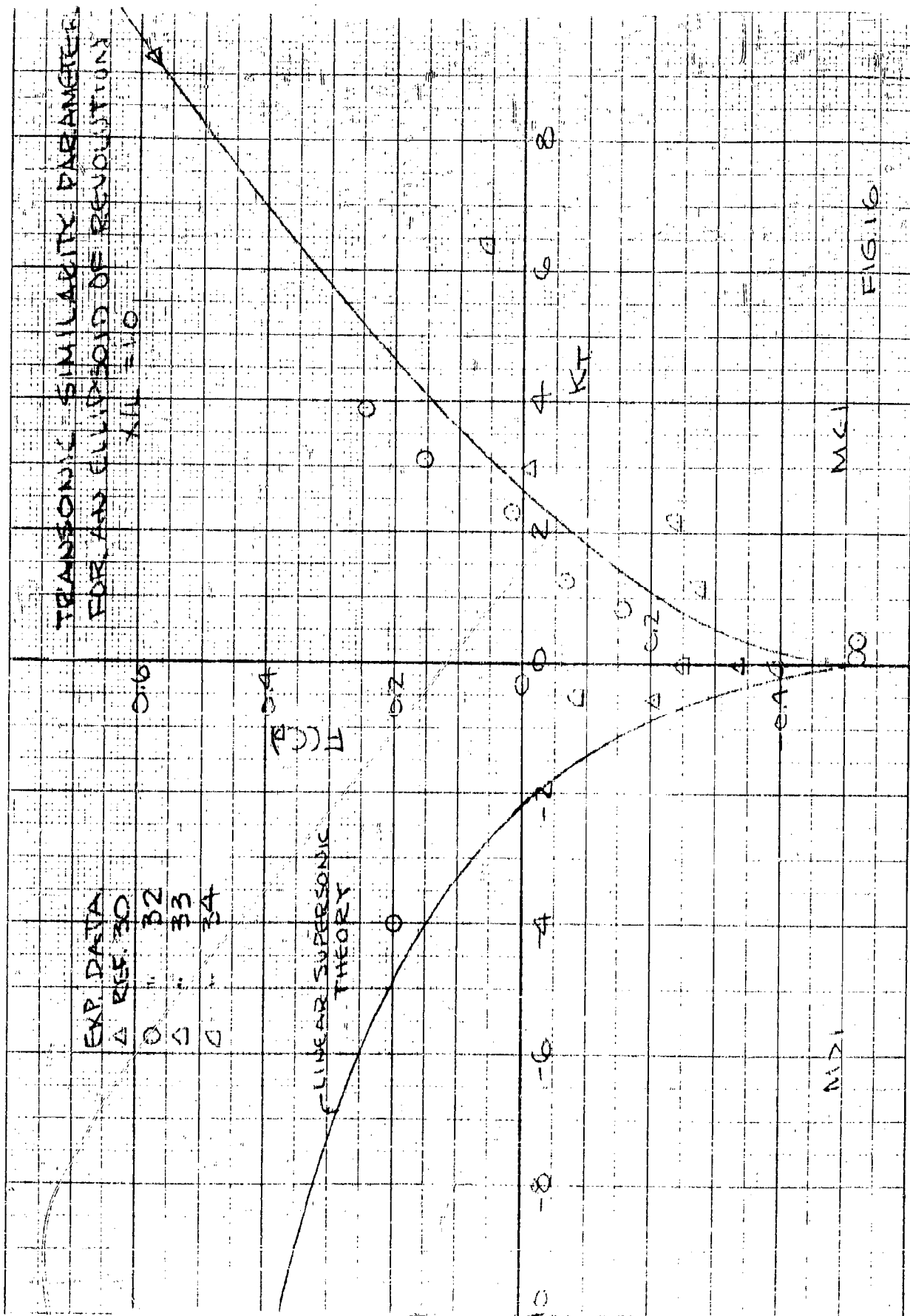
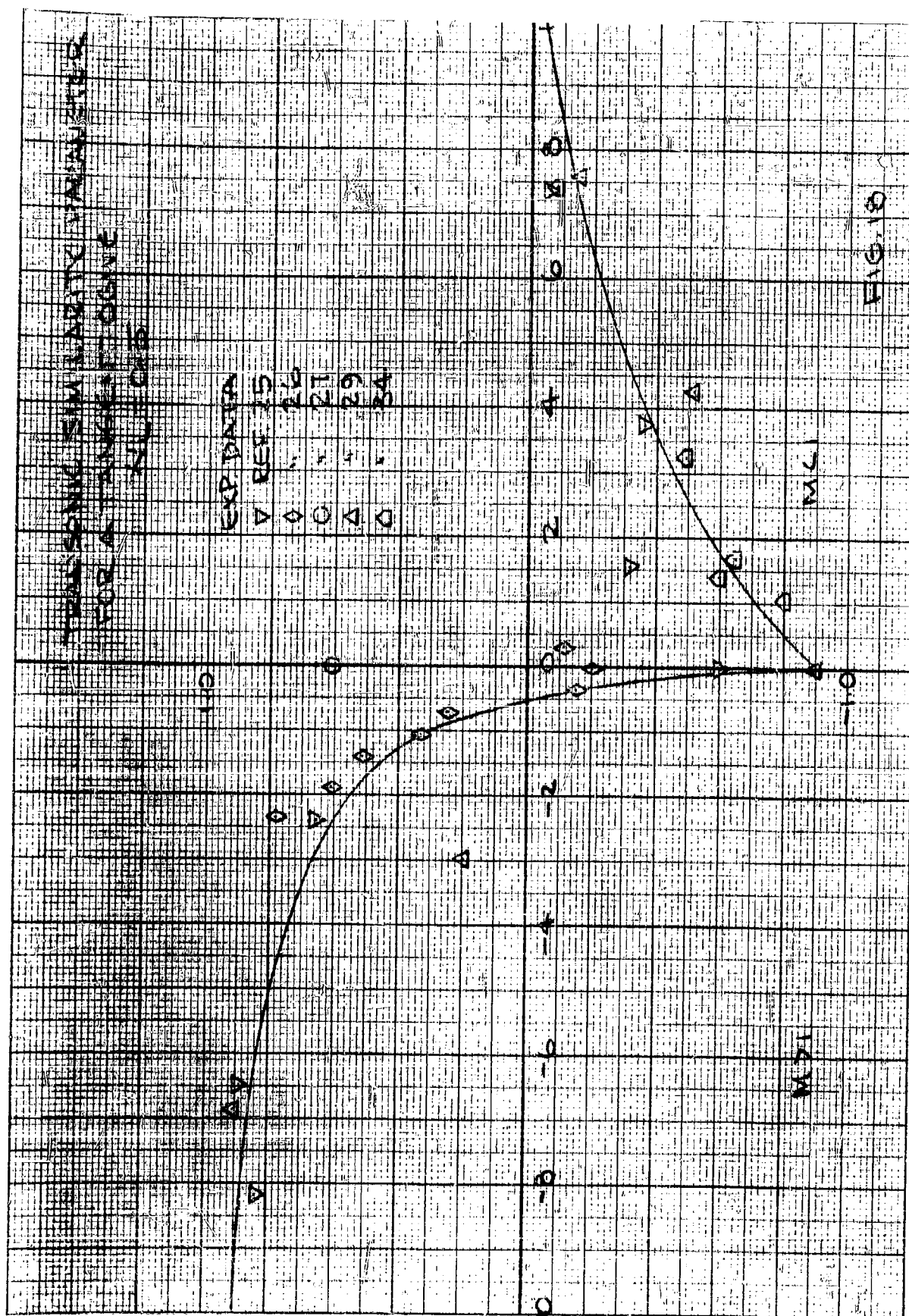
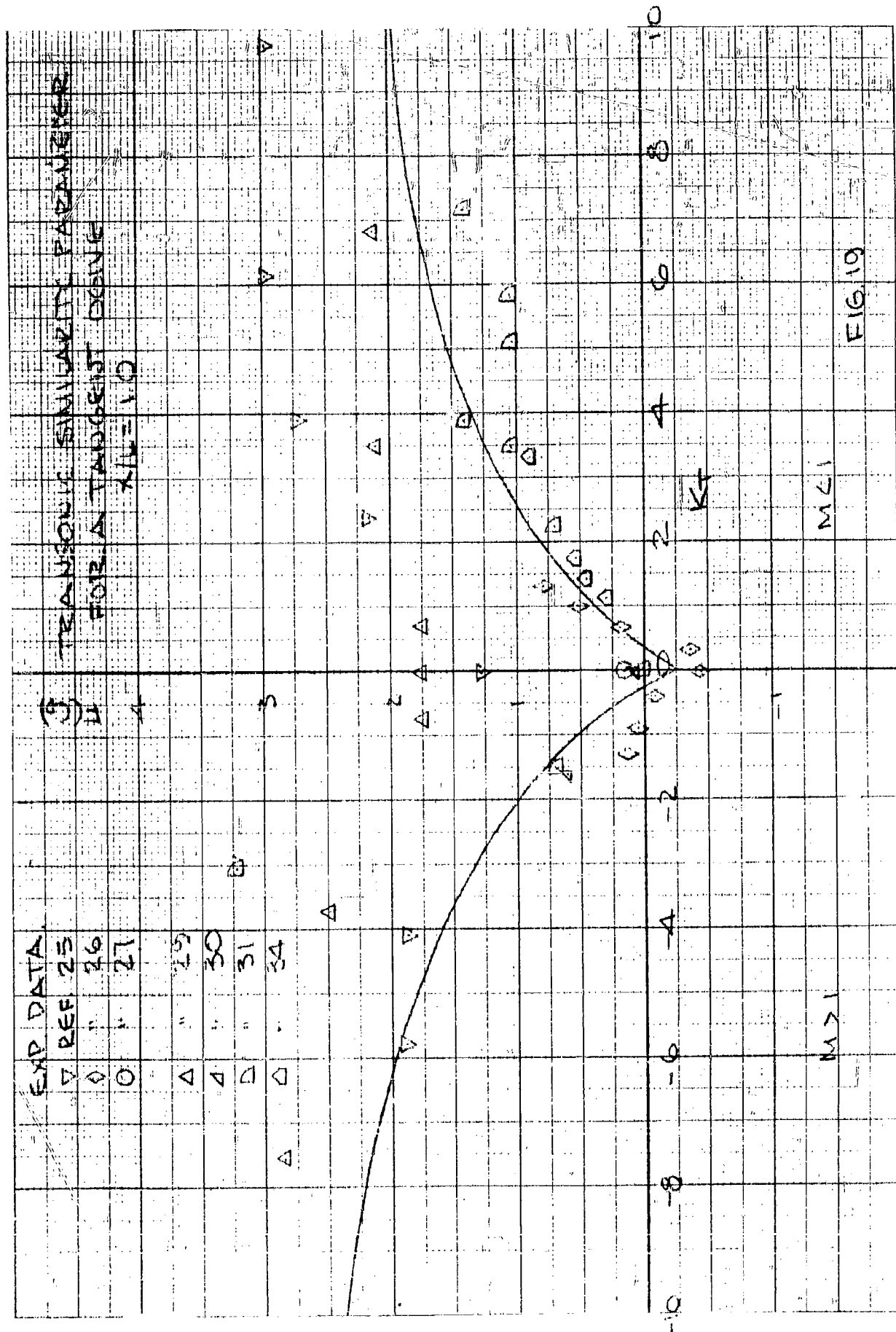


FIG. 16





CHAPTER I - PART C

METHODS OF CALCULATING THE PRESSURE DISTRIBUTION ON
VARIOUS NOSE SHAPES AT SMALL ANGLE OF ATTACK IN THE
RANGE OF MACH NUMBERS FROM 0.9 to 7.0

by Ernest D. Kennedy

TABLE OF CONTENTS

	<u>Title</u>	<u>Page</u>
	Summary	77
	Symbols	78
1.	Introduction	79
2.	Shock Expansion Method	80
3.	Newtonian Flow Theory	81
4.	Linear Theory	82
5.	Similarity Rules	82
6.	MIT Cone Tables	83
7.	Application of the Above Methods to the Calculation of Pressure Distribution on:	84
	a. Tangent Ogives	84
	b. Cones	84
	c. Ellipsoids and Paraboloids of Revolution	85
8.	Transonic Range	86
9.	Conclusions	87
	References	88
	Appendix A	91
	Figures	95

C. METHODS OF CALCULATING THE PRESSURE DISTRIBUTION ON
VARIOUS NOSE SHAPES AT SMALL ANGLE OF ATTACK IN THE
RANGE OF MACH NUMBER FROM 0.9 TO 7.0

SUMMARY

A survey has been made of the methods of calculating pressure distributions on bodies of revolution at small angles of attack in the range of Mach number from 0.9 to 7.0.

For sharp-nosed bodies in the Mach number range above transonic, the linear theory and the shock expansion method will yield results in good agreement with experiment except on the leeward side where separation occurs.

For blunt-nosed bodies, the Newtonian flow theory is used in the high Mach number range (greater than 2) and the linear theory at lower Mach numbers. The linear theory is applicable only for portions of the body far from the nose.

In the transonic range, there is no theory available for any of the shapes and any information must come from experimental data.

SYMBOLS

$K = \frac{M_0}{L/D}$, the hypersonic similarity parameter

α angle of attack (measured in radians)

δ slope of meridian section of a body of revolution referred to the body axis

P static pressure

C_p pressure coefficient = $\frac{\Delta P}{q}$

ϕ angular coordinate measured counterclockwise from extreme windward meridian.

M Mach number

L/D fineness ratio (the ratio of the nose length of a body to its base diameter)

γ ratio of specific heats

ψ angle between normal to surface and free stream direction

$K_\alpha = M\alpha$, the similarity parameter for angle of attack

Subscripts

S, N conditions on the surface of the body immediately behind the shock wave

o free stream conditions

max. maximum

1. INTRODUCTION

This study is an extension to small angle of attack of the work presented in Part B. As before, the modified Newtonian theory, the generalized shock expansion method and the linearized theory cover most of the range. The hypersonic and supersonic similarity rules apply as before except that in addition to thickness, the angle of attack must also be transformed to maintain similarity.

In the transonic range there are no theories and the similarity rule has not yet been applied to bodies of revolution at angle of attack. Any information must therefore come from experimental data, which are not plentiful.

2. SHOCK EXPANSION METHOD

This method is based on the observation that for certain combinations of Mach number, fineness ratio and angle of attack, the surface streamlines over a slender sharp-nosed body of revolution are approximated very closely by the meridians and the flow downstream of the nose is very nearly two-dimensional. The development of the method is given in Reference 1 where it is shown by comparison with experimental data on cones and ogives that reasonable results are obtained for $K \geq 0.6$ and $\alpha/\delta_N \leq 1$. (K is the so-called hypersonic similarity parameter $M/\sqrt{L/D}$ introduced by Tsien Reference 23.) In general, the prediction is better on the windward side than on the leeward side. The poorer agreement is, of course, the result of boundary layer separation and, as expected, is most severe at locations far from the nose and for the higher angles of attack.

The expression for pressure coefficient is

$$C_p = \frac{2}{\gamma M_0^2} \left[\frac{P_s}{P_0} \right]_{\phi=0} \left\{ \frac{M_s}{M_0} \left(\frac{P_s}{P_0} \right)_{\phi=0} - \frac{\gamma-1}{2} \left(\frac{M_s}{M_0} \right)_{\phi=0}^2 \left(1 - \frac{\delta}{\delta_0} \right)^2 \right\} - 1$$

where δ is the slope of the body referred to its axis and ϕ is the angular coordinate as shown in Figure 8. The required parameters are given in Table I (reproduced from Reference 1) in terms of the angular coordinate ϕ .

3. NEWTONIAN FLOW THEORY

In order to apply the Newtonian concept it is necessary to know only the angle between the normal to the surface and the free stream velocity, since the pressure coefficient is given simply by $C_p = C_{p \max} \cos^2 \psi$ (for the case when $\alpha = 0$, $\psi = \pi/2 - \delta$). It follows from geometry that the expression for ψ is (Reference 2), $\cos \psi = \cos \alpha \sin \delta + \sin \alpha \cos \delta \cos \phi$ with δ and ϕ defined as before. For a body of revolution, δ is independent of ϕ and is constant at any axial location. (In the usual case, δ is positive forward of the maximum diameter and negative aft of this location.) For an ellipsoid, $\delta = -\frac{D}{2L} \frac{X/L - 1}{\sqrt{1 - (X/L - 1)^2}}$ and for a paraboloid, $\delta = \frac{D}{4L} \sqrt{\frac{L}{X}}$ where L/D is the fineness ratio and X/L is the distance from the nose as a fraction of the nose length. The condition $C_p = 0$ defines a curve on the surface of the body given by $\cos \phi = -\tan \delta / \tan \alpha$, downstream of which the surface of the body is negatively inclined to the free stream and, hence, the Newtonian approximation is not valid. In this region, C_p is taken equal to zero which is the limit for infinite Mach number. This expansion region will cover increasing amounts of the body as the angle of attack is increased.

4. LINEAR THEORY

In the linear approximation the flow over a slender body at small angle of attack can be treated as two separate flows - one parallel and one normal to the body axis. The pressures are calculated for each flow separately and added to get the pressure due to the inclined flow. The result of the analysis is (Reference 4 or 5)

$$C_p = C_{p_{\alpha=0}} + 4\alpha \cos \theta + (1 + \alpha^2 \sin^2 \theta) \alpha^2$$

where $C_{p_{\alpha=0}}$ is the pressure coefficient at zero angle of attack.

5. SIMILARITY RULES

The hypersonic and supersonic similarity rules apply as before except that now an additional parameter, $K_\alpha = M_\infty \alpha$ or $\sqrt{M^2 - 1} \alpha$ appears. Since the angle of attack similarity is valid only for angles of the same order as the nose angle, K_α has the same Mach number and fineness ratio limitations as K . (Valid only for $M > 2$, $L/D > 2$ for tangent ogives and for $M > 1.5$, $L/D > 2$ for cones.)

6. MIT CONE TABLES

These tables (References 7 and 10) are based on the perturbation analysis of Reference 11 and give values of velocity, pressure and density at any point between the body and the conical shock. The coordinate system in terms of which the various parameters are listed is aligned with the shock axis rather than the body axis. At first sight this would seem to require a coordinate transformation to obtain the flow parameters in terms of the more usual body axes. It was shown in Reference 12, however, that for small angle of attack, the correction terms are of the order of terms already neglected so that the tables may be used directly. In the nomenclature of the tables, the pressure is given by $p = \bar{p} + \eta \epsilon \cos \phi$ where p is the pressure at angle of attack

\bar{p} is the pressure at zero angle of attack

ϵ is the angle of attack (in our coordinate system $\epsilon = -\alpha$)

η is the pressure correction for angle of attack

ϕ is the angular coordinate but is measured from the extreme leeward station in the tables.

In our nomenclature then $\frac{p}{\bar{p}} = 1 + \frac{\eta}{\bar{p}} \alpha \cos \phi$ where $\frac{\eta}{\bar{p}}$ must be read from Reference 10 and \bar{p} is given in Reference 9 in terms of the free stream pressure. (For cones at large angle of attack, the analysis has been extended (Reference 3) to include terms of second order in ϵ .)

7. APPLICATION OF THE ABOVE METHODS TO THE CALCULATION OF PRESSURE DISTRIBUTION ON:

a. Tangent Ogives

Figure 2 shows the range of interest of fineness ratio and Mach number and the available experimental data. The following procedures are suggested for small angle of attack:

1. For $K \geq 0.6$, the shock expansion method using the quantities in Table I should be used.
2. For $K < 0.6$, the pressure distribution at angle of attack can be derived from that at zero angle of attack by adding the cross flow contribution according to the linear theory.
3. For $L/D = 0.5$ (i.e., a hemisphere) the Newtonian approximation as outlined above should be used.

b. Cones

In the range of $K > 0.6$, the shock expansion method and the MIT tables overlap. Figure 6 shows the pressure distribution on a 10° cone at Mach number 6.9 at an angle of attack of 6.7° ($K = 1.2$, $K_n = 0.8$) as calculated by each of the two methods and experimental data from Ref. 7. It is noted that near $\phi = 0$ and 180° , the shock expansion method gives more accurate results while in the remainder of the range there is little to choose between the two methods. In view of this superiority of the shock expansion method, it is to be preferred in the range of $K > 0.6$.

There is also the fact that the Mach number increments in the MIT tables are large and, in general, interpolation in the tables is required.

For $K \leq 0.6$, the MIT tables can be used with the similarity rules extending the region of application to fineness ratios greater than 5.7 which is the largest value for which tabulated data are available.

c. Ellipsoids and Paraboloids of Revolution

There are no pressure data available for either of these bodies at angle of attack in the range above transonic - hence, the recommended methods of calculation are subject to experimental verification. Following the pattern suggested for $\alpha = 0$, the Newtonian concept should be used for $M > 2$ and the linear theory for $M < 2$ and $L/D > 3$. As shown in Figure 3, there are several sets of experimental data for ellipsoids in the transonic range, but none in the super or hypersonic ranges.

Reference 25 gives force data (i.e., lift and drag) of a paraboloid of revolution and a so-called $3/4$ power body ($3/4$ refers to the power of X in the equation defining the meridians. For example, a paraboloid of revolution ($\propto X^{1/2}$) would be called a $1/2$ powerbody). These data are compared with the lift and drag obtained from the Newtonian theory and in the range of Mach number reported (2.75 - 5.0), excellent agreement is shown. Although good correlation of force data does not necessarily imply good correlation of pressure data, it adds a certain degree of confidence in this method of calculation.

8. TRANSONIC RANGE

There are no theories available in the transonic range and the validity of a transonic similarity rule has not yet been established. The available experimental data are shown in Figures 1, 2 and 3 for cones, ogives and ellipsoids, respectively. No data are available for paraboloids of revolution.

9. CONCLUSIONS

Methods have been given which may be used to calculate the pressure distribution on certain bodies of revolution at small angle of attack in the range of Mach number from low supersonic to hypersonic.

The pressure distribution on sharp-nosed bodies such as cones or ogives may be calculated from the linear theory and the shock expansion method with good accuracy except on the windward side of the body.

In the case of the blunt-nosed bodies of revolution, the Newtonian approximation may be used for Mach numbers above 2 and the linear theory below this.

In the transonic range, experimental data alone must suffice since no theory has as yet been developed.

REFERENCES

1. Eggers, A. J. Jr. and Savin, Raymond C. - A Unified Two-Dimensional Approach to the Calculation of Three-Dimensional Hypersonic Flows, With Application to Bodies of Revolution - NACA Report No. 1249, 1955
2. Grimminger, G., Williams, E. P. and Young, G. B. W. - Lift on Inclined Bodies of Revolution in Hypersonic Flow - Journal of the Aeronautical Sciences, Vol. 17, No. 11, p.675, November 1950
3. Staff of the Computing Section under direction of Zdenek Kopal - Tables of Supersonic Flow Around Cones at Large Yaw - Department of Electrical Engineering, Technical Report No. 5, Massachusetts Institute of Technology 1949.
4. Munk, Max M. - The Aerodynamic Forces on Airship Hulls - NACA Report No. 184, 1924
5. Allen, H. Julian and Perkins, Edward W. - A Study of Effects of Viscosity on Flow Over Slender Inclined Bodies of Revolution - NACA Report No. 1048, 1951
6. Perkins, Edward W. and Kuehn, Donald M. - Comparison of the Experimental and Theoretical Distributions of Lift on a Slender Inclined Body of Revolution at $M = 2$ - NACA Technical Note 3715, May 1956
7. Ferri, Antonio - Supersonic Flow Around Circular Cones at Angles of Attack - NACA Report No. 1045, 1951
8. Hamaker, Frank M., Neice, Stanford E., and Wong, Thomas J. - The Similarity Law for Hypersonic Flow and Requirements for Dynamic Similarity of Related Bodies in Free Flight - NACA Report No. 1147, 1953
9. Massachusetts Institute of Technology - Tables of Supersonic Flow Around Cones - Department of Electrical Engineering Technical Report No. 1, Cambridge, Massachusetts, 1947

10. Staff of the Computing Section, Center of Analysis (Under Direction of Zdenek Kopal) - Tables of Supersonic Flow around Yawing Cones - Technical Report No. 3, M.I. T., 1947
11. Stone, A. H. - On Supersonic Flow Past a Slightly Yawing Cone - Journal of Mathematics and Physics, Vol 27, No. 1, 1948
12. Roberts, R. C. and Riley, J. D. - A Guide to the Use of the M.I. T. Cone Tables - Journal of the Aeronautical Sciences, May 1954
13. Cole, Richard I. - Pressure Distributions on Bodies of Revolution at Subsonic and Transonic Speeds - NACA RM L52D30 July 21, 1952
14. Matthews, Clarence W. - Pressure Distributions Over a Wing-Fuselage Model at Mach Numbers of 0.4 to 0.99 and at 1.2 - NACA RM No. L8H06, November 3, 1948
15. Boltz, Frederick W. and Beam, Benjamin H. - The Effects of Compressibility on the Pressures on a Body of Revolution and on the Aerodynamic Characteristics of a Wing-Nacelle Combination Consisting of the Body of Revolution Mounted on a Swept-Back Wing - NACA RM a50E09, July 26, 1950
16. Loving, Donald L. and Estabrooks, Bruce B. - Transonic-Wing Investigation in the Langley 8-Foot High-Speed Tunnel at High Subsonic Mach Numbers and at a Mach Number of 1.2 - Analysis of Pressure Distribution of Wing-Fuselage Configuration Having a Wing of 45° Sweepback, Aspect Ratio 4, Taper Ratio 0.6, and NACA 65A006 Airfoil Section - NACA RM L51F07, September 6, 1951
17. Perkins, Edward W. and Jorgensen, Leland H. - Comparison of Experimental and Theoretical Normal-Force Distributions (Including Reynolds Number Effects) on an Ogive-Cylinder Body at Mach Number 1.98 - NACA Technical Note 3716, May 1956
18. Estabrooks, Bruce B. - An Analysis of the Pressure Distribution Measured on a Body of Revolution at Transonic Speeds in the Slotted Test Section of the Langley 8-Foot Transonic Tunnel - NACA RM L52D21a, June 25, 1952

19. Robinson, Harold L. - Pressures and Associated Aerodynamic and Load Characteristics for Two Bodies of Revolution at Transonic Speeds - NACA RM L53L28a, March 11, 1954
20. Matthews, Clarence W. - A Comparison of the Experimental Subsonic Pressure Distributions About Several Bodies of Revolution with Pressure Distributions Computed by Means of the Linearized Theory - NACA Report No. 1155, 1953
21. Savin, Raymond C. - Application of the Generalized Shock-Expansion Method to Inclined Bodies of Revolution Traveling at High Supersonic Airspeeds - NACA Technical Note 3349, April 1955
22. Centolanzi, Frank J. - Characteristics of a 40° Cone for Measuring Mach Number, Total Pressure, and Flow Angles at Supersonic Speeds - NACA Technical Note 3967, May 1957
23. Tsien, H. S. - Similarity Laws of Hypersonic Flow - Journal of Mathematics and Physics, 25 (1946)
24. Holt, Maurice and Blackie, John - Experiments on Circular Cones at Yaw in Supersonic Flow - Journal of the Aeronautical Sciences, October 1956
25. Dennis, David H. and Cunningham, B. E. - Forces and Moments on Pointed and Blunt Nosed Bodies of Revolution at Mach Numbers from 2.75 to 5.0 - NACA RM A52E22, August 1952

APPENDIX A

SAMPLE CALCULATIONS

1. Tangent Ogives

a. Shock Expansion Method

As an example of the shock expansion method, the circumferential pressure distribution on an ogive of fineness ratio 5 will be calculated for $M_0 = 5$ at two streamwise locations. Experimental data for this body are available in Reference 1. The equation to be used is

$$C_p = \frac{2}{\gamma M_0^2} \left\{ \frac{p_s}{p_0} \right\}_{\varphi=0} \left[\frac{M_s}{M_N} \right]_{\varphi=0} - \frac{\gamma-1}{2} (M_s \delta_N)_{\varphi=0} \left(1 - \delta/\delta_N \right)^{\frac{2\gamma}{\gamma-1}} - 1 \right\}$$

where $(p_s/p_0)_{\varphi=0}$, $\frac{M_s}{M_N} \right]_{\varphi=0}$ and $M_s \delta_N$ are given in Table I in terms of $M_0 \delta_N$ and α/δ_N for various values of φ .

Following the method of Appendix C of Part B, the value of δ_N , the semi-nose angle is found to be 0.20 and, therefore, $M_0 \delta_N = 1.0$. We choose $\alpha/\delta_N = 0.80$ to avoid interpolation in Table I. Corresponding to $M_0 \delta_N = 1.0$ and $\alpha/\delta_N = 0.8$ we have $(p_s/p_0)_{\varphi=0} = 5.188$ and $(M_s \delta_N)_{\varphi=0} = .744$ and hence

$$C_p = \frac{2}{1.4(5)^2} \left\{ 5.188 \left[\frac{M_s}{M_N} \right]_{\varphi=0} - 0.2(0.744) \left(1 - \frac{\delta}{\delta_N} \right)^7 - 1 \right\}$$

For any axial location δ/δ_N is known and $M/M_N)_{\varphi=0}$ is available for any angular position from the table.

The calculations for $\delta = \delta_N$ and $\delta = 0$ (the nose and shoulder positions, respectively) are carried out in Table II and plotted in Figure 4.

For $\delta = \delta_N$,

$$C_p = 0.0571 \left[5.188 \left(\frac{M_s)_{\varphi=0}}{M_N} \right)^7 - 1 \right]$$

and for $\delta = 0$

$$C_p = 0.0571 \left\{ 5.188 \left[\frac{M_s)_{\varphi=0}}{M_N} - 0.1488 \right]^7 - 1 \right\}$$

b. Linear Theory

As an illustration of the linear theory, the circumferential pressure distribution on an ogive of fineness ratio 5.75 at Mach number 1.98 will be calculated at a location 46.5% of the nose length aft of the vertex. We use the equation

$$C_p - C_{p_{\alpha=0}} = (4 \cos \varphi) \delta + (1 - 4 \sin^2 \varphi) \alpha^2$$

For the location chosen, $\delta = .09$ and for $\alpha = 8^\circ$ the equation becomes

$$C_p - C_{p_{\alpha=0}} = 0.078 \cos^2 \varphi + 0.0516 \cos \varphi - 0.0585$$

The calculation is compared with the experimental data in Figure 5.

2. Cones

a. For $K > 0.6$, the shock expansion method is used, the procedure being identical with that given for tangent ogives. In the case of a cone, of course, $\delta = \delta_N$, independent of the streamwise coordinate, and so

$$C_p = \frac{2}{\gamma M_0^2} \left[\frac{P_s}{P_0} \right]_{\varphi=0} \left\{ \frac{M_s}{M_N} \right\}_{\varphi=0}^{\frac{2\gamma}{\gamma-1}} - 1$$

b. MIT Cone Tables

As an illustration of the use of the cone tables, the pressure distribution on a 7.5° cone at $M_0 = 1.6$ will be calculated. Experimental data are available for this body in Ref. 7. On page 471 of Ref. 9 for a cone angle of 7.5° read (interpolating in Mach number) $p_s/p_w = 1.1143$ and $p_w/p_1 = 1.0159$ and, hence, $p_s/p_1 = 1.1320$ where in the nomenclature of the tables, p_s is the pressure on the surface of the cone at zero angle of attack and p_1 is the free stream pressure. From Ref. 10, page 71, for a cone angle of 7.5° read $\eta/\bar{p} = 0.7377$ for $M = 1.5462$, and on page 75 $\eta/\bar{p} = 0.9320$ for $M = 1.7610$ (interpolating gives $\eta/\bar{p} = 0.7730$ for $M_0 = 1.60$).

Therefore, $\frac{p}{\bar{p}} = 1 + 0.7730 \alpha \cos \varphi$, and since $\frac{\bar{p}}{p_0} = 1.1320$, $p/p_0 = 1.1320 + 0.8750 \alpha \cos \varphi$. This expression can be rewritten straightaway as

$$C_p = 0.0737 + 0.4883 \alpha \cos \varphi$$

Figure 7 shows a comparison of the above calculation for $\alpha = 4^\circ$ with experimental data from Ref. 7.

3. Ellipsoids

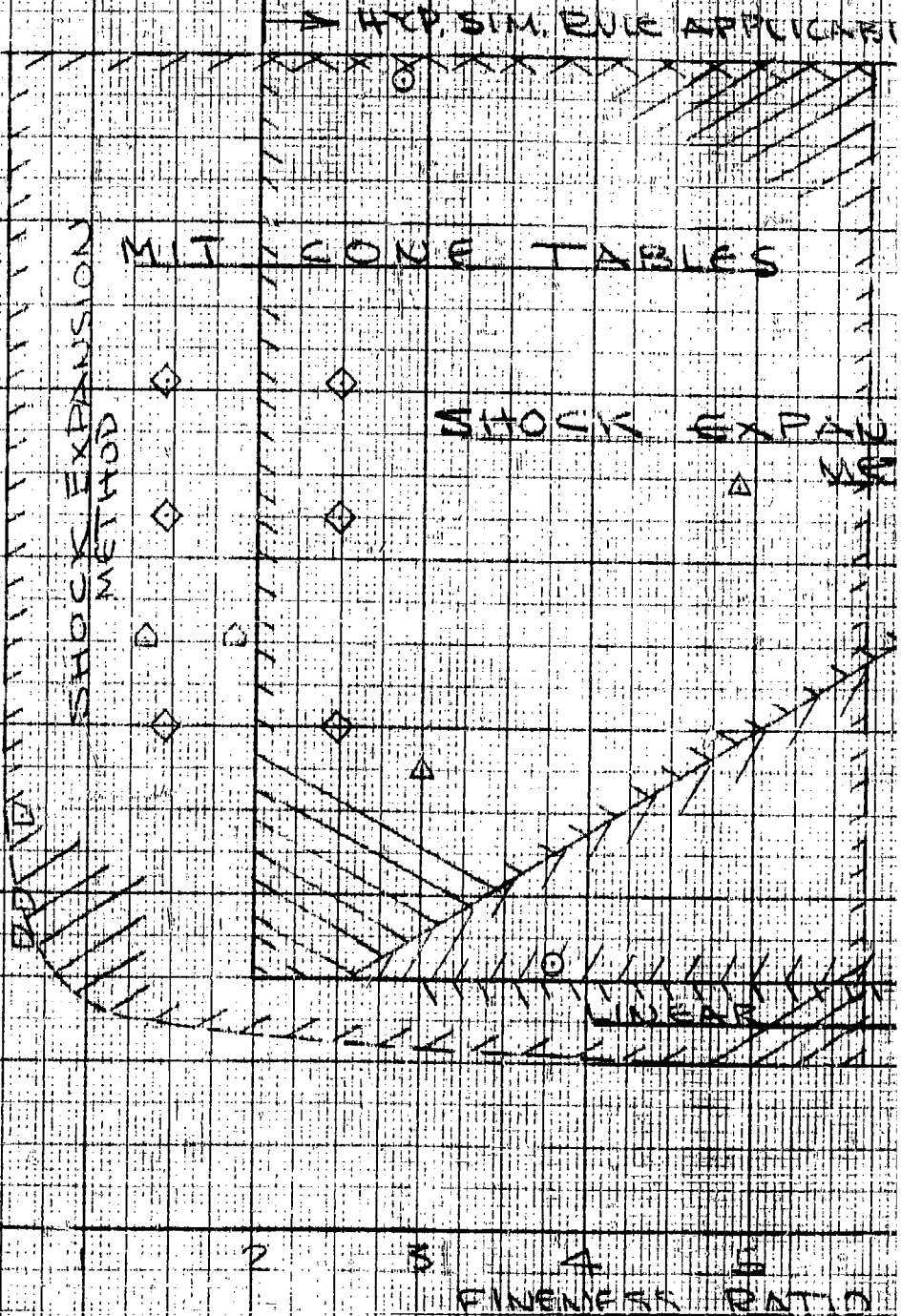
In the range of $M > 2$, the Newtonian flow concept is used with the pressure being calculated from the equation $C_p = C_{p \text{ max.}} \cos^2 \psi$ where $\cos \psi = \cos \alpha \sin \delta + \sin \alpha \cos \delta \cos \phi$. The pressure will be calculated along the line $\phi = \pi$ (the extreme leeward meridian in which case $\cos \psi = \sin(\delta - \alpha)$). We arbitrarily assume $\alpha = 0.10$, $L/D = 5.0$ and $M_0 = 3.0$ ($C_{p \text{ max.}} = 1.75$). The calculations for pressure coefficient are carried out in Table III. Note that when $\frac{x}{L} = 0.292$, $\delta = \alpha$ and $C_p = 0$. Hence, this is the limit of application of the theory for this particular meridian. For any other meridian, the limit will be further aft on the body.

REGIONS OF APPLICABILITY OF CALCULATING PRESSURE ANGLE OF ATTACK

EXPERIMENTAL DATA

	REF.	α (DEG)	
○	7	4-14	6
○	21	5-15	
○	22	0-36	
△	8	0-5	5
○	24	5-25	

2
3
4
5
6
7



1

OF APPLICABILITY OF VARIOUS METHODS COUNTING PRESSURE ON CONES AT SMALL ANGLE OF ATTACK

SIM. RULE APPLICABLE

E TABLES

SHOCK EXPANSION
 METHOD

MIT TABLES
 SIM. RULE

SIM. RULE APPLICABLE

LINEAR THEORY

FINENESS RATIO 4 5 6 7 8 9 10

2

FIG 1

REGIONS OF APPLICABILITY OF CALCULATING PRESSURE ON TANG SMALL ANGLE OF ATTACK

EXPERIMENTAL DATA

REF.	α (DEG)
6	16
7	17
8	18
9	19
10	20
11	21
12	22
13	23
14	24
15	25
16	26
17	27
18	28
19	29
20	30
21	31
22	32
23	33
24	34
25	35
26	36
27	37
28	38
29	39
30	40
31	41
32	42
33	43
34	44
35	45
36	46
37	47
38	48
39	49
40	50
41	51
42	52
43	53
44	54
45	55
46	56
47	57
48	58
49	59
50	60

MACH NO

CONSTANT
ANGLE
METHOD

SHOCK EXPANSION

SHOCK EXPANSION
METHOD

REGION OF APPLICABILITY

SHOCK DETACHMENT LINEAR
FOR $\alpha = 0.5$

FINESS RATIO

1

APPLICABILITY OF VARIOUS METHODS OF PRESSURE ON TANGENT OBLICS AT WALL ANGLE OF ATTACK

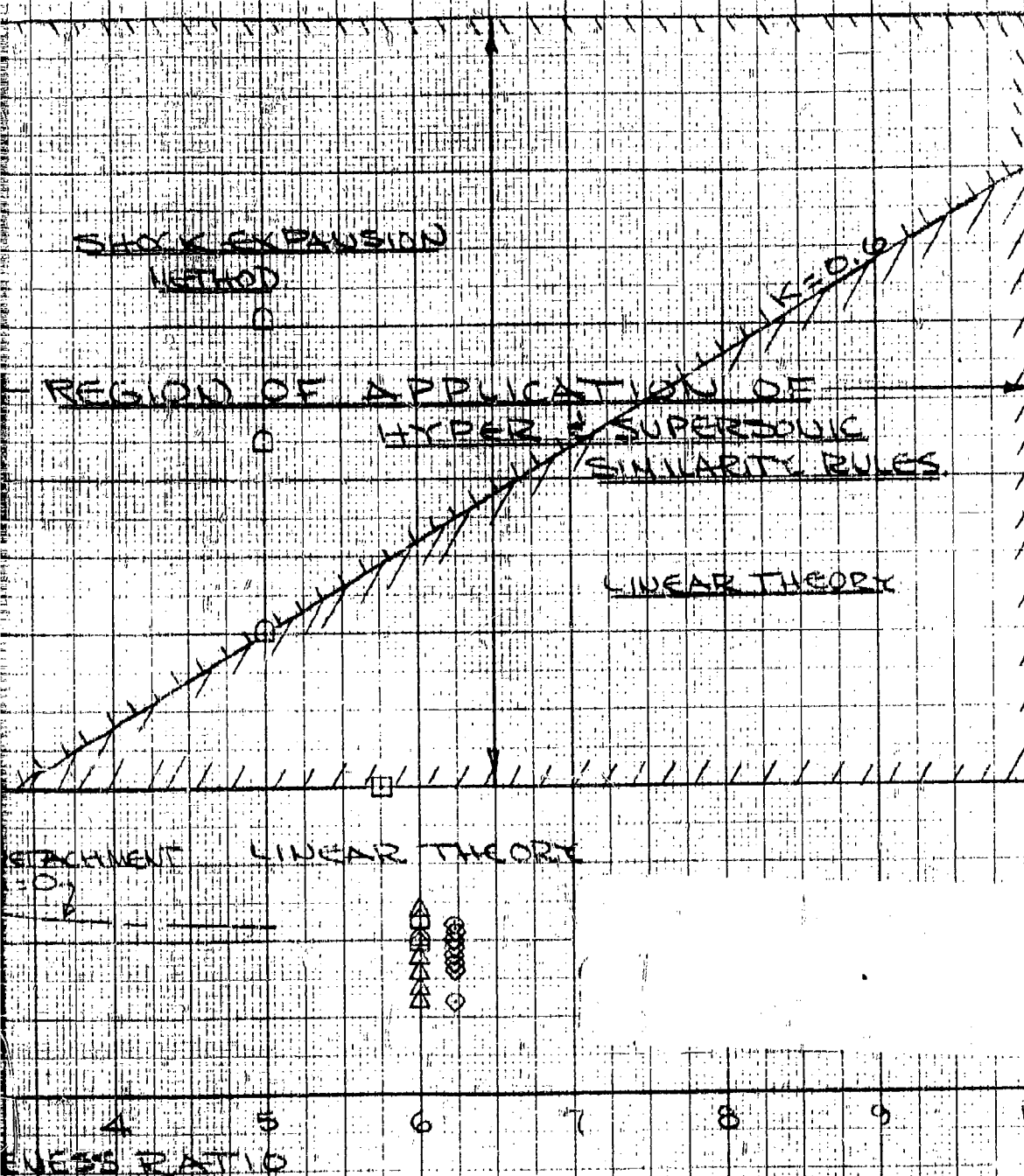


FIG 2

2

REGIONS OF APPLICABILITY OF CALCULATING PRESSURES ON ELLIP AT SMALL ANGLE OF

EXPERIMENTAL DATA

	REF.	α (deg)
△	13	10-20°
○	14	10-20°
◇	15	2-8°

NEWTONIAN THEORY

LINEAR

1

THICKNESS RATIO

APPLICABILITY OF VARIOUS METHODS OF PRESSURES ON ELLIPSOIDS OF REVOLUTION AT SMALL ANGLE OF ATTACK

NEWTONIAN THEORY

LINEAR THEORY

C
D
D

4 5 6 7 8 9 10
FINENESS RATIO

FIG. 3

2

CIRCUMFERENTIAL VARIATION OF PRESSURE COEFF ON A FINENESS RATIO 5 OGIVE AT $M_\infty = 5$

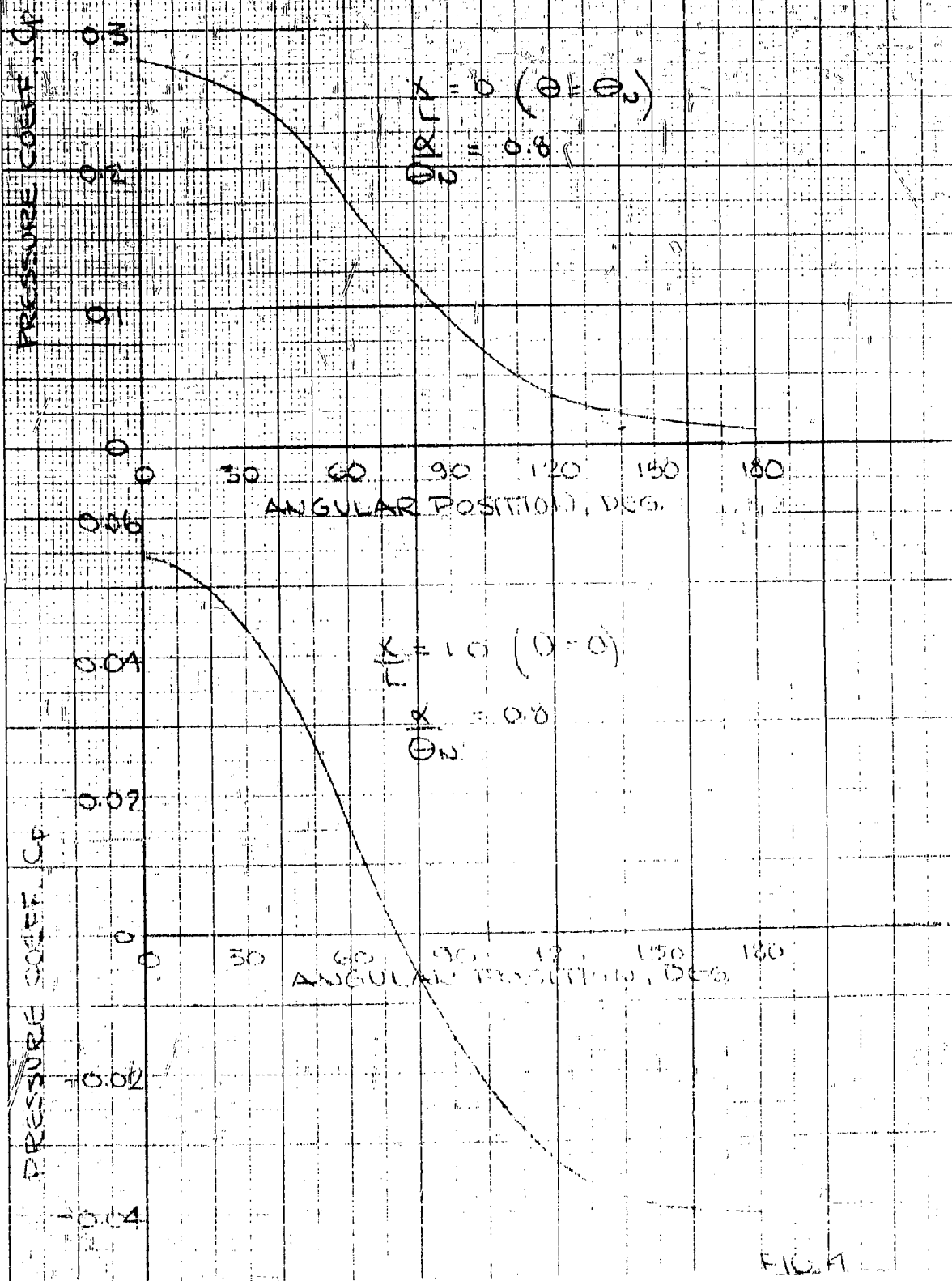
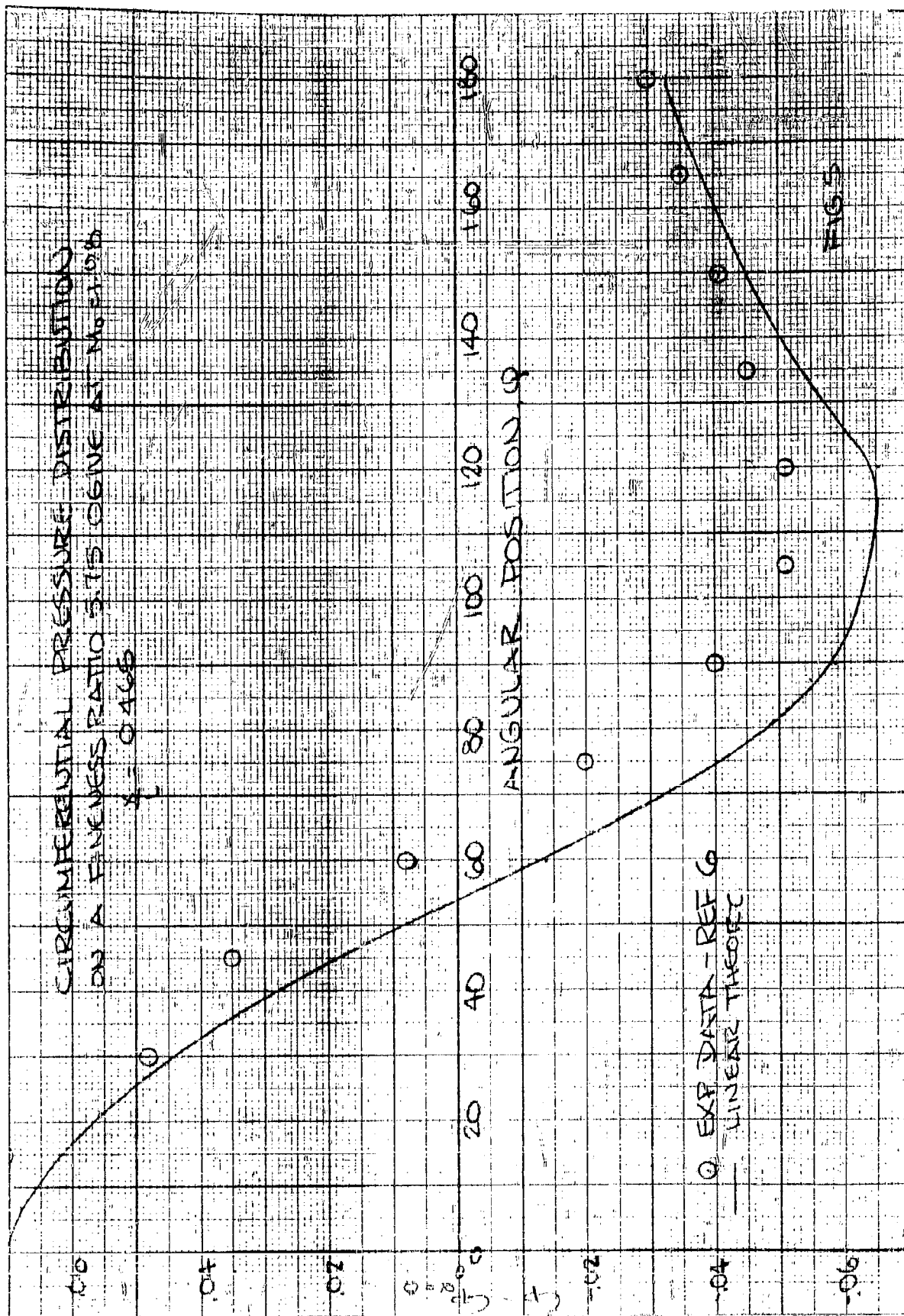
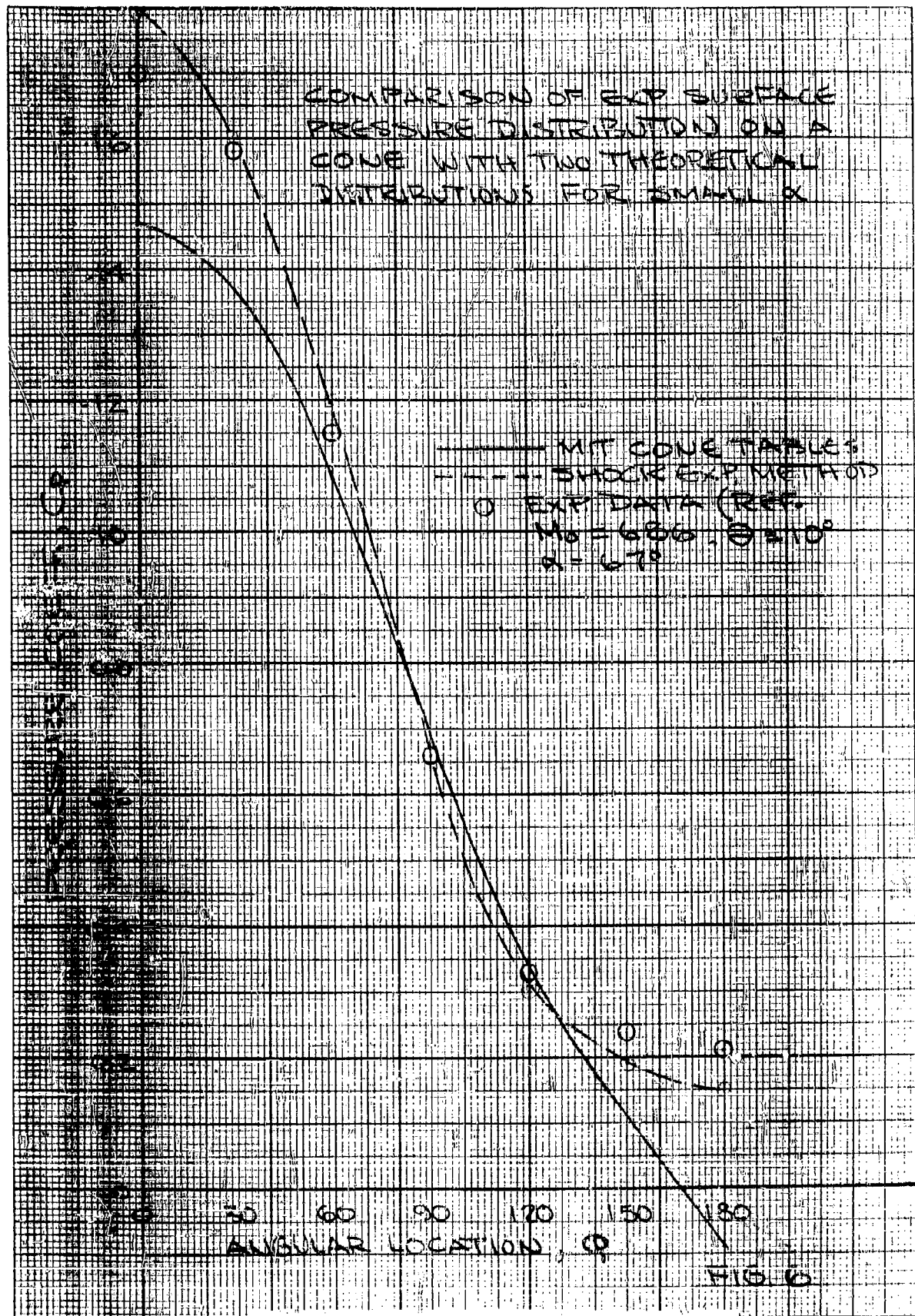


FIG. A





PRESSURE DISTRIBUTION ON A
7.5° CONE AT $M_\infty = 1.6$, $\alpha = 4^\circ$

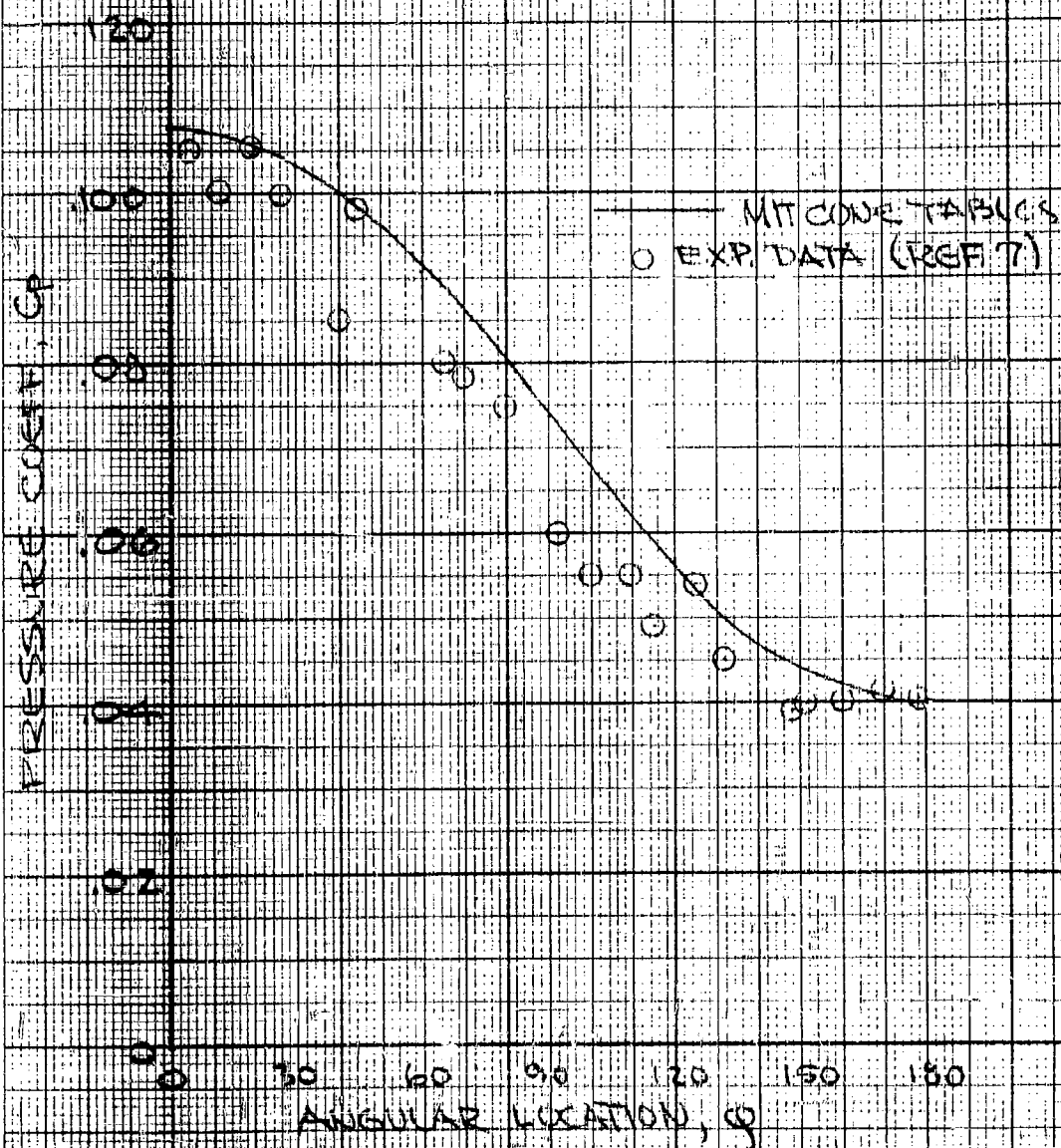
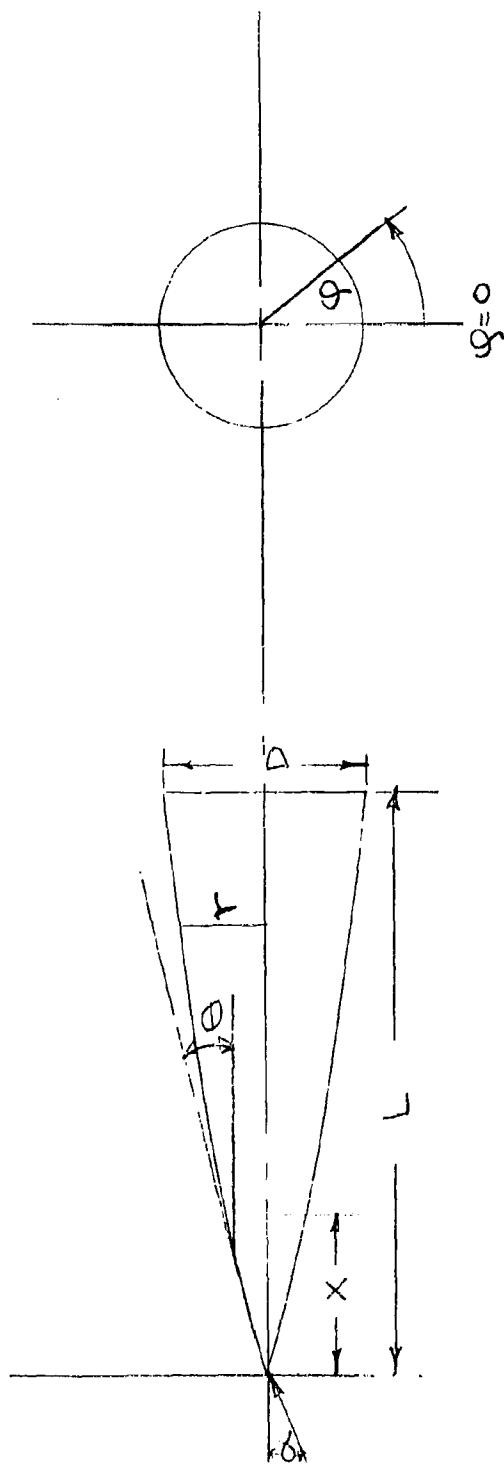


FIG. 7



NONENCLATURE

FIG. 8

TABLE I
TABLE OF FUNCTIONS
FOR SHOCK EXPANSION METHOD

$\frac{p_s/p_\infty}{(M_\infty \delta_N)^2}$ for $\varphi=0^\circ$		$\frac{(M_s)_{\varphi=0}}{M_N}$ for $\varphi=30^\circ$						$\frac{(M_s)_{\varphi=0}}{M_N}$ for $\varphi=120^\circ$							
$M_\infty \delta_N$	α/δ_N	0	0.20	0.40	0.60	0.80	1.00	$M_\infty \delta_N$	α/δ_N	0	0.20	0.40	0.60	0.80	1.00
0.60	4.178	4.753	5.406	6.143	6.969	7.817	8.685	0.60	0.60	1.021	1.021	0.9803	0.9556	0.9271	0.8942
0.80	2.963	3.517	4.161	4.898	5.732	6.645	7.635	0.80	0.80	1.021	0.9818	0.9600	0.9247	0.8850	0.8396
1.00	2.400	2.952	3.590	4.343	5.188	6.131	7.161	1.00	1.00	1.019	0.9812	0.9405	0.8961	0.8465	0.7891
1.20	2.094	2.640	3.301	4.052	4.903	5.853	6.891	1.20	1.20	1.017	0.9717	0.9238	0.8720	0.8139	0.7460
1.40	1.910	2.468	3.125	3.881	4.737	5.691	6.731	1.40	1.40	1.016	0.9638	0.9102	0.8527	0.7876	0.7109
1.60	1.791	2.352	3.013	3.773	4.632	5.589	6.629	1.60	1.60	1.014	0.9574	0.8993	0.8371	0.7666	0.6828
1.80	1.709	2.273	2.937	3.700	4.562	5.518	6.558	1.80	1.80	1.013	0.9523	0.8907	0.8247	0.7501	0.6607
2.00	1.650	2.217	2.884	3.648	4.512	5.471	6.511	2.00	2.00	1.012	0.9483	0.8839	0.8152	0.7372	0.6436
2.50	1.540	2.132	2.802	3.569	4.436	5.398	6.438	2.50	2.50	1.011	0.9412	0.8723	0.7989	0.7164	0.6161
3.00	1.511	2.086	2.759	3.529	4.396	5.359	6.400	3.00	3.00	1.010	0.9369	0.8656	0.7893	0.7053	0.6024
4.00	1.462	2.041	2.716	3.489	4.357	5.321	6.362	4.00	4.00	1.009	0.9324	0.8587	0.7782	0.6917	0.5881
6.00	1.428	2.008	2.686	3.459	4.329	5.294	6.335	6.00	6.00	1.008	0.9289	0.8540	0.7716	0.6863	0.5811
10.00	1.410	1.992	2.671	3.446	4.315	5.280	6.321	10.00	10.00	1.007	0.9271	0.8518	0.7668	0.6811	0.5760
∞	1.400	1.983	2.662	3.437	4.307	5.272	6.313	∞	∞	1.007	0.9260	0.8507	0.7665	0.6811	0.5760

$M_\infty \delta_N$ for $\varphi=0^\circ$		$\frac{(M_s)_{\varphi=0}}{M_N}$ for $\varphi=60^\circ$						$\frac{(M_s)_{\varphi=0}}{M_N}$ for $\varphi=150^\circ$							
$M_\infty \delta_N$	α/δ_N	0	0.20	0.40	0.60	0.80	1.00	$M_\infty \delta_N$	α/δ_N	0	0.20	0.40	0.60	0.80	1.00
0.60	5.635	5.577	5.432	5.319	5.203	5.095	4.995	0.60	0.60	1.021	0.9977	0.9716	0.9436	0.9132	0.8797
0.80	4.724	4.707	4.683	4.654	4.624	4.595	4.565	0.80	0.80	1.021	0.9849	0.9467	0.9060	0.8626	0.8150
1.00	4.066	4.045	4.020	4.000	3.979	3.958	3.937	1.00	1.00	1.019	0.9720	0.9228	0.8709	0.8158	0.7559
1.20	3.606	3.586	3.561	3.540	3.519	3.498	3.477	1.20	1.20	1.017	0.9606	0.9021	0.8408	0.7756	0.7042
1.40	3.226	3.206	3.181	3.160	3.139	3.118	3.097	1.40	1.40	1.016	0.9511	0.8852	0.8161	0.7424	0.6618
1.60	2.938	2.918	2.893	2.872	2.851	2.830	2.809	1.60	1.60	1.014	0.9434	0.8716	0.7964	0.7156	0.6277
1.80	2.713	2.693	2.668	2.647	2.626	2.605	2.584	1.80	1.80	1.013	0.9373	0.8609	0.7808	0.6942	0.5999
2.00	2.556	2.536	2.511	2.490	2.469	2.448	2.427	2.00	2.00	1.012	0.9324	0.8525	0.7686	0.6774	0.5782
2.50	2.307	2.287	2.262	2.241	2.220	2.199	2.178	2.50	2.50	1.011	0.9241	0.8379	0.7481	0.6492	0.5429
3.00	2.167	2.147	2.122	2.101	2.080	2.059	2.038	3.00	3.00	1.010	0.9190	0.8305	0.7381	0.6382	0.5266
4.00	1.813	1.793	1.768	1.747	1.726	1.705	1.684	4.00	4.00	1.009	0.9138	0.8234	0.7313	0.6318	0.5161
6.00	1.643	1.623	1.598	1.577	1.556	1.535	1.514	6.00	6.00	1.008	0.9101	0.8199	0.7281	0.6281	0.5124
10.00	2.022	1.711	1.453	1.309	1.171	1.060	0.967	10.00	10.00	1.007	0.9082	0.8194	0.7273	0.6273	0.5124
∞	2.070	1.740	1.501	1.321	1.180	1.067	0.961	∞	∞	1.007	0.9073	0.8194	0.7273	0.6273	0.5124

$\frac{(M_s)_{\varphi=0}}{M_N}$ for $\varphi=0^\circ$		$\frac{(M_s)_{\varphi=0}}{M_N}$ for $\varphi=30^\circ$						$\frac{(M_s)_{\varphi=0}}{M_N}$ for $\varphi=180^\circ$							
$M_\infty \delta_N$	α/δ_N	0	0.20	0.40	0.60	0.80	1.00	$M_\infty \delta_N$	α/δ_N	0	0.20	0.40	0.60	0.80	1.00
0.60	1.021	1.024	1.025	1.025	1.025	1.025	1.025	0.60	0.60	1.021	0.9960	0.9688	0.9405	0.9107	0.8795
0.80	1.021	1.022	1.023	1.023	1.023	1.023	1.023	0.80	0.80	1.021	0.9817	0.9423	0.9008	0.8584	0.8157
1.00	1.019	1.020	1.020	1.020	1.020	1.020	1.020	1.00	1.00	1.019	0.9687	0.9168	0.8636	0.8097	0.7547
1.20	1.017	1.018	1.018	1.018	1.018	1.018	1.018	1.20	1.20	1.017	0.9566	0.8947	0.8316	0.7680	0.7042
1.40	1.016	1.016	1.016	1.016	1.016	1.016	1.016	1.40	1.40	1.016	0.9465	0.8766	0.8052	0.7332	0.6611
1.60	1.014	1.015	1.015	1.015	1.015	1.015	1.015	1.60	1.60	1.014	0.9384	0.8620	0.7840	0.7047	0.6209
1.80	1.013	1.014	1.014	1.014	1.014	1.014	1.014	1.80	1.80	1.013	0.9319	0.8505	0.7672	0.6821	0.5989
2.00	1.012	1.013	1.013	1.013	1.013	1.013	1.013	2.00	2.00	1.012	0.9267	0.8415	0.7540	0.6650	0.5822
2.50	1.011	1.011	1.011	1.011	1.011	1.011	1.011	2.50	2.50	1.011	0.9178	0.8264	0.7321	0.6381	0.5562
3.00	1.010	1.010	1.010	1.010	1.010	1.010	1.010	3.00	3.00	1.010	0.9126	0.8183	0.7218	0.6212	0.5342
4.00	1.009	1.009	1.009	1.009	1.009	1.009	1.009	4.00	4.00	1.009	0.9072	0.8114	0.7165	0.6192	0.5282
6.00	1.008	1.009	1.010	1.010	1.010	1.010	1.010	6.00	6.00	1.008	0.9034	0.8092	0.7143	0.6170	0.5262
10.00	1.007	1.008	1.009	1.010	1.010	1.010	1.010	10.00	10.00	1.007	0.9018	0.8077	0.7128	0.6155	0.5247
∞	1.007	1.008	1.009	1.010	1.010	1.010	1.010	∞	∞	1.007	0.9018	0.8077	0.7128	0.6155	0.5247

TABLE II

PRESSURE DISTRIBUTION ON A TANGENT OGIVE

 $L/D = 5$ $M_0 = 5$ $\alpha/\theta_0 = 0.8$ $X_L = 0$ $X/L = 1.0$

① φ	② M_x/M_0	③ θ	④ $\sin \theta$	⑤ $\cos \theta$	⑥ C_p	⑦ θ	⑧ $\sin \theta$	⑨ $\cos \theta$	⑩ $\sin \theta$	⑪ C_p
0	1.019	1.141	5.919	4.919	.281	.870	.377	1.956	.956	.055
30	1.007	1.050	5.447	4.447	.254	.858	.342	1.774	.774	.044
60	.967	.790	4.098	3.098	.177	.818	.245	1.271	.271	.015
90	.906	.500	2.594	.594	.091	.757	.142	.737	-.263	-.015
120	.847	.312	1.619	.619	.035	.698	.081	.420	-.580	-.033
150	.816	.240	1.245	.245	.014	.667	.059	.305	-.695	-.040
180	.810	.228	1.183	.183	.010	.661	.055	.285	-.715	-.041

TABLE III

PRESSURE DIST. ALONG $\varphi = \pi$ FOR AN ELLIPSOID OF REV. $L/D = 5$, $M_0 = 3.0$, $\alpha = 0.10$

① X/L	② $\tan \theta$	③ θ	④ $\theta - \alpha$	⑤ $\sin(\theta - \alpha)$	⑥ $\cos^2 \eta$	⑦ C_p
0	∞	1.571	1.471	.995	.990	1.730
.05	.3045	.296	.196	.1945	.038	.066
.10	.2064	.204	.104	.1037	.0108	.019
.15	.1613	.160	.060	.0599	.0036	.006
.20	.1333	.133	.033	.0326	.00106	.002
.25	.1135	.113	.013	.0131	.0002	0
.292	.1004	.100	0	0	0	0

CHAPTER I - PART D
CALCULATION OF HEAT TRANSFER TO
RADOME-SHAPED BODIES

By Martin H. Bloom* and Melvin Epstein

* Professor of Aeronautical Engineering, Polytechnic Institute of Brooklyn

TABLE OF CONTENTS

	<u>Title</u>	<u>Page</u>
	Summary	107
	Symbols	108
1.	Introduction	110
2.	Physical Description of Heat Transfer Processes	112
3.	Thermal Properties of Air	117
4.	Atmospheric Properties	125
5.	Convective Heat Transfer	126
6.	Concluding Remarks	140
	References	141
	Bibliography	145
	Figures	155

D. CALCULATION OF HEAT TRANSFER TO
RADOME SHAPED BODIES

SUMMARY

Presented herein are procedures by which estimates of the heat transfer rates can be made for radome shaped bodies in flight, that is, blunt-nosed and pointed-nosed bodies of revolution. Non-axially symmetric shapes are not considered. A brief qualitative account is given of the physical nature of various modes of heat transfer and the governing parameters. The thermal properties of air and atmospheric properties required for execution of the procedure are presented in chart form. Primary emphasis is given to flight conditions between Mach numbers of 0 to 12 at altitudes up to 150,000 feet. Laminar and turbulent heat rates for both zero and moderate angles of attack are treated. Real gas effects are included in a manner sufficient for most engineering purposes. Charts for facilitating computation procedures have been constructed.

SYMBOLS

a	speed of sound
C_p	coefficient of specific heat at constant pressure
G	function defined in Equation 13
h	static enthalpy
k	coefficient of thermal conductivity
M	Mach number = u/a
Nu	Nusselt number - defined in Equation 16
p	pressure
Pr	Prandtl number = $\mu C_p/k$
q	heat transfer rate
r_o	radius of body
R_o	radius of curvature of nose in meridian plane
Re	Reynolds number = $\frac{\rho u x}{\mu}$
s	distance along meridian curve
T	absolute temperature
u	velocity
x	distance along meridian curve
α	angle of attack
γ	ratio of specific heats

$\bar{\gamma}$ reduced ratio of specific heats for use at high temperatures
 ϵ emmisivity
 μ coefficient of absolute viscosity
 ρ density

Subscripts

aw adiabatic wall
B base conditions (Ref. 5)
e conditions at outer edge of boundary layer
f free stream conditions
r reference value
s stagnation values
w wall value
o stagnation point value
z condition downstream of normal shock wave

1. INTRODUCTION

The design of radomes for high speed aircraft is subject to a complication which does not exist at low speeds; that is, at high speeds the rate at which heat is generated aerodynamically by virtue of compressive and viscous effects at the exterior surface of the body is sufficiently great to create undesirable high surface temperatures. These large temperatures complicate the design problem in a number of ways. For example, marked changes in the strength and dielectric properties of the radome occur at elevated temperatures. In addition, radiation from the hot surface into the interior of the radome may result in undesirably large environmental temperatures for the electronic gear.

A considerable amount of effort, both theoretical and experimental, has been expended during the last decade, with the aim of understanding and predicting the heat transfer to bodies of various geometries at high flight speeds. Because of the complexity of the problem, several approximate methods of analysis are available for many problems involving aerodynamic heating. It is the purpose of this report to describe those methods which appear to be best suited for engineering calculations

of heat transfer to radome shaped bodies. The reader is referred to References 1 and 2 for extensive bibliographies of reports dealing with the development of the various methods of analysis and with comparison with experiment. Procedures for computing the pressure distributions required for making heat transfer estimates have been discussed in Parts B and C.

2. PHYSICAL DESCRIPTION OF HEAT TRANSFER PROCESSES

The calculation of the heat transfer to a body in high speed flight requires the analysis of the so-called "boundary layer" surrounding the body. In aerodynamic problems the behavior of air flowing past a surface can usually be studied in two parts. One is a relatively thin boundary layer which is appreciably affected by the adhesive decelerating action of the surface and by the accompanying viscous and heat conduction effects. The other part, outside the boundary layer, is primarily affected by the disturbances caused by the surface contour. In this outer region, the explicit effects of viscosity and thermal conductivity are usually negligible. A major simplification in aerodynamic studies results from the fact that the outer region is usually affected only slightly by occurrences within the boundary layer, and by the boundary layer's distortion of the streamlines, provided that the layer does not become separated from the surface. In effect, therefore, the outer flow slides frictionlessly over the boundary layer. A correction for the influence of the boundary layer on the outer flow can often be made, if necessary, by considering a slightly altered surface contour. The additional fact that the pressure variation through the boundary layer in a direction normal to the surface is negligible in most cases, makes it possible to compute force effects, aside from viscous drag, without considering the boundary layer. On the other

hand, boundary layer phenomena are often largely dependent on the characteristics of the outer flow, which, together with the conditions at the solid surface are usually considered to be the boundary conditions of the boundary layer flow. For this reason, the surface heat transfer rates, the temperature and velocity distributions within the boundary layer, and the surface friction drag are usually expressed in terms of the parameters of the outer flow and the surface.

In general, the boundary layer may be characterized by its condition, i. e., laminar, turbulent, or transitional. In a laminar flow, transport of momentum and energy in a direction perpendicular to the streamlines takes place because of the random motion of the molecules which make up the fluid. When the flow is turbulent, there is in addition a strong mixing action within the boundary layer, because of the presence of randomly distributed turbulent eddies.

One of the principal processes of heat transfer is conduction. In this mode of heat transfer the heat flux is proportional to the temperature gradient at the point in question. The proportionality factor, the thermal conductivity, k , is a property of the energy transport on a molecular scale. Mechanically enforced relative motion which brings fluid masses into contact permitting conduction to take place is termed "forced convection" whereas relative motion of the fluid induced by body forces such as

gravity give use to the term "free convection". Although body forces may have an influence on the transition from laminar to turbulent flow under special circumstances, they have a negligible effect on the heat transfer rates on the external surface of a body in high speed flow. On the other hand, free convection is responsible for a large part of the energy transfer on the inside of a closed structure. The analysis of free convection problems will not be considered here.

The conductive transport resulting from the random motion of the molecules may be augmented if the fluid motion is turbulent, by an additional transport due to the intermixing of the random turbulent eddies on a macroscopic scale. One cannot show conclusively that the heat transfer rate due to forced convection in turbulent flow is directly proportional to the mean temperature gradient. However, an empirical proportionality factor between the turbulent heat flux and the mean temperature gradient is often defined and termed the "turbulent eddy conductivity" by analogy with laminar flow.

At sufficiently high temperatures, air dissociates into a mixture of atoms and molecules. The diffusion of the various components through each other influences the heat transfer process. The diffusion process, characterized by the proportionality between the rate of change of concentration and the concentration gradient at a point, influences the

composition of the gas at each point as well as the flow properties. Thus, it affects the transport properties, such as the thermal conductivity, as well as the temperature distribution in the flow. Furthermore, dissociated components of a gas, having absorbed energy in the process of dissociation may diffuse toward the surface and recombine there, releasing their dissociation energy. In a manner analogous to turbulent eddy conductivity, diffusion on a molecular scale can also be augmented by turbulent eddy diffusion.

Another mechanism by which heat can be transferred is that of radiation. In this mode of heat transfer, molecular energy is transported by electromagnetic waves or the equivalent quanta. The physical characteristics of the gas are not affected by the presence of the quanta. However, they may transfer part of their energy to the molecules of the gas because of the collisions that occur between the quanta and the molecules. Air is essentially transparent to thermal radiation, i. e., it absorbs very little of the thermal radiation passing through it. The rate at which thermal radiation is emitted by a material can be shown to be proportional to the fourth power of the absolute temperature. The constant of proportionality, ϵ , is known as the emissivity of the substance. Under the flight conditions of interest, air has a very low emissivity and hence, its radiation to the surface of the body may be neglected for design purposes.

The temperature of a point on the surface of a body is determined by striking a balance between the heat transferred to the surface by forced convection of the air adjacent to the surface, conduction to or from the surface due to temperature gradients within the body, and radiation from the surface of the body. The rate of radiation of heat from a body is given as

$$q = .481 \epsilon \left(\frac{T}{1000} \right)^4 \frac{\text{BTU}}{\text{ft}^2 \text{sec.}} \quad (1)$$

where ϵ is the emmissivity which depends on the material of the radiating surface.

3. THERMAL PROPERTIES OF AIR

In the temperature range below approximately 3500°R, the coefficient of absolute viscosity, coefficient of thermal conductivity, and the heat capacities of dry air vary essentially only with temperature. When the temperature exceeds 3500°R, the pressure dependence of these properties of air may become quite significant. Since these three quantities are related to the Prandtl number by the relation $Pr = \frac{\mu C_p}{k}$, if the Prandtl number and any two of the other quantities are known, the remaining quantity may be found.

The Prandtl number may be interpreted physically as representing a qualitative balance between the frictional heating, the heat stored and the heat conducted at a point. The variation of Prandtl number with temperature for $T \leq 1800^\circ R$ is presented in Reference 3. Values of Prandtl number for high temperatures are presented in Reference 2. The variation with temperature and pressure may be conveniently summarized by plotting Prandtl number vs. enthalpy as in Figure 1.

The coefficient of absolute viscosity μ is also presented in Reference 3 for temperatures up to 3420°R. An empirical relationship which fits the data of Reference 3 is

$$\mu = .227 \times 10^{-7} \frac{T^{3/2}}{T + 178.7} \quad (2)$$

where T is in $^{\circ}\text{R}$ and μ has the units of slug/ft. sec. Precise determinations for μ are not available for high temperatures. However, an empirical relation which fits the observed and predicted data reasonably well is presented in Reference 5. This relationship which relates μ to the density ρ and the static enthalpy h is particularly convenient for heat transfer calculations and is given as follows:

$$\frac{\rho\mu}{\rho_B\mu_B} = \left(\frac{h}{h_B}\right)^{-.28} \quad (3)$$

where ρ_B is the density at the local pressure and $T = 400^{\circ}\text{R}$, μ_B is the viscosity at 400°R , and h_B is the static enthalpy at $T = 400^{\circ}\text{R}$. The value of μ_B is $30.4 \times 10^{-8} \frac{\text{slugs}}{\text{ft. sec.}}$ and h_B is 3092 Btu/slug.

The variation of the specific heat at constant pressure with temperature is also presented in Reference 3 for temperatures up to 3400°R . The data is plotted in Figure 2 for a pressure of one atmosphere. The following formula, given in Reference 6, closely represents the values of Reference 3.

$$\frac{C_p}{.06856} = \frac{7}{2} + \frac{5526}{T} \left[-1 + \exp\left(\frac{5526}{T}\right) \right]^{-2} \exp\left(\frac{5526}{T}\right) \quad (4)$$

where T is in $^{\circ}\text{R}$ and C_p has the units of $\frac{\text{Btu}}{\text{lb } ^{\circ}\text{F}}$.

A summary of the state of knowledge concerning the coefficient of thermal conductivity of air has been given in Reference 7. Several

empirical equations which describe the variation of the thermal conductivity with temperature are cited in Reference 7, the most reliable of which are

$$k = .00114T^{1/2} \left[1 + 441.2 T^{-1} \times 10^{-\frac{26.1}{T}} \right]^{-1} \quad (5)$$

and

$$k = .001091T^{3/2} (T + 362)^{-1} \quad (6)$$

where k has the units of BTU/hr. ft²R and T is in degrees Rankine.

Equation 5 is used in the NBS-NACA tables (Ref. 3) up to 1800°R, and is estimated therein to be reliable within four percent. Equations 5 and 6 are plotted in Figure 3. They agree with each other within three percent up to 4460°R.

It is helpful to consider heat transfer processes as resulting from a difference in energy levels between two points. Hence, the difference between the surface temperature and a representative temperature of the surroundings may be considered to be a temperature potential which generates a heat flux. For modes of heat transfer other than radiation, this potential is roughly proportional to the heat flux. At high gas temperatures the static enthalpy h may replace the temperature T as a natural indicator of energy levels with the result that the enthalpy potential replaces the temperature potential as the significant parameter.

The enthalpy $h = h(p, T)$ is a property of the state of the gas. The variation of the enthalpy with pressure and temperature is shown in Figures 4 and 5. For $T \leq 3600^\circ\text{R}$, the enthalpy may be considered to be a function of temperature only, i.e., $h = \int_0^T C_p(T) dT$. For $T < 600^\circ\text{R}$, C_p is essentially constant. For $T \geq 3600^\circ\text{R}$, the air no longer behaves like a perfect gas, but dissociates according to the laws of chemical reaction. High temperature phenomena related to the effects of dissociation are frequently referred to as "real gas" effects.

To characterize more concretely the heat transfer potential of the ambient fluid over a surface, a reference value of temperature or enthalpy may be defined. Values which are often used are the "stagnation" temperature T_s or enthalpy h_s , or the "adiabatic wall" temperature T_{aw} or enthalpy h_{aw} . The latter values are sometimes referred to as recovery values.

Since, under adiabatic conditions, the sum of the enthalpy and kinetic energy per unit mass of fluid remains constant, the stagnation enthalpy is that value of the enthalpy that would be acquired by a moving air mass if an adiabatic deceleration to zero velocity were to occur. On the other hand, the adiabatic wall enthalpy is that value of the enthalpy which would arise at the surface of a solid body if the surface were everywhere perfectly insulated. The adiabatic wall enthalpy is generally different

from the stagnation enthalpy because of viscous, conductive and heat storage effects in the fluid, and because of "slip" and "free-molecule" effects arising at the surface when the flight condition is such that the molecular mean free paths are not much smaller than the surface dimensions so that the fluid does not behave as a continuum. In a continuum the stagnation enthalpy and the adiabatic wall enthalpy are found to be related empirically as follows:

$$\frac{h_{aw} - h_e}{h_s - h_e} = \begin{cases} Pr^{1/2} & \text{for laminar flow} \\ Pr^{1/3} & \text{for turbulent flow} \end{cases} \quad (7)$$

where

$$h_s - h_e = \frac{1}{2} u_e^2 \quad (8)$$

and subscript e denotes conditions at the outer edge of the boundary layer. The right hand side of Equation 7 is referred to as the "enthalpy recovery factor". When the temperatures are sufficiently low the left hand side of Equation 7 may be written in terms of temperatures rather than enthalpies, in which case the right hand side is referred to as the "temperature recovery factor". For air, the Prandtl number is always less than unity, so that the adiabatic wall enthalpy is always less than the stagnation enthalpy.

Another value of the enthalpy which frequently arises in heat transfer calculations is the so-called "reference enthalpy". The reference enthalpy

is an empirically obtained quantity which is found to correlate quite well high speed and low speed boundary layers. It is determined from the following formula

$$h_r = .5h_w + .22 h_s + .28 h_e \quad (9)$$

When the temperature is sufficiently low so that real gas effects may be neglected, the enthalpy may be replaced by the temperature in Equation 9.

As an example of real gas effects, one may calculate the effect of dissociation on say the stagnation temperature at high flight speeds. For example, at the nose of a blunt body which is moving at a supersonic speed, a detached shock wave is formed. At the axis of symmetry, the shock wave is perpendicular to the flow direction and the flow passing through this "normal shock" continues to the nose of the body where it stagnates. Since this process is adiabatic, the value of the stagnation enthalpy may be determined from the principle of conservation of energy

$$h_s = h_f + \frac{1}{2} u_f^2$$

where subscript f denotes flight conditions. It is useful to note that the change in pressure across a normal shock is hardly influenced by real gas effects. Hence, the stagnation pressure behind the shock can be estimated from conventional tables for perfect gases (e.g., Ref. 8). Knowing the pressure and the enthalpy, the stagnation temperature can be determined from Figure 4 or 5. For example, for a body moving at a Mach number of

twenty at an altitude of 100,000 feet, the stagnation temperature, determined in this way is 12,000°R. On the other hand, if the formula for a perfect gas is used, with the low temperature value of $\gamma = 1.4$, i. e.,

$$\frac{T_s}{T_f} = 1 + \frac{\gamma - 1}{2} M_f^2 \quad (11)$$

the stagnation temperature is calculated to be 32,000°R.

The point has recently been discussed (Refs. 9, 10) that certain dissociation effects in thermodynamic processes, such as isentropic processes, and correspondingly in flow phenomena, can be taken into account simply by utilizing reduced constant values of γ . For example, the correct value of stagnation temperature can be obtained quite simply in the illustrative example above by using Equation 11 if it is assumed that $\gamma = 1.15$. Logan and Treanor have indicated that an appropriate value of γ to be used in a particular isentropic process may be obtained by making a log-log plot of the true variation of the quantities in question for a given value of the entropy (using Ref. 4, for example). The appropriate value of γ is then defined from the isentropic expressions for the particular process in question from the slope of the approximately straight line that results. For example, in a true isentropic process with constant γ , the relation between p and ρ is $\frac{p_1}{p_2} = \left(\frac{\rho_1}{\rho_2}\right)^\gamma$. At high temperatures,

the appropriate value of γ can be obtained by plotting (on log-log paper) p vs. ρ at constant entropy using Reference 4, say, and measuring the slope of the straight line that results, since $\ln(p_1/p_2) = \gamma \ln(\rho_1/\rho_2)$. This procedure has been carried out for the special case of a body with a blunt nose. The results are plotted here as a function of flight condition in Figure 6.

4. ATMOSPHERIC PROPERTIES

The variation of ambient pressure, temperature, density and speed of sound is given in Reference 11 for altitudes up to 65,800 feet. Values of these quantities at higher altitudes are given in Reference 12. A summary of this data is given in Figure 7. At altitudes above 250,000 feet, one must take into consideration the changing chemical composition of the atmosphere with altitude. It should be noted that the atmospheric properties appearing in the above-mentioned references are for the so-called "standard day". Data for "hot" and "cold" days may be found in Reference 13.

5. CONVECTIVE HEAT TRANSFER RATES

The calculation of convective heat transfer rates may proceed in several different directions depending on the state of the boundary layer and the shape of the body. In what follows, recommended procedures for the calculation of convective heat transfer are presented. The proposed methods are not necessarily the most accurate, but are believed to represent reasonable procedures for engineering calculations, at least within the state of the art at the present time.

The prediction of heat transfer rates is accomplished by first determining the pressure distribution over the surface neglecting the effects of viscosity. Methods for calculating the inviscid pressure distribution for zero and small angle of attacks have already been summarized. In the procedures recommended below, it is assumed that the pressure distribution is known.

A. Zero Angle of Attack

1. Laminar Boundary Layer

a. Blunt Body

i. Stagnation Point

One of the critical points on a body from the standpoint of aerodynamic heating is the stagnation point. At this point the air

outside the boundary layer reaches its maximum temperature due to the severe compression involved in bringing the air to rest. At sufficiently high speeds the compression of the air is great enough to raise the temperature of the air to a level where the effects of dissociation must be taken into account. Lees (Ref. 15) has obtained an approximate solution to this problem, employing the assumption of thermodynamic equilibrium for which the reaction between atoms and molecules proceeds at an infinitely fast rate. His results were derived assuming in addition that the wall enthalpy is much less than the stagnation enthalpy outside the boundary layer. However, the wall enthalpy can be introduced into the equation he determines for the heat flux by replacing h_{se} by $(h_{se} - h_w)$. This is only a slight modification which should give better results for relatively high wall temperatures. The relation to be used is,

$$q_{w0} = \frac{.50\sqrt{2}}{\bar{Pr}^{2/3}} (h_{se} - h_{sw}) \sqrt{\frac{(\rho_e \mu_e)_0 u_f}{R_0}} G(M_f, \bar{\gamma}, \gamma_f) \quad (12)$$

where

$$G(M_f, \bar{\gamma}, \gamma_f) = \left(\frac{\bar{\gamma} - 1}{\bar{\gamma}} \right)^{1/4} \left(1 + \frac{2}{\gamma_f - 1} \frac{1}{M_f^2} \right)^{1/4} \left(1 - \frac{1}{\gamma_f M_f^2} \right)^{1/4} \quad (13)$$

R_0 is the radius of curvature of the body at the stagnation point. \bar{Pr} is the Prandtl number at some average condition behind the shock wave.

In view of the lack of reliable experimental data for the Prandtl number

at very high temperatures, Lees suggests using $\bar{Pr} = .71$ when the temperature immediately behind the shock wave exceeds 1800°R .

The quantity $\bar{\gamma}$ is the ratio of specific heats which, when used in the ordinary isentropic pressure-density relation, gives approximately the same results as the true pressure-density relation which takes into account the variation of γ due to real gas effects. Logan and Treanor (Ref. 9) have shown that the use of such an average constant value of γ correlates the true variation of pressure with density over large temperature ranges. The variation of $\bar{\gamma}$ with flight conditions is shown in Figure 6.

Probstein (Ref. 16) has indicated that the $p\mu$ product in Equation 12 should be evaluated at some point inside the boundary layer. In a calculated example, he shows that Equation 12 overestimates the heat transfer by about 15% when compared to the result obtained using a more correct value of $p\mu$. On the other hand, it has been suggested that a rough surface may result in increased heat transfer rates. In view of the fact that Probstein's correction requires considerable calculation and that both Equation 12 and Probstein's results apply to smooth bodies, it is suggested that Equation 12 be used without any correction.

ii. Downstream region

Lees has also shown (Ref. 15) that the variation of the laminar heat transfer rate along the surface of the body may be expressed as

$$\frac{q_w}{q_{w0}} = \frac{\frac{1}{2} \frac{p}{p_{s2}} \frac{u_e}{u_f} r_o}{\left[\int_0^s \frac{p}{p_{s2}} \frac{u_e}{u_f} r_o^2 ds \right]^{1/2}} \cdot \frac{\sqrt{R_o}}{G(M_f, \gamma, \gamma_f)} \quad (14)$$

where s is the distance along the body surface measured from the stagnation point, and r_o is the radius of the cross-section of the body of revolution measured at the station s . The pressure and velocity distributions outside the boundary layer are obtained from the inviscid flow solutions as described in Part B. The integral in Equation 14 must generally be evaluated numerically.

b. Pointed body

When the nose of the body is pointed, it is found that the heat transfer rate may be satisfactorily approximated by utilizing the equations for the heat transfer to a flat plate parallel to the air stream with the following modifications. In calculating the heat transfer to a flat plate, the external velocity and pressure are constant. In this application it is assumed that at each point on the body, the heat transfer is that given by the flat plate formula wherein the velocity and pressure are locally equal to the value at the outer edge of the boundary layer at the point in question. In addition, the thermal properties of the air are evaluated at the reference enthalpy (Eq. 9).

On a conical surface, the laminar heat transfer rate is $\sqrt{3}$ times the value for a flat plate. When the body is almost cylindrical, on the other hand, the heat transfer rate is well approximated by the flat plate formula. The factor "A" is therefore inserted into Equation 15 below to take into account the transition from the cone heat transfer value to the flat plate heat transfer value. It is assumed that it is conservative to begin the change from the conical to the flat plate value when the inclination of the surface of the body of revolution with respect to the axis of the body has the value $\Theta = 25^\circ$.

The recommended formula for the calculation of the heat transfer then takes the form:

$$q_w = \frac{.332 A \rho_r u_e}{(\text{Pr}_r)^{2/3} (\text{Re}_r)^{1/2}} (h_{aw} - h_w) \quad (15)$$

where

$$A = \begin{cases} \sqrt{3} & \Theta \geq 25^\circ \\ (\sqrt{3} - 1) \frac{\Theta^\circ}{25} + 1 & \Theta \leq 25^\circ \end{cases}$$

and where the subscript r implies that the fluid properties are to be evaluated at the reference enthalpy and the pressure corresponding to the local external pressure. The value h_{aw} is obtained from Equation 7, and

$$\text{Re}_r = \frac{\rho_r u_{ex}}{\mu_r} \text{ is the local Reynolds number.}$$

It should be noted that this equation for the heat transfer predicts an infinite heat transfer rate at the nose of a pointed body. However, since $q_w \rightarrow \infty$ as $x^{-1/2}$, it is found that the total heat transfer to the nose region, which is obtained by integrating q_w over the surface through which heat is being transferred, is finite, since $\int_0^x q_w dx \sim x^{1/2}$. In practice, it is sufficient, for the purpose of heat conduction calculations to approximate the heat transfer distribution in the immediate neighborhood of the nose by a linear variation which gives the same total heat transfer as Equation 15. In any case, it is conventional to assume that the temperature at the apex of a completely insulated sharp-nosed body is the adiabatic wall temperature.

2. Turbulent Boundary Layer

When a fluid flows over a smooth body, it generally starts out at the stagnation point as a laminar flow. In some region downstream, the transition to a turbulent flow takes place. The mechanism of transition and the transport of momentum and energy by the turbulent fluctuations is still not well understood. For this reason, the analysis of turbulent boundary layer heat transfer rates is largely empirical.

Several comparisons of the various approximate methods of analysis have been made with experimental results (see, for example, Ref. 17).

It has been found that for engineering purposes, a reasonably accurate, and consistently conservative method consists of using the analysis for the turbulent heat transfer rate to a flat plate. As in the laminar case, the values of pressure and external velocity to be used are the local values at the point in question. Also, the reference enthalpy method is used again.

The formula for the turbulent heat transfer rate may be written as

$$Nu = \frac{q_w x Pr}{(\mu_r \rho_r)(h_{aw} - h_w)} = .03 \frac{(Re_r)^{4/5}}{(Pr_r)^{2/3}} \quad (16)$$

In this formula, x is taken to be the distance from the nose of the body measured along the body surface and the quantity Nu is a nondimensional heat transfer parameter, termed the Nusselt number.

When a detached shock wave exists ahead of the nose of the body, the various quantities entering into Equation 16 have been calculated, and are presented here in Figures 8-10 as a function of local pressure, for various flight conditions of interest. Real gas effects were taken into account as follows. The $p\mu$ product was calculated according to Equation 3. The Prandtl number was taken from Figure 1. The properties of state were taken from Reference 3 for $T < 3600^\circ R$, and from Reference 4 for $T \geq 3600^\circ R$. For flight Mach numbers of $M \geq 6$, the isentropic relations were used for

the $p(\rho)$ and $p(T)$ variations, except that in each case the value of γ used was that given by Figure 6. It should be noted that the data of Reference 3, for air, are slightly in error at the higher temperatures. Hence, if one must consider a temperature range which necessitates the use of both References 3 and 4, a slight discontinuity in the thermodynamic variables is observed. This discontinuity, together with the fact that when calculating local velocities at high flight Mach numbers, one must calculate small differences of large numbers (enthalpies), makes the calculations at the higher Mach numbers tend to be less accurate. The apparently irregular behavior of the curves of Figures 8-10 should be interpreted in this light.

If the nose of the body is pointed with an apex angle sufficiently small so that the shock wave remains attached, the compression experienced by the gas in passing through the shock wave is sufficiently small that real gas effects and detailed tip effects can be neglected for design purposes in the Mach number range under consideration. Hence, Equation 16 may be applied directly without any corrections for real gas effects. However, as in the laminar case, the heat transfer on a conical surface is higher than that on a flat surface. However, the turbulent heat transfer on a cone is only about fifteen percent greater than the turbulent heat transfer on a flat surface. It is therefore recommended that in the analysis of a pointed body, Equation 16 be used with the numerical factor .03 replaced by .0345.

3. Transition

As mentioned previously, the boundary layer begins, at the nose of a body, as a laminar boundary layer. At some point on the surface of the body, the transition to a turbulent boundary layer takes place. Since the turbulent heat transfer rates are substantially higher than the laminar rates except in the immediate vicinity of the nose, it is important to determine the location of the transition point. Unfortunately, a reliable method for determining the transition point has not yet been developed. Some success has been had in several special cases (e.g., References 19, 20, 21). However, the position at which transition occurs depends on a large number of parameters (e.g., pressure gradient, surface roughness, surface temperature, Mach number, free stream turbulence, etc.), some of which are not easily evaluated. Hence, the reliability of these methods is usually in doubt.

As a rough measure of when to change from a laminar boundary analysis to a turbulent boundary layer analysis, one may use the following method for the blunt nose case. Carry both the laminar and turbulent boundary layer analyses to the point where the two curves of laminar heat transfer and turbulent heat transfer intersect (see Fig. 11). Use the laminar boundary layer analysis for the region upstream and the turbulent boundary layer analysis for the region downstream of the intersection point. It

should be noted that this method does not really predict a transition point.

Rather, it gives a conservative design method by using the analysis which predicts the higher heat transfer at a given point. Actually, it is conceivable that in the small region in which the change from a fully laminar to a fully turbulent boundary layer takes place, the heat transfer may be higher than either the laminar or the turbulent rates. However, no method has yet been devised for calculating the heat transfer in the transition region. Furthermore, it is possible that the transition to turbulence may occur at a position prior to that indicated by the intersection of the laminar and turbulent values. However, this possibility cannot be taken into account in a general way without making a precise evaluation of the location of the transition region. Hence, a reasonable preliminary design procedure would be to assume that this will not occur. An additional degree of conservatism may be obtained by fairing the curves together in the region of the intersection point as indicated by the dotted line in Figure 11.

When the nose of the body is pointed, the predicted turbulent heat transfer rate increases as the vertex is approached, and, hence, the method outlined above does not apply. The most conservative procedure in this case is to assume that the boundary layer is turbulent over the entire body. If this assumption results in an intolerable design, one must resort to experimental data to determine the transition point.

As pointed out above, the location of the transition point depends on factors such as surface cooling and heating, body shape and pressure gradient, surface roughness, and body forces such as those due to acceleration and deceleration. In References 22, 23, and 14, critical discussions are presented on all but the last of the factors mentioned above. It appears that while, in some cases, the correlation of experimental transition data may be accomplished using the proposed theories, in general, additional factors, beyond those with which the theories are concerned, must be taken into account. It is suggested therefore that the reader use the method proposed above as a first approximation. If a better approximation is desired, the reader is referred to References 22, 23, and 14 for surveys of experimental data. The location of the transition point by the proposed method should at least fall within the range predicted by the experimental data.

It must be emphasized, however, that the correlation of experimental wind tunnel data with actual flight results has not yet reached a reliable state of the art, as regards transition. The determination of the transition point is therefore strongly dependent on the degree of conservatism which the designer employs.

B. Bodies at Angle of Attack

When the axis of the body is not aligned with the line of flight of the body, the body is said to be yawed or at an angle of attack. The pressure

distribution changes appreciably when the angle of attack, α , is altered and so the heat transfer rates also change. The problems of heat transfer and pressure distribution become considerably more complicated when the angle of attack is not zero. At present, no satisfactory theoretical solution has been obtained for either of these problems for a blunt body. Approximate methods for determining the pressure distribution are outlined in Reference 18. The best that can be done at this time is to recommend an empirical approach to the problem which should be satisfactory for engineering purposes.

For blunt bodies, the recommended procedure is as follows: Draw the profile of the body in a meridian plane containing the plane of yaw. Draw the line parallel to the remote velocity vector, which intersects the surface of the body normal to a local tangent (see Fig. 12). This point of intersection is to be regarded as the new stagnation point. Since the flow is no longer axially symmetric, the heat transfer distribution will be different in each meridian plane. To calculate the heat transfer in any meridian plane, consider, for example, the meridian plane shown in Figure 12. Assume that the line AB is an axis of symmetry, so that in each plane one can generate 2 bodies of revolution, one corresponding to the upper part of the profile COC' and one corresponding to the lower part of the profile DOD'. Calculate the heat transfer to each part of the

actual body, using the methods suggested for the zero angle of attack case, assuming that each contour is part of the body of revolution generated as described above. This procedure should be carried out for a sufficient number of meridian planes so that the variation of heat transfer with meridian angle can be determined.

For pointed bodies, the same procedure is used as for the case of a blunt body except that the new axis of revolution is simply a line parallel to the remote velocity vector passing through the apex of the body. (See Addendum)

If the angle of attack becomes sufficiently large, it is possible that the boundary layer may become separated from the surface. In this case a region of low velocity turbulent air exists between the surface and the boundary layer. Unfortunately, the prediction of both the point of separation and heat transfer rates in separated flow have not yet reached a satisfactory degree of reliability. Chapman (Ref. 18) has developed an approximate method for predicting heat transfer rates when the boundary layer is either laminar or turbulent just ahead of the point of separation. His results indicate that if the boundary layer is laminar at the point of separation, the heat transfer in the separated region is lower than the laminar value; on the other hand, if the boundary layer is turbulent at the point of separation, the heat transfer may be higher in the separated region. However, there is not yet sufficient experimental evidence to bear out Chapman's predictions.

In view of the present state of the art of predicting heat transfer in separated regions, it can only be suggested that a turbulent heat transfer rate be used in regions of separated flow. This procedure will at least yield a conservative design.

6. CONCLUDING REMARKS

Procedures have been presented by which estimates of the heat transfer rates can be made for radome shaped bodies in flight, that is, blunt-nosed and pointed-nosed bodies of revolution. Non-axially symmetric shapes have not been considered. A brief qualitative account has been given of the physical nature of various modes of heat transfer and the governing parameters. The thermal properties of air and atmospheric properties required for execution of the procedures have been presented in chart form. Primary emphasis has been given to flight conditions between Mach numbers of 0 to 12 at altitudes up to 150,000 ft. Laminar and turbulent heat rates for both zero and moderate angles of attack have been treated. Real gas effects have been included in a manner sufficient for most engineering purposes. Charts for facilitating computation procedures have been constructed.

REFERENCES

1. Bloom, M. H. - Thermal Conditions Associated with Aircraft in Flight - WADC Technical Report 55-169, March 1956.
2. Bloom, M. H. - External Sources of Heat (in Aeronautics) - Chapter 2 of High Temperature Effects in Aircraft Structures (N.J. Hoff, editor)- NATO AGARDograph.
3. Hilsenrath, J. et al - Tables of Thermal Properties of Gases - National Bureau of Standards Circular 564, November 1955.
4. Hilsenrath, J. and Beckett, C. W. - Tables of Thermodynamic Properties of Argon-Free Air to 15,000°K - AEDC TN 56-12, September 1956.
5. Romig, M. F. - Stagnation Point Heat Transfer for Hypersonic Flow - Jet Propulsion, Vol. 26, No. 12, p. 1098, December 1956.
6. Donaldson, C. DuP. - Note on the Importance of Imperfect-Gas Effects and Variation of Heat Capacities on the Isentropic Flow of Gases - NACA RM No. L8J14, December 10, 1948.
7. Glassman, I. and Bonilla, C. F. - Thermal Conductivity and Prandtl Number of Air at High Temperatures - Chemical Engineering Progress Symposium Series, Vol. 49, No. 5, 1953. Published by American Institute of Chemical Engineers.

8. Ames Research Staff - Equations, Tables and Charts for Compressible Flow - NACA Technical Report 1135.
9. Logan, J. and Treanor, C. - Polytropic Exponents for Air at High Temperatures - Journal of the Aeronautical Sciences, Vol. 24, No. 6, p. 467, June 1957.
10. Ferri, A. and Libby, P. - The Hypersonic Facility of the Polytechnic Institute of Brooklyn and Its Application to Problems of Hypersonic Flight - Presented at the AGARD WT and MT Panel, Netherlands, July 1957.
11. ICAO and NACA - Standard Atmosphere - Tables and Data for Altitudes to 65,800 Feet - NACA Technical Report 1235, 1955.
12. Anon. - Standard Atmosphere (ICAO Extension) - Jet Propulsion, Vol. 26, No. 12, p. 1097, December 1956.
13. ANA Bulletin No. 421
14. Rubesin, M. W., Rumsey, C. B. and Varga, S. A. - A Summary of Available Knowledge Concerning Skin Friction and Heat Transfer and Its Application to the Design of High-Speed Missiles - NACA RM A51J25a, 1951.
15. Lees, L. - Laminar Heat Transfer Over Blunt-Nosed Bodies at Hypersonic Flight Speeds - Jet Propulsion, Vol. 26, No. 4, p. 259, April 1956.

16. Probst, R. - Methods of Calculating the Equilibrium Heat Transfer Rate at Hypersonic Flight Speeds - Jet Propulsion, Vol. 26, No. 6, p. 497, June 1956.
17. Libby, P. A. and Cresci, R. J. - Evaluation of Several Hypersonic Turbulent Heat Transfer Analyses by Comparison with Experimental Data - WADC TN 57-72, July 1957.
18. Chapman, D. R. - A Theoretical Analysis of Heat Transfer in Regions of Separated Flow - NACA TN 3792, 1956.
19. Lees, L. and Lin, C. C. - Investigation of the Stability of a Laminar Boundary Layer in a Compressible Fluid - NACA TN 1115, 1946.
20. Lees, L. - The Stability of the Laminar Boundary Layer in a Compressible Fluid - NACA Report 876, 1947.
21. Lees, L. - Stability of the Supersonic Laminar Boundary Layer with a Pressure Gradient - Princeton University, Aeronautical Engineering Laboratory Report No. 167, November 20, 1950.
22. Probst, R. F. and Lin, C. C. - A Study of the Transition to Turbulence of the Laminar Boundary Layer at Supersonic Speeds - I. A. S. Preprint No. 596, 1956.

23. Czarnecki, K. R. and Sinclair, A. R. - Factors Affecting Transition
at Supersonic Speeds - NACA RM L53I18a, 1953.

BIBLIOGRAPHY

(This list consists of typical works; it is not exhaustive or arranged chronologically.)

1. L. Howarth (editor) - Modern Developments in Fluid Dynamics, High Speed Flow - Oxford at the Clarendon Press, London 1953.
2. H. Schlichting - Boundary Layer Theory - McGraw-Hill, New York, 1955.
3. A. H. Shapiro - The Dynamics and Thermodynamics of Compressible Fluid Flow - Ronald Press, New York 1953.
4. S. I. Pai - Fluid Dynamics of Jets - Van Nostrand, New York, 1955.
5. H. Gortler and W. Tollmien (editors) - Fifty Years of Boundary Layer Research - I. R. Maxwell, London, 1955.
6. G. N. Patterson - Molecular Flow of Gases - Wiley, New York, 1956.
7. J. O. Hirschfelder, C. O. Curtiss, and R. B. Bird - Molecular Theory of Gases and Liquids - Wiley, New York, 1954.
8. S. S. Penner - Chemical Reactions in Flow Systems, AGARD, NATO, Butterworths, London, 1955.
9. R. C. L. Bosworth - Heat Transfer Phenomena - Wiley, New York, 1952.
10. H. W. Liepmann and A. Roshko - Elements of Gas Dynamics, Wiley, New York, 1957.
11. M. Bloom - Thermal Conditions Associated with Aircraft in Flight - U.S. Air Force WADC TR 55-169, March 1956 (Polytechnic Institute of Brooklyn, PIBAL Rept. 241, Jan. 1954). Also see N. J. Hoff, et al., Theory and Experiment in the Solution of Structural Problems of Supersonic Aircraft. U.S. Air Force WADC TR 55-291, March 1956. Also see M. Bloom, Appendix I of The Structural Effects of Aerodynamic Heating by N. J. Hoff, AGARD Proceedings Third General Assembly AG 6/P3 September 1953.

12. E. R. G. Eckert - Survey on Heat Transfer at High Speeds - U.S. Air Force WADC TR 54-70, April 1954.
13. M. W. Rubesin, C. B. Rumsey, and S. A. Varga - A Summary of Available Knowledge Concerning Skin Friction and Heat Transfer and Its Application to the to the Design of High-Speed Missiles - NACA RM A51J25a, November 9, 1951.
14. Heat Transfer, A Symposium (contributors: A. S. Faust, S. S. Manson, H. F. Poppendiek, W. M. Rohsenow, M. Summerfield, E. R. G. Eckert, M. Tribus and J. Klein, S. A. Schaaf, R. V. Churchill) Held at University of Michigan in 1952, Engineering Research Institute, University of Michigan, 1953.
15. Fundamentals Review, Industrial and Engineering Chemistry, American Chemical Society, Washington, D. C., March 1955. Contributors: E. F. Johnson; A. K. Oppenheim and R. R. Hughes; E. R. G. Eckert, J. P. Hartnett, and H. S. Isbin; C. R. Wilke; C. O. Bennett and J. M. Smith.
16. T. von Karman - Solved and Unsolved Problems of High-Speed Aerodynamics - Proc. of Conf. on High-Speed Aeronautics, Polytechnic Institute of Brooklyn, New York, January 1955.
17. M. Roy - Aerodynamic Heating Versus Speed - Thermodynamic Aspects of the Struggle - AGARD Proceedings Fifth General Assembly AG 20/P10, June 1955.
18. M. Finston - Survey on the Present Status of Supersonic Heat Transfer - M.I.T. Naval Supersonic Lab. TR 62, December 1954.
19. J. A. F. Hill - Supersonic Heat Transfer Coefficients for Engineering Use - M.I.T. Naval Supersonic Lab. Internal Memo A. and R. 110, February 1954, ASTIA, AD 69305.
20. J. Kaye - Survey of Friction Coefficients, Recovery Factors and Heat Transfer Coefficients for Supersonic Flow - Journal of the Aeronautical Sciences, Vol. 21, No. 2, 1954, pp. 117-129.
21. H. H. Kurzweg - The Status of Heat Transfer and Friction Investigations at Supersonic Speeds - Seventh Meeting, WT and MT Panel. AGARD, NATO, June 1955.

22. E. R. Van Driest - The Problem of Aerodynamic Heating - Aeronautical Engineering Review, V. 15, No. 10, October 1956, pp. 26-41.
23. W. H. Dorrance - Some Problems in the Aerothermodynamics of Hypersonic Flight - Aeronautical Engineering Review, Vol. 16, No. 1, January 1957, pp. 26-28, 46.
24. T. Nonweiler - Aerodynamic Heating at High Speeds - Journal of the British Interplanetary Society, Vol. 10, No. 4, July 1951, pp. 160-176.
25. J. R. Stalder - A Survey of Heat Transfer Problems Encountered by Hypersonic Aircraft - American Rocket Society Preprint 457-57, June 1957.
26. J. F. Brahtz and A. Dean - An Account of Research Information Pertaining to Aerodynamic Heating of Airframe, Part II, Bibliography, V. I., External Environment - Aerophysics Development Corp., U.S. Air Force WADC TR 55-99, March 1955.
27. M. S. Krzwoblocki - The Forces Acting on an Air Vehicle - A Review of the Literature, Advisory Board on Simulation, University of Chicago, January 1955.
28. J. J. Brophy - A Report Bibliography on Thermoaerodynamics - ASTIA, AD 24885, January 1954.
29. F. K. Moore and S. Ostrach - Average Properties of Compressible Laminar Boundary Layer on Flat Plate with Unsteady Flight Velocity - NACA TN 3886, December 1956.
30. N. A. Carhart - The Problem of Cooling Electronic Equipment in High Performance Aircraft - Aeronautical Engineering Review, Vol. 15, No. 5, May 1956, pp. 76-81, 109.
31. J. P. Welsh - Cooling Procedures Necessary to Avionic Reliability - Aeronautical Engineering Review, Vol. 15, No. 5, May 1956, pp. 110-113.
32. Anon., Heat Transfer in Minaturized Electronic Equipment - U.S. Government Printing Office. Catalog No. D211.2: E1 2/2, 1956.

33. Anon., Guide Manual of Cooling Methods for Electronic Equipment - U. S. Government Printing Office. Catalog No. D211.6: E1 2/2, 1956.
34. J. G. Logan, Jr. - Relaxation Phenomena in Hypersonic Aerodynamics - IAS Preprint 728, January 28, 1957.
35. J. S. Evans - Method for Calculating Effects of Dissociation on Flow Variables in the Relaxation Zone Behind Normal Shock Waves - NACA TN 3860, December 1956.
36. J. Hilsenrath and C. W. Beckett - Tables of Thermodynamic Properties of Argon-Free Air to 15000°K - AEDC TN 56-12, ASTIA No. AD 98974. Arnold Engineering Development Center and U.S. National Bureau of Standards, September 1956.
37. J. G. Logan, Jr. - Thermodynamic Charts for High Temperature Air Calculations - Cornell Aeronautical Labs., Inc. Report AD 1052-A-3, AF OSR TN 56-342, ASTIA No. AD 95218, July 1956.
38. M. F. Romig - The Normal Shock Properties for Air in Dissociation Equilibrium - Journal of the Aeronautical Sciences, Reader's Forum, Vol. 23, No. 2, February 1956, pp. 185-186.
39. W. E. Moeckel - Oblique Shock Relations at Hypersonic Speeds for Air in Chemical Equilibrium - NACA TN 3895, January 1957.
40. S. Feldman - Hypersonic Gas Dynamic Charts for Equilibrium Air - AVCO Research Laboratory, Everett, Massachusetts, January 1957.
41. L. L. Moore - A Solution of the Laminar Boundary-Layer Equations for a Compressible Fluid with Variable Properties, Including Dissociation - Journal of the Aeronautical Sciences, Vol 19, No. 8, August 1952, pp. 505-518.
42. S. Feldman - The Chemical Kinetics of Air At High Temperatures: A Problem in Hypersonic Aerodynamics - 1957 Heat Transfer and Fluid Mechanics Institute, Stanford University Press, June 1957.
43. P. H. Rose and F. R. Riddell - An Investigation of Stagnation Point Heat Transfer in Dissociated Air - 1957 Heat Transfer and Fluid Mechanics Institute, Stanford University Press, June 1957.

44. L. Lees - Laminar Heat Transfer Over Blunt-Nosed Bodies at Hypersonic Flight Speeds - Jet Propulsion, Vol. 26, No. 4, p. 259, April 1956.
45. J. A. Fay, F. R. Riddell and N. H. Kemp - Stagnation Point Heat Transfer in Dissociated Air Flow - Jet Propulsion, Vol. 27, No. 6, p. 672, June 1957.
46. J. Keck, B. Kivel and T. Wentink, Jr. - Emissivity of High Temperature Air - 1957 Heat Transfer and Fluid Mechanics Institute, Stanford University Press, June 1957.
47. C. F. Hansen - Prandtl Number for Dissociated Air - Journal of the Aeronautical Sciences, Vol. 20, No. 11, p. 789, November 1953.
48. M. F. Romig - Stagnation Point Heat Transfer for Hypersonic Flow - Jet Propulsion, Vol. 26, No. 12, p. 1098, December 1956.
49. J. G. Logan and C. E. Treanor - Polytopic Exponents for Air at High Temperatures - Journal of the Aeronautical Sciences, Vol 24, No. 6, p. 467, June 1957.
50. A. Ferri and P. A. Libby - The Hypersonic Facility of the Polytechnic Institute of Brooklyn and Its Application to Problems of Hypersonic Flight - Presented at the AGARD WT and MT Panel, Netherlands, July 1957.
51. N. Rott - Unsteady Viscous Flow in the Vicinity of a Stagnation Point - Quarterly of Applied Mathematics, Vol. 13, No. 4, p. 444, 1955.
52. H. E. Roberts - The Earth's Atmosphere - Aeronautical Engineering Review, Vol. 8, No. 10, p.18, October 1949.
53. Anon., Standard Atmosphere (ICAO Extension) - Jet Propulsion, Vol. 26, No. 12, December 1956, p. 1097.
54. J. Kaplan, G. F. Schilling, and H. K. Kallman - Methods and Results of Upper Atmosphere Research, Geophysical Research Papers No. 43, AFCRC TR 55-224, Air Force Cambridge Research Center, November 1955.

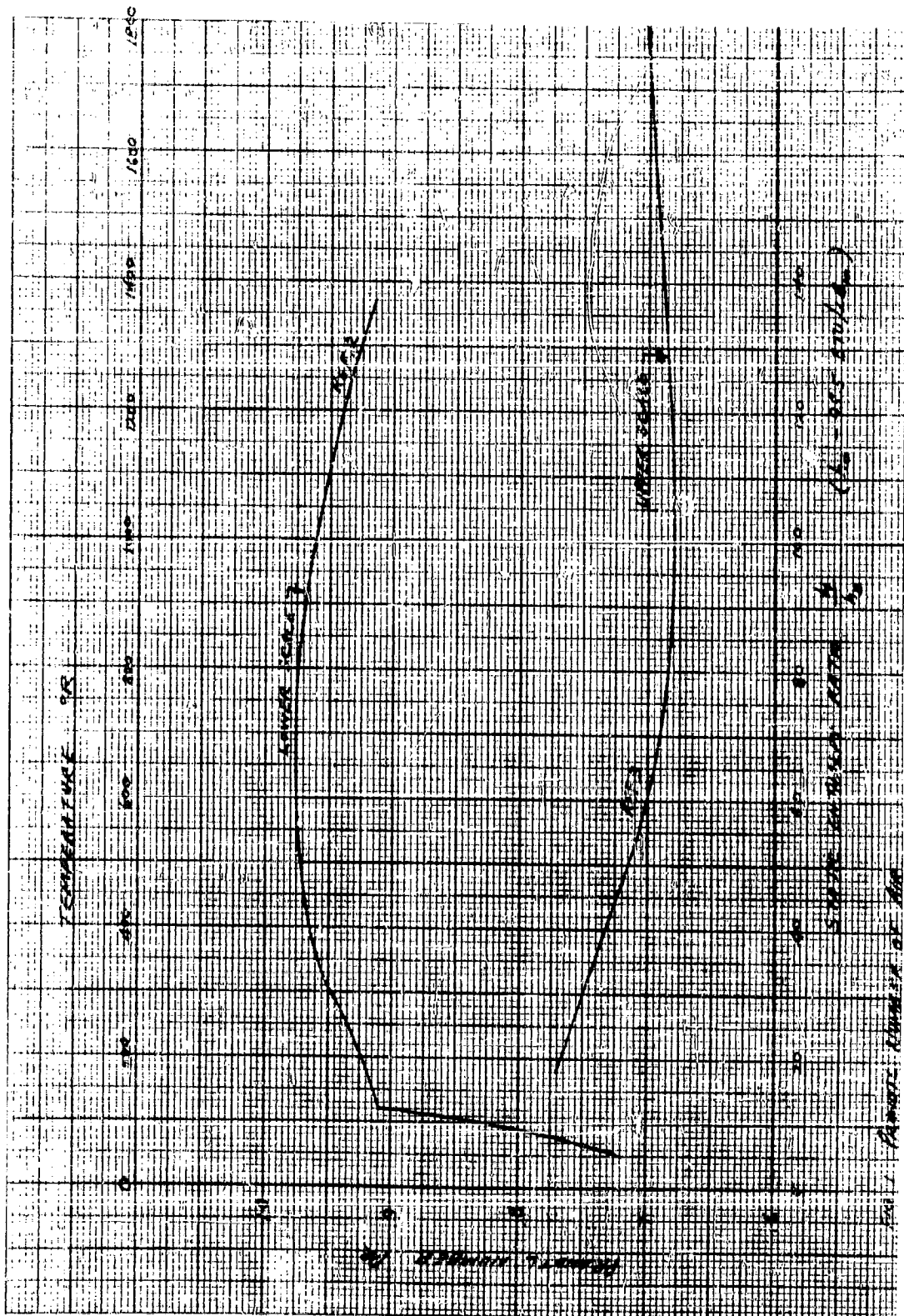
55. C. N. Warfield - Tentative Tables for the Properties of the Upper Atmosphere - NACA TN 1200, January 1947.
56. R. E. Holzer and W. E. Smith - Proceedings on the Conference on Atmospheric Electricity - Geophysical Research Papers, No. 42, AFRC TR 55-222, Air Force Cambridge Research Center, November 1955.
57. D. Brunt - Physical and Dynamical Meteorology - Second Ed., Cambridge University Press, 1952.
58. C. F. Hansen - Some Characteristics of the Upper Atmosphere Pertaining to Hypervelocity Flight - American Rocket Society Preprint 458-57, June 1957.
59. E. H. Kennard - Kinetic Theory of Gases - McGraw-Hill, New York, 1938.
60. H. S. Tsien - Superaerodynamics - Journal of the Aeronautical Sciences, Vol. 13, No. 12, December 1946, pp. 653-664.
61. S. A. Schaaf - Rarified Gas Dynamics - Applied Mechanics Reviews, Vol. 9, No. 10, p. 413, October 1956.
62. S. A. Schaaf - Theoretical Considerations in Rarified Gas Dynamics - Heat Transfer Symposium, Engineering Research Institute, University of Michigan, 1953.
63. L. Lees - Recent Developments in Hypersonic Flow - American Rocket Society, Preprint 455-57, June 1957.
64. N. H. Kemp and F. R. Riddell - Heat Transfer to Satellite Vehicles Re-entering the Atmosphere - American Rocket Society, Preprint 358-56, November 1956.
65. K. A. Ehricke - The Satelloid - Astronautica Acta, Vol. 2, 1956.
66. D. J. Masson and C. Gazley, Jr. - Surface-Protection and Cooling Systems for High-Speed Flight - Aeronautical Engineering Review, Vol. 15, No. 11, p. 46, November 1956.

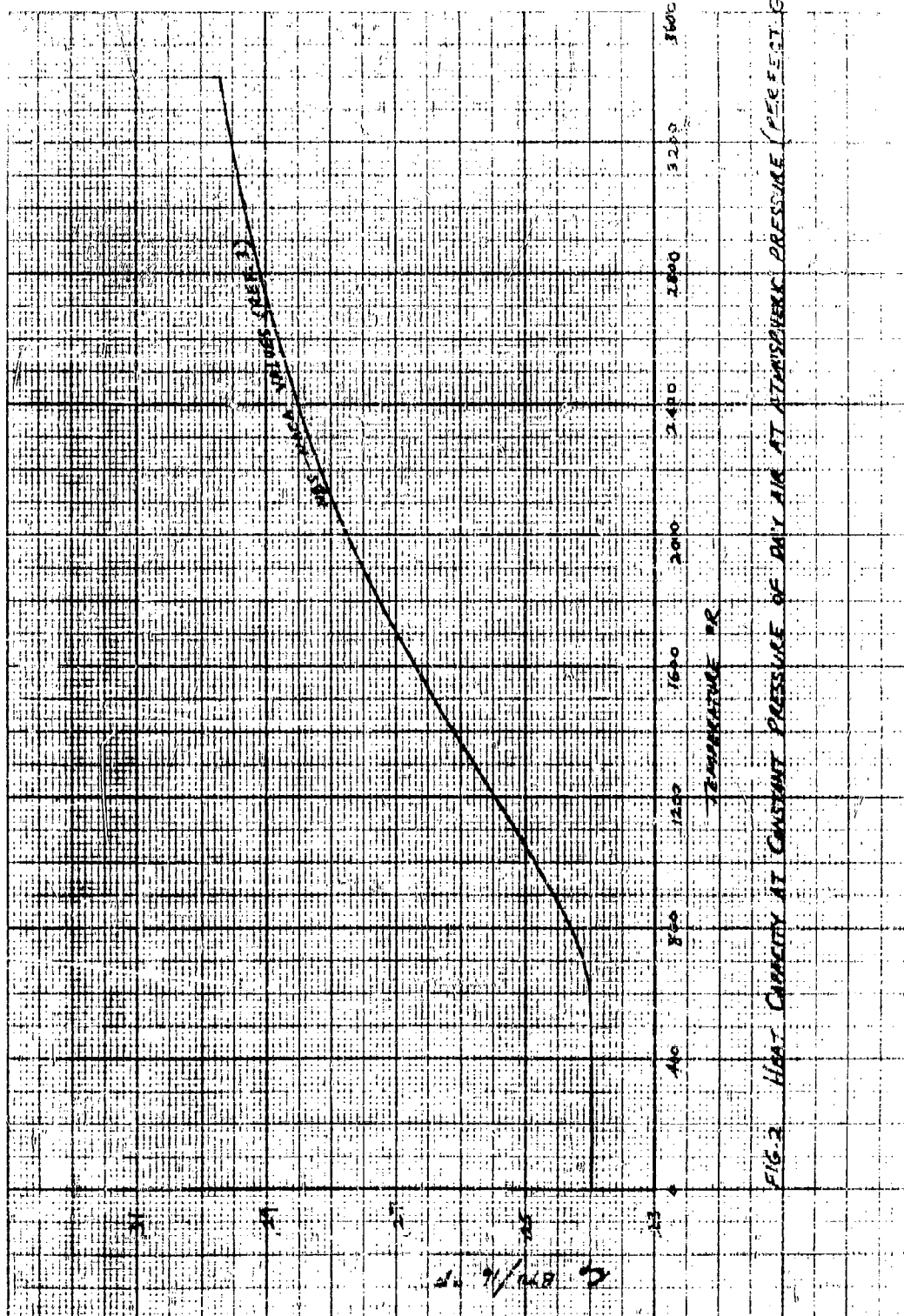
67. H. J. Allen and A. J. Eggers, Jr. - A Study of the Motion and Aerodynamic Heating of Missiles Entering the Earth's Atmosphere at High Supersonic Speeds - NACA RM A53D28, August 25, 1953.
68. J. F. Vandrey - Upper Bounds and Conservative Estimates for Aerodynamic Heating at Great Altitudes - Jet Propulsion, Vol. 27, No. 5, p. 522, May 1957.
69. A. J. Eggers, Jr. - Performance of Long Range Hypervelocity Vehicles - American Rocket Society, Preprint 456-57, June 1957.
70. E. R. G. Eckert - Engineering Relations for Friction and Heat Transfer to Surfaces in High Velocity Flow - Journal of the Aeronautical Sciences, Vol. 22, No. 8, p. 585, August 1955.
71. L. Lees - On the Boundary Layer Equations in Hypersonic Flow and Their Approximate Solutions - Journal of the Aeronautical Sciences, Vol 20, No. 2, p. 143, February 1953.
72. Ting-Yi Li and H. T. Nagamatsu - Hypersonic Viscous Flow on a Non-insulated Flat Plate - Proceedings of the Fourth Midwestern Conference on Fluid Mechanics, Purdue University, September 1955.
73. C. B. Cohen and E. Roshotko - The Compressible Laminar Boundary Layer with Heat Transfer and Arbitrary Pressure Gradient - NACA TN 3326, April 1955.
74. E. Roshotko and I. Beckwith - Compressible Laminar Boundary Layer Over a Yawed Infinite Cylinder With Heat Transfer and Arbitrary Prandtl Number - NACA TN 3986, June 1957.
75. F. K. Moore - Three-Dimensional Boundary Layer Theory - Advances in Applied Mechanics, Academic Press, New York, 1956.
76. A. May and T. J. Williams - Free Flight Ranges at the Naval Ordnance Laboratory - U.S. Naval Ordnance Laboratory, NAVORD Report 4063, July 18, 1955.
77. A. Seiff - A Free-Flight Wind Tunnel for Aerodynamic Testing at Hypersonic Speeds - NACA Report 1222, 1955.

78. A. J. Eggers, Jr. - A Method for Simulating the Atmospheric Entry of Long Range Ballistic Missiles - NACA RM A55115, December 1955.
79. D. H. Crawford and Wm. D. McCauley - Investigation of the Laminar Aerodynamic Heat-Transfer Characteristics of a Hemisphere-Cylinder in the Langley 11-Inch Hypersonic Tunnel at a Mach Number of 6.8 - NACA TN 3706, July 1956.
80. M. H. Bloom and A. Pallone - Heat Transfer to Surfaces in the Neighborhood of Protuberances in Hypersonic Flow - U. S. Air Force WADC TN 57-95, 1957 Heat Transfer and Fluid Mechanics Institute, California Institute of Technology, June 1957.
81. M. H. Bloom - A High Temperature-Pressure Air Heater (Suitable for Intermittent Hypersonic Wind-Tunnel Operation) U.S. Air Force WADC TN 55-694, November 1956.
82. A. Ferri, P. A. Libby, M. H. Bloom and V. Zakkay - Development of the Polytechnic Institute of Brooklyn Hypersonic Facility, U. S. Air Force WADC TN 55-695, November 1955.
83. A. Ferri and M. H. Bloom - Achievement of High Heat Fluxes in a Wind Tunnel - May 9, 1957 - Journal of the Aeronautical Sciences Reader's Forum.
84. D. R. Chapman - Some Possibilities of Using Gas Mixtures Other Than Air in Aerodynamic Research - NACA Report 1259, 1956.
85. A. P. Sabol and J. S. Evans - Investigation of the Use of the Thermal Decomposition of Nitrous Oxide to Produce Hypersonic Flow of a Gas Closely Resembling Air - NACA TN 3624, March 1956.
86. A. Ferri and P. A. Libby - A New Technique for Investigating Heat Transfer and Surface Phenomena Under Hypersonic Flow Conditions - Journal of the Aeronautical Sciences, Reader's Forum, Vol. 24, No. 6, p. 464, June 1957.
87. A. Hertzberg - The Application of the Shock Tube to the Study of the Problems of Hypersonic Flight - Jet Propulsion, Vol. 26, No. 7, p. 549, July 1956.

88. A. Hertzberg - The Application of the Shock Tube to the Study of High Temperature Phenomena in Gases - Applied Mechanics Review, Vol. 9, No. 12, December 1956.
89. A. Hertzberg and R. Weatherston - A New Method for Providing Continuous High Temperature Air Flow for Hypersonic Research - Cornell Aeronautical Laboratory Inc., U.S. Air Force, AFOSR Contract No. AF 18(603)-19, January 1957.
90. S. A. Schaaf - Experimental Methods and Results in Rarified-Gas Dynamics - Heat Transfer Symposium, Engineering Research Inst., University of Michigan, 1953.
91. W. R. Sears - A Brief Review of Three-Dimensional Boundary Layer Flows - Seventh Meeting, WT and MT Panel AGARD, NATO, June 1955.
92. A. Ferri, and A. Pallone - Note on the Flow Fields on the Rear Part of Blunt Bodies - U. S. Air Force WADC TN 56-294, July 1956.
93. L. Trilling - Viscous Flows Near Side Edges and Leading Edges - U. S. Air Force AFOSR TN No. 55-220, June 1955.
94. E. R. G. Eckert, J. P. Hartnett and R. Birkebak - Simplified Equations for Calculating Local and Total Heat Flux to Nonisothermal Surfaces - Journal of the Aeronautical Sciences, Vol. 24, No. 7, p. 549, July 1957.
95. N. J. Hoff - Notes on Thermal Effects in Structures - Polytechnic Institute of Brooklyn, 1957.
96. R. F. Probst and C. C. Lin - A Study of the Transition to Turbulence of the Laminar Boundary Layer at Supersonic Speeds - Institute of the Aeronautical Sciences, Preprint 596, January 1956.
97. A. M. O. Smith and N. Gamberoni - Transition, Pressure Gradient and Stability Theory - Douglas Aircraft Company, Inc., Report No. ES 26388, August 31, 1956.
98. V. J. Rossow - On Flow of Electrically Conducting Fluids Over a Flat Plate in the Presence of a Transverse Magnetic Field - NACA TN 3971, May 1957.

99. J. L. Neuringer - Two-Dimensional Flow in the Vicinity of the Stagnation Point of an Incompressible, Viscous, Electrically Conducting Fluid in the Presence of a Magnetic Field - Republic Aviation Corporation, June 12, 1957.
100. D. Altman and H. Wise - Effect of Chemical Reactions in the Boundary Layer on Convection Heat Transfer - Jet Propulsion, Vol. 26, No. 4, p. 256, April 1956.
101. D. R. Bartz - A Simple Equation for Rapid Estimation of Rocket Nozzle Convective Heat Transfer Coefficients - Jet Propulsion, Vol. 27, No. 1, p. 49, January 1957.
102. W. Unterberg - An Analysis of Heating Problems in Supersonic Ramjet Tailpipes - Jet Propulsion, Vol. 27, No. 5, p. 514, May 1957.
103. D. R. Chapman - A Theoretical Analysis of Heat Transfer in Regions of Separated Flow - NACA TN 3792, October 1956.
104. Wm. T. Bryant and R. M. Machell - An Experimental Investigation of Flow Over Blunt Nosed Cones at a Mach Number of 5.8 - Journal of the Aeronautical Sciences, Vol. 23, No. 11, p. 1054, November 1956.
105. E. Reshotko - Laminar Boundary Layer with Heat Transfer on a Cone at Angle of Attack in Supersonic Stream - NACA TN 4152, December 1957.
106. E. Reshotko - Heat Transfer to a General Three-Dimensional Stagnation Point - Jet Propulsion, Vol. 28, No. 1, January 1958.





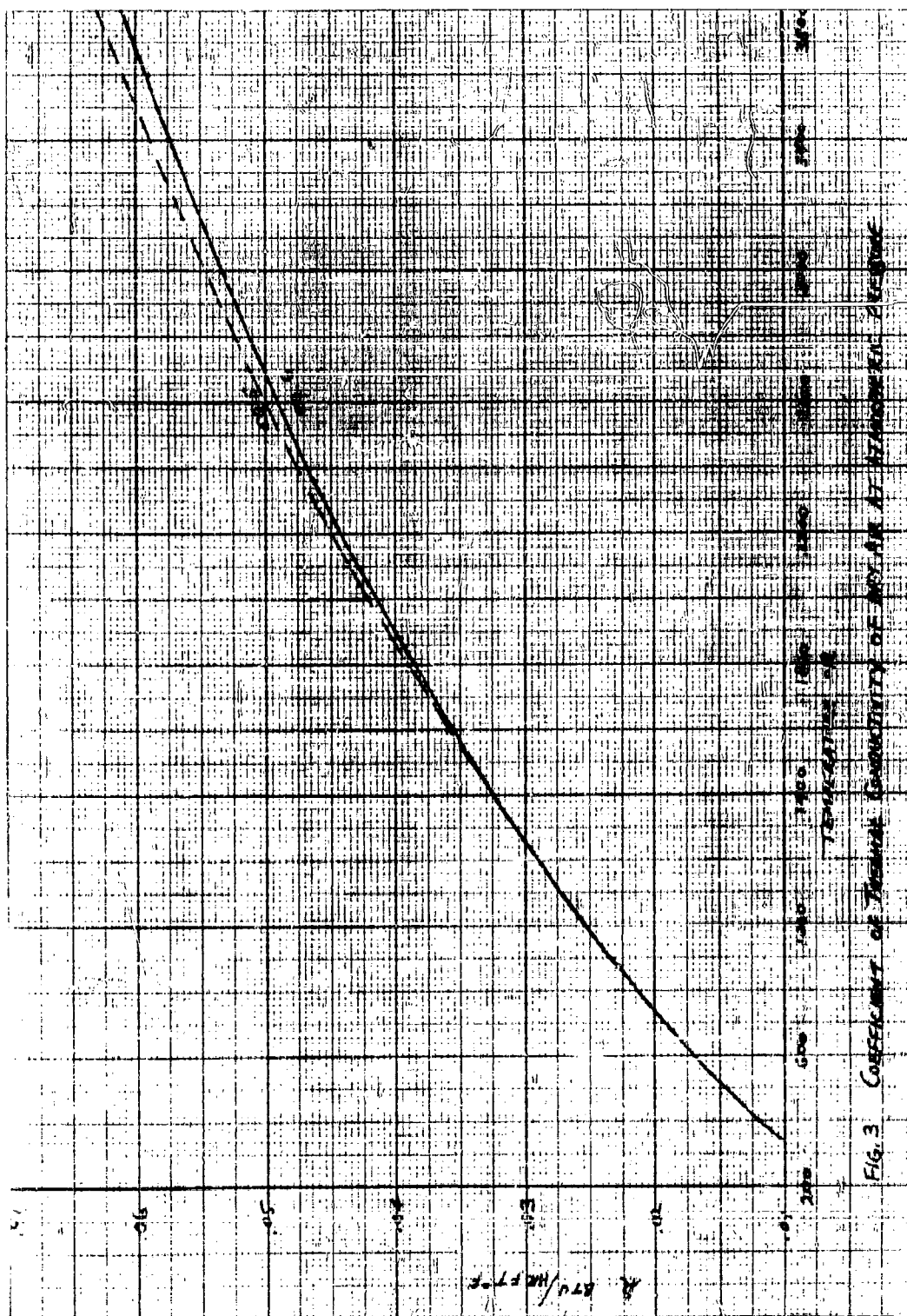


FIG. 3 COEFFICIENT OF THERMAL CONDUCTIVITY OF DRY AIR AT STANDARD PRESSURE

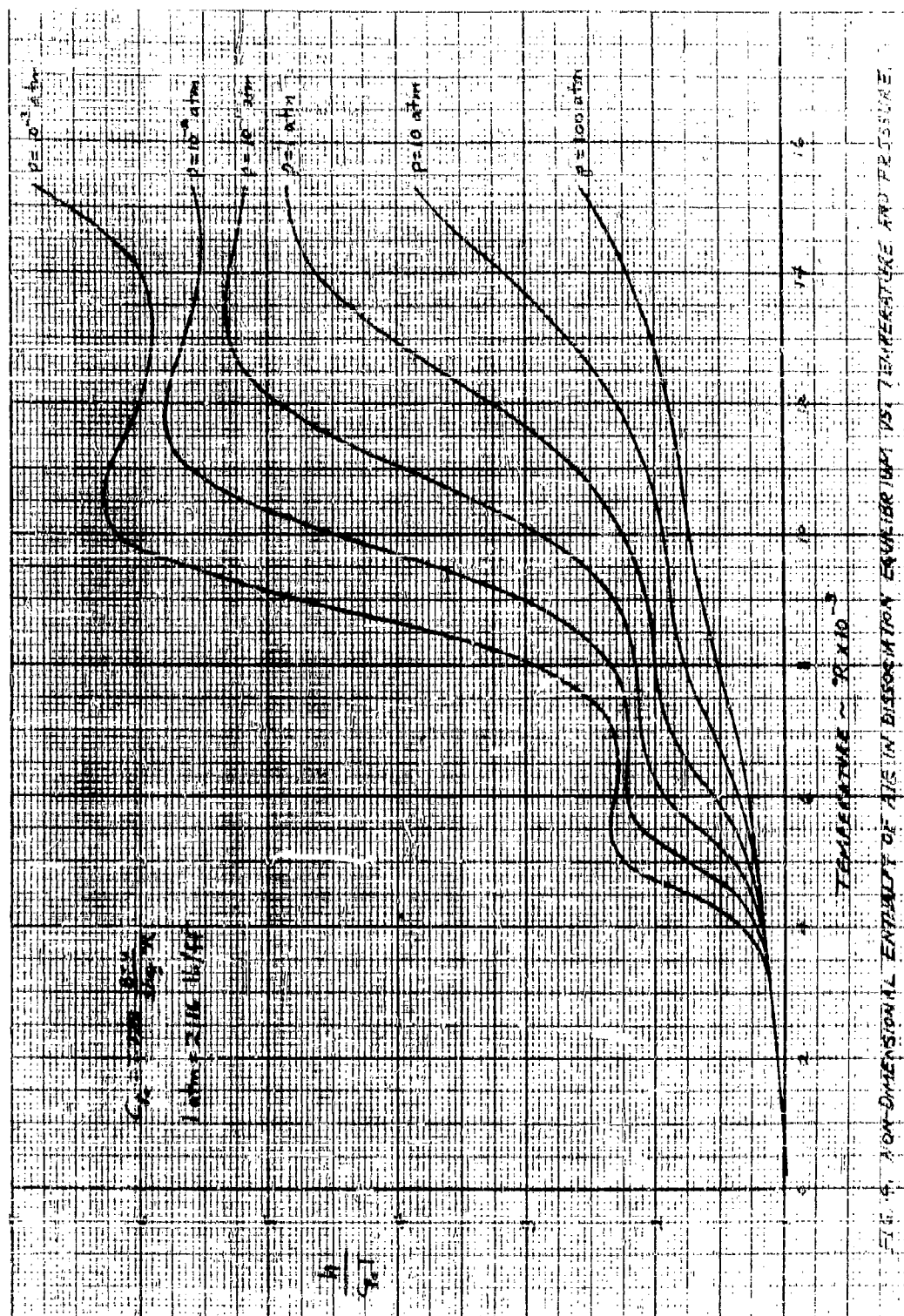
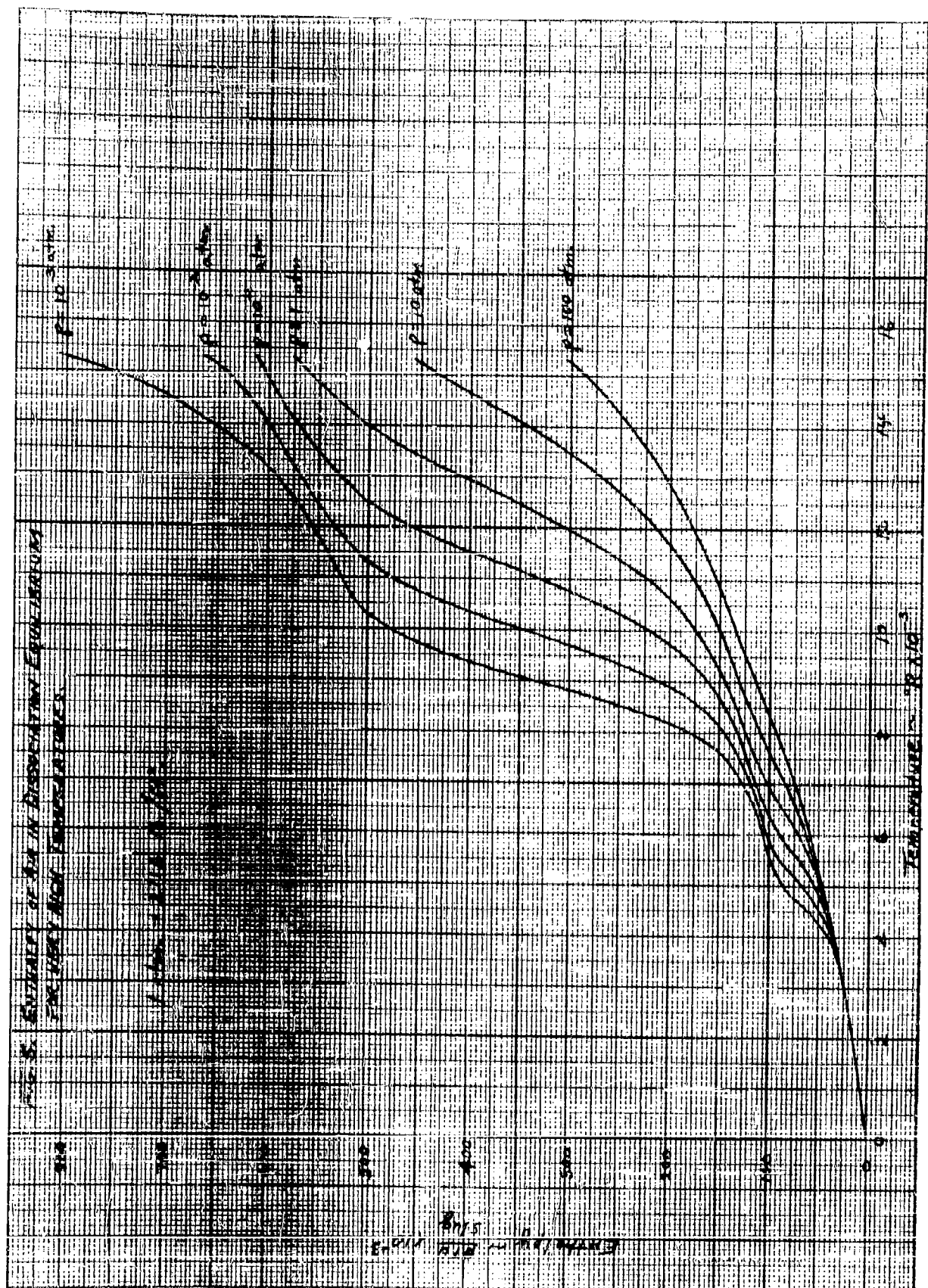
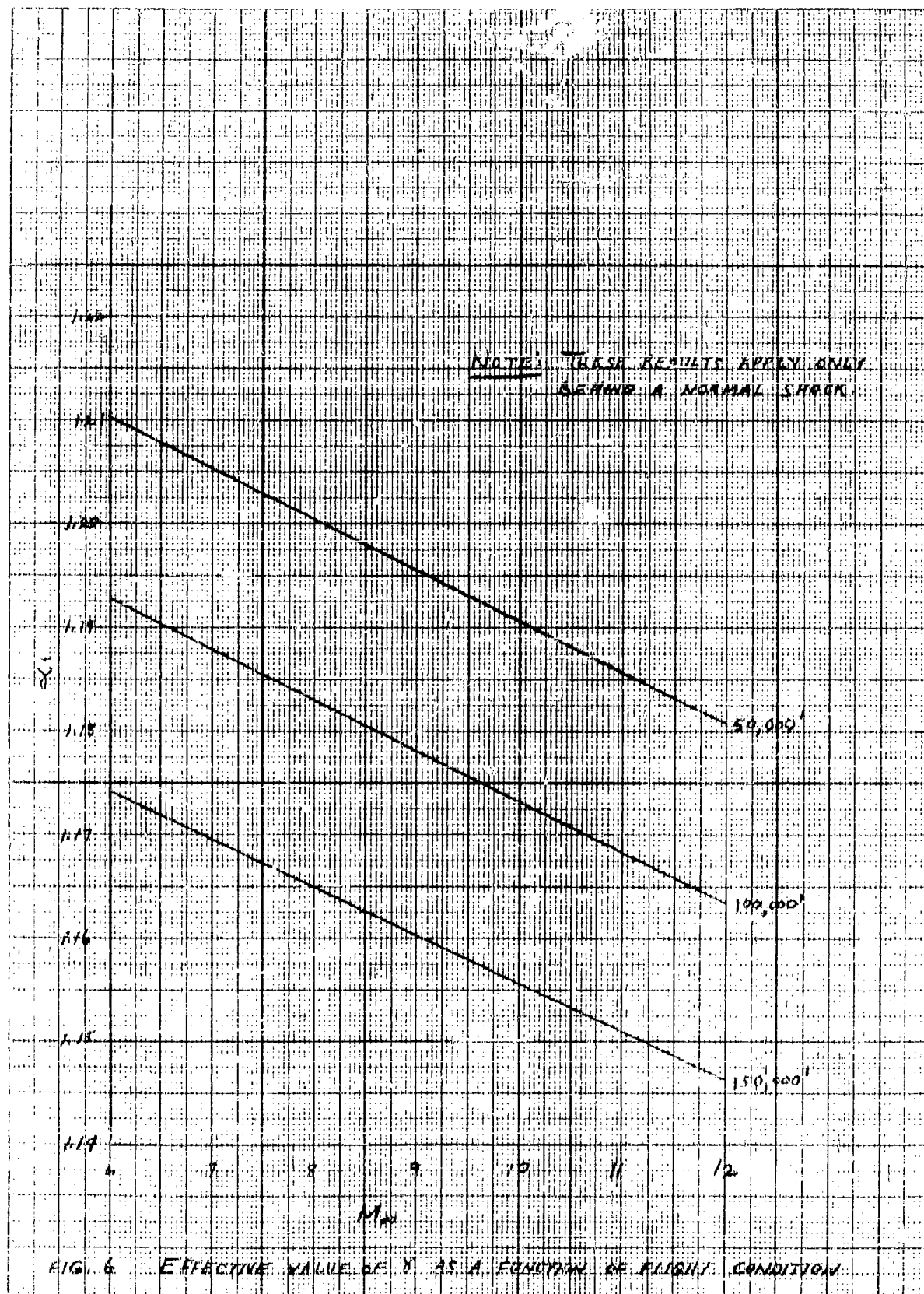
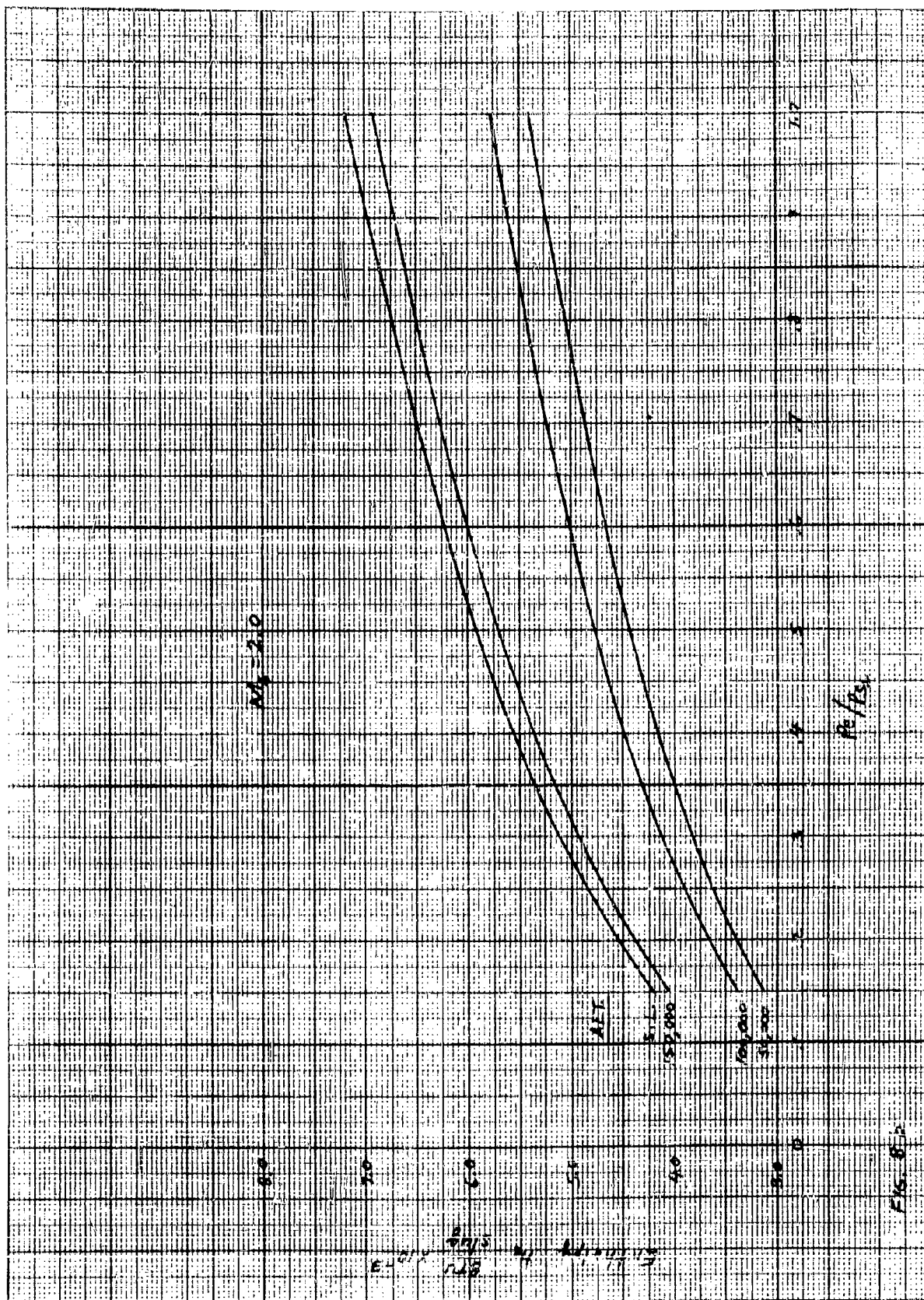
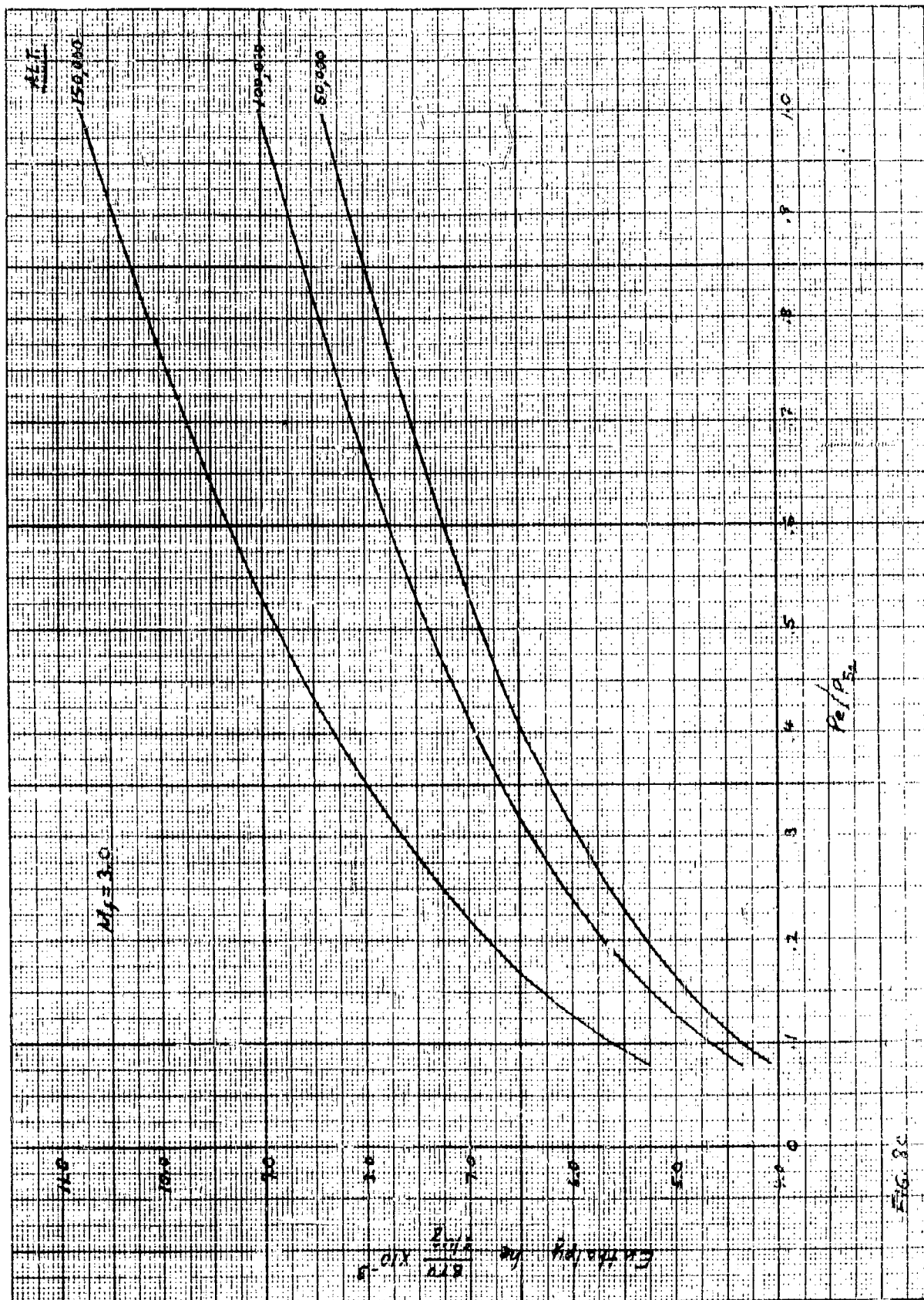


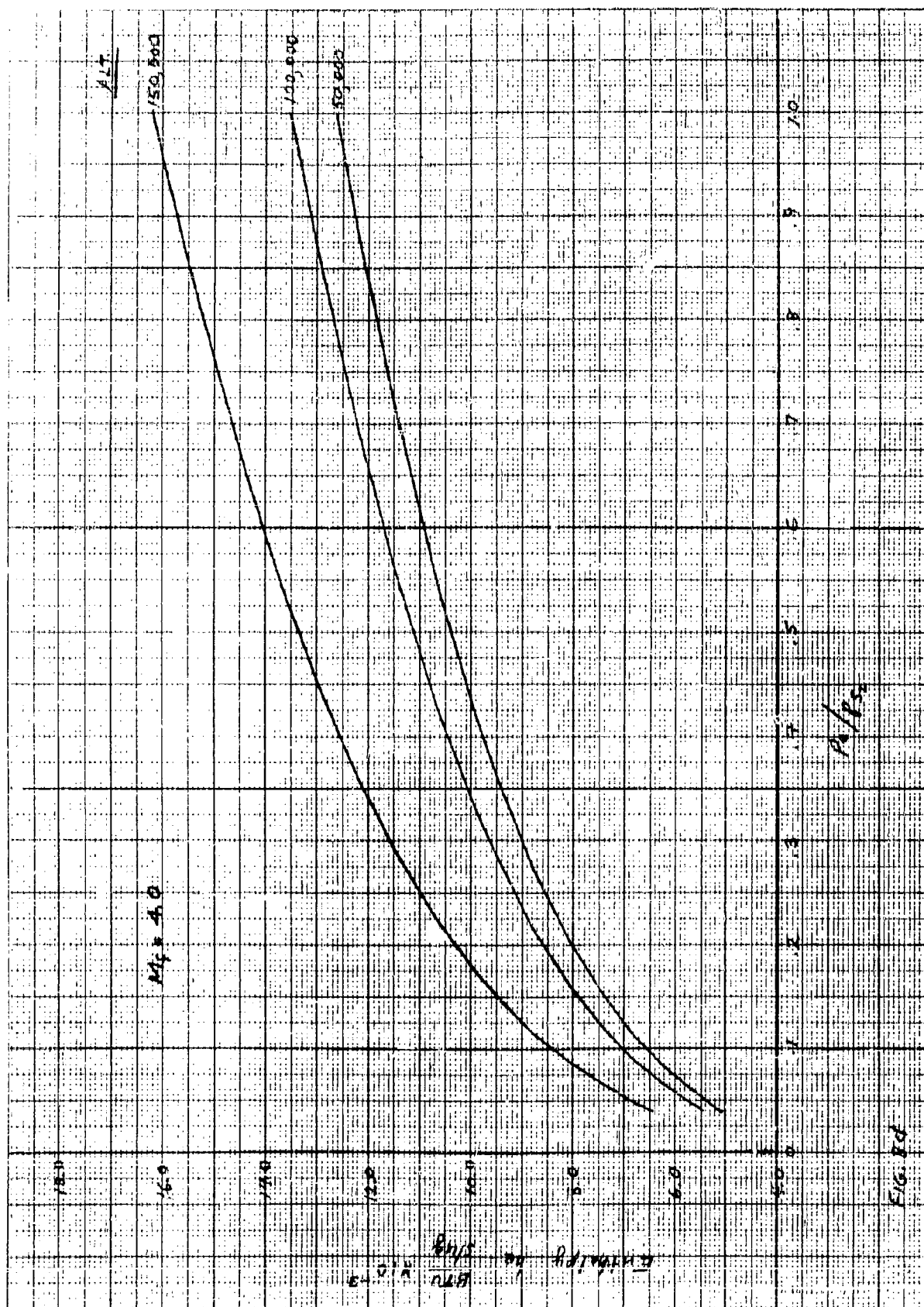
FIG. 5. NON-DIMENSIONAL ENTHALPY OF AIR IN DISSOCIATION EQUILIBRIUM VS. TEMPERATURE AND PRESSURE.

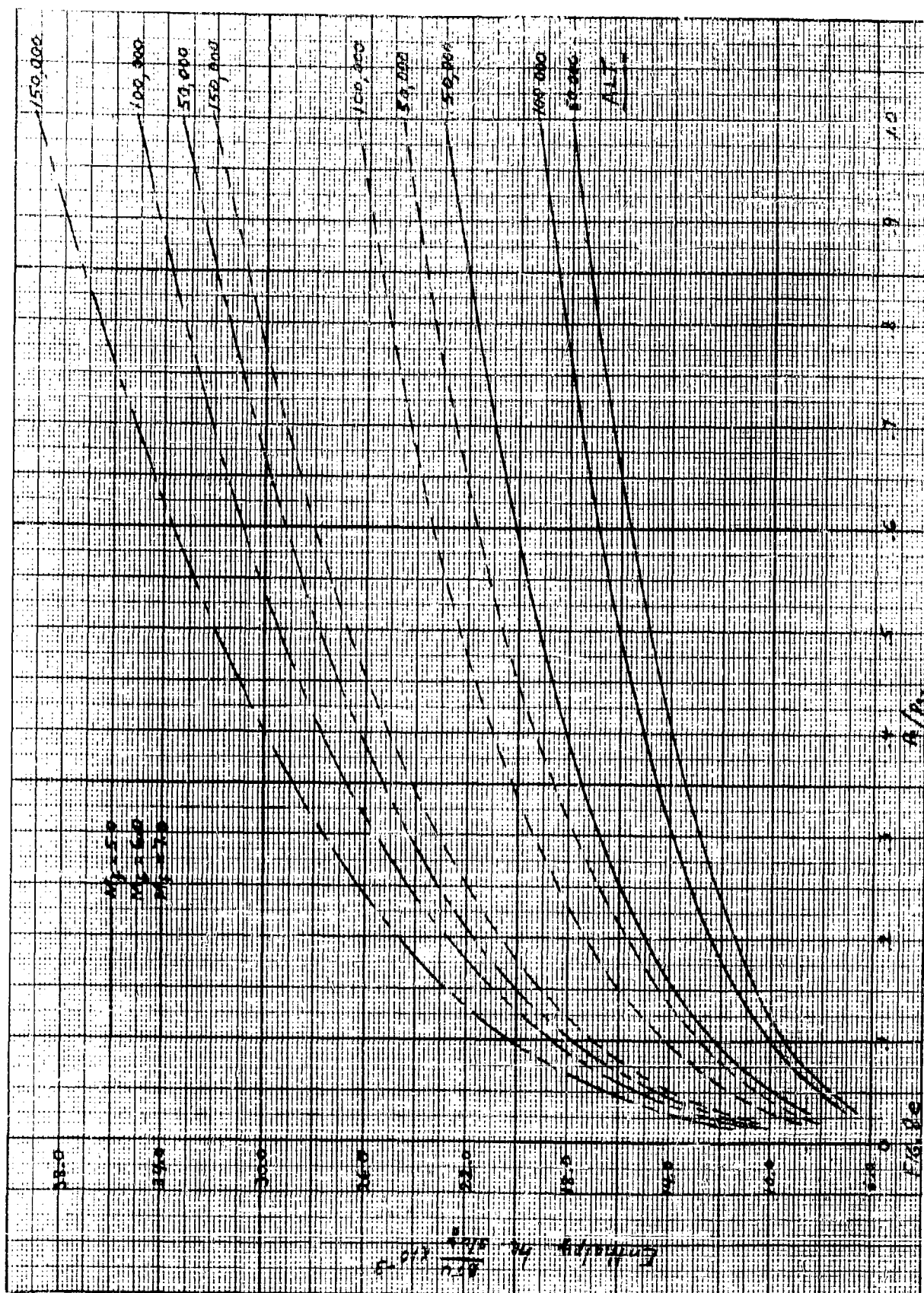












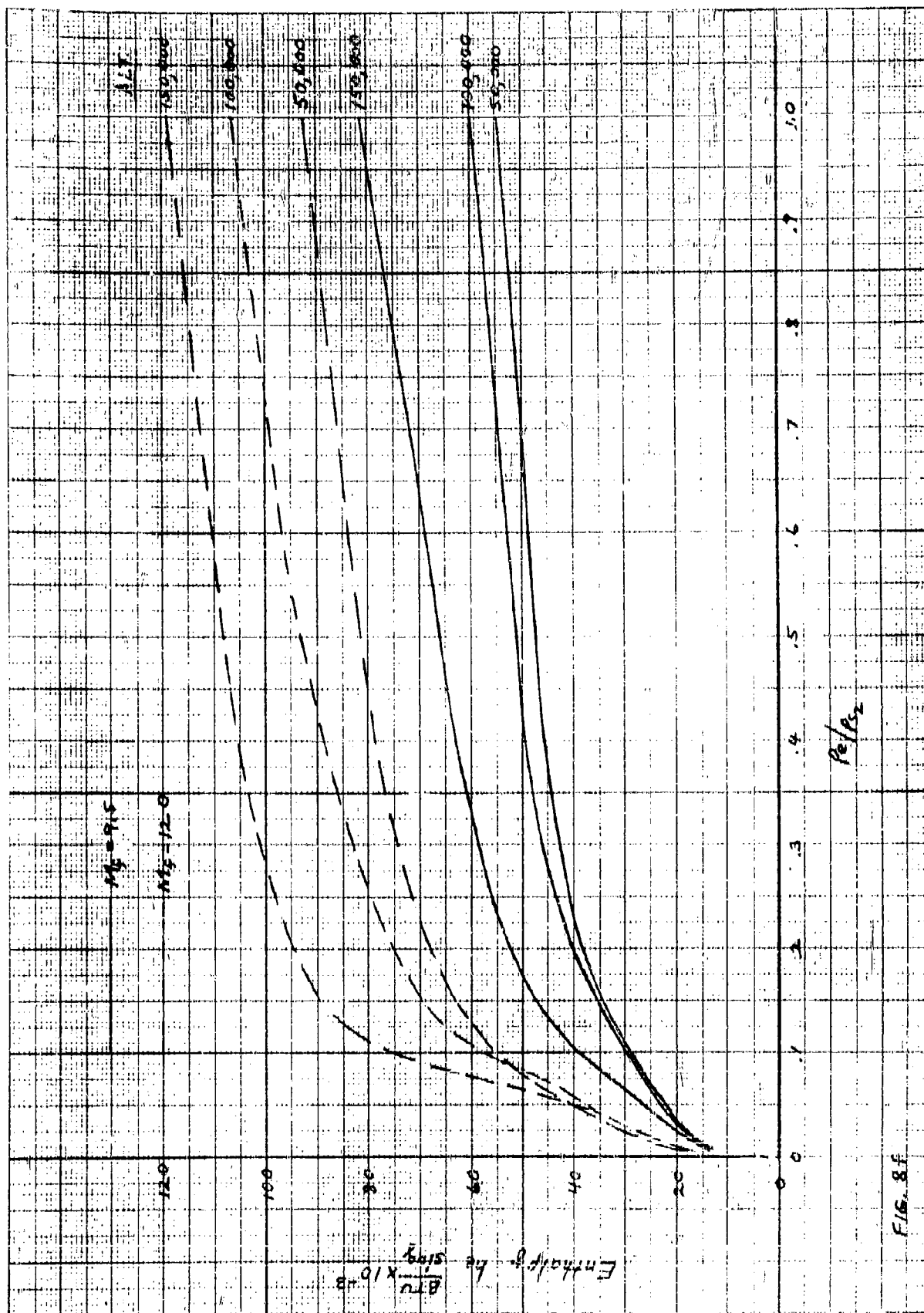


FIG. 8f

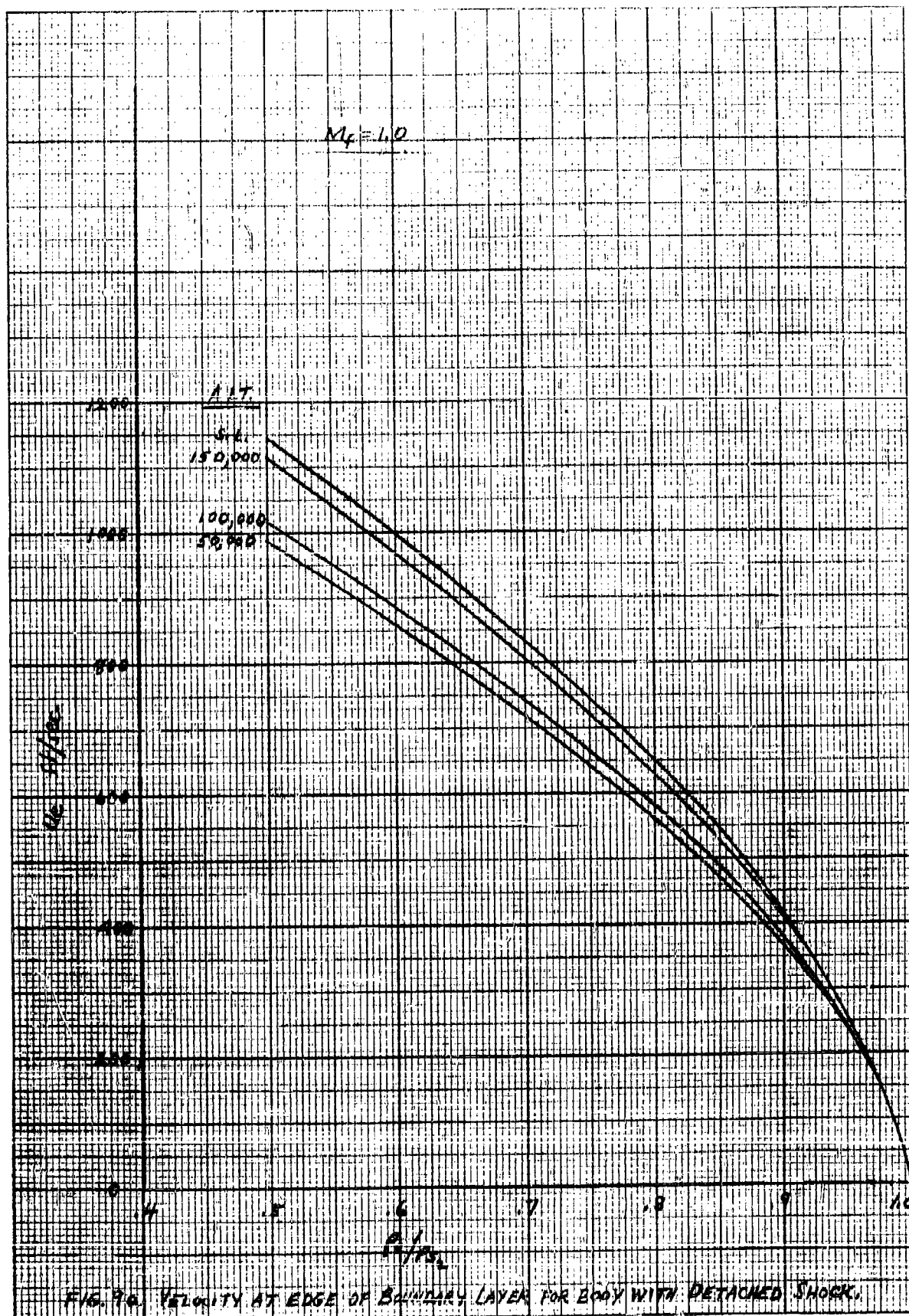
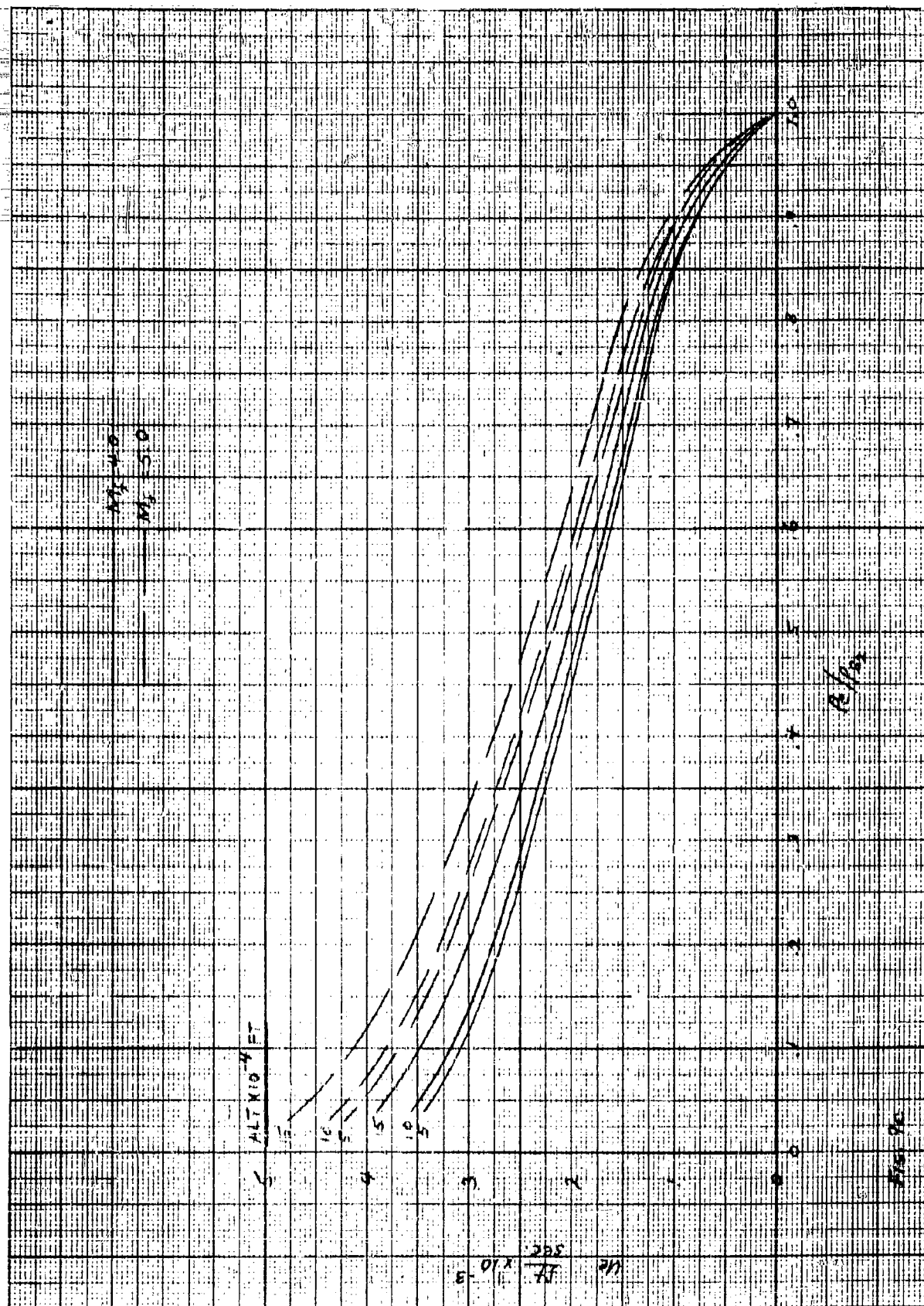
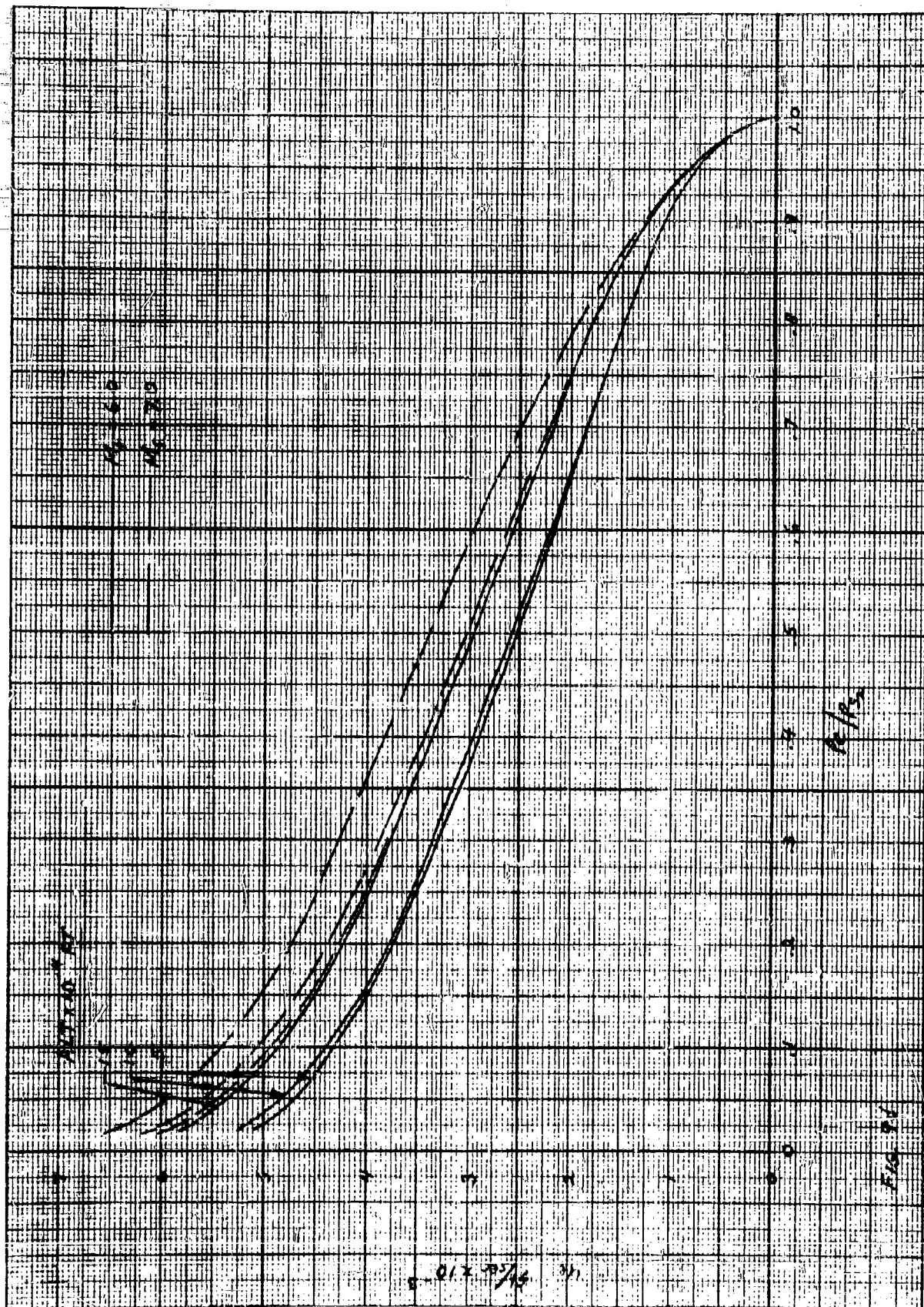


FIG. 70. VELOCITY AT EDGE OF BOUNDARY LAYER FOR BODY WITH DETACHED SHOCK.





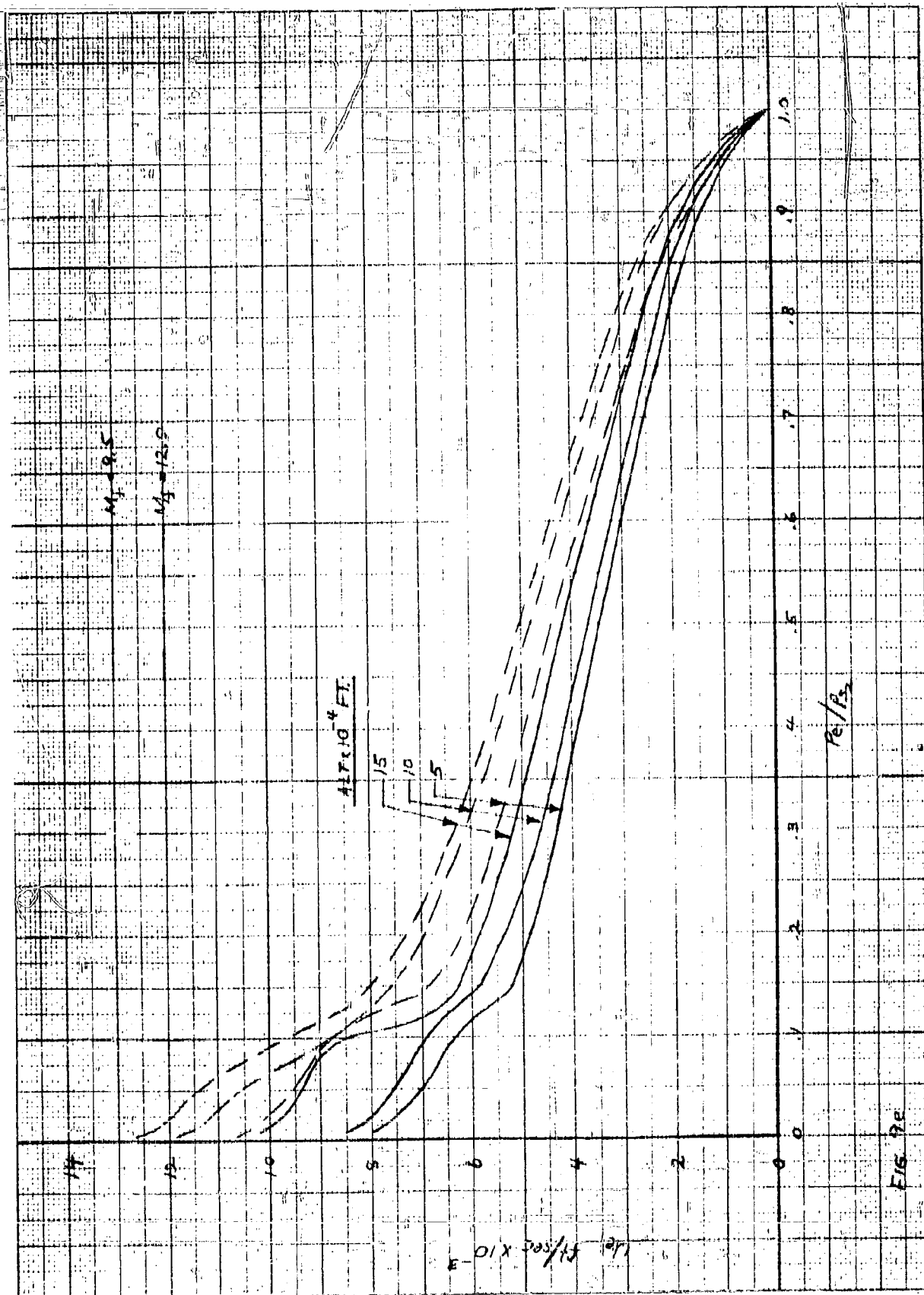
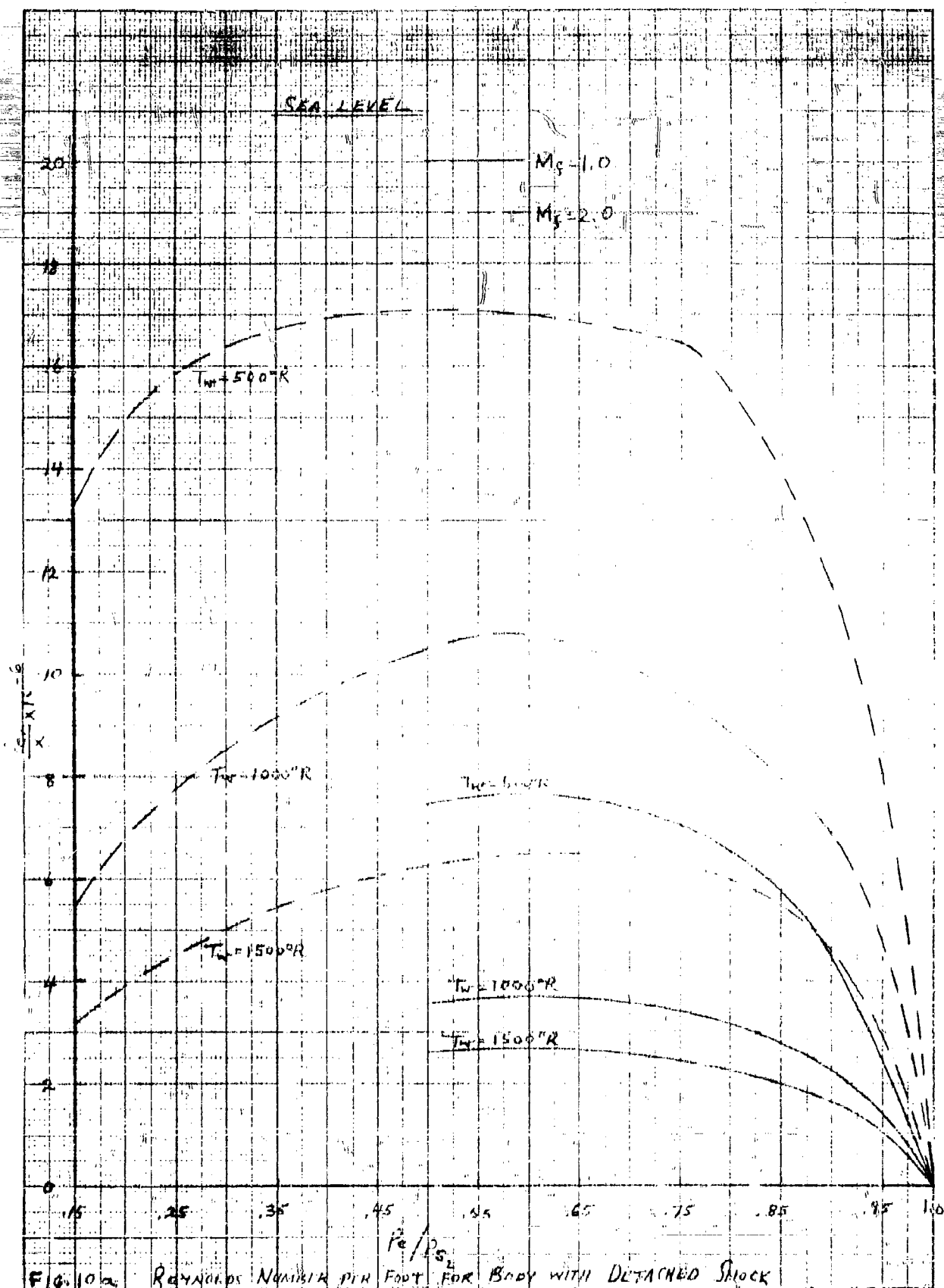


FIG. 7e



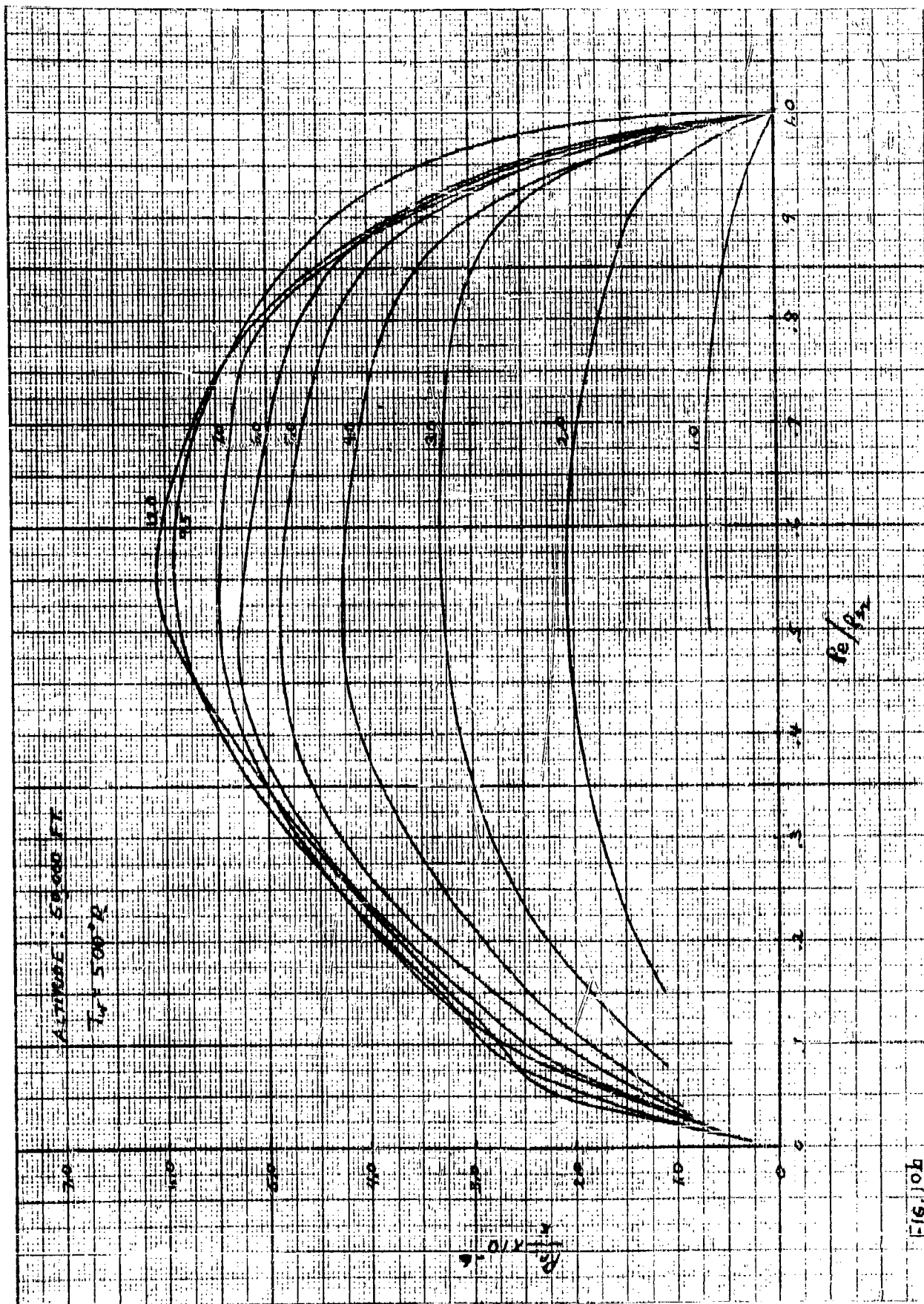
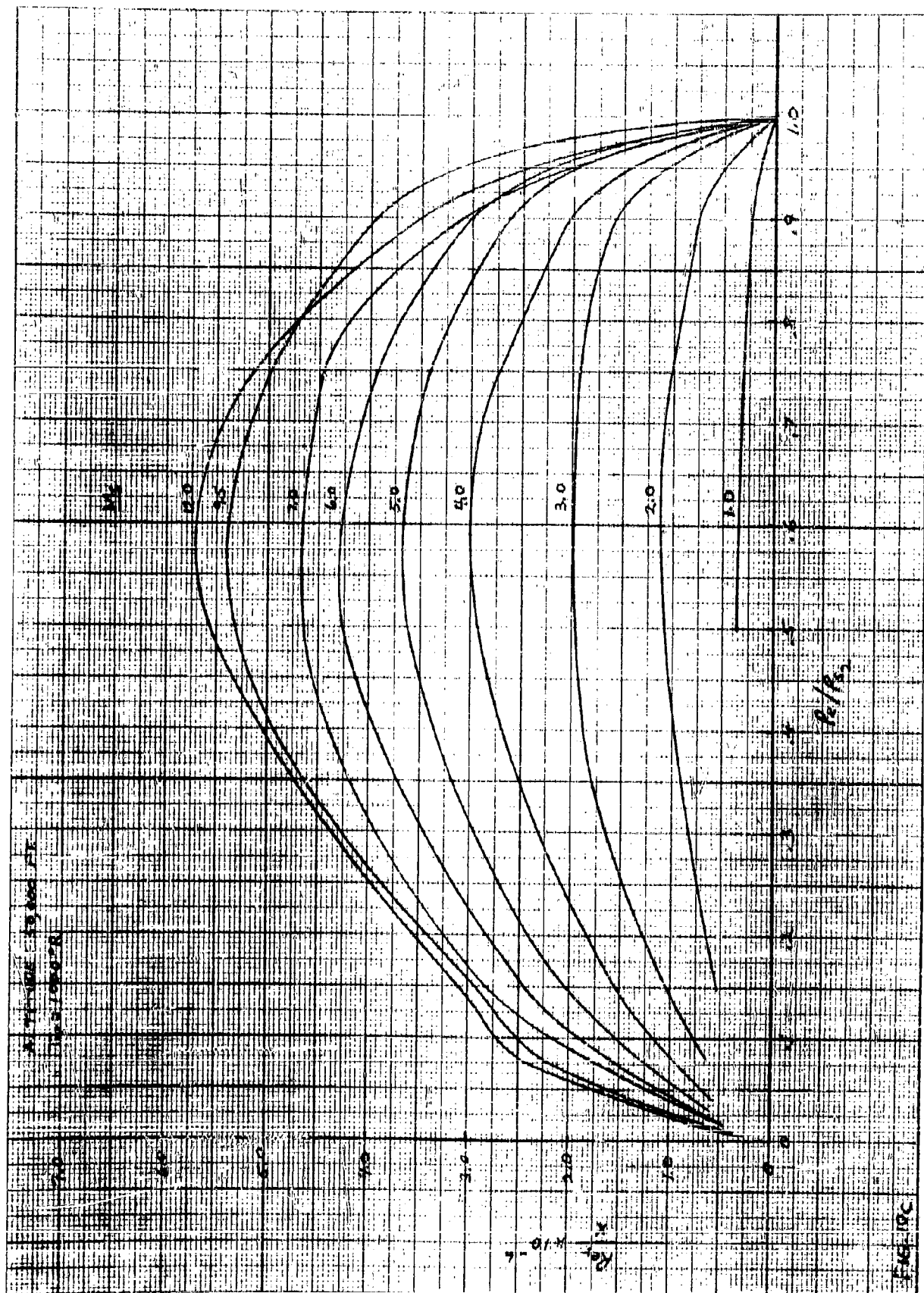
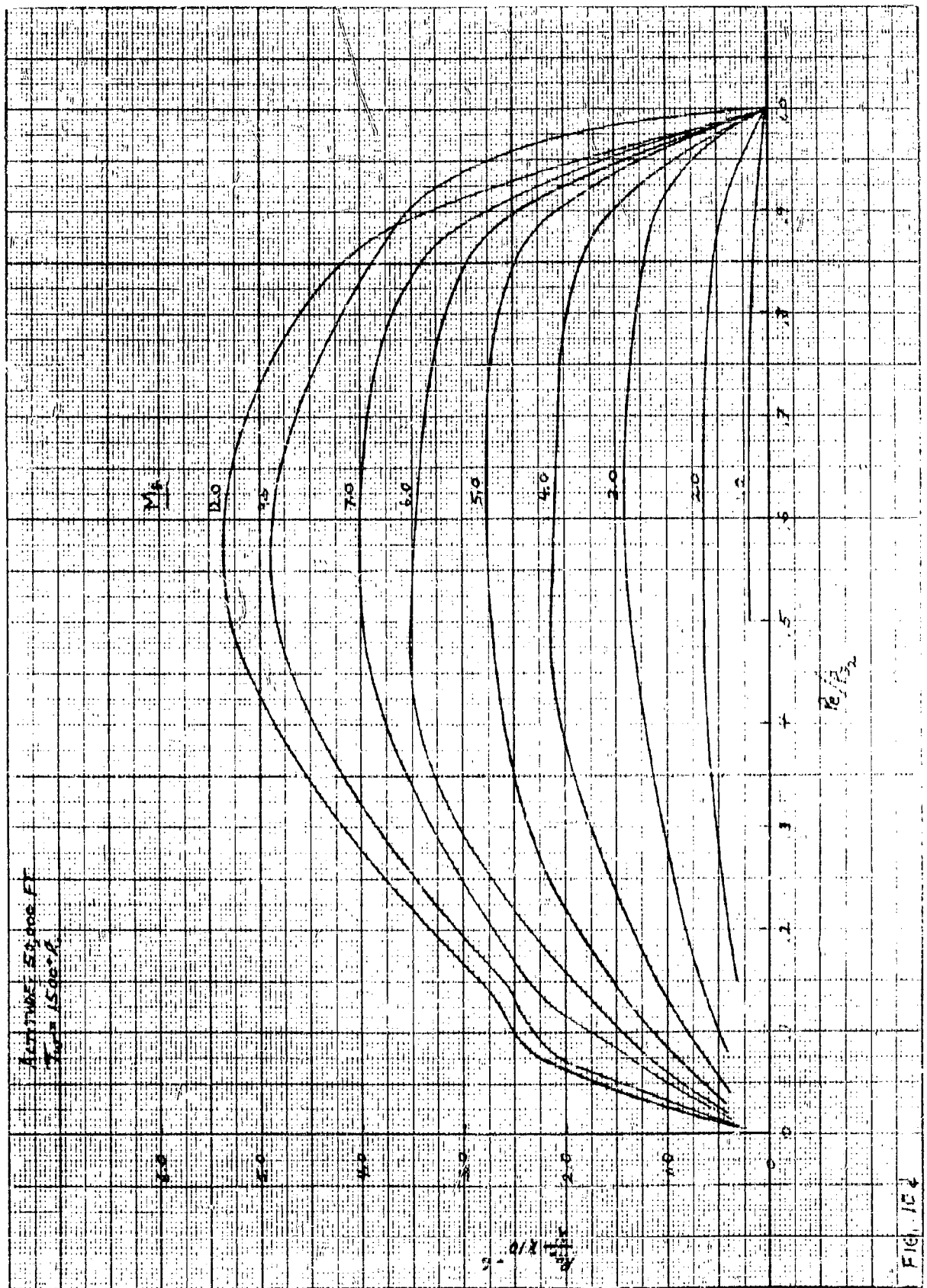
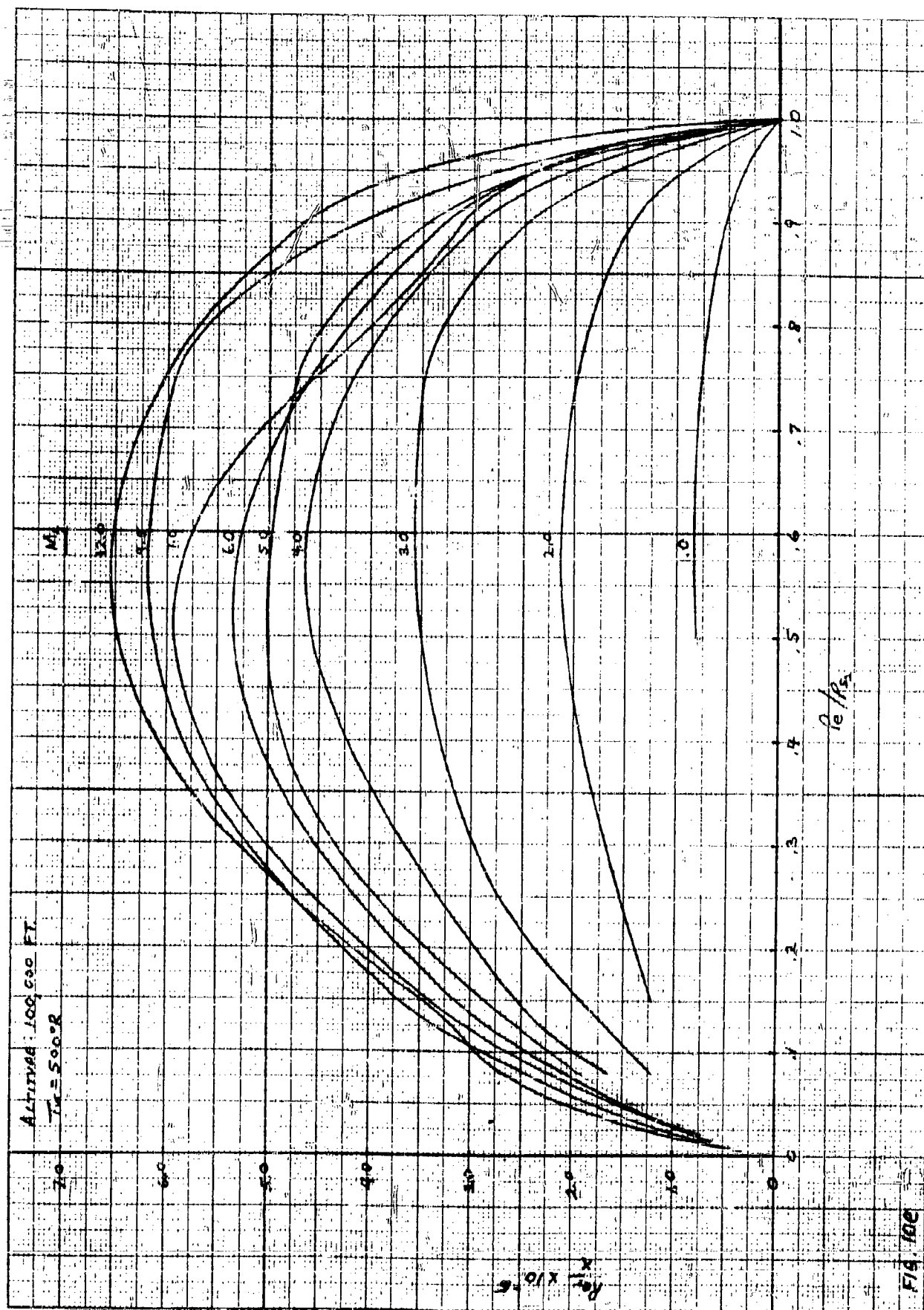
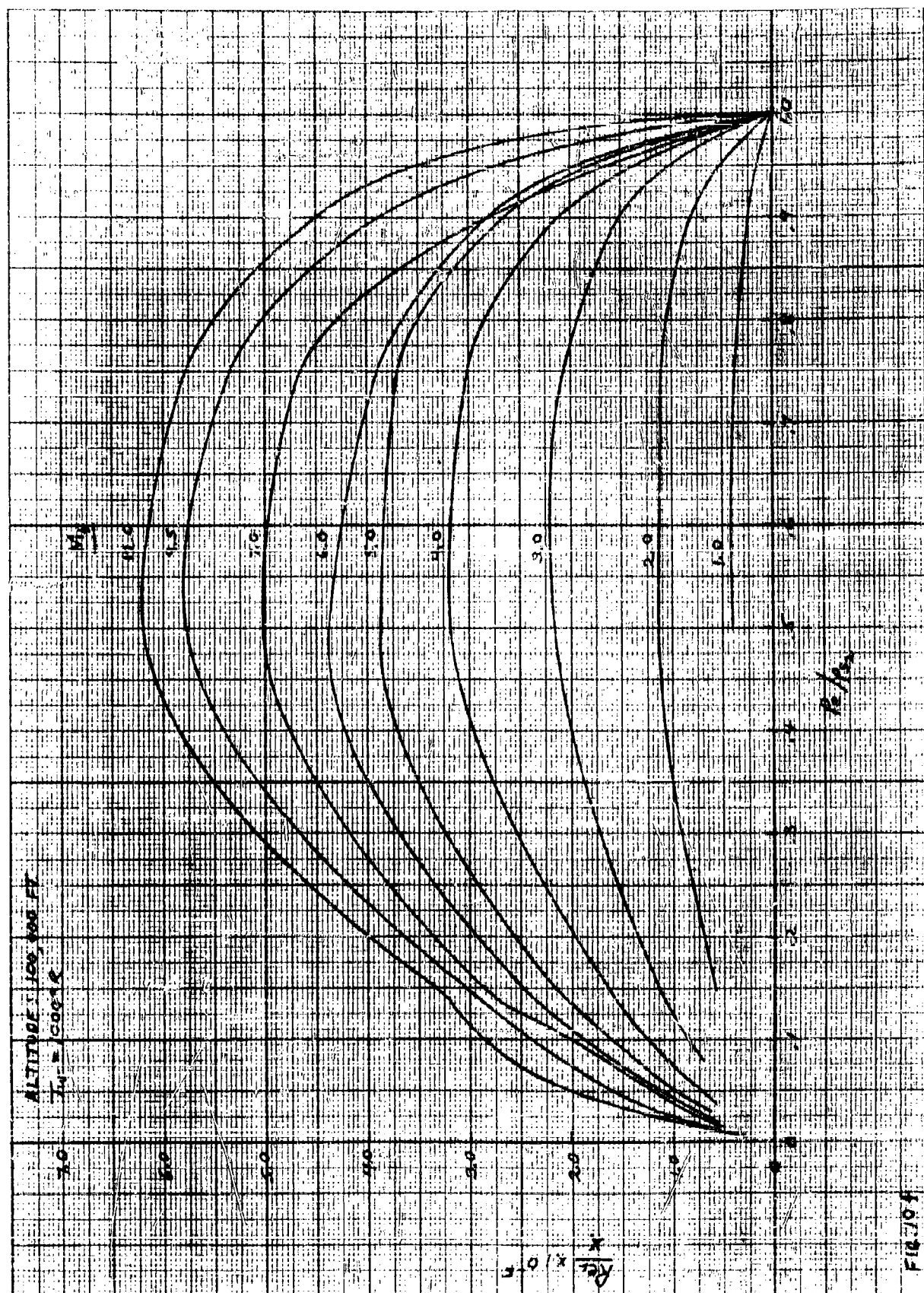


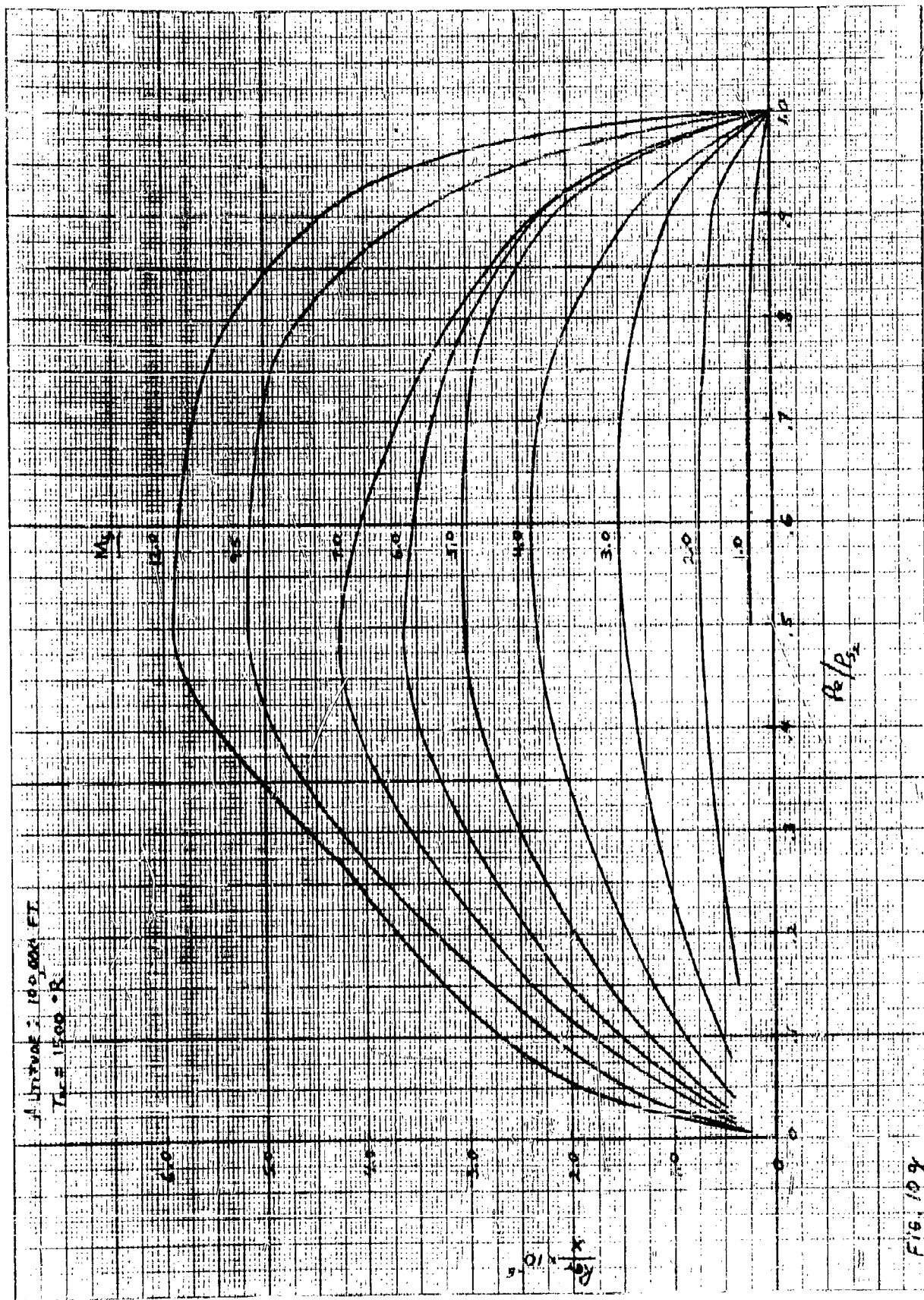
FIG. 10b

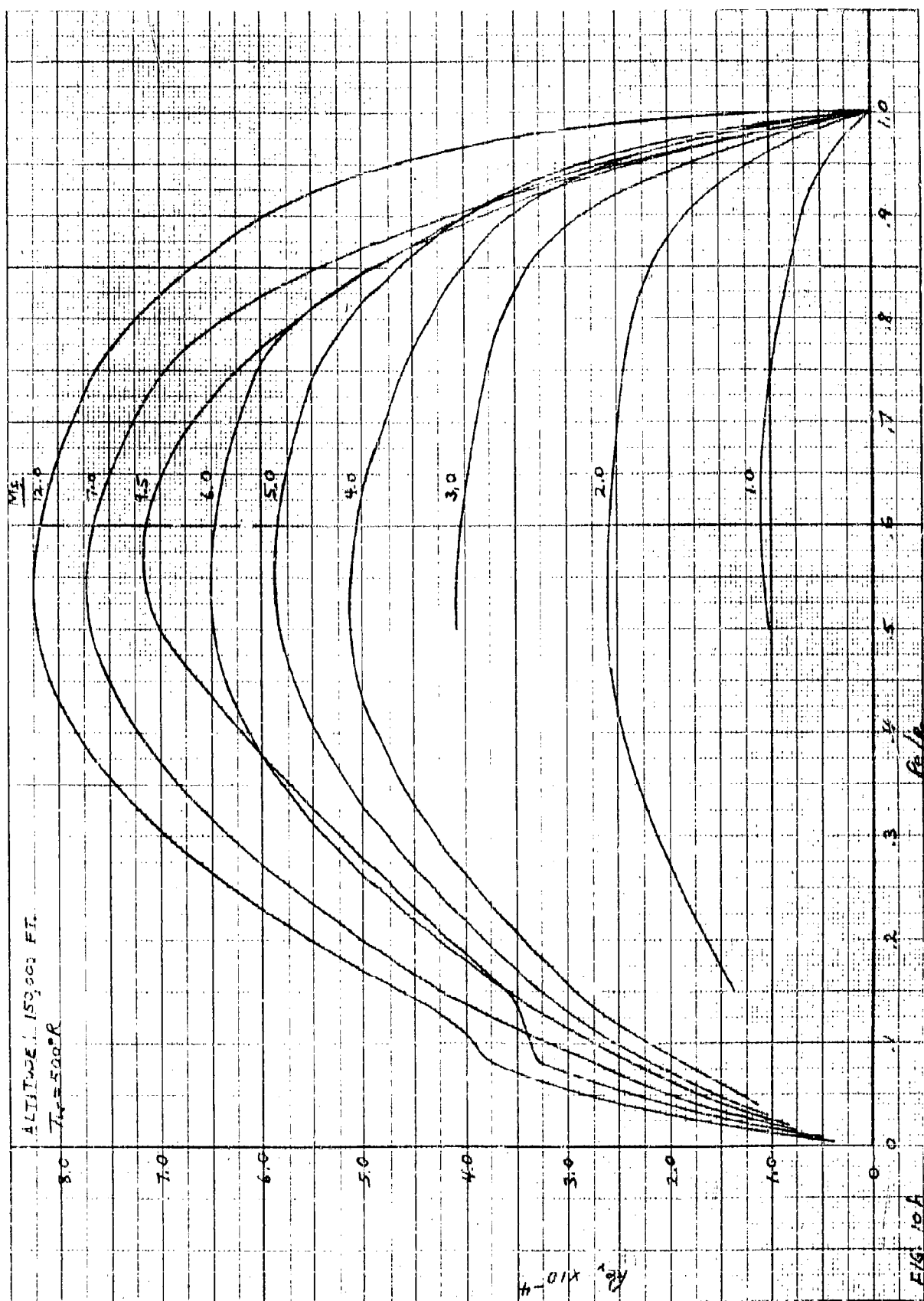


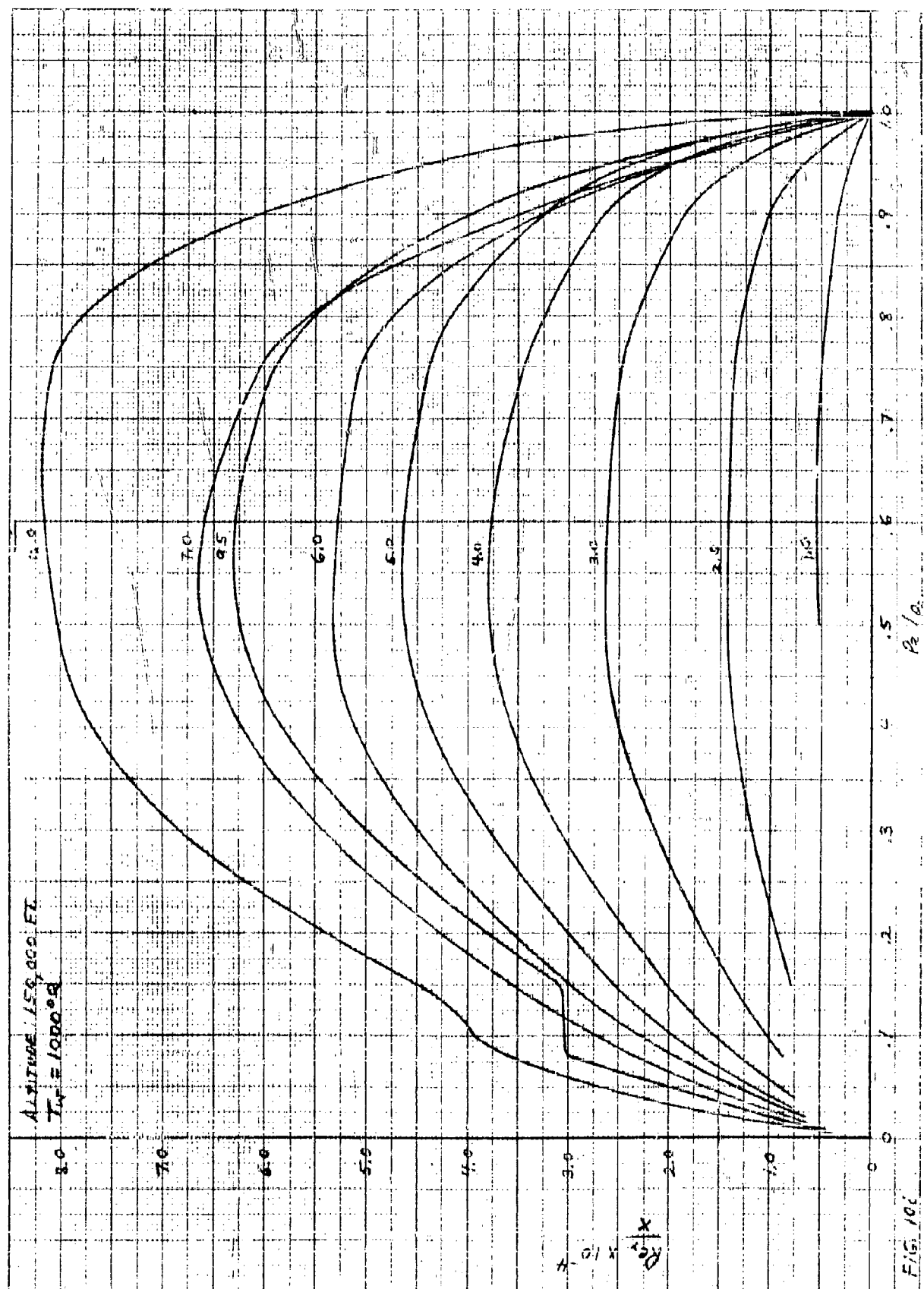


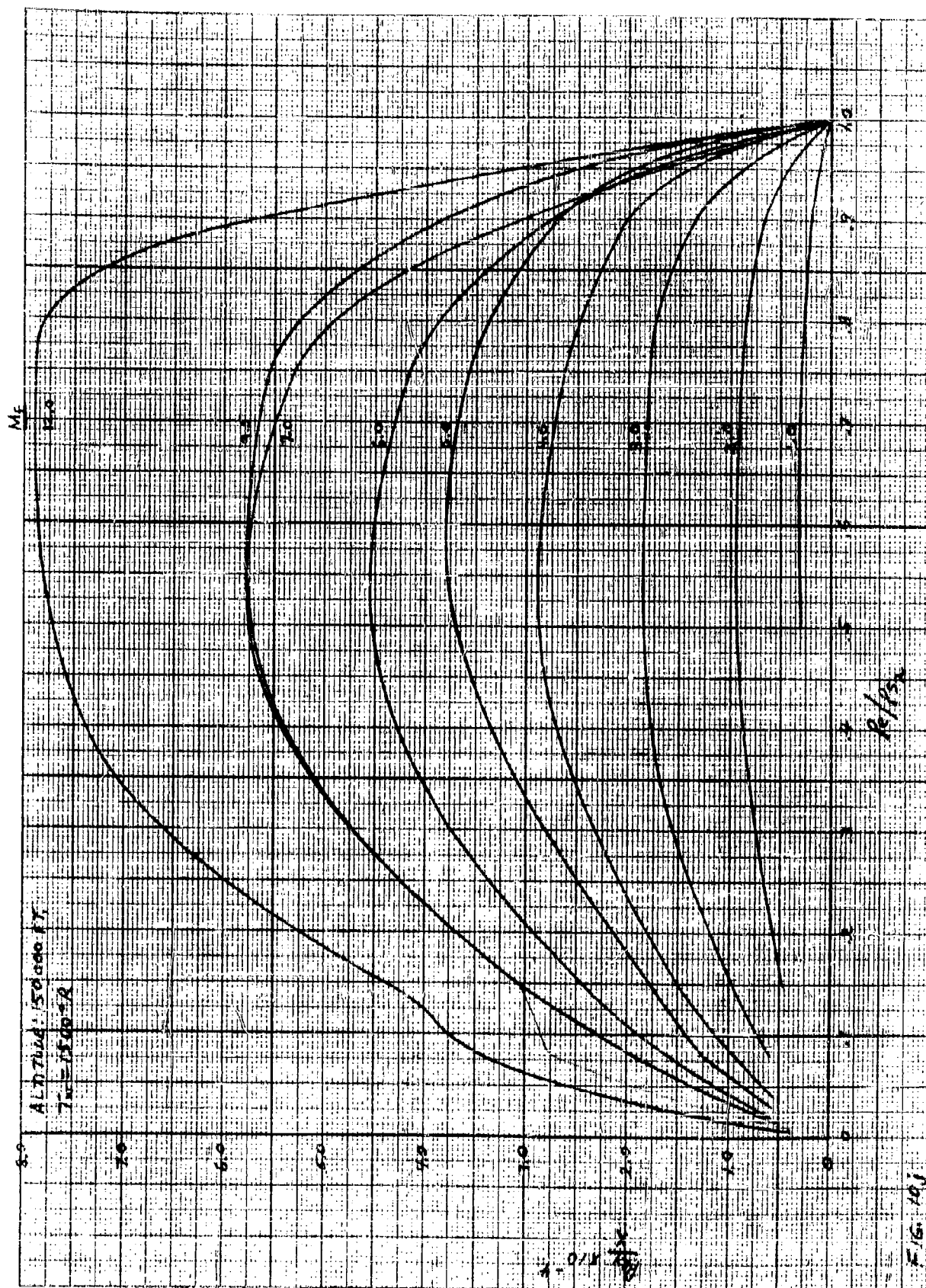












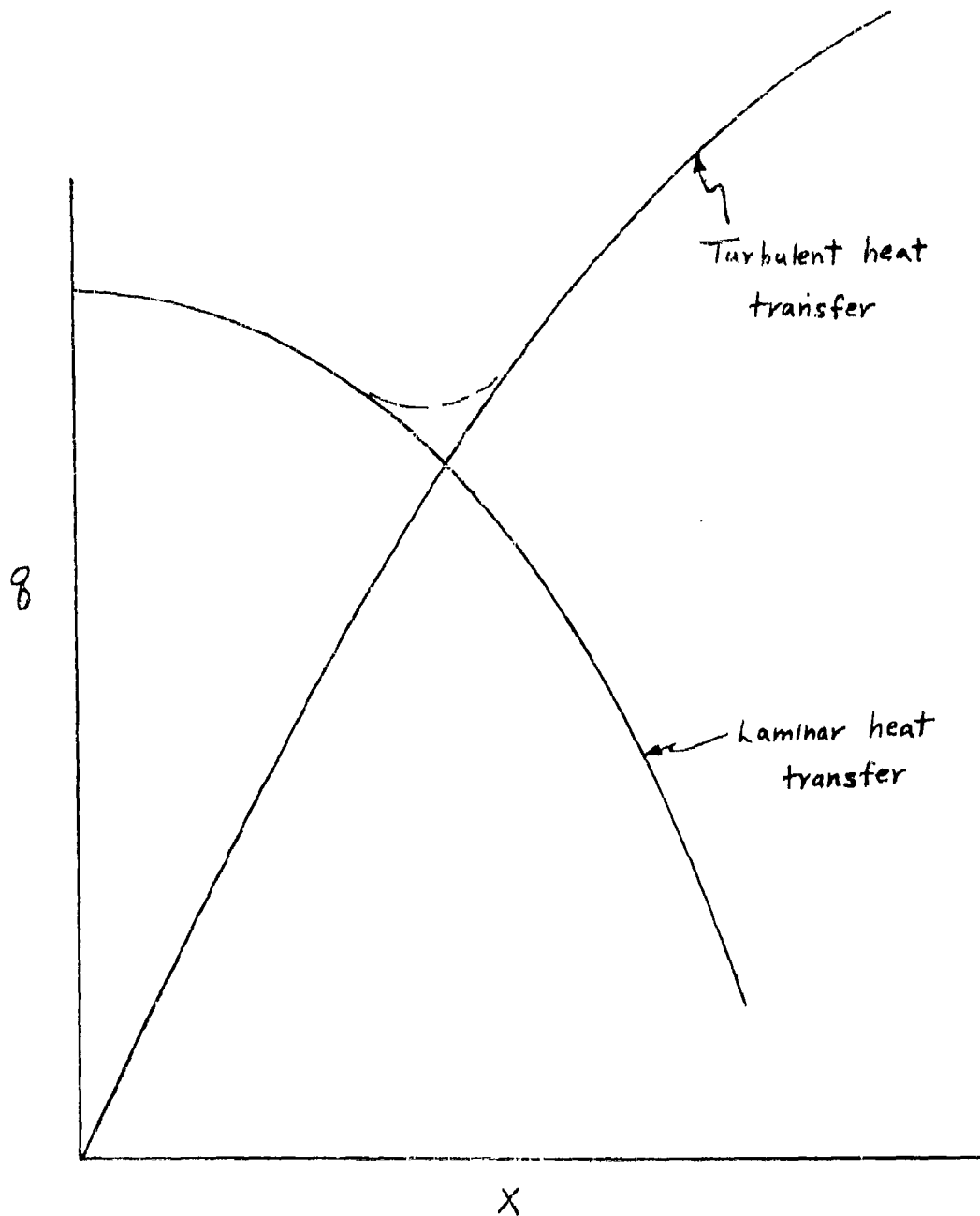


FIG. II VARIATION OF LAMINAR AND TURBULENT HEAT TRANSFER
RATES WITH DISTANCE

CHAPTER I - PART E

CHARTS AND EQUATIONS FOR THE DETERMINATION OF
AERODYNAMIC HEAT TRANSFER TO RADOME-SHAPED BODIES

by Harold S. Pergament and Melvin Epstein

TABLE OF CONTENTS

	<u>Title</u>	<u>Page</u>
	Summary	187
	Symbols	188
	List of Figures	190
1.	Introduction	192
2.	Blunt Bodies	194
	Stagnation Point	194
	Laminar Flow	195
	General Bodies	195
	Sphere-Cone	198
	Turbulent Flow	200
	General Bodies	200
	Sphere-Cone	203
3.	Pointed Bodies	205
	Ogives	205
	Laminar Flow	205
	Turbulent Flow	209
	Cones	211
	Laminar Flow	211
	Turbulent Flow	215
4.	Transition	217
	References	219
	Figures	220

E.

CHARTS AND EQUATIONS FOR THE
DETERMINATION OF AERODYNAMIC
HEAT TRANSFER TO
RADOME-SHAPED BODIES

SUMMARY

A series of curves and equations are presented which will facilitate the computation of the heat transfer rate along blunt and pointed-nosed bodies of revolution. The free stream Mach number range is from 2 to 7 and the altitude extends from sea level to 150,000 feet. Methods are included for both laminar and turbulent flow with a discussion of the approximate location of the transition point. Only bodies at zero angle of attack are considered.

SYMBOLS

a	sonic velocity, ft/sec.
a*	sonic velocity at point where $M = 1$, ft/sec.
A	factor defined by Equation (8)
D	diameter of body at base, ft.
f	fineness ratio - L/D
h	enthalpy, Btu/lb _m
k	thermal conductivity, Btu/sec-ft-°R
L	length of body, ft.
M	Mach number, u/a
p	static pressure, lb/ft ²
Pr	Prandtl number, $\frac{\mu c_p}{k}$ (where c_p is specific heat at constant pressure)
q	heat transfer rate, Btu/sec-ft ²
r	radial distance from centerline of body to surface, ft.
R ₀	radius of curvature at nose, ft.
s	distance along body measured from nose, ft.
T	absolute temperature, °R
u	velocity, ft/sec.
x	axial distance measured from nose, ft.
α_i	$\left\{ \begin{array}{l} \text{initial inclination angle of ogive} \\ \text{semi-vertex angle of cone} \end{array} \right.$
γ	ratio of specific heats

$\bar{\gamma}$	reduced ratio of specific heats for use at high temperatures
θ	angle between a normal to the surface and the horizontal (turning angle).
ρ	density, lb_m/ft^3
μ	coefficient of viscosity, $\text{lb}_m/\text{ft-sec.}$

Subscripts

aw	adiabatic wall value
e	local value at edge of boundary layer
m	mass
o	value at stagnation point
r	reference value
s	stagnation value
w	wall value
2	value behind a normal shock (downstream of detached shock)
2'	value behind an attached conical shock
∞	free stream value

LIST OF FIGURES

<u>Figure</u>	<u>Title</u>	<u>Page</u>
1	$\frac{q_0 \sqrt{R_0}}{(h_s - h_w)}$ vs. M_∞	220
2	Stagnation Enthalpy vs. M_∞	222
3	Enthalpy vs. Temperature	223
4	$\frac{q_w}{q_0} \sqrt{\frac{s}{R_0}}$ vs. Turning Angle	224
5	Axial Location vs. Turning Angle	225
6	Distance Along Body vs. Turning Angle	226
7	Ratio of Local Pressure to Stagnation Pressure Behind Normal Shock	227
8	$\frac{p_e}{p_{s2}}$ vs. $\frac{u_e}{a^*}$ and $\frac{T_e}{T_s}$	228
	$\frac{p_e}{p_{s2}}$ vs. $\frac{u_e}{a^*}$ and $\frac{T_e}{T_s}$	
9	a^* vs. Altitude	230
10	Stagnation Pressure Behind Normal Shock vs. M_∞	231
11	Stagnation Temperature vs. Altitude	234
12	Coefficient of Viscosity vs. Temperature	235
13	Prandtl Number vs. Temperature	236
14 - 19	Ratio of Local Pressure to Stagnation Pressure Behind Conical Shock for M_∞ from 2-7	237

<u>Figure</u>	<u>Title</u>	<u>Page</u>
20	$\frac{P_{s2}'}{P_{\infty}}$ vs. a_i	249
21	Free Stream Pressure vs. Altitude	251
22	Free Stream Temperature and Sonic Velocity vs. Altitude	253

1. INTRODUCTION

The methods presented herein are sufficiently general for use in computing the heat transfer rates along most bodies suitable to radome application. These bodies are divided into two main classifications, blunt-nosed and pointed-nosed. The former is characterized by a detached shock ahead of the body while the latter has a shock attached to the body. Because of this distinction, different methods are needed to evaluate the aerodynamic parameters (pressure, velocity, etc.) for each. These properties have been determined for all cases of interest and are given here in a form suitable for use in the heat transfer equations.

A discussion of the transition from laminar to turbulent flow indicates the position on the body where each type of flow is likely to exist. This analysis is approximate since extensive information on the exact location of the transition point is not available. However, it is felt that the method shown is suitable for engineering calculations since it should always yield results on the conservative side.

Real gas effects are included only in determining the heat transfer rate at the stagnation point. For all other cases, perfect gas relations are used. This procedure is approximately correct for Mach numbers up to 5. For higher Mach numbers, errors are incurred by the use of a perfect gas analysis, but since this investigation extends to Mach 7,

the error is still relatively small and likely to yield a conservative value for the heat transfer rate.

There should be no aerodynamic heating problem below Mach 2, but if it is necessary to determine the heat transfer rate at low Mach numbers, it is suggested that the properties be calculated individually⁽¹⁾ instead of extrapolating the curves needed for the given equations. Under no circumstances should the curves be extrapolated above Mach 7, since real gas effects would make this analysis invalid.

From the given information, only the local value of the heat transfer rate can be found. If it is necessary to determine the total heat transfer to the body, one has to integrate the local value over the surface (usually by numerical methods).

There are some cases that cannot be included in a general study such as this (e.g., detached shock in front of a pointed-nosed body). However, these problems can be solved individually by means which are familiar to the aerodynamicist.

(1) (e.g.) Parts B and D, and Reference 3

2. BLUNT BODIES (DETACHED SHOCK)

A. Stagnation Point

The equation used to calculate the heat transfer rate at the stagnation point is given in Part D as,

$$q_o = \frac{.50\sqrt{2}}{\bar{P}_R^{2/3}} \sqrt{\frac{(\rho_e \mu_e)_o u_\infty^2}{R_o}} (h_s - h_w) G(M_\infty, \bar{\gamma}, \gamma_f) \frac{\text{Btu}}{\text{sec-ft}^2} \quad (1)$$

where

$$G(M_\infty, \bar{\gamma}, \gamma_\infty) = \left(\frac{\bar{\gamma} - 1}{\bar{\gamma}} \right)^{1/4} \left(1 + \frac{2}{\gamma_\infty - 1} \frac{1}{M_\infty^2} \right)^{1/4} \left(1 - \frac{1}{\gamma_\infty M_\infty^2} \right)^{1/4} \quad (1a)$$

For the flight conditions under consideration:

$$\gamma_\infty = 1.4$$

$$\bar{\gamma} = 1.4$$

$$\bar{P}_R = 0.71$$

Figure 1 plots $\frac{q_o \sqrt{R_o}}{(h_s - h_w)}$ vs. M_∞ with altitude as a parameter. Thus, for any flight condition, this quantity can be found. From Figure 2, h_g is determined and in Figure 3, the enthalpy is plotted as a function of temperature. From this curve, the wall enthalpy (h_w) can be found from the corresponding wall temperature (T_w). The wall temperature is one of the variables which must be known before the heat transfer rate can be computed.

Example 1

Flight Conditions: $M_\infty = 5$, alt. = 100,000 ft., $T_w = 1000^\circ\text{R}$, $R_o = 0.3$ ft.

Step 1

From Figure 1B, $\frac{q_o \sqrt{R_o}}{h_s - h_w} = .0215$

Step 2

From Figure 2, $h_s = 604 \text{ Btu/lb}_m$

Step 3

From Figure 3, $h_w = 240 \text{ Btu/lb}_m$

then $q_o = \frac{.0215(605 - 240)}{\sqrt{0.3}}$

$$q_o = 14.3 \frac{\text{Btu}}{\text{sec-ft}^2}$$

B. Laminar Flow

1. General Bodies

The most generally accepted equation to be used for the laminar heat transfer distribution around a blunt body is given by Lees⁽¹⁾ as

$$\frac{q_w}{q_o} = \frac{0.5 \left(\frac{Pe}{Pe_2} \right) \left(\frac{u_e}{u_\infty} \right) r}{\left[\int_0^s \left(\frac{Pe}{Pe_2} \right) \left(\frac{u_e}{u_\infty} \right) r^2 ds \right]^{1/2}} \frac{\sqrt{R_o}}{G(M_\infty, \gamma, \gamma_\infty)} \quad (2)$$

For a given flight condition $\left(\frac{Pe}{Pe_2} \right) \left(\frac{u_e}{u_\infty} \right)$ is found to be a function of turning angle (θ) ⁽²⁾ only. Therefore, at a given angle, the heat transfer is

(1) Reference 2

(2) In order to calculate the pressure distribution, Newtonian flow is used up to $\theta = 50^\circ$. From 50° to 90° , Prandtl-Meyer flow is assumed.

only a function of the geometry (1). However, if a heat transfer parameter, $\frac{q_w}{q_o} \sqrt{\frac{s}{R_o}}$ is plotted against θ , the resulting curves (Figure 4) prove to be independent of the geometry also, for ellipsoids and paraboloids in the fineness ratio range of 1/2 to 10. Although only the bodies mentioned above have been investigated, it is felt that the heat transfer distribution for any body shape, that has (for a given fineness ratio and base radius) a radius of curvature at the nose between that of the parabola and ellipse, can be found by using the given curves. For bodies outside this range, it is advisable to examine the similarity between them and the body shapes investigated here. If the geometry compares favorably, the use of this analysis is recommended.

In general, the error that can be expected from these curves depends upon the turning angle. Up to 50 degrees, the error is within 5 percent of the value indicated. From 50 through 90 degrees, the error will vary from 5 to 15 percent, being greatest in the range from 80-90 degrees.

(1) Relation between radius and distance along the surface.

Notice that these curves are independent of altitude (and only slightly dependent upon free stream Mach number). However, in order to get q_w , one must first calculate the heat transfer rate at the stagnation point (q_0), which is a function of altitude.

The relations between turning angle, distance along the body and axial location are presented in Figures 5 and 6 for the ellipse and parabola with fineness ratios of 1/2 and 10.

Example 2

Flight Conditions: $M_\infty = 5$, alt. = 100,000 ft., Ellipsoid ($L/D = 1/2$)

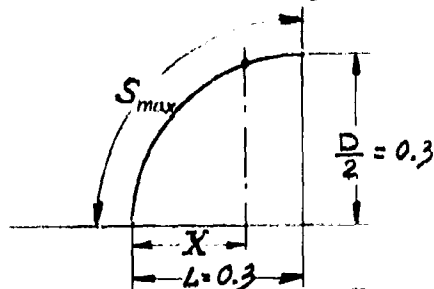
$$\theta = 50^\circ, R_0 = 0.3 \text{ ft.}$$

Step 1

From Figure 4, $\frac{q_w}{q_0} \sqrt{\frac{s}{R_0}} = 0.490$

Step 2

From Figure 6, $s/s_{\max} = 0.57$



$$s_{\max} = \frac{2\pi(0.3)}{4} = 0.471$$

$$s = .57(.471) = 0.268 \text{ ft.}$$

Also from Figure 5, $\frac{x}{L} = 0.35$

Step 3

$$\frac{q_w}{q_0} = 0.49 \sqrt{\frac{0.3}{.268}} = 0.52$$

From Example 1, $q_0 = 14.3 \frac{\text{Btu}}{\text{sec-ft}^2}$

$$q_w = .52(14.3)$$

$$q_w = 7.34 \frac{\text{Btu}}{\text{sec-ft}^2}$$

2. Sphere-Cone

Figure 4 is also applicable to a spherically blunted cone (shown below)

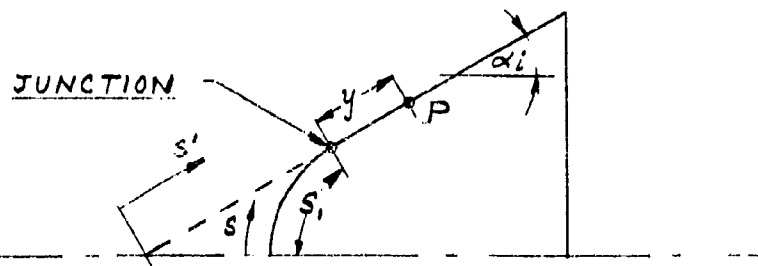


Figure A

The heat transfer for the spherical section can be determined from the curve for the ellipsoid, $\frac{L}{D} = 1/2$ (sphere).

The procedure for the conical section is as follows:

Step 1

At the junction of the sphere and cone ($\theta = 90 - \alpha_i$), determine $\frac{q_w}{q_0} \sqrt{\frac{s}{R_0}}$, which is constant for the rest of the body.

Step 2

Determine $q_w \sqrt{s}$ at the junction (point 1).

Step 3

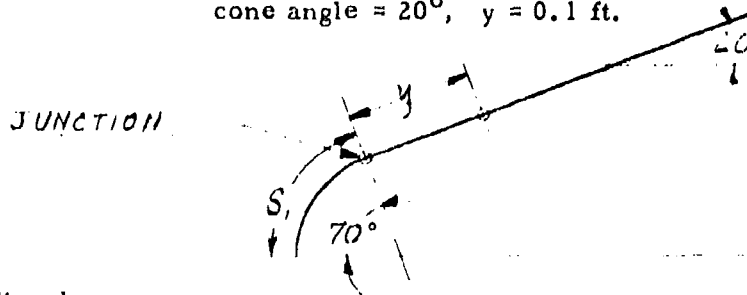
Find q_w at point P from $q_w \sqrt{s_1} = q_p \sqrt{(s_1 + y)}$

This analysis for the conical section is only approximate since the value of $q_w \sqrt{s}$ is not a constant, but increases with s . "Far" from the junction (when s is almost equal to s') a constant value is approached, which agrees with the results obtained from Equation 7 (see page 205). In general, the above method gives quite accurate results near the junction, and decreases in accuracy as s increases. The entire procedure is, however, recommended as a good engineering estimate.

Example 2a

Flight Conditions: $M_\infty = 5$, alt. = 100,000 ft., $R_0 = 0.3$ ft.

cone angle = 20° , $y = 0.1$ ft.



Step 1

From Figure 4 at $\theta = 70^\circ$

$$\frac{q_w}{q_0} \sqrt{\frac{s}{R_0}} = 0.28$$

$$s_1 = R_0 \theta = 0.3(70) \times \frac{\pi}{180} = 0.366 \text{ ft.}$$

$$\frac{q_w}{q_0} = 0.28 \sqrt{\frac{0.3}{0.366}} = 0.254$$

From Example 1, $q_o = 14.3 \frac{\text{Btu}}{\text{sec-ft}^2}$

$$q_w = .254(14.3) = 3.64 \frac{\text{Btu}}{\text{sec-ft}^2}$$

Step 2

Now since $q_w s^{1/2} = \text{constant}$,

$$(q_w)_{s_1} s_1^{1/2} = (q_w)_{s_1 + y} (s_1 + y)^{1/2}$$

$$(q_w)_{s_1 + y} = 3.64 \sqrt{\frac{0.366}{0.466}}$$

$$(q_w)_{s_1 + y} = 3.27 \frac{\text{Btu}}{\text{sec-ft}^2}$$

C. Turbulent Flow

1. General Bodies

The following equation is used to calculate the turbulent heat transfer rate around a blunt body,

$$q_w = 0.0072 \frac{u_e^{0.8} \rho_r^{0.8} \mu_r^{0.2}}{(P_{R_r})^{0.667}} \frac{(T_{aw} - T_w)}{s^{0.2}} \frac{\text{Btu}}{\text{sec-ft}^2} \quad (3)$$

The quantities that must be known for each calculation are: M_∞ , altitude, T_w , s (which defines θ for a given body).

Step 1

From Figure 7, determine the ratio of the local pressure to the stagnation pressure behind a normal shock $\left(\frac{P_e}{P_{s_2}}\right)$ for a given free stream Mach number and turning angle.

Step 2

From Figure 8, find T_e/T_s and u_e/a^* for the previously determined value of $(\frac{P_0}{P_{S_2}})$.

Step 3

From Figures 9, 10 and 11, get a^* , p_{S_2} and T_s , which are functions of Mach number and altitude. Then calculate p_e , T_e and u_e .

Step 4

Calculate the reference temperature, T_r , from the following equation:

$$T_r = 0.5 T_w + 0.22 T_s + 0.28 T_e \quad (4)$$

Step 5

Calculate ρ_r from,

$$\rho_r = \frac{p_e}{53.3 T_r} \frac{\text{lb}_m}{\text{ft}^3} \quad (5)$$

where p_e is in lb/ft^2 and T_r is in $^\circ\text{R}$.

Step 6

Find μ_r and P_{R_r} from Figures 12 and 13

Step 7

Calculate the adiabatic wall temperature (T_{aw}) from,

$$T_{aw} = P_{R_r}^{1/3} T_s + (1 - P_{R_r}^{1/3}) T_e \quad (6)$$

Step 8

Calculate q_w from Equation (3)

Example 3

$$q_w = 0.0072 \frac{u_e^{0.8} p_r^{0.8} \mu_r^{0.2} (T_{aw} - T_w)}{(PR_r)^{0.667} s^{0.2}}$$

Flight Conditions: $M_\infty = 5$, alt. = 100,000 ft, $T_w = 1000$, $\theta = 45^\circ$
($s = 0.236$ ft.)

Step 1

From Figure 7, $\frac{p_e}{p_{s2}} = 0.517$

Step 2

From Figure 8, $\frac{u_e}{a^*} = 1.015$ $\frac{T_e}{T_s} = .828$

Step 3

From Figure 9 $a^* = 2240$ fps

Figure 10c $p_{s2} = 738$ lb/ft²

Figure 11 $T_s = 2500$ °R

$$u_e = 1.015 (2240) = 2280 \text{ fps}$$

$$p_e = 0.517 (738) = 382 \text{ lb/ft}^2$$

$$T_e = .828 (2500) = 2070 \text{ °R}$$

Step 4

$$T_r = 0.5 (1000) + .22 (2500) + .28 (2070)$$

$$T_r = 1630^\circ\text{R}$$

Step 5

$$p_r = \frac{382}{53.3 (1630)} = .00440 \text{ lb}_m/\text{ft}^3$$

Step 6

From Figures 12 and 13

$$\mu_r = 0.264 \times 10^{-4} \text{ lb}_m/\text{ft-sec}$$

$$P_{R_r} = .705$$

$$(P_{R_r})^{1/3} = .890$$

$$(P_{R_r})^{2/3} = .792$$

Step 7

$$T_{aw} = .890 (2500) + (1 - .890) 2070$$

$$T_{aw} = 2440^\circ\text{R}$$

Step 8

$$q_w = \frac{0.0072(2280)^{0.8} (.0044)^{0.8} (2.64 \times 10^{-5})^{0.2} (2440 - 1000)}{.792 (0.236)^{0.2}}$$

$$q_w = 13.4 \text{ Btu/sec-ft}^2$$

2. Sphere-Cone

The turbulent heat transfer about a sphere-cone can be calculated in a similar manner to the laminar heat transfer about a sphere-cone.

Step 1

Determine q_w at the junction of the sphere and cone by using the turbulent blunt body equations

Step 2

Assume $q_w s^{0.2} = \text{constant}$ from the junction to the back of the body (as in the laminar case⁽¹⁾), this gives most accurate results near

(1) See page 199

the junction.

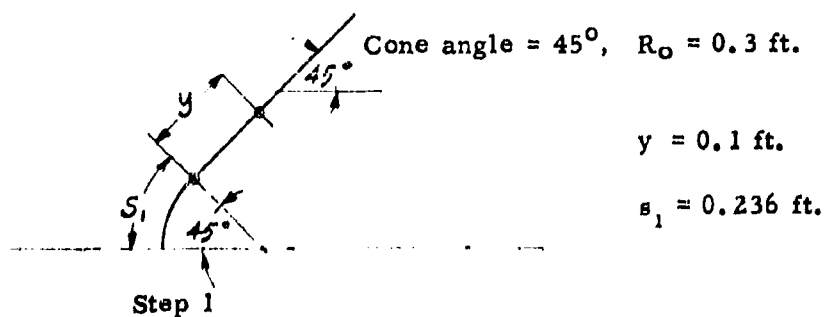
Step 3

Determine q_w at a given value of s .

Note that for the spherical section, the method described in the previous section is used.

Example 3a

Flight Conditions: $M_\infty = 5$, alt. = 100,000 ft., $T_w = 1000^\circ\text{R}$



From Example 3, $(q_w)_{s_1} = 13.4$ Btu/sec-ft²

Step 2

$$(q_w)_{s_1} s_1^{0.2} = (q_w)_{s_1 + y} (s_1 + y)^{0.2}$$

$$(q_w)_{s_1 + y} = 13.4 \left(\frac{0.236}{0.336} \right)^{0.2}$$

$$(q_w)_{s_1 + y} = 12.5 \text{ Btu/sec-ft}^2$$

3. POINTED BODIES (ATTACHED SHOCK)

A. Ogives

1. Laminar Flow

The following equation is used to calculate the laminar heat transfer rate around a pointed-nosed body,

$$q_w = \frac{0.0796 A \rho_r^{0.5} u_e^{0.5} \mu_r^{0.5} (T_{aw} - T_w)}{(P_{Rr})^{0.667} s^{0.5}} \frac{\text{Btu}}{\text{sec-ft}^2} \quad (7)$$

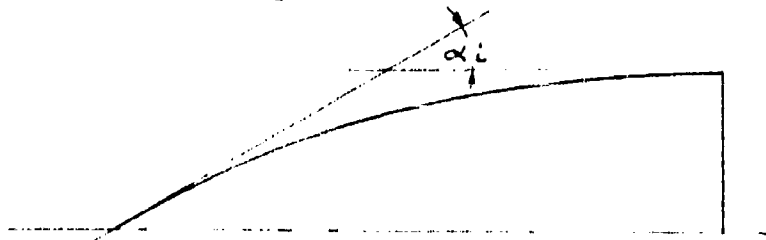


Figure B

The quantities that must be known for each calculation are: M_∞ , altitude, T_w , s (which defines θ for a given body), α_i (inclination angle at the nose).

Step 1

From Figures 14-19 (depending on M_∞), the ratio of local pressure to stagnation pressure behind a conical shock ($\frac{P_e}{P_{s2}}$) can be found for a given initial inclination angle and turning angle.

Step 2

From Figure 8 get $\frac{u_e}{a^*}$ and $\frac{T_e}{T_s}$ for a given value of $\frac{P_e}{P_{s2}}$.

Step 3

From Figure 9, get a^*

From Figure 11, get T_s

} For a given M_∞ and altitude

Then calculate u_e and T_e .

Step 4

From Figure 20, get $\frac{p_{s2}}{p_\infty}$ for a given M_∞ and initial inclination angle.

Step 5

From Figure 21, get p_{o1} for a given altitude and calculate p_{s2} . Then find p_o .

Step 6

Calculate the reference temperature (T_r)

$$T_r = 0.5 T_w + 0.22 T_s + 0.28 T_e$$

Step 7

Calculate ρ_r from $\rho_r = \frac{p_e}{53.3 T_r} \frac{\text{lb}_m}{\text{ft}^3}$

where p_e is in lb/ft^2 and T_r is in $^\circ\text{R}$.

Step 8

Find μ_r and P_{R_r} from Figures 12 and 13.

Step 9

Calculate the adiabatic wall temperature (T_{aw}) from,

$$T_{aw} = P_{R_r}^{1/2} T_s + (1 - P_{R_r}^{1/2}) T_e$$

Step 10

From the following equation, solve for A

$$A = \begin{cases} \sqrt{3} & \theta \leq 65^\circ \\ (\sqrt{3} - 1) \frac{90 - \theta}{\alpha_i} + 1 & \theta \geq 65^\circ \end{cases} \quad (8)$$

Step 11

Solve for q_w from Equation (7).

It should be noted that this equation for the heat transfer rate predicts an infinite value at the nose of a pointed body. Since this is not the actual value, it is suggested that the equation be used only up to one wall thickness of the apex. In the region where the heat transfer cannot be predicted accurately, assume that the temperature at the wall is equal to the adiabatic wall temperature.

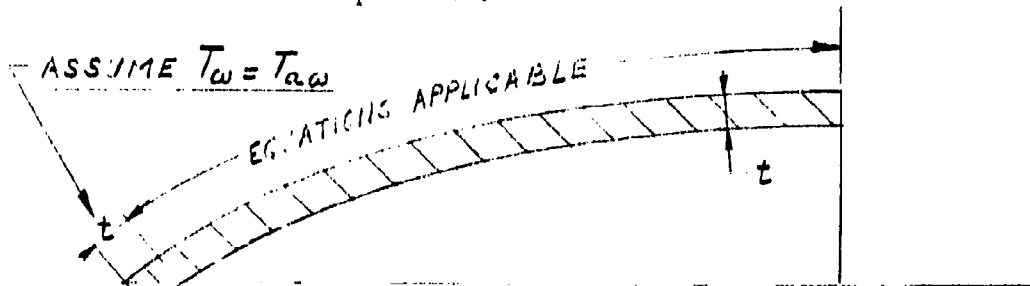


Figure C

Example 4

$$q_w = \frac{.0796 A \rho_r^{0.5} u_e^{0.5} \mu_r^{0.5} (T_{aw} - T_w)}{(P_{R_r})^{0.667} s^{0.5}}$$

Flight Conditions: $M_\infty = 5$, alt. = 100,000 ft., $T_w = 1000^\circ\text{R}$

$$\alpha_i = 35^\circ, \quad \theta = 70^\circ (\bar{s} = 0.5 \text{ ft.})$$

Step 1

From Figure 17B $\frac{p_e}{p_{s_2}} = .038$

Step 2

From Figure 8 $\frac{T_e}{T_s} = .393 \quad \frac{u_e}{a^*} = 1.91$

Step 3

From Figure 9 $a^* = 2240 \text{ fps}$

Figure 11 $T_s = 2500^\circ\text{R}$

$$u_e = 1.91(2280) = 4280 \text{ fps} \quad T_e = .393(2500) = 983^\circ\text{R}$$

Step 4

From Figure 20 $\frac{p_{s_2}}{p_\infty} = 130$

Step 5

From Figure 21B $p_\infty = 22.5 \text{ lb/ft}^2$

$$p_{s_2} = 130(22.5) = 2930 \text{ lb/ft}^2$$

$$p_e = .038(2930) = 111 \text{ lb/ft}^2$$

Step 6

$$T_r = .5(1000) + .22(2500) + .28(983)$$

$$T_r = 1325^\circ\text{R}$$

Step 7

$$\rho_r = \frac{111}{53.3(1325)} = .00158 \text{ lb}_m/\text{ft}^3$$

Step 8

From Figures 12 and 13

$$\mu_r = 0.230 \times 10^{-4} \text{ lb}_m/\text{ft-sec} \quad (p_r)^{1/2} = .832$$

$$P_{R_r} = 0.692 \quad (p_r)^{2/3} = .782$$

Step 9

$$T_{aw} = .834 (2500) + (.832) (.168)$$

$$T_{aw} = 2240^\circ\text{R}$$

Step 10

$$A = (1.732 - 1) \left(\frac{20}{35} \right) + 1 = 1.418$$

Step 11

$$q_w = \frac{.0796 (1.418) (.00158)^{0.5} (4280)^{0.5} (.230 \times 10^{-4})^{0.5} (2240 - 1000)}{.782 (0.5)^{0.5}}$$

$$q_w = 3.16 \text{ Btu/sec-ft}^2$$

2. Turbulent Flow

The following equation ⁽¹⁾ is used to calculate the turbulent heat transfer rate around a pointed-nosed body,

$$q_w = \frac{0.00828 u_e^{0.8} p_r^{0.8} \mu_r^{0.2} (T_{aw} - T_w)}{(P_{R_r})^{0.667} s^{0.2}} \quad \frac{\text{Btu}}{\text{sec-ft}^2} \quad (9)$$

(1) See page 207 for method used near the apex.

Step 1

Use the same method to get the properties (except T_{aw}) as for laminar flow around an ogive ⁽¹⁾ (previous section)

Step 2

$$T_{aw} = P_{R_r}^{1/3} T_s + (1 - P_{R_r}^{1/3}) T_e$$

Step 3

Calculate q_w from Equation (9)

Example 5

Step 1

$$\rho_r = .00158 \text{ lb}_m/\text{ft}^3$$

$$P_{R_r} = .692$$

$$u_e = 4280 \text{ fps}$$

$$s = 0.5 \text{ ft}$$

$$\mu_r = 0.230 \times 10^{-4} \text{ lb}_m/\text{ft-sec.} \quad T_s = 2500^\circ\text{R}$$

$$T_e = 983^\circ\text{R}$$

Step 2

$$(P_{R_r})^{1/3} = .885$$

$$T_{aw} = .885(2500) + (.115)(983)$$

$$T_{aw} = 2330^\circ\text{R}$$

(1) Note that it is not necessary to calculate the factor A for turbulent flow.

Step 3

$$q_w = \frac{.00828 (4280)^{0.8} (.00158)^{0.8} (2.30 \times 10^{-5})^{0.2} (2330 - 1000)}{.782 (0.5)^{0.2}}$$

$$q_w = 8.70 \text{ Btu/sec-ft}^2$$

B. Cones

For cones at a given flight condition, all properties are assumed constant along the surface. Therefore, q_w is a function of s only.

1. Laminar Flow

Equation (7) is used to calculate q_w for laminar flow around cones.

The quantities which must be known are, M_∞ , altitude, T_w , α_i (cone-semi-vertex angle)

Step 1

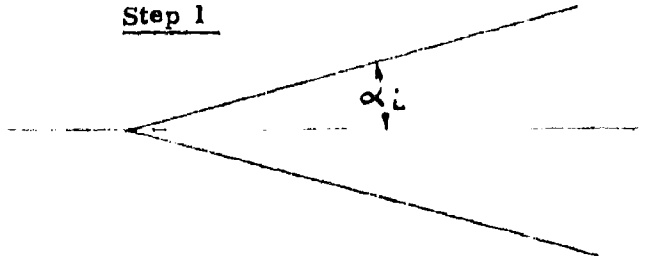


Figure D

In order to get the local pressure along the cone, Figures 14-19 are used. For a given M_∞ , $\frac{P_e}{P_{s_2}}$ is found at the first point on the curve for the desired α_i (i.e., the point where $\theta = 90 - \alpha_i$).

Step 2

From Figure 8 get $\frac{u_c}{a^*}$ and $\frac{T_c}{T_s}$ for the value of $\frac{P_e}{P_{s_2}}$ gotten in

Step 1.

Step 3

From Figure 9, get a^*

From Figure 11, get T_s

} For a given M_∞ and altitude

Then calculate T_e and u_e .

Step 4

From Figure 20, get $\frac{p_{s2}'}{p_\infty}$ for a given M_∞ and cone semi-vertex angle.

Step 5

From Figure 21, get p_∞ for a given altitude and calculate p_{s2}' , then find p_e .

Step 6

Calculate the reference temperature (T_r)

$$T_r = 0.5 T_w + 0.22 T_s + 0.28 T_e$$

Step 7

Calculate ρ_r from, $\rho_r = \frac{p_e}{53.3 T_r} \frac{\text{lb}_m}{\text{ft}^3}$

where p_e is in lb/ft^2 and T_r is in $^\circ\text{R}$.

Step 8

Find μ_r and P_{Rr} from Figures 12 and 13.

Step 9

Calculate the adiabatic wall temperature (T_{aw}) from

$$T_{aw} = P_{Rr}^{1/2} T_s + (1 - P_{Rr}^{1/2}) T_e$$

Step 10

For cones, $A = \sqrt{3}$

Step 11

Solve for q_w from Equation (7)⁽¹⁾.

Example 6

Flight Conditions: $M_\infty = 5$, alt. = 100,000 ft., $T_w = 1000^\circ\text{R}$

$\alpha_i = 35^\circ$, $s = 0.5$ ft.

Step 1

From Figure 17A $\frac{p_e}{p_{s2}^*} = 0.1005$

Step 2

From Figure 8 $\frac{u_e}{a^*} = 1.696$ $\frac{T_e}{T_s} = .520$

Step 3

From Figure 9 $a^* = 2240$ fps

From Figure 11 $T_s = 2500^\circ\text{R}$

$T_e = .520(2500) = 1300^\circ\text{R}$ $u_e = 1.696(2240) = 3800$ fps

Step 4

From Figure 20B $\frac{p_{s2}^*}{p_\infty} = 130$

Step 5

From Figure 21B $p_\infty = 22.5$ lb/ft²

(1) See page 207 for method used near the apex.

$$p_{s_2}' = 22.5(130) = 2930 \text{ lb/ft}^2 \quad p_e = .1005(2930) = 294 \text{ lb/ft}^2$$

Step 6

$$T_r = 0.5(1000) + 0.22(2500) + 0.28(1300)$$

$$T_r = 1410^\circ\text{R}$$

Step 7

$$\rho_r = \frac{p_e}{53.3(T_r)} = \frac{294}{53.3(1410)}$$

$$\rho_r = .00392 \text{ lb}_m/\text{ft}^3$$

Step 8

From Figures 12 and 13

$$\mu_r = 0.240 \times 10^{-4} \text{ lb}_m/\text{ft-sec.} \quad (P_{R_r})^{1/3} = .886$$

$$P_{R_r} = 0.695 \quad (P_{R_r})^{1/2} = .834$$

$$(P_{R_r})^{2/3} = .784$$

Step 9

$$T_{aw} = P_{R_r}^{1/2} T_R + (1 - P_{R_r}^{1/2}) T_e$$

$$T_{aw} = .834(2500) + .166(1300)$$

$$T_{aw} = 2300^\circ\text{R}$$

Step 10

$$A = 1.732$$

Step 11

$$q_w = \frac{0.0796(1.732)(.00392)^{0.5}(3800)^{0.5}(0.240 \times 10^{-4})^{0.5}(2300-1000)}{0.784(0.5)^{0.5}}$$

$$q_w = 6.13 \text{ Btu/sec-ft}^2$$

2. Turbulent Flow

Step 1

Use the same method to get the properties T_{aw} as for laminar flow around a cone⁽¹⁾, (previous section).

Step 2

$$T_{aw} = P_{R_r}^{1/3} T_s + (1 - P_{R_r}^{1/3}) T_e$$

Step 3

Calculate q_w from Equation (9)⁽²⁾.

Example 7

Flight Conditions: same as Example 6

Step 1

$$u_e = 3800 \text{ fps}$$

$$P_{R_r} = 0.695$$

$$\rho_r = .00392 \text{ lb}_m/\text{ft}^3$$

$$s = 0.5$$

$$\mu_r = 0.240 \times 10^{-4} \text{ lb}_m/\text{ft-sec.}$$

$$T_e = 1300^\circ\text{R}$$

$$T_s = 2500^\circ\text{R}$$

Step 2

$$T_{aw} = P_{R_r}^{1/3} T_s + (1 - P_{R_r}^{1/3}) T_e \quad P_{R_r}^{1/3} = .886$$

$$T_{aw} = .886(2500) + .114(1300)$$

$$T_{aw} = 2370^\circ\text{R.}$$

(1) Note that it is not necessary to calculate the factor A for turbulent flow.

(2) See page 207 for method used near the apex.

Step 3

$$q_w = \frac{.00828 (3800)^{0.8} (.00392)^{0.8} (2.40 \times 10^{-5})^{0.2} (2370 - 1000)}{.784 (0.5)^{0.2}}$$

$$q_w = 17.4 \text{ Btu/sec-ft}^2$$

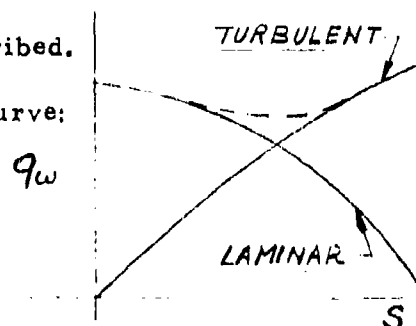
4. TRANSITION

It is expected that transition from laminar to turbulent flow will take place while the fluid passes over the body. The exact location of the transition point is usually not known for bodies of revolution. Therefore, approximate methods must be used to determine which heat transfer rate (laminar or turbulent) should be used at a given point on the body. Different methods are used for blunt and pointed-nosed bodies.

Blunt Bodies

1. Determine both the laminar and turbulent heat transfer rates along the body from methods previously described.
2. Using these rates, draw the following curve:

Figure E



3. For points before the intersection, use the laminar rate and for points after the intersection, use the turbulent rate. This probably gives the most conservative (highest) value of heat transfer at a given point.

The intersection of these two curves is not necessarily the transition point, and it is possible that in the transition region the heat transfer rate is higher than indicated by either curve. However, this cannot be taken into account because of the lack of available information. Therefore,

the above method is suggested as a good engineering estimate.

An additional degree of conservatism is obtained by fairing the curves together in the region of the intersection point (dotted line).

Pointed-Nosed Bodies

The method used for blunt bodies does not apply here since the turbulent heat transfer rate increases as the nose of the body is approached. The most conservative procedure in this case is to assume that the boundary layer is turbulent over the entire body. If this assumption results in an intolerable design, a reasonable estimate of the transition point (by experimental or other means) must be made.

REFERENCES

1. Bloom, M. H. - Thermal Conditions Associated with Aircraft in Flight - WADC Technical Report 55-169, March 1956.
2. Lees, L. - Laminar Heat Transfer Over Blunt-Nosed Bodies at Hypersonic Flight Speeds - Jet Propulsion, Vol. 26, No. 4, April 1956.
3. Ames Research Staff - Equations, Tables and Charts for Compressible Flow - NACA Technical Report 1135.
4. ICAO and NACA - Standard Atmosphere Tables and Data for Altitudes to 55,800 Feet - NACA Technical Report 1235, 1955.
5. Anon. - Standard Atmosphere (ICAO Extension) - Jet Propulsion, Vol. 26, No. 12, p. 1097, December 1956.
6. Keenan and Kaye - Gas Tables - Wiley, New York, 1948.
7. Jahnke, E. and Emde, F. - Tables of Functions - Dover Publications, New York 1945.

Z_{eff} vs M_{∞}
($P_{\infty} = P_{ref}$)

FOR ALTITUDES 0' TO 50,000'

FOR STAGNATION POINT HEAT TRANSFER

SEA LEVEL

25,000'

1

32

36

40

44

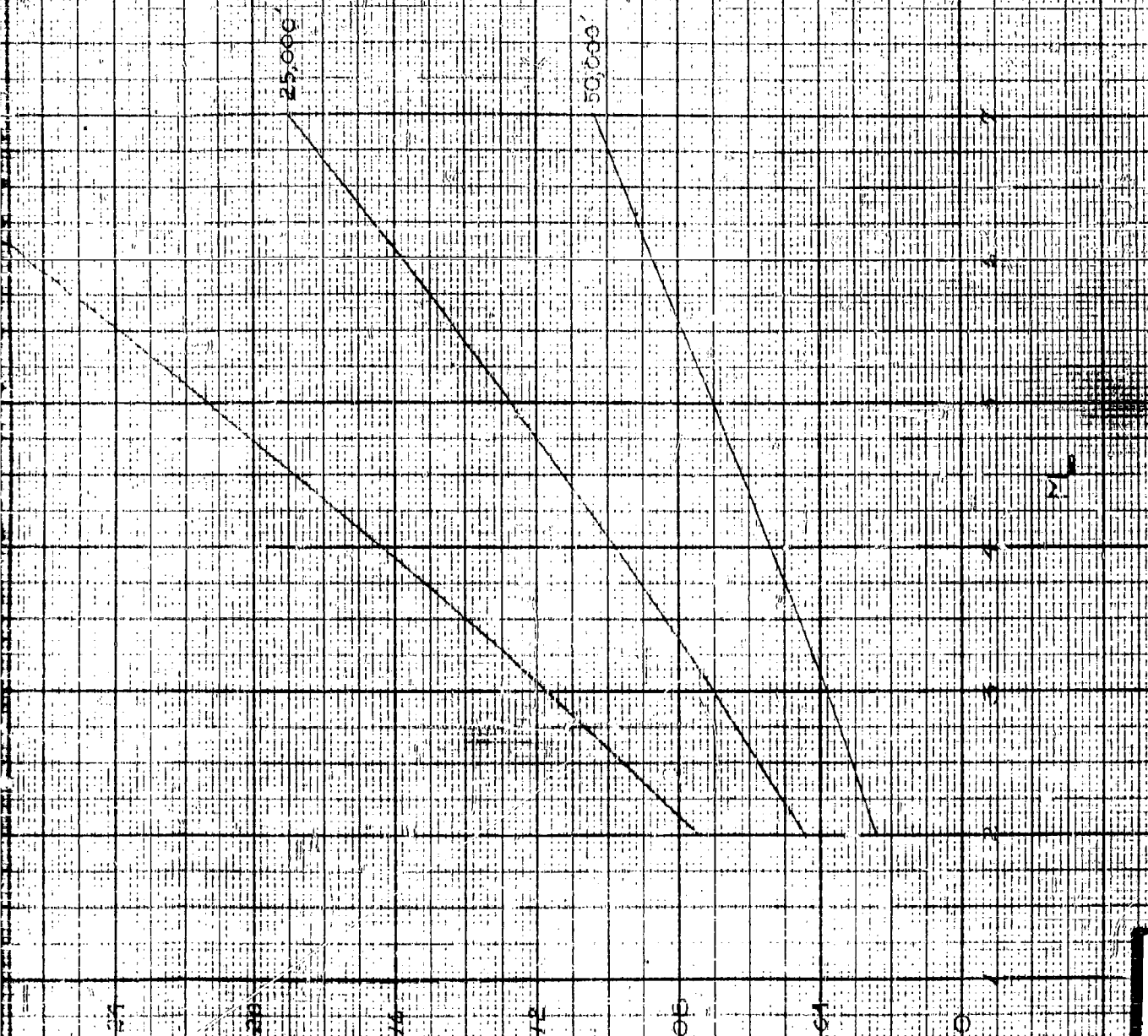
48

$$\left(\frac{h_{ref}}{h_{ref,0}} \right)_{ref}$$

$$\times \left(\frac{h_{ref}}{h_{ref,0}} \right)_{ref}$$

$$= \frac{(h_{ref})_{ref}}{h_{ref,0}}$$

FIG. 1A



2

1

$$\frac{Z}{(R_2 - R_1)} \cdot \frac{V}{M_\infty}$$

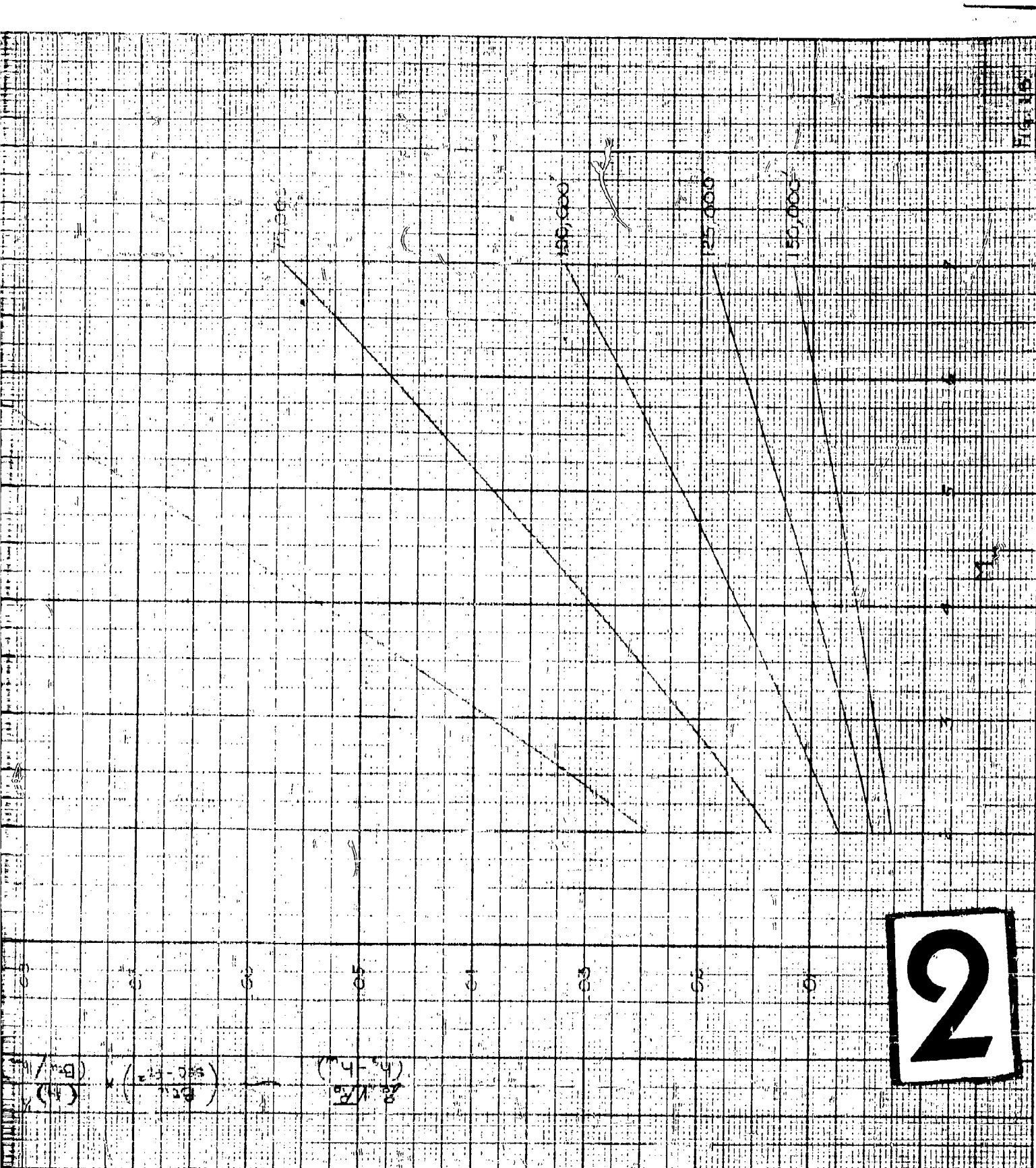
FOR ALTITUDES 5000' TO 150,000'

FOR STAGNATION POINT HEAT TRANSFER

5000'

75000'

$$\frac{(R_2 - R_1)}{(R_2 - R_1)} \cdot \frac{(R_2 - R_1)}{(R_2 - R_1)}$$



2

1

STAGNATION ENTHALPY VS. M
FOR ALTITUDES FROM 0' TO 50,000'

SEA LEVEL

300

400

500

600

700

800

900

1000

1100

150,000

175,000

200,000

225,000

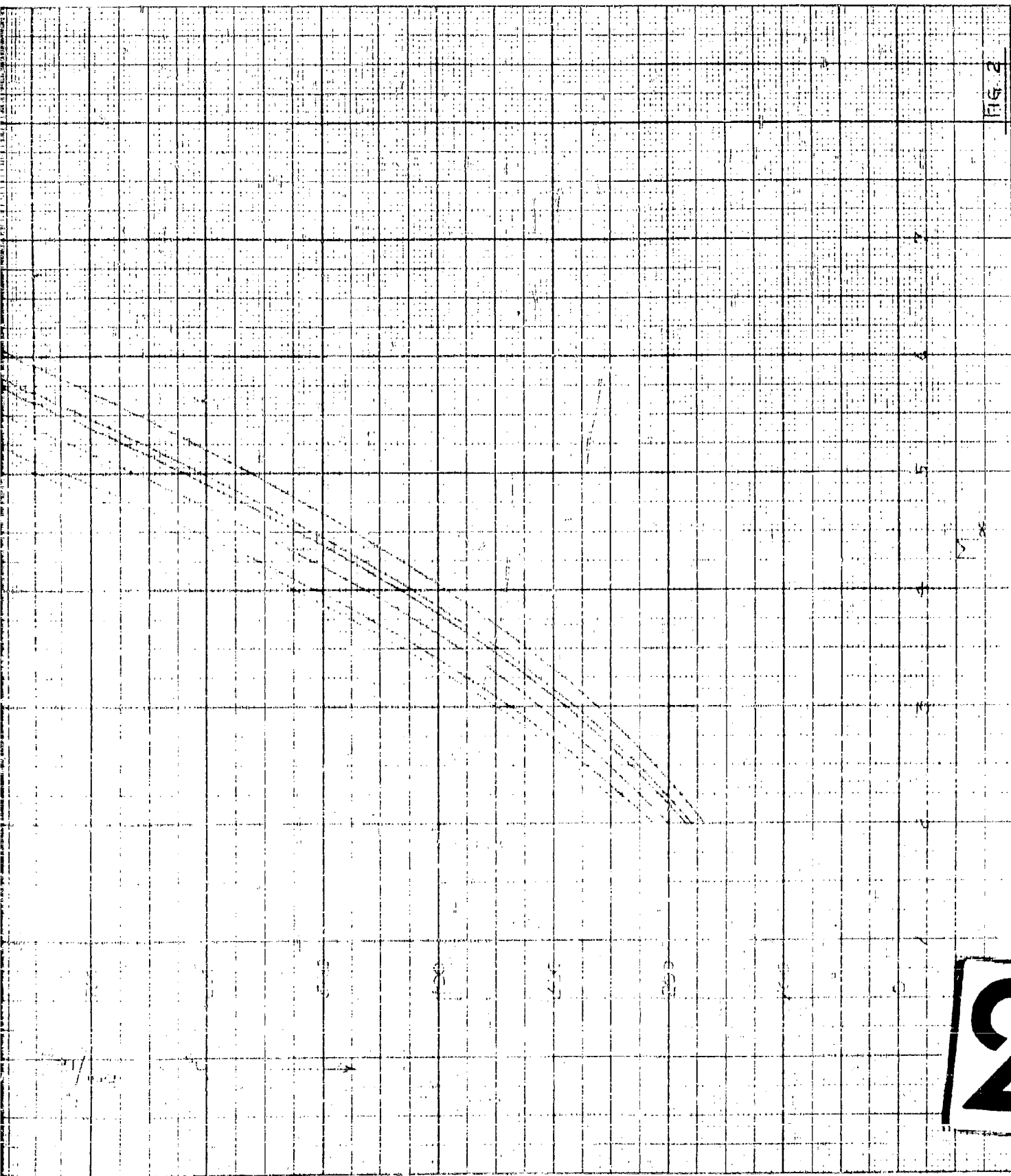
250,000

275,000

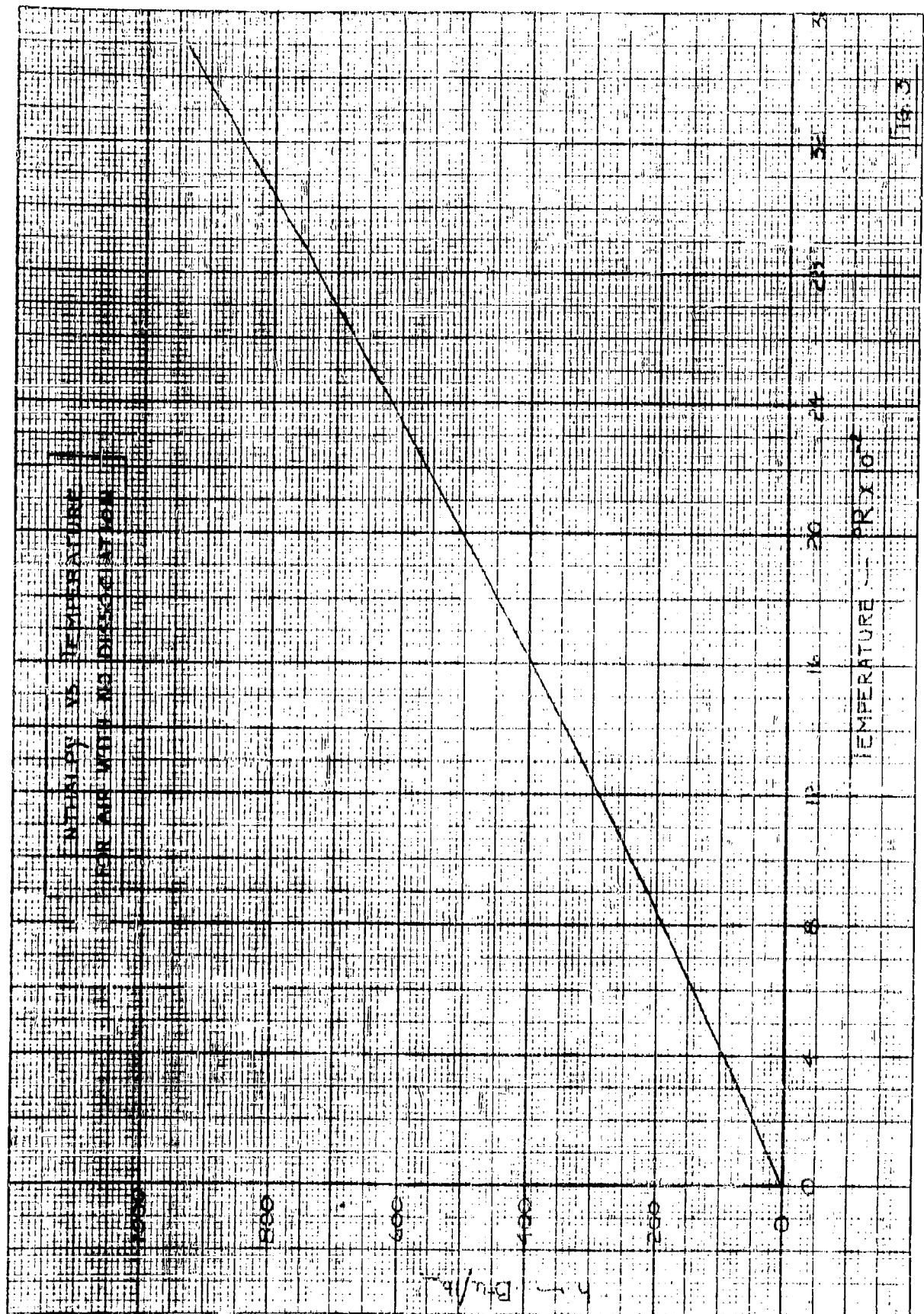
SEA LEVEL

STAGNATION ENTHALPY VS. M
FOR ALTITUDES FROM 0' TO 50,000'

FIG. 2

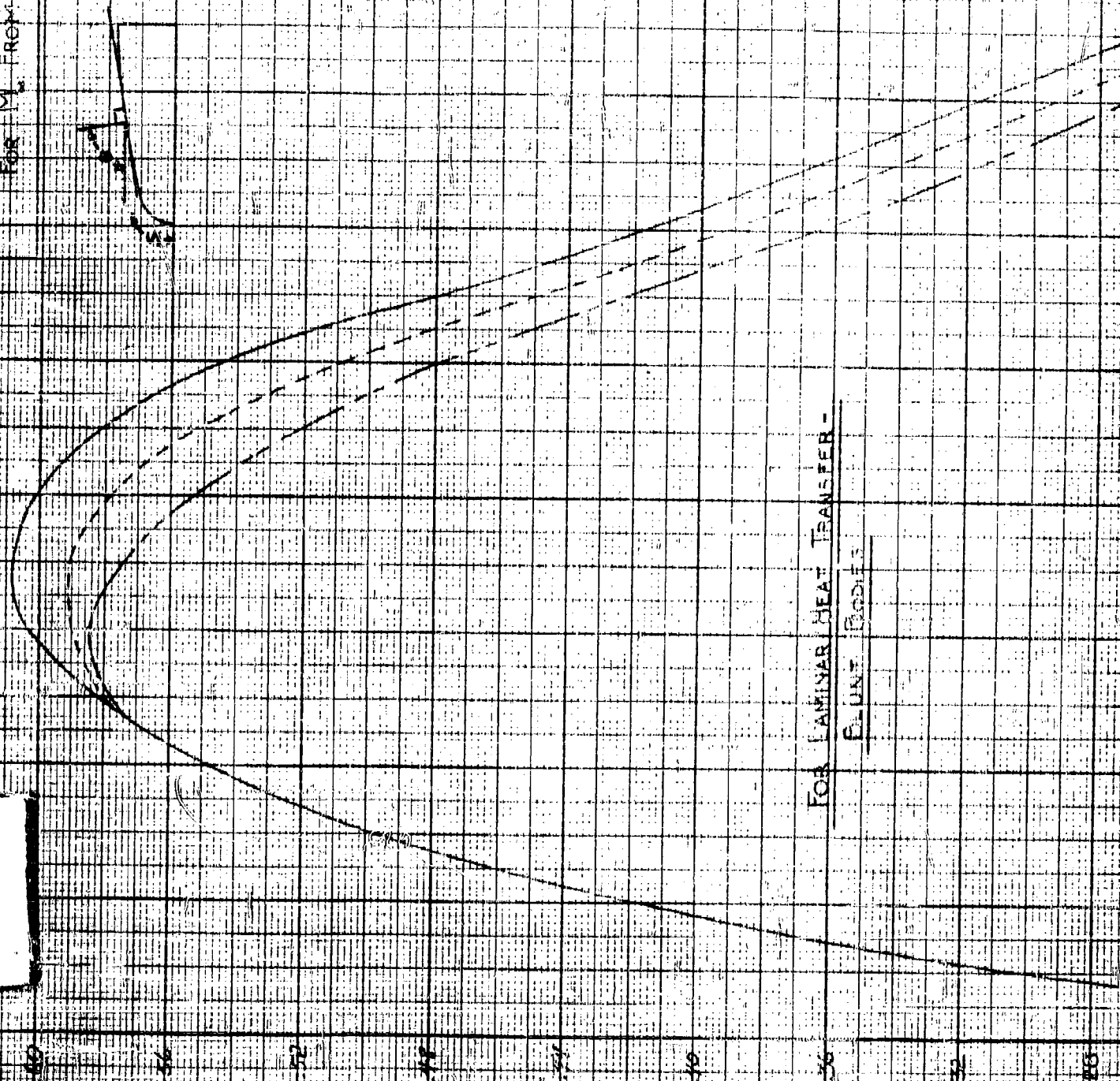


2



1

$\frac{1}{2} \sqrt{\frac{2}{\pi}}$ VS. TURNING ANGLE
 FOR M_∞ FROM 2 TO 7

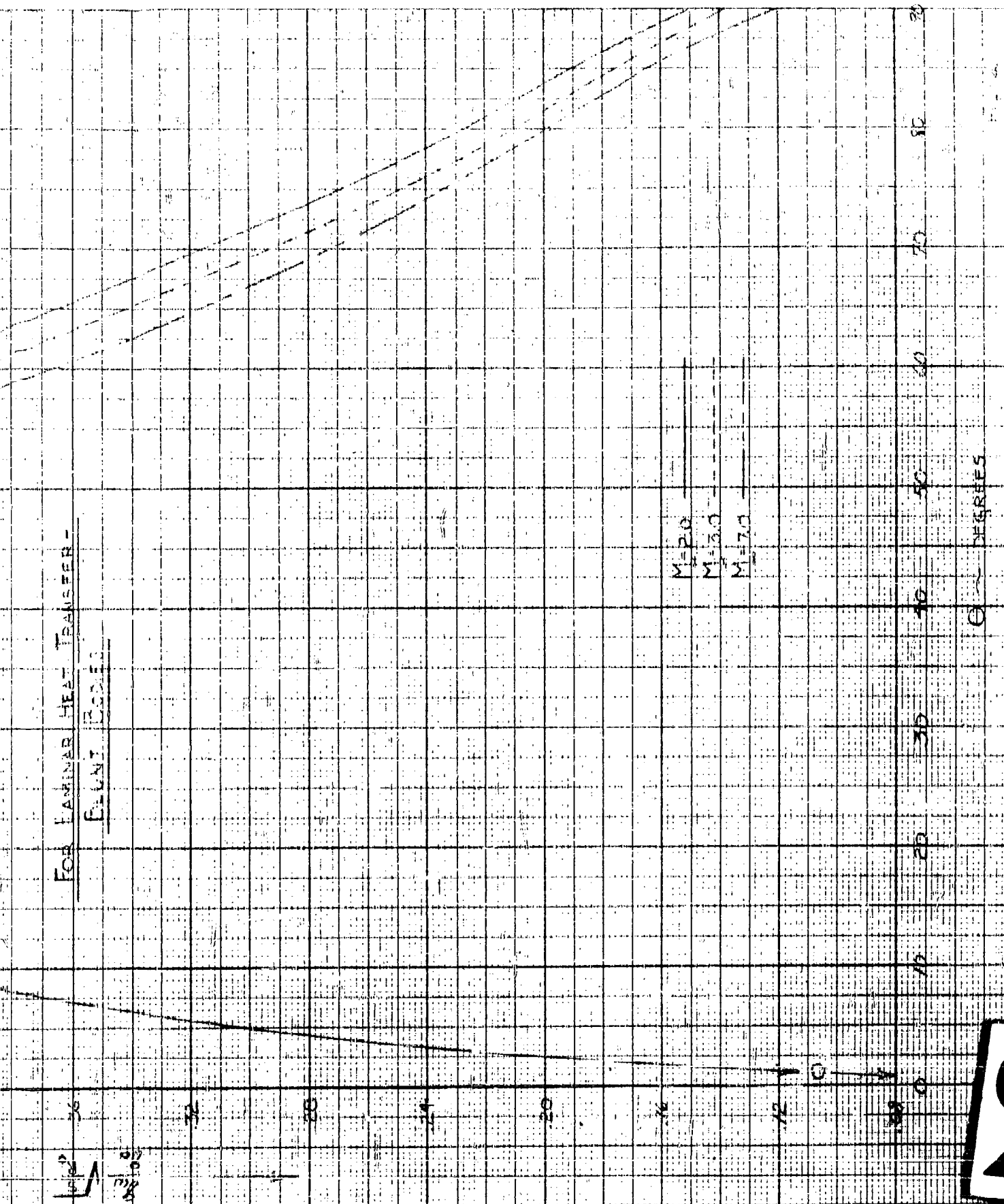


FOR LAMINAR HEAT TRANSFER -
 BLUNT BODIES

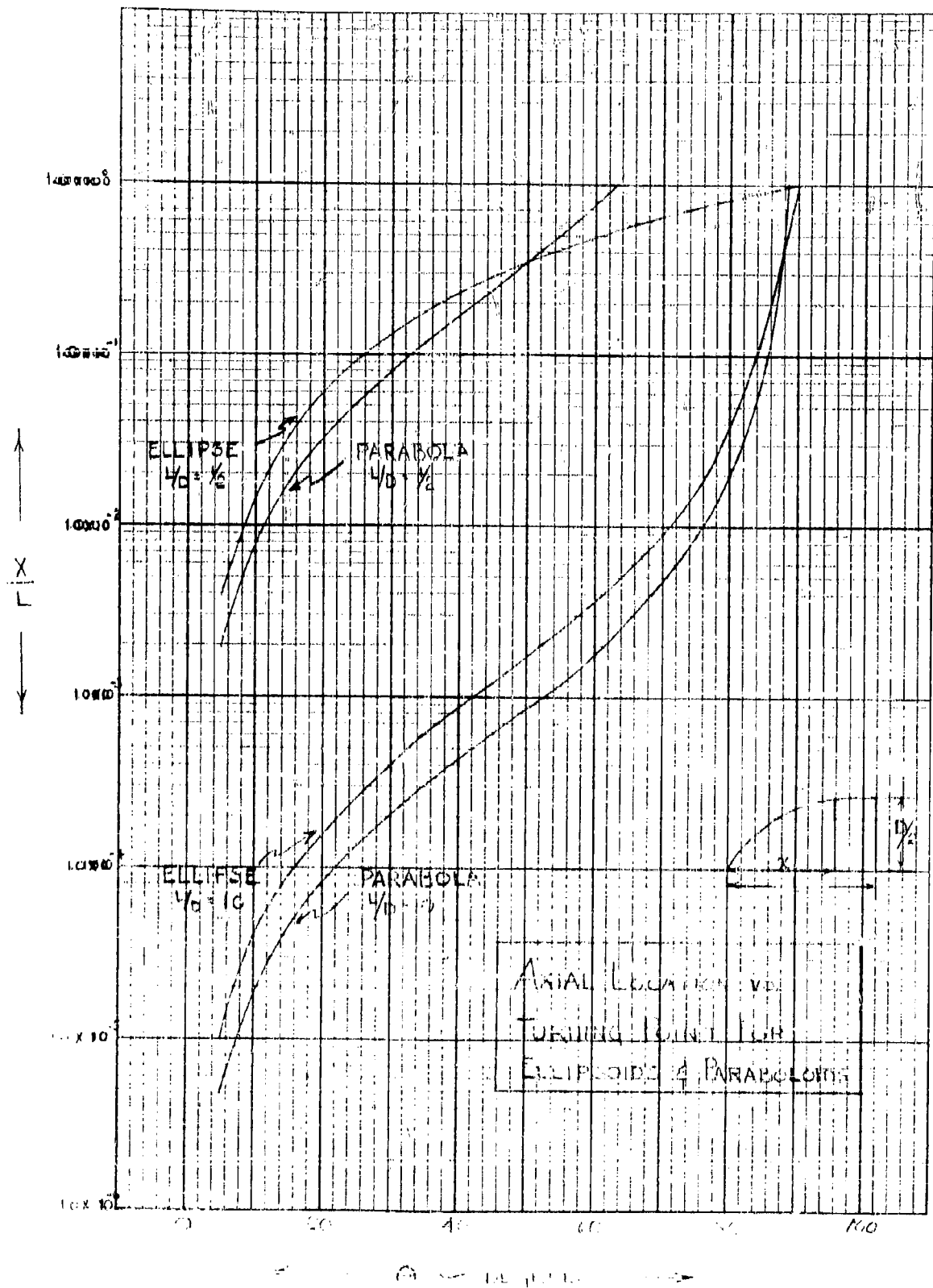
FOR LAMINAR HEAT TRANSFER -

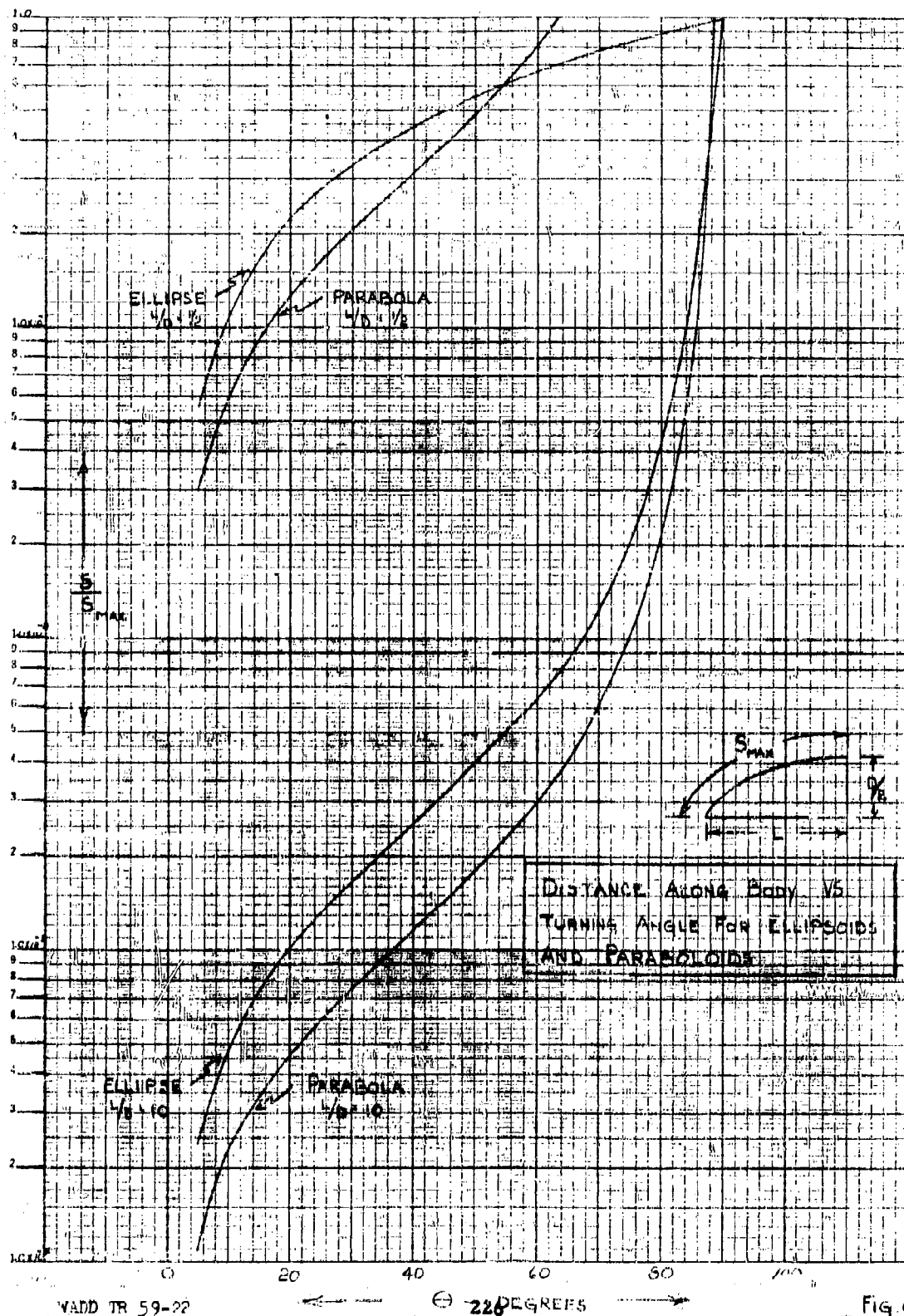
FLUNT BODIES

$\frac{h}{k} \sqrt{\frac{A}{P}}$



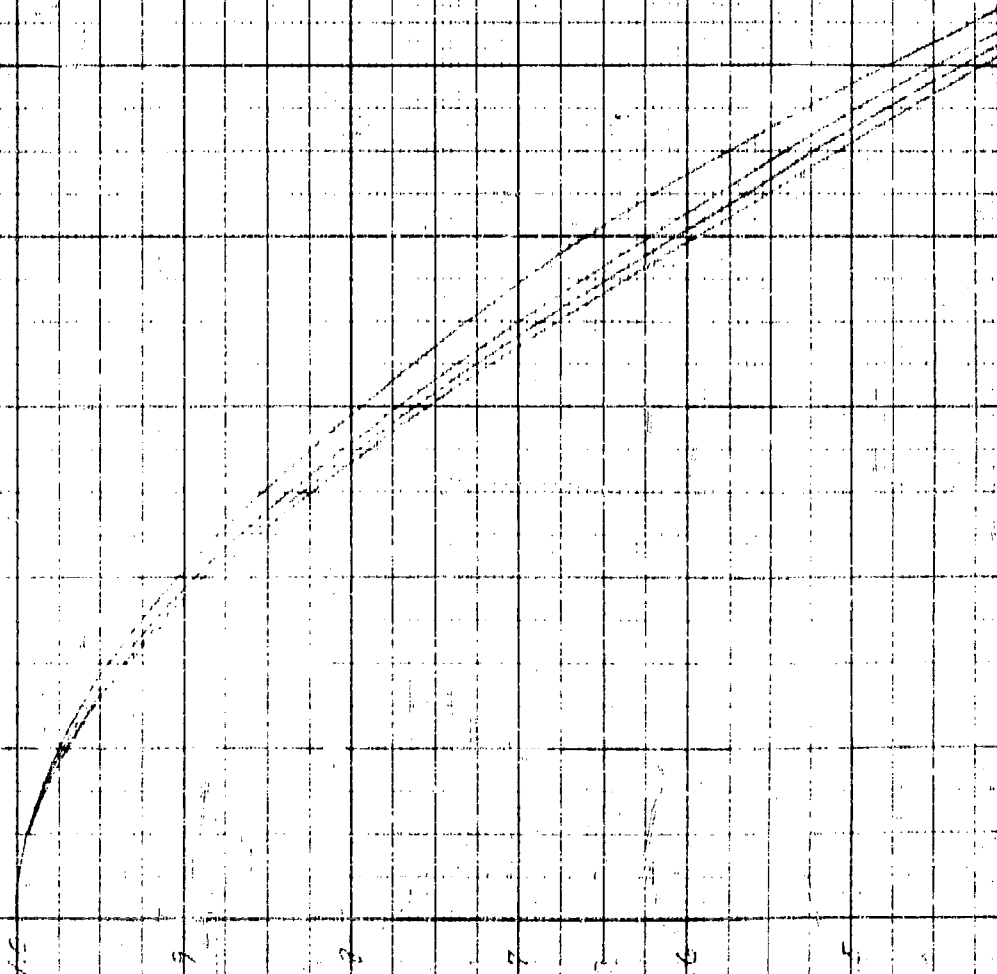
2

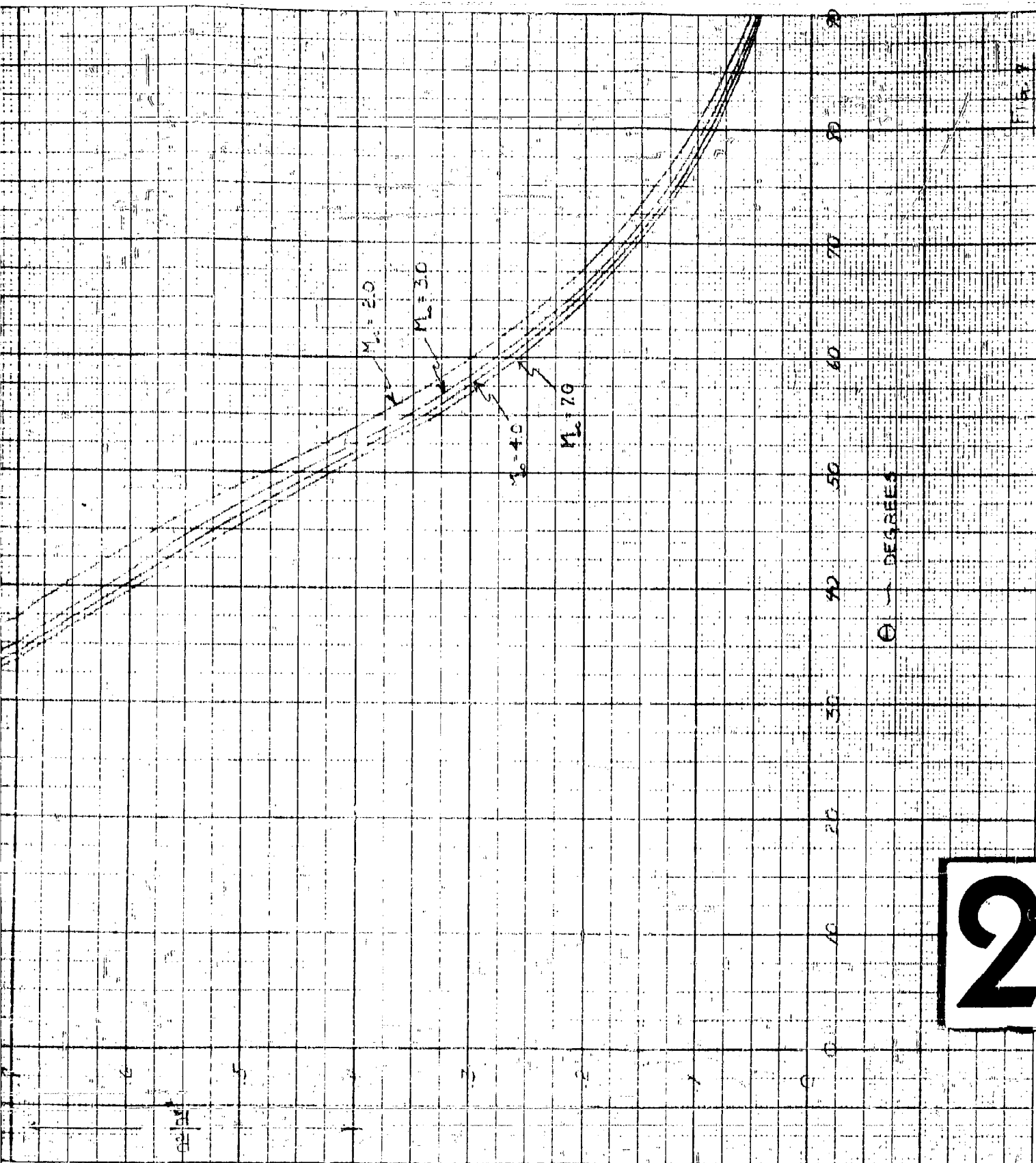




1

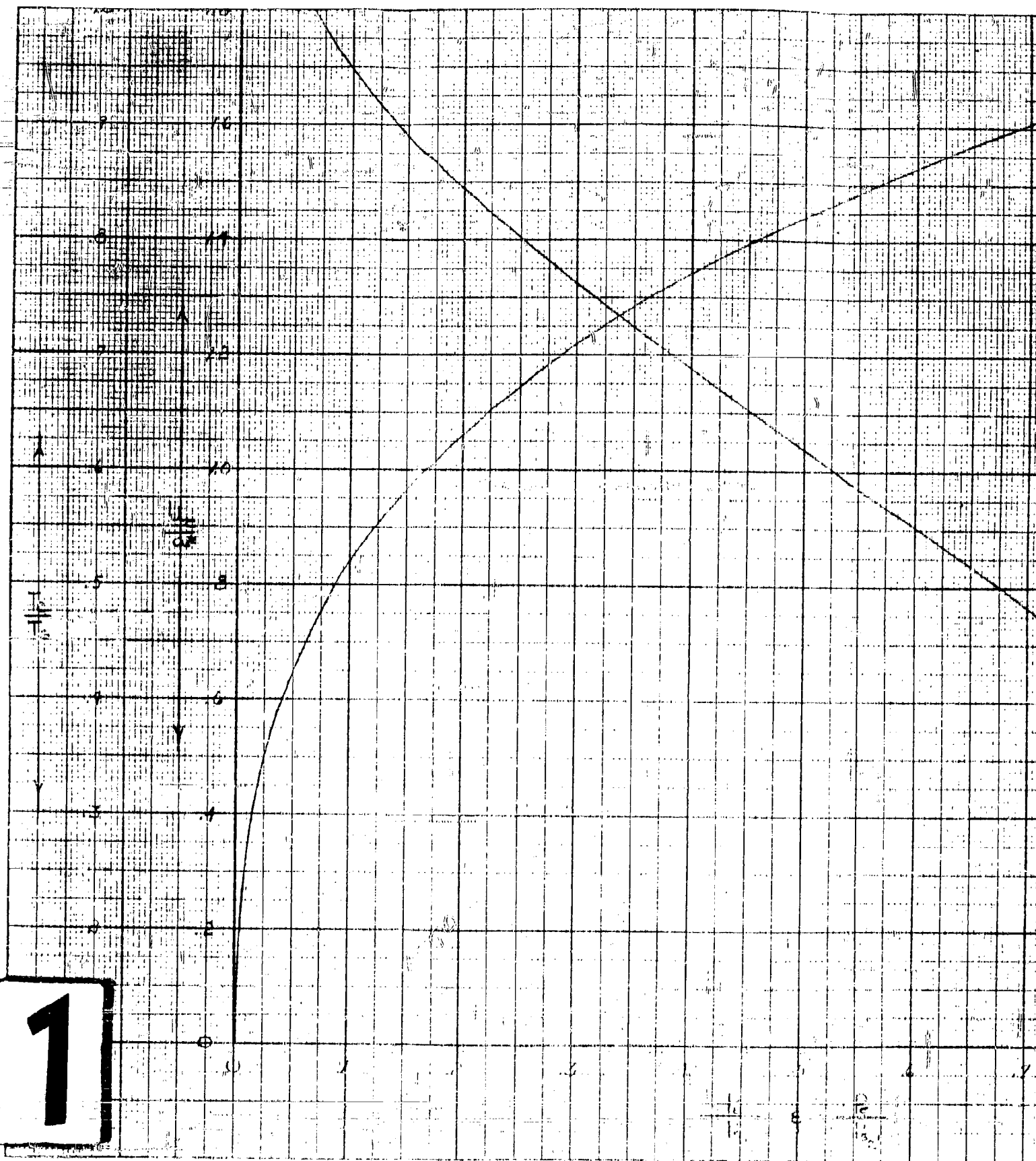
RATIO OF LOCAL PRESSURE TO STAGNATION
PRESSURE BEHIND NORMAL SHOCK VS
TURNING ANGLE FOR M_0 FROM 2 TO 7

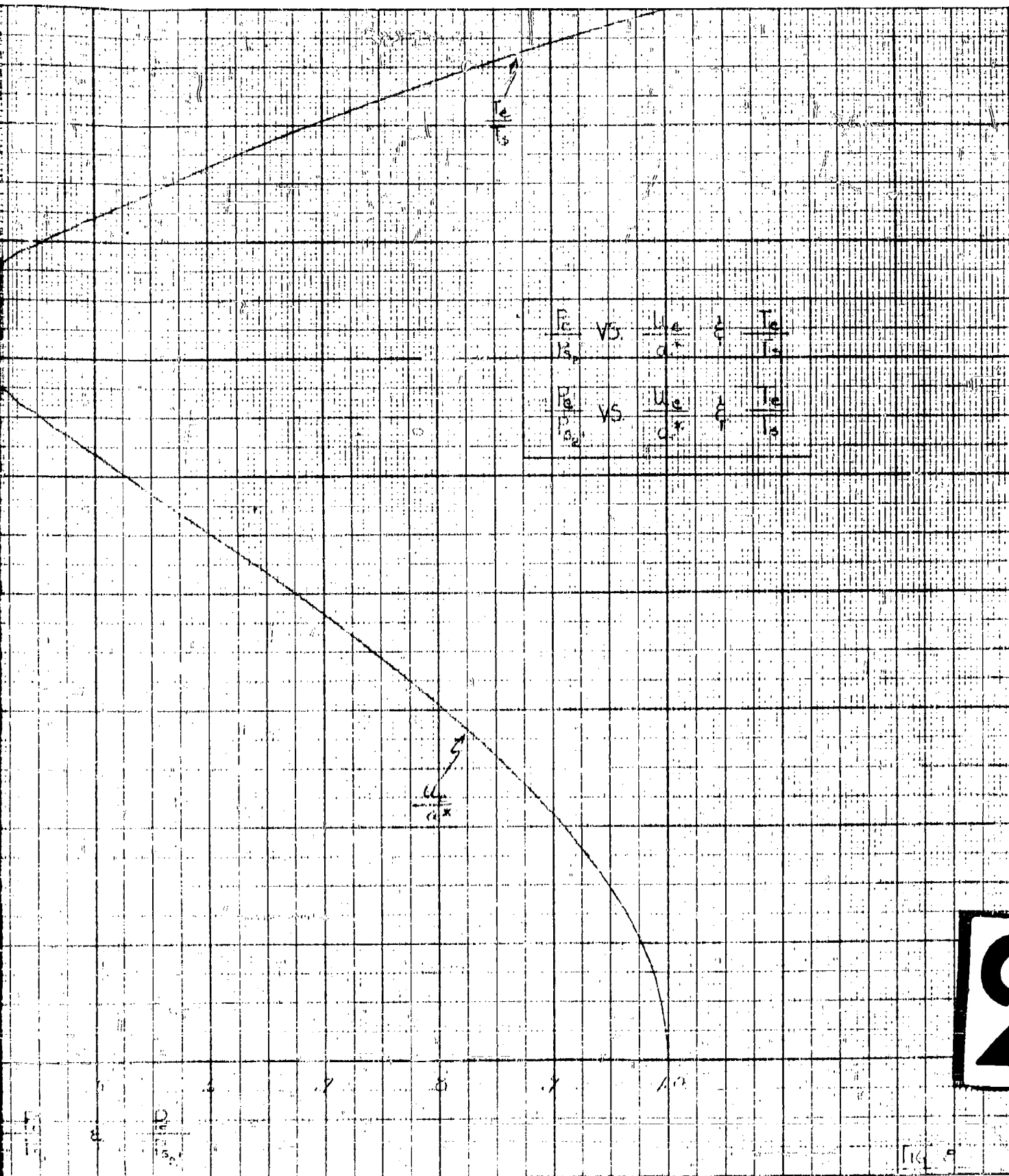




2

1





2

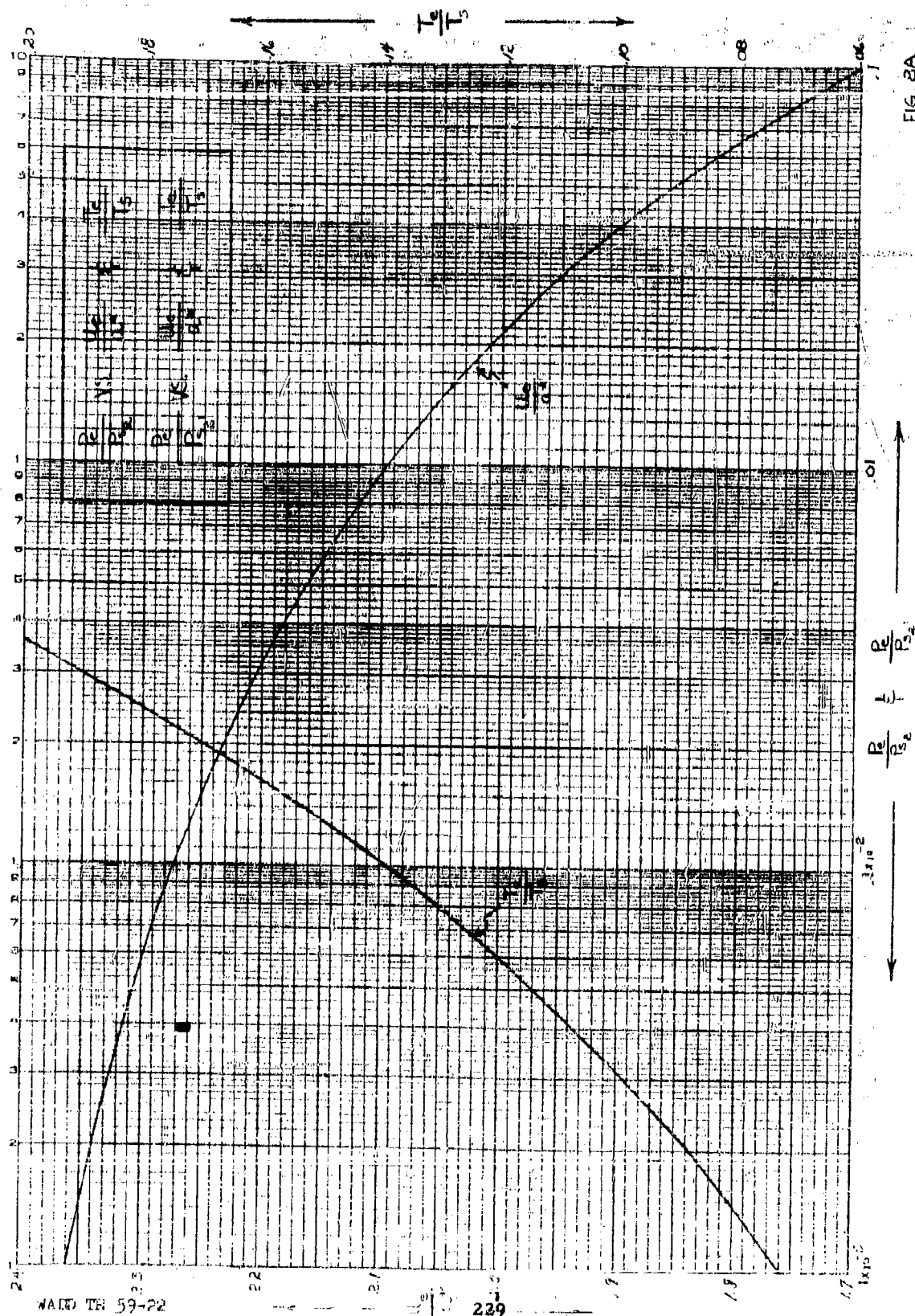
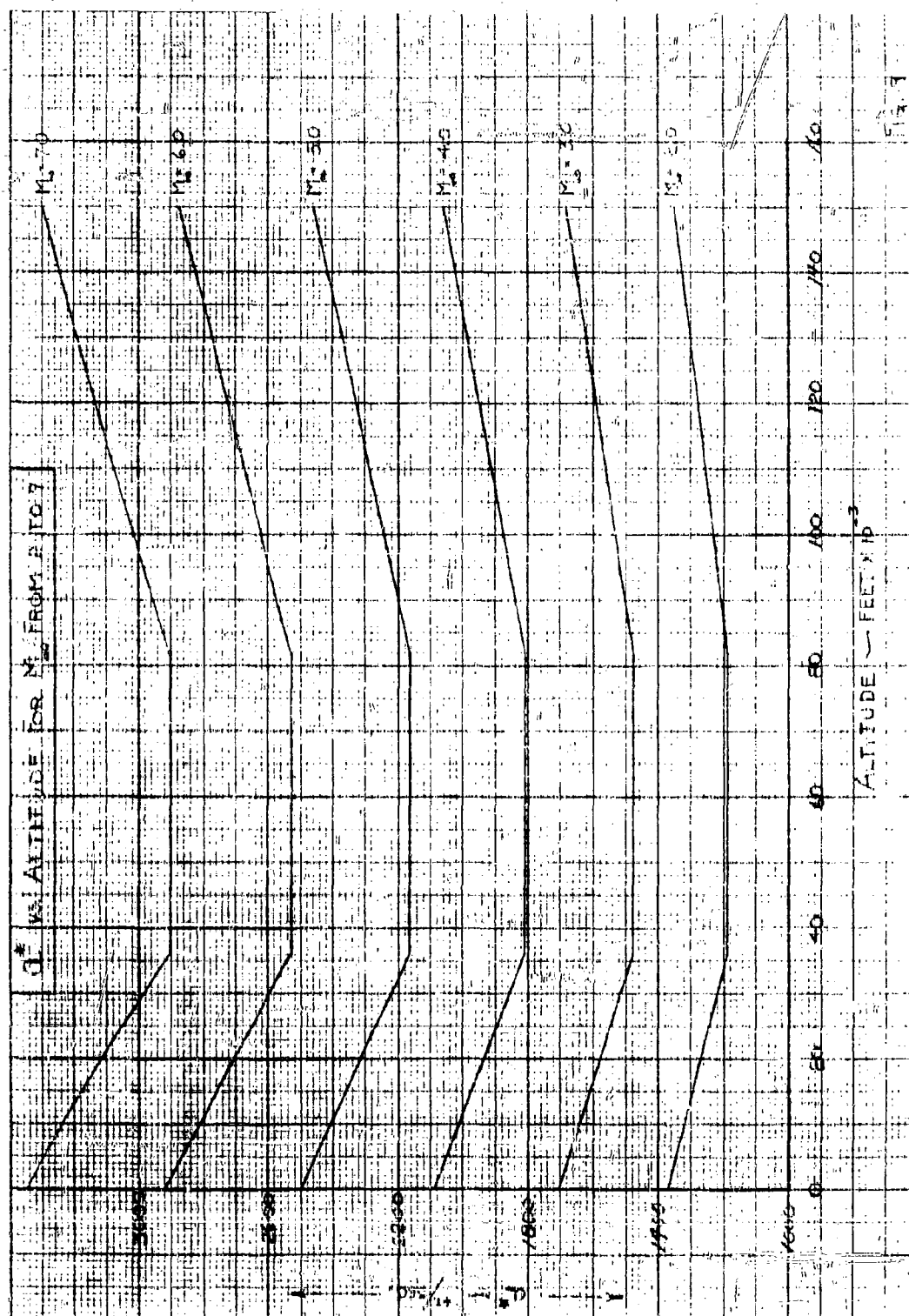
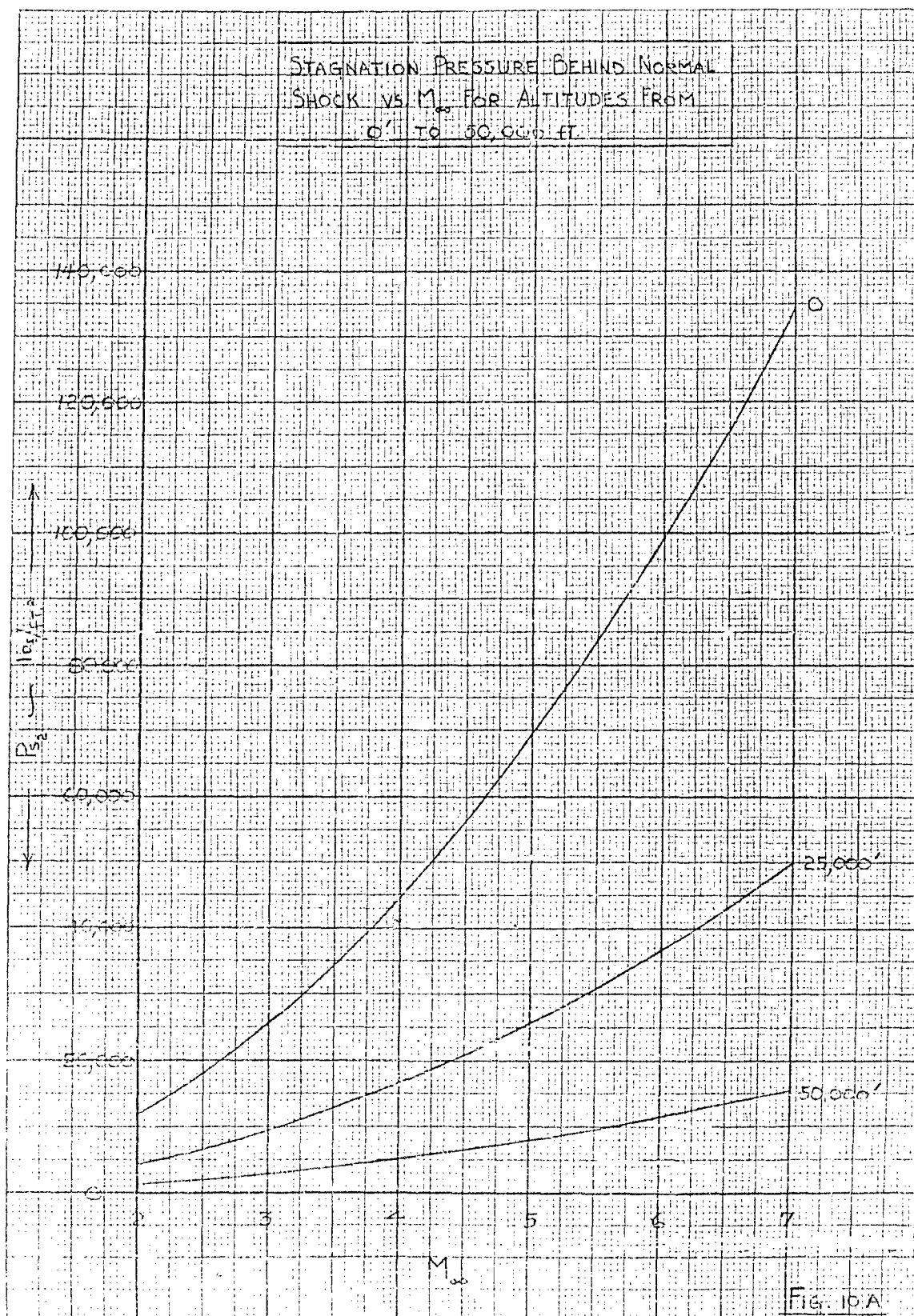
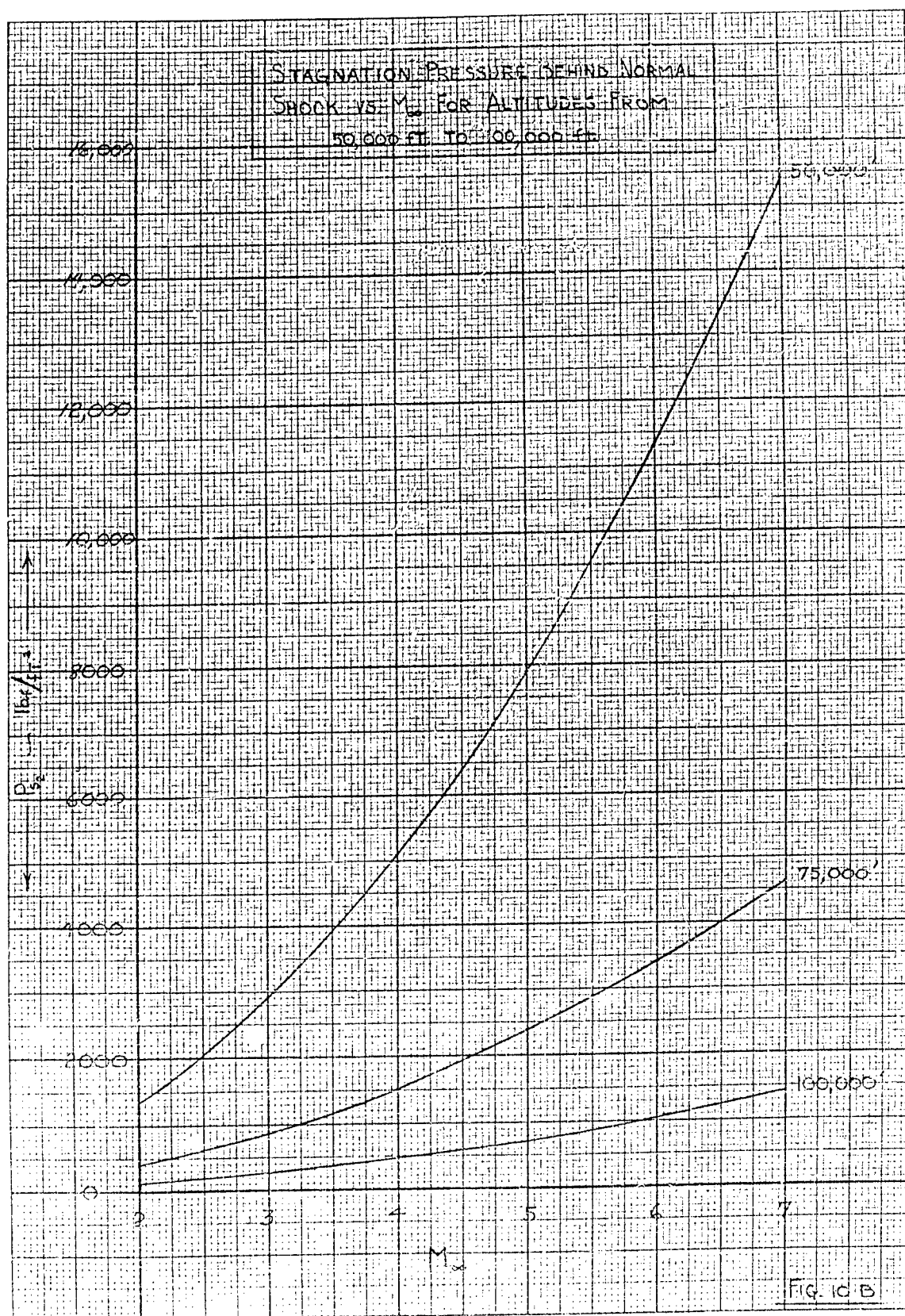
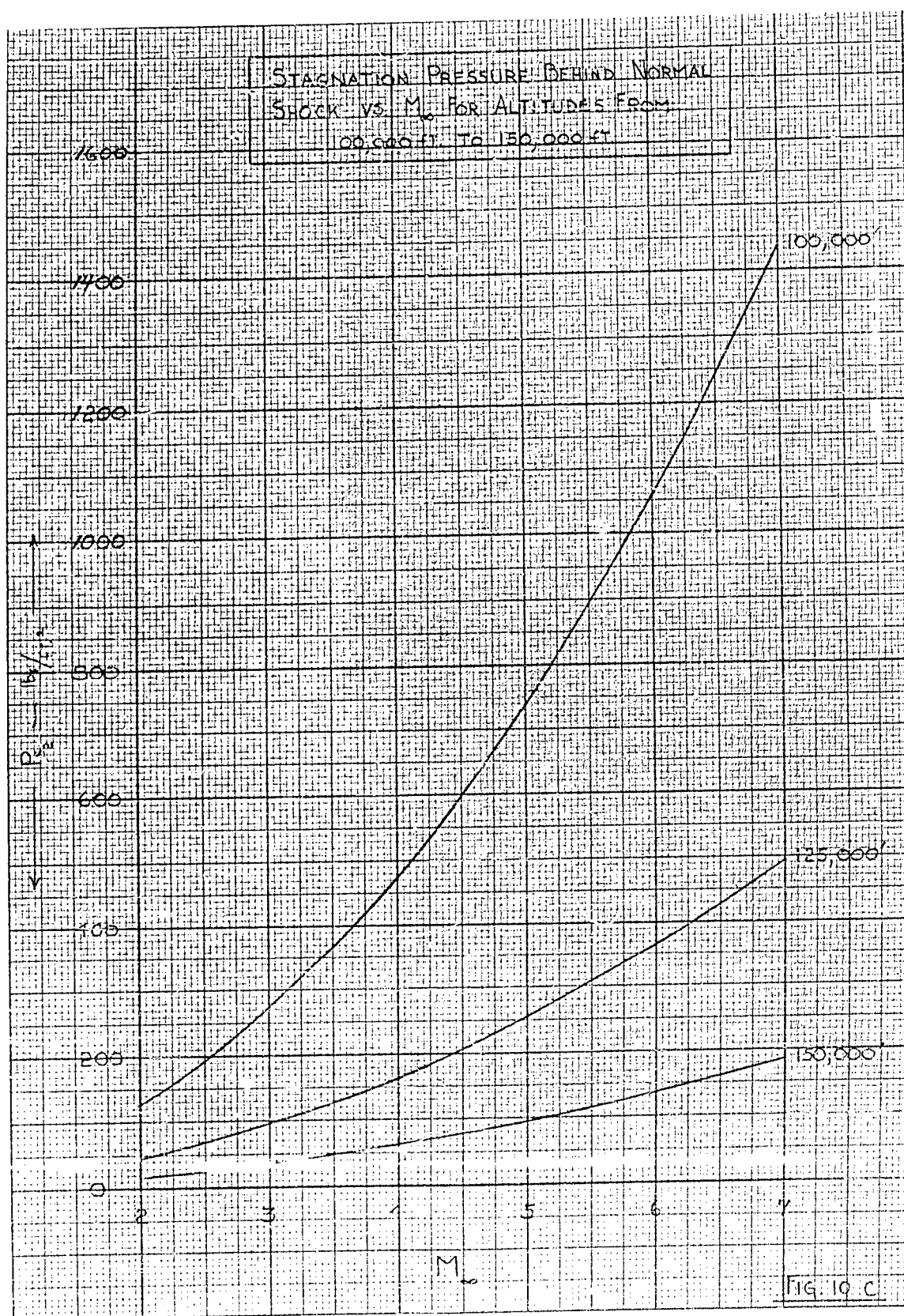


FIG. 2A









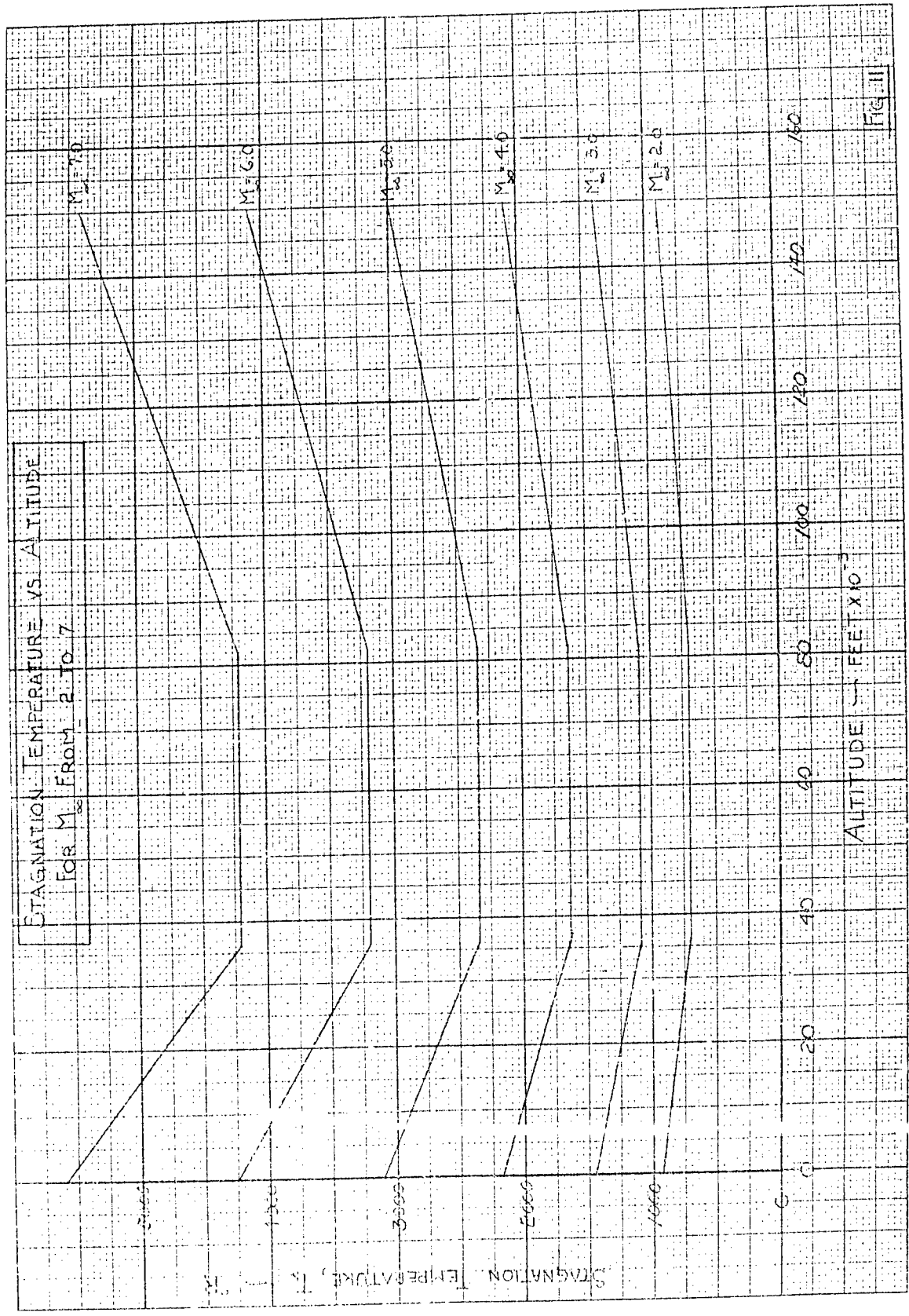
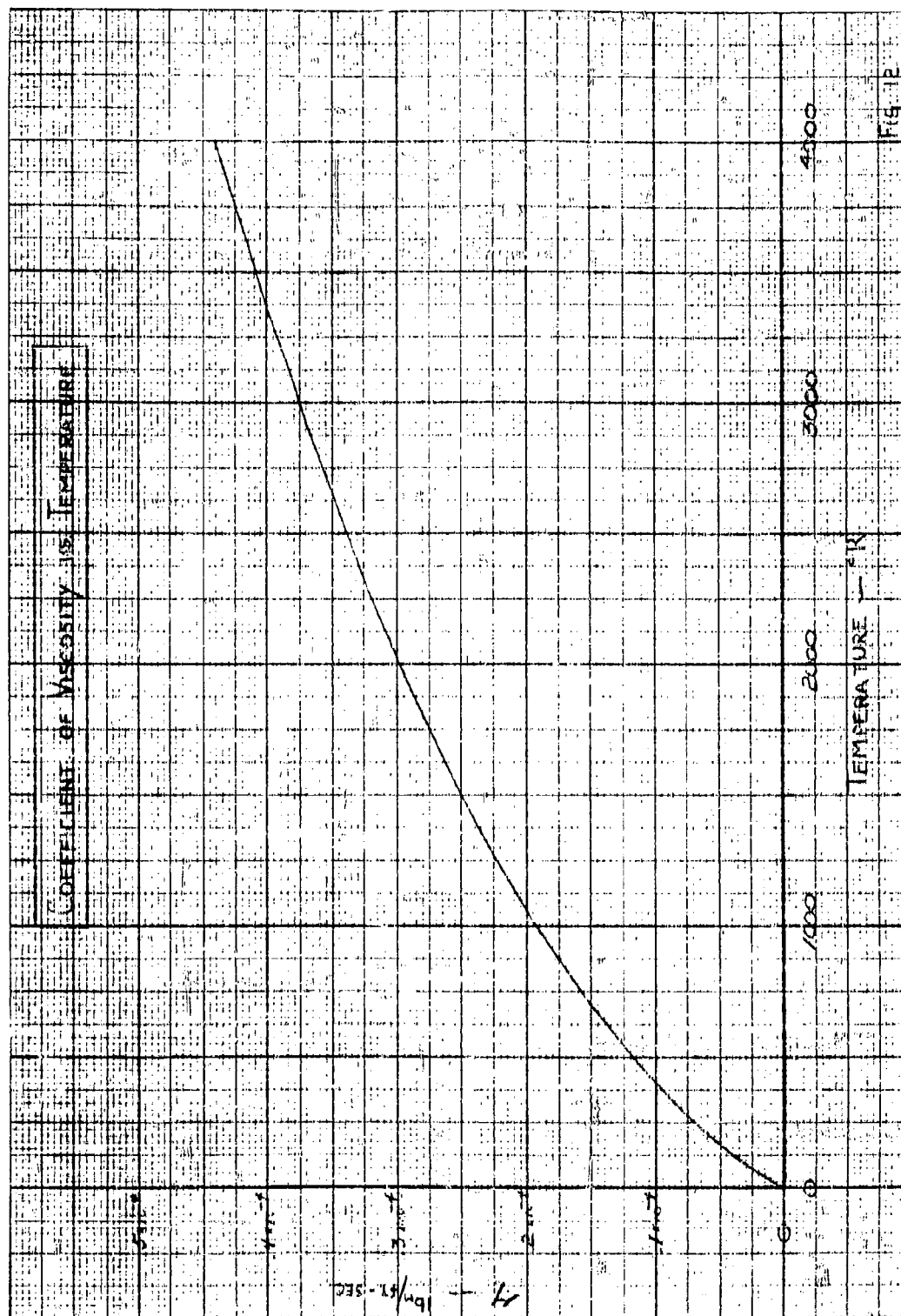
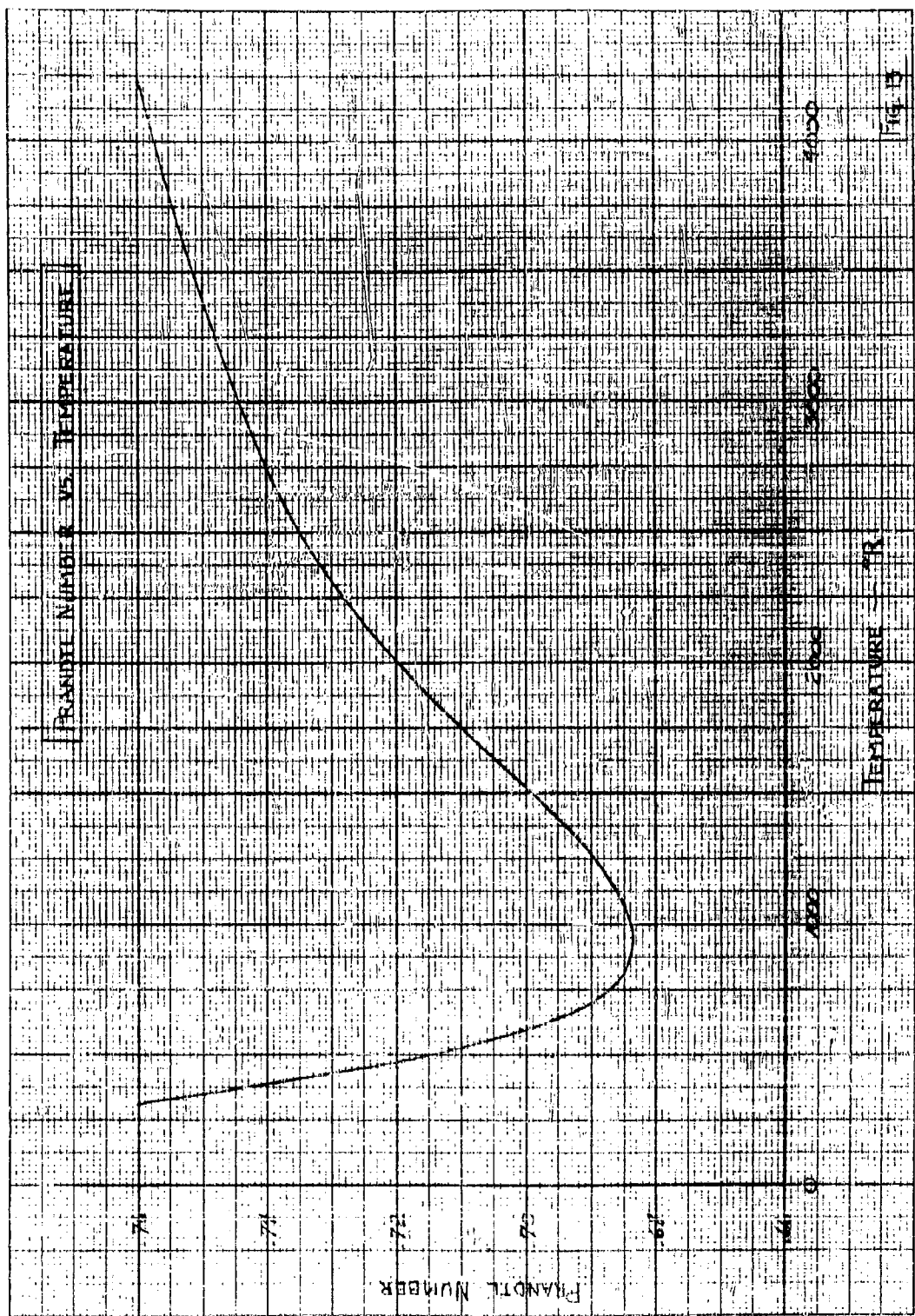


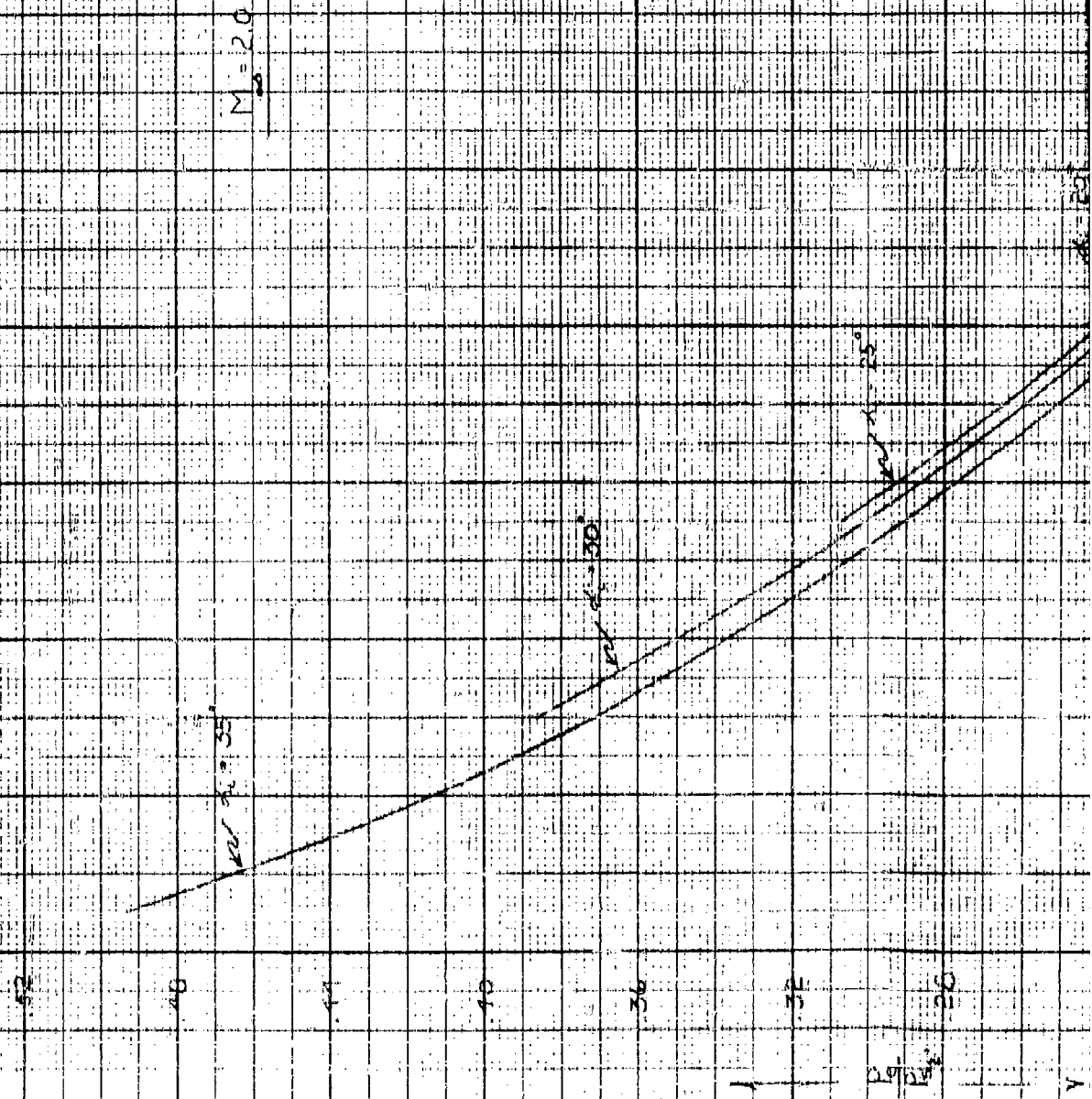
FIG. III





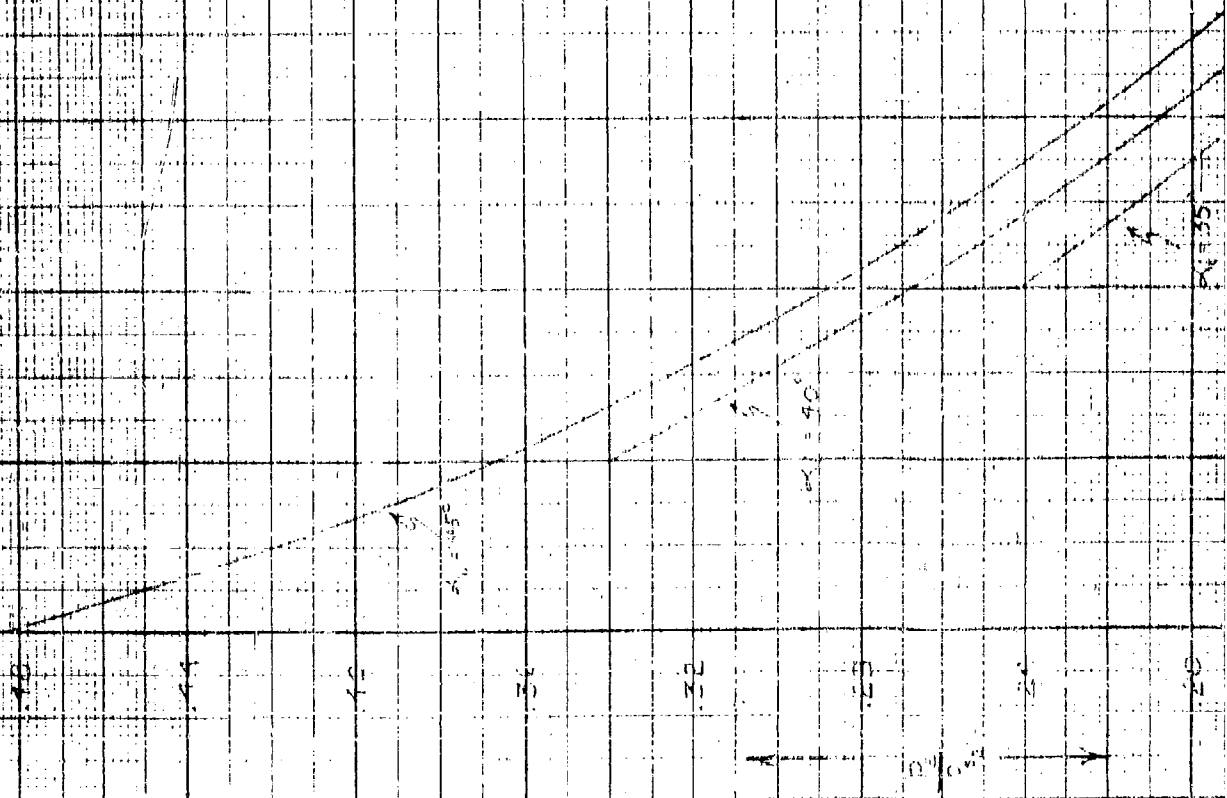
1

RATIO OF TOTAL PRESSURE TO STAGNATION
PRESSURE BEHIND CONICAL SHOCK FOR
INITIAL INCLINATION ANGLES FROM 5° TO 35°



RATIO OF LOCAL PRESSURE TO STAGNATION
PRESSURE, BEHIND CENTRAL SHOCK FOR
INITIAL INCLINATION ANGLES FROM 5° TO 45°

$$M_1 = 3.0$$



RATIO OF LOCAL PRESSURE TO STAGNATION
PRESSURE BEHIND CONICAL SHOCK FOR
INITIAL INCLINATION ANGLES FROM 5° TO 35°

$M_\infty = 10$

10

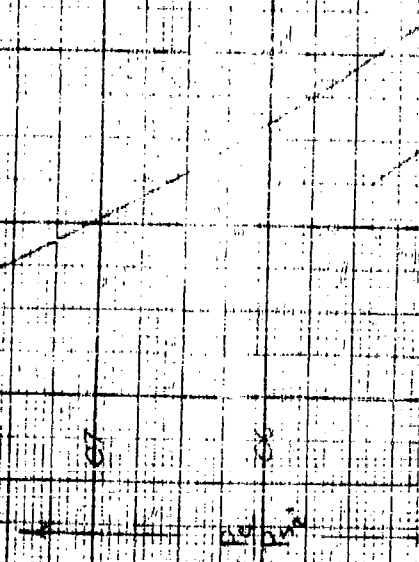
09

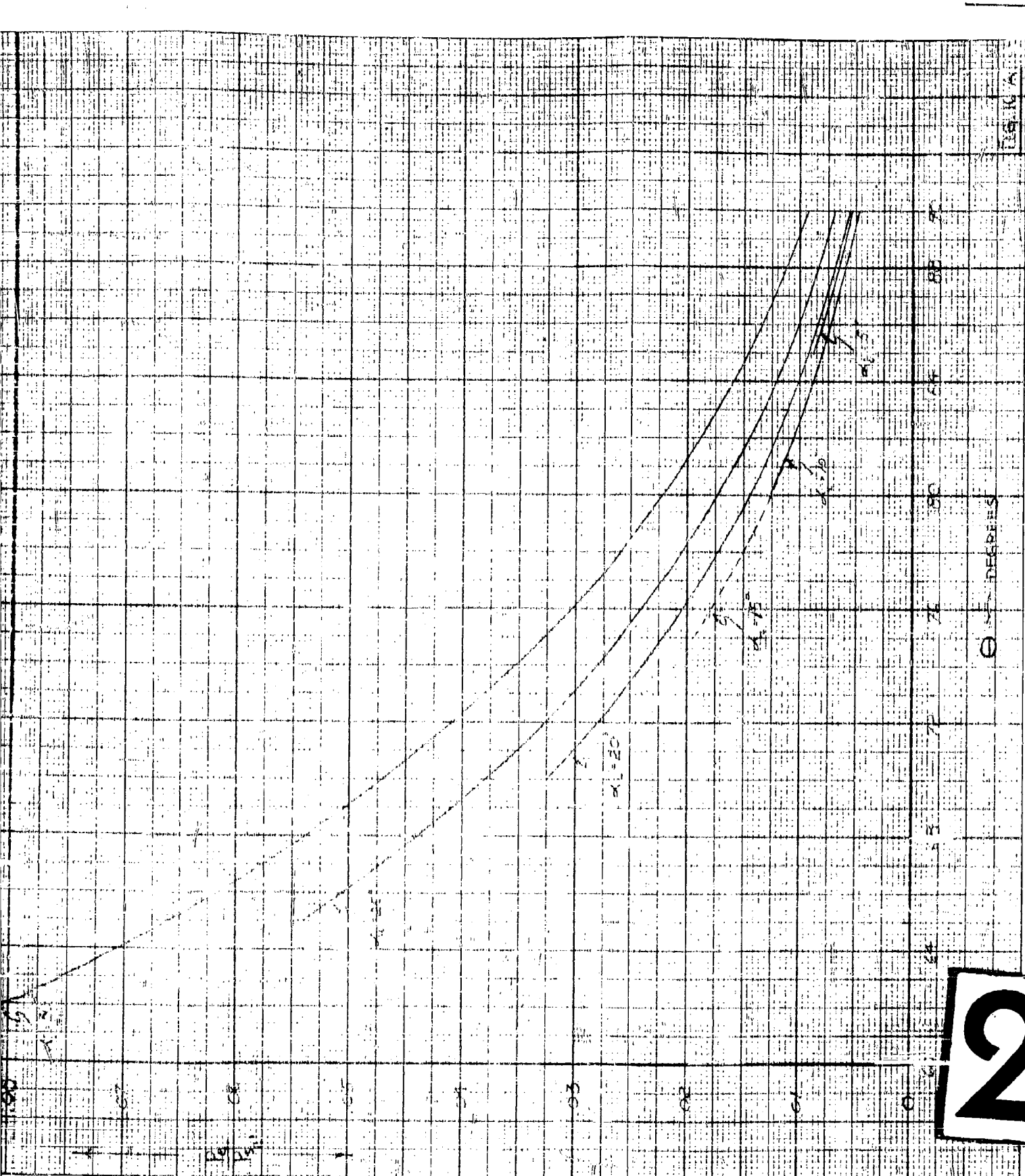
08

07

06

P_0/P_∞





2

1

WADD TR 59-2252

RATIO OF LOCAL PRESSURE TO STAGNATION
PRESSURE BEHIND CENTRAL SHOCK FOR
INITIAL INCIDENCE ANGLES FROM 10 TO 60

$M_0 = 4.0$

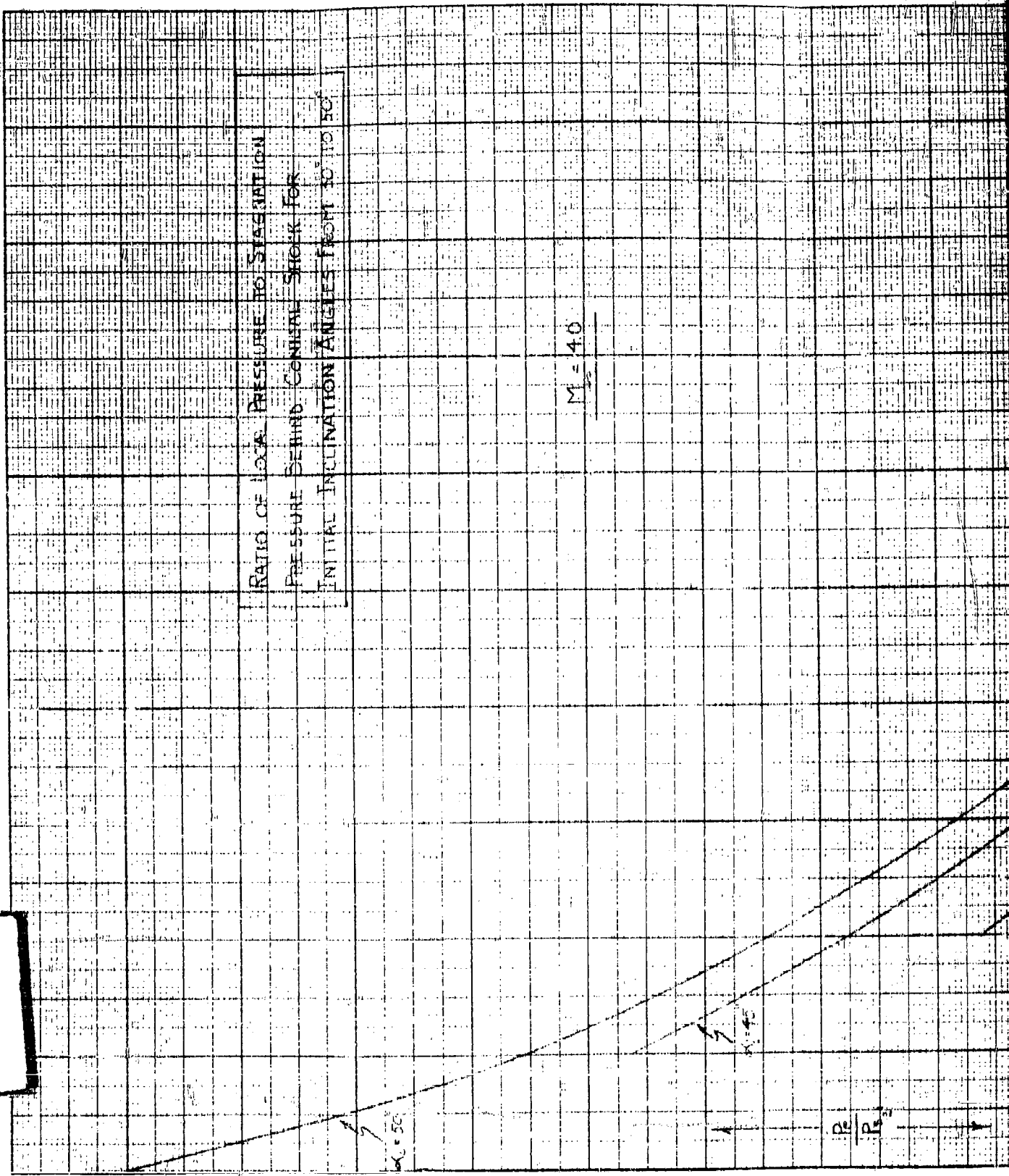
$\alpha = 50^\circ$

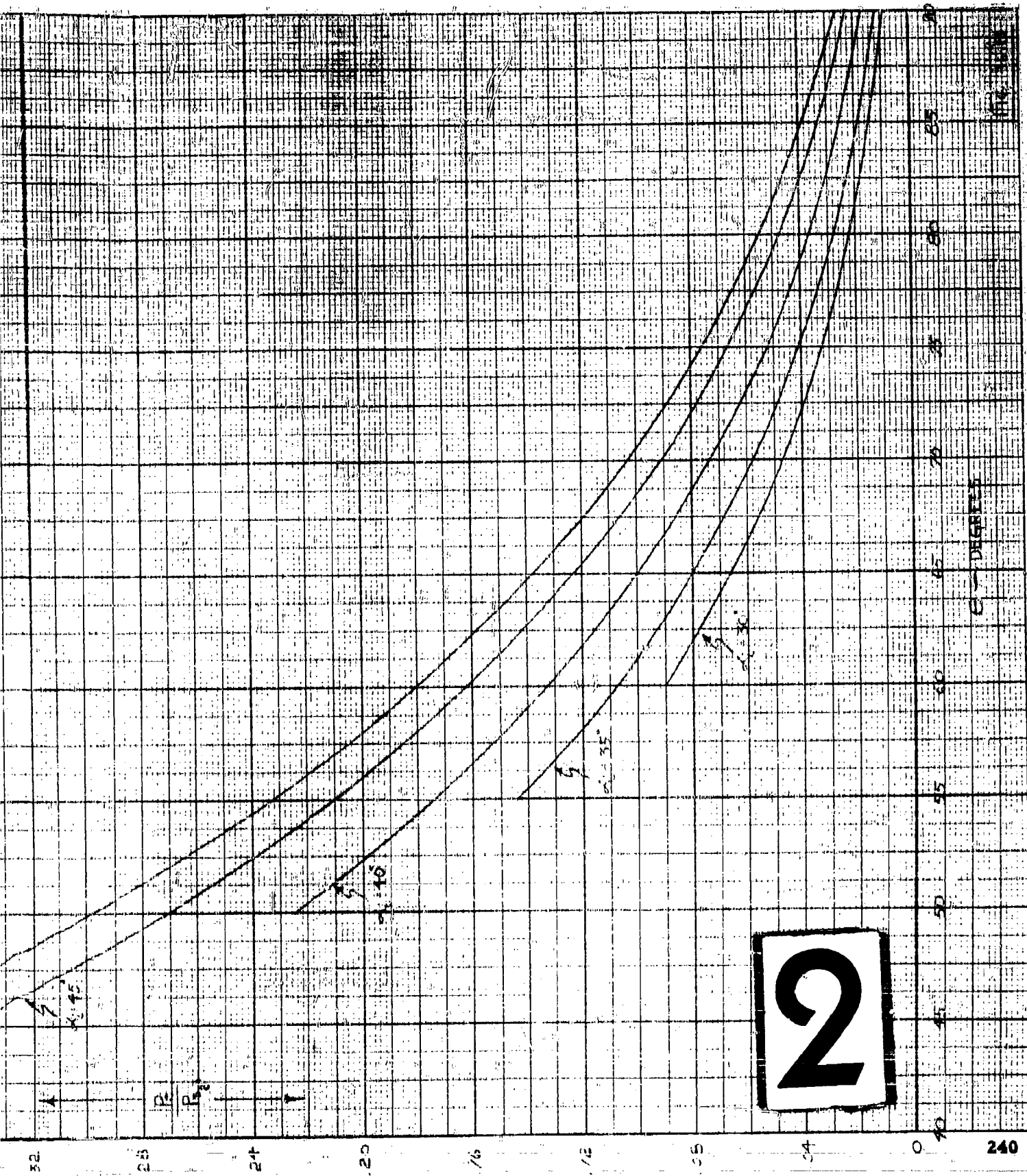
$\alpha = 45^\circ$

P/P_0

P/P_0

P/P_0

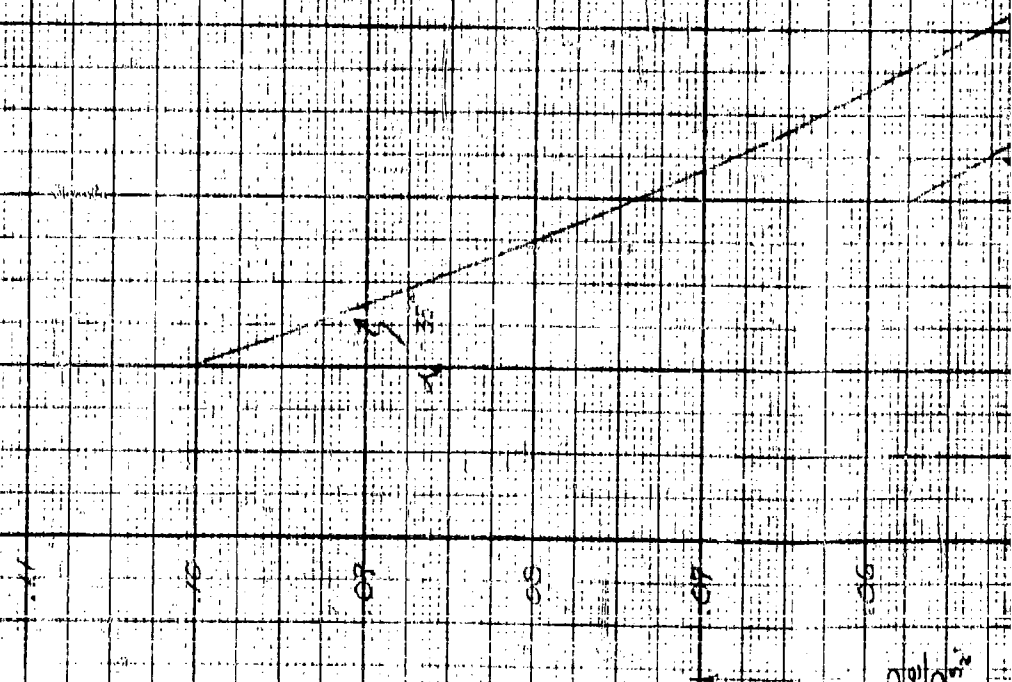


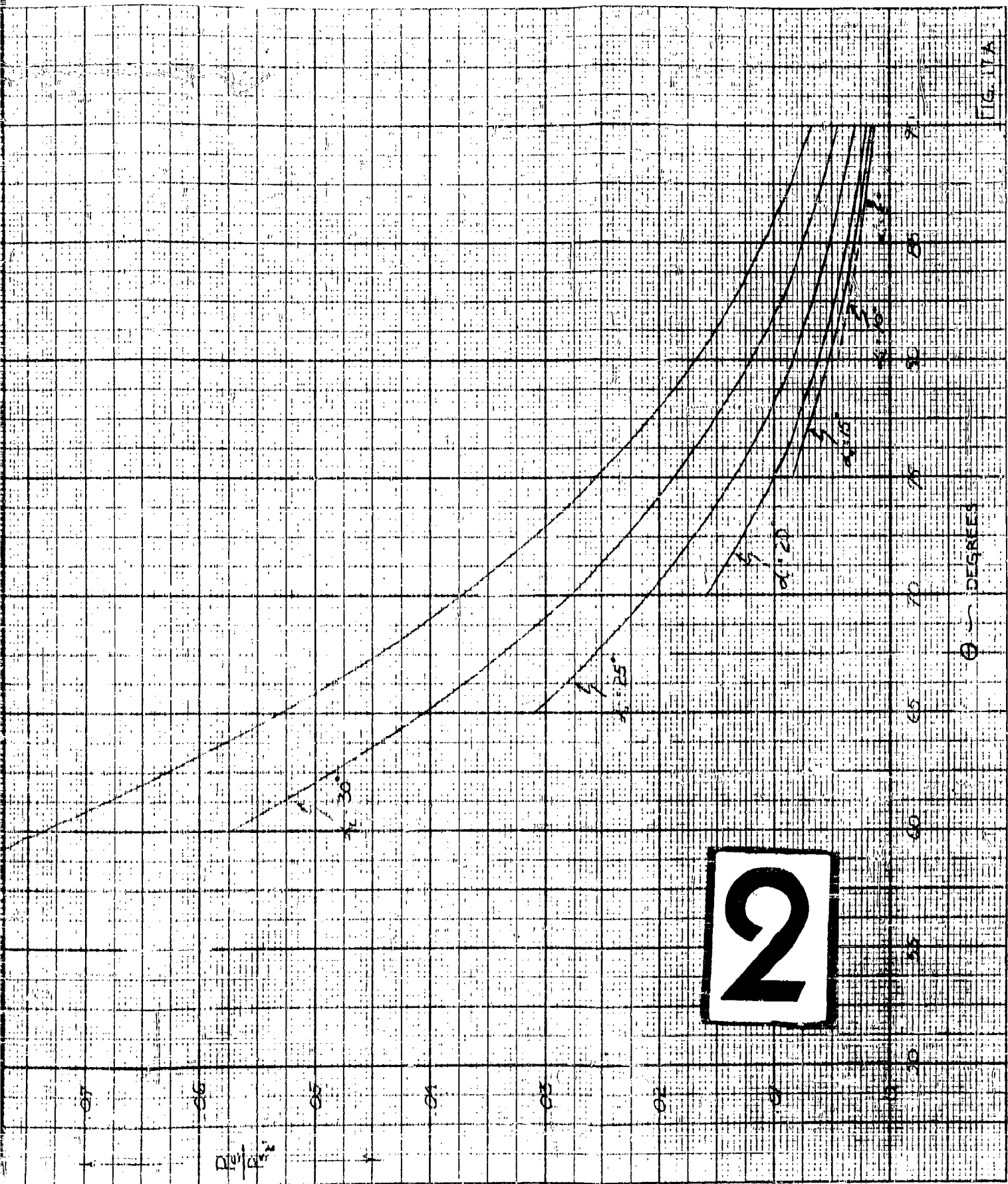


1

RATIO OF TOTAL PRESSURE TO STAGNATION
PRESSURE BEHIND CONICAL SHOCK FOR
INITIAL INCLINATION ANGLES FROM 5 TO 55

M = 5.0



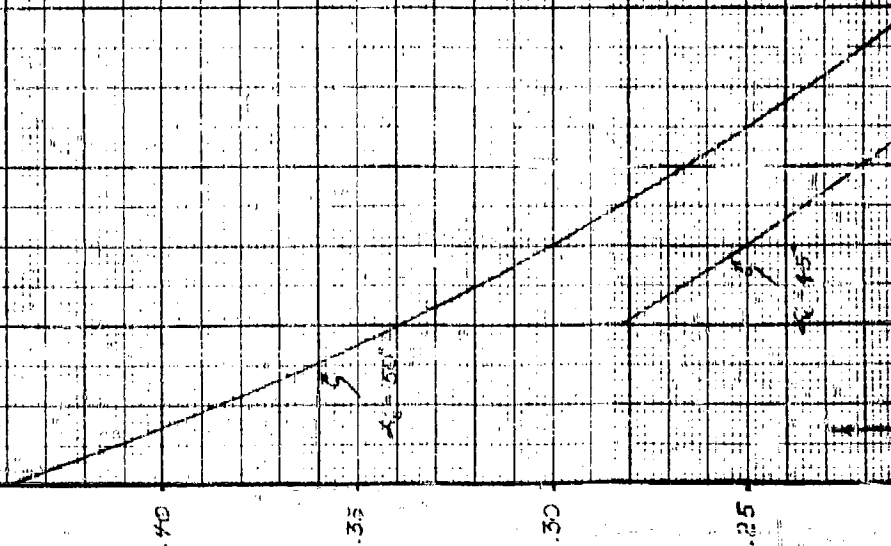


1

WARD TR 59-22

RATIO OF LOCAL PRESSURE TO STRAIN RATE
PRESSURE BEHIND CONICAL SHOCK FOR
INITIAL INCLINATION ANGLES FROM 15 TO 45

$$M = 50$$



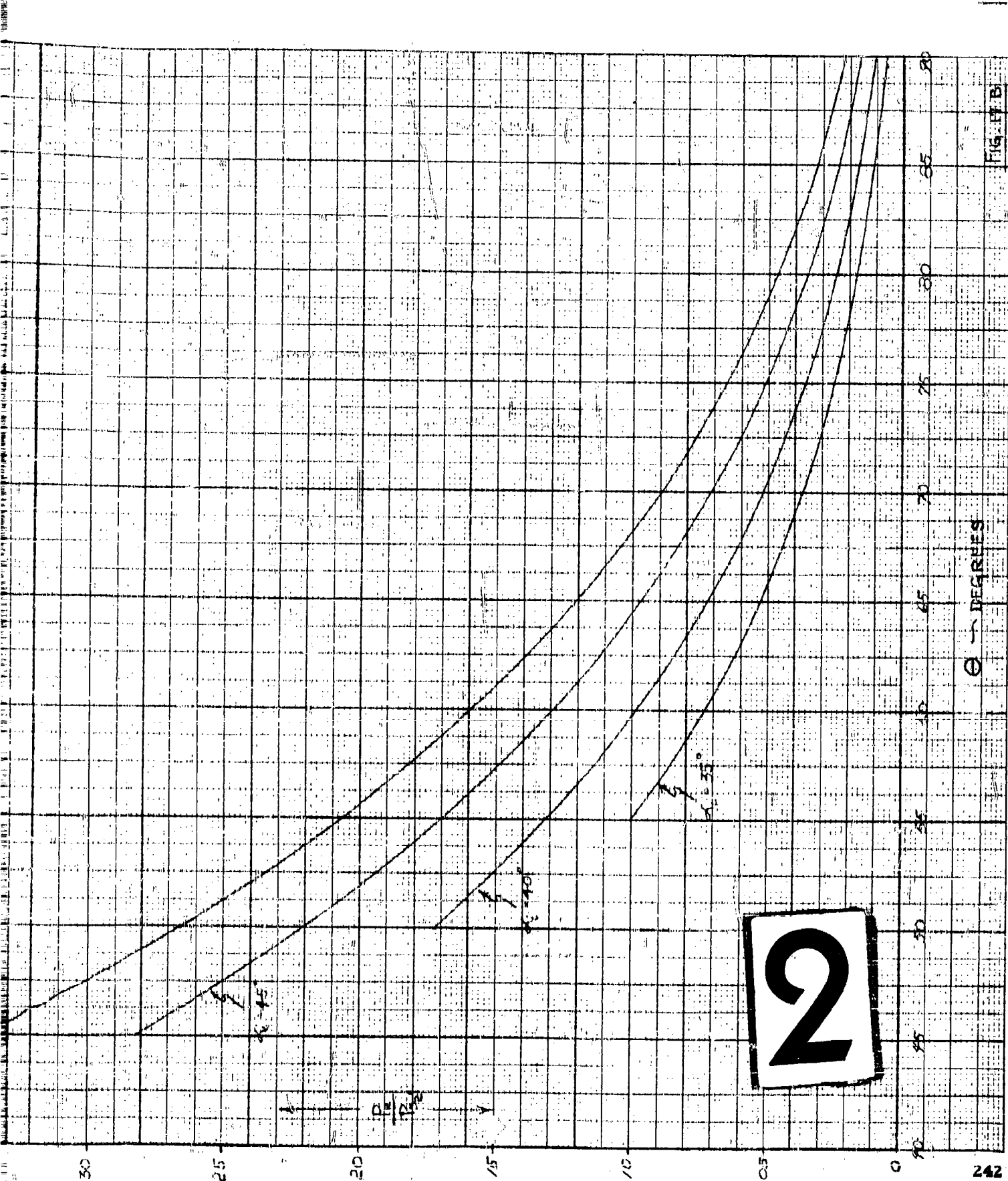


FIG. 17 B

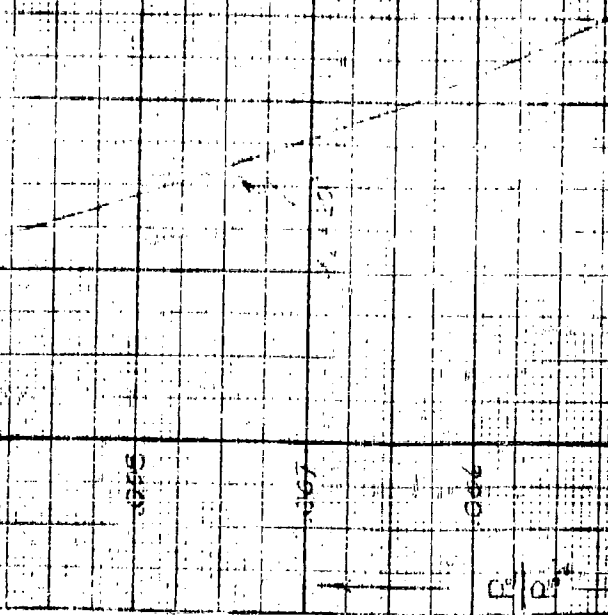
θ - DEGREES

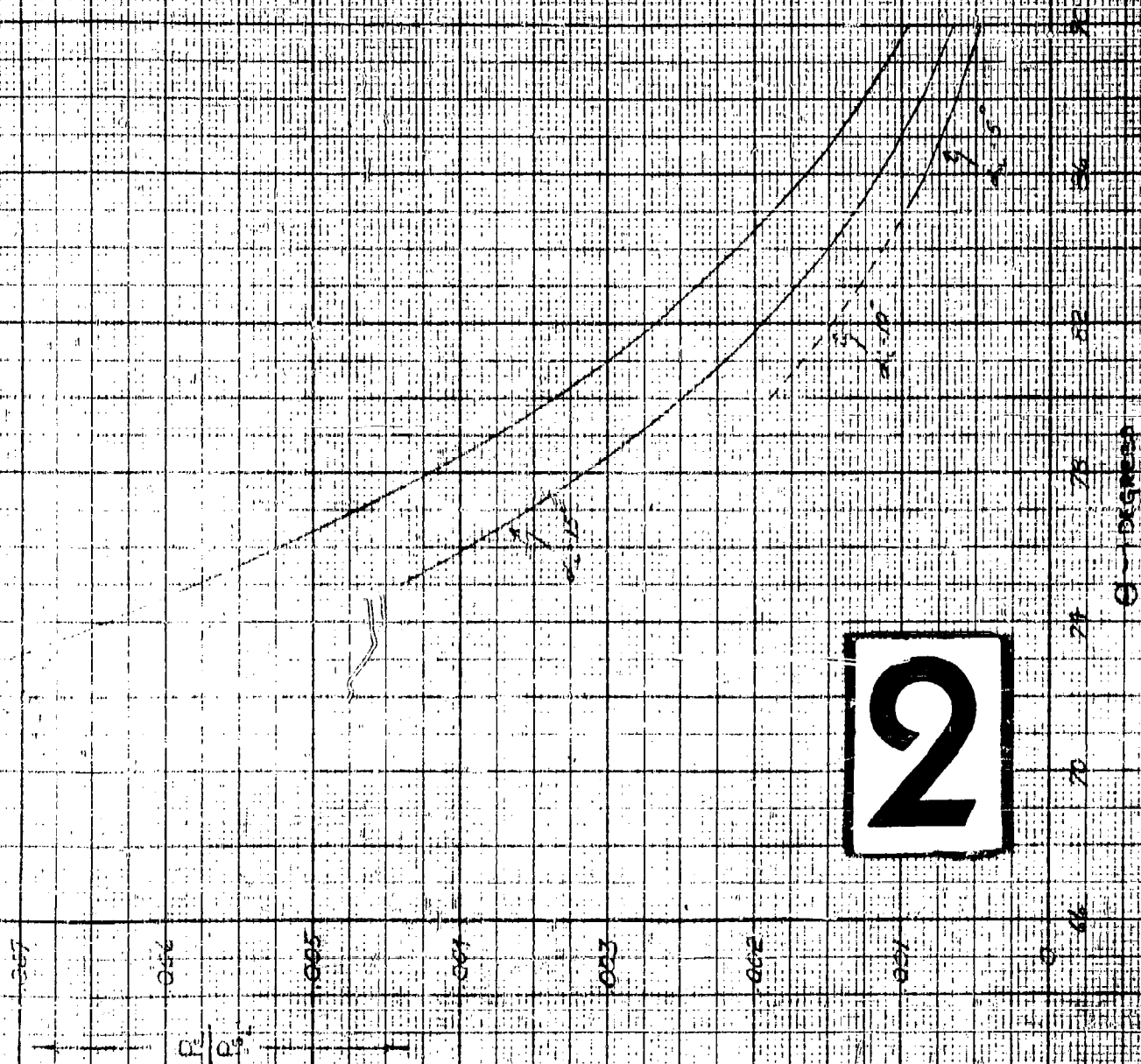
2

1

RATIO OF LOCAL PRESSURE TO STAGNATION
PRESSURE BEHIND CONICAL SHOCK FOR
INITIAL INCINATION ANGLES FROM 5° TO 20°

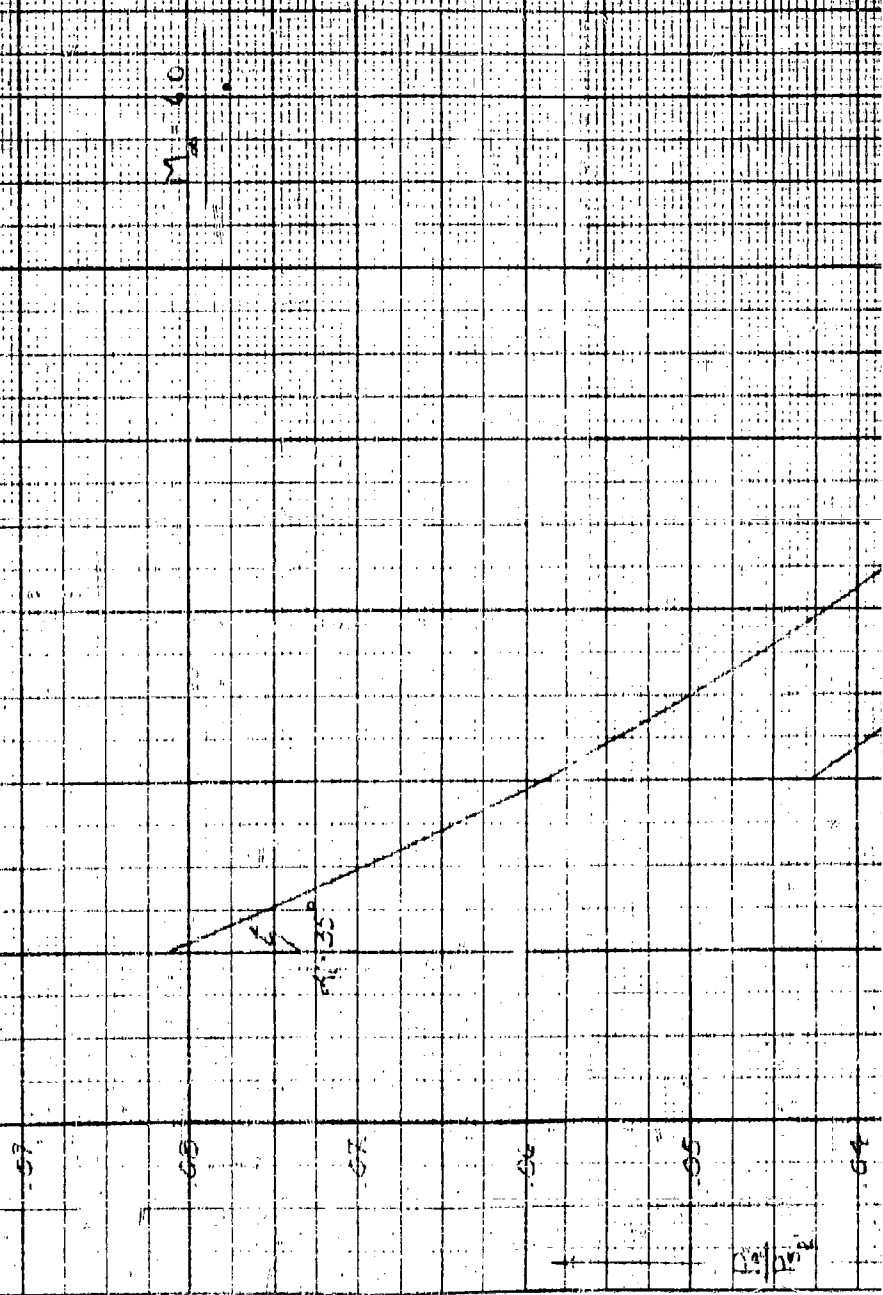
M = 2.0

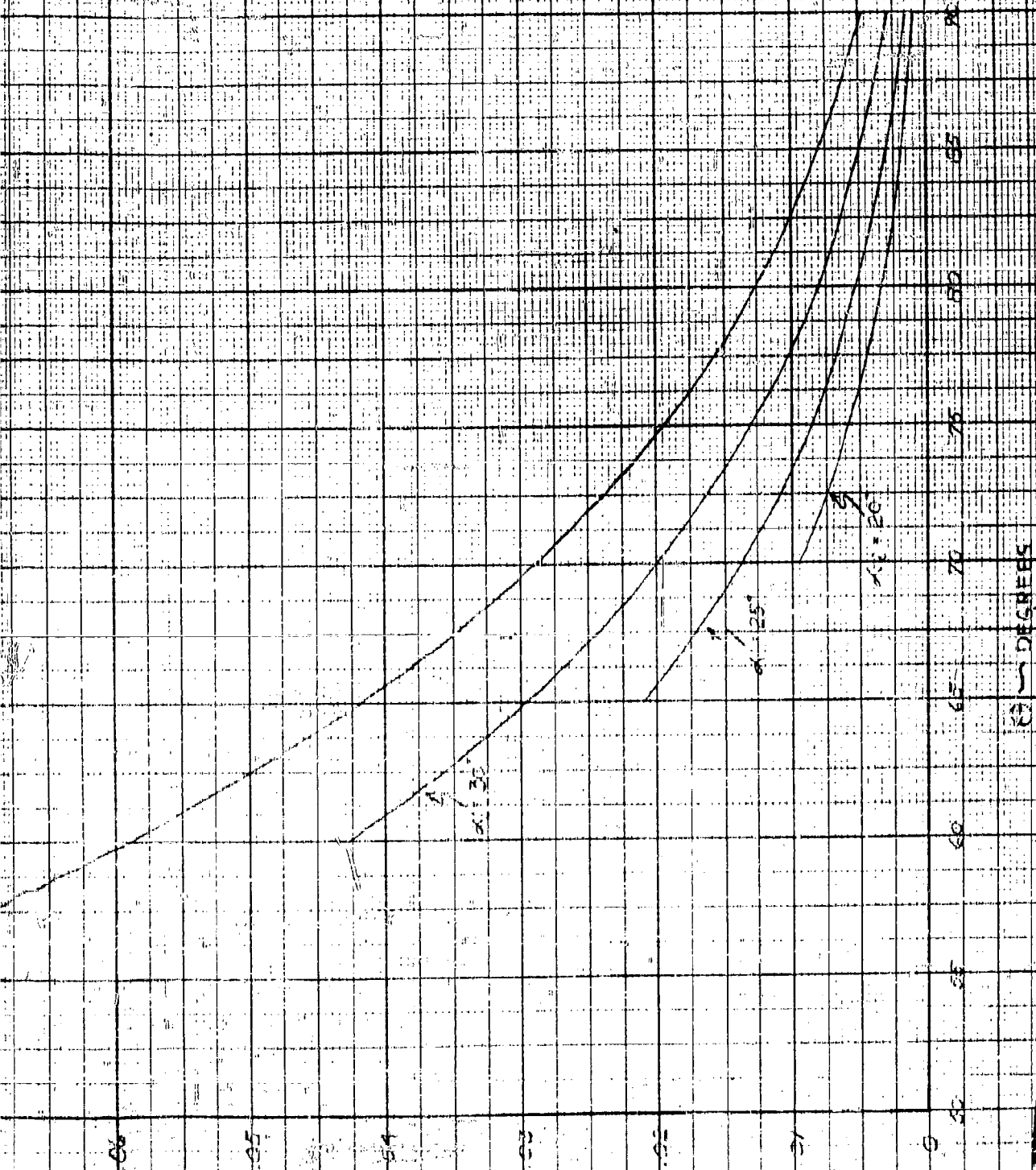




1

RATIO OF SEAL PRESSURE TO STAGNATION
PRESSURE BEHIND CONICAL SHOCK FOR
INITIAL INCLINATION ANGLES FROM 20° TO 55°

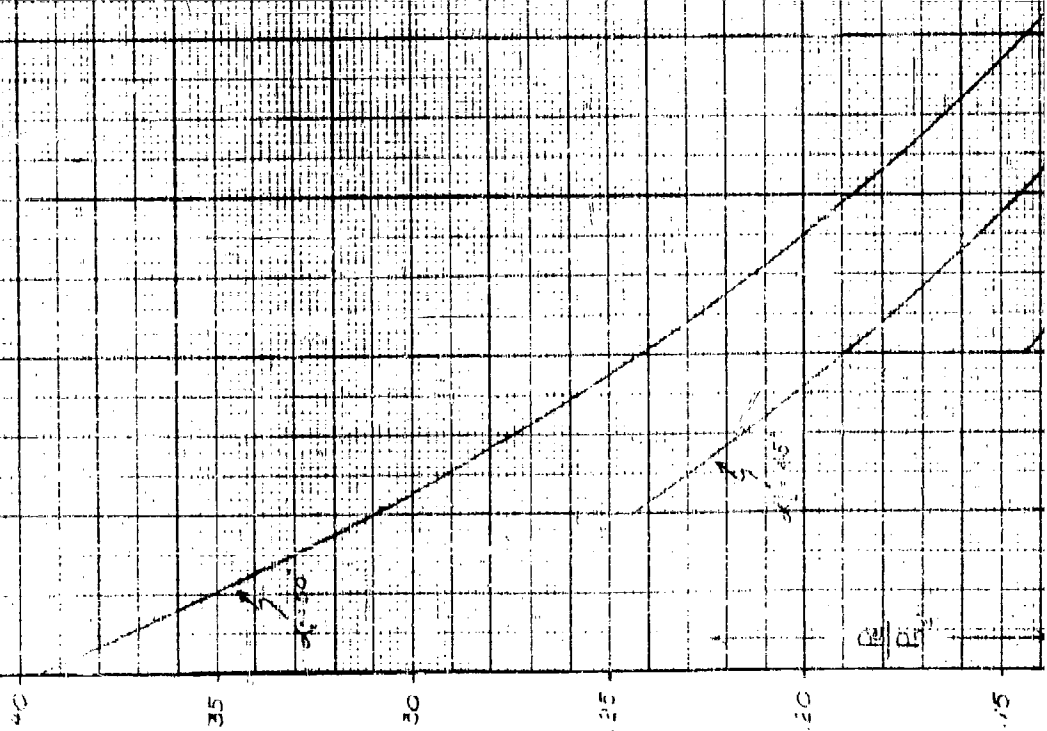




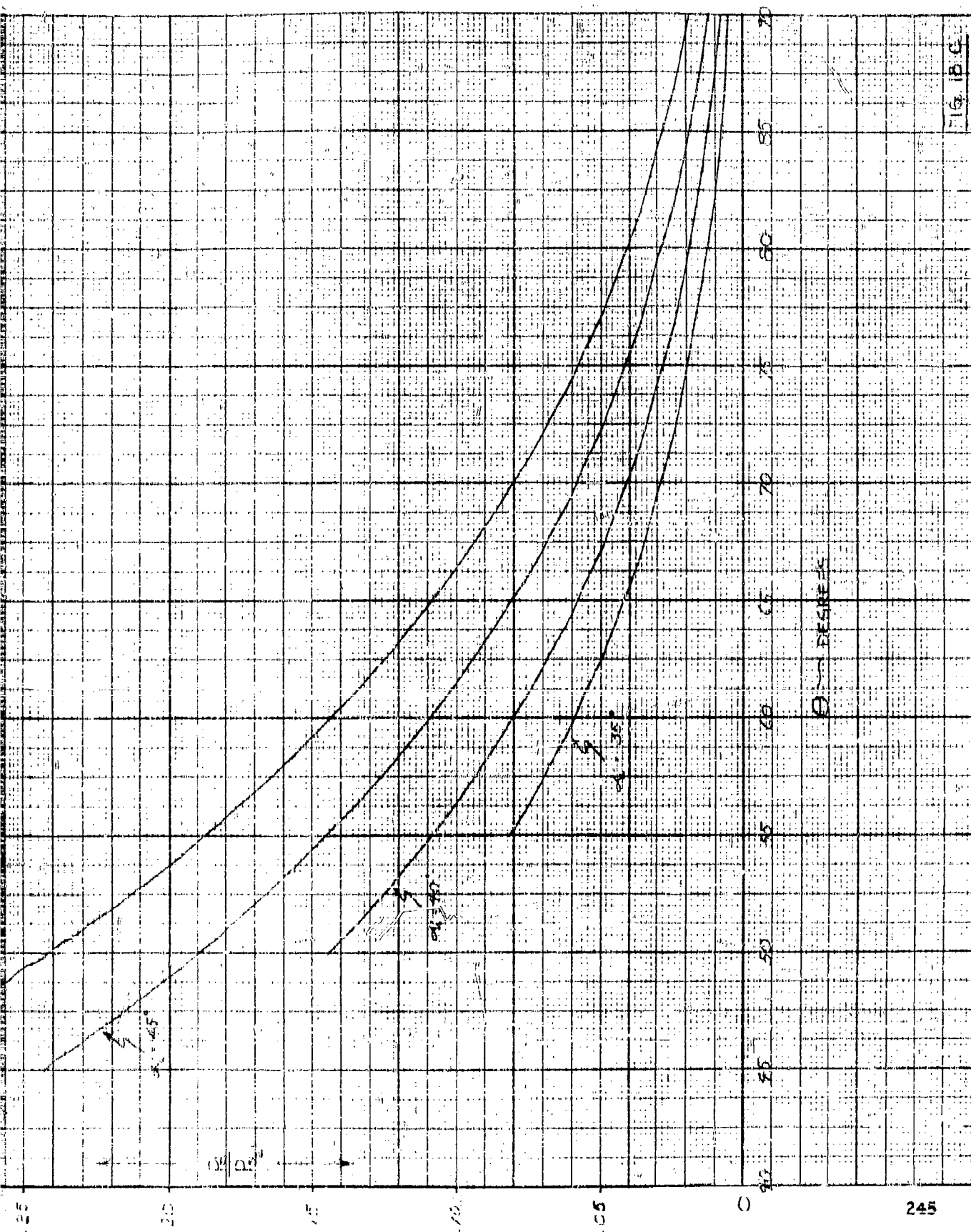
2

1

RATIO OF LOCAL PRESSURE TO STAGNATION
PRESSURE BEHIND CENTRAL SHOCK FOR
INITIAL INCLINATION ANGLES FROM 35° TO 50°



$M = 6.0$



15. B.C.

2

1

RATIO OF TOTAL PRESSURE TO STAGNATION
PRESSURE BEHIND CONICAL SHOCK FOR
INITIAL INCIDENCE ANGLES FROM 5° TO 20°

$M_1 = 2.0$

305

649

735

105

145

$\frac{P_2}{P_1}$

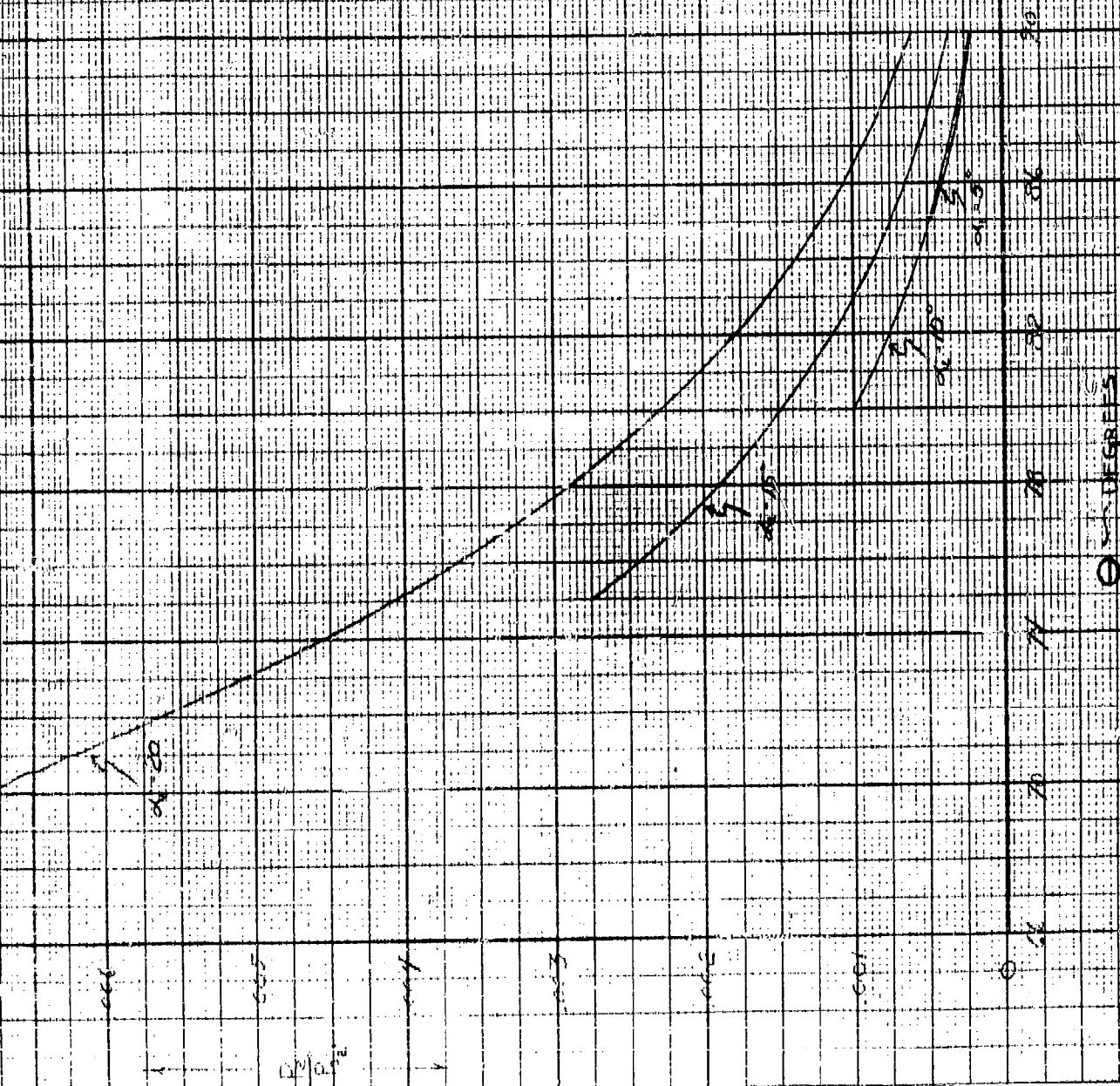


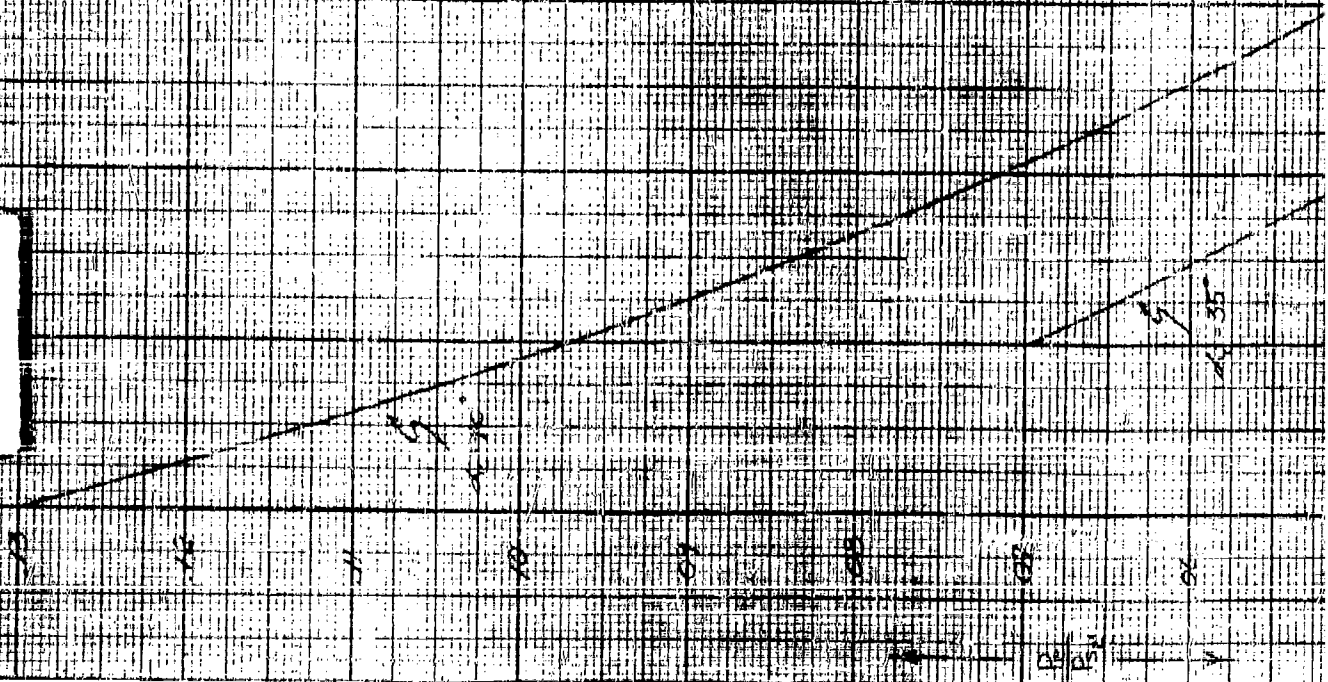
Fig. 19 A

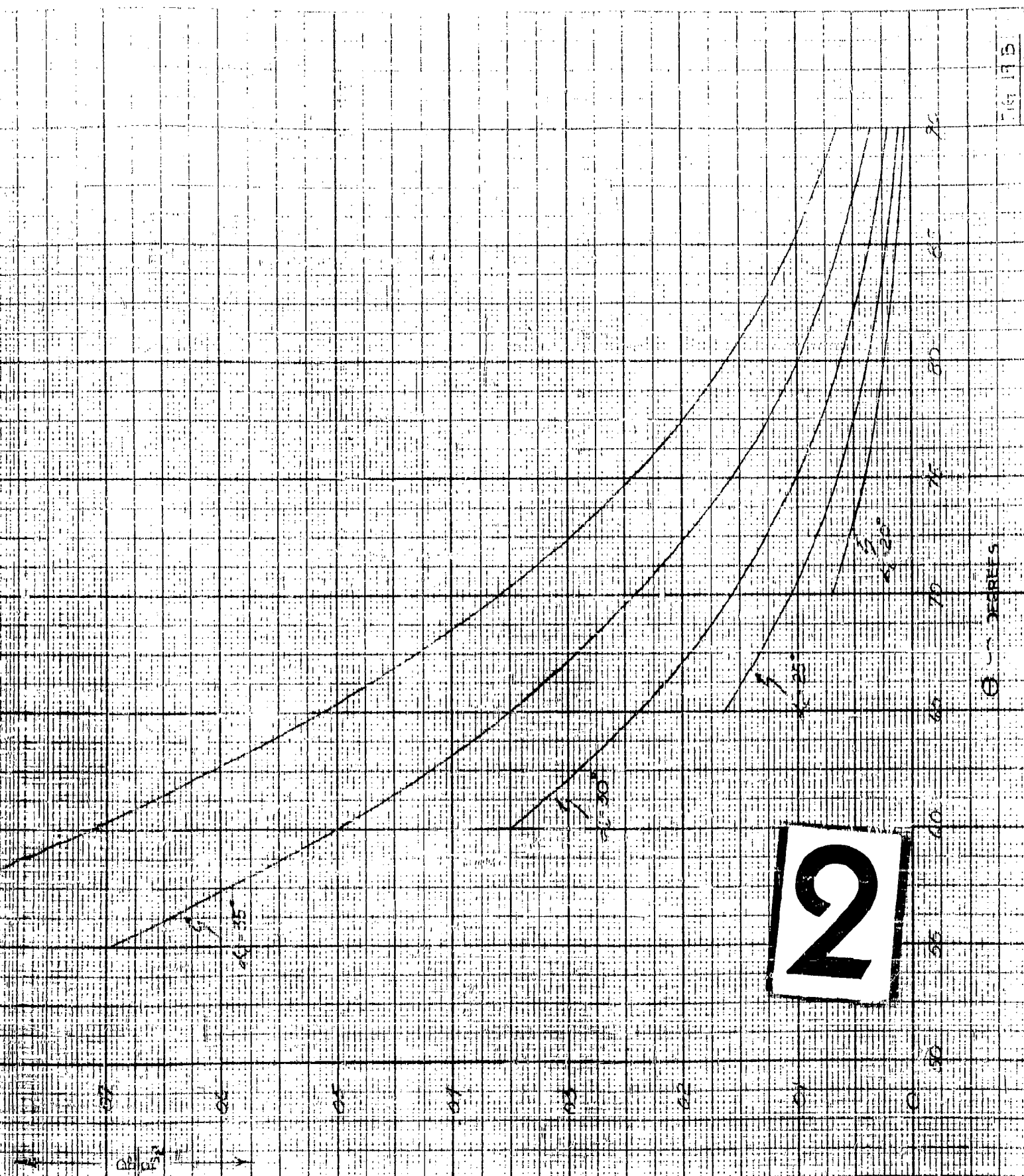
2

1

RATIO OF LOCAL PRESSURE TO FREE STREAM
PRESSURE BEHIND CONICAL SHOCK FOR
INITIAL INCINATION ANGLES FROM 0

$$M_{\infty} = 7.0$$



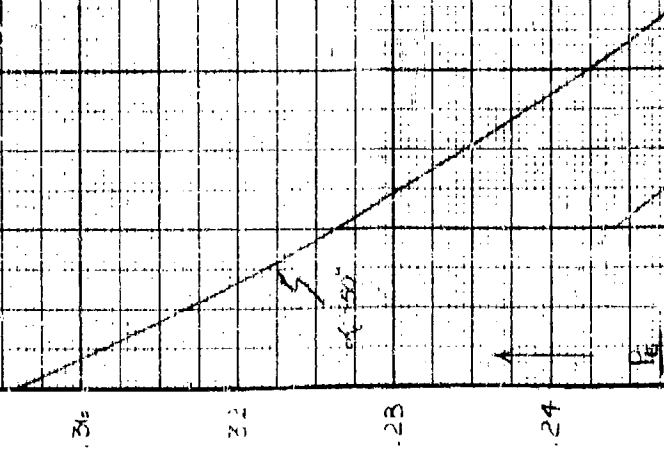


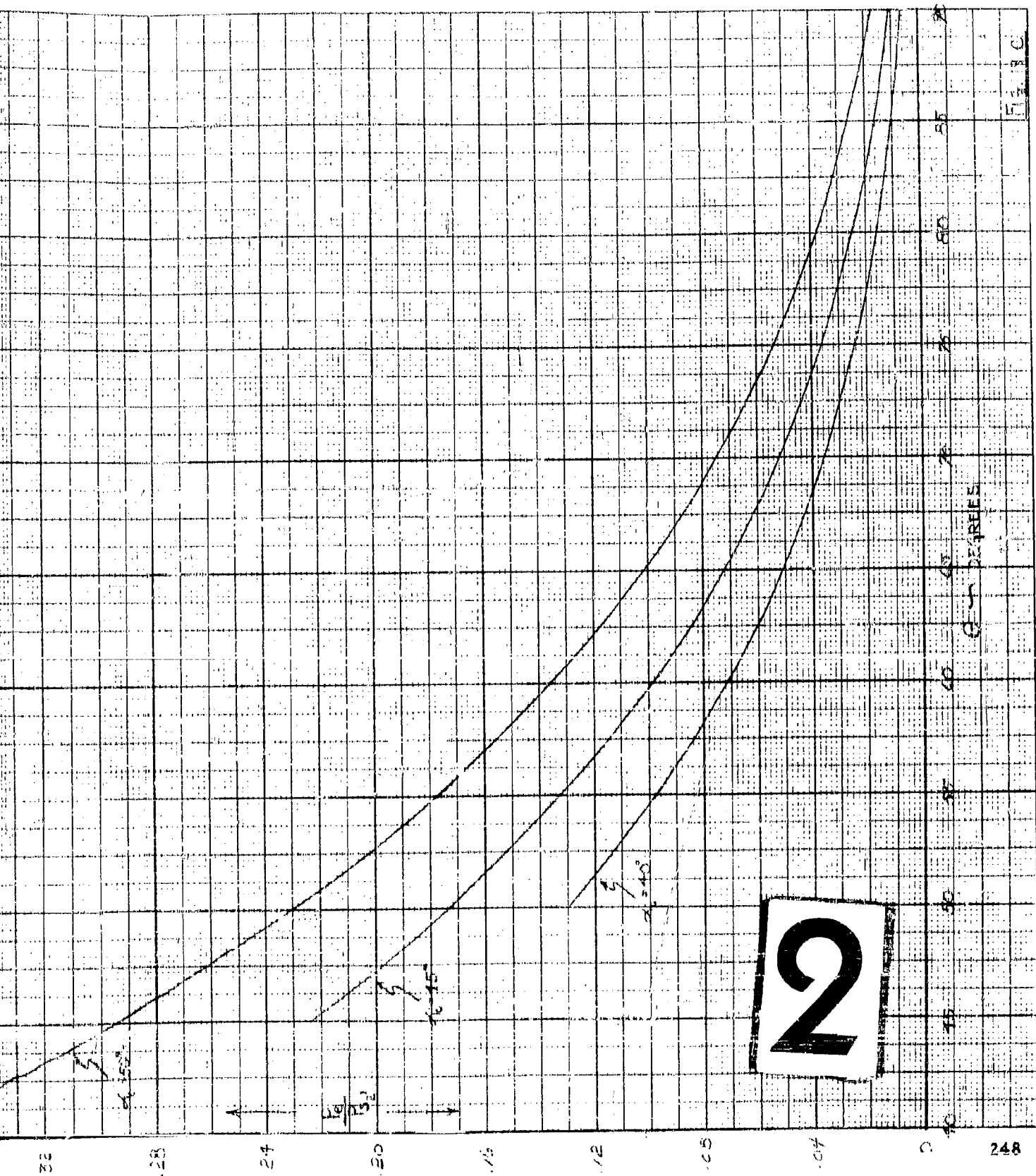
1

RATIO OF TOTAL PRESSURE TO STAGNATION
PRESSURE BEHIND CONICAL SHOCK FOR

INITIAL INCLINATION ANGLES FROM 10° TO 50°

$$M_1 = 7.0$$

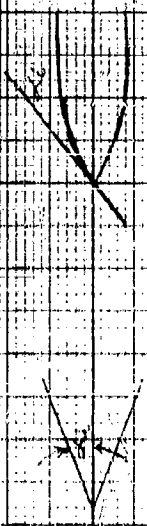




2

1

$\frac{P_2}{P_1} = \frac{V_2}{V_1} \propto \frac{1}{V_1}$ FOR M_1 FROM 20 TO 45
 $\frac{P_2}{P_1}$



320

280

240

200

160

$\frac{P_2}{P_1} = \frac{V_2}{V_1} \propto \frac{1}{V_1}$
 $\frac{P_2}{P_1}$

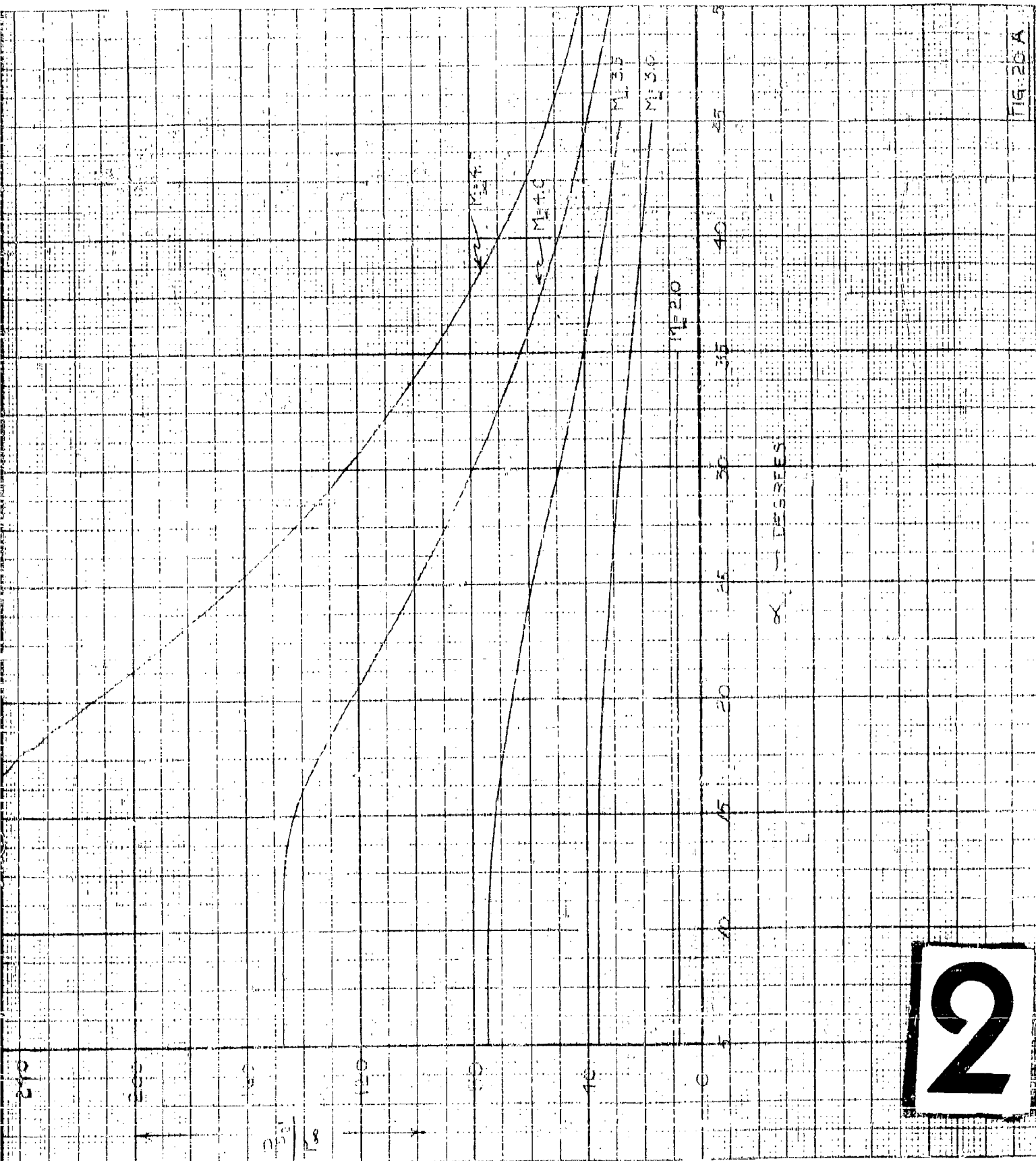
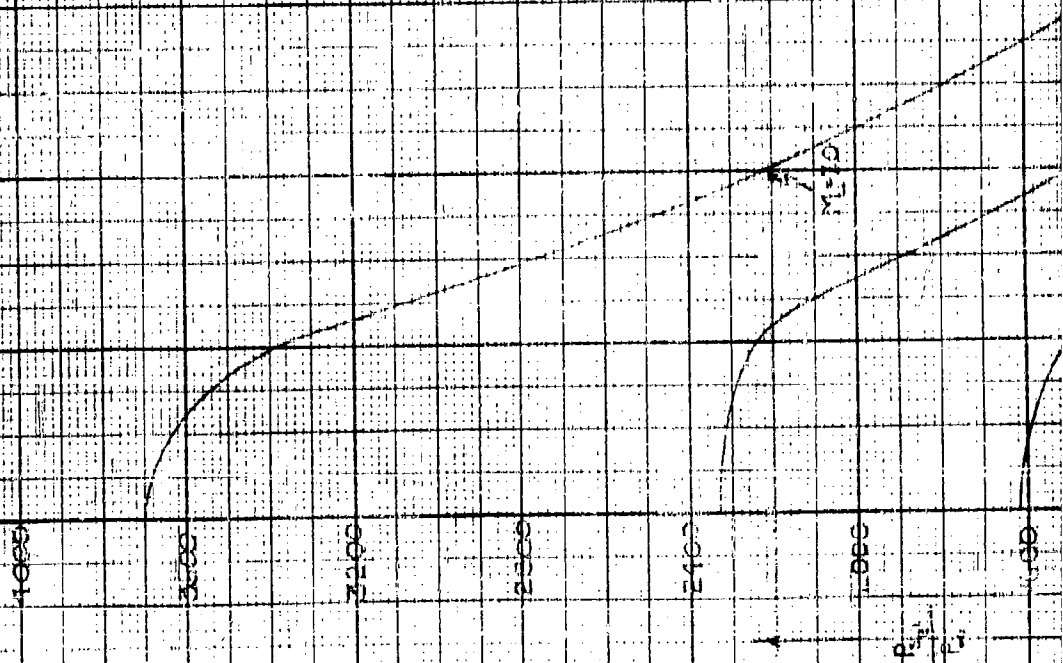
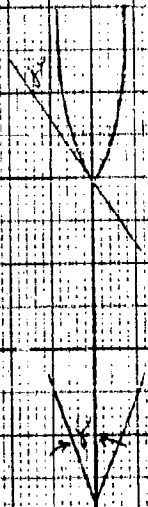


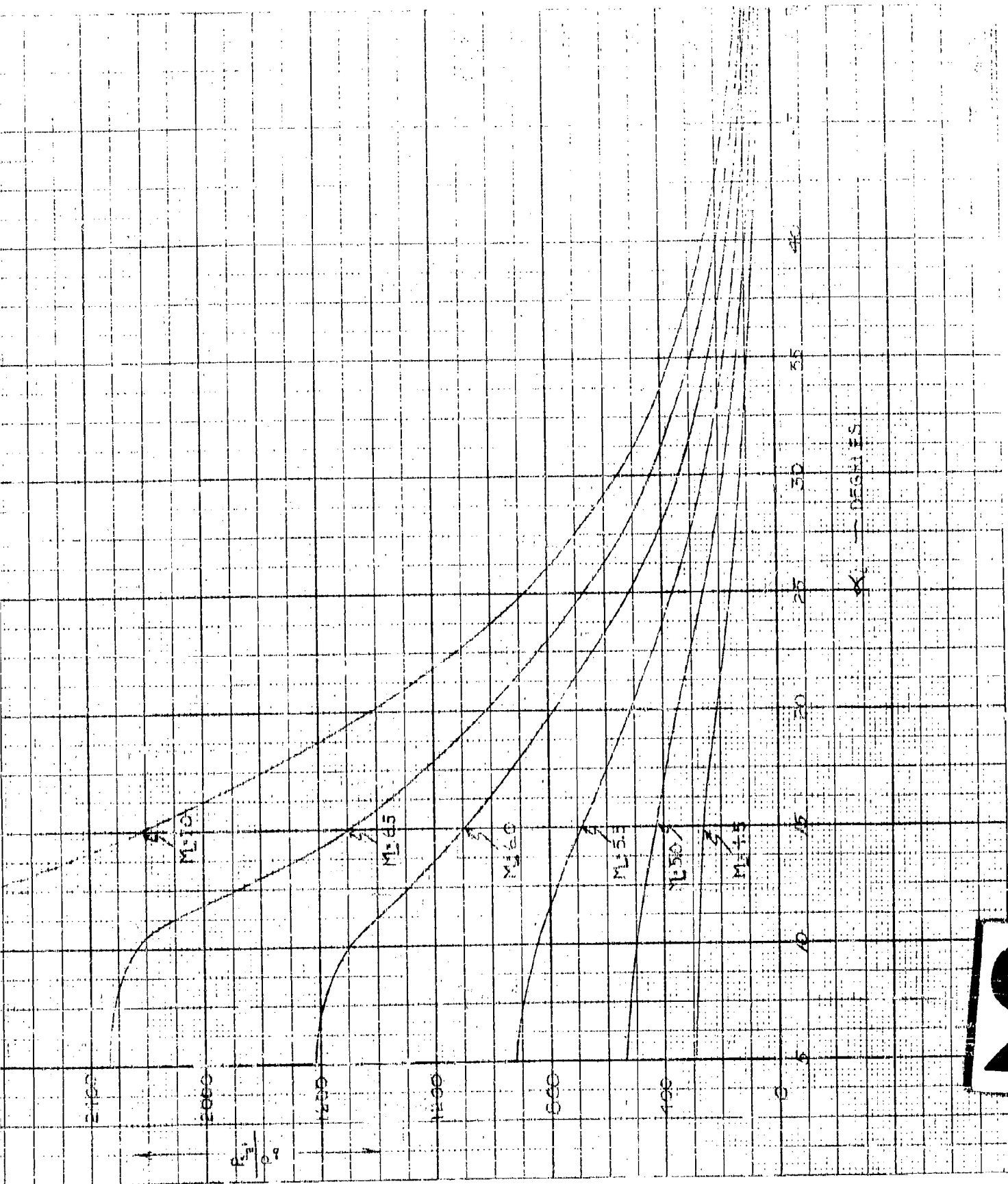
FIG. 20 A

2

1

$\frac{K_s}{P_0}$ vs α FOR M_1 FR-M-45 TO 70

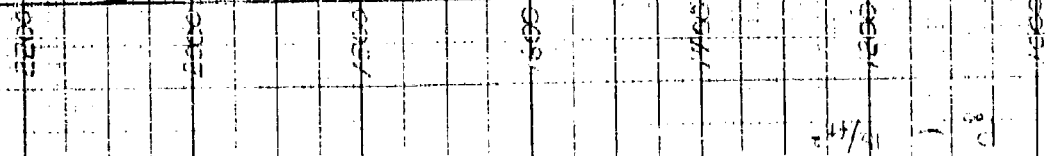


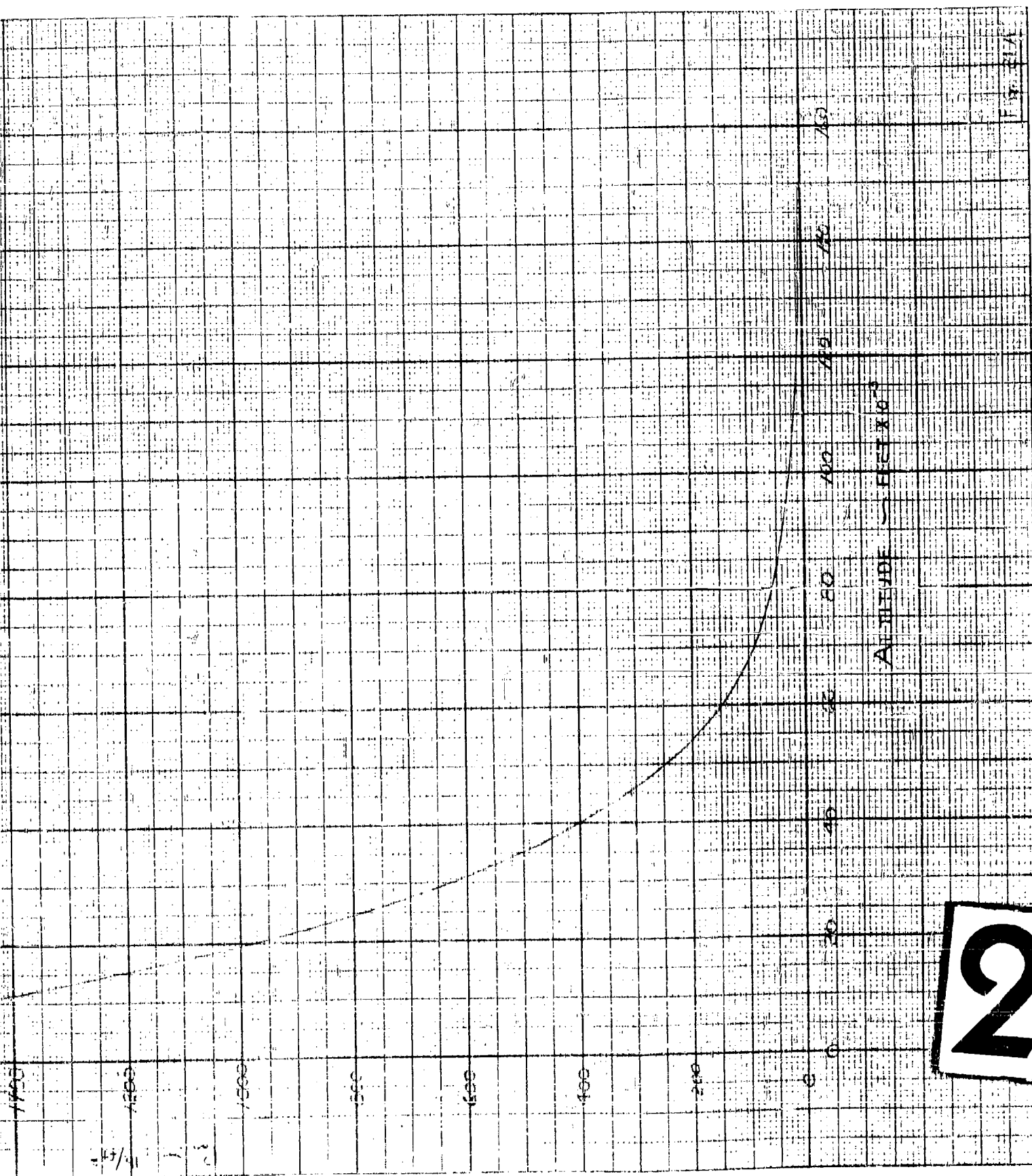


FIERF STREAM PRESSURE VS ALTITUDE

FROM 0' TO 150,000'

1





2

1

FREE SURFACE PRESSURE VS. ALTITUDE
FROM 10000 TO 100000

270

240

160

140

120

100

80

60

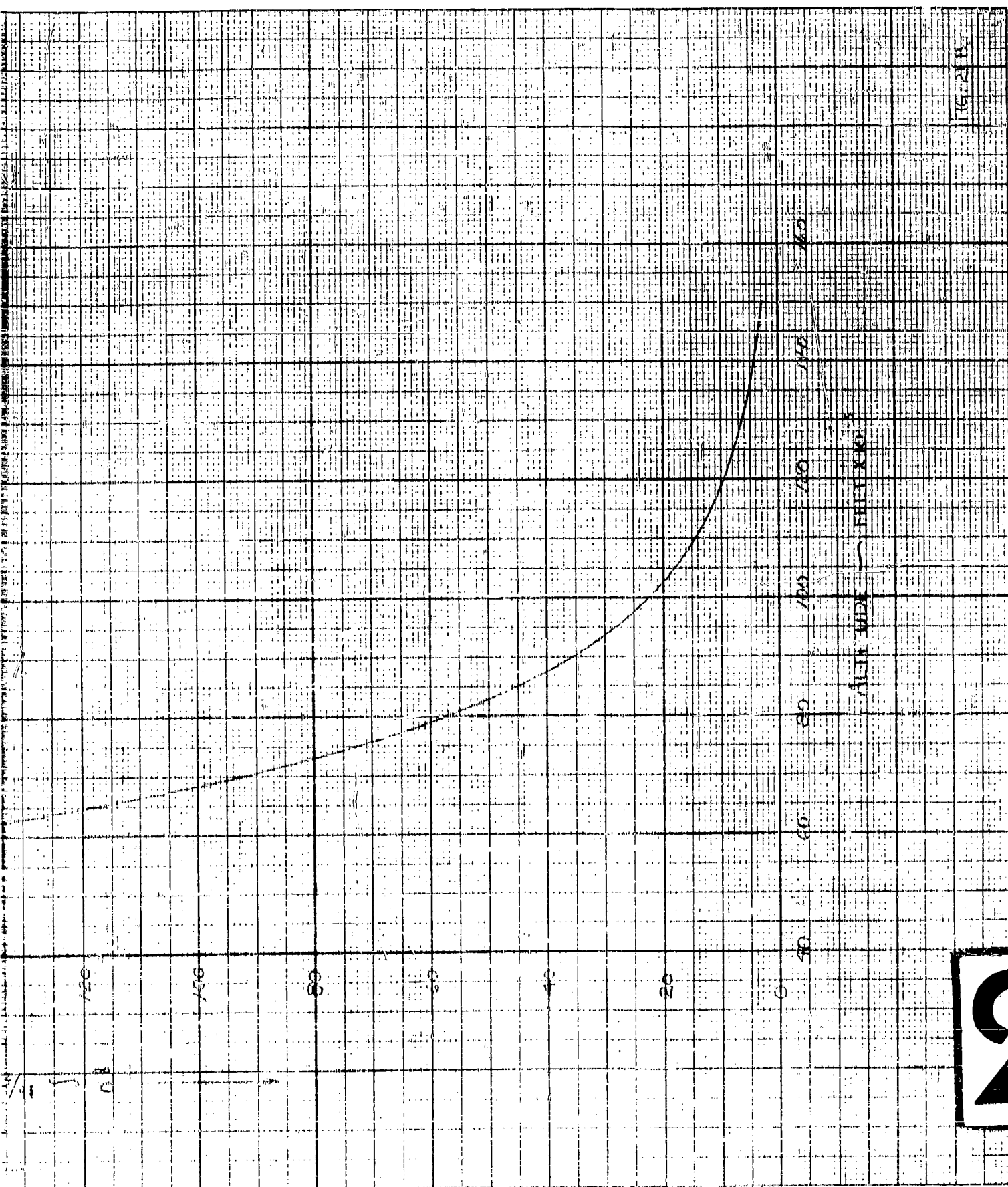
1

100

100

100

100



116-2113

2

1

REF. STATION TEMPERATURE
SINK VELOCITY VS. ALTITUDE

1000

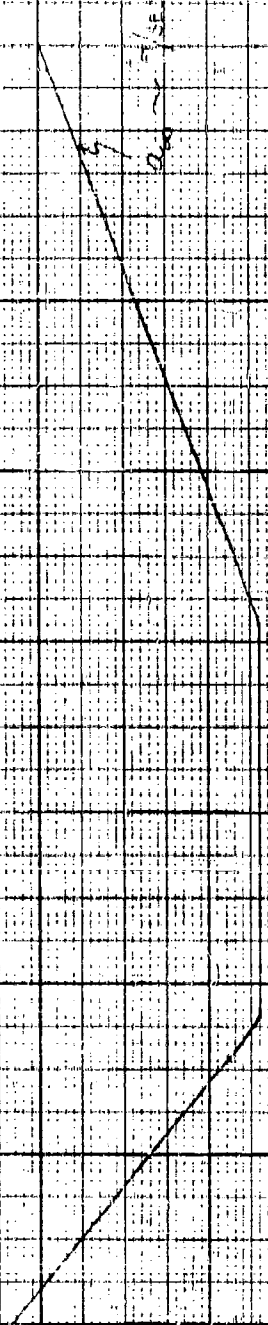
1100

1200

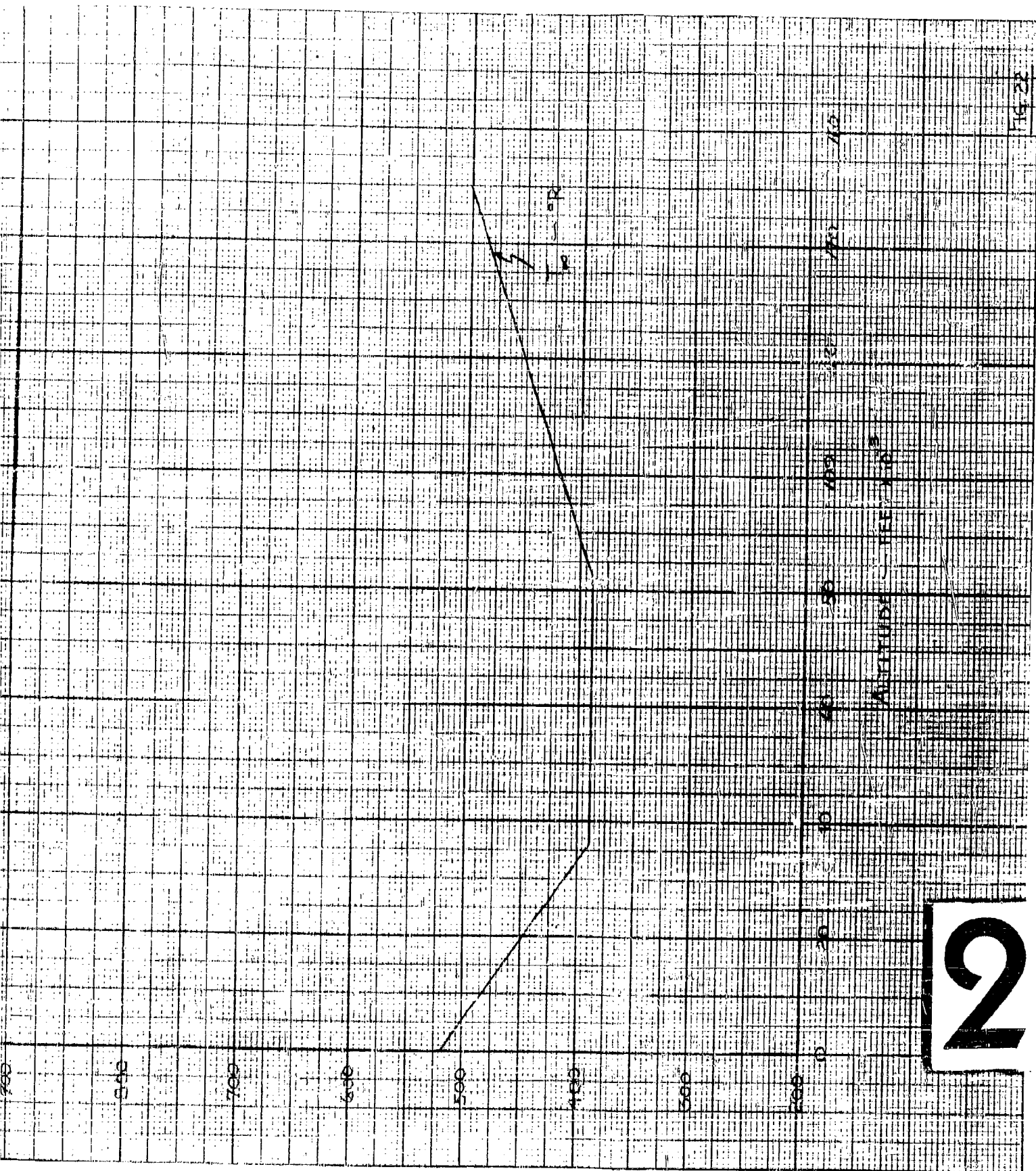
1300

1400

1500



$Q_{10} \sim 1.5$



2

Fig. 22

CHAPTER II

COOLING TECHNIQUES FOR RADOMES

PART A

GENERAL DISCUSSION OF COOLING PROBLEMS

A. GENERAL DISCUSSION OF COOLING PROBLEMS *

All structural materials lose their strength as their temperatures are increased. Hence, no matter what material is under consideration, a speed will be reached at which the material fails. If flight is to be accomplished at very high speeds, some means of cooling must be employed to keep the temperature of the structure within tolerable limits. It is the purpose of this section to discuss several possible cooling methods. The schemes which appear promising for radome applications will be considered in detail.

There appear to be two basic approaches to the cooling problem. In the first approach, the heat transferred to the body is absorbed by the structure, that is, the structure is made a heat sink. This approach has two essential variations.

1. High thermal conductivity scheme. The structure is made of a high heat capacity, high thermal conductivity material so that heat flows readily from the hot to cold regions of the structure. A high heat capacity is required so that a large amount of heat may be absorbed per unit of mass without the temperature becoming excessively high. Since the temperature ultimately attained by the material depends on the quantity of heat absorbed, it is obvious that such a scheme would find application only for short duration flights. Of course, there also exists the problem of finding a material which

*Most of the material in this part has been taken from GASL Scientific Reports Nos. 6 and 9-Part I.

has both the required thermal properties and electrical properties necessary for radome applications.

2. Ablation scheme. For flights wherein the heating is very intense but of short duration, it may be feasible to allow the outer surface of the structure to ablate. The latent heat of melting or sublimation may be used to absorb a large part of the heat load. The problem of suitable choice of materials, of course, exists for this scheme also, and probably in an even more aggravated form since in this case, the material must possess the required strength under conditions of large temperature gradients. Further, the gradually changing shape of the radome due to the ablating action may cause serious optical problems.

The methods discussed above are seen to be applicable to flights of short duration. Their success depends essentially on the proper selection of materials. For flights of longer duration, or when a material cannot be found that has the required thermal, strength and electrical properties, a different approach must be used. This other approach makes use of a material, other than the structure, to absorb the heat. In the present discussion, attention will be restricted to the latter approach since analysis of the heat sink approach requires detailed knowledge of the vehicle trajectory.

Again, one may divide the possible schemes into two classes.

1. Convection cooling. In this scheme a coolant is circulated in a channel in the interior of the radome. The heat absorbed by the radome wall is transferred to the coolant by conduction. The coolant is then either passed

through the radome, or it is discharged from the vehicle and a fresh supply of coolant is delivered to the radome.

2. Coolant injection. In these schemes coolant is injected through the radome surface either through discrete slots as in the case of film cooling, or through sections of the radome which are made of a porous material. In both of these methods, the cooling is accomplished by two mechanisms. First, heat is absorbed by the coolant as its temperature is raised from its initial state to its final state. Secondly, the injection of the coolant into the air outside the radome changes the nature of the boundary layer flow so that less heat is transferred to the radome than would occur if the same wall temperature were maintained without coolant injection.

In all of the schemes where a coolant is used, the problem of coolant supply must be considered. One may carry the required supply of coolant along with the vehicle (together with a heat exchanger system if convection cooling is to be used). In this case, the weight of the coolant to be carried may become prohibitive especially for long flights. Alternatively, one may make use of the air through which the vehicle is flying for the coolant supply. In this case, some device would have to be carried which would reduce the temperature of the ram air without too great a loss in pressure. The weight and efficiency of such a device would depend, of course, on the amount of coolant weight flow required. A discussion of such a system is given in Part B of this Chapter. In either case, it is seen that the rate at which coolant must be supplied is an important factor in the design of the cooling system.

In Reference 1, a comparison has been made of the weight flows required to maintain a given wall temperature on a flat plate using convection cooling, transpiration cooling and film cooling. It was found that transpiration cooling required the least weight flow, convection cooling was second and one slot or film cooling was last. The results for film cooling depend on the number of slots being used (transpiration cooling is the limiting case of film cooling when the number of slots become infinite). The analysis of Reference 1 was performed for essentially low speed conditions. In Part B a similar comparison will be made for a body of revolution at the high speed flight conditions which are of more interest for the present investigations. Also, deviations from optimum performance which arise from practical considerations of coolant supply will be considered. The calculations were performed for only one configuration, namely, a spherically blunted cone of 20° semi-apex angle, base radius of 1.5 ft., and radius at the cone-sphere junction of 0.3 ft. (Fig. 1, Pt. B-b). This configuration was selected in order to simplify the aerodynamic calculations. The variations of the coolant weight flow with coolant temperature, flight conditions, etc. should be qualitatively the same for other shapes of interest for radome applications. Air was the only coolant for which calculations were performed. Again, the trends obtained from these calculations should apply to other coolants.

Parts C and D of this Chapter are concerned with the effect of upstream transpiration (porous region near the nose of the radome) cooling on both the turbulent and laminar boundary layers. This problem is considered

here since a completely porous radome would hinder the transmission and reception of radar waves to such an extent as to render the unit ineffective.

It has been suggested that removing the radome from the nose and placing it underneath the forward section of the missile (chin radome) would alleviate the heating problem. However, when in this position the radome causes the flow to separate. This separated region has a different effect on the aerodynamic heating than the ordinary boundary layer flow. Part E considers the heat transfer to the chin radome for both laminar and turbulent separation. The effect of injecting a cool gas in the separated region is also investigated.

Part F of this Chapter deals with the effect of placing a spike in front of a nose radome on the heat transfer to the body. A discussion is now given of several aerodynamic features of spikes which project upstream along the axes of bodies of revolution.

Studies have been made of the drag-reducing possibilities of forward projecting spikes (see for example Reference 2). As slender bodies their aerodynamic behavior has been well understood (Reference 3), particularly when they have been faired gradually into bodies of moderate cone angle. In the latter cases flow separation from the spikes occurs only near the faired junction if at all.

Investigations have also been made on the aerodynamic effects of placing spikes upstream of blunt bodies (Reference 2, 4 to 8). Primarily, these studies have been concerned with drag-reduction of the blunt bodies

and with heat transfer reduction on the noses of blunt bodies. In all the cases cited, solid spikes, such as cone cylinders, were used. In some instances, enlarged conical tips or flat-disk tips were placed on the ends of the spikes. The spike diameters were small compared to the base diameters of the blunt bodies. Their lengths were on the order of one-half to seven body diameters.

The flows associated with the spikes on blunt bodies in the instances cited above are characterized by the fact that the flow on the spike becomes separated under the influence of the strong adverse pressure gradients generated at the stepwise junction between the spike and the body. As a result a conical wake is generally formed which envelopes the frontal region of the body. A region of low pressure is thus generated on the front of the body and a reduction in drag follows. Furthermore, the spike causes a conical shock to form and thus ameliorates the momentum loss through the strong shock region which normally forms before a blunt body. This results in a further drag reduction. From the standpoint of drag reduction the spike has the general effect of making the blunt body sharp.

The details of the flow field engendered by the spike on the blunt body are complex. The flow in separated wakes cannot readily be analyzed. Furthermore, the interaction between the conical shock on the spike and parts of the bow shock remaining in the region of the blunt nose, and between the shocks and the separated flow complicates matters further. As a result, the heat transfer rates associated with this flow are difficult to estimate. In the work of Stalder and Nielsen (Reference 6) at Mach 1.75 and 2.67 the heat

rates on the nose were double the value on the unspiked nose regardless of the spike configuration. The heat rates without spikes in these tests varied approximately as the square root of the test Reynolds number, thus indicating laminar boundary layer flow. The heat rates with the spikes showed a slightly stronger variation with Reynolds number, but not one sufficient to suggest a turbulent heat rate variation which usually increases with the 0.8 power of the Reynolds number. However, it has been suggested that the free boundary layer on the boundary of the separated region had turned turbulent and that this influenced the doubling of the heat transfer level despite the reduction in pressure level on the nose.

The tests of Bogdonoff and Vas (Reference 8) were made in helium at a Mach number of 14. These indicated forebody pressure reductions by factors of 10 to 40 when spikes were used. Contrary to the aforementioned low Mach number results, the hypersonic tests indicated decreases in the forebody heat rates by factors of 2 and 3. It has been speculated that the separated flows in this case remained laminar. A further reduction in the heat transfer might be accomplished by the injection of a coolant in the separated region.

It should be noted that spikes placed at angles of attack generate cross-forces which may result in appreciable deflections and bending moments. Furthermore, the separated flows of Stalder and Nielsen were found to be somewhat oscillatory in nature.

REFERENCES

1. Eckert, E. R. G. and Livingood, J. N. B.: Comparison of Effectiveness of Convection - Transpiration - and Film-Cooling Methods with Air as Collant. NACA Report 1182, 1954.
2. Moeckel, W. E.: Flow Separation ahead of Blunt Bodies at Supersonic Speeds. NACA Report TN 2418, 1951.
3. Allen, H. J. and Perkins, E. W.: Study of Effects of Viscosity on Flow Over Slender Inclined Bodies of Revolution. NACA Report 1048, 1951.
4. Mair, W. A.: Experiments on Separation of Boundary Layers on Probes in Front of Blunt-Nosed Bodies in a Supersonic Airstream. The Philosophical Magazine, Vol. 43, No. 342, p. 695, July 1952.
5. Jones, J. J.: Flow Separation from Rods ahead of Blunt Noses at Mach Number 2.72. NACA Report RM L52E05a, July 1952.
6. Stalder, J. R. and Nielsen, H. V.: Heat Transfer from a Hemisphere-Cylinder Equipped with Flow-Separation Spikes. NACA Report TN 3287, September 1954.
7. Beastall, D. and Turner, J.: The Effect of a Spike Protruding in Front of a Bluff Body at Supersonic Speeds. British R. and M. Report No. 3007, 1957.
8. Bogdonoff, S. M. and Vas, I.: Preliminary Investigations of Spiked Bodies at Hypersonic Speeds. Princeton University Report No. 412, March 1958 (Sponsored by A. R. L. of WADC).
9. Fourteenth Quarterly Progress Report, The Naval Supersonic Laboratory: Aerodynamic Spike, Massachusetts Institute of Technology, N. S. L., WTR 188, October-November 1956 (Confidential).
10. Ferri, A., Zakkay, V. and Libby, P. A.: A Theoretical and Experimental Analysis of a New Method of Reducing Aerodynamic Heating. Polytechnic Institute of Brooklyn, AFOSR TN 57-113, March 1957, (Confidential).
11. Martellucci, A. and Visich, M., Jr.: An Experimental Investigation at $M=3.09$ of the Pressure Distribution over a Tangent Ogive with Upstream Spikes. OSR TN 58-838, ASTIA Document No. AD 302 096, September 1958 (Confidential).

CHAPTER II - PART B

RADOME COOLING ANALYSIS

- a. Transpiration Cooling - by Melvin Epstein

TABLE OF CONTENTS

	<u>Title</u>	<u>Page</u>
	Summary	265
1.	Analysis and Discussion of Results	266
2.	References	276
3.	Symbols	277
	Figures	279

B. RADOME COOLING ANALYSIS

a. TRANSPIRATION COOLING

SUMMARY

An engineering analysis is presented for the purpose of studying the feasibility of using a transpiration cooling system to cool a radome shaped body. An empirical correlation of known solutions for the turbulent flow over a flat plate with transpiration is used to establish a simple formula for the determination of the mass flow rate required as a function of flight condition, coolant properties, and desired wall temperature. This result is used to determine the coolant weight flow requirements of a radome shaped body for both ideal (non-uniform) and realistic (uniform) distributions of porosity. Discussions are presented concerning the problems of coolant pressure requirements, coolant supply systems and problems related to the use of a porous material.

1. ANALYSIS AND DISCUSSION OF RESULTS

An approximate analysis is presented below for determining the amount of coolant required to protect a radome utilizing a transpiration cooling scheme. To the writer's knowledge, no analysis of the present problem appears in the literature. Since the purpose of the present investigation is to determine the feasibility of a transpiration cooling system, an approximate engineering approach will be used. In the analysis, it is assumed that the boundary layer is entirely turbulent. Since porous injection is known to have a destabilizing effect on the boundary layer, the surface area wetted by the laminar part of the boundary layer on a body of revolution is only a small part of the total surface area and, hence, the assumption of all turbulent flow appears to be reasonable.

It is realized that the completely porous radome is not practical (see Part A, Chapter II). However, this assumption will suffice for a comparison of the three methods of cooling discussed in this part of the report.

It has been found that in the limiting case of zero transpiration, the heat transfer on a body of revolution can be determined to a degree of accuracy adequate for engineering purposes by applying the turbulent flat plate formulas, with the free stream parameters replaced by the local values of the parameters which exist outside the boundary layer on the actual body. In addition, for conical bodies, the local Reynolds number is divided by a factor of two. Since an analysis of the compressible turbulent boundary layer on a body of revolution with transpiration

cooling has not yet been accomplished, the same approximation will be used here.

In Reference 1 an analysis is presented by Rubesin of the compressible turbulent flat plate boundary layer with porous injection. In Reference 2, Rubesin shows that for a wide range of flow conditions, all of his solutions fall into a rather narrow band if the results are plotted as St/St_0 vs. F/St_0 (Figure 2), where St is the Stanton number,

$$St = \frac{q}{C_p(T_{aw} - T_w) \rho_e u_e} \quad (1)$$

F is a non-dimensional injection parameter defined by

$$F = \frac{\rho_w v_w}{\rho_e u_e} \quad (2)$$

and subscript zero denotes zero transpiration conditions. In analogy with the zero transpiration case, it is assumed that local application of the flat plate results to axially symmetric problems is permissible providing one uses the zero transpiration Stanton number corresponding to the axially symmetric case.

$$St_0 = \frac{.0345}{P_R^{2/3} Re^{1/5}} \quad (3)$$

The Reynolds number should be evaluated at the so-called "reference temperature", but for simplicity in this analysis, it will be evaluated at the conditions existing at the outer edge of the boundary layer. The error

involved in this approximation should not be significant for the purpose of this analysis.

A further approximation is now introduced which is suggested by the narrow band into which Rubesin's solutions fall in Figure 2. It can be seen that the curve given by

$$\frac{St}{St_0} = e^{-.5 \frac{F}{St_0}} \quad (4)$$

is within approximately plus or minus ten percent of all of Rubesin's solutions for a wide range of parameters (Figure 2). It will therefore be assumed that Equation 4 can be used to relate the heat transfer with transpiration to the heat transfer without transpiration at the same conditions.

The amount of coolant required to maintain a given wall temperature can be deduced by striking a heat balance between the heat transferred toward the wall and the heat absorbed by the coolant. Thus

$$q = C_p(T_{aw} - T_w)\rho_e u_e St_0 e^{-.5 \frac{F}{St_0}} = \rho_w v_w C_p(T_w - T_1) \quad (5)$$

If one defines

$$z \equiv \frac{F}{St_0}, \quad \eta \equiv \frac{T_{aw} - T_w}{T_w - T_1} \quad (6)$$

Equation 4 reduces to

$$z = \eta e^{-.5z} \quad (7)$$

Equation 7 is plotted in Figure 3. It represents a very simple approximate solution to the transpiration cooling problem. Given the flight condition, coolant temperature, pressure distribution and zero transpiration heat transfer, one can determine the amount of coolant required to maintain a given wall temperature.

Equation 7 has been applied to the determination of the amount of coolant required to protect the spherically blunted cone illustrated in Figure 1. The spherical part was assumed to be protected by injecting the coolant at a discrete slot at the stagnation point. Since the surface area of the spherical region is only a very small part of the total surface area, the amount of coolant required to protect the nose is small compared to the amount required to protect the conical surface. This amount was estimated (by assuming that the maximum local coolant flux rates required at any point on the body was supplied over the entire spherical region) to be less than 4% of the total required coolant.

The amount of coolant required to cool the conical part of the surface is simply

$$W = 2\pi g \sin \theta_c \int_{L_1}^{L_1 + L} \rho_w v_w x dx \quad (8)$$

It is seen from Equations 2, 3, 6 and 7, that the minimum coolant rate is obtained when the local injection rate ($\rho_w v_w$) varies as $x^{-1/5}$.

In this case, Equation 8 becomes

$$W = \frac{.0383 \pi g R_B \mu_e}{Pr^{2/3}} Re_B^{4/5} z \left[1 - \left(\frac{L_1}{L} \right)^{9/5} \right] \quad (9)$$

where Re_B is the Reynolds number based on the base radius and z is determined from the known values of adiabatic wall temperature, coolant temperature, wall temperature and Equation 7.

For the configuration under consideration, a varying injection rate would require either a varying internal pressure or a nonuniform distribution of porosity. It does not appear that a controlled distribution of pressure in the interior of the radome would be feasible. Quantity production of porous radomes with variable porosity is also not within the present state-of-the-art. Hence the coolant weight flow predicted by Equation 9 may be regarded as an ideal weight flow which probably cannot be obtained in practice. For the purpose of illustration, the variation of this ideal weight flow with Mach number and coolant temperature at an altitude of 100,000 feet and $T_w = 1000^\circ R$ is shown in Figure 4 for the configuration under consideration.

It is of interest to calculate the weight flow required under more practical conditions, i.e., with constant internal pressure and uniform

porosity. Since the pressure is essentially constant on the conical part of the surface, the injection rate is then also constant. Hence, the coolant rate flow may be expressed as

$$W = 2\pi g \sin \theta_c \rho_w v_w \int_{L_1}^{L_1+L} x dx = \pi g \rho_w v_w \left[(L_1+L)^2 - L_1^2 \right] \sin \theta_c \quad (9)$$

The value of $\rho_w v_w$ to be used in Equation 9 is the value required to keep the point of maximum heating at the required wall temperature. On the conical part of the surface, this is at the sphere-cone junction. Thus, given T_{aw} , T_w at the shoulder, and T_1 , one can determine η and hence the value of z at the shoulder. Then, using Equations 6 and 3, the expression for the coolant weight flow required to keep the maximum temperature below T_w becomes

$$\frac{W}{\pi R_B^2 \rho_e u_e} = \frac{.0345 g \left[1 - \left(\frac{L_1}{L_1+L} \right)^2 \right]}{Re_B^{1/5} \sin^{4/5} \theta_c} \cdot \frac{z}{(L_1/L)^{1/5}} \quad (10)$$

The variations of coolant weight flow required vs. coolant temperature, Mach number, altitude and maximum wall temperature are presented in Figure 5. Comparison with the ideal porosity case of Figure 4 shows that approximately twenty-five percent more coolant weight flow must be supplied for the constant porosity, constant internal pressure case.

In the scheme considered above, it was assumed that the spherical part of the body is cooled by means of a discrete injection of coolant at the stagnation point. In order to have as simple a system as possible, it would be desirable that the pressure drop across the porous part of the surface be sufficiently large so that the pressure on the inside of the radome is greater than the stagnation pressure behind the bow shock wave. In this way, the same coolant source could be used for the entire system, the division of mass flow between the nose slot and the porous wall being accomplished by appropriately designing the shape of the nose slot.

As an example of the pressure levels required in such a system, calculations were performed assuming the porous surface to have a pressure drop of 1 psi per inch of thickness for a flow rate of one cubic foot per minute of air at standard temperature and pressure. This corresponds to a low porosity refractory ceramic. The results of this calculation are presented in Figure 6 for a 1/4 inch thick wall. It is seen that the required pressure level on the inside of the radome varies considerably with altitude and Mach number. This fact complicates the problem of controlling the coolant supply with changing flight conditions. The problem may not be as severe as one might first expect, however, since the device which supplies the coolant will also probably have

characteristics which depend in a similar manner on flight condition.
(assuming a ram-air intake is used).

One possible device for supplying the coolant is a turbo-cooler which takes ram air and expands it to the required coolant pressure. If the temperature at the end of the expansion is equal to or less than the required coolant temperature, then such a device could, by itself, serve as a coolant supply system. If the temperature at the end of the expansion is higher than the required coolant temperature then an additional means of reducing the cooling temperature must be coupled into the system. A more detailed discussion of such a system is given in Appendix IV of the portion of Part B on convective cooling (page 350). However, it is of interest here to make a rough calculation to see whether such a system could find application in a transpiration cooling scheme.

The feasibility of such a system depends, of course, on the flight condition and the heat load to be absorbed. To illustrate the effect of these conditions on the feasibility of a turbo-cooler system, approximate sample calculations were made for 1) the ideal case, wherein the ram air was obtained through an inlet with one hundred percent pressure recovery and 2) a more realistic case wherein the ram air was obtained through an inlet with sixty percent pressure recovery. The final temperature was determined by assuming that the air expands isentropically from the final total pressure to the required coolant pressure. The results are presented in Figure 6. The region in which the cooling system would

operate is to the right of the shaded curves. For the 1000°R wall temperature condition, the heat load is too great for this system to operate by itself. For the 2000°R wall temperature condition, it is seen that the turbo-cooler by itself is capable of providing the required cooling air over a wide range of conditions if an efficient inlet is used. Even for an inlet with a pressure recovery of sixty percent, the turbo-cooler is still satisfactory for a somewhat restricted range of conditions.

A few words are in order here concerning the fabrication of a porous wall. One of the principal difficulties associated with a transpiration cooling system is the manufacturing of an acceptable porous wall. It is necessary that the porosity be closely controlled with respect to uniformity and reproducibility. The state-of-the-art of the manufacturing of porous ceramics has been developed to the point where these characteristics can be adequately controlled, at least for simple shapes (cylinders and disks). Good results have also been obtained for radome shaped bodies in laboratory applications. In radome applications, it may also be necessary that the wall thickness be closely controlled because of optical considerations. Present porous ceramic forming practice allows the thickness to be controlled to within about one percent on simple shapes.

Another difficulty associated with the use of porous walls is that of maintenance. Experience with porous ceramic linings in combustion

chambers and gas turbine blades indicates that the pores frequently become clogged. It is expected that in radome applications this problem may not be so severe since the fluid passing through the material is relatively clean.

The strength characteristics of porous materials depend very much on the type of materials being used and the method of manufacture. The presence of myriads of tiny pores tends to weaken the structure considerably because of the stress concentrations that they introduce. This condition appears to be worst for materials with a crystalline structure. Ceramics made from a glassy substance seem to be better in this respect although the loss of strength due to porosity is still quite large. The successful use of porous wall radomes may hence depend principally on whether the desired strength properties can be obtained. The porous materials which are now available appear to be marginal with respect to strength characteristics.

2. REFERENCES

1. Rubesin, Morris W. - An Analytical Estimation of the Effect of Transpiration Cooling of the Heat-Transfer and Skin-Friction Characteristics of a Compressible Turbulent Boundary Layer - NACA TN 3341, December 1954.
2. Rubesin, Morris W. - The Influence of Surface Injection on Heat Transfer and Skin-Friction Associated with the High-Speed Turbulent Boundary Layer - NACA RM A55L13, February 20, 1956.

3. SYMBOLS

C_p	specific heat at constant pressure
F	$\frac{p_{wv_w}}{p_{e u_e}}$
L, L_1	slant height of body, slant distance to cone-sphere junction
M_∞	free stream Mach number
p	pressure
Pr	Prandtl number
q	heat flux
R	radius
Re	$\frac{\rho_e u_e x}{\mu_e}$
St	Stanton number
T	temperature
u	velocity
v	velocity normal to surface
W	weight flow
x	distance along meridian of body
z	F/St_0
η	$\frac{T_{aw} - T_w}{T_w - T_1}$
θ_c	cone semi-apex angle
ρ	density

Subscripts .

aw.	adiabatic-wall
B	base
c	cone
e	local inviscid flow
0	zero transpiration
t ₁	free stream total value
t ₂	total value downstream of normal shock
w	wall
l	coolant

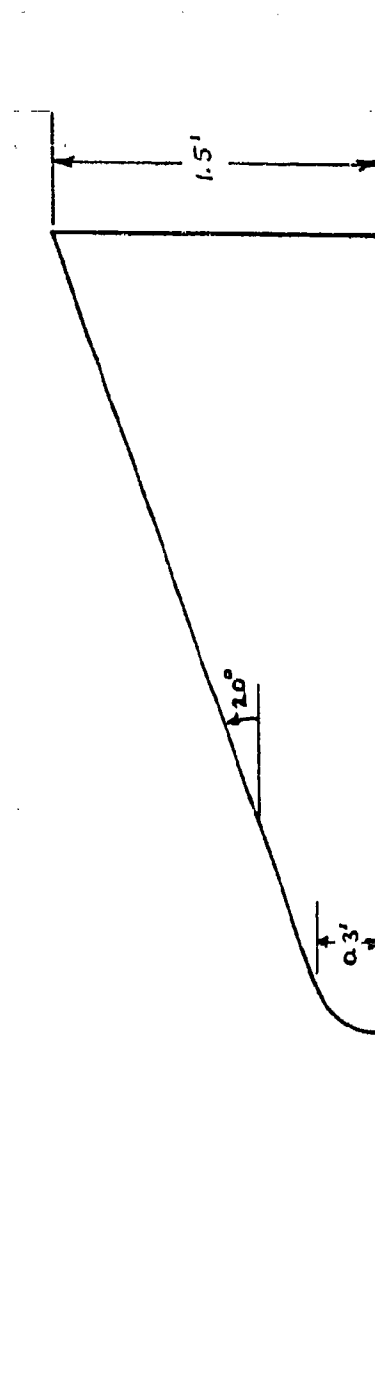
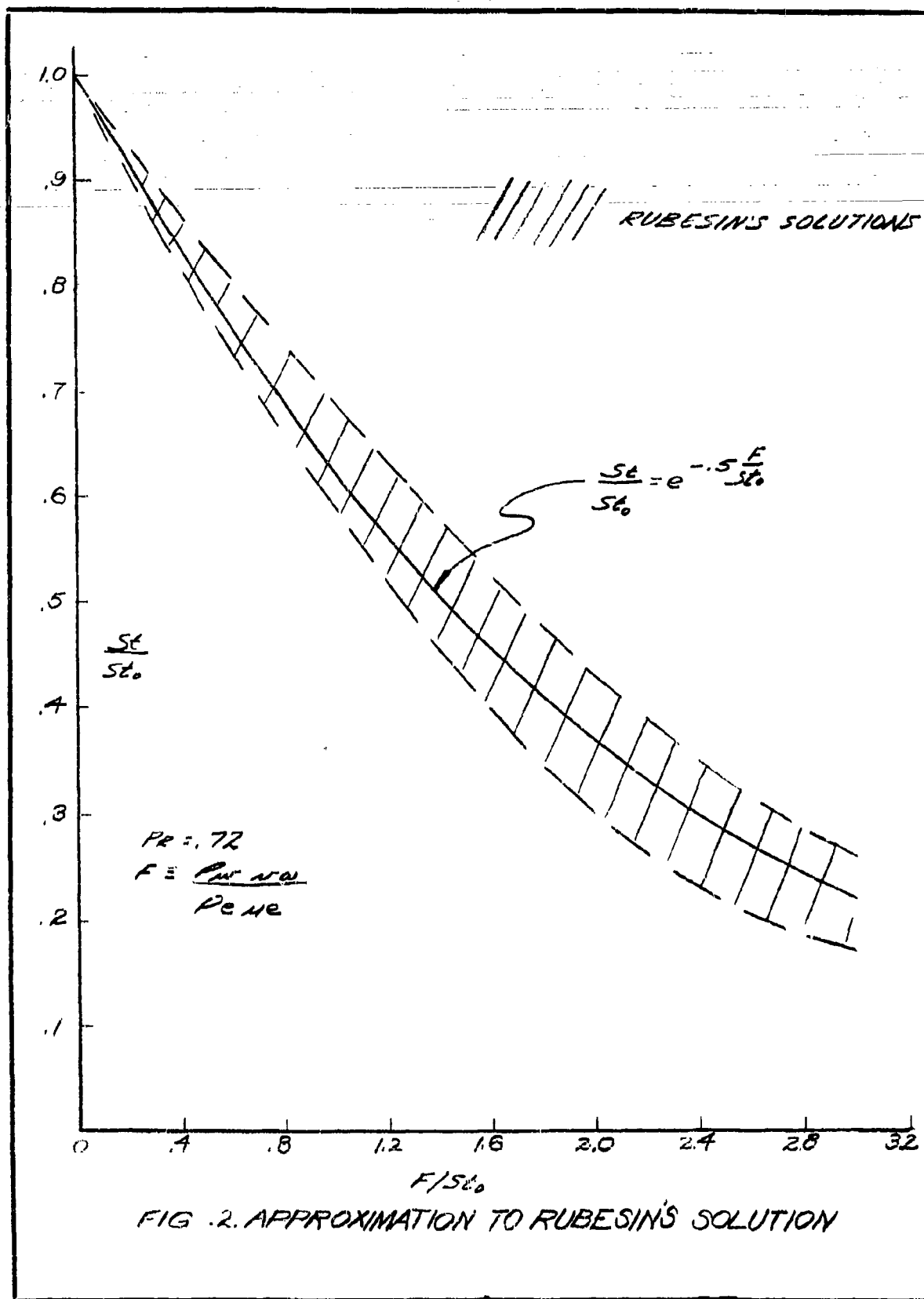


FIG. 1. CONFIGURATION STUDIED.



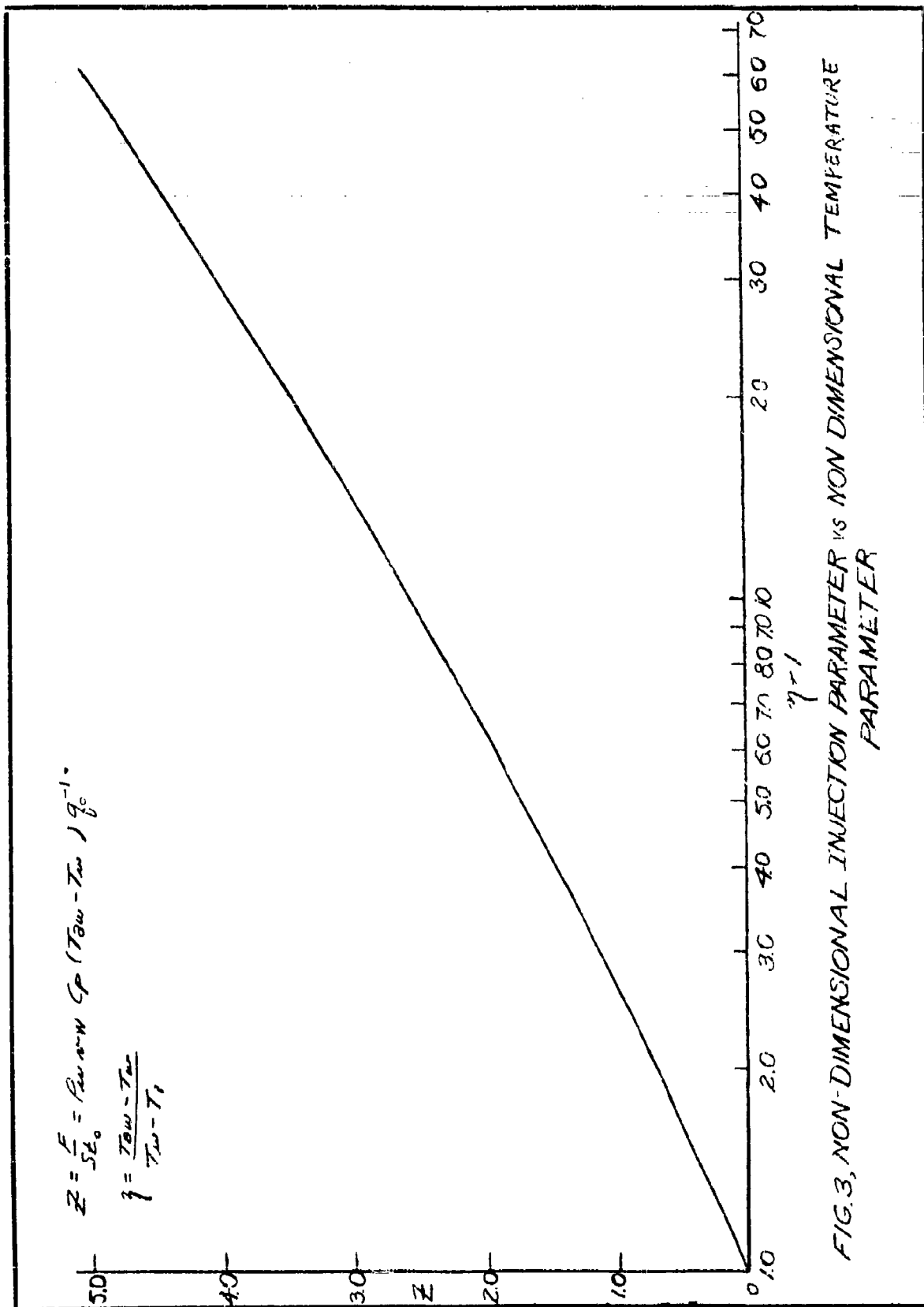


FIG. 3, NON-DIMENSIONAL INJECTION PARAMETER VS NON DIMENSIONAL TEMPERATURE PARAMETER

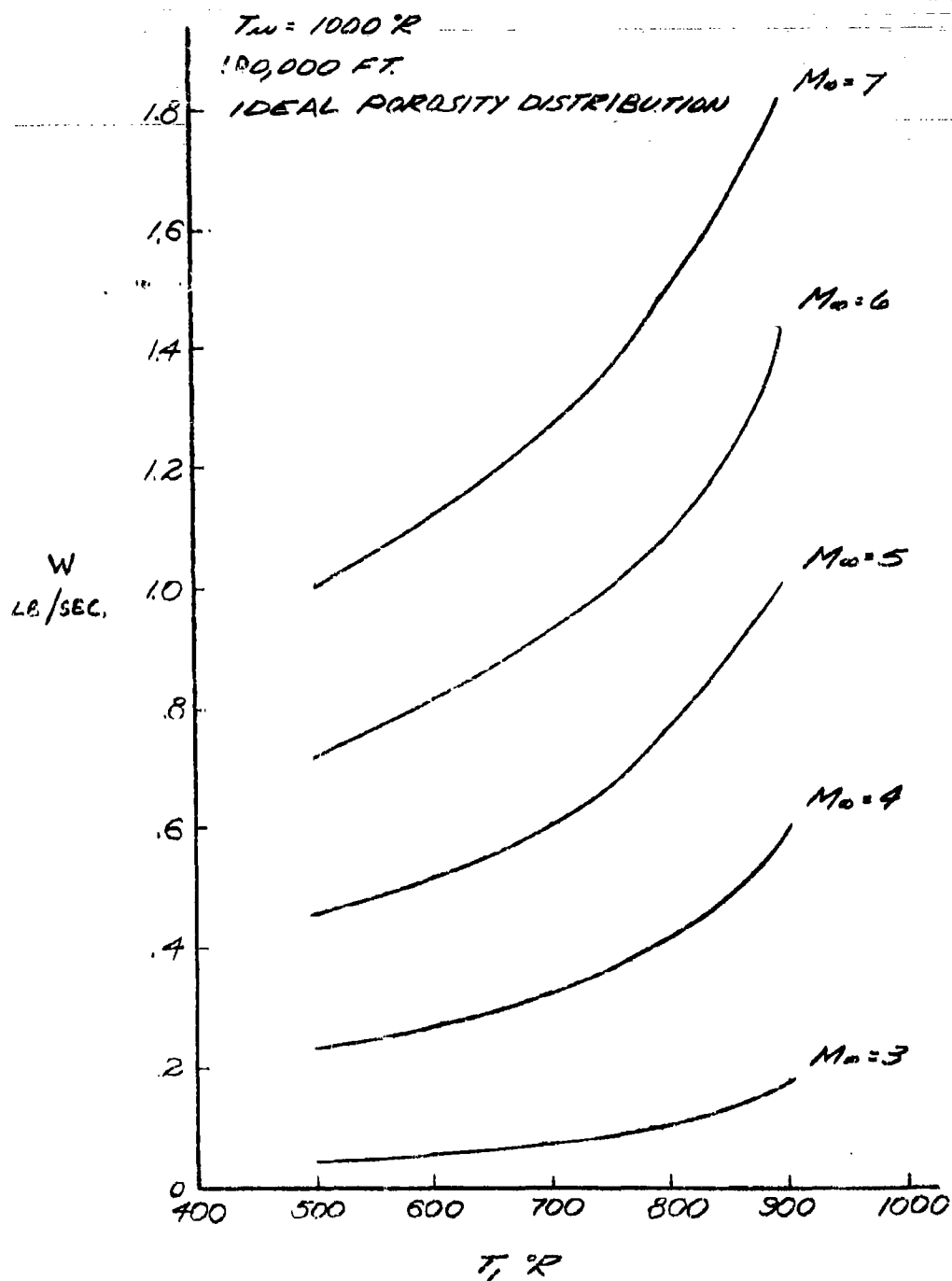


FIG. 4. COOLANT WEIGHT FLOW REQUIREMENTS WITH IDEAL POROSITY DISTRIBUTION.

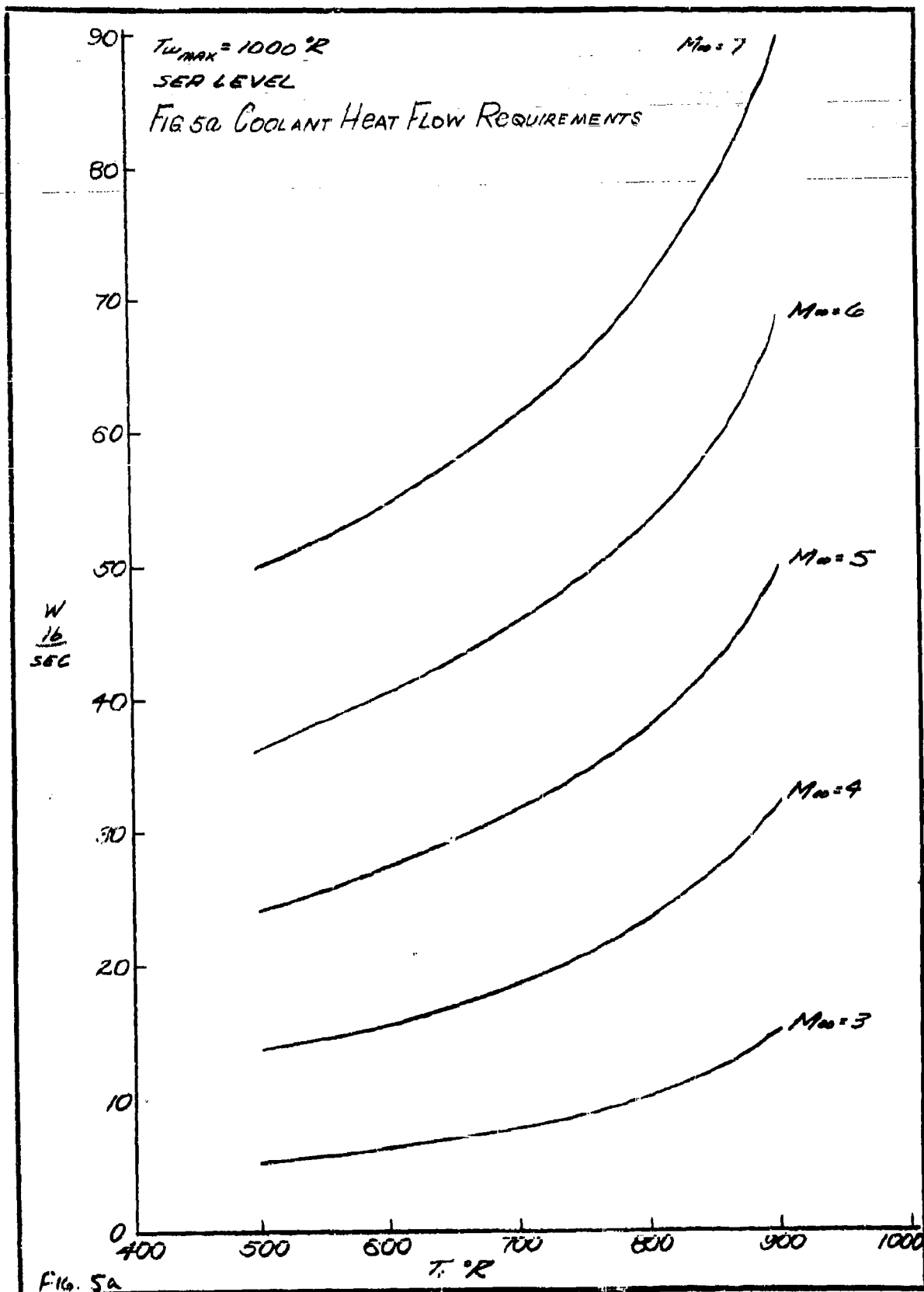
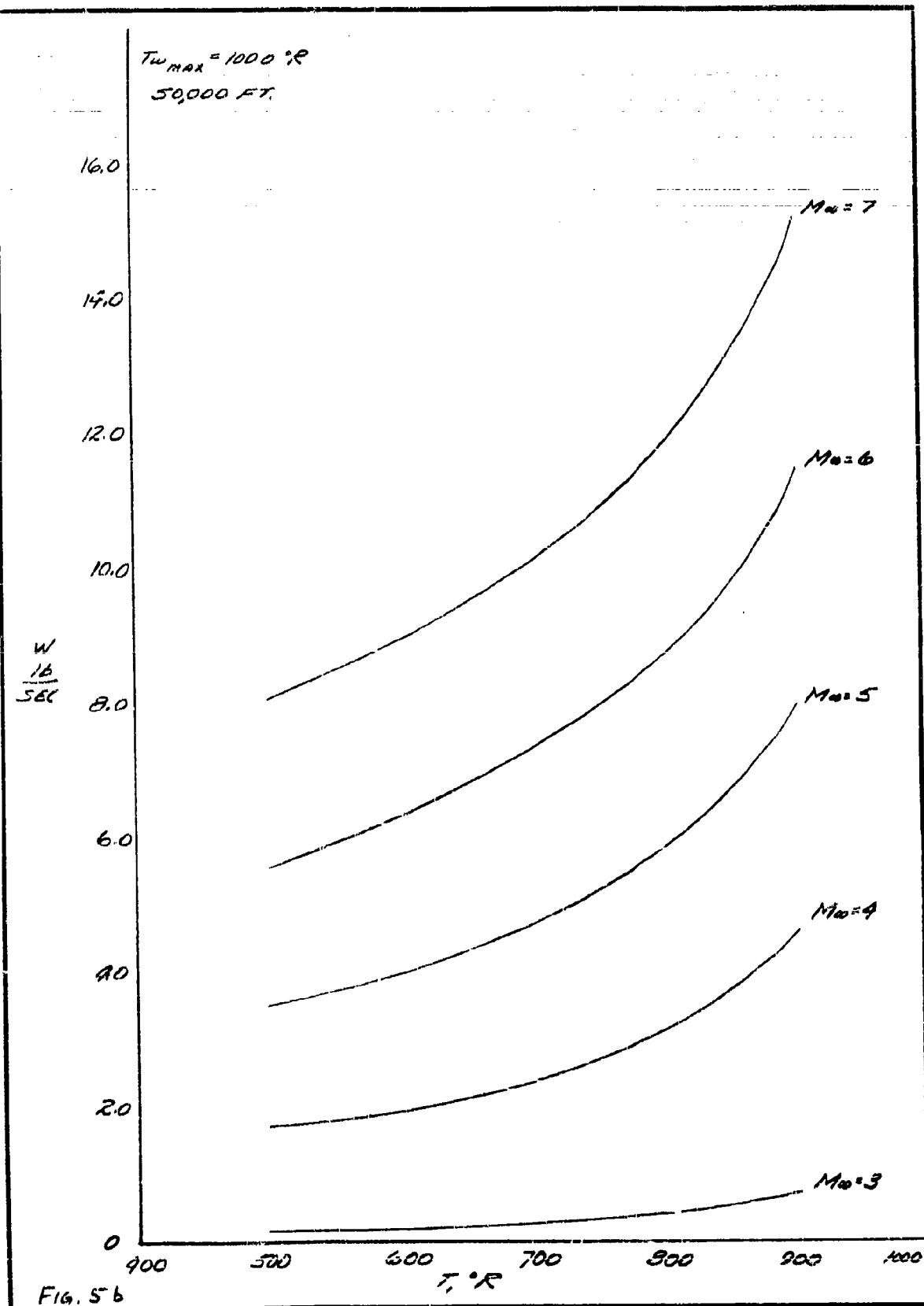


FIG. 5a



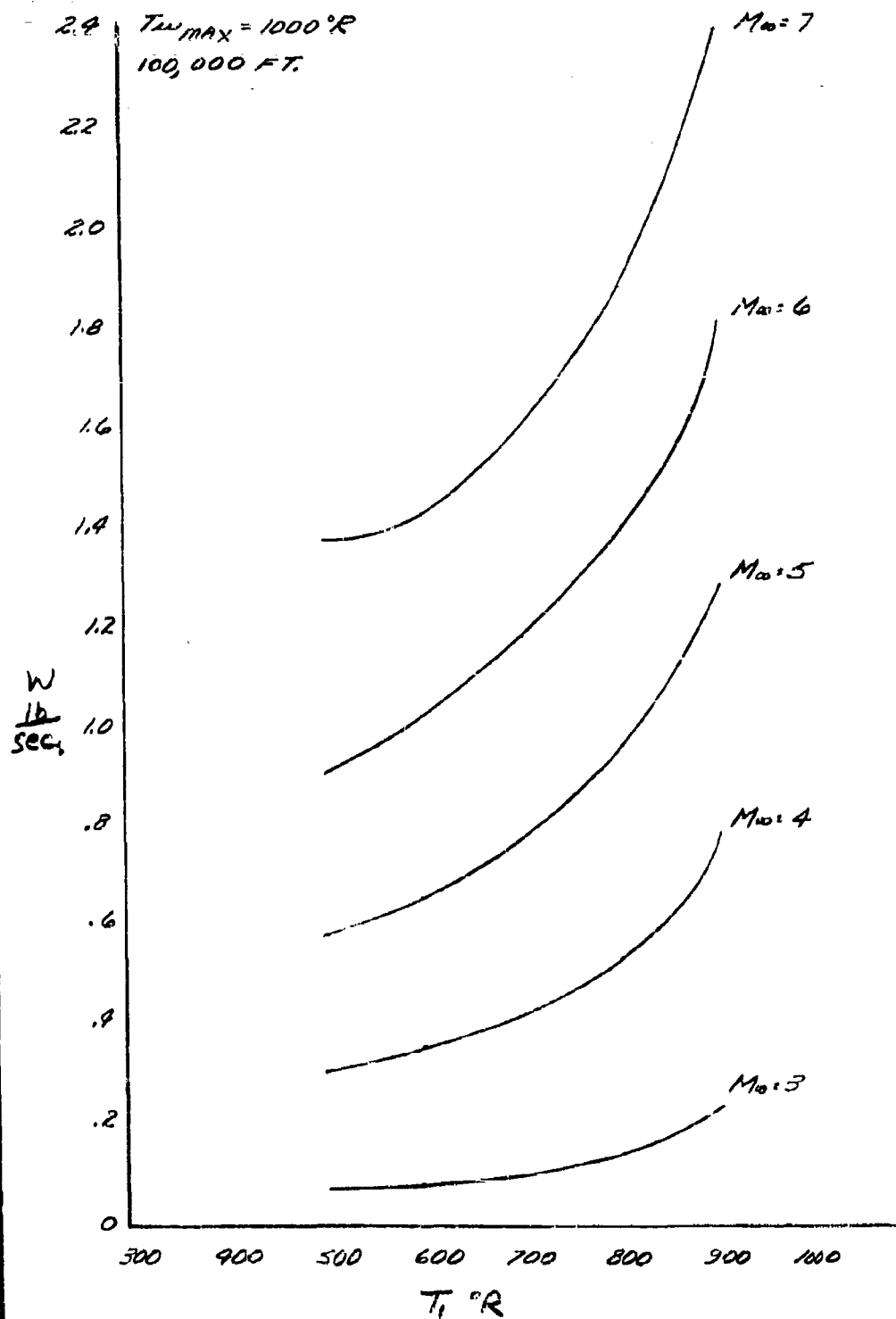


Fig. 5c

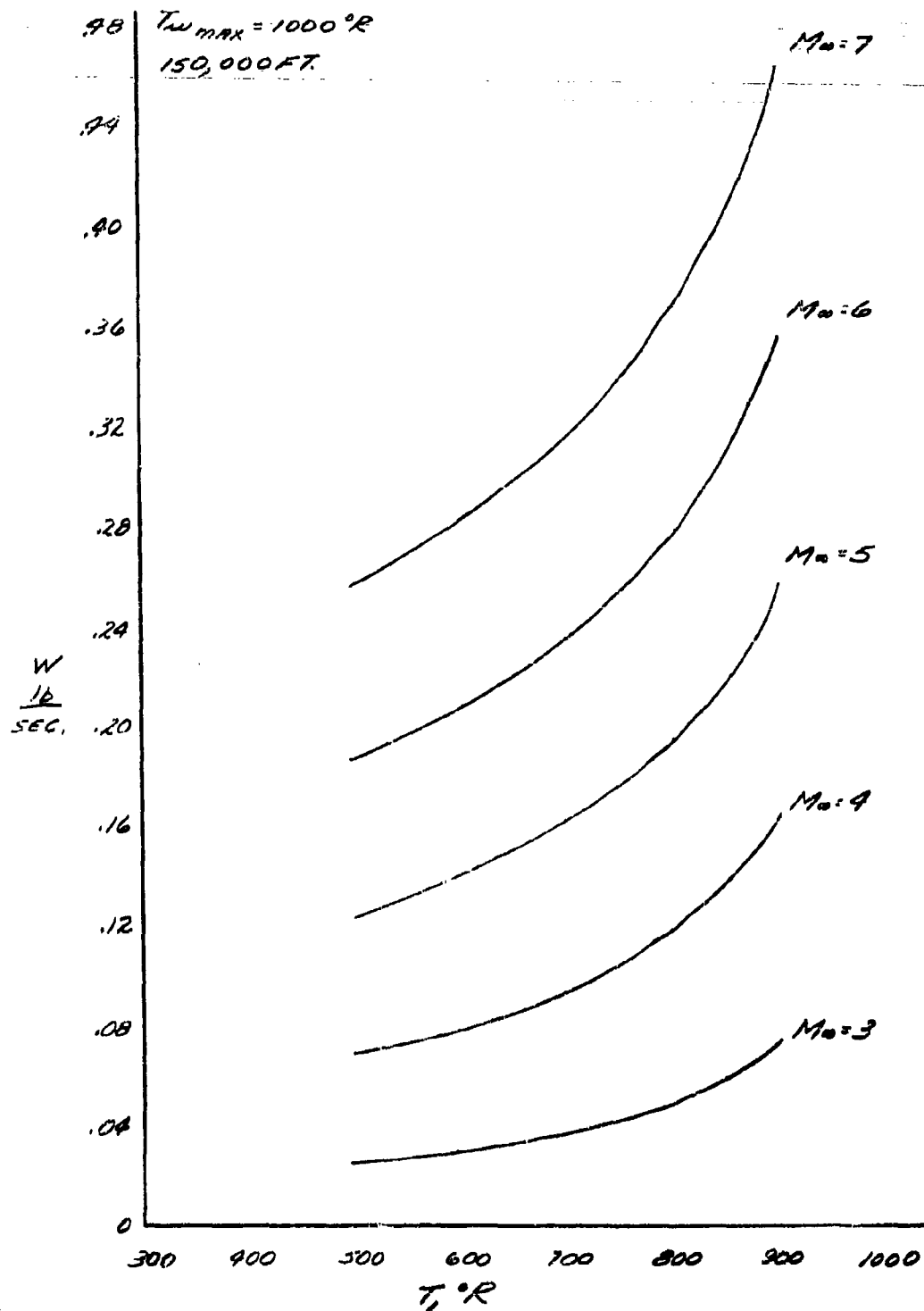
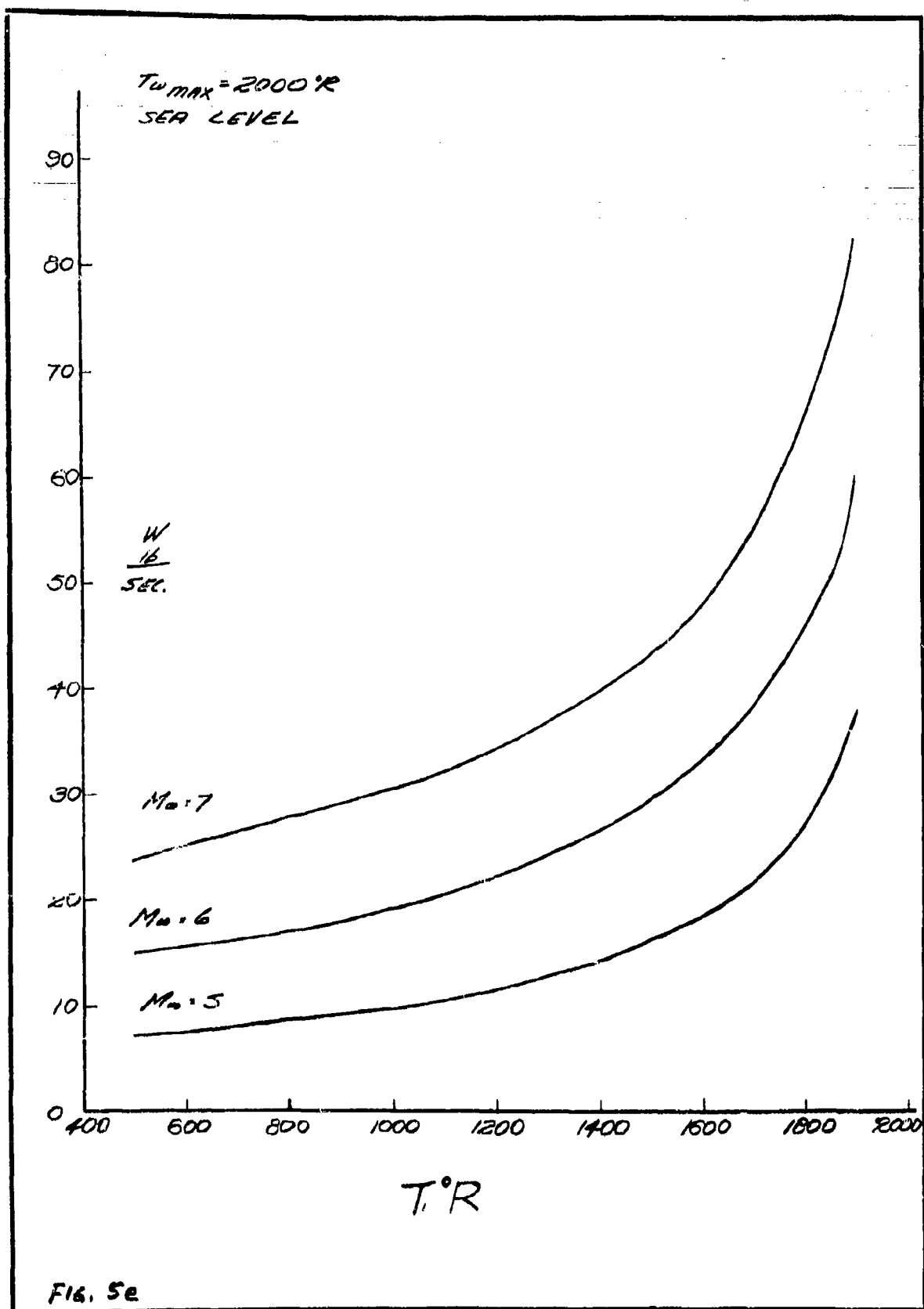


FIG. 5d



$T_{w, \max} = 2000^{\circ}R$
 50,000 FT.

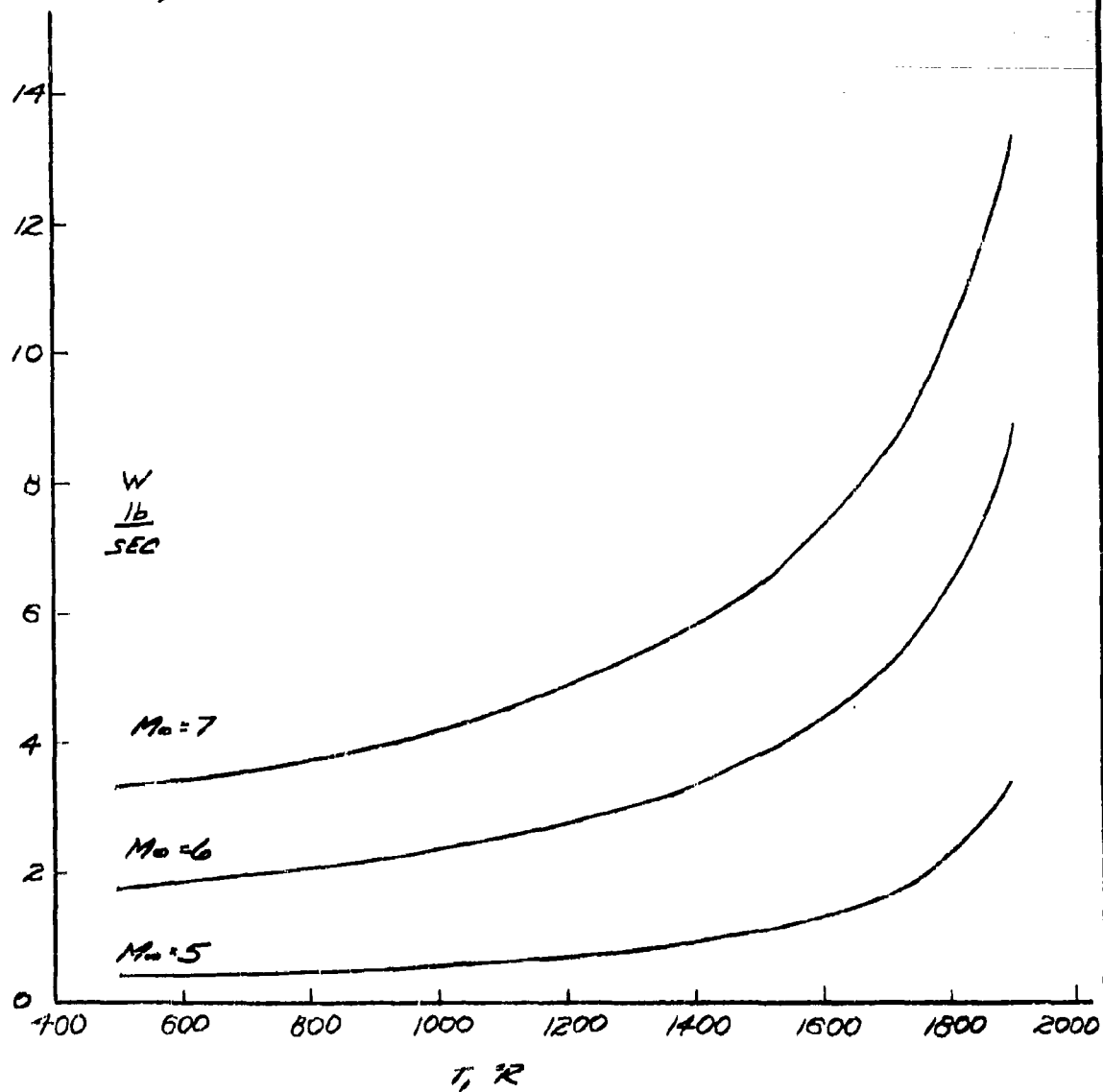


FIG. 5f

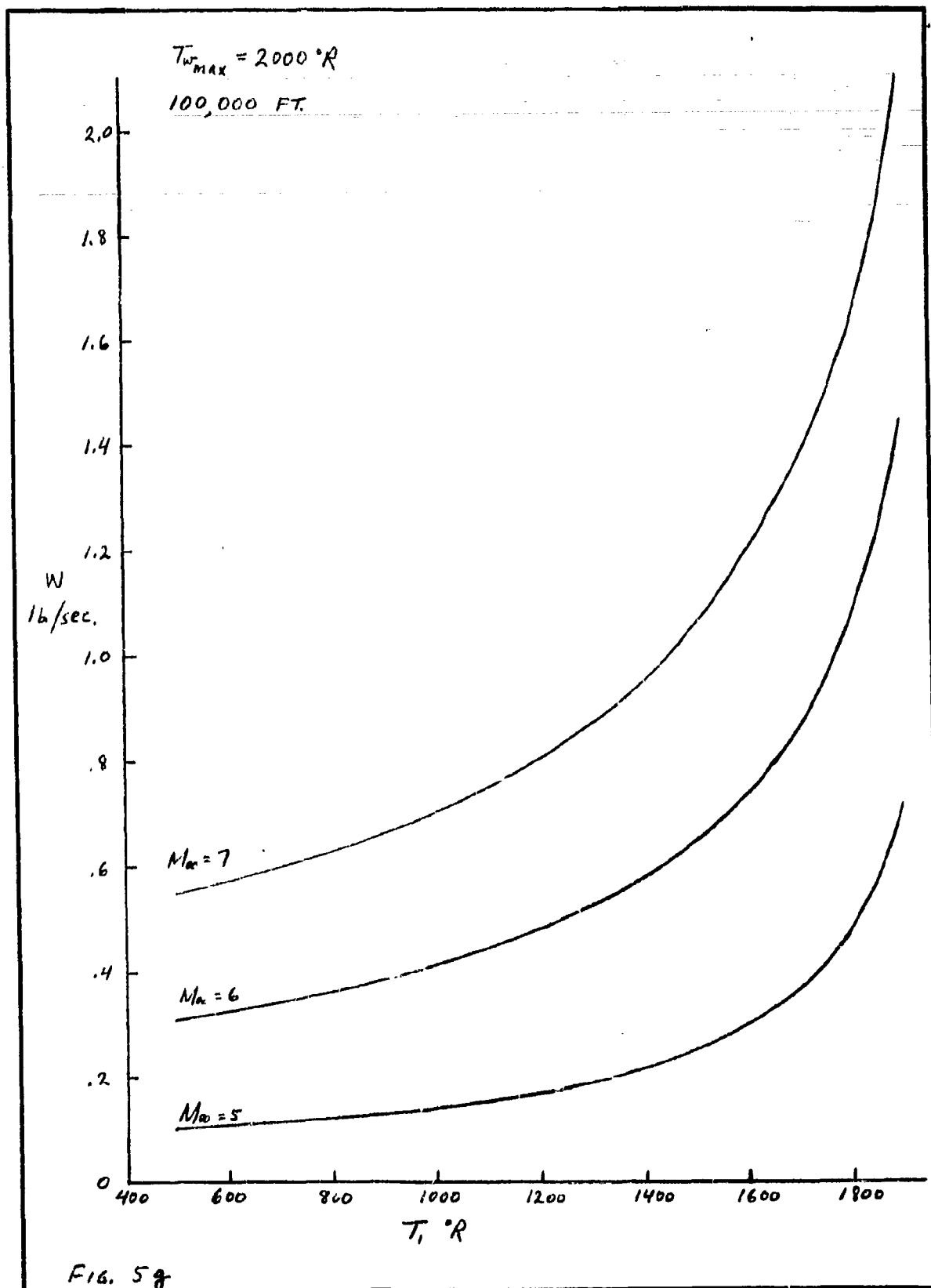


FIG. 5g

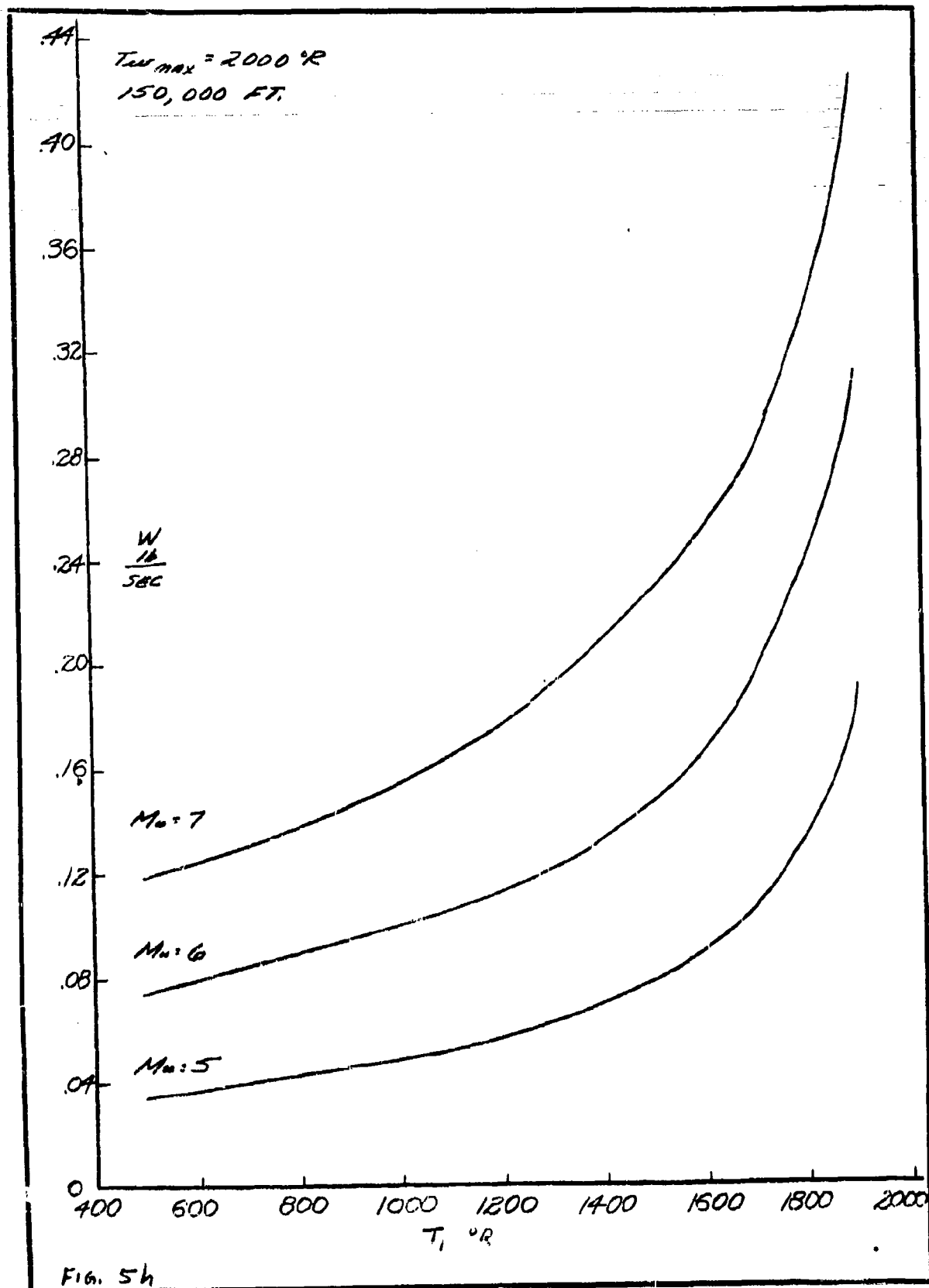
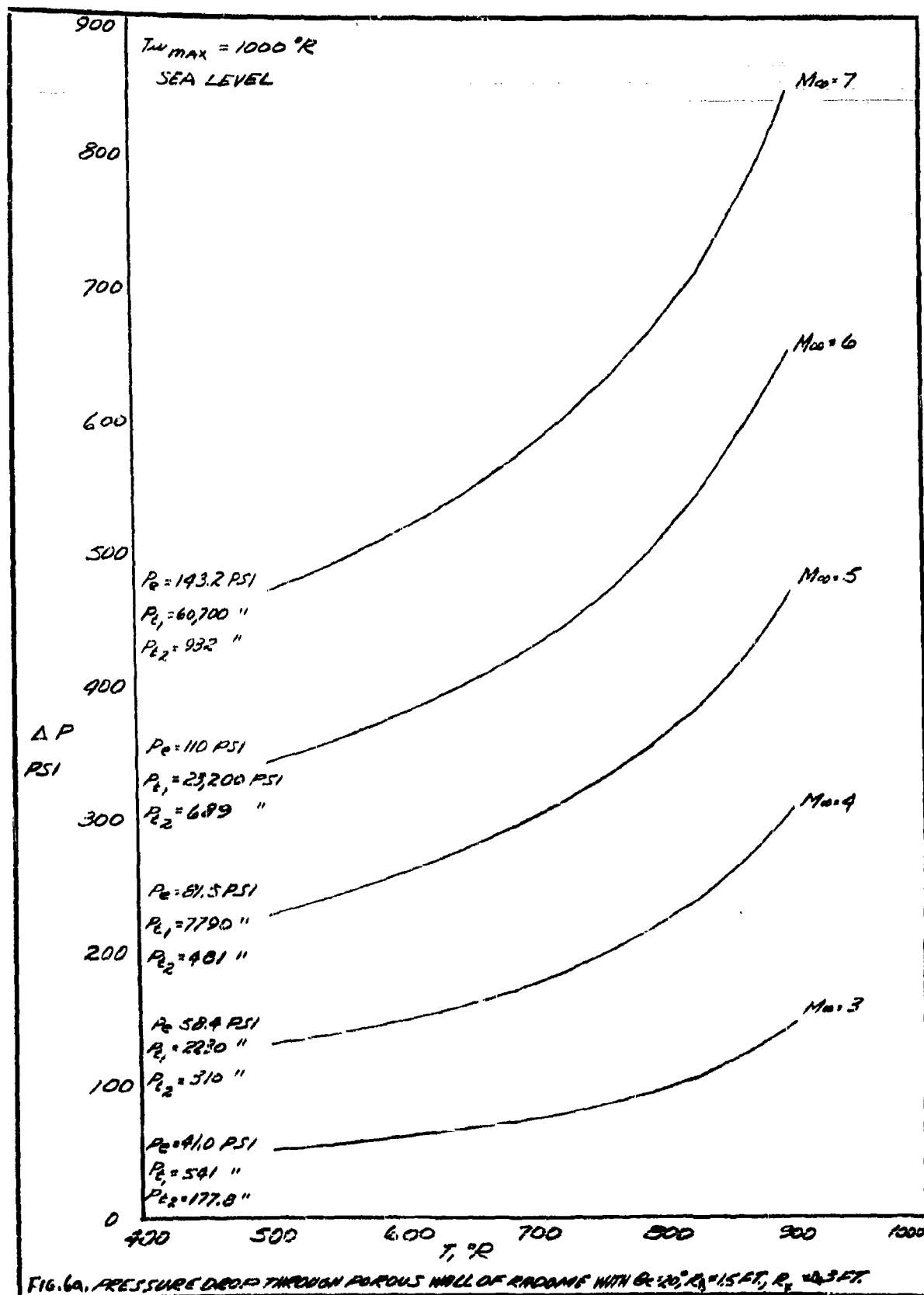


Fig. 5h



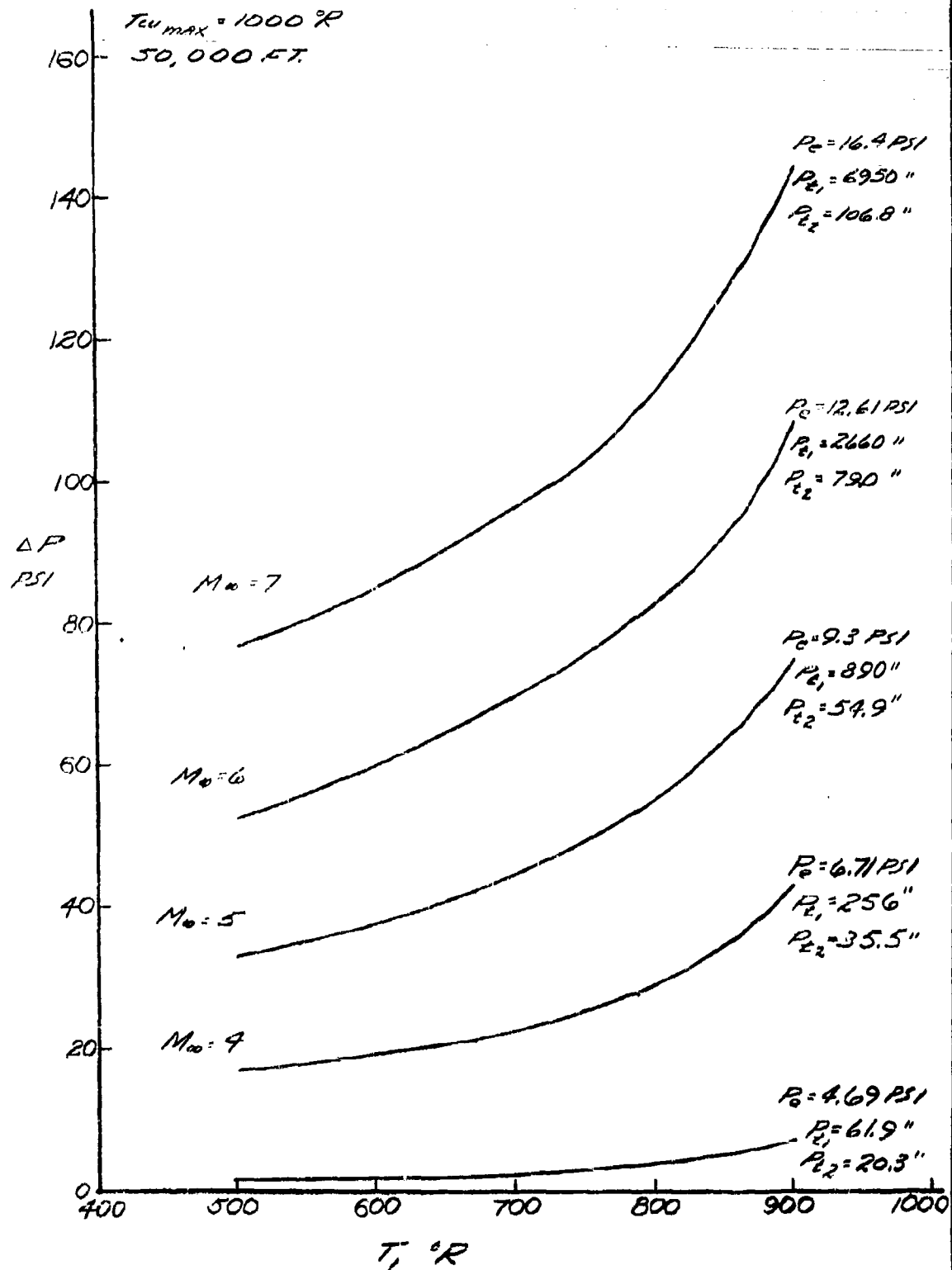
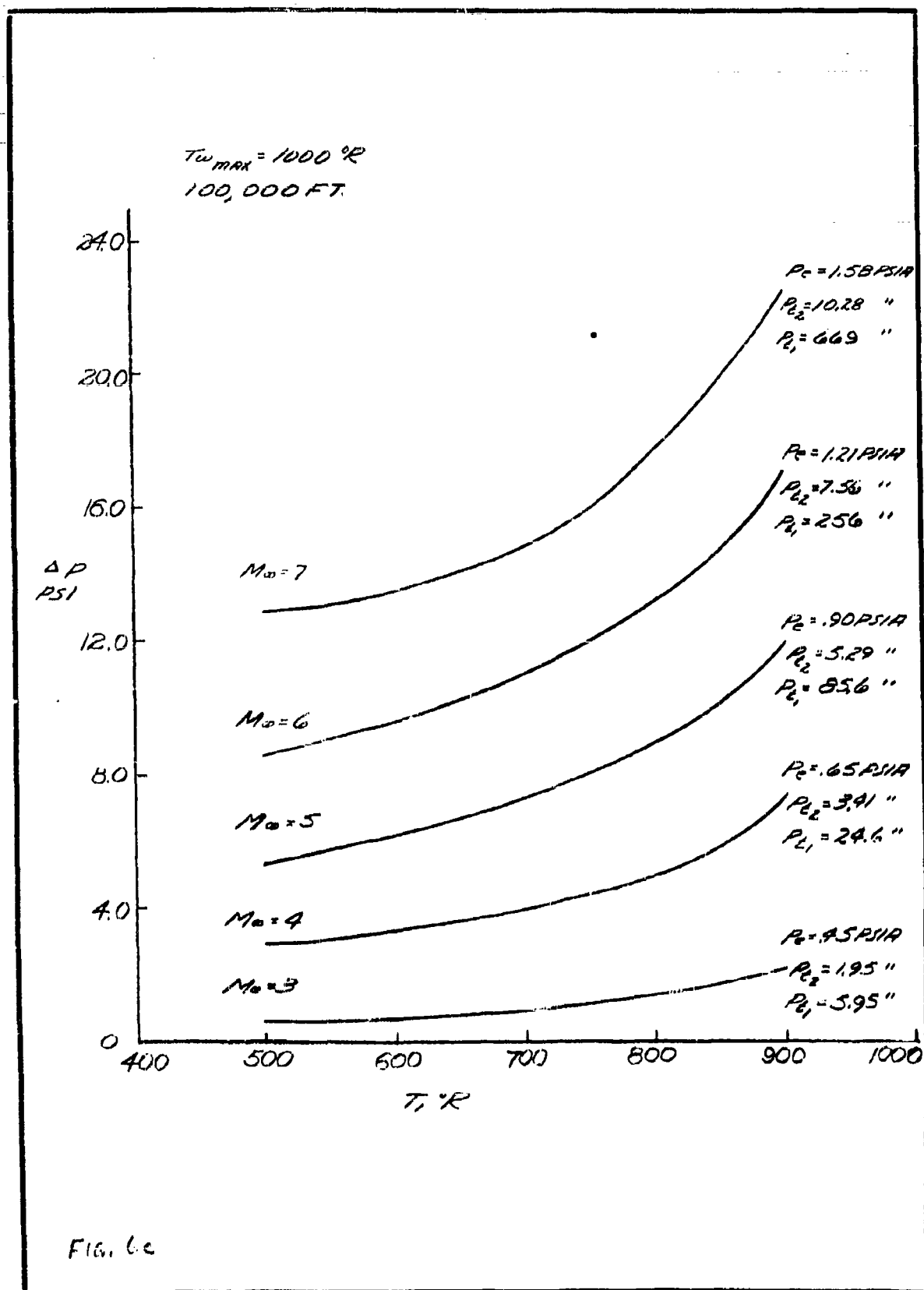
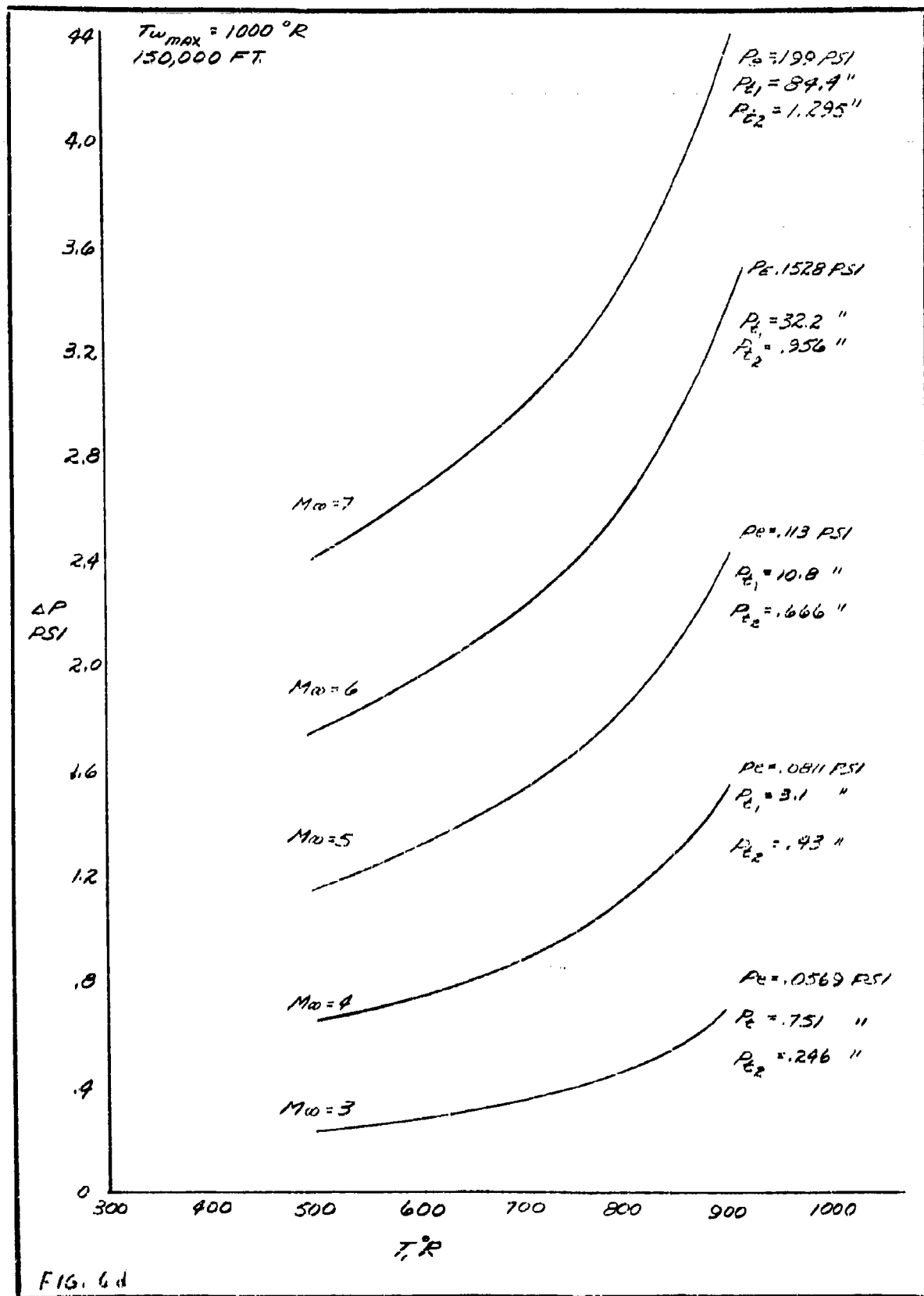


FIG. 66





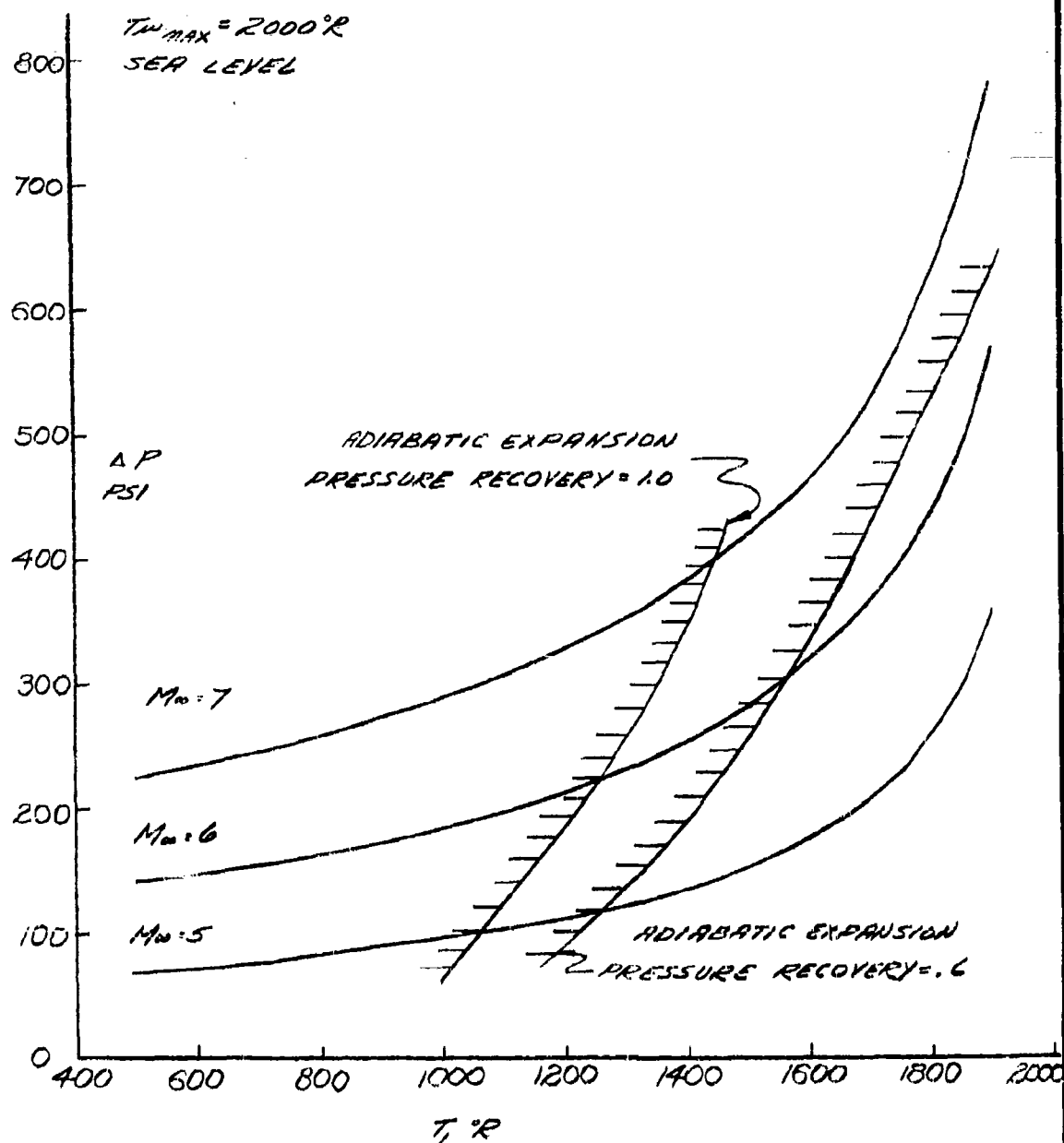


FIG. 6e

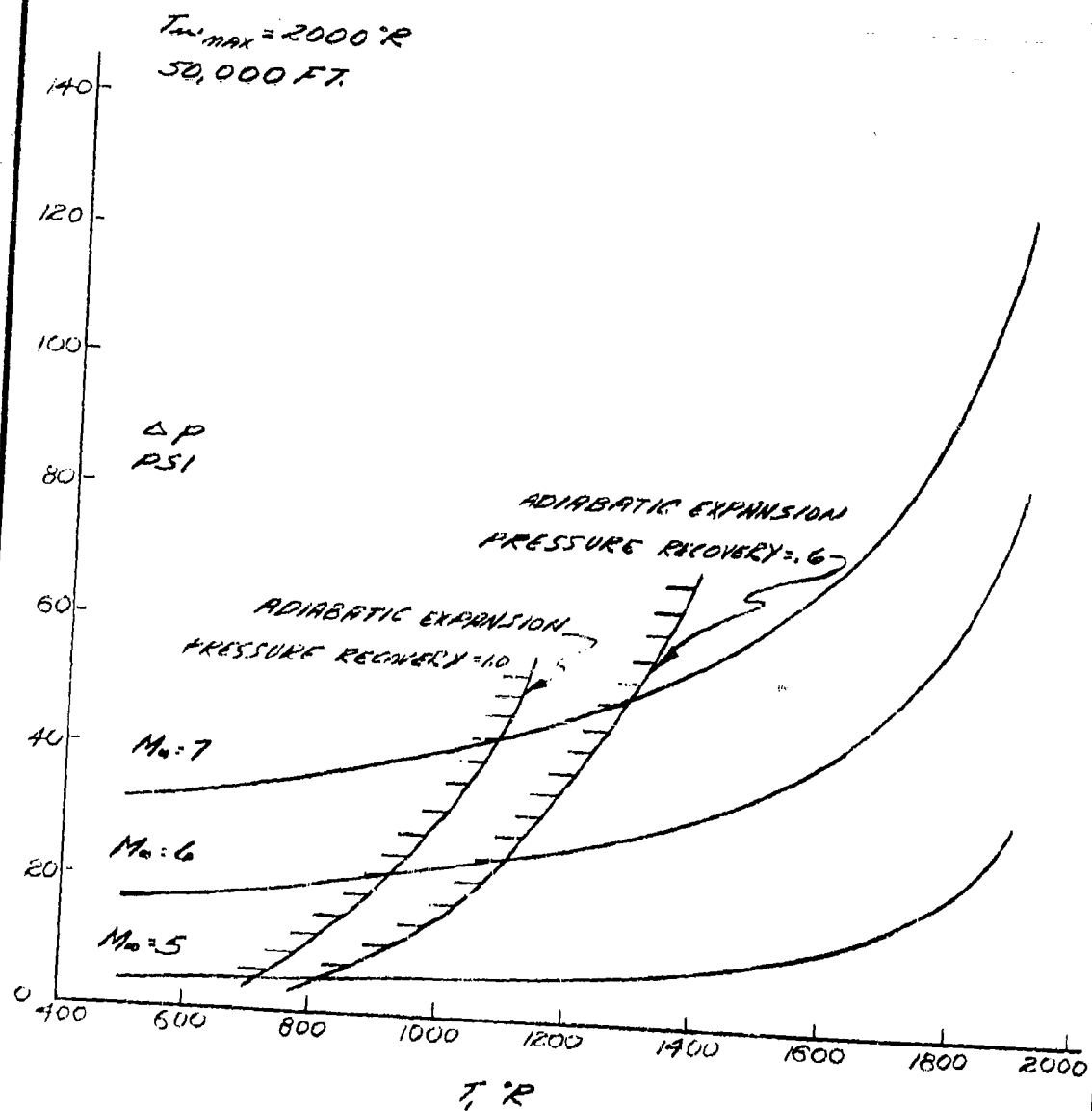


Fig. 6f

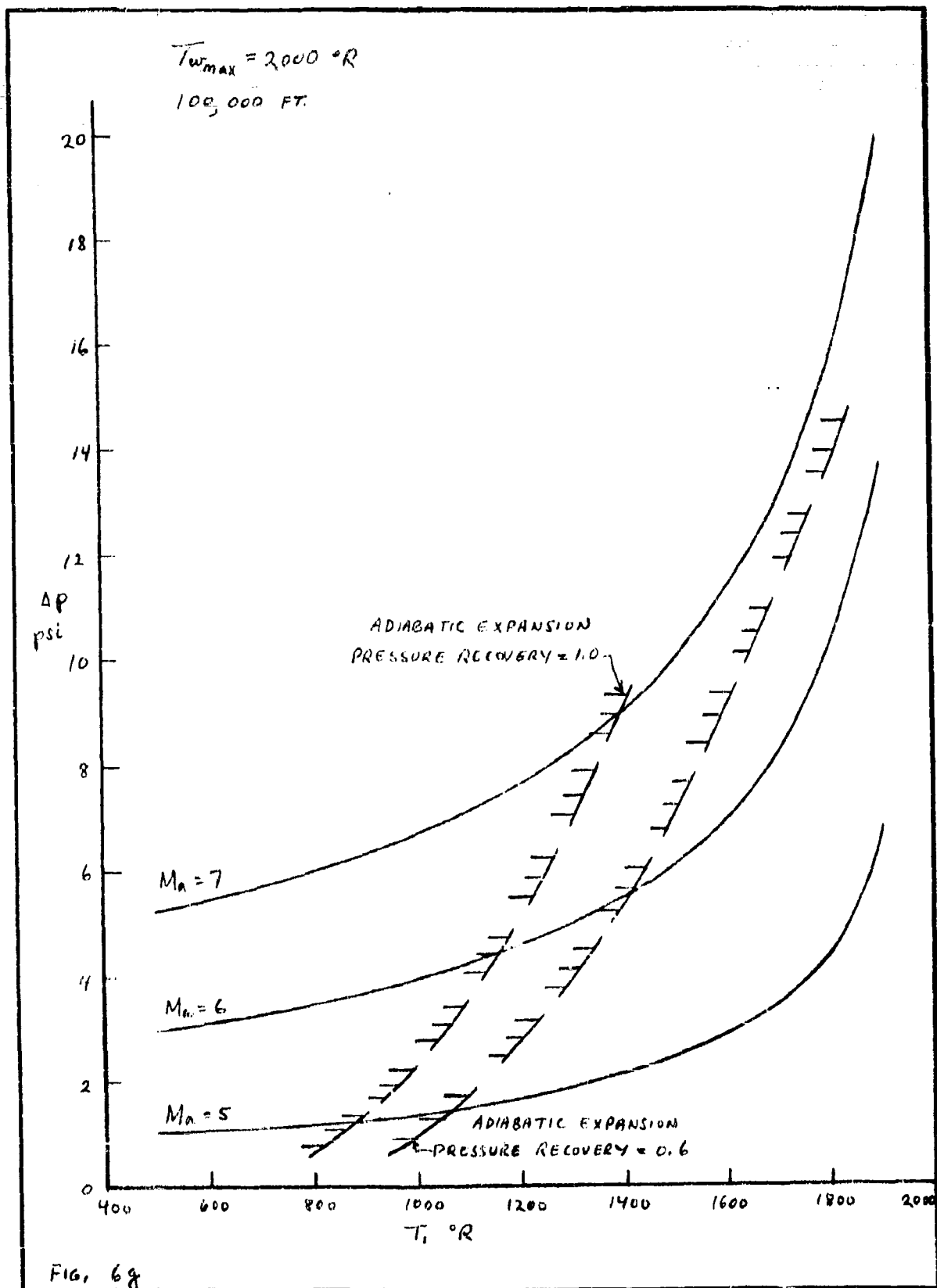
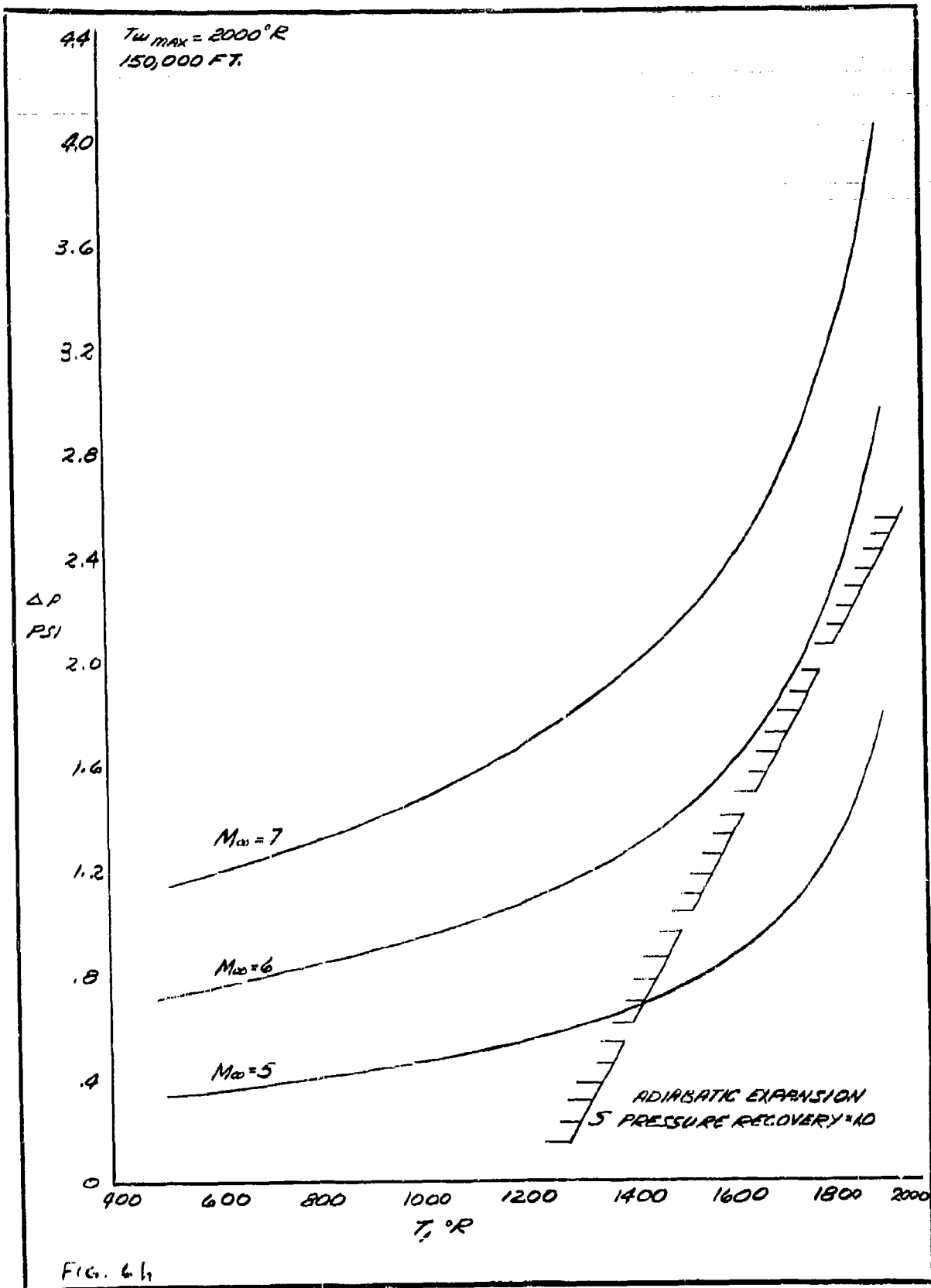


FIG. 6g



CHAPTER II - PART B

RADOME COOLING ANALYSIS

b. Convective Cooling - by Alfred A. Marino

TABLE OF CONTENTS

<u>Section</u>	<u>Title</u>	<u>Page</u>
	Summary	304
1	Scope of Study	305
2	Cooling Charts	307
3	Turbulent Heat Flux Variation	312
4	Constant Heat Flux Variation	313
5	Flow Direction	313
6	Correction for α	314
7	Effect of Thermal Resistance of Radome Material	315
8	Exit Temperature	315
9	Depth of Cooling Gap	316
10	Mach Number	318
11	Application	318
12	Discussion of Results	324
13	Application to Cooling System	327
14	Capability Limit	330
App. I	General Cooling Analysis	334
App. II	Application to Conical Radome	343
App. III	Effect of Conductivity of Radome Material	348
App. IV	Turbo-Cooler Systems	350

<u>Section</u>	<u>Title</u>	<u>Page</u>
References		352
Symbols		353
Figures		356

LIST OF FIGURES

<u>Figure No.</u>	<u>Title</u>
1.	Temperature Factor Y for Air
2.	Cooling Chart - Turbulent Heat Flux Variation Rearward Cooling Flow
3.	Do - Forward Cooling Flow
4.	Do - Constant Heat Flux Variation
5.	Correction for α
6.	Cooling Chart with Thermal Resistance of Radome
7.	Factor for Determining Coolant Temperature Rise
8.	Required Cooling Air Flow - Without Radiation
9.	Required Cooling Air Flow - With Radiation
10.	Exit Temperature of Cooling Air - Without Radiation
11.	Exit Temperature of Cooling Air - With Radiation
12.	Water Consumption - Without Radiation
13.	Water Consumption - With Radiation
14.	Capability Limit With Convection Cooling
15.	Pressure and Temperature at Capability Limit
16.	Heat Flux at Capability Limit
17.	Turbulent Convective Heat Transfer to Cone
18.	Schematics of Turbo-Cooler Systems

Figure No.

Title

- | | |
|-----|---|
| 19. | Discharge Pressures and Temperatures of Turbo-Cooler System 1 |
| 20. | Water Consumption with Turbo-Cooler System 2 |

B. RADOME COOLING ANALYSIS

b. CONVECTIVE COOLING

SUMMARY

General methods are developed for determining the cooling requirements of a radome with convective cooling in which the radome is constructed of two shells forming a gap through which the cooling medium is passed. The depth of the gap is varied along the radome to maintain a constant surface temperature of the outer shell. Charts are presented for the rapid calculation of the cooling requirements of radomes of conical shape. The limits of the capability of convection cooling are pointed out.

An example is given of the cooling requirements of a 20° conical radome of 1.5 feet base radius flying at a Mach number of 6 at 100,000 feet, using air as the cooling medium. Several systems for obtaining the required cooling air are discussed.

1. SCOPE OF STUDY

This part of the report presents and discusses the results of an analysis for determining required cooling flows and radome designs with convection cooling. The term "convection cooling" denotes the system of cooling in which the radome is constructed of two shells forming a gap through which the coolant is passed.

The coolant considered is gaseous. The treatment is for the steady state condition. The effect of radiation and of the thermal resistance of the radome material are considered.

Results are presented for the design condition of a constant temperature of the outside shell. In order to achieve a constant temperature, it is necessary that the cooling gap vary along the length of the radome. As opposed to other possible design conditions, for example, a constant cooling gap, the constant temperature condition results in the minimum required cooling flows for maintaining a given maximum temperature.

Results are presented for shapes consisting of frustrums of cones. The nose region is not considered. In practice, the nose must be treated in a special manner, possibly by injection cooling. Since the nose region comprises a very small surface, the cooling requirements are of minor importance as far as magnitude of the requirements are concerned.

Turbulent flow of the coolant was assumed in the analysis. This condition will apply in the flight regimes of major interest where high rates of heat flux occur.

The analysis was made assuming low or moderate Mach numbers of the cooling flow. This assumption was adopted in line with the desirability of small or moderate pressure drops. Small pressure drop is a design requirement where the effect of the cooling system on the performance of the aircraft is important, particularly of aircraft designed for long range or long duration.

Where performance is not an overriding consideration, high Mach numbers may be tolerated. The results presented herein are then not strictly applicable. This aspect of the cooling problem has been earmarked for future study. Until such a study has been accomplished, a tentative criterion for the accuracy of the present results is suggested as an exit Mach number around .5.

A design based on high Mach numbers of the cooling flow may result in a choked condition at the exit of the cooling gap. The choked condition represents the limit of the capability of convection cooling. The determination of this capability limit is a worthwhile subject for future study. For the present, a rough criterion has been tentatively established, as discussed in Section 14 in order to give some idea of the significance of this limit.

The results of the cooling analysis are presented in general form for ready application to any gaseous cooling medium. An example is worked out in detail to illustrate the method of application.

The example considered is the case of cooling with air at a flight condition of $M = 6$ at 100,000 ft. The results are discussed in the light of several systems devised for producing the required air.

2. COOLING CHARTS

Cooling charts for the determination of required cooling flows are developed from the general analysis presented in Appendix I which can be applied to any radome shape. The application to the conical radome is given in Appendix II. The analysis applies to cases where the thermal resistance of the radome material may be neglected. The effect of thermal resistance is treated in Section 7.

The charts consist of curves of the dimensionless quantities ϵ_B vs. σ_B for constant values of b .

The quantity b defines the cone geometry

$$b = \frac{R_B - R_F}{R_F}$$

R_B base radius of the cone frustrum

R_F front radius of frustrum

The quantity ϵ_B is defined as

$$\epsilon_B = \frac{q_B S}{W c_p (T_w - T_1)}$$

W cooling flow rate

c_p average specific heat of cooling flow

S surface area of frustrum

T_w temperature of surface

T_1 temperature of coolant at inlet

q_B reference heat flux at base of frustrum

The heat flux q_B is made up of the external convection to and the external radiation from the radome surface

$$q_B = q_{cB} - q_r$$

The heat flux q_{cB} which represents the convective heat flux at the base of the radome is determined from

$$q_{cB} = \frac{q_{cF}}{(1 + b)^{1/5}}$$

q_{cF} is the convective heat flux at the front of the frustrum which can be determined according to the methods of Parts D & E of Chapter I. For conservative results, turbulent flow should be assumed. The value of q_{cB} depends on the distance from the stagnation point and is therefore dependent on the shape of the nose of the radome. However, for any normal nose shape,

the value of q_{cB} determined as indicated above will always be greater than the actual turbulent heat flux at the base.

The radiation flux is given by

$$q_r = e \sigma T_w^4$$

σ Stefan-Boltzman radiation constant

e emissivity of the radome surface

Since the surface temperature is constant, q_r is constant over the entire surface.

The quantity σ_B is defined as

$$\sigma_B = \frac{q_B}{B(T_w - T_i)}$$

B is a quantity with the dimensions of a heat transfer coefficient.

It is a function of the conditions of the cooling flow

$$B = a^{5/6} \left(\frac{z}{2n}\right)^{5/12} \left(\frac{d}{d_h}\right)^{1/4} Y_1 P_1^{5/6} L^{-1/6}$$

The quantity a is an experimental constant in the normal heat transfer correlation for turbulent flow (see App. I). On the basis of data in Reference 1, a value of $a = .020$ is recommended.

n is the theoretical constant in the Reynolds heat transfer-friction analogy. It has the value of 2.

z is a pressure drop parameter defined by

$$z = \frac{\Delta P}{P_1} \left(1 - \frac{1}{2} \frac{\Delta P}{P_1} \right)$$

ΔP pressure drop of coolant from inlet to exit

P_1 pressure at inlet

d/d_h is the ratio of the depth of the cooling gap to the hydraulic diameter. For the annular shape of the gap, it has the value of 1/2.

Y_1 is a function of temperature and the physical properties of the cooling medium

$$Y_1 = c_p \mu^{1/6} \left(\frac{g}{RT_1} \right)^{5/12} (Pr)^{-5/9}$$

c_p specific heat

μ viscosity

g acceleration of gravity

R gas constant

T_1 inlet temperature

Pr Prandtl number

For accurate results, the physical properties should be evaluated at a temperature which is a mean of the wall temperature and the bulk temperature of the cooling medium.

For present purposes of estimation, it is sufficiently accurate to evaluate the properties at the inlet temperature. This has the advantage of making Y_1 a function only of T_1 as given in Figure 1 for air.

P_1 is the inlet pressure

L is the length of the cooling run from inlet to exit (length of the frustrum)

(To obtain B in $\text{BTU/sec-ft}^2\text{-}^\circ\text{F}$, the following dimensions should be used

c_p	$\text{BTU/lb-}^\circ\text{F}$	T_1	$^\circ\text{R}$
μ	lb/sec-ft	P_1	lb/ft^2
g	ft/sec^2	L	ft.
R	$\text{ft/}^\circ\text{R}$		

All other quantities involved are dimensionless)

Note that the quantity B is set up so that a cooling design is performed for a given pressure drop of the coolant. Pressure drop is important in considering the overall performance of a cooling system, for example, the drag produced when the cooling medium is air which is taken aboard or the pumping requirements if the cooling medium is circulated. A high pressure drop leads to lower cooling flows, but also results in decreased performance. The design value chosen must be a compromise between these two effects. For preliminary estimates, a value of $\Delta P/P_1 = .20$ is considered a practical compromise.

In a cooling design problem, all quantities for the determination of σ_B are given data. Entering the cooling charts at the value of σ_B and the proper value of b , the value of ϵ_B is read. The cooling flow is then determined from ϵ_B and the given design data.

3. TURBULENT HEAT FLUX VARIATION

The cooling charts are set up in terms of q_B which defines the heat flux at the base of the radome. In deriving one set of cooling curves (Figures 2 and 3), it is assumed that the variation along the surface follows the law (see App. II)

$$q/q_B = (x_B/x)^{1/5}$$

q is the flux at the distance x from the nose

q_B is the flux at the base, distance x_B from the nose.

This variation is denoted as the "turbulent variation" because it follows the law of the external convective heat transfer in turbulent flow.

In a cooling design, it is conservatively assumed that the frustrum is entirely behind the transition point so that the convective flux is turbulent. If the effect of radiation is negligible, the net flux to the radome is entirely due to convection. Then the actual variation of flux is the "turbulent variation" and the cooling curves of Figures 2 and 3 apply accurately. (There is a small conservatism in the method for finding q_B as noted above in Section 2.) Therefore, when the effect of radiation is relatively small, the cooling charts of Figures 2 and 3 should be used.

4. CONSTANT HEAT FLUX VARIATION

Cooling charts are also presented for the case where the heat flux is constant along the radome surface (Figure 4). These curves are useful when radiation is important. With a constant surface temperature, the radiation flux is constant. It is apparent that the true flux variation will fall somewhere between the "turbulent variation" of Sec. 3 and a constant variation. In effect, the true cooling curve could be considered to be between those of Figures 2 and 3 (turbulent variation) and those of Figure 4 (constant variation).

The radiation considered above is the radiation from the outer surface of the radome into the surrounding atmosphere. There exists another effect of radiation which tends to modify the cooling curves. This is the interchange of radiation between the two shells of the radome across the cooling gap. The effect of this internal radiation is to reduce the cooling flow requirements.

The effect of internal radiation is considered of minor importance. It is felt that the data of Figure 4 which overestimates the benefit of radiation compensates for this effect. Therefore, the cooling curves of Figure 4 are used when radiation is important.

5. FLOW DIRECTION

The cooling charts of Figures 2, 3 and 4 present data for the flow of the

coolant in both the rearward (from the nose to the base of the cone) and the forward (from the base to the nose) direction. Figures 2 and 3 for the turbulent heat flux variation indicate that for large values of b , the rearward direction results in a measurable reduction in cooling flows. Figure 4 for the constant heat flux variation shows a similar but smaller advantage.

Another relative disadvantage of the forward direction is that the exit Mach numbers are higher, thus aggravating the bad effect of compressibility on pressure drop.

For these reasons, the rearward direction is chosen for design.

6. CORRECTION FOR α

An additional quantity affecting the cooling requirements is a parameter α defined by

$$\alpha = \frac{T_w - T_1}{T_1}$$

The cooling curves presented above are for the case of $\alpha = 0$. The effect of α is to decrease the value of ϵ_B at a given value of σ_B , that is, to increase the required cooling flow. Figure 5 gives a factor by which the value of ϵ_B determined from the cooling charts for $\alpha = 0$ must be divided (or the cooling flow multiplied). The data of Figure 5 were determined for the special case of $b = 0$. The correction may be applied to other values of b with small error.

7. EFFECT OF THERMAL RESISTANCE OF RADOME MATERIAL

The radome material introduces a resistance to the flow of heat from the outside to the coolant. In general, because of the small thickness of the radome, this resistance is small. However, when the external heat flux is high, the resistance becomes important in increasing the cooling flow required to maintain a given temperature of the outside surface.

In App. III, the analysis of App. I has been extended to include the effect of this thermal resistance. It is shown that the effect is measured by the parameter ψ_B defined by

$$\psi_B = \frac{q_B}{C(T_w - T_i)}$$

where C is the conductance of the radome outer shell (= thermal conductivity of material/thickness of shell).

Cooling charts for the special case of $b = 0$, $a = 0$ are given in Figure 6 to illustrate the effect of the thermal resistance of the radome. The curves show that as the value of ψ_B increases, the value of ϵ_B decreases, that is, the cooling flow requirements increase. It appears that for very high heat fluxes (large values of ψ_B) the resistance of the radome material may be of primary importance.

8. EXIT TEMPERATURE

In many applications the temperature of the coolant leaving the radome is sufficiently low to be useful for cooling other parts of the aircraft, for

example, the engine. Cooling charts provide a means of estimating the exit temperature by calculating the temperature rise of the coolant.

For the "turbulent heat flux variation", the temperature rise is given by:

$$\Delta T = \frac{\epsilon_B}{k} (T_w - T_i)$$

k is a factor depending only on b as given in Figure 7.

For the constant heat flux variation, the temperature rise is simply,

$$\Delta T = \epsilon_B (T_w - T_i)$$

The value of ϵ_B to be used in these determinations is the value of ϵ_B corrected for the effect of a.

9. DEPTH OF COOLING GAP

The depth may be found from the general equation

$$\frac{d}{L} = D \cdot b$$

where D is a non-dimensional function of the conditions of the cooling flow

$$D = a^{5/6} \left(\frac{z}{Z_n} \right)^{-1/12} \left(\frac{d}{d_h} \right)^{1/4} (Pr)^{-5/9} \left(\frac{\mu}{P_1 L} \sqrt{\frac{RT_1}{g}} \right)^{1/6}$$

The quantity δ depends on the variation of the heat flux and the cooling flow direction. It is reported here only for the rearward direction since this is the preferred direction. For "turbulent heat flux variation", (and negligible thermal resistance of the radome material)

$$\delta = \frac{1}{\sigma_B^{1/5} \epsilon_B^{4/5}} \frac{1 - \epsilon_B \eta}{(1 + by)^{3/5}} \frac{(1 + b/2)^{4/5}}{(1 + b)^{1/5}}$$

where

$$\eta = \frac{5}{9b} \frac{(1 + b)^{1/5}}{1 + b/2} \left[(1 + by)^{9/5} - 1 \right]$$

For the constant heat flux variation (and negligible thermal resistance of the radome material):

$$\delta = \frac{1}{\sigma_B^{1/5} \epsilon_B^{4/5}} \frac{1 - \epsilon_B \eta}{(1 + by)^{4/5}} (1 + b/2)^{4/5}$$

where

$$\eta = \frac{(1 + by)^2 - 1}{2b(1 + b/2)}$$

In these equations, y is the fraction of the total cooling run from the inlet (at inlet, $y = 0$, at exit $y = 1$).

Note that the value of ϵ_B corrected for a should be used.

When the thermal resistance of the radome is appreciable, the expressions for δ given above must be modified by replacing the quantity $(1 - \epsilon_B \eta)$ by the quantity $(1 - \epsilon_B \eta - \psi_B)$. Of course, the value ϵ_B is the value determined from a cooling chart which takes the effect of ψ_B into account, such as the chart of Figure 6.

10. MACH NUMBER

The Mach number may be found from the general equation

$$M = N \cdot \phi$$

At inlet,

$$N_1 = \sqrt{\frac{1}{\gamma} \frac{z/2n}{d/d_h}}$$

At exit

$$N_2 = N_1 \frac{\sqrt{T_2/T_1}}{1 - \Delta P/P_1}$$

The expression for ϕ depends on the flow direction. For the rearward flow,

$$\text{At inlet} \quad \phi_1 = \frac{\sigma_B}{\epsilon_B} \frac{1 + b/2}{\delta_1}$$

$$\text{At exit} \quad \phi_2 = \frac{\sigma_B}{\epsilon_B} \frac{1}{\delta_2} \frac{1 + b/2}{1 + b}$$

The values of δ_1 and δ_2 are the values determined as indicated above in Section 9 at inlet and exit, respectively.

These equations as they stand apply equally to cases where the radome thermal resistance is important as long as the proper cooling chart and the proper value of δ are used as explained in Section 9 above.

11. APPLICATION

The radome considered is a 20° conical frustrum with a base radius of 1.5 feet and a front radius of .3 feet giving a cooling length (slantheight

of frustrum) of 3.51 feet, a surface area of 19.9 sq. ft. and a value of $b = 4$.

The flight considered is around $M = 6$ at 100,000 ft. The design surface temperature is chosen as 2000R, representative of a high temperature radome material. For these conditions, the convective turbulent heat flux at the front end of the frustrum is estimated to be 7.2 BTU/sec-ft².

From Sec. 2

$$q_{cB} = \frac{7.2}{(1+b)^{1/5}} = \frac{7.2}{(1+4)^{1/5}} = 5.2 \text{ BTU/sec-ft}^2$$

An emissivity of .3 is assumed. The thermal resistance is not considered because of the moderate severity of the heat flux. The radiation heat flux is

$$q_r = .476e \left(\frac{T_w}{1000} \right)^4 = .476 \times .3 \times (2)^4 = 2.3 \text{ BTU/sec-ft}^2$$

$$\text{Then } q_B = q_{cB} - q_r = 5.2 - 2.3 = 2.9 \text{ BTU/sec-ft}^2$$

An inlet cooling air temperature of 1000R and an inlet cooling air pressure of 5 psia are assumed.

$$a = \frac{T_w - T_1}{T_1} = \frac{2000 - 1000}{1000} = 1.0$$

The value of B is found from

$$B = a^{5/6} \left(\frac{z}{2r} \right)^{5/12} \left(\frac{d}{d_h} \right)^{-1/4} Y_1 P_1^{5/6} L^{-1/6}$$

From Sec. 2

$$a = .020$$

$$a^{5/6} = .038$$

$$n = 2$$

$$\Delta P/P_1 = .20$$

$$z = .20 \times .90 = .18$$

$$z/2n = .045$$

$$(z/2n)^{5/12} = .275$$

$$d/d_h = .5$$

$$(d/d_h)^{-1/4} = 1.189$$

From Figure 1 at $T_1 = 1000R$, $Y_1 = .0026$

$$P_1 = 5 \text{ psia} = 720 \text{ psfa} \quad P_1^{5/6} = 240$$

$$L = 3.51 \text{ ft.}$$

$$L^{-1/6} = .81$$

$$B = .038 \times .275 \times 1.189 \times .00226 \times 240 \times .81 = .00546 \text{ BTU/sec-ft}^2\text{-}^\circ\text{F}$$

$$\sigma_B = \frac{q_B}{B(T_w - T_1)} = \frac{2.9}{.00546(2000 - 1000)} = .53$$

Because radiation is appreciable, the cooling curves of Figure 4 are used. At $\sigma_B = .53$, $b = 4.0$ and rearward cooling flow, $\epsilon_B = .680$.

From Figure 5, the correction factor at $\sigma_B = .53$ and $a = 1.0$ is 1.11.

Hence, the corrected value of ϵ_B is $\frac{.680}{1.11} = .613$

The cooling flow is found from

$$W = \frac{q_B S}{\epsilon_B c_p (T_w - T_1)}$$

Using a value of $c_p = .24 \text{ BTU/lb-}^\circ\text{F}$,

$$W = \frac{2.9 \times 19.9}{.613 \times .24 \times 1000} = .39 \text{ lb/sec.}$$

From Sec. 8, the temperature rise of the cooling air is

$$\Delta T = \epsilon_B (T_w - T_1) = .61 \times 100 = 610$$

Exit temperature $T_2 = 1000 + 610 = 1610R$.

From Section 9 to find the channel depth,

$$D = a^{5/6} \left(\frac{z}{2n}\right)^{-1/12} \left(\frac{d}{d_h}\right)^{1/4} \left(\frac{\mu}{P_1 L} \frac{RT_1}{g}\right)^{1/6} (Pr)^{-5/9}$$

$$a = .020$$

$$a^{5/6} = .038$$

$$\frac{z}{2n} = .045$$

$$\left(\frac{z}{2n}\right)^{-1/12} = 1.294$$

$$d/d_h = .70$$

$$(d/d_h)^{1/4} = .842$$

$$Pr = .70$$

$$(Pr)^{-5/9} = 1.22$$

$$R = 53.3 \text{ ft/}^\circ R$$

$$g = 32.2 \text{ ft/sec}^2$$

$$T_1 = 1000R$$

$$\mu_1 = 1.95 \times 10^{-5} \text{ lb/sec-ft.}$$

$$P_1 = 720 \text{ psfa}$$

$$L = 3.5 \text{ ft.}$$

Using these numbers, $D = .00415$

From Section 9,

$$\eta = \frac{(1+by)^2 - 1}{2b(1+b/2)}$$

For $b = 4$

$$\eta = \frac{(1+4y)^2 - 1}{24}$$

From Sec. 9, the equation for δ is:

$$\delta = \frac{1}{\sigma_B^{1/5} \epsilon_B^{4/5} (1 - \epsilon_B \eta)} \frac{(1 + b/2)^{4/5}}{(1 + by)^{4/5}}$$

$$\sigma_B = .53 \qquad \sigma_B^{1/5} = .881$$

$$\epsilon_B = .613 \qquad \epsilon_B^{4/5} = .676$$

$$(1 + b/2)^{4/5} = 3^{4/5} = 2.41$$

Hence,

$$\delta = \frac{1}{.881} \times \frac{1}{.676} \times 2.41 \frac{1 - .613\eta}{(1 + 4y)^{4/5}}$$

Calculating η and δ for various values of y from 0 to 1.0:

y	η	δ	d , inches
0	0	4.03	.705
.2	.0933	2.38	.416
.4	.240	1.60	.280
.6	.440	1.11	.194
.8	.684	.74	.129
1.0	1.00	.43	.076

The depth is found from

$$d = D \times L \times \delta = .00415 (3.51 \times 12) \delta = .175 \delta, \text{ inches}$$

giving variation of d as tabulated above.

To find Mach numbers from Section 10:

$$M = N \phi$$

At entrance;

$$N_1 = \sqrt{\frac{1}{\gamma} \frac{z/2n}{d/d_h}}$$

$$\gamma = 1.4, \frac{z}{2n} = .045, d/d_h = .5$$

$$N_1 = \sqrt{\frac{1}{1.4} \times \frac{.045}{.5}} = .253$$

$$\phi_1 = \frac{\sigma_B}{\epsilon_B} \frac{(1+b/2)}{\delta_1} = \frac{.53}{.613} \times \frac{3}{4.03} = .651$$

$$M_1 = .253 \times .651 = .165$$

At exit,

$$N_2 = \frac{N_1 \sqrt{T_2/T_1}}{1 - \Delta P/P_1} = \frac{.253 \sqrt{1610/1000}}{1 - .2} = .402$$

$$\phi_2 = \frac{\sigma_B}{\epsilon_B \delta_2} \frac{1+b/2}{1+b} = \frac{.530}{.613 \times .430} \frac{3}{5} = 1.20$$

$$M_2 = .402 \times 1.20 = .48$$

The Mach number range is not likely to lead to severe compressibility effects on the pressure drop.

A check on the Reynolds number is provided by:

$$Re = \frac{W}{\mu r (d/d_h)}$$

At inlet,

$$T_1 = 1000R \quad \mu_1 = 1.95 \times 10^{-5} \text{ lb/sec-ft}$$

$$r_1 = 2\pi R_F = 2\pi \times .3 = 1.86 \text{ ft.}$$

$$Re_1 = \frac{.39}{1.95 \times 10^{-5} \times 1.86 \times .5} = 2.15 \times 10^4$$

At exit,

$$T_2 = 1610R \quad \mu_2 = 2.6 \times 10^{-5} \text{ lb sec-ft.}$$

$$r_2 = 2\pi R_B = 2\pi \times 1.5 = 9.4 \text{ feet}$$

$$Re_2 = 3.2 \times 10^3$$

It appears that at the exit, the Reynolds number may be in the transition region. To offset this effect, it will be necessary to increase the cooling gap and the cooling flow a small amount.

The calculations for cooling flows outlined above were carried out for a range of inlet temperatures and pressures with results as shown in Figure 9. Similar calculations (Figure 8) were made neglecting radiation. In this case, the value of q_B is the convective value of 5.2 BTU/sec-ft²-°F and the cooling chart of Figure 2 is used. Exit temperatures are shown in Figures 10 and 11.

12. DISCUSSION OF RESULTS

It is pointed out that the cooling flows shown in Figures 8 and 9 do not really exist above the line labelled "capability limit". The significance of this limit is discussed below in Section 14. The present discussion applies to the data below this limit.

The data show that at low cooling inlet temperatures, the decrease of cooling flow as the temperature decreases is small. Considering the performance penalties involved in supplying a low temperature cooling medium, it is concluded that a moderately low coolant temperature is probably best for most applications.

The data indicate the importance of inlet pressure. To fully appreciate the effect of pressure, it is necessary to understand the meaning of the curves labeled "minimum limit". These curves represent the best that can be done with convective cooling. At this limit, the exit temperature of the cooling air is equal to the wall temperature of the radome, that is, all the cooling potential of the cooling air has been utilized. On the cooling charts, this corresponds to a value of $\sigma_B = 0$ which in turn implies an infinite inlet pressure. In practice, the pressure which can be used will be limited by consideration of the structural design of the radome. The data indicate that moderately high pressures approach the limiting condition. Therefore, efficient cooling can be performed without penalizing the radome structure.

With respect to the effect of pressure, it is pointed out that the increased flows required at low pressures result in lower exit temperatures as shown in Figures 10 and 11. They may be regarded as a compensating effect, since the air leaving the radome may be used for cooling other parts of the airplane, such as the engine.

Comparison of Figures 8 and 9 indicate the importance of radiation in the present case, even the moderate value of emissivity of .30 has a large effect on reducing the cooling flow. The effect is important only if the design surface temperature of the radome is high. A reduction of the design temperature from 2000R to 1500R would reduce the radiation heat flux to 1/3 of the value; at 1000R, radiation would be negligible.

The importance of radiation is measured by its value relative to the convective flux. The flight condition chosen in the example leads to convective fluxes which are not very severe. An increase in Mach number or a decrease in altitude would diminish the importance of radiation.

The calculations above in Section 11 indicated the Reynolds numbers near the exit are in the transition region, so that results derived from the cooling charts do not apply exactly. Such a condition is handled by increasing the gap and the gap and the cooling flow. This results in a decreased temperature rise of the air so that the heat transfer coefficient required near the exit is reduced. (It may be mentioned that because the initial Reynolds number is in a well defined turbulent region, transition will be delayed. This tends to diminish the harmful effect of transition flow.)

The design procedure in such cases involves a step-wise calculation of each individual case. The details of such a procedure have not been undertaken in the present report, but it is a suitable study for the future.

It is pointed out that extreme cases which involve very low Reynolds numbers, possibly in the laminar region, are not of practical interest.

Such cases imply very small external heat fluxes which are best eliminated by some other means such as a small reduction of the flight Mach number.

13. APPLICATION OF COOLING SYSTEM

The turbo-cooler system 1 discussed in Appendix IV and shown in Figure 19 can provide the required conditions for the cooling air with reasonable size. For example, at an inlet pressure of 5 psia and an inlet temperature of 1000R, the data for the lower heat flux (Figure 9 with radiation) shows that a flow of around .4 lb/sec. is required. At $M=6$, 100,000 ft, this corresponds to a free stream tube diameter around 3.5 inches. From Figure 19, it is seen that the turbo-cooler system can provide these conditions with a pressure ratio of around 35 for turbine 1 and around 15 for turbine 2.

The system of Figure 19 can also provide cooling for the higher heat flux (Figure 8 - without radiation), but the pressure required is greater. At a pressure ratio of 40 for turbine 1 and a cooling discharge pressure of 5 psia (pressure ratio of turbine 2 around 15), the discharge temperature according to Figure 19 is around 970R. Entering the cooling flow curves of Figure 8 at 970R and 5 psia, a point is obtained which lies above the "capability limit", which shows that the cooling is not possible. Consider now an inlet pressure of 20 psia. The turbo-cooler system of Figure 19

gives a temperature of 1300R (pressure ratio of turbine 1 = 40, pressure ratio of turbine 2 = 3.5). Entering Figure 8 at 20 psia and 1300R, the required flow is read as around .9 lb/sec and lies well below the "capability limit". This flow too is small, corresponding to a free stream tube diameter around 5 inches.

If lower altitudes are considered, the ability of the turbo-cooler system to furnish suitable discharge conditions is relatively unchanged in spite of the increased heat flux because the convective heat flux varies as the atmospheric pressure to the $4/5$ power whereas the cooling inlet pressure which varies directly as the atmospheric pressure, enters into cooling as the $5/6$ power. Of course, this assumes that the radome structure can withstand the increased available pressure. The effect of lower altitudes on equipment size will be somewhat beneficial since the required cooling flow varies as the $4/5$ power of the atmospheric pressure, whereas the stream tube size varies inversely to the pressure.

The observation on equipment size applies if the thermal resistance of the radome shell is small. As noted in Section 7, high heat fluxes magnify the effect of thermal resistance in increasing cooling flow requirements. It is possible that the increase in cooling flow due to this effect may result in larger equipment sizes.

For higher Mach numbers or much lower design wall temperatures, this turbocooler system is not suitable unless it is supplemented with a

heat sink, such as fuel or water.

Consider now the use of turbo-cooler system 2 (Appendix IV) using water as a heat sink which can easily provide cooling temperatures as low as 650R. By means of the water consumption curves of Figure 20, the water required for cooling the radomes can be determined as shown in Figures 12 and 13. With a circulating system in which only the heat transferred through the radome must be removed by the heat sink, the water consumption is less as indicated on the figures. The difference in water consumption becomes greater at the higher heat flux. At the lower flux (Figure 13) an increase of around 10% is required with the turbo-cooler system; at the higher flux (Figure 12) an increase of around 40% is required.

As far as equipment is concerned, the turbo-cooler system and the circulating system are probably comparable since the turbine and compressor of the turbo-cooler system are equalized by the turbine and pump required by the circulating system. The advantage of the turbo-cooler system is that the air leaving the radome which is at a fairly low temperature can be used for cooling other components of the aircraft, for instance, the engine.

The above remarks will also apply to a heat sink consisting of fuel if the water consumption is interpreted as fuel temperature rise. In this case, the increased temperature rise of the fuel with turbo-cooler system 2 is not objectionable as long as it is within the limits prescribed for the fuel.

The ultimate choice of the cooling system depends on a detailed comparison of drag and weight penalties for the specific application. The only general statement which can be made is that for long flights, turbo-cooler system 1 which uses no heat sink which must be carried by the aircraft, has definite advantages where fuel is not available as a heat sink. For example, with a circulating system, the water required for one hour flight is around 200 lbs. for the lower heat flux (Figure 13) and 400 lbs. for the high heat flux (Figure 12). At lower altitudes, the consumption would be greater. It is likely that a turbo-cooler system 1 can be designed for less weight.

14. CAPABILITY LIMIT

The capability limit of convection cooling is defined by choking at the exit of the cooling gap. Generally, such a condition is to be avoided because it results in very high pressure losses. However, when performance is not a prime consideration, a design with choking at the exit may be tolerated.

It should be recognized that the limit discussed here is the limit for performing cooling at a constant surface temperature. It is possible to extend this limit by overcooling the radome at the front end (inlet of the coolant). However, this is not usually desirable since it increases the cooling requirements.

The determination of the capability limit has not been undertaken in the present study which is intended to provide designs for small pressure

drops. However, it is an important phenomenon which should be studied in the future. In the meantime, a criterion is suggested which can be used at present to draw some useful conclusions.

The criterion suggested is a Mach number of .3 at the inlet of the cooling gap. This selection is based on the judgment that above this Mach number, compressibility effects start to become appreciable. In most cases, this criterion is probably conservative.

The value of σ_B corresponding to an inlet Mach number $M_1 = .3$ and a given value of b can be determined by means of the Mach number equations in Section 10. For a given value of $\Delta P/P_1$ and a given γ , the value of N_1 may be calculated. For the assumed M_1 , the value of the quantity ϕ may be found. Then by means of the expression for δ in Section 9 and the cooling curves of ϵ_B vs. σ_B , the value of σ_B may be determined. The results for the "turbulent heat flux variation" and rearward cooling flow are shown in Figure 14.

For a given heat flux q_B and a given wall temperature T_w , the value of σ_B can be translated in terms of cooling inlet pressure and inlet temperature as shown in Figure 15 for the conditions of the example in Figure 8. It is pointed out that the values of $\Delta P/P_1$ are nominal pressure drops and no longer true values because the effect of compressibility increases the pressure drop. The curves at different values of $\Delta P/P_1$

are intended to show that the relationship between pressure and temperature is not affected much by the assumed value of $\Delta P/P_1$.

The relationship in Figure 15 transferred to the cooling flow data of Figure 8 represents a limit beyond which the cooling flow curves do not exist and in the region of which the pressure drop will be greater than the nominal value. A similar procedure for the case of the constant heat flux variation leads to the limit indicated in Figure 9. It is always true that the limit for the case of the constant heat flux variation is less severe than the limit for the turbulent variation.

In a similar manner, the variation of the heat flux q_B with cooling temperature T_1 at various values of cooling pressure P_1 can be determined as shown in Figure 16 for the turbulent flux variation and a value of surface temperature $T_w = 2000R$. These data are interpreted as: for a given q_B and a given T_1 , the value of P_1 represents the minimum pressure which can be employed in the radome to perform cooling. Furthermore, the pressure loss accompanying the cooling will be very large, so that if performance considerations require small pressure drops, the pressure P_1 must be even greater than the value indicated.

Representative values of the convective heat flux in turbulent flow at a distance of 5 feet from the nose of a 20° conical radome are shown in Figure 17. Comparing Figures 16 and 17, it appears that the heat fluxes

at 100,000 feet do not present a severe problem. However, at 50,000 feet, the pressure requirements are quite severe. For example, at flight Mach number of 7, Figure 17 indicates a value of heat flux around 50 BTU/sec-ft². Entering the curves of Figure 16 at this value of q_B at a temperature T_1 around 650R (roughly the temperature which would be available with a water heat sink), the pressure read is around 75 psia. This is the minimum pressure for performing cooling. The pressure requirement is more severe for lower wall temperatures and higher cone angles.

These estimates of the minimum pressures required for convection cooling apply to the case of negligible thermal resistance of the radome shell. Where the resistance is not negligible, the pressure requirements are even more severe.

Since the external pressures on the radome are small in comparison with the internal pressures required for cooling, it appears that at high heat fluxes, the structural limit of the radome will dictate the capability limit of convection cooling. For a given structural limit, the cooling limit can be increased by using a gas with better heat transfer characteristics, such as helium. Of course, the use of such a gas would require a circulating system of cooling.

APPENDIX I

GENERAL COOLING ANALYSIS

It is assumed that the heat absorbed by the coolant is entirely a result of the heat transferred from the outer radome shell. There is no heat transferred to or from the coolant from the inner shell. This implies no cooling of the space within the radome. It also implies no radiation across the cooling gap or across the space inside the radome. These effects are of minor importance. Furthermore, they tend to decrease cooling requirements so that neglecting them leads to conservative results.

It is assumed that conditions at any station along the radome are uniform and that the heat flow is one-dimensional. Since the radome shell is thin, its resistance to heat flow is ignored. The coolant is assumed to be a gap. The fluid properties are treated as constant, with the premise that an average value is used in application.

The analysis is made for a constant temperature of the outer radome surface. With this condition, the heat flux for a given flight condition at any station along the radome is a function only of the location.

Under steady state conditions, the coolant absorbs all the heat flux through the radome shell so that the temperature of the coolant at any station y is given by:

$$W c_p (T - T_1) = \int_0^y q dS$$

where W - coolant flow
 c_p - specific heat of coolant
 T - temperature
 q - local heat flux
 dS - differential surface area of radome

Introducing the dimensionless parameters

$$\lambda = \frac{\int_0^y q dS}{W c_p (T_w - T_1)}$$

$$\alpha = \frac{T_w - T_1}{T_1}$$

The temperature at station y is written

$$\frac{T}{T_1} = 1 + \alpha \lambda \quad (1)$$

To maintain the surface temperature T_w , the convective heat transfer coefficient of the coolant h must balance the heat flux from the outside to the wall with the heat flux from the wall to the cooling medium, that is

$$h(T_w - T) = q$$

which may be written

$$h = \frac{q}{T_w - T_1} \frac{1}{1 - \lambda} \quad (2)$$

The convective coefficient h is determined from the normal heat transfer correlation for turbulent flow:

$$St = a(Re)^{-1/5}(Pr)^{-2/3} \quad (3)$$

St Stanton number $(= \frac{h}{c_p} \frac{rd}{W})$

Re Reynolds number $(= \frac{d_h}{\mu} \frac{W}{rd})$

Pr Prandtl number

a experimental constant

From this relationship, h may be expressed as:

$$h = \frac{a}{(Pr)^{2/3}} \frac{c_p (\mu d/d_h)^{.2}}{d} \left(\frac{W}{r}\right)^{.8} \quad (4)$$

μ viscosity

d depth of cooling gap

d_h hydraulic diameter of cooling gap =

r perimeter of shell

Note that in obtaining (4) and in all following analyses, the flow area of the gap is taken as rd , the justification being that the gap depth d is small compared to the diameter of the radome.

Substituting h from (2) into (4) and solving for d ,

$$d = \frac{a}{(Pr)^{2/3}} c_p (\mu d/d_h)^{.2} \left(\frac{W}{r}\right)^{.8} \frac{(T_w - T_1)}{q} (1 - \lambda) \quad (5)$$

This equation expresses the required depth of the gap to perform cooling.

In treating the pressure drop, it is assumed that the Mach number of the cooling flow is low enough so that the total and static temperature and pressures may be taken as the same with small error.

The pressure drop across the differential length of the cooling run dl is given by

$$-\frac{dP}{P} = \frac{4f}{d_h} \frac{\gamma M^2}{2} dl$$

dP pressure drop

P pressure

f friction coefficient

M Mach number

γ specific heat ratio

The Mach number is related to the flow conditions by

$$\gamma M^2 = \frac{R T}{g P^2} \left(\frac{W}{rd} \right)^2$$

R is gas constant

g acceleration of gravity

so that the pressure drop may be written:

$$-P dP = \frac{4f}{d_h} \frac{R T}{2g} \left(\frac{W}{rd} \right)^2 L dy \quad (6)$$

where the dl is written in terms of the total length of the cooling run L and the dimensionless station y ($dl = L dy$).

The friction factor is related to the flow conditions by means of

Reynolds friction-heat-transfer analogy

$$f = n(St)$$

where n is a constant having the theoretical value of 2.

By means of (3)

$$f = \frac{na}{(Pr)^{2/3}} (\mu d/d_h)^{.2} \left(\frac{r}{W}\right)^{.2}$$

Using this in (6)

$$-P dP = \frac{2na}{(Pr)^{2/3}} \mu^{.2} \left(\frac{d}{d_h}\right)^{1.2} \left(\frac{RT}{g}\right) \left(\frac{W}{r}\right)^{1.8} \frac{L}{d^3} dy$$

Substituting for d from (5) and for T from (1),

$$-P dP = \frac{2n}{a^2} \frac{(Pr)^{4/3}}{c_p^3} \left(\frac{d}{d_h}\right)^{.6} \frac{1}{\mu^{.4}} \left(\frac{RT_1}{g}\right) \left(\frac{r}{W}\right)^{.6} L \left(\frac{q}{T_w - T_1}\right) \frac{1 + a\lambda}{(1 - \lambda)^3} dy \quad (7)$$

The quantities q and r vary with y . For convenience, they are expressed in terms of reference values q_R and r_R as:

$$q = \beta q_R$$

$$r = \rho r_R$$

The reference r_R is taken as the average value based on the total heat transfer surface area.

$$r_R L = S$$

L is the length of the cooled surface

S is the surface area

A dimensionless quantity ϵ is now introduced defined by

$$\epsilon = \frac{q_R S}{W_{cp}(T_w - T_1)}$$

with these substitutions, Equation (7) becomes:

$$-P dP = \frac{2n}{a^2} \frac{(Pr)^{4/3}}{\mu^{.4}} \left(\frac{d}{d_h}\right)^{.6} \left(\frac{RT_1}{g}\right) L^{.4} \left(\frac{W}{S}\right)^{2.4} \epsilon^3 \beta^3 \rho^{.6} \frac{(1+\alpha\lambda)}{(1-\lambda)^3} dy$$

Integrating this equation from the inlet ($y = 0, P = P_1$) to the exit ($y = 1, P = P_2$),

$$\frac{P_1^2 - P_2^2}{2} = \frac{2n}{a^2} \frac{(Pr)^{2/3}}{\mu^{.4}} \left(\frac{d}{d_h}\right)^{.6} \left(\frac{RT_1}{g}\right) L^{.4} \left(\frac{W}{S}\right)^{2.4} \epsilon^3 \int_0^1 \beta^3 \rho^{.6} \frac{(1+\alpha\lambda)}{(1-\lambda)^3} dy \quad (8)$$

A pressure drop function z is introduced by

$$z = \frac{P_1^2 - P_2^2}{2P_1^2} = \frac{\Delta P}{P_1} \left(1 - \frac{1}{2} \frac{\Delta P}{P_1}\right)$$

where ΔP is the pressure drop over the cooling run.

A quantity with the dimensions of a heat transfer coefficient is now introduced by

$$B = a^{5/6} \left(\frac{z}{2n}\right)^{5/12} \left(\frac{d}{d_h}\right)^{-1/4} \frac{c_p \mu^{1/6}}{(Pr)^{5/9}} \left(\frac{g}{RT_1}\right)^{5/12} P_1^{5/6} L^{-1/6}$$

so that (8) may be written

$$\left(\frac{1}{\sigma}\right)^{2.4} = \epsilon^{.6} \int_0^1 \frac{\beta^3 \rho^{.6} (1+\alpha\lambda)}{(1-\lambda)^3} dy \quad (9)$$

where

$$\sigma = \frac{q_R}{B(T_w - T_1)}$$

The quantity λ is also related to ϵ , β , and ρ . From the definition of λ ,

$$\lambda = \frac{\int_0^y q dS}{W_{cp}(T_w - T_1)}$$

With the use of β , this is written

$$\lambda = \epsilon \int_0^y \beta \frac{dS}{S}$$

Now $dS = r d\theta = rL dy$

and $S = r_R L$

so that $\frac{dS}{S} = \frac{r}{r_R} dy = \rho dy$.

Hence, λ may be written

$$\lambda = \epsilon \int_0^y \beta \rho dy$$

so that Equation (9) may be written

$$\left(\frac{1}{\theta}\right)^{2.4} = \epsilon^{.6} \int_0^1 \beta^3 \rho^{.6} \frac{(1 + a \epsilon \eta)}{(1 - \epsilon \eta)^3} dy \quad (10)$$

$$\text{where } \eta = \int_0^y \beta \rho dy \quad (11)$$

Equations (10) and (11) relate the required cooling flow W (through the quantity ϵ) to the conditions of the coolant and the heat flux (through the quantity σ). For a given heat flux variation (expressed by β) and a given radome shape (expressed by ρ), η is found from (11). It is then used in (10) together with the heat flux variation and the radome shape to determine σ . In this process, of course, the quantity ϵ is held constant. The procedure results in "cooling charts", that is, curves of ϵ vs. σ for constant values of α .

The temperature rise of the coolant is determined from Equation (1) as

$$\frac{\Delta T}{T_w - T_1} = \epsilon \eta_1 \quad (12)$$

where
$$\eta_1 = \int_0^1 \beta \rho \, dy$$

Also, a convenient form for the exit temperature is

$$\frac{T_2}{T_1} = 1 + \alpha \epsilon \eta_1 \quad (13)$$

The depth of the cooling gap as given in (5) may be written in terms of the quantities explained above:

$$\frac{d}{L} = D \times \delta \quad (14)$$

where
$$\delta = \frac{1}{0.2 \epsilon \cdot 8} \frac{1 - \epsilon \eta}{\beta \rho \cdot 8}$$

and D is a dimensionless quantity dependent on the flow conditions of the cooling flow.

$$D = a^{5/6} \left(\frac{z}{2n}\right)^{-1/12} \left(\frac{d}{dn}\right)^{1/4} (Pr)^{5/9} \left(\frac{\mu}{P_1} \sqrt{\frac{RT_1}{g}}\right)^{1/6}$$

Through its dependence on β , ρ and η , the cooling gap is a function of the location along the radome.

The Mach number of the cooling flow is found from

$$M = \sqrt{\frac{RT}{rg}} \frac{W}{Pr d}$$

In terms of the quantities treated above, this may be written as

$$M = N \times \phi \quad (15)$$

where $\phi = \frac{\sigma}{\epsilon \rho \delta}$

$$N = \sqrt{\frac{1}{\gamma} \frac{z/2n}{d/dh} \frac{\sqrt{T/T_1}}{P/P_1}}$$

where the values of ρ , δ , T/T_1 and P/P_1 are determined by the location along the radome.

APPENDIX II

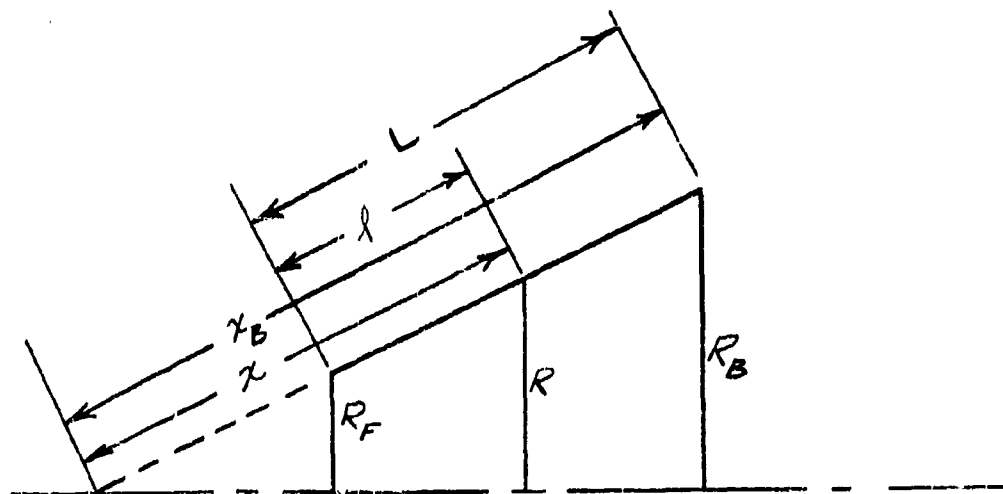
APPLICATION TO CONICAL RADOME

The equations derived in Appendix I are applied to a radome whose shape is the frustrum of a cone. The case of cooling flow direction from the nose to the base (rearward cooling flow) is treated. The external heat flux variation treated is the "turbulent heat flux variation". The reference value of the heat flux is taken at the base of the radome. The heat flux variation is defined by the equation:

$$q/q_B = (x_B/x)^{1/5}$$

where q is the heat flux at the distance x from the nose

q_B is the heat flux at the base distance x_B from the nose



Conical Radome

The distance x is measured from the nose of the radome formed by extending the frustrum to an apex.

In terms of the station parameter $y (=l/L)$, the local perimeter r is:

$$r = 2\pi R = 2\pi R_F (1 + by)$$

where
$$b = \frac{R_B - R_F}{R_F}$$

The reference value of r is defined by:

$$r_R L = S \text{ (Surface area)}$$

so that
$$r_B = 2\pi R_F (1 + b/2)$$

Hence,
$$\rho = \frac{r}{r_R} = \frac{1 + by}{1 + b/2} \quad (16)$$

The value of β is

$$\beta = q/q_B = (x_B/x)^{1/5}$$

which in terms of y is:

$$\beta = \left(\frac{1 + b}{1 + by} \right)^{1/5} \quad (17)$$

Using (16) and (17) in Equation (11) of Appendix I,

$$\eta = \frac{(1 + b)^{1/5}}{1 + b/2} \int_0^y (1 + by)^{4/5} dy$$

from which

$$\eta = \frac{5}{9b} \frac{(1+b)^{1/5}}{(1+b/2)} \left[(1+by)^{9/5} - 1 \right] \quad (18)$$

From (16) and (17)

$$\beta^3 p \cdot 6 = \frac{(1+b)^{3/5}}{1+b/2}$$

Using this in Equation (10) of Appendix I,

$$\left(\frac{1}{\sigma_B} \right)^{2.4} = \epsilon_B \cdot 6 \frac{(1+b)^{3/5}}{(1+b/2)} \int_0^1 \frac{1 + a \epsilon_B \eta}{(1 - \epsilon_B \eta)^3} dy \quad (19)$$

Note that the subscript B is used with ϵ and σ to denote that the value of q entering into these quantities is the value q_B .

With the use of (18), the integration in (19) can be performed. A closed analytical solution is not possible. A graphical solution can be handled easily. The solution for the case of $a = 0$ is shown in Figure 2.

For the special case of $b = 0$ (cylinder), the expression for η becomes simply

$$\eta = y$$

In this case, Equation (19) can be handled analytically to give:

$$\sigma_B = \epsilon_B^{1/6} \left[\frac{(1 - \epsilon_B)^2}{\epsilon_B - (1-a) \frac{\epsilon_B^2}{2}} \right]^{5/12} \quad (20)$$

From this equation, a correction factor to ϵ_B for the effect of a can be readily determined (Figure 5).

From Equation (12) Appendix I, the temperature rise is given by:

$$\frac{\Delta T}{T_w - T_1} = \epsilon \eta_1$$

where the value of η_1 determined from (18) is:

$$\eta_1 = \frac{5}{9b} \frac{(1+b)^{1/5}}{(1+b/2)} \left[(1+b)^{9/5} - 1 \right] \quad (21)$$

By means of (16) and (17) the expression for δ in (13) Appendix I becomes

$$\delta = \frac{1}{\sigma_B \cdot 2 \epsilon_B \cdot 8} \frac{1 - \epsilon_B \eta}{(1+by)^{3/5}} \frac{(1+b/2)^{4/5}}{(1+b)^{1/5}} \quad (22)$$

With this equation and (18), the variation of the depth of the cooling gap along the radome can be determined.

The values of ϕ entering into the determination of the Mach number of the cooling flow as given in Equation (15) Appendix I, are:

At inlet:

$$\phi_1 = \frac{\sigma_B}{\epsilon_B \delta_1} (1+b/2) \quad (23)$$

At exit:

$$\phi_2 = \frac{\sigma_B}{\epsilon_B \delta_2} \frac{(1+b/2)}{1+b} \quad (24)$$

where δ_1 and δ_2 are the value of δ determined from (22) at inlet ($y = 0$) and exit ($y = 1$), respectively.

APPENDIX III

EFFECT OF CONDUCTIVITY OF RADOME MATERIAL

The resistance of the radome material to heat flow causes a temperature drop across the thickness of the outer shell which is given by:

$$C(\Delta T_w) = q$$

$$\Delta T_w = T_w - T_i$$

C conductance of the shell (conductivity/thickness)

T_w temperature of the outside surface of the outer shell

T_i temperature of the inside surface of the shell

q external heat flux

The presence of the resistance modifies Equation (2) of Appendix I to:

$$\frac{hC}{h + C} (T_w - T) = q$$

By a procedure similar to that followed in Appendix I, it is found that Equation (10) of Appendix I is modified to:

$$\left(\frac{1}{\theta}\right)^{2.4} = \epsilon^{.6} \int_0^1 \frac{\beta^3 \rho^{.6} (1 + \alpha \epsilon \eta)}{(1 - \epsilon \eta - \beta \psi)^3} dy \quad (25)$$

where $\psi = \frac{q_R}{C(T_w - T_i)}$

The quantity ψ is not exactly constant because the conductance C is a function of the mean temperature of the material. Even with the outside

surface at the constant temperature T_w , the mean temperature varies because of variation of the inside temperature T_i . However, this effect is not of prime importance and to illustrate the effect of the thermal conductivity of the radome material ψ is treated as constant.

For the conical radome, the handling of Equation (25) may be performed along the lines discussed in Appendix II. For the special case of $b = 0$, the equation can be handled analytically for it simplifies to:

$$\left(\frac{1}{\sigma}\right)^{2.4} = \epsilon_B^{-6} \int_0^1 \frac{1 + a \epsilon_B y}{(1 - \epsilon_B y - \psi_B)^3} dy$$

which integrates to:

$$\sigma_B = \epsilon_B^{1/6} \left[\frac{(1 - \psi_B)^2 (1 - \psi_B - \epsilon_B)^2}{(1 - \psi_B) \epsilon_B - (1 - a(1 - \psi_B)) \frac{\epsilon_B^2}{2}} \right]^{5/12}$$

Cooling curves obtained from this equation for $a = 0$ are shown in Figure 6.

APPENDIX IV
TURBO-COOLER SYSTEMS

The systems considered (Figure 18) are turbo-cooler system 1 which uses cooled ram air as a heat sink and turbo-cooler system 2 which uses water as a heat sink.

In System 1, ram air for cooling is passed through a heat exchanger where it is cooled by ram air which has been passed through a cooling turbine 1. The cooled air is then further cooled in turbine 2 from which it goes to the cooling load (radome and possible other components of the aircraft). The air then passes through a compressor which loads the turbine and is discharged through a nozzle for thrust recovery. This "bootstrap" arrangement of the compressor is believed to result in the least drag for the system compared to other possible arrangements. The compressor loading turbine 1 is also used in a bootstrap arrangement.

The discharge temperatures and pressures calculated for this system at a flight condition $M = 6$, 100,000 ft are shown in Figure 19. The data used were:

Turbine efficiencies = .85

Heat exchanger effectiveness = .90

Ram recovery to heat exchanger = .30

Pressure drop fraction through heat exchanger = .20

It is pointed out that the ram recovery to turbine 1 can be much higher than to the heat exchanger since this turbine can be designed with supersonic Mach numbers at the inlet. Such a design is useful in increasing the downstream pressure and consequently reducing the size of the heat exchanger.

In turbo-cooler system 2, ram air for cooling is passed through a cooling turbine and then to a water evaporator for further cooling. After passing through the cooling load, it goes to the compressor which is in bootstrap arrangement with the turbine.

The water consumption required for various discharge temperatures are shown in Figure 20 based on the following:

Turbine efficiency = .85

Ram recovery to turbine = .60

Pressure drop fraction across evaporator = .10

Latent heat of vaporization of water = 1000 BTU/lb.

It is noted that a high ram recovery at the turbine is used because the turbine is designed for supersonic inlet Mach numbers.

REFERENCES

1. McAdams, W. H. - Heat Transmission - McGraw-Hill Book Company, 1954.

SYMBOLS

Dimensional

C	conductance
c_p	specific heat
d	depth of cooling gap
d_h	hydraulic diameter
g	acceleration of gravity
h	convective heat transfer coefficient
L	length of cooling run
P	pressure
ΔP	pressure drop
q	net heat flux
q_c	convective heat flux
q_r	radiant heat flux
r	perimeter of radome
r_R	reference perimeter (= S/L)
R	radius of radome
R	gas constant
S	surface area
T	temperature of coolant
T_w	surface temperature

ΔT temperature rise of coolant

W cooling flow

x distance along surface from nose

$$B = a^{5/6} \left(\frac{z}{2n}\right)^{5/12} \left(\frac{d}{d_h}\right)^{-1/4} Y_1 P_1^{5/6} L^{-1/6}$$

$$Y_1 = c_p \mu^{1/6} \left(\frac{q}{RT_1}\right)^{5/12} (Pr)^{-5/9}$$

Non-dimensional

a constant in heat transfer correlation

$$b = \frac{R_B - R_F}{R_F}$$

$$D = a^{5/6} \left(\frac{z}{2n}\right)^{-1/12} \left(\frac{d}{d_h}\right)^{1/4} (Pr)^{-5/9} \left(\frac{\mu}{P_1} \sqrt{\frac{RT_1}{g}}\right)^{1/6}$$

e emissivity

M Mach number

n constant in Reynolds heat transfer-friction analogy

$$N = \sqrt{\frac{1}{Y} \frac{z/2n}{d/d_h} \frac{\sqrt{T/T_1}}{P/P_1}}$$

Pr Prandtl number

Re Reynolds number

St Stanton number

γ station along radome

$$z = \frac{\Delta P}{P_1} \left(1 - 1/2 \frac{\Delta P}{P_1} \right)$$

$$\alpha = \frac{T_w - T_1}{T_1}$$

$$\beta = q/q_B$$

γ specific heat ratio

$$\delta = \frac{d}{DL}$$

$$\epsilon = \frac{qS}{W_{cp}(T_w - T_1)}$$

$$\rho = r/r_R$$

$$\sigma = \frac{q}{B(T_w - T_1)}$$

$$\phi = M/N$$

$$\psi = \frac{q}{C(T_w - T_1)}$$

Subscripts

- 1 inlet of cooling gap
- 2 outlet of cooling gap
- B base of radome
- F front of radome

FIG. 1 - TEMPERATURE FACTOR Y FOR AIR

$$Y = \frac{C_p \mu^{1/2}}{(Pr)^{5/4}} \left(\frac{g}{RT} \right)^{5/12}$$

$$g = 32.2 \text{ FT/SEC}^2$$

$$R = 53.3 \text{ FT/}^\circ\text{R}$$

C_p SPECIFIC HEAT, BTU/LB- $^\circ\text{F}$

μ VISCOSITY, LB/SEC-FT

T TEMPERATURE, $^\circ\text{R}$

Pr PRANDTL NUMBER

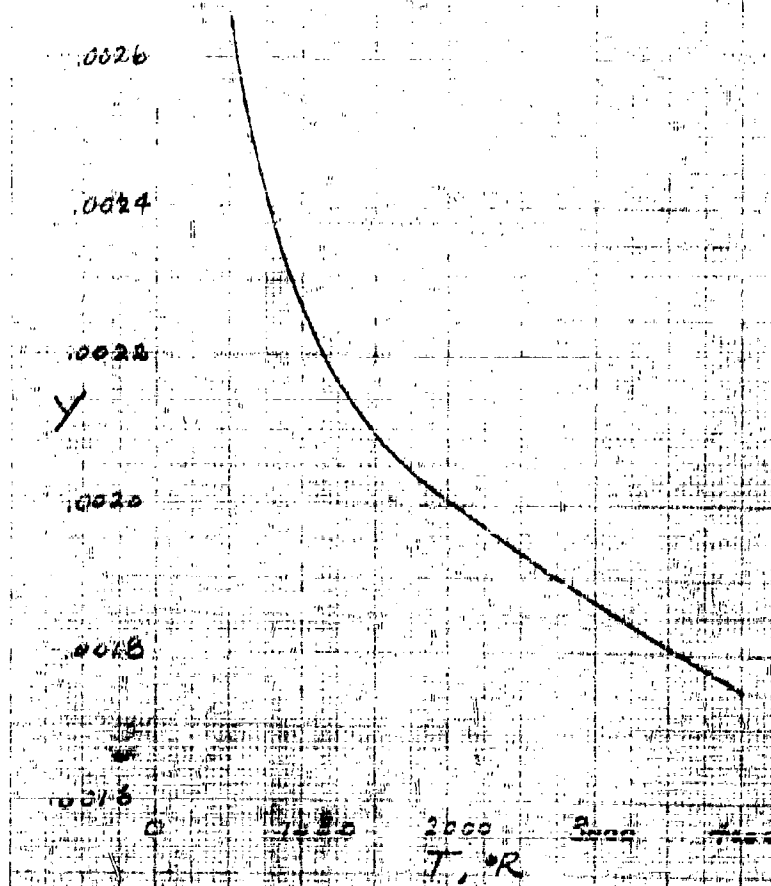


Figure 1

FIG. 2- CONVECTION COOLING OF CONICAL B
 CONSTANT SURFACE TEMPERATURE
 TURBULENT HEAT FLUX VARIATION
 REARWARD COOLING FLOW

$\alpha = 0$
 $\psi_B = 0$

b
 0
 1
 5
 8

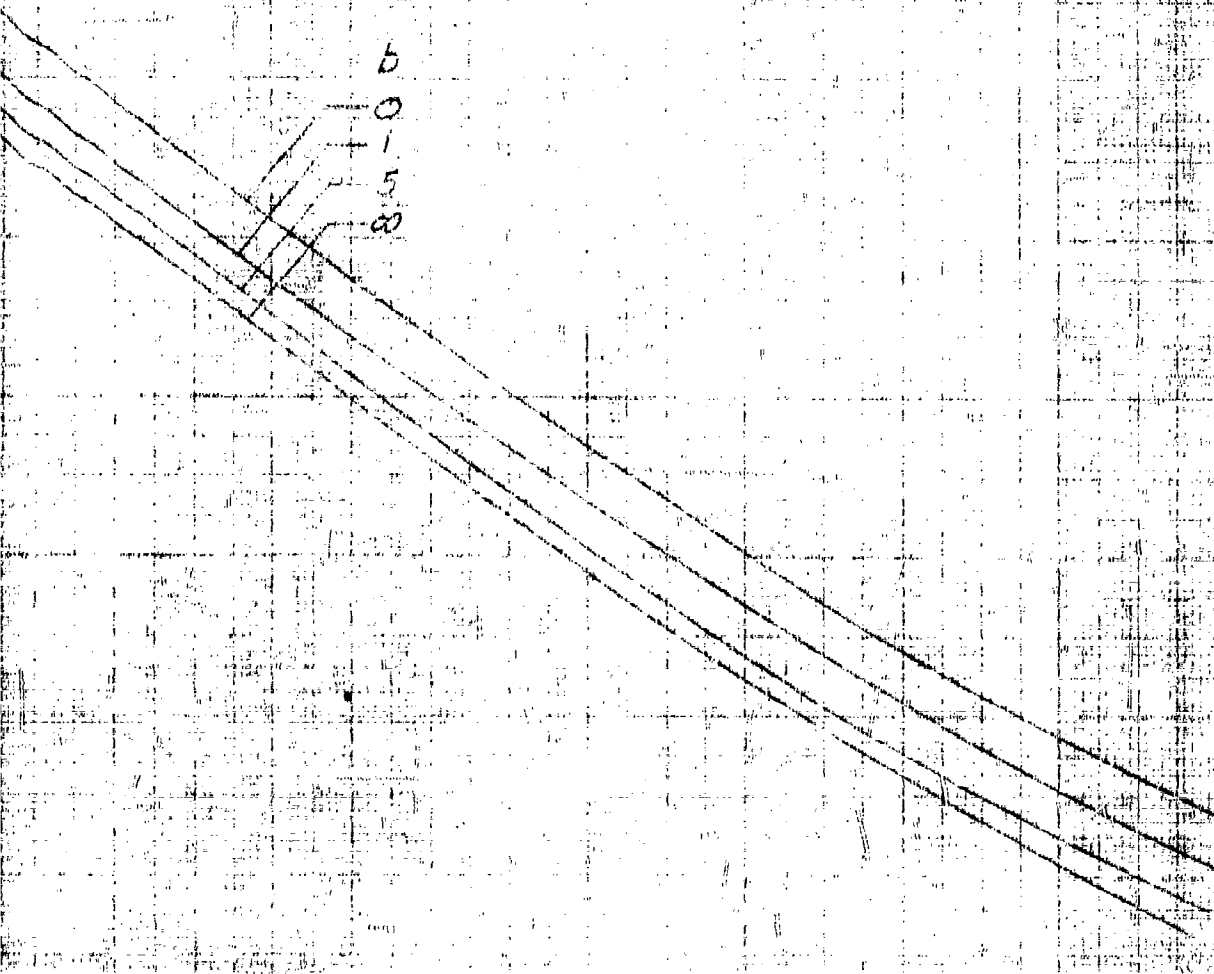
1

$\sigma_B = \frac{q_B}{B(T_w - T_f)}$

CONVECTION COOLING OF CONICAL RADOME
 CONSTANT SURFACE TEMPERATURE
 TURBULENT HEAT FLUX VARIATION
 REARWARD COOLING FLOW

$$\alpha = 0$$

$$\psi_B = 0$$



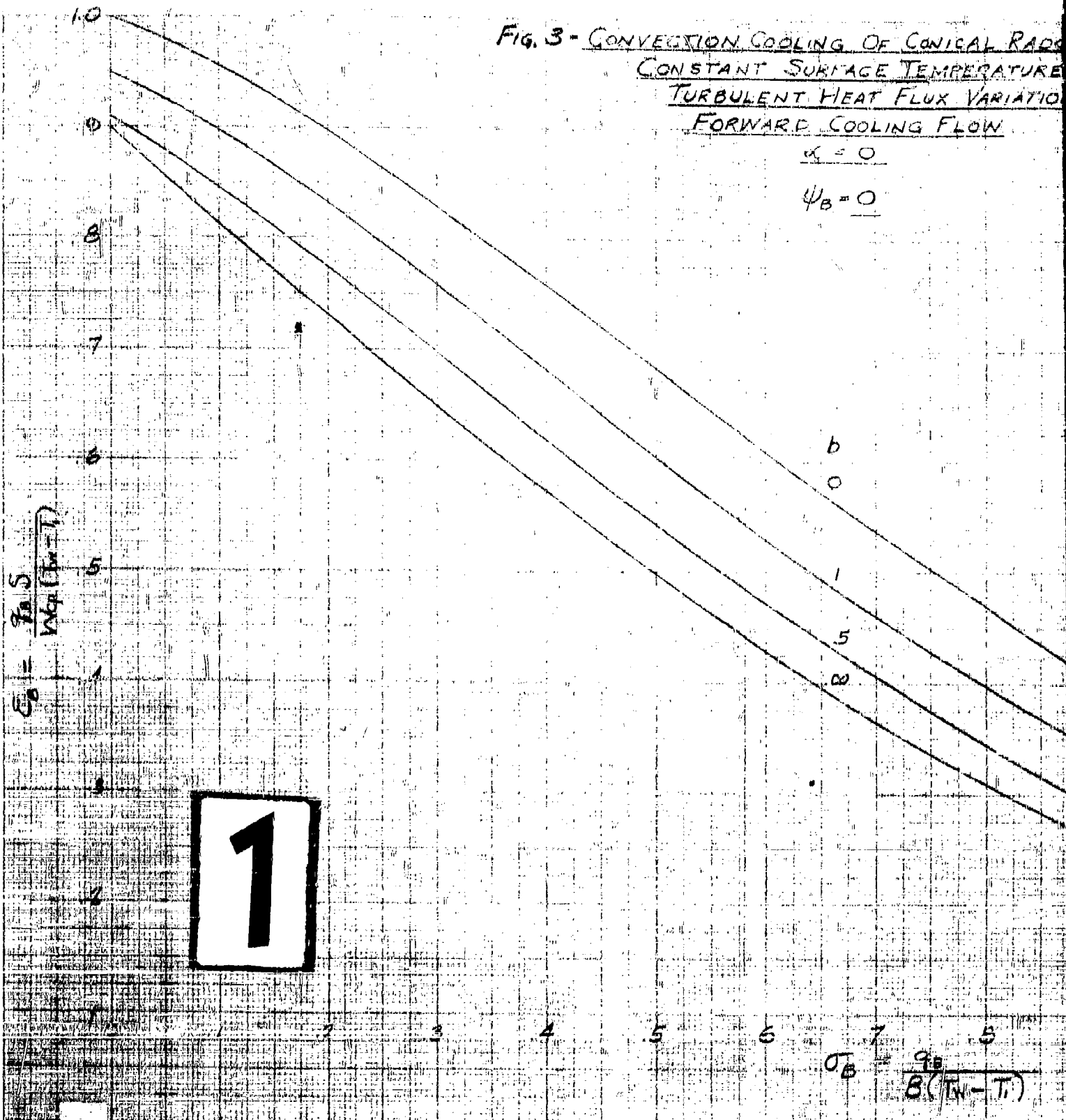
2

$$\sigma_B = \frac{q_B}{B(T_w - T_i)}$$

FIG. 3 - CONVECTION COOLING OF CONICAL RADAR
 CONSTANT SURFACE TEMPERATURE
 TURBULENT HEAT FLUX VARIATION
 FORWARD COOLING FLOW

$$\alpha = 0$$

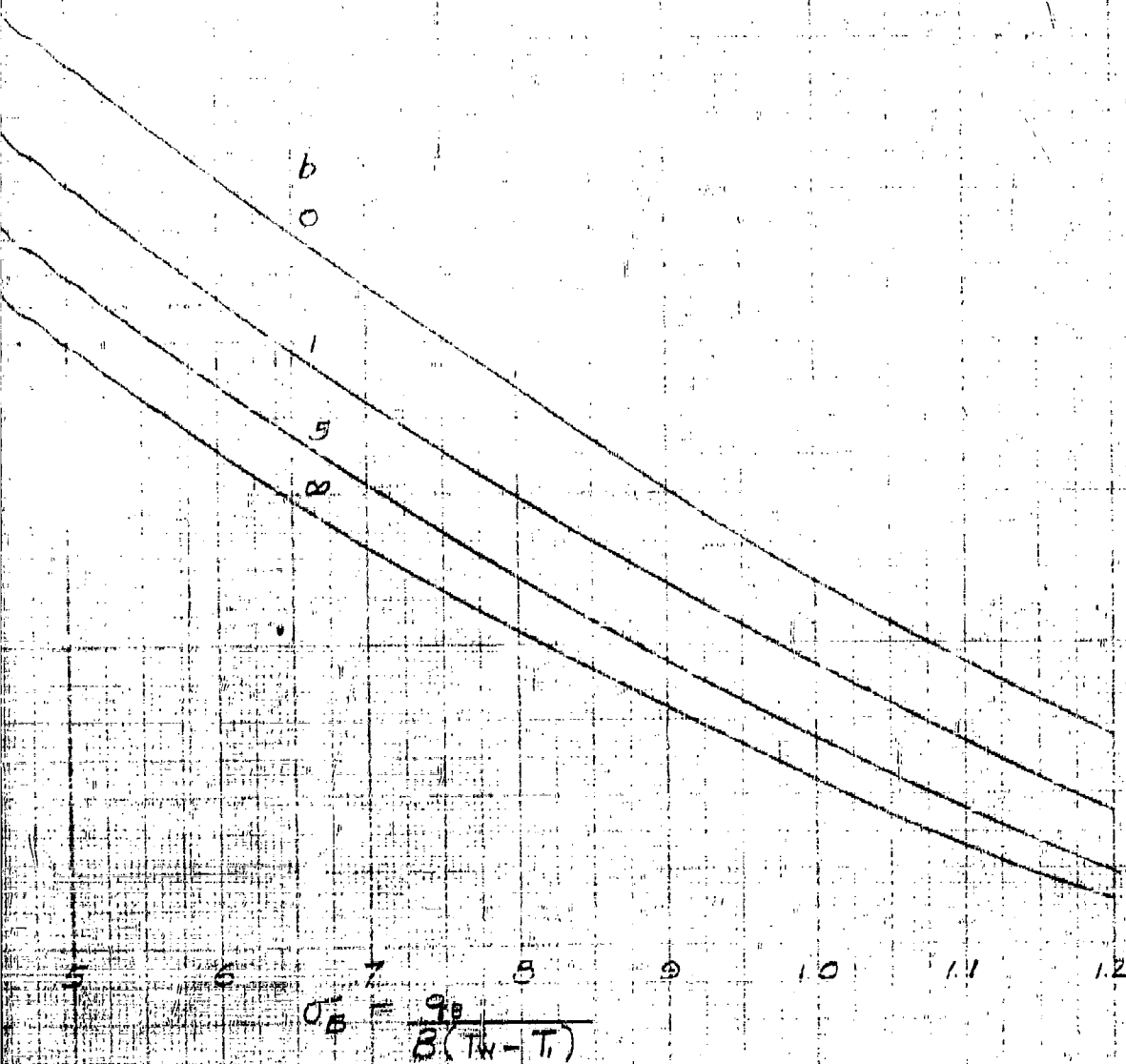
$$\psi_B = 0$$



CONVECTION COOLING OF CONICAL RADOME
 CONSTANT SURFACE TEMPERATURE
 TURBULENT HEAT FLUX VARIATION
 FORWARD COOLING FLOW

$$\alpha = 0$$

$$\psi_B = 0$$



$$q_B = \frac{q_0}{B(T_w - T_i)}$$

Figure 3

FIG. 4 - CONVECTION COOLING OF CONICAL
 CONSTANT SURFACE TEMPER
 CONSTANT HEAT FLUX

$$Pe = 0$$

$$\psi_b = 0$$

REARWARD
 COOLING FLOW

b

0

1

5

∞

FORWARD
 COOLING FLOW

b

0

∞

1

$$\frac{q_b}{B(T_w - T_i)} = 9$$

CONVECTION COOLING OF CONICAL RADOME
 CONSTANT SURFACE TEMPERATURE
 CONSTANT HEAT FLUX

$Re = 0$

$Pr = 0$

REARWARD
 COOLING FLOW

0
 1
 5
 ∞

FORWARD
 COOLING FLOW

0
 1
 ∞

$\frac{q_B}{B(T_w - T_f)}$

2

Figure 4

FIG. 5- CORRECTION TO COOLING FLOW FOR EFFECT OF α

$$b = 0$$

$$\text{CORRECTED } W = C \times W_{\alpha=0}$$

$$\alpha = \frac{T_w - T_i}{T_i}$$

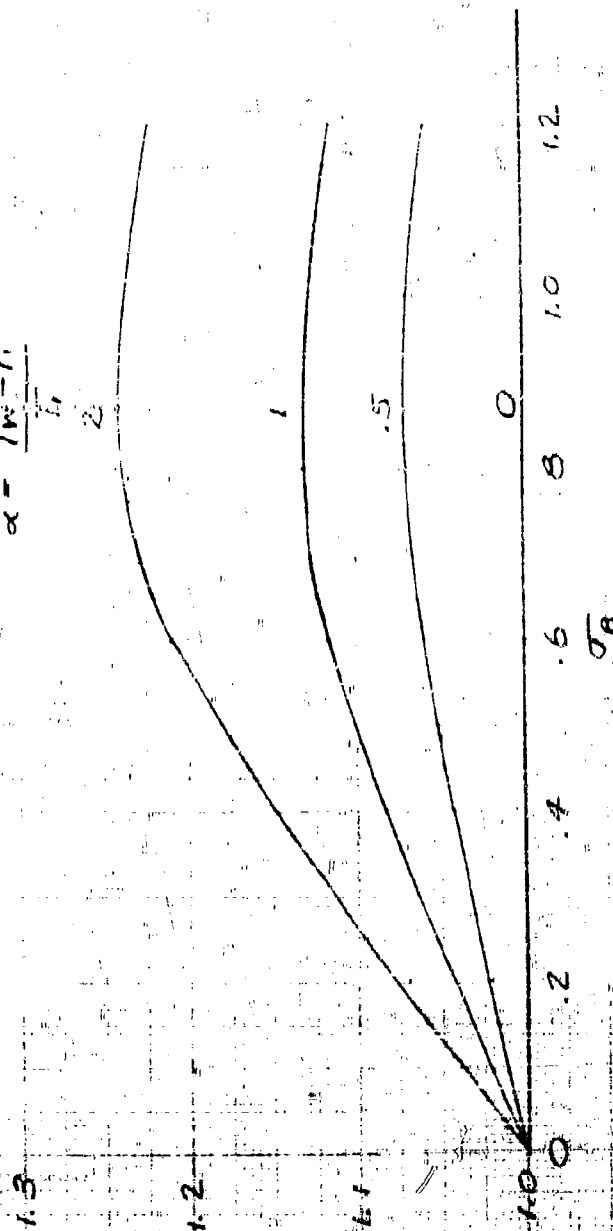
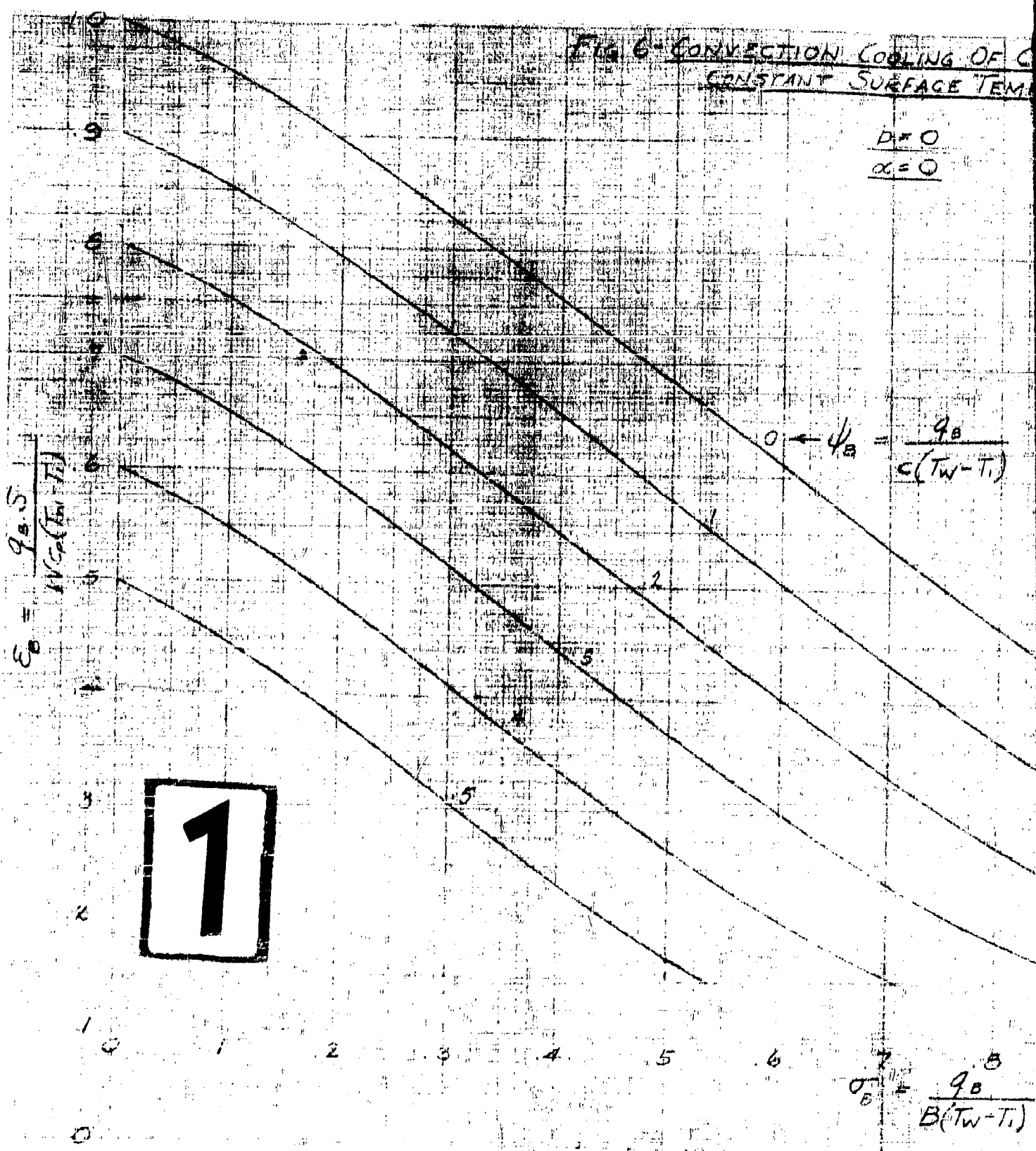


Figure 5

FIG. 6- CONVECTION COOLING OF C
CONSTANT SURFACE TEMP

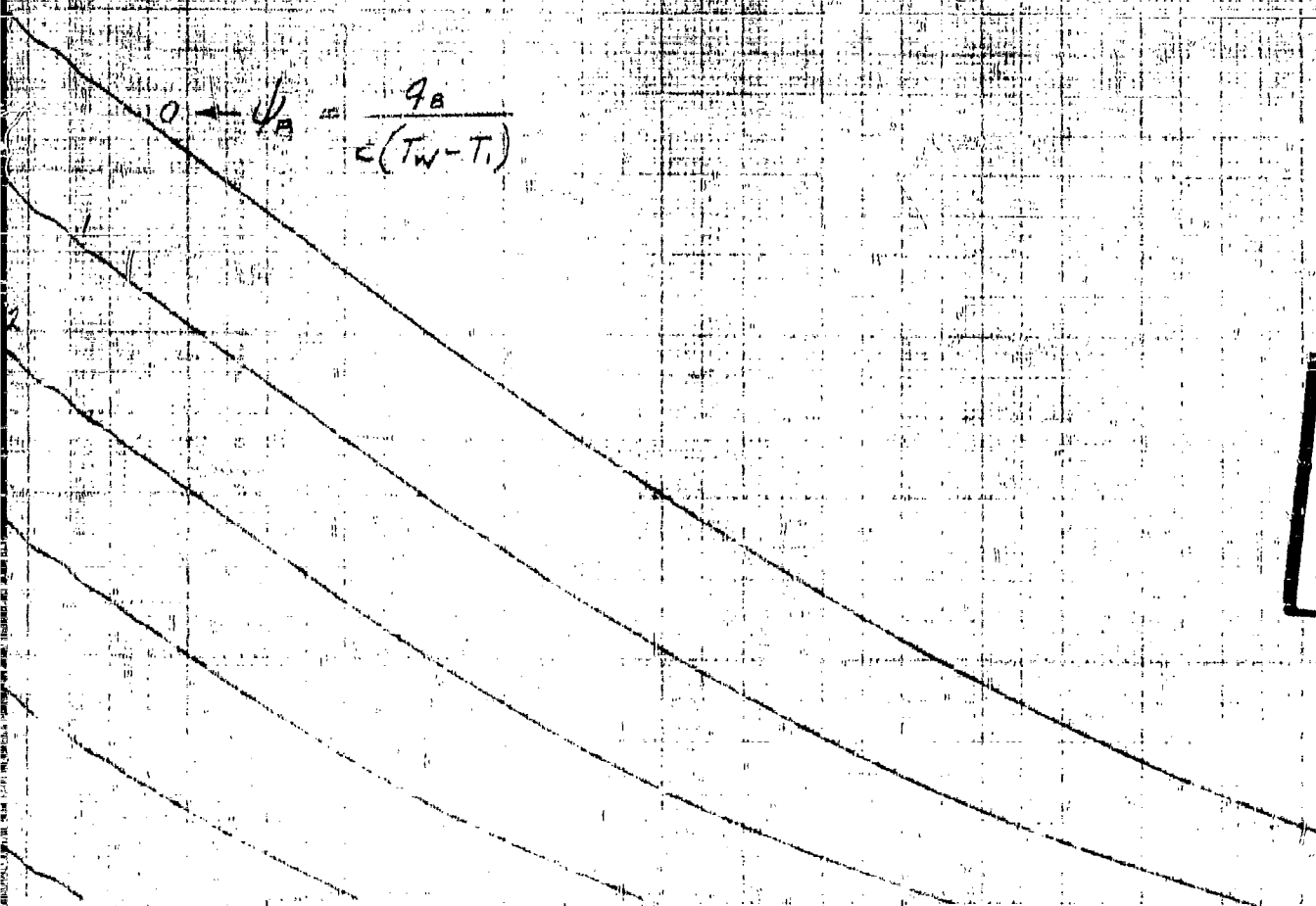
$D = 0$
 $\alpha = 0$



CONVECTION COOLING OF CONICAL RADIOME CONSTANT SURFACE TEMPERATURE

$$b = 0$$

$$\alpha = 0$$



2

$$\tau_B = \frac{q_B}{B(T_W - T_i)}$$

Figure 6

FIG. 7. FACTOR FOR DETERMINING TEMPERATURE RANGE OF COOLING MEDIUM

TURBULENT HEAT FLUX VARIATION

1.12

1.08

K

1.04

1.0

0

2

4

5

6

8

10

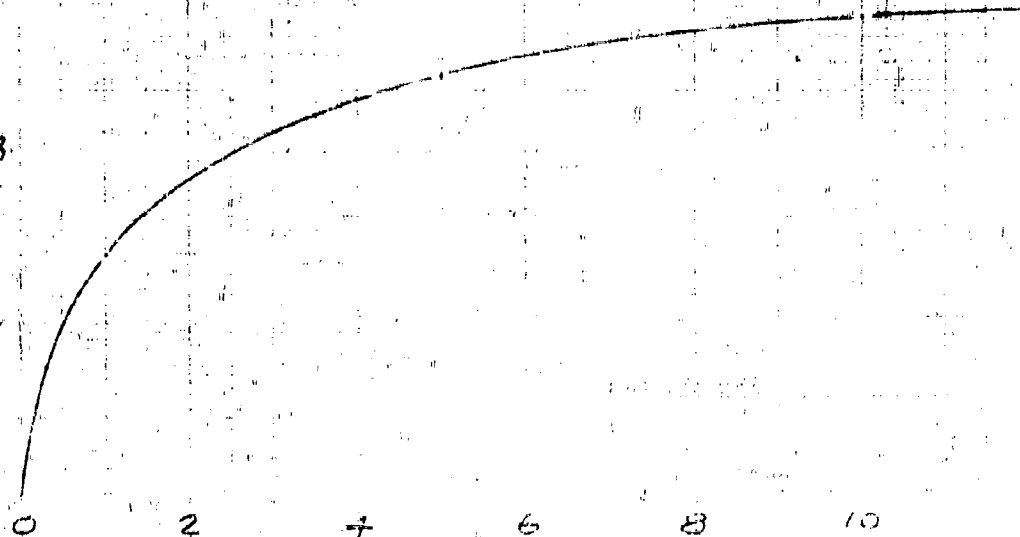


Figure 7

FIG 7-FACTOR FOR DETERMINING TEMPERATURE
RISE OF COOLING MEDIUM

TURBULENT HEAT-FLUX VARIATION

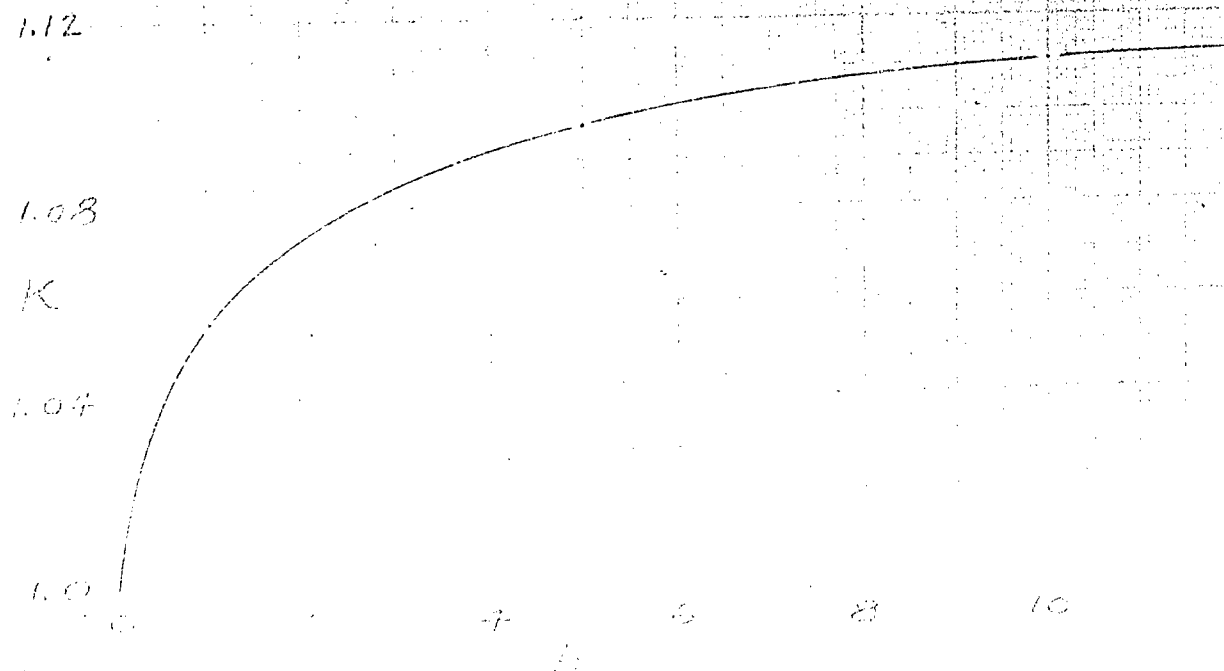


Figure 7

FLUX VARIATION WITH DETERMINING TEMPERATURE
COOLING MEDIUM

FLUX VARIATION

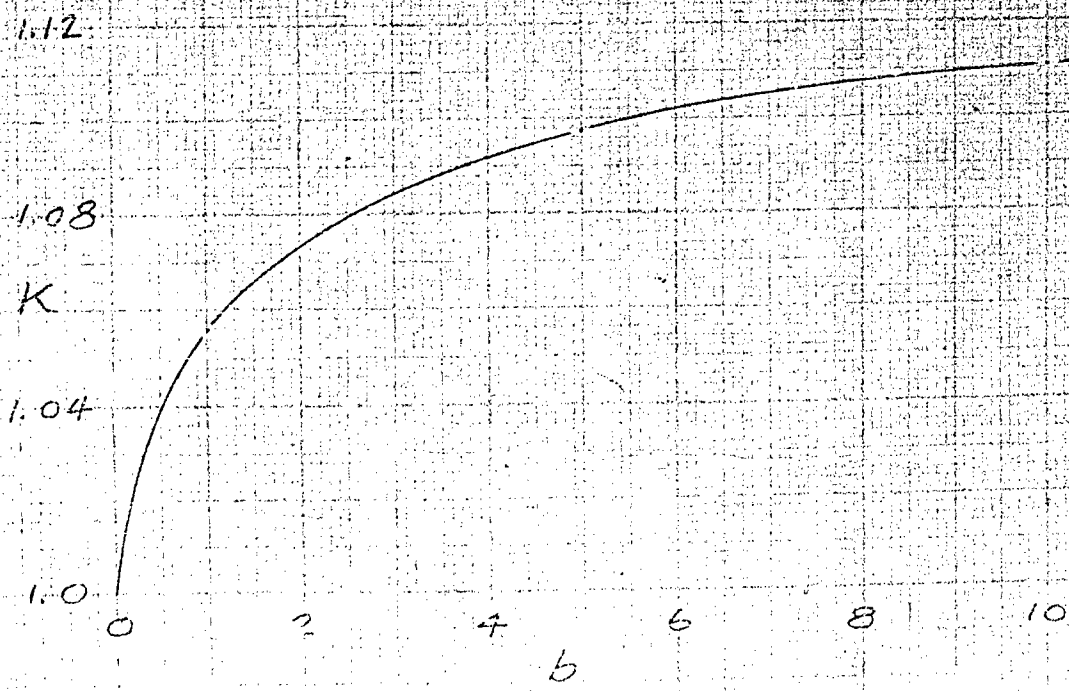


Figure 7

FIG. 8 - REQUIRED AIRFLOW FOR RADOME COOLING WITHOUT RADIATION

MFE 100,000 FT

CONICAL (FRUSTRUM) RADOME
CONE ANGLE 20°

RADOME TEMPERATURE 2000R

BASE DIAMETER 3 FT

PRESSURE DROP FRACTION

FRONT DIAMETER 6 FT

OF COOLING AIR $\Delta P/P = .20$

SLANT HEIGHT 3.51 FT

SURFACE AREA 19.9 FT²

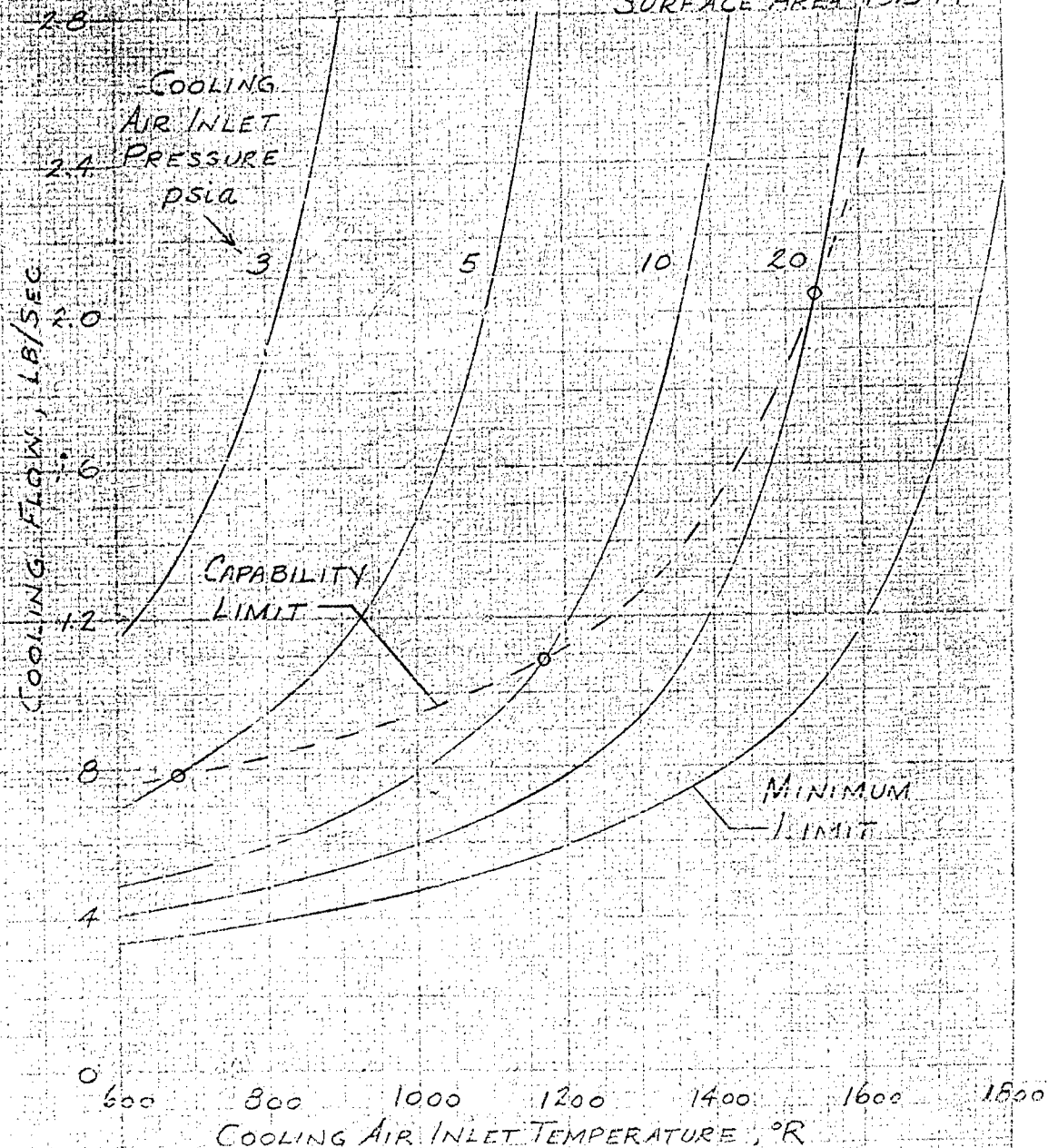


Figure 8

FIG. 9. REQUIRED AIR FLOW FOR RADOME COOLING WITH RADIATION

MT # 6 100,000 FT

CONICAL (FRUSTRUM) RADOME

CONE ANGLE 20°

RADOME TEMPERATURE 2000 R

BASE DIAMETER 3 FT

RADOME EMISSIVITY .30

FRONT DIAMETER .6 FT

PRESSURE DROP FRACTION

SLANT LENGTH 3.51 FT

OF COOLING FLOW $\Delta P/P = .20$

SURFACE AREA 12.9 FT²

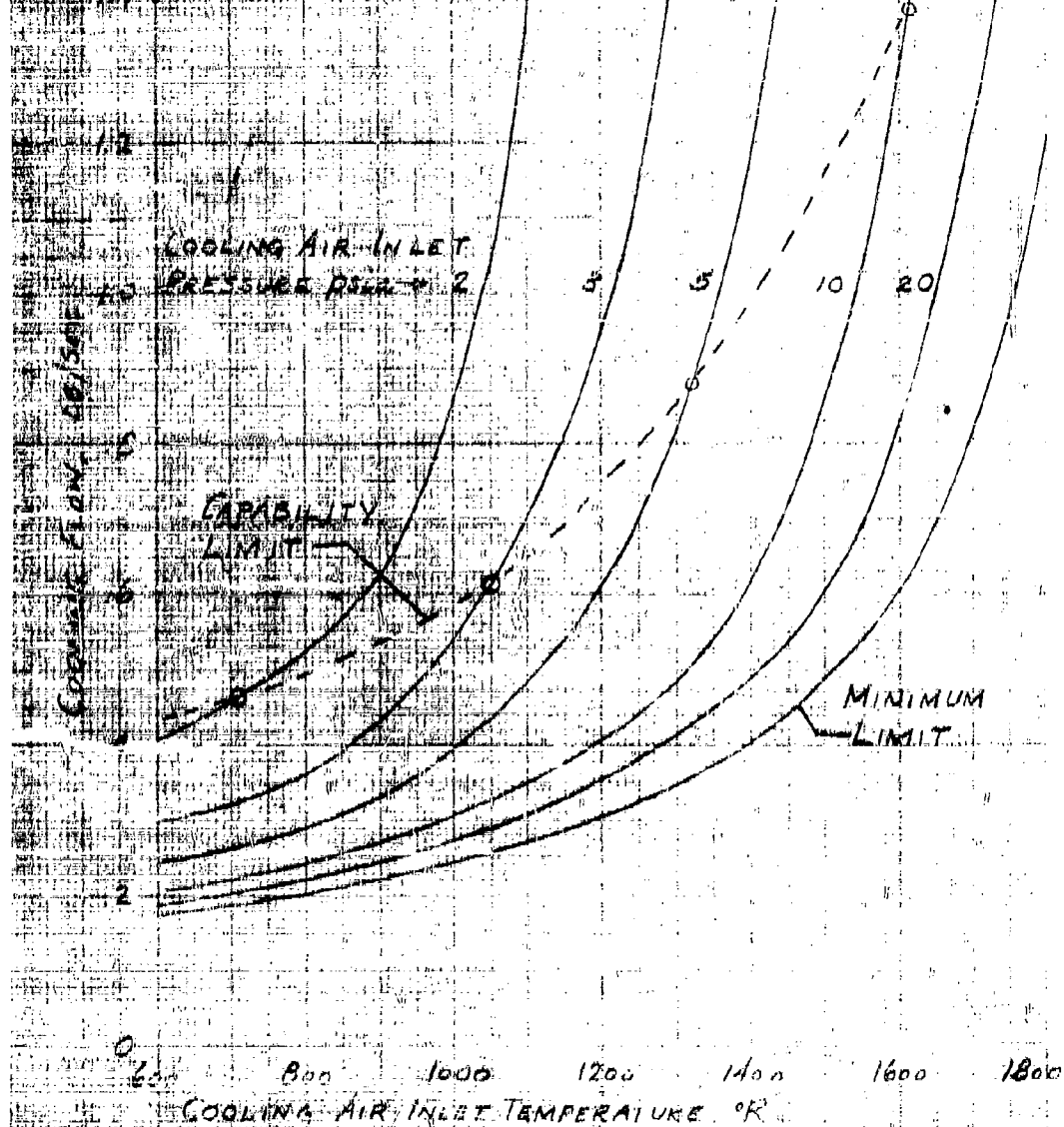


Figure 9

FIG 9. REQUIRED AIRFLOW FOR RADOME COOLING
WITH RADIATION

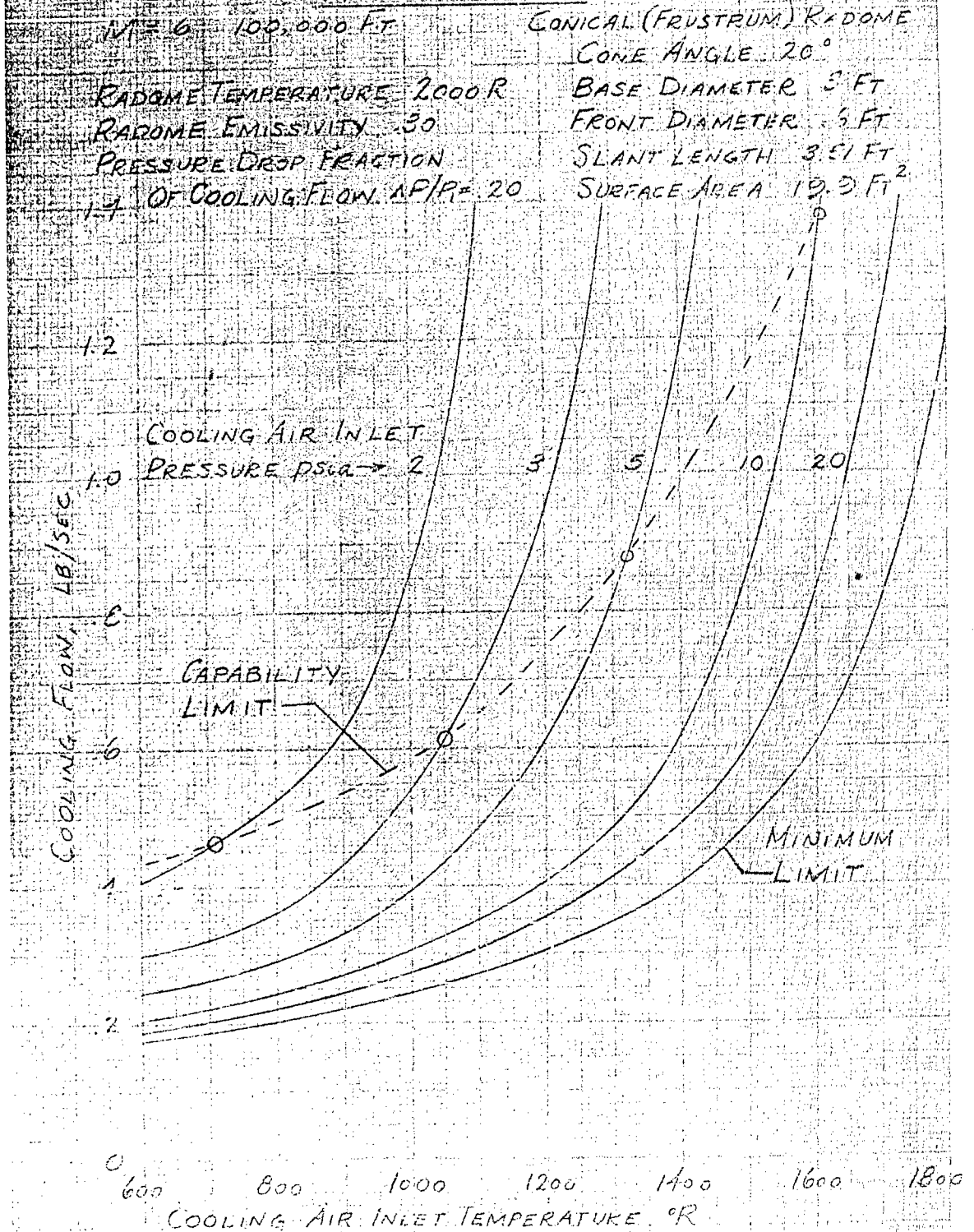


Figure 9

FIG. 10 - COOLING AIR EXIT TEMPERATURE
WITHOUT RADIATION

$M = 6$ 100,000 FT

CONICAL (FRUSTRUM) RADOME

CONE ANGLE 20°

SURFACE TEMP. 2000 R

BASE DIAMETER 3 FT

PRESSURE DROP FRACTION

FRONT DIAMETER 6 FT

OF COOLING AIR $\Delta P/P = 1.20$

SLANT LENGTH 3.5 FT

SURFACE AREA 12.9 FT²

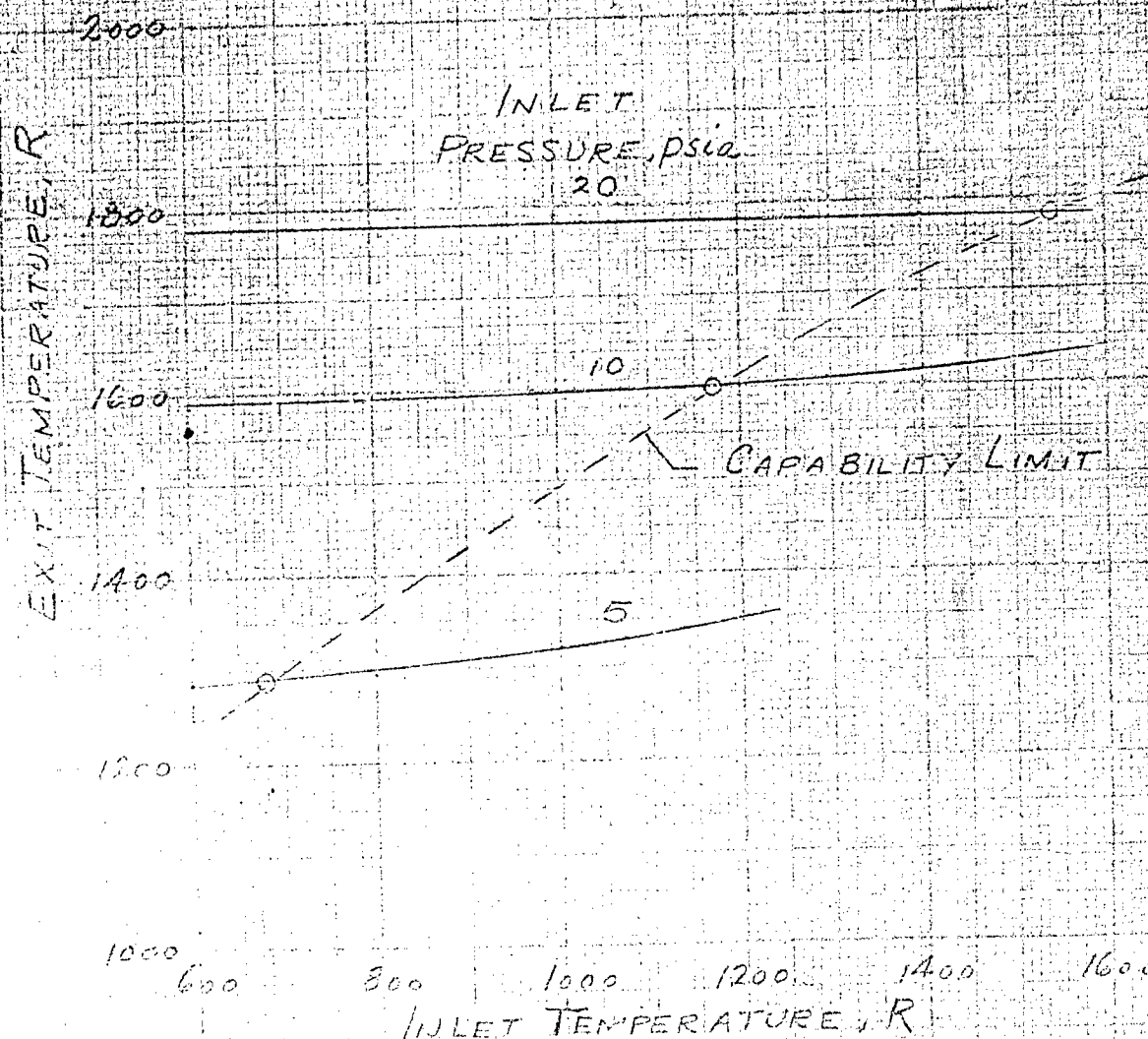


Figure 10

FIG. 10 - COOLING AIR EXIT TEMPERATURE
WITHOUT RADIATION

$M = 6$ 100,000 FT

CONICAL FRUSTUM PARABOLIC

CONE ANGLE 20°

SURFACE TEMP. 2000 R

BASE DIAMETER 3 IN

PRESSURE DROP FRACTION

FRONT DIAMETER 6 IN

OF COOLING AIR $\Delta P/P = 1.20$

SLANT LENGTH 3 IN

SURFACE AREA 1.5 IN²

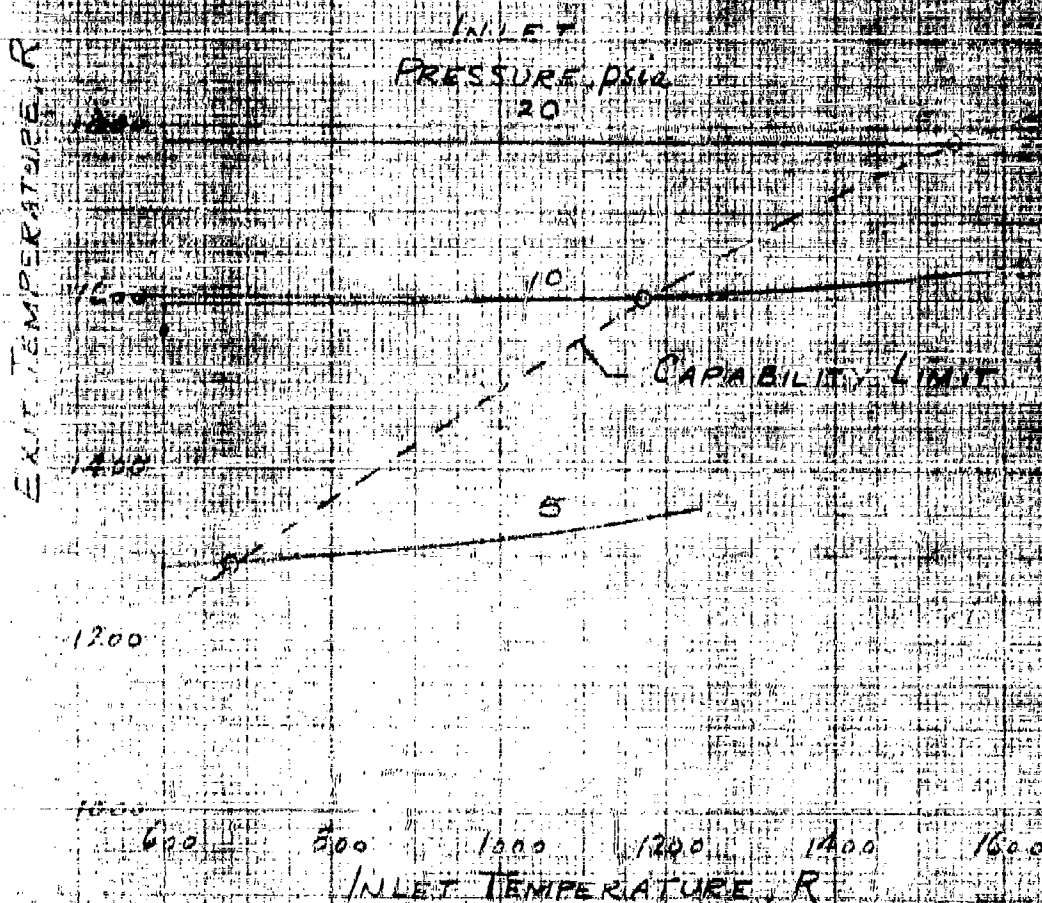


Figure 10

FIG 11- COOLING AIR EXIT TEMPERATURE WITH RADIATION

$M = 6$ 100,000 Ft

CONICAL (FRUSTUM) RADOME

CONE ANGLE 20°

RADOME TEMPERATURE 2000R

BASE DIAMETER 3 Ft

RADOME EMISSIVITY .90

FRONT DIAMETER 6 Ft

PRESSURE DROP FRACTION
OF COOLING AIR $\Delta P/P = .20$

SLANT LENGTH 3.51 Ft

SURFACE AREA 199 Ft²

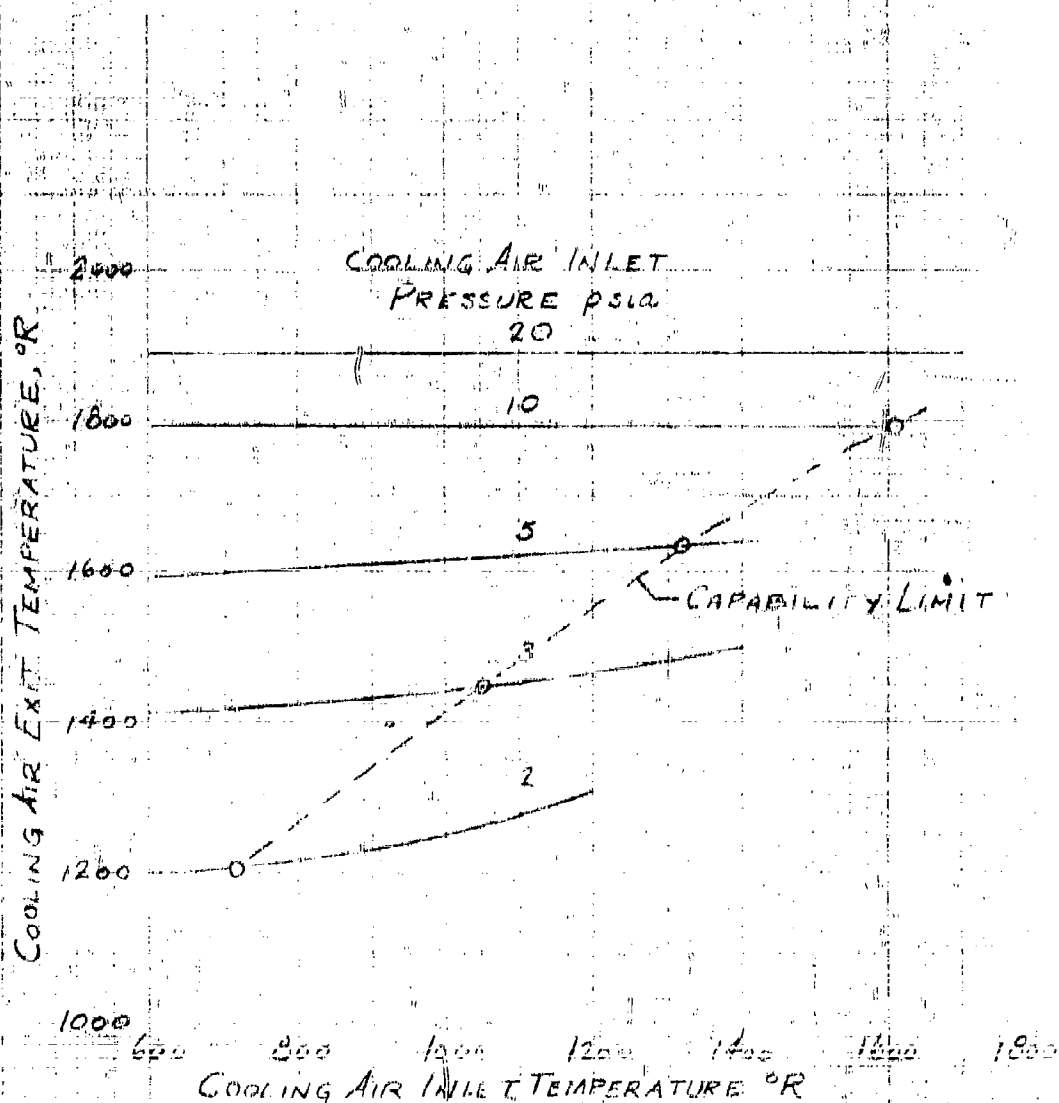


Figure 11

FIG. 12- WATER CONSUMPTION FOR RADOME COOLING
WITH TURBO-COOLER SYSTEM-2
NO RADIATION

M=6 100,000 FT

CONICAL (FRUSTRUM) RADOME

CONE ANGLE 20°

BASE DIAMETER 3 FT

FRONT DIAMETER 16 FT

SLANT LENGTH 9.5 FT

SURFACE AREA 129 FT²

SURFACE TEMP. 2000 R

PRESSURE DROP FRACTION
OF COOLING FLOW $\Delta P/P = .20$

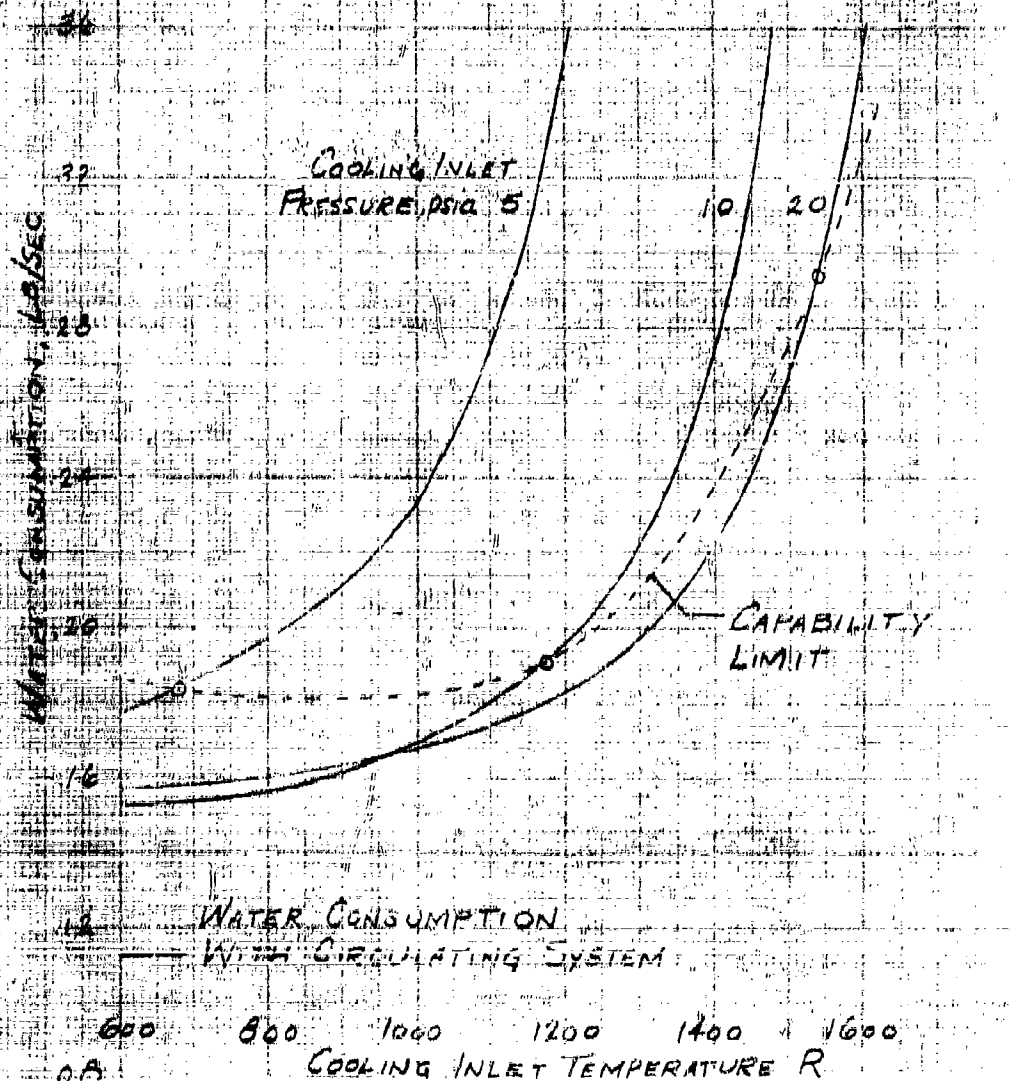


FIG. 13- WATER CONSUMPTION FOR RADOME COOLING
WITH TURBO-COOLER SYSTEM-2
WITH RADIATION

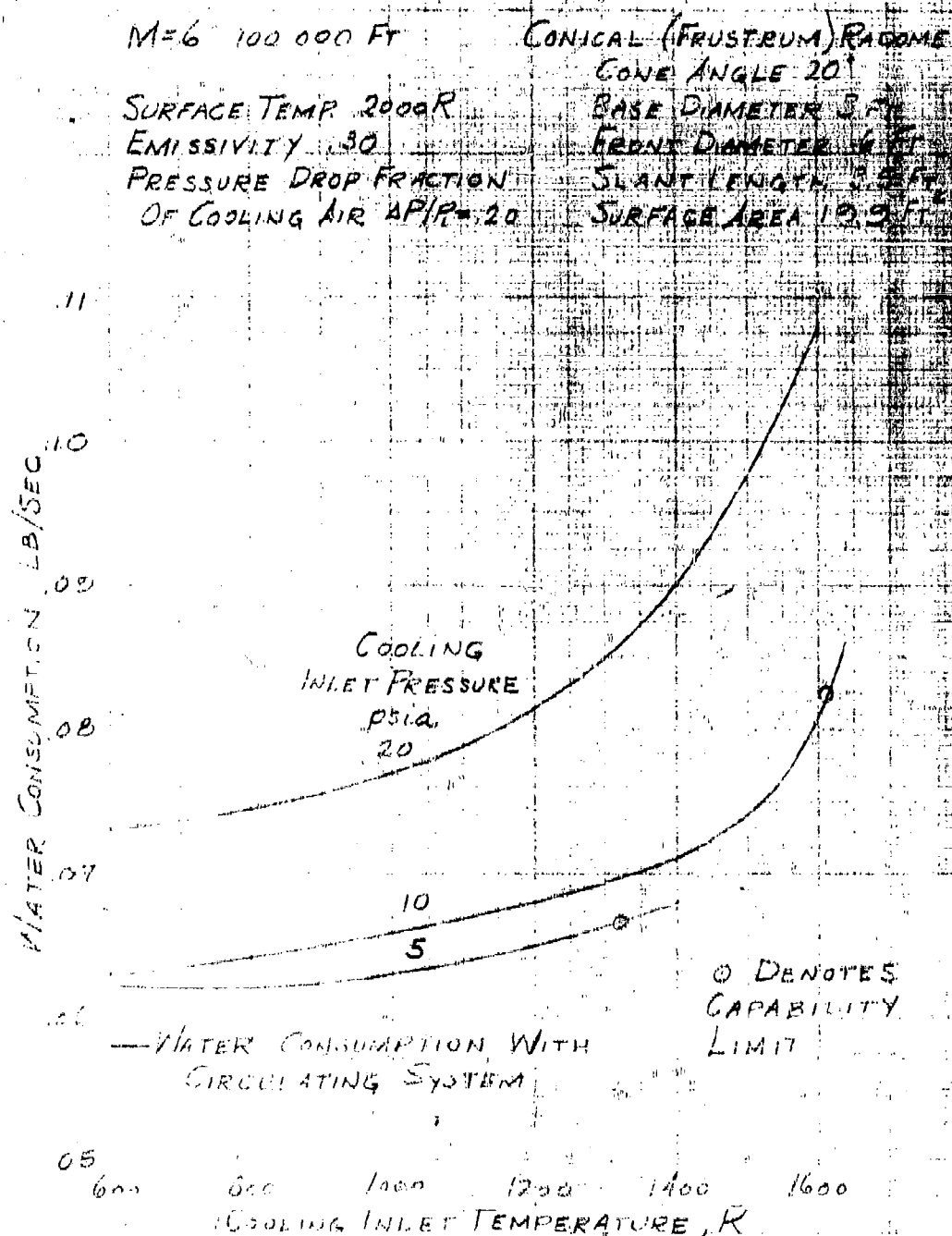


Figure 13

FIG. 14. CAPABILITY LIMIT FOR CONVECTION COOLING

BASED ON INLET MACH NUMBER = .30

TURBULENT HEAT FLUX VARIATION
REARWARD COOLING FLOW.

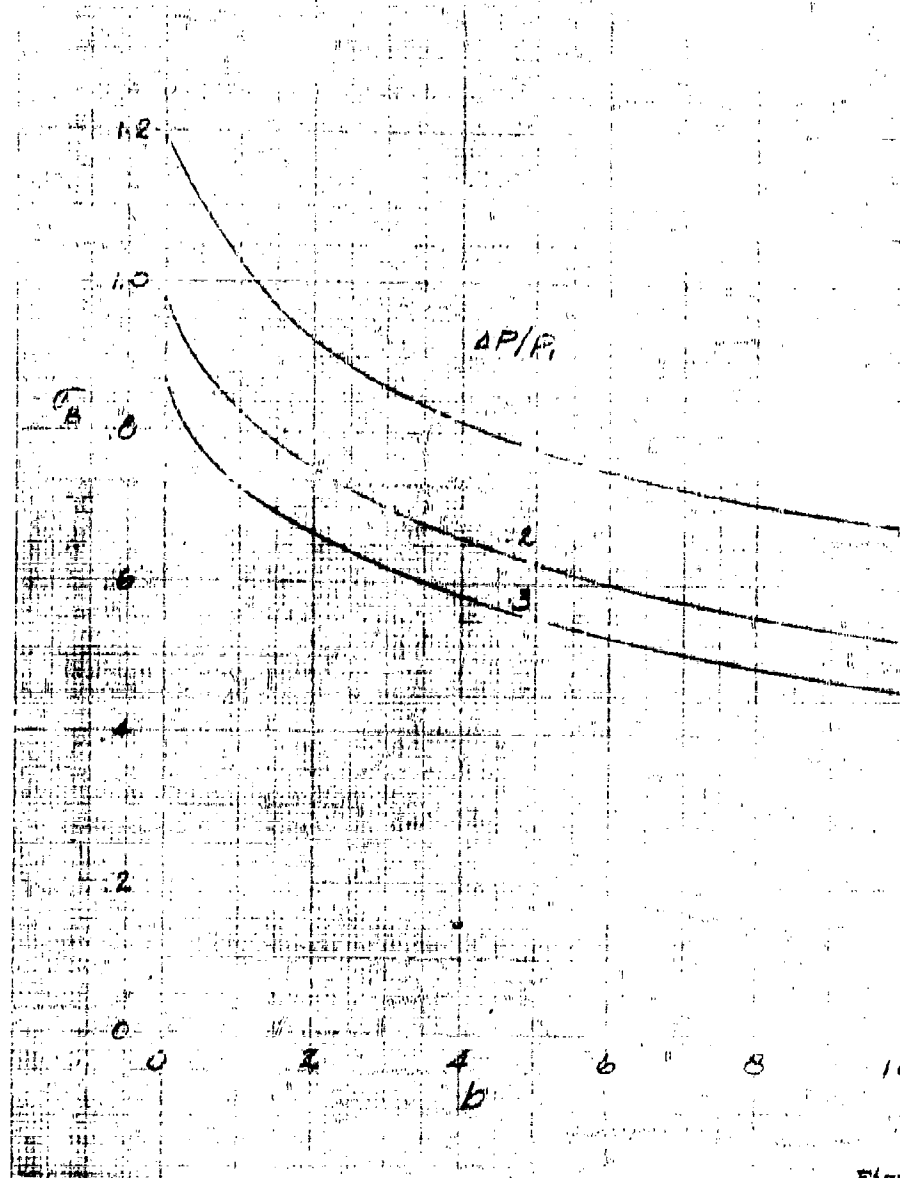


Figure 14

FIG. 15 - PRESSURE AND TEMPERATURE AT CAPABILITY
LIMIT OF CONVECTION COOLING WITH AIR

32

$$q_b = 5.2 \text{ BTU/SEC} \cdot \text{FT}^2$$

$$T_w = 2000^\circ \text{R}$$

28

$$b = 4$$

BASED ON INLET MACH NUMBER $M = 3.0$
TURBULENT HEAT FLUX VARIATION
REARWARD COOLING FLOW

24

COOLING AIR INLET PRESSURE, PSIA

20

16

12

8

4

0

600

800

1000

1200

1400

1600

COOLING AIR INLET TEMPERATURE, $^\circ \text{R}$

$\Delta P/P$

1

2

3

Figure 15

FIG. 15 - PRESSURE AND TEMPERATURE AT CAPABILITY
LIMIT OF CONVECTION COOLING WITH AIR

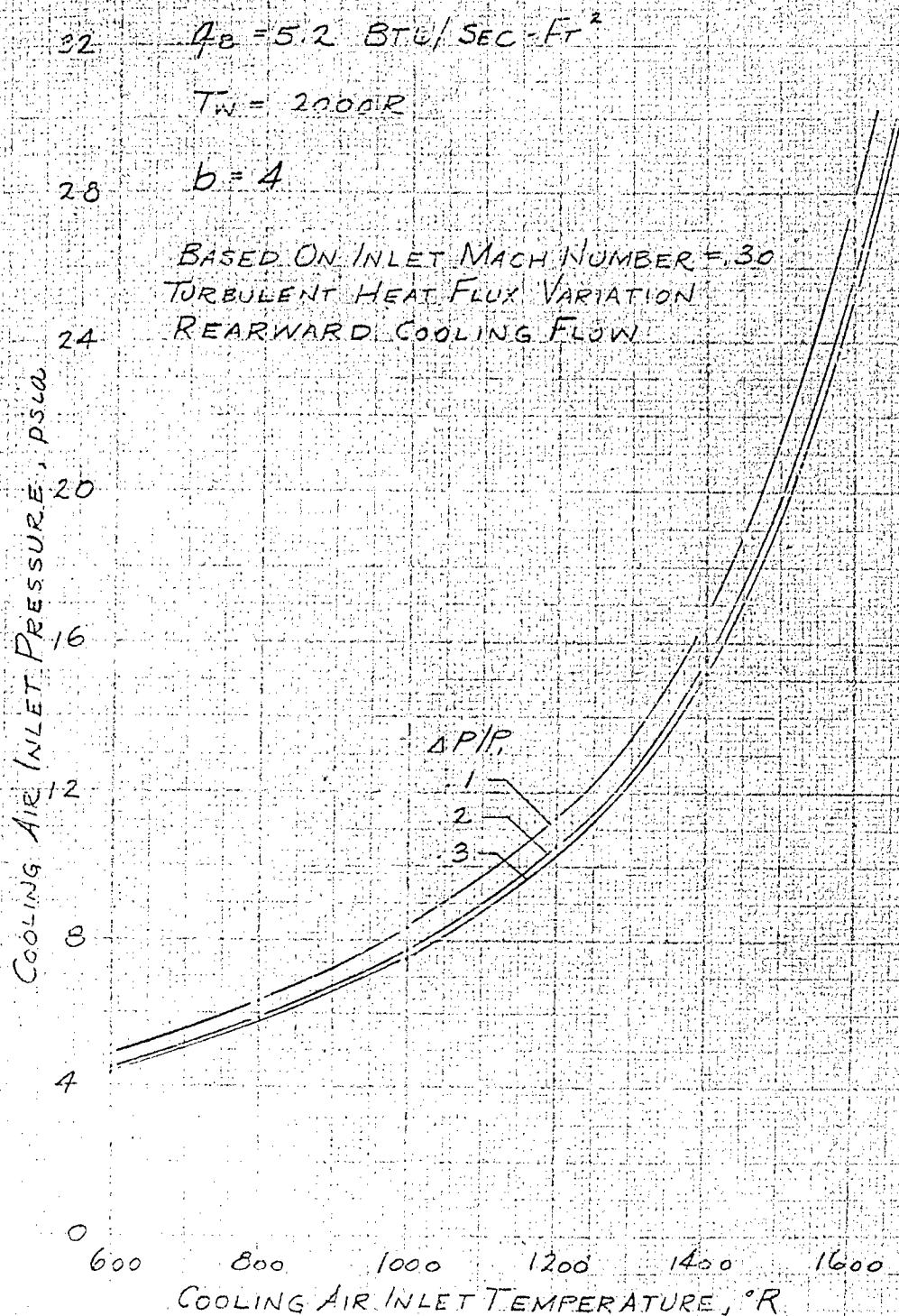


Figure 15

FIG. 16-HEAT FLUX AT CAPABILITY LIMIT OF
CONVECTION COOLING WITH AIR

BASED ON INLET MACH NUMBER = .30
TURBULENT HEAT FLUX VARIATION
REARWARD COOLING FLOW
APIR = 2.0

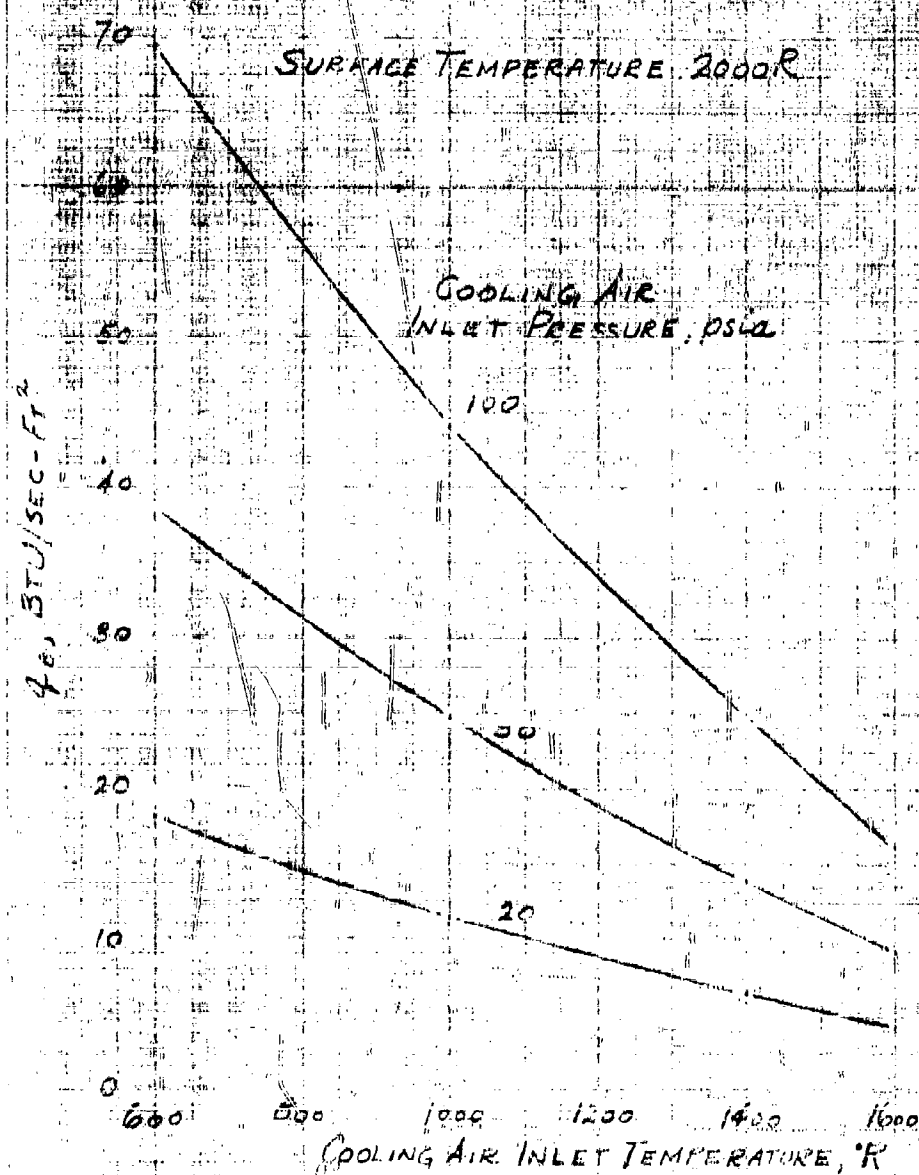


Figure 16

FIG. 17- TURBULENT CONVECTIVE HEAT TRANSFER TO CONE

CONE ANGLE = 20°

DISTANCE FROM NOSE = 5 FT

$T_w = 2000^\circ R$

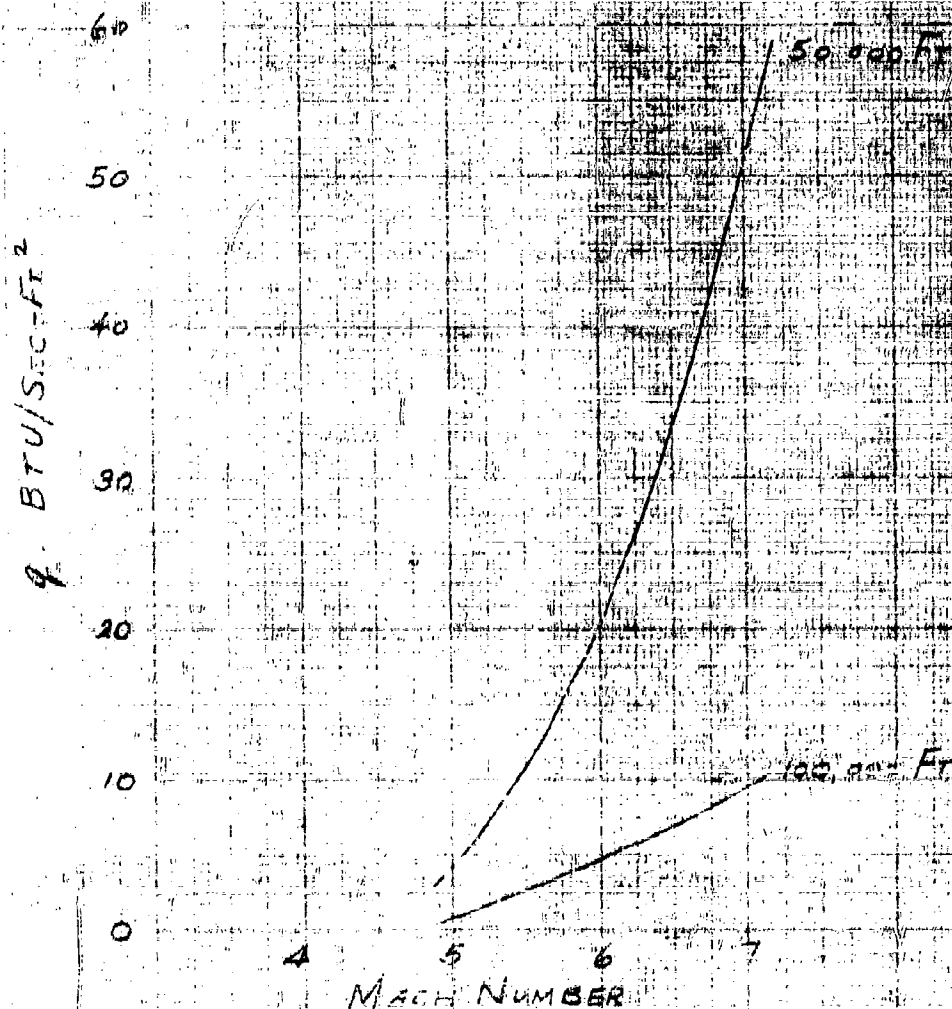


Figure 17

FIG. 17- TURBULENT CONVECTIVE HEAT
TRANSFER TO CONE

CONE ANGLE = 20°

DISTANCE FROM NOSE = 5 FT

$T_w = 2000^\circ R$

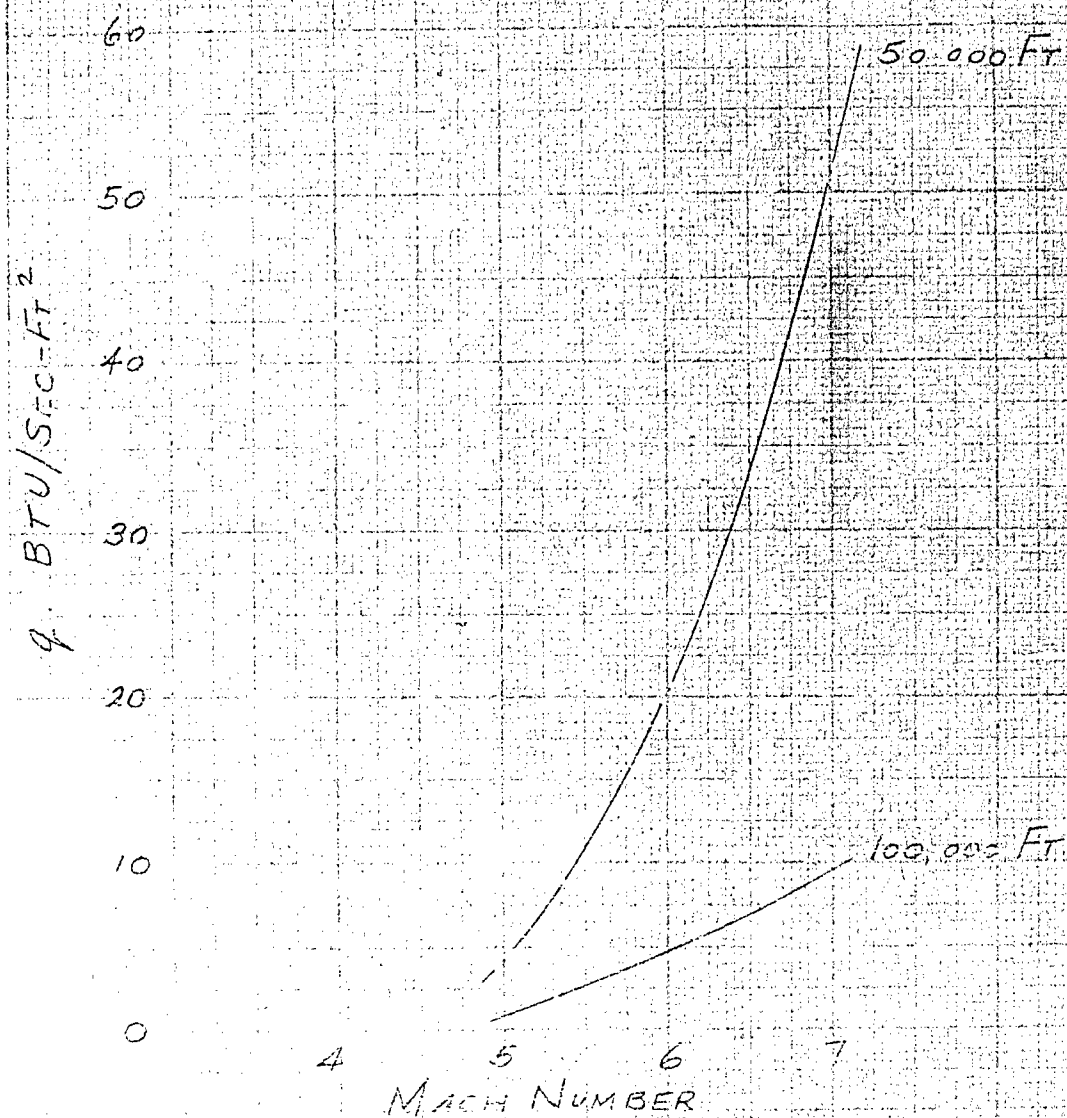
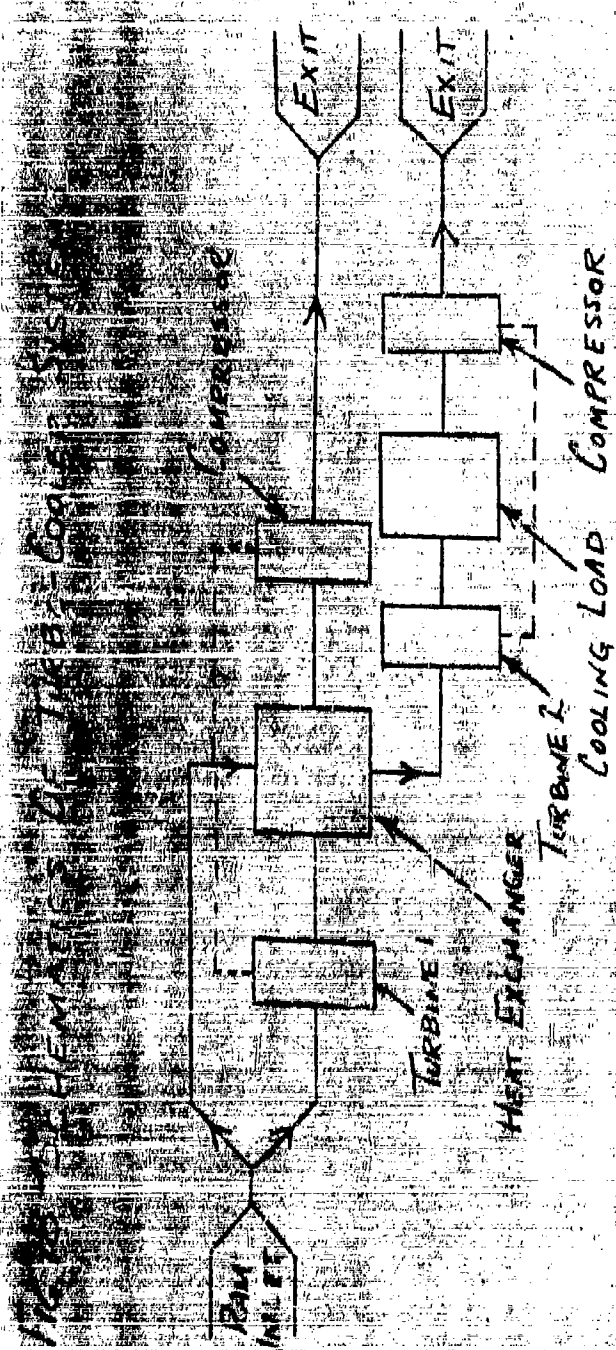
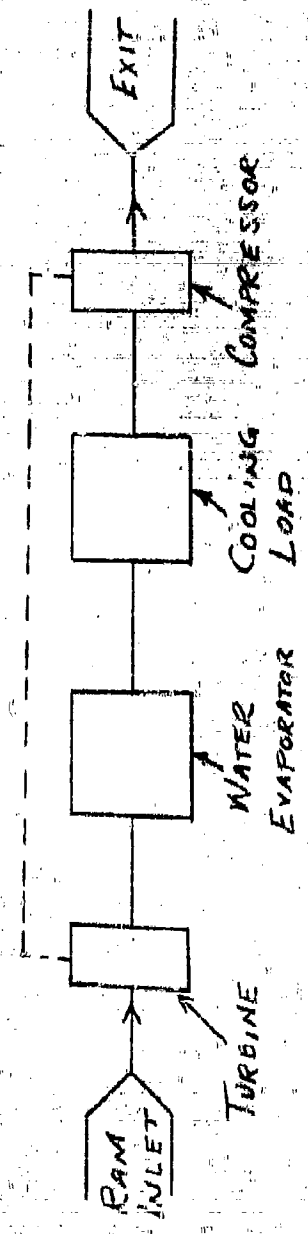


Figure 17



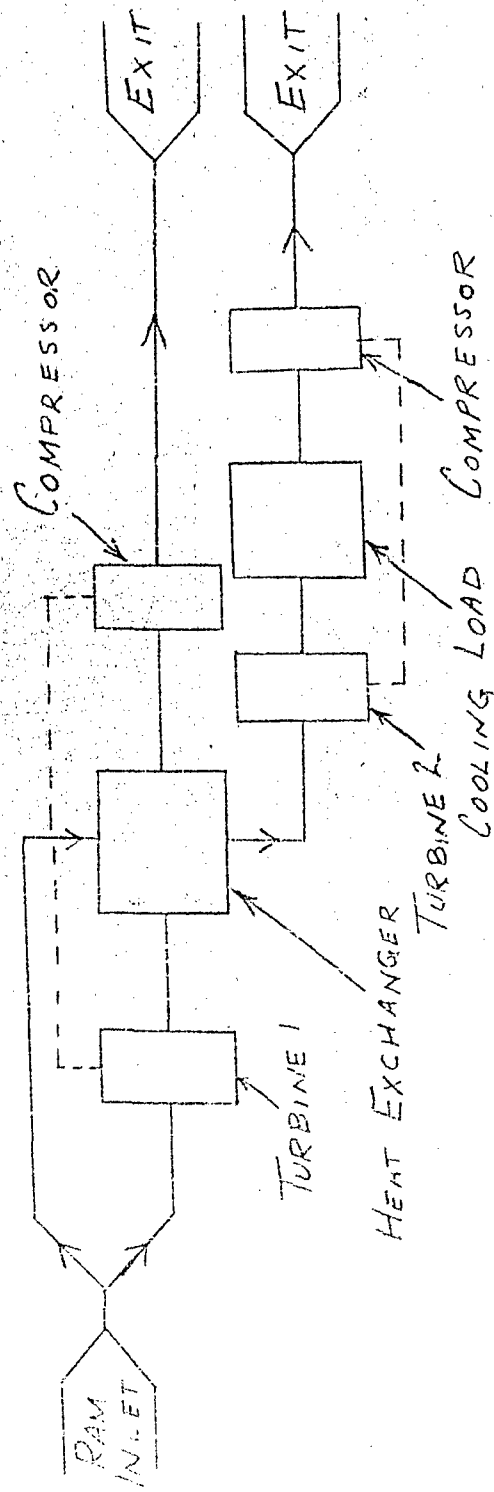
TURBO-COOLER SYSTEM 1



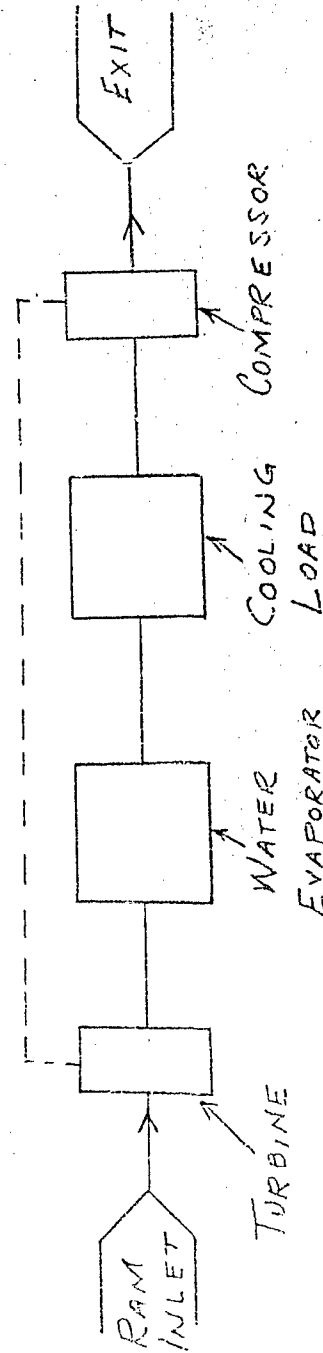
TURBO-COOLER SYSTEM-2

Figure 18

FIG. 18 - SCHEMATICS OF TURBO-COOLER SYSTEMS



TURBO-COOLER SYSTEM 1



TURBO-COOLER SYSTEM-2

FIG. 19-DISCHARGE PRESSURES AND TEMPERATURES
OF TURBO-COOLER SYSTEM I

$M=6$ 100,000 FT

2200 TURBINE EFFICIENCIES = .85

HEAT EXCHANGER EFFECTIVENESS = .90

RAM RECOVERY TO EXCHANGER = .30

2000 PRESSURE DROP FRACTION
ACROSS HEAT EXCHANGER = .20

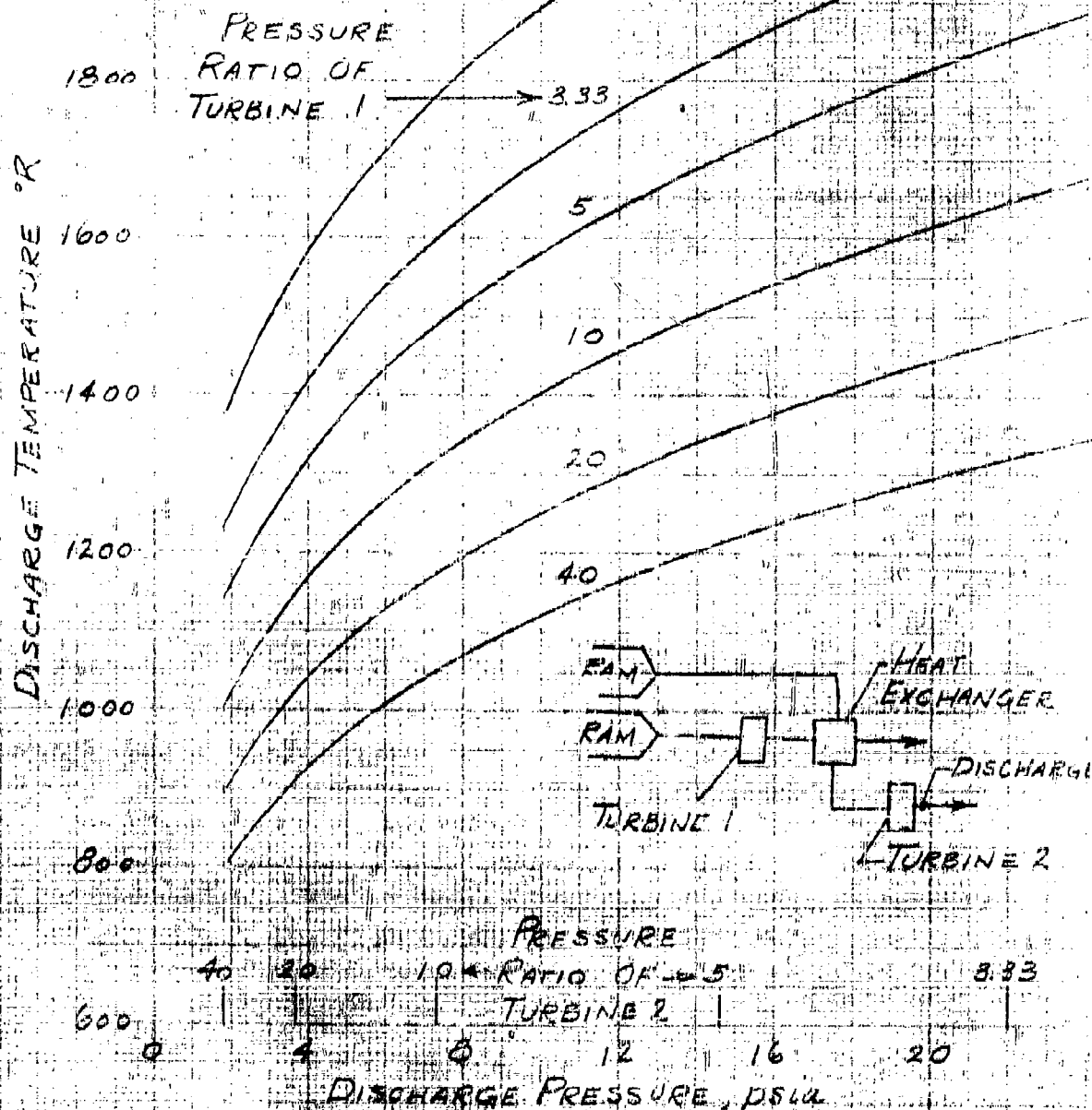


Figure 19

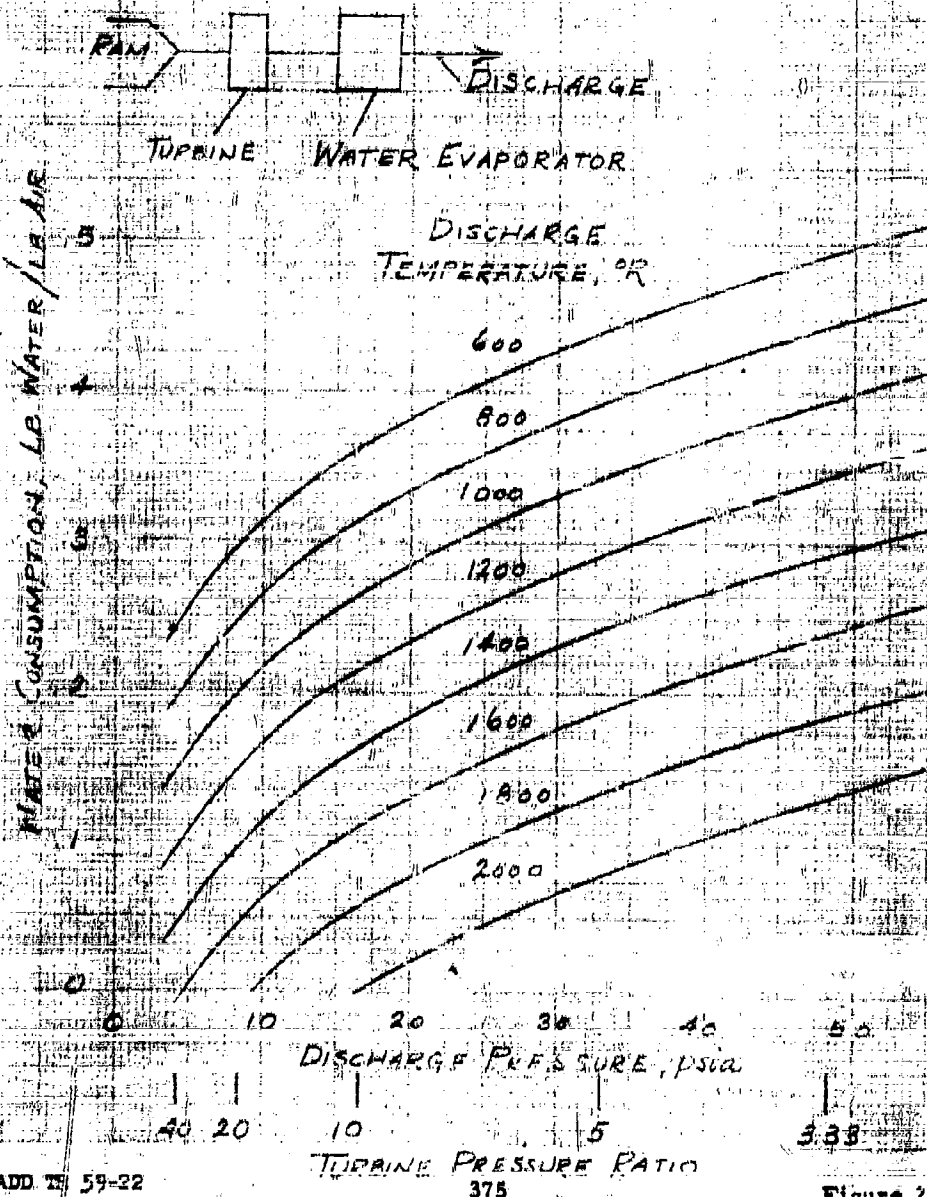
FIG. 20-WATER CONSUMPTION OF TURBO-COOLER SYSTEM 2

$M = 6 \quad 100,000 \text{ ft}$

RAM RECOVERY TO TURBINE = .60

PRESSURE DROP FRACTION ACROSS EVAPORATOR = .10

TURBINE EFFICIENCY = .85



CHAPTER II - PART B

RADOME COOLING ANALYSIS

c.. Cooling Effects of Localized Mass Addition -
by Martin H. Bloom*

*Professor of Aeronautical Engineering, Polytechnic Institute of Brooklyn.

TABLE OF CONTENTS

<u>Section</u>	<u>Title</u>	<u>Page</u>
	Summary	378
	Symbols	379
1.	Introduction	381
2.	Engineering Analysis and Calculation	392
	References	396
	Figures	398

B. RADOME COOLING ANALYSIS

c. COOLING EFFECTS OF LOCALIZED MASS ADDITION

SUMMARY

An engineering calculation based on the current state-of-the-art is presented to estimate some effects of local coolant addition on the surface temperature of a blunt-nosed body in steady supersonic flight. A review of the current state of knowledge concerning the cooling effects of local mass addition is presented as an introduction.

SYMBOLS

G	mass-flow-rate (lb/sec)
M	Mach number
P	Prandtl number assumed constant and equal to 0.72 for air
T	temperature ($^{\circ}\text{R}$)
u	streamwise velocity (ft/sec)
x	streamwise distance along body surface measured from injection slot (ft)
α	cone half-angle (degrees or radians)
ϵ	effectiveness factor (non-dimensional)
μ	absolute viscosity (slugs/ft. sec)
ρ	density (slugs/ft ³)

Subscripts

aw	adiabatic surface (different from equilibrium surface)
e	local inviscid conditions
j	coolant
max.	maximum value
r	reference condition for evaluation at some reference temperature (see note following equation 4)
s	stagnation conditions

w surface conditions
we surface conditions under equilibrium
 ∞ undisturbed flight conditions

1. INTRODUCTION

The purpose of this paper is to present an engineering estimate of some effects of localized cooling or mass addition on radome-type bodies under typical flight conditions. First, however, a review of some pertinent available information will be given.

The literature concerning the effects of local mass addition on surface temperatures and heat transfer is not extensive. Much of this work has dealt with cooling by means of liquid films, for example, as such films are applied to combustion chamber linings. In these studies, the persistence of the film in its liquid state has usually been considered to be an important factor (see for example References 1 to 3). Less work has been done with gaseous injection or with injected liquids which are immediately vaporized to the gaseous state. Pertinent in this regard are References 4 to 10.

The present paper is concerned only with the gaseous injection case, and more particularly with air-to-air injection effects. The boundary layer flow is considered to be turbulent, since mass addition has a strong destabilizing effect, and since a conservative estimate of the heat loads is desired. Bodies of revolution, specifically blunted cones, are dealt with primarily and are expected to yield results which will be reasonably valid for other similar shapes.

The manner in which mass is added to a local region may have a significant influence on the propagation of the cooling effect and on its subsequent effectiveness. Studies have been made of the following types of procedure:

Case 1. Mass addition through a strip of porous material located at the leading edge of a flat plate. Theoretical analyses of compressible laminar flow are given in References 5 and 6. Comparable analyses for bodies of revolution have not been made. In this case injection velocities are quite small. In fact it is demonstrated in Reference 6 that a major part of the cooling effect would be obtained by replacing the porous strip by a solid strip kept cool by some other means such as internal convective cooling. The cooled strip thus acts as a heat-sink. The primary effect of the porous injection is to keep the leading edge strip cool; although the mass addition gives an additional cooling effect which, while secondary, may be significant if the coolant mass flow is sufficiently large. For this reason theoretical analyses such as that of Ref. 11 which permit a treatment of discrete cooled strips along a surface, but without mass addition, can still be of use in the present case to provide first-order cooling effects of a sequence of local cooling regions. The analysis of Reference 11 applies to turbulent incompressible flow on a flat plate. Useful adaptation of its results are given in References 4 and 12.

Cooling strips located downstream of the leading edge as well as multiple strips can be treated by this method. Comparable cases with true mass addition through porous strips have not been treated. Experimental data on the effects of porous strips are not available.

Case 2. Mass addition through a single slot with the coolant flow directed tangent to the surface in the same direction as the main stream. Experiments in this category for low-speed, constant-density, turbulent flow over flat plates with air-to-air injection have been described in References 4, 10 and 12. Early work of Weighardt is described in all these references. Additional experimental results are given in Reference 10. Theoretical correlations based on the heat-sink analysis cited previously under Case 1 are presented in References 4 and 12.

In the aforementioned low-speed experiments, the momentum of the injected coolant jet ($\rho_j u_j$) was always smaller than the outer flow momentum ($\rho_e u_e$). In fact it was concluded that the alteration of the original boundary layer velocity distribution because of mixing with the coolant had a negligible influence on the thermal properties in a region "far" from the slot (say on the order of 50 or more slot-widths downstream of the slot). It is this far-region which can be correlated analytically. Fortunately, it is this far-region which governs the main decay of the cooling effect and is therefore of prime interest.

The region very near the slot is dominated by the boundary layer within the coolant jet alone. It can be analyzed by considering a conventional boundary layer to exist at the surface, the flow conditions at the outer limit of this boundary layer being equal to the velocity, pressure and thermodynamic state of the coolant stream alone. The intermediate region between this near-the-slot region and the aforementioned far-from-the-slot region has not been treated theoretically up to now. However, in practice it is suitable to consider that the surface temperature up to the far-region will be maintained at the temperature of the coolant. This implies that in the region near the slot the coolant stream completely blocks external heat transfer, and moreover assumes that there is no additional heat transfer from the surface-interior through the surface to the coolant. This simplification is sufficiently accurate for engineering purposes.

A different type of tangential slot injection is described in Reference 9. Helium, chosen for a special reason, is utilized as the coolant when air is the mainstream gas. In this system the purpose is to minimize mass-mixing of the coolant-film with the mainstream by minimizing the difference in velocity of the two streams, over a range of velocities if necessary. Thus, the integrity of the low-temperature insulating layer is maintained for a significant distance and the heat transfer through the coolant takes place primarily by a more static form of conduction. In

Reference 9 it was desired to keep the stagnation pressure of the coolant on the same order as that of the mainstream. Therefore, since the local static pressures in the two streams would be equal, it was necessary to have the stagnation enthalpies of the coolant and air about equal to enforce equality of the velocities. Since the heat capacity of helium is about 5 times that of air, the stagnation temperature in the air could be about 5 times that of the helium for matching velocities. In this method the point must be considered that the thermal conductivity of helium is on the order of 7 times that of air, a property which works to the disadvantage of the insulating system.

In Reference 9, the helium-film method was applied to the cooling of a nozzle throat. Velocities were matched between the Mach number 0.4 and 3.0 stations. Effective cooling was achieved with helium mass flows of 3 to 4% of the main air flow. Air injection at 6 and 12% of the main air mass flow was appreciably less effective; velocity matching was not achieved with air.

Some additional effects of tangential injection obtained by injection near the stagnation point of a blunt body of revolution (Reference 8) will be cited at the end of the discussion of Case 3.

Case 3. Mass addition through a single slot with the coolant flow injected in a direction other than that of the main stream. Some

experimental data of coolant injection perpendicular to a flat plate in turbulent low-speed flow, utilizing a single slot in an air-to-air system, is presented in Reference 10. This data generally indicates a decrease in effectiveness over that achieved with tangential injection; although with non-tangential injection, consideration must be given to whether the injected jet disturbs appreciably the flow outside the boundary layer, that is, the consequent inviscid flow pattern. No information on this factor is given in Reference 10, but presumably the pressure distribution over the plate was not severely altered by the injection. An idea of the relative effectiveness of the tangential and normal injection systems can be obtained by considering the following results of Reference 10 giving the temperature distribution on an insulated plate "far" downstream of the injection slot;

$$\text{tangential injection: } \frac{T_{we} - T_e}{T_j - T_e} \approx 15 \text{ to } 30 \left(\frac{\rho_j u_j d_j}{\rho_e u_e x} \right)^{0.7} \quad (1)$$

$$\text{normal injection: } \frac{T_{we} - T_e}{T_j - T_e} = 2.2 \left(\frac{\rho_j u_j d_j}{\rho_e u_e x} \right)^{0.5} \quad (2)$$

where all quantities are defined in the list of symbols. The numerical coefficients in (1) and (2) are Reynolds-number-dependent. More precisely that of (1) is given as $0.83 (\rho_j u_j d_j / \mu_j)^{1/3}$ for $(\rho_e u_e x / \rho_j u_j d_j) > 40$, and in the range $1000 < (\rho_j u_j d_j / \mu_j) < 10,000$. The results of Weighardt,

cited for example in Reference 10, give an exponent of 0.8 rather than 0.7 in expression (1) for tangential injection.

It is seen from (1) and (2) that for a given distance x downstream of the slot and for equal coolant and external flow conditions the temperature factor (left-hand side of (1)) for tangential injection is on the order of 3 to 5 times higher than that for normal injection; that is, the surface temperature T_{aw} is closer to the coolant temperature T_j .

The cooling effect of a single jet of coolant directed upstream with respect to the main flow and located at the nose of a body of revolution has been studied in References 7 and 8 at Mach numbers of about 6. Jets of this kind generally stagnate against the oncoming mainstream and then are blown back over the surface of the body aiding the formation of a layer of low-energy air which has an insulating effect. Both air and liquid water which subsequently vaporized were used as coolants in Reference 7. Nitrogen and helium were used in Reference 8. When a liquid is used as coolant, its heat of vaporization may have an important additional cooling effect by acting as a heat-sink which absorbs an appreciable part of the energy contained in a streamtube of air approaching the body. In the tests of Reference 8 it was found that helium, a light gas with a specific heat about 5 times higher than air, was much more effective than nitrogen for a given mass-flow-rate of coolant. This comparatively good cooling effect of helium or other light gases usually is found in other types of

mass addition systems as well.

In cooling by means of a jet directed upstream, it may be necessary to take into account the influence of the jet on the surrounding flow field not only in the viscous region but outside as well. Jets of large momentum or mass-flow may distort the shock shape or oncoming streamlines, thereby altering the effective shape of the body. For example, the upstream jet may effectively "sharpen" a blunt body reducing the pressure in the forward nose region, thus reducing the pressure drag as well as the heat transfer over the body.

The experimental cooling results obtained at Mach 6 in Reference 7 using an upstream jet of air at the nose of a cone will be utilized later in this report to provide the order of magnitude of an empirical "effectiveness factor" for localized mass addition on bodies of revolution. This empirical factor is roughly analogous to the numerical coefficients in (1) and (2) for example.

In Reference 8 a slot-injection system was also examined by placing a small button-like deflector in front of the jet at the nose of the body. Thus the coolant was injected tangent to the blunt nose of the body. The "sharpening" effect of the jet was diminished in this way, and the pressure decrease at the nose was much less pronounced. However, it is interesting to observe that this tangentially directed cooling was significantly

less effective than the open jet for a given mass-flow-rate of coolant for both nitrogen and helium.

For the types of slot injection categorized under Case 3, no work has been reported of the cooling effects of local-mass-addition positions located away from the most forward nose station, or of a series of discrete cooling positions. Furthermore, the influence of the detailed velocity and momentum characteristics of the injected jets on their cooling effectiveness has not been studied.

As previously mentioned, the purpose of this paper is to provide an engineering estimate, within the current state-of-the-art, of the cooling effect of one or more local air injection slots or orifices on blunted bodies of revolution characteristic of radome or other similar nose shapes. For this purpose only blunted cones will be considered here as a representative shape insofar as cooling effects are concerned. Moreover the detailed nature of the blunted foremost region will not be considered, since this rather small region can be cooled with relatively little difficulty by coolant added in its immediate vicinity or by special means such as internal convective cooling. Rather, emphases will be placed on the cooling of the conical skirt.

The following assumptions will be employed in addition:

1. Steady conditions of continuous supersonic flight
2. The cones are sufficiently blunt that the stagnation pressure

in the inviscid flow over the skirt is equal to the stagnation pressure behind a detached normal bow shock. This will also be the case if a sharp cone is "blunted" by a sufficiently large jet injected upstream at its vertex.

3. The static pressure over the conical skirt is not appreciably disturbed by the coolant and is equal in value to the static pressure on a sharp cone of the same cone angle.

4. The cooling effect of an injection point or slot can be represented as a heat-sink whose functional form can be deduced analytically, but whose strength, expressed in terms of an "effectiveness factor", must be determined empirically.

5. The ratio of the effect of a series of streamwise-spaced injection slots to the effect of a single slot can be deduced for two-dimensional low-speed flow (see Figure 9 of Reference 4). This ratio will be assumed to be the same for supersonic flow over bodies of revolution, although this has not been proved. This assumption is in keeping with the current state-of-the-art and is expected to yield a reasonable concept of the order of magnitude.

6. The effects of heat loss from the surface by radiation are neglected.

7. The specific heat at constant pressure c_p is assumed constant.

8. When a series of cooling slots is considered, the slots are assumed to be so spaced that the same value of the maximum allowable

surface temperature is reached immediately before each slot, and the total mass-flow-rate of coolant from all the slots in a given series is equally distributed among the individual slots. It will be noted that under these conditions the slots will not be equally spaced.

9. The heat loss to the interior of the body is assumed to be negligible in the steady state, since no other cooling devices except local mass addition are assumed to be active here.

10. In the numerical calculations, the following values are considered:

altitudes	sea level to 150,000 ft.
flight Mach numbers	3 to 7
cone half-angle	20°
cone base-diameter	3 ft.
length of cone-generator	4.39 ft.

2. ENGINEERING ANALYSIS AND CALCULATION

For calculating the surface temperature of a body in steady flight when no heat is transmitted to the interior of the body by conduction or other cooling media, we consider the body to act as a perfect insulator as far as heat transmission to the interior is concerned. Under these conditions, the surface of the body assumes the temperature of the air in the boundary layer directly adjacent to it. When no other influences such as external cooling media or radiation are present, the resulting surface temperature is usually termed the "adiabatic surface temperature" T_{aw} . This temperature is close in value to the stagnation temperature T_s of the flow, although it may be as much as 10 or 15% below T_s . For constant c_p , the value of T_{aw} is given by the following relation:

$$\frac{T_{aw} - T_e}{T_s - T_e} = r \text{ (recovery factor)} \quad (3)$$

where $r \approx 0.9$ for turbulent boundary layers.

When cooling or heating media are present at the exterior of the body or when radiation heat transfer occurs, the resulting surface temperature may be changed from the value T_{aw} , and the altered temperature may be termed the "equilibrium surface temperature" T_{we} .

It is shown in Reference 7 that on a conical surface, when one coolant injection point is located near the vertex of the cone the equilibrium surface

temperature may be expressed as follows:

$$\frac{T_s - T_{we}}{T_s - T_j} = \left(\frac{132 P^{2/3}}{2\pi \sin \alpha} \right) \frac{\epsilon G_j}{\mu_e} \left(\frac{T_r}{T_e} \right)^{-0.6} \left(\frac{\rho_e u_e}{\mu_e} \right)^{-0.86} x^{-1.86} \quad (4)$$

(Note: The reference temperature T_r here is analogous to the "reference temperature" of Rubesin-Johnson and Eckert (see Reference 7 for example). It is used in boundary layers without mass addition to take into account empirically some compressibility effects, and depends on surface temperature and inviscid flow conditions. For present purposes it will not be evaluated explicitly (see Equation 6).)

An equation analogous to (4) is derived in Reference 7 for two-dimensional flow as well as for conical flow. The two-dimensional relation of Reference 7 is shown to be reducible in form to that of (1) of this paper.

From a series of tests in Reference 7 for upstream jet injection on cones the following value of the effectiveness factor ϵ is obtained.

$$\epsilon = 0.045 \quad (5)$$

Although this value may vary somewhat with Mach number and Reynolds number, as well as with the precise method of coolant injection, it is assumed to apply in the present case for order of magnitude purposes. (The test conditions of Reference 7 were Mach 6, stagnation pressure

600 psia, stagnation temperature 1700°R, test Reynolds number per foot 3.8×10^6 , cone half-angle 25°.) The required mass flows calculated using (5) can be considered to vary inversely with ϵ if new data should become available.

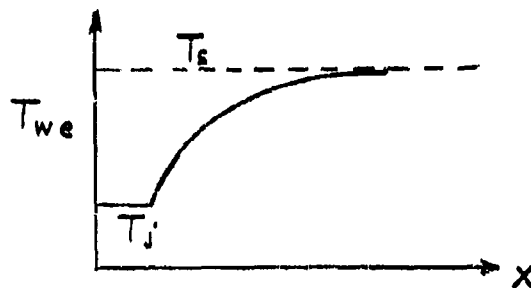
For calculation purposes here, it is sufficient to assume that in (4)

$$(T_r/T_e)^{-0.6} \approx 1 \quad (6)$$

With (5) and (6) we can now proceed to calculate the value of G_j required if a given maximum value of T_{we} is prescribed to exist at the end of the cone, that is, at

$$x = 4.39 \text{ ft.} \quad (7)$$

It should be noted that the surface temperature along the cone will vary in the following qualitative manner:



Calculations show that over the altitude and Mach number range specified, (4) can be approximated as follows:

$$G_j/K = 0.08 M_\infty \left(\frac{T_s - T_{we, \max.}}{T_s - T_j} \right) x_{\max.}^{1.86} \quad (8)$$

where K is a factor which varies with altitude as follows:

Table 1

<u>Altitude (ft.)</u>	<u>K</u>
0	47.
50,000	7.5
100,000	1.0
150,000	0.17

Values of G_j are calculated from (8) for the case of $M_\infty = 6$ and 100,000 ft. ($k = 1.0$). These are presented in Figure 1. A range of values $400 \leq T_j \leq 2000^\circ\text{R}$ and values of $T_{we, \max.} = 1500^\circ\text{R}$ and 2000°R were assumed. To make estimates for other Mach numbers, it must be remembered that T_s in (8) depends on M_∞ . However, it will be found that G_j increases with increasing M_∞ .

To obtain the effect of using several slots with the total coolant rate distributed equally among them, the proportionate coolant flow for a given temperature factor $\left(\frac{T_s - T_{we, \max.}}{T_s - T_j} \right)$ was obtained directly from Figure 9 of Reference 4. The proportional scaling down of the mass flow is not sensitive to variations in the temperature factor.

From the results of this calculation the expected trends are noted; the required mass flow of coolant increases with decreasing altitude, with increased Mach number and with a decrease in the number of slots utilized.

REFERENCES

1. Knuth, E. L., The Mechanics of Film Cooling - Parts 1 and 2 - Jet Propulsion, November-December, 1954, pp. 359-364 and January 1955, pp. 16-25.
2. Kinney, G. R. - Abramson, A. E. and Sloop, J. L. - Internal-Liquid-Film-Cooling Experiments with Air-Stream Temperatures to 2000°F in 2- and 4-Inch-Diameter Horizontal Tubes - NACA TN 1087, 1952.
3. Warner, C. F. and Reese, B. A. - Investigation of the Factors Affecting the Attachment of a Liquid Film to a Solid Surface - Presented at American Rocket Society Fall Meeting, Buffalo, New York, September 24-26, 1956.
4. Eckert, E. R. G. and Livingood, J. N. B. - Comparison of Effectiveness of Convection-, Transpiration-, and Film-Cooling Methods with Air as Coolant, NACA Report No. 1182, 1954
5. Libby, P. A. and Pallone, A. - A Method for Analyzing the Insulating Properties of the Laminar Compressible Boundary Layer - Journal of the Aeronautical Sciences, Vol. 21, No. 12, December 1954, p. 825.
6. Rubesin, M. W. and Inonye, M. - A Theoretical Study of the Effect of Upstream Transpiration Cooling on the Heat-Transfer and Skin-Friction Characteristics of a Compressible, Laminar Boundary Layer -

NACA TN 3969, May 1957.

7. Ferri, A. and Bloom, M. H. - Cooling by Jets Directed Upstream in Hypersonic Flow - Polytechnic Institute of Brooklyn, WADC TN 56-382, May 1957.
8. McMahon, H. M. - An Experimental Study of the Effect of Mass Injection at the Stagnation Point of a Blunt Body - California Institute of Technology CALCIT, Hypersonic Research Project, Memo No. 42, May 1, 1958.
9. Ferri, A. and Libby, P. A. - The Use of Helium for Cooling Nozzles Exposed to High Temperature Gas Streams - WADC TN 55-318, July 1955.
10. Seban, R. A., Chan, H. W., and Scesa, S. - Heat Transfer to a Turbulent Boundary Layer Downstream of an Injection Slot - Presented at A.S.M.E. Annual Meeting, December 1957, A.S.M.E. Paper 57-A-36.
11. Rubesin, M. W. - The Effect of an Arbitrary Surface-Temperature Variation Along a Flat Plate on the Convective Heat Transfer in an Incompressible Turbulent Boundary Layer - NACA TN 2345, April 1951.
12. Tribus, M. and Klein, J. - Forced Convection from Nonisothermal Surfaces - Proceedings of the 1952 Heat Transfer Symposium, University of Michigan, 1953.

$$G_j/K = 0.08 M_\infty \left(\frac{T_s - T_{w_e, \text{MAX}}}{T_s - T_j} \right) T_{\text{MAX}}$$

$$\epsilon = 0.045 \text{ (FROM REF. 7), } G_j \sim \frac{1}{\epsilon}$$

alt,	K
0	47
50,000	7.5
100,000	1.0
150,000	0.17

SLOTS SPACED TO GIVE
SAME $T_{w, \text{MAX}}$ BEFORE EACH
SLOT (NACA REP 1182
EXTRAPOL.)

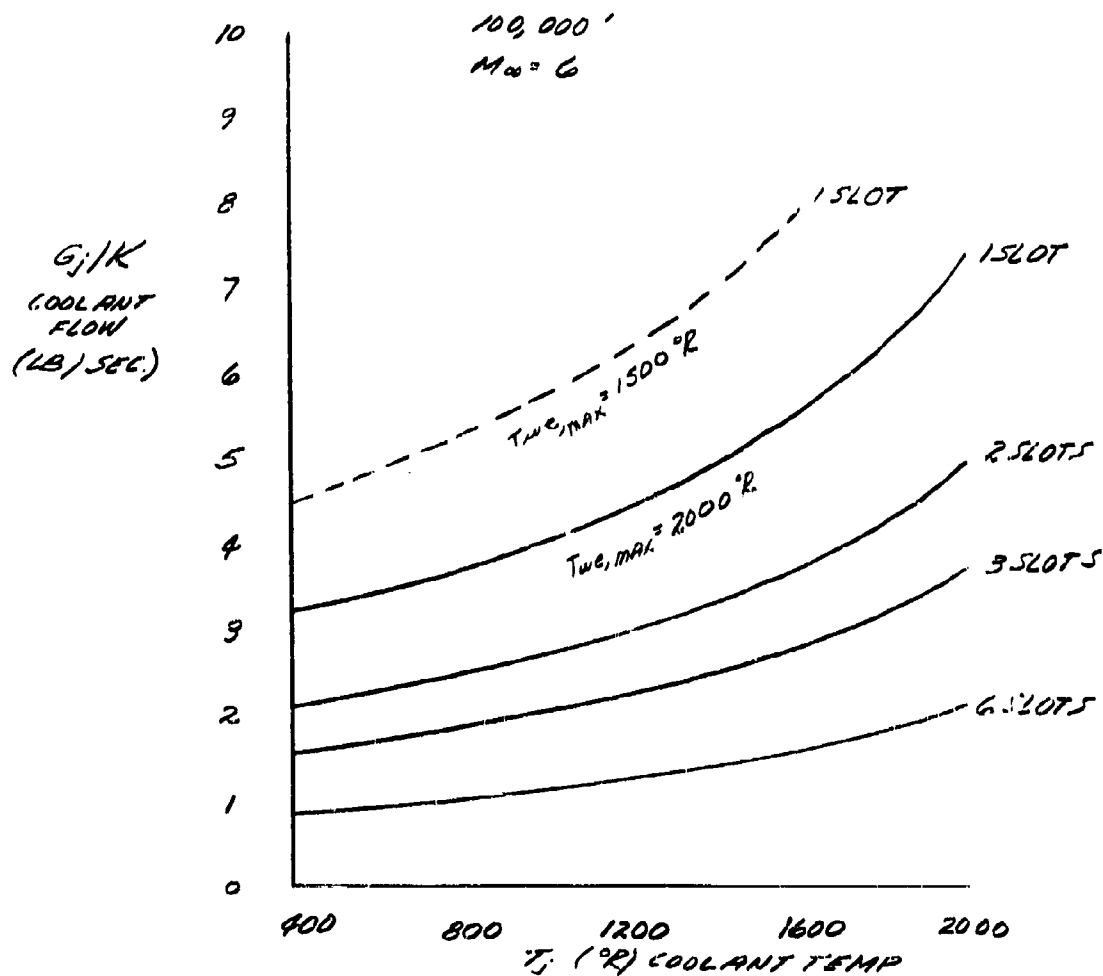


FIG. 1. ESTIMATE OF COOLING EFFECTS OF LOCAL SLOT
AIR-TO-AIR INJECTION ON AN INSULATED BLUNT CONE

CHAPTER II - PART B

RADOME COOLING ANALYSIS

- d. Comparison of Transpiration, Convective and Film Cooling - by Melvin Epstein, Alfred A. Marino and Martin H. Bloom *

*Professor of Aeronautical Engineering, Polytechnic Institute of Brooklyn

B. RADOME COOLING ANALYSIS

d. COMPARISON OF TRANSPIRATION, CONVECTIVE AND FILM COOLING

In Part A of this Chapter it was pointed out that one of the important parameters which determined the feasibility of a cooling system is the rate at which coolant must be supplied. If the coolant is carried along with the vehicle, large coolant flow rates over long periods of time cannot be tolerated because of weight and space requirements. Alternatively, if ram air is used as the coolant, the size, weight and complexity of the machinery necessary to reduce the temperature of the ram air increases. Further, large coolant flow rates require large internal pressures which may be unacceptable from the strength standpoint.

A comparison of the coolant flow rates required using a transpiration cooling system, a convection cooling system and a slot cooling system has been made utilizing the analyses presented in Sections a, b and c. Such a comparison is presented in Figure 1 for the spherically blunted cone described in the Introduction. The data are presented in the form of curves of coolant weight flow versus coolant air temperature at a typical flight condition of $M_{\infty} = 6$ and an altitude of 100,000 feet. The wall temperature is taken to be 2000°R . The curve for transpiration cooling was obtained assuming a uniform porosity material with a pressure drop of 1 psi per cubic foot per minute per inch of thickness. Three curves are presented for the convection cooling case. The lower curve corresponds to the ideal case of infinite coolant pressure, i. e, minimum weight

flow. The upper curve is obtained by using the same pressure that is required to cool the radome by transpiration cooling. The middle curve gives the variation of weight flow required for cooling when the pressure has the value which just causes choking of the channel. It is seen that convection cooling cannot be accomplished at the same pressure as transpiration cooling, but must be accomplished at a higher pressure (in this particular example). The results of the slot cooling analysis are presented for one- and two-slot systems.

The effects of radiation are not considered in this comparison. It was shown in the discussion of convection cooling that at a wall temperature of 2000°R , radiation has a significant effect on the required cooling rates. However, the radiation heat transfer depends only on the wall temperature. All cooling methods would therefore be affected to the same extent by radiation.

Inspection of Figure 1 shows that, from purely weight flow considerations, transpiration cooling is superior to the other two methods of cooling. At low temperatures, convection cooling requires weight flows which are only slightly higher than those required for transpiration cooling; at high coolant temperatures a larger difference between the two methods exists. The coolant flow rates required for slot cooling are apparently much greater than those required by the other two methods. It is noted, however, that the state-of-the-art of both the theoretical and experimental work

concerned with slot cooling is still in a quite primitive form. In the present slot cooling analysis, it is necessary to employ an empirical cooling effectiveness parameter which can only be obtained from experiment. The experiments from which the cooling effectiveness parameter was obtained for this investigation, were essentially of an exploratory nature. There is little doubt that the cooling effectiveness measured in those experiments could be considerably improved upon by, say, proper shaping of the slots.

It is important to note that the selection of a method of cooling is by no means determined solely by coolant weight flow considerations. The above results should be interpreted rather as the fluid-mechanical part of the analysis of a radome cooling study. There are many other considerations which have to be made in evaluating the proper system to use for a given application. For example, the particular trajectory that the vehicle is flying may very well be an overriding consideration. Thus, if the vehicle is flying a ballistic trajectory, a heat sink or ablation scheme may be the appropriate one to use.

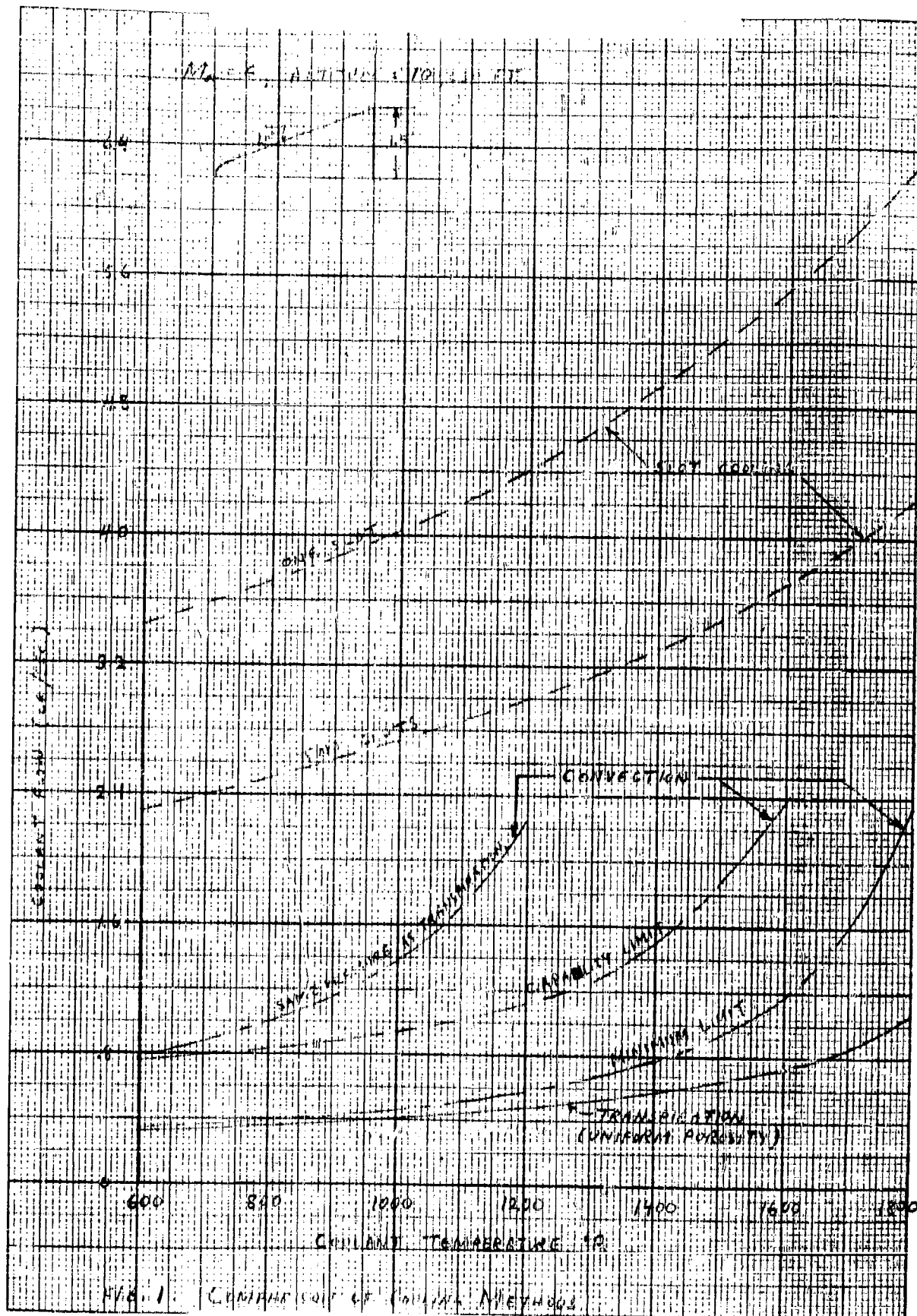
The strength and electrical characteristics of the radome material must also be carefully considered when the cooling analysis is made. In all methods using a coolant, the interior of the radome must be pressurized. For high coolant flow rates, the pressure differential across the radome wall may become intolerable from the strength standpoint.

At first glance, it might appear that since transpiration cooling requires a smaller internal pressure than convection cooling, the former might be preferred under high weight flow conditions. However, at a given temperature, a porous wall has considerably less strength than a solid wall. It may therefore be preferable to use convection or slot cooling. This problem is further complicated by the fact that the average wall temperature, for a given external skin temperature, is higher for convection cooling than for transpiration cooling so that the supposed high strength of the solid wall may not really exist. Under very high coolant flow rate conditions, the internal pressures required for transpiration and convection cooling may be so high that a slot scheme might be more appropriate.

It can be seen from these discussions, that the proper choice of a cooling system must take into consideration all of the factors discussed above. Thus suppose that the vehicle trajectory is such that one of the three methods discussed above must be chosen. If the peak heating load occurs at a sufficiently high altitude so that the internal pressure is tolerable, then transpiration cooling may be the better system to use, providing that there are no other design factors which have to be compromised with. On the other hand, if the peak heating load occurs at a low altitude with the associated high internal pressures, it would be necessary to make a detailed study of the structural problem to decide which system to use.

It is also noted that each of these cooling systems have an effect on the performance of the vehicle which may be significant, especially for long range aircraft. Thus, it is known that transpiration cooling reduces not only the heat transfer to the body but also the skin friction. In the convection cooling case, it may be possible to discharge the heated coolant in such a manner as to gain some thrust. Similarly, in the slot cooling method, appropriate designing of the shape and location of the slots may result in a small amount of thrust.

As mentioned in Part A of this Chapter, the investigations reported herein were carried out for only one body shape using air as the coolant. Although the qualitative trends predicted above should hold for other closely related shapes and other coolants, it is believed that further study is warranted to define more clearly the limits of applicability of the various cooling techniques. For example, the slot cooling method is extremely effective in the immediate neighborhood of the slot. It may therefore compare much more favorably with the other methods of cooling when applied to bodies of small fineness ratio. It appears that in order to draw any more specific conclusions regarding the choice of a cooling system, it is necessary to consider a specific configuration traveling a particular trajectory.



CHAPTER II - PART C

THE EFFECT OF UPSTREAM TRANSPIRATION COOLING ON
THE COMPRESSIBLE, TURBULENT BOUNDARY LAYER

- a. Analytical Investigation -
by Harold S. Pergament

TABLE OF CONTENTS

<u>Section</u>	<u>Title</u>	<u>Page</u>
	Summary	408
	Symbols	410
1.	Introduction	413
2.	General Method of Analysis	420
3.	Porous Section	423
4.	Non-Porous Section	428
5.	Effects of Convective and Radiative Heat Transfer in Non-Porous Section	434
6.	Results and Conclusions	436
	References	439
	Table I	440
	Appendix A	441
	Appendix B	448
	Appendix C	451
	Figures	452

C. THE EFFECT OF UPSTREAM TRANSPIRATION
COOLING ON THE COMPRESSIBLE, TURBULENT
BOUNDARY LAYER

a. ANALYTICAL INVESTIGATION

SUMMARY

An analysis of the compressible turbulent boundary layer over a cone with upstream transpiration cooling has been made, and the results applied to a free stream Mach number range of 5 to 7. Modifications of existing studies (Refs. 1 and 2) have been used to determine the skin friction and other important properties in both the porous and non-porous regions. From this knowledge, and the use of the momentum and energy integral equations, an engineering solution for the adiabatic wall temperature downstream of the junction is obtained. The effectiveness of this cooling technique is shown to be measured by the rate of increase of adiabatic wall temperature along the body. Curves are presented which show this increase as a function of flight condition and injection rate. The coolant mass flow requirements are also shown for a few cases.

It is concluded that the use of upstream transpiration is a feasible method for cooling radomes. Further studies will indicate more specifically the range of flight conditions and possible configurations for which this cooling method is applicable.

The author is indebted to Dr. Paul A. Libby for his many helpful suggestions in the preparation of this report.

SYMBOLS

a	parameter defined by Eq. (20)
A	parameter defined by Eq. (A15)
A'	parameter defined by Eq. (C2)
B	parameter defined by Eq. (A16), also different parameter defined by Eq. (27)
c_f	local skin friction coefficient
c_p	specific heat at constant pressure
$f(o)$	parameter defined by Eq. (18)
F	$\rho_w v_w / \rho_1 u_1$
$F[k_m, \phi_m]$	elliptic integral of first kind
g	exponential term defined by Eqs. (A22) and (A23)
g_c	conversion factor $(32.2 \frac{\text{ft-lbm}}{\text{lb}_f\text{-sec}^2})$
h	film coefficient $(\frac{q}{T_{aw} - T_w})$
H	stagnation enthalpy
k	thermal conductivity
K	mixing length parameter, $l = ky$ - also, proportionality constant for $c_f \sim x^{-1/5}$
$k_{m,n}$	parameter defined by Eqs. (A32a) and (A32b)
l	mixing length
M	Mach number
p	pressure
Pr	Prandtl number
Pr_t	turbulent Prandtl number

q	heat transfer
r	distance from axis of cone to surface
R	specific gas constant
Re_x	Reynolds number based on length
Re_θ	Reynolds number based on momentum thickness
T	absolute temperature
u	velocity in x direction
v	velocity in y direction
w_i	total mass flow of coolant
x	coordinate measured along cone surface
y	coordinate measured normal to cone surface
α	parameter defined by Eq. (A32c)
β	parameter defined by Eq. (A32d)
γ	ratio of specific heats
δ	boundary layer thickness
ϵ	emissivity
ϵ_H	eddy thermal conductivity
ϵ_M	eddy viscosity
η	dimensionless momentum thickness, defined by Eq. (22)
θ	momentum thickness
μ	coefficient of viscosity
ξ	dimensionless length, defined by Eq. (23)
ρ	density

σ	Stefan-Boltzmann constant, also parameter defined by Eq. (A32e)
τ	shear stress
ϕ	dimensionless enthalpy thickness, defined by Eq. (32)
$\phi_{m,n}$	parameter defined by Eqs. (A32a) and (A32b)
Ω	enthalpy thickness
ω	exponent in temperature-viscosity relation, see Eq. (A21)

Subscripts

a	value at edge of laminar sub-layer
aw	adiabatic wall value
c	coolant value
NT	value for no transpiration
o	value at end of porous section
r	reference value
s	stagnation value
w	wall value
1	value at edge of boundary layer
∞	free stream value

Superscripts

-	quantity averaged with respect to time
'	instantaneous fluctuating quantity
\sim	dimensionless quantity, see Eq. (A17)
+	dimensionless quantity, see Eqs. (A19) and (A20)

1. INTRODUCTION

The aerodynamic heating that accompanies high speed flight usually causes the outside surface of a missile to reach extreme temperatures. One of the methods to reduce the surface temperature is that of injecting a cool fluid through a porous wall. The principal effect of porous injection is that the coolant absorbs most of the heat, thus reducing considerably the temperature rise of the material. There are other, secondary effects, however. One of these is that the introduction of the low energy coolant decreases the energy level in the boundary layer, thus decreasing the aerodynamic heat input. Also, the injected fluid serves to decrease the velocity gradient at the wall, which, of course, indicates a smaller local skin friction coefficient. (However, since injection induces earlier transition from laminar to turbulent flow, it is possible that the overall drag will increase.)

Since the heat transfer is decreasing along the body, it is not necessary (or practical) to make the entire radome of a porous material. Only the front portion need be cooled by this method with the expectation that the downstream effect is sufficient to cool the rear. The figure on page 420 shows the configuration considered in this report.

It is always possible to keep the porous section at a low temperature by adding enough coolant. The real problem to be solved is how much mass need be injected into the boundary layer per unit time for a given flight condition, such that the surface temperature downstream of injection is kept below a prescribed maximum value. Then, for a specified trajectory, the

total amount of coolant can be computed and the feasibility of this method of cooling shown.

The use of a porous section has certain disadvantages which could reduce the usefulness of this method of cooling. The major disadvantage is that the porous region acts as a "blind spot" to the transmission and reception of radar waves. Thus, it must be reduced to the minimum possible size that will still cool the rear of the radome effectively.

The criterion for the allowable size of "blind spot" is the ratio of the cross-sectional area of the base of the radome to the cross-sectional area removed from "sight" by the porous material. No exact figures for the minimum ratio are presently available, but recent estimates * indicate that a ratio greater than from 50-100:1 should not interfere with the operation of the radar.

Other difficulties to be encountered with the use of a porous material are: method of manufacture, strength of the material, and attachment to the non-porous section. If these difficulties could be overcome and the size of the porous section does not have to be made so small that its effectiveness is curtailed, this scheme shows promise for radome cooling.

It should be pointed out here that no rational analysis presently exists for the turbulent case, which is considered in this report. This is because of the lack of fundamental information concerning the mechanics of turbulent

*Private Communication, Jack Richmond, Antenna Laboratory, Ohio State University, Columbus, Ohio

shear flows. All analyses of this type of flow require experimental data which can be incorporated in semi-empirical theories.

In the problem of the turbulent boundary layer on a partially porous wall no experimental data exist for the boundary layer properties near the discontinuity in injection ($x = x_0$) which is precisely the region of interest. Because of this unfortunate state of knowledge, crude assumptions concerning the boundary layer behavior must be made with the expectation of later experimental evaluation. Thus, in order to get an engineering solution, the momentum and energy integral equations are used and the variation of the skin friction coefficient downstream of injection is assumed.

It is known that the effects of transpiration will decrease with increasing x , and that eventually the boundary layer profiles will approach those for no upstream cooling. With this in mind there are several assumptions that can be made for c_f in the non-porous region.

For the completely non-porous wall, experiments have shown that the relation between skin friction and momentum thickness can be expressed by:

$$c_f \sim \theta^{-1/4}$$

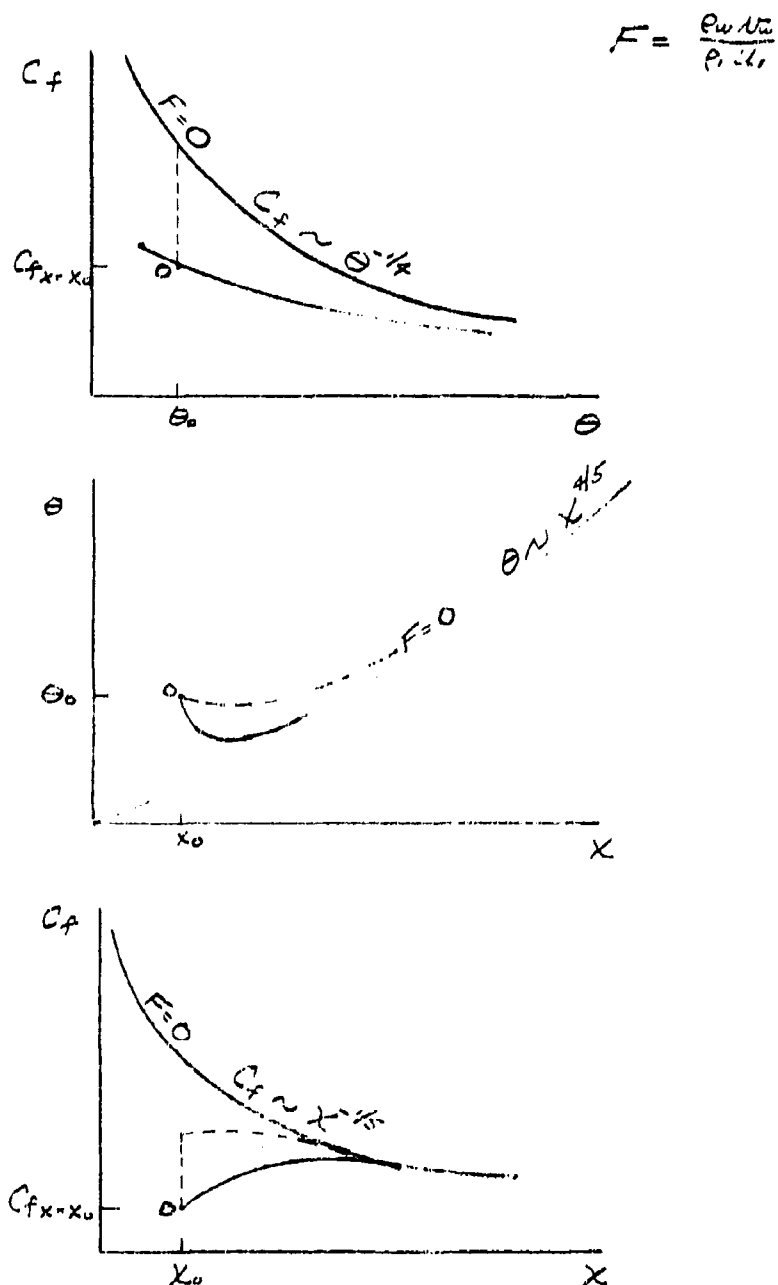
Using this in the momentum integral equation gives the relation between θ and x as,

$$\theta \sim x^{4/5}$$

and thus,

$$c_f \sim x^{-1/5}$$

The sketches below indicate some of the possibilities for the variation of c_f in the non-porous sections (point 0 indicate the values at the end of the porous region).



The most conservative assumption (largest c_f) would be that the skin friction instantaneously reverts to its zero transpiration value at $\theta = \theta_0$ (dotted path). This indicates a discontinuity in c_f at $x = x_0$, and is certainly conservative since the adjustment to the zero transpiration c_f — θ relation is not expected to take place until some distance downstream of $x = x_0$. This estimate was made by Epstein (Ref. 8) in his turbulent flow analysis. A less conservative method is to assume continuity of c_f and some kind of asymptotic approach to the zero transpiration value. It is clear that there are many reasonable assumptions that meet this requirement (e.g., solid path above).

A more exact analysis of the equivalent problem for laminar flow can be made and several reports have been written on the subject (Refs. 1, 3 and 6). In References 3 and 6 a discontinuity in c_f at $x = x_0$ results, while in Ref. 1, c_f is assumed continuous. Howe compares the different expressions for $c_f(x)$ and it is shown that the results of Ref. 1 are the most conservative of the three.

We will assume here that the solution of Ref. 1 for $c_f(x)$ (see Figure 3) can be applied to the turbulent case. Remember, this is only an assumption, made with the hope of providing more realistic results than those obtained by the method of Reference 8, and must certainly be verified experimentally.

This report then will analyze the effect of upstream transpiration cooling on the surface temperatures and heat flux to the body. The only coolant to be considered is air, although the analysis could be adopted to some other

fluids with a small modification. The results obtained from such an analysis depend on whether the flow is laminar or turbulent. This in turn depends upon the flight condition, surface roughness, pressure gradient, etc. Also, as indicated previously, the injection of fluid into the boundary layer tends to decrease the stability and induces turbulence at lower Reynolds numbers than the zero transpiration case. Thus, analyses of both laminar and turbulent flow are important since either condition could prevail along a given trajectory.

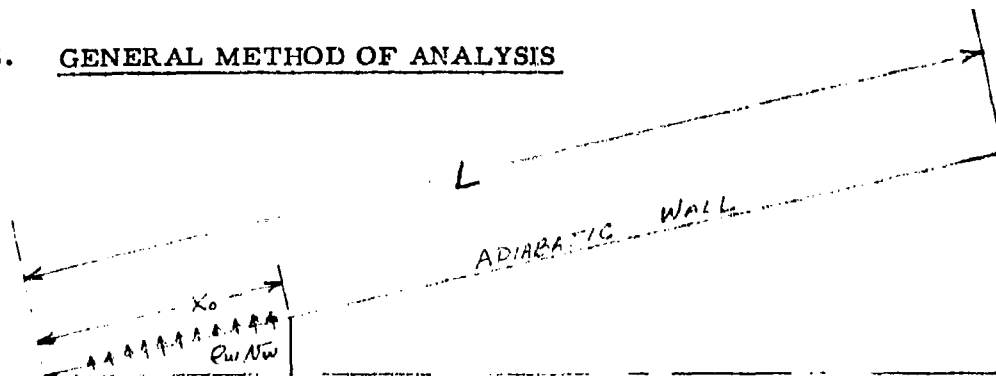
Only turbulent flow over a cone will be considered in this report. It will be assumed that this condition exists from the apex so that the problem of transitional flow need not be treated. This does not seem unreasonable since at the flight conditions where turbulent flow is expected (relatively high densities and Mach numbers) only a small portion of the cone should be able to sustain laminar flow, due to the aforementioned destabilizing effect of injection. The case of completely laminar flow over a flat plate with upstream transpiration has been treated in Ref. 1. An outline of the method used there will be given in a following section.

The turbulent flow analysis can be most conveniently handled by treating the porous and non-porous sections separately. The problem of transpiration cooling in compressible flow over a flat plate has been treated by Rubesin in Ref. 2. It will be shown how these results may be applied to supersonic flow over a cone with but a slight change in the basic equations. When this is done, the important physical quantities in the porous sections can be

computed. Then, since it is necessary to find the variation of adiabatic wall temperature in the non-porous region, the aforementioned assumption for the skin friction is made. This allows the solution of the momentum integral equation, which along with the energy integral equation enables the determination of the adiabatic wall temperature around the radome. It is then possible to compute the heat flux to the body for cooled walls.

These results are then applied to a number of steady state flight conditions in order to indicate the range in which upstream transpiration cooling is effective.

2. GENERAL METHOD OF ANALYSIS



The problem to be solved can be simply stated as follows: What is the adiabatic wall temperature in the range from x_0 to L ? This is the temperature the downstream surface will reach (neglecting radiation) if steady flight is achieved and the wall is perfectly insulated.

This computation is made by assuming the Crocco relation (which connects velocity and temperature distributions through the boundary layer) to hold in the downstream region. Actually, the Crocco relation applies strictly to a region of constant wall temperature, but since it will only be used here to relate integrated quantities (momentum and enthalpy thicknesses) it is felt that the error incurred by using it for zero heat transfer will not be significant. The relation can be written in the following form (for a perfect gas),

$$\frac{T}{T_{s_1}} = \frac{T_w}{T_{s_1}} + \left(1 - \frac{T_w}{T_{s_1}}\right) \frac{u}{u_1} \quad (1)$$

The momentum and enthalpy thicknesses are defined respectively as

$$\theta = \int_0^{\delta} \frac{\rho u}{\rho_1 u_1} \left(1 - \frac{u}{u_1}\right) dy \quad (2)$$

$$\Omega = \int_0^{\delta_t} \frac{\rho u}{\rho_1 u_1} \left(1 - \frac{T}{T_{s_1}}\right) dy \quad (3)$$

Consistent with the assumption of the Crocco relation, the thermal (δ_t) and hydrodynamic boundary layer thicknesses are considered equal. This is usually considered satisfactory for air. The combination of Eqs. (1), (2) and (3) gives,

$$\Omega = \theta \left(1 - \frac{T_w}{T_{s_1}}\right) \quad (4)$$

It is obvious that once the momentum and enthalpy thicknesses are known in the downstream section, the adiabatic wall temperature can be determined as a function of x .

For a cone the momentum and energy integral equations are respectively,

$$\frac{d\theta}{dx} + \frac{\theta}{x} = \frac{c_f}{2} = \frac{\tau_w}{\rho_1 u_1^2} \quad (5)$$

$$\frac{d\Omega}{dx} + \frac{\Omega}{x} = \frac{q_w}{\rho_1 u_1 H_1} \quad (6)$$

Eq. (5) can be solved if c_f is known as a function of x or θ . However, it is clear that since Eq. (5) is of the first order there will be one arbitrary constant which must be evaluated from the "initial conditions", i. e., the value of θ at $x = x_0$. Thus it can be said that θ is matched (assumed continuous) at the junction of the porous and non-porous sections.

The solution to Eq. (6) for an adiabatic wall ($q_w = 0$) is,

$$\Omega x = \text{Constant} = \Omega_0 x_0 \quad (7)$$

The equations for the porous section will then be used to compute Ω_0 .

Therefore, the general method of analysis can be described as follows:
solving the pertinent equations for both the porous and non-porous sections
and matching important parameters at the junction.

3. POROUS SECTION

As shown in Section II one of the quantities that must be computed in the porous section is the momentum thickness at the end of transpiration. Since a variable in this study is the length of the porous region, a curve of θ vs. x is needed. This can be obtained from the solution of the momentum integral equation for a cone, which is,*

$$\frac{d\theta}{dx} + \frac{\theta}{x} = \frac{c_f}{2} + \frac{\rho_w v_w}{\rho_1 u_1} \quad (8)$$

A solution to the problem of porous cooling of a flat plate has been obtained by Rubesin (Ref. 2). If one considers the comparison between the equations for a cone and a flat plate for no injection, it can be shown (Ref. 4), that the flat plate equations (used to compute, e.g., skin friction) can be applied to a cone if one-half the cone Reynolds number (based on length) is substituted for the flat plate Reynolds number. This means that when the conditions at the edge of the boundary layer and the surface are the same for both the cone and the flat plate, the skin friction coefficient for the cone is the same as that for the flat plate for one-half the cone Reynolds number. Thus at corresponding x locations, the local skin friction is larger on a cone than on a flat plate. It might be expected that injection into the boundary layer through a porous wall should not seriously affect this relation. Before this analogy is investigated further, the analysis made in Ref. 2 will be outlined.

*Note that the variable x is used to denote distance along the surface for both the porous and non-porous sections.

The principal assumptions made by Rubesin are:

1. The coolant fluid (air) is the same as the boundary layer fluid and enters the boundary layer at the temperature of the surface of the plate.
2. The boundary layer is composed of a laminar sub-layer and a fully turbulent outer layer (with velocity, temperature, shear and heat flux assumed continuous at interface).
3. In the fully turbulent region, the transport of heat is proportional to the transport of momentum (Reynolds analogy).
4. The variation of the dependent variables with respect to x (in the boundary layer equations) is assumed negligible compared with their variations with respect to y . (This reduces the boundary layer equations to a set of ordinary differential equations). Notice the similarity to Couette flow.

The details of this analysis may be found in Appendix A.

Once the flat plate has been analyzed, we are in a position to show the similarity of the equations to those for the cone. If it is assumed that the boundary layer thickness is much less than the radial distance from the axis of the cone to the surface, the only difference in the boundary layer equations appears in the equation of continuity.

Flat Plate

$$\frac{\partial}{\partial y} (\bar{\rho} \bar{u}) + \frac{\partial}{\partial y} (\bar{\rho} \bar{v} + \rho' v') = 0 \quad (9)$$

Cone

$$\frac{\partial}{\partial x} (\bar{\rho} \bar{u}) + \frac{\partial}{\partial y} (\bar{\rho} \bar{v} r + \rho' v' r) = 0 \quad (10)$$

With the assumption that the $\frac{\partial}{\partial x}$ terms are negligible, we see that the continuity equations for the cone and the flat plate are identical, since r is not a function of y . Thus, the velocity and temperature distributions, as determined from the solution to the boundary layer equations, are the same for the cone and the flat plate. This means that the momentum thicknesses are identical.

The momentum equation can be rewritten as,

$$\frac{dRe_\theta}{dx} + \frac{Re_\theta}{Re_x} = \frac{c_f}{2} + \frac{\rho_w v_w}{\rho_1 u_1} \quad (11)$$

or

$$Re_x d Re_x = \frac{d(Re_\theta \cdot Re_x)}{\left(\frac{c_f}{2} + \frac{\rho_w v_w}{\rho_1 u_1}\right)} \quad (12)$$

To continue the demonstration, it is assumed (as for the flat plate) that the demoninator of the right hand side of Eq. (12) is approximately constant. Integration of Eq. (12) then gives,

$$\frac{Re_x^2}{2} = \frac{Re_0 \cdot Re_x}{\frac{c_f}{2} + \frac{\rho_w v_w}{\rho_1 u_1}} \quad (13)$$

or

$$\frac{Re_x}{2} = \frac{Re_0}{\frac{c_f}{2} + \frac{\rho_w v_w}{\rho_1 u_1}} \quad (14)$$

The validity of the approximation ($\frac{c_f}{2} + \frac{\rho_w v_w}{\rho_1 u_1} = \text{constant}$) may be

shown by an a posteriori examination of the results. Since $\frac{\rho_w v_w}{\rho_1 u_1}$ is taken to be constant, it is clear that for high injection rates (with correspondingly low values of c_f), the above approximation is good. Figure 1, which was computed from the equations derived in Appendix A, shows the variation of c_f with Re_x for a number of Mach numbers and injection rates (note: $F \equiv \frac{\rho_w v_w}{\rho_1 u_1}$). For practical application of this cooling technique, it is probable that values of $\frac{\rho_w v_w}{\rho_1 u_1}$ will be greater than 0.005, with a Reynolds number at the end of injection about 10^6 . This gives skin friction coefficients which are at least an order of magnitude less than the injection rates. Thus the assumption of taking $\frac{c_f}{2} + F$ to be constant in order to integrate Eq. (13) is shown to be reasonable.

Comparing Eqs. (14) and (A28) then shows that the similarity between the results for the cone and flat plate is the same as for no injection. That is, the results for the flat plate may be applied to a cone if one-half the cone Reynolds number is used.

The momentum thickness is then computed from,

$$\theta = \frac{x}{2} \left(\frac{c_f}{2} + \frac{\rho_w v_w}{\rho_1 u_1} \right) \quad (15)$$

In order to evaluate Eq. (A33), the wall temperature must be known. It has been shown (Ref. 5) that (for no radiation) the outside wall temperature must be equal to the temperature of the coolant entering the boundary layer. Thus a heat balance in the porous region gives

$$h(T_{awNT} - T_w) = \rho_w v_w c_p (T_w - T_c) \quad (16)$$

where T_{awNT} is the adiabatic wall temperature for no transpiration and T_c is the coolant temperature inside the radome. If T_{awNT} and T_c are assumed to be constant along the cone, it is apparant that both the injection rate and wall temperature cannot be held constant since h is a function of x . In order to keep a constant wall temperature, the porosity must vary with h (which is roughly proportional to $x^{-1/5}$). This means that either the internal pressure must vary or the material has a controlled variable porosity. Since neither of these alternatives appear (at the present time) to be feasible, the more practical case seems to be a constant injection rate and varying wall temperature. Thus T_w must be computed at each point under consideration in the porous region.

The method for computing T_w is described in Part B-a. In this Part, some of Rubesin's results (Ref. 2) for the Stanton number ($\frac{h}{\rho_1 u_1 c_p}$) are used in making the heat balance indicated in Eq. (16). Figure 3 of Part B-a plots the results in a convenient non-dimensional form from which the wall temperature can be calculated.

An example is shown in Appendix B which indicates how the skin friction coefficient is determined for a given flight condition.

4. NON-POROUS SECTION

It was shown in Section 2 that once the initial conditions (θ_0 , Ω_0 , etc.) are known for the non-porous region, the energy and momentum integral equations can be solved provided a reasonable assumption for $c_f = c_f(x)$ or $c_f = c_f(\theta)$ is made. As indicated previously, the assumption to be used comes from a solution to the same problem considered here, except for laminar flow (Ref. 1).

In Ref. 1 an existing solution for the laminar flow in the porous region, is used (e.g., Low, NACA TN 3404) to determine the important quantities (c_f , θ , Ω) at the end of injection. These are assumed continuous at this point and can therefore be used as initial conditions for the solution to the problem in the non-porous region.

To begin the downstream solution, the velocity distribution at $x = x_0$ must match that at the end of injection. Therefore, non-similarity of profiles is to be expected since they must change from those characteristic of transpiration to the characteristic of flow along a solid surface with no upstream cooling. Because this makes the solution of the boundary layer equations quite difficult, an integral approach was adopted for the downstream section, and the boundary layer profile was assumed to be approximate by seventh degree polynomial in terms of y/δ ,

$$\frac{u}{u_1} = \sum_{n=1}^7 a_n(x) \left(\frac{y}{\delta}\right)^n \quad (17)$$

The coefficient a_1 is proportional to the skin friction coefficient. It is shown that all other coefficients can be expressed in terms of a_1 by the use of boundary conditions at $y = 0$ and $y = \delta$. This leads to an ordinary differential equation in a_1 , δ and x which can be solved simultaneously with the momentum equation to give the variation of skin friction coefficient with x . The actual matching of profiles at the junction is accomplished by equating the slopes at the wall (skin friction) and the boundary layer thicknesses, which serve as the initial conditions to be used in the solution of the differential equations.

The results that we are interested in are presented in Figure 5 of Ref. 1 and are reproduced here in Figure 3. The parameter $f(0)$ in the figure is defined as,

$$f(0) = -2 \frac{\rho_w v_w}{\rho_1 u_1} \sqrt{Re_{x_0}} \quad (18)$$

Notice that the ordinate is the ratio of the local skin friction to the skin friction for zero transpiration. Therefore, at large distances from the porous region, it would be expected that the ordinate approaches unity since the effect of upstream transpiration would be negligible. This, of course, does not depend upon whether the flow is laminar or turbulent.

Now, the problem we are trying to solve is how the skin friction increases from its initial value at the end of injection to its zero transpiration level far downstream, for turbulent flow. It is felt that the solution to the laminar problem in its non-dimensional form can be applied directly to turbulent flow, because the rate at which the skin friction recovers from the

effect of upstream transpiration should be relatively independent of whether the flow is laminar or turbulent. Note that this does not say that the laminar and turbulent skin friction coefficients are identical, but rather that at the same distance downstream of the end of injection (with the same initial conditions) the ratio $c_f/c_{fF=0}$ is the same. The actual values of c_f are different because, first of all, the initial values will be different, and secondly, the zero transpiration values are different functions of x ($c_{fF=0} \sim x^{-1/2}$ - Laminar, $c_{fF=0} \sim x^{-1/5}$ - Turbulent).

It was found that one curve could be fitted to the four shown in Fig. 3 so that the effect of the parameter $f(0)$ is negligible. The equation of this curve is,

$$\frac{c_f}{c_{fF=0}} = 1 - a e^{-1.40(\xi - 1)^{1/3}} \quad (19)$$

where,

$$a = 1 - \left(\frac{c_f}{c_{fF=0}} \right)_{\xi=1} \quad (20)$$

Notice that the effect of injection rates appears only in the value of a ($c_{f\xi=1}$ decreasing with increasing F). Then, with this variation of c_f with x (or ξ), the momentum integral equation in the non-porous section can be integrated.

Rewriting Eq. (5) in dimensionless form gives,

$$\frac{d\eta}{d\xi} + \frac{\eta}{\xi} = \frac{x_0}{\theta_0} \frac{c_f}{2} \quad (21)$$

where

$$\eta = \frac{\theta}{\theta_0} \quad (22)$$

$$\xi = \frac{x}{x_0} \quad (23)$$

Now, for the turbulent boundary layer with no transpiration,

$$\frac{c_f}{2} = Kx^{-1/5} = Kx_0^{-1/5} \xi^{-1/5} \quad (24)$$

so that Eq. (19) becomes

$$\frac{c_f}{2} = (1 - ae^{-1.4(\xi-1)^{1/3}}) Kx_0^{-1/5} \xi^{-1/5} \quad (25)$$

Substituting in Eq. (21) gives,

$$\frac{d\eta}{d\xi} + \frac{\eta}{\xi} = \frac{x_0^{4/5}}{\theta_0} K \xi^{-1/5} \left[1 - ae^{-1.4(\xi-1)^{1/3}} \right] \quad (26)$$

Let $B = \frac{x_0^{4/5} K}{\theta_0}$ (27)

Then multiplying Eq. (26) by ξ ,

$$\frac{d}{d\xi}(\eta\xi) = B\xi^{4/5} - aB\xi^{4/5} e^{-1.4(\xi-1)^{1/3}} \quad (28)$$

Integrating gives,

$$\eta\xi \Big|_1^\xi = \frac{5}{9} B \xi^{9/5} \Big|_1^\xi - aB \int_1^\xi s^{4/5} e^{-1.4(s-1)^{1/3}} ds \quad (29)$$

Letting $I(\xi)$ equal the integral in Eq. (29), and inserting the limits results in,

$$\frac{\eta - 1/\xi}{B} = \frac{5}{9} (\xi^{4/5} - \frac{1}{\xi}) - \frac{aI(\xi)}{\xi} \quad (30)$$

Once $I(\xi)$ is determined (by numerical methods) $\frac{\eta - 1/\xi}{B}$ can be plotted, as shown in Figure 4. Since the momentum thickness is now known as a function of x , the Crocco integral and the energy equation can be combined to give the adiabatic wall temperature.

The Crocco relation in non-dimensional form is,

$$\phi = \frac{\theta_0}{\Omega_0} \eta (1 - \frac{T_w}{T_{s1}}) \quad (31)$$

$$\text{where } \phi = \frac{\Omega}{\Omega_0} \quad (32)$$

The energy equation for an adiabatic wall is

$$\frac{d\phi}{d\xi} + \frac{\phi}{\xi} = 0 \quad (33)$$

Integrating gives,

$$\phi \xi = \text{constant} = \phi_0 \xi_0 = 1 \quad (34)$$

Then,

$$\frac{1}{\xi} = \frac{\theta_0}{\Omega_0} \eta (1 - \frac{T_w}{T_{s1}}) \quad (35)$$

but at $\xi = 1$

$$\Omega_0 = \theta_0 (1 - \frac{T_{w0}}{T_{s1}})$$

where T_{w0} is the wall temperature at the end of the porous section.

Finally,

$$\eta \left(1 - \frac{T_w}{T_{s1}} \right) = \frac{1}{\xi} \left(1 - \frac{T_{w0}}{T_{s1}} \right) \quad (36)$$

The left hand side of Eq. (36) is plotted in Figure 5 vs. ξ for different values of initial temperature ratio. This can be used along with Figures 4 and 2 to get the variation of adiabatic wall temperature along the body for a given flight condition and coolant inlet temperature.

5. EFFECTS OF CONVECTIVE AND RADIATIVE HEAT TRANSFER IN NON-POROUS SECTION

If the non-porous wall is not insulated but is instead assumed to remain at a temperature below that of the adiabatic wall, then it is of importance to compute the convective heat transfer to the wall. This can be represented as,

$$q_{\text{conv.}} = h(T_{\text{aw}} - T_w) \quad (37)$$

In the usual aerodynamic heating problem, with no transpiration, the adiabatic wall temperature is somewhat less than the stagnation temperature at the edge of the boundary layer (for $Pr < 1$). In this case, however, the adiabatic wall temperature is considerably less than this stagnation temperature (due to the effect of upstream transpiration), and approaches it asymptotically (see Figure 6). Thus, a reduction in heat transfer is obtained downstream of the porous region if it is assumed that the film coefficient remains the same as in the zero transpiration case. Since h depends largely on the properties at the edge of the boundary layer, this assumption is probably good. For turbulent flow over a cone, h can be expressed by,

$$h = \frac{0.00828 (u_1 p_r)^{0.8}}{(Pr_r)^{0.667}} \left(\frac{\mu_r}{\mu_s}\right)^{0.2} \frac{\text{Btu}}{\text{sec-ft}^2\text{-}^\circ\text{R}} \quad (38)$$

Thus, the convective heat transfer to the body can be computed.

If it is assumed that the missile is in steady flight and the effects of radiation are included, the surface reaches its radiation equilibrium temperature (if the inside wall is insulated). This means that the convective heat

flux to the body equals the heat radiated from the wall. The expression for radiant heat transfer into free space is,

$$q_{\text{rad.}} = \sigma \epsilon T_w^4 \quad (39)$$

When equilibrium is achieved, the following expression is used to calculate the wall temperature,

$$h(T_{aw} - T_w) = \sigma \epsilon T_w^4 \quad (40)$$

6. RESULTS AND CONCLUSIONS

Figures 1 and 2 give the important results for the porous section. It can be shown that these curves are only slightly dependent upon altitude, which therefore does not appear as a parameter. Curves of c_f vs. Re_x indicate the large reduction in c_f with increasing injection rate. Figure 2 presents the variation of wall temperature in the porous region as a function of injection rate and Mach number. Notice that as $x \rightarrow 0$ the temperature approaches that of an adiabatic wall for no transpiration. This temperature (for the Mach number range under consideration) is, of course, much higher than the melting point of most materials, and therefore special means of cooling must be used for this small area. This could be accomplished by cutting a slot at the tip and injecting coolant into the stream.

Figure 6 shows the rate at which the adiabatic wall temperature in the non-porous section approaches the value which would be achieved for no upstream cooling. This is the measure of effectiveness for this cooling technique.

Before discussing these results it should be noted that there is a slight inconsistency in the presentation of the curves. The ordinate is non-dimensionalized with respect to the stagnation temperature at the edge of the boundary layer. This is done because this ratio appears in the Crocco relation from which these curves are obtained (see Section IV). However, it is known that with no transpiration, an adiabatic wall will reach a temperature somewhat lower than the stagnation temperature. Thus the maximum

temperature that can be reached (for large values of ξ) is about 10% less than is indicated in Figure 6. Therefore, the calculated values are higher than the true temperatures, and in this sense are conservative.

At each flight condition, the effect of injection rate and transpiration length can be seen. Relatively large values of F (greater than 0.01) are needed to obtain a sustained depression of the adiabatic wall temperature, while changing the initial transpiration length effects the curves very little (of course, the actual length is twice as large for $x_0 = 1'$ at a given ξ).

The effectiveness of this method of cooling is seen to increase with increasing Mach number and decrease with altitude. However, for the practical application of upstream transpiration cooling, one must be concerned with the mass flow of coolant needed to give a required downstream temperature. For a constant injection rate ($\rho_w v_w / \rho_1 u_1$) the mass flow is found to increase with both increasing Mach number and decreasing altitude.

A calculation was made to show the difference between the more conservative method of Ref. 8 and the present analysis. The result is given in Figure 6B. Notice that the difference in adiabatic wall temperatures is largest near $\xi = 1$, which is to be expected since the assumptions for the skin friction approach each other for large values of ξ (see Introduction).

Figure 7 gives an indication of the mass flow requirements for a particular configuration. This calculation was only made at 100,000 ft. At a given Mach number, a decrease in altitude means that a larger mass flow is needed to give the same cooling effectiveness.

Recall that all calculations in this report have been made for a coolant temperature of 600°R . A reduction of this temperature will increase the effectiveness of the scheme.

The only conclusion pertaining to radome cooling that can be drawn from an analytical study such as this is that the use of a porous plug in the front of a radome may be a feasible method of protecting the surface. The following part (C-b) deals with the application of the curves and equations presented here to a possible radome configuration. In that part, the mass flow required to keep the radome at a given maximum temperature for variations in M_{∞} , altitude, coolant temperature and injection rate will be computed. This, in turn, will prescribe the method of obtaining the coolant (e.g., ram air inlet-refrigeration, carried on board, etc.). An examination of the weight and volume of this system will then determine to a large extent, its feasibility for cooling a particular radome.

It should be emphasized that experimental results are needed (as in all turbulent flow problems) to verify the accuracy of the results obtained.

REFERENCES

1. Rubesin, M. W. and Inouye, M.: A Theoretical Study of the Effect of Upstream Transpiration Cooling on the Heat-Transfer and Skin Friction Characteristics of a Compressible, Laminar Boundary Layer. NACA TN 3969, May 1957.
2. Rubesin, M.: An Analytical Estimation of the Effect of Transpiration Cooling on the Heat-Transfer and Skin-Friction Characteristics of a Compressible, Turbulent Boundary Layer. NACA TN 3341, Dec. 1954.
3. Howe, John T.: Some Finite Difference Solutions of the Laminar Compressible Boundary Layer Showing the Effects of Upstream Transpiration Cooling. NASA Memo 2-26-59A, February 1959.
4. Van Driest, E. R.: Turbulent Boundary Layer on a Cone in a Supersonic Flow at Zero Angle of Attack. Journal of the Aeronautical Sciences, January 1952.
5. Eckert, E. R. G. and Livingood, J. N. B.: Comparison of Effectiveness of Convection, Transpiration and Film Cooling Methods with Air as Coolant. NACA Report No. 1182, 1954.
6. Libby, P. A. and Pallone, A.: A Method for Analyzing the Heat Insulating Properties of the Laminar Compressible Boundary Layer. Journal of the Aeronautical Sciences, December 1954.
7. Bloom, M. H. and Martellucci, A.: A Method for Calculating Turbulent Boundary Layer Properties in High Speed Flow. General Applied Science Laboratories, Inc., Technical Report No. 27A, March 1957.
8. Epstein, M.: Heat Transfer on Cone with Upstream Coolant Injection. General Applied Science Laboratories, Inc., Technical Report No. 18, March 1957.

TABLE 1
VALUES OF $K^{(1)}$ FOR $\left(\frac{C_f}{2}\right)_{F=0} = K x^{-1/5}$

<u>M_∞</u>	<u>Altitude</u>		
	<u>50,000</u>	<u>100,000</u>	<u>150,000</u>
5	-	.00153	-
6	-	.00143	-
7	.000828	.00137	.00220

(1) See Appendix C for method used to determine K.

APPENDIX A

The result that we are looking for is a relation between c_f and Re_x and c_f and Re_0 . The first step is to determine the velocity and temperature distributions in both the laminar sub-layer and fully turbulent region.

The boundary layer equations are (using assumption (4), page 424

$$\frac{d}{dy} (\bar{\rho} \bar{v} + \overline{\rho'v'}) = 0 \quad (A1)$$

$$(\bar{\rho} \bar{v} + \overline{\rho'v'}) \frac{d\bar{u}}{dy} = \frac{d}{dy} (\bar{\mu} \frac{d\bar{u}}{dy} - \overline{\rho u'v'}) \quad (A2)$$

$$(\bar{\rho} \bar{v} + \overline{\rho'v'}) \frac{d}{dy} (c_p \bar{T} + \frac{\bar{u}^2}{2}) = \frac{d}{dy} (\bar{k} \frac{d\bar{T}}{dy} + \bar{\mu} \bar{u} \frac{d\bar{u}}{dy} - \overline{\rho c_p v'T'} + \overline{u\rho u'v'}) \quad (A3)$$

Note that Eq. (A1) can be integrated directly to give,

$$\bar{\rho} \bar{v} + \overline{\rho'v'} = \text{constant} \quad (A4)$$

with the boundary conditions

$$y = 0 : \quad \bar{\rho} \bar{v} = \rho_w v_w \quad \rho'v' = 0 \quad (A5)$$

$$\text{Thus,} \quad \bar{\rho} \bar{v} + \overline{\rho'v'} = \rho_w v_w \quad (A6)$$

The concepts of eddy viscosity and eddy thermal conductivity are introduced here. The definitions are,

$$\epsilon_M = - \frac{\overline{\rho u'v'}}{\frac{d\bar{u}}{dy}} \quad (A7)$$

$$\epsilon_H = - \frac{\bar{\rho} c_p \overline{v'T'}}{\frac{dT}{dy}} \quad (A8)$$

Now, a turbulent Prandtl number may be defined which relates the turbulent transfer of momentum and energy,

$$Pr_t = \frac{\epsilon_M c_p}{\epsilon_H} \quad (A9)$$

When Eqs. (A6) through (A9) are introduced into (A2) and (A3), there results,

$$\rho_w v_w \frac{du}{dy} = \frac{d}{dy} \left[(\mu + \epsilon_M) \frac{du}{dy} \right] \quad (1) \quad (A10)$$

$$\rho_w v_w \frac{d}{dy} \left(c_p T + \frac{u^2}{2} \right) = \frac{d}{dy} \left[\left(\frac{\mu}{Pr} + \frac{\epsilon_M}{Pr_t} \right) \frac{d}{dy} (c_p T) + (\mu + \epsilon_M) \frac{d}{dy} \left(\frac{u^2}{2} \right) \right] \quad (A11)$$

Eqs. (A10) and (A11) can now be solved for velocity and temperature distributions through the boundary layer.

An assumption that will simplify the solution considerably is that $Pr = Pr_t = 1$. When this is asserted, it will be noticed that Eqs. (A10) and (A11) have the same form, and if u is a solution to (A10), then,

$$c_p T + \frac{u^2}{2} = au + b \quad (2) \quad (A12)$$

is a solution to (A11), since it is linear. The constants a and b are evaluated from the boundary conditions:

-
- (1) Since the fluctuating components no longer appear, all quantities now refer to average values.
 - (2) It should be noted that this is also a statement of the Crocco relation.

$$\begin{aligned}
 y = \delta & : T = T_1 & u = u_1 \\
 y = 0 & : T = T_w & u = 0
 \end{aligned}
 \tag{A13}$$

Thus Eq. (A12) becomes

$$\frac{T}{T_w} = 1 + B \tilde{u} - A^2 \tilde{u}^2
 \tag{A14}$$

where,

$$A^2 = \frac{\frac{\gamma-1}{2} M_1^2}{\left(\frac{T_w}{T_1}\right)}
 \tag{A15}$$

$$B = \frac{1 + \frac{\gamma-1}{2} M_1^2}{\left(\frac{T_w}{T_1}\right)} - 1
 \tag{A16}$$

$$\tilde{u} = \frac{u}{u_1}
 \tag{A17}$$

Eqs. (A10) and (A11) are now integrated (note that in the sub-layer $\epsilon_M \ll \mu$, while in the turbulent core, $\mu \ll \epsilon_M$) to give:

Sublayer (Assuming $\mu = \mu_w$ in the integration)

$$y^+ = \frac{\sqrt{\frac{c_f}{2}} \left(\frac{T_w}{T_1}\right)^\omega}{\frac{\rho_w v_w}{\rho_1 u_1}} \ln \left(1 + \frac{\rho_w v_w}{\rho_1 u_1} \frac{u^+}{\sqrt{\frac{c_f}{2}}} \right)
 \tag{A18}$$

$$\text{where, } y^+ = \frac{\rho_1 u_1 \sqrt{\frac{c_f}{2}} y}{\mu_1}
 \tag{A19}$$

$$u^+ = \frac{\tilde{u}}{\sqrt{\frac{c_f}{2}}}
 \tag{A20}$$

$$\frac{\mu_1}{\mu_w} = \left(\frac{T_1}{T_w}\right)^\omega
 \tag{A21}$$

Turbulent Case (Assuming the Prandtl mixing-length theory - $\epsilon_M = \rho l^2 \frac{du}{dy}$,

and letting $l = Ky$)

$$y = y_a \exp \int_{u_a}^u \frac{K \rho^{1/2} du}{\sqrt{\rho_w u_w u + \tau_w}} \quad (A22)$$

$$\text{or} \quad y = y_a g \quad (A23)$$

It should be noticed that the skin friction, which appears in both profiles, is still an unknown.

Combining Eqs. (2), (A18) and (A23) gives a relation between θ and $c_f^{(1)}$,

$$\theta = \frac{y_a}{K} \sqrt{\frac{c_f}{2} + \frac{\rho_w v_w}{\rho_1 u_1}} g(1) \quad (A24)$$

This can be put in the form,

$$\ln \frac{Re_0 K}{y_a + \sqrt{1 + \frac{\rho_w v_w / \rho_1 u_1}{c_f / 2}}} = \int_{\tilde{u}_a}^1 \frac{K (\frac{\rho}{\rho_1})^{1/2} d\tilde{u}}{\sqrt{\frac{\rho_w v_w}{\rho_1 u_1} + \frac{c_f}{2}}} \quad (A25)$$

From the momentum equation, a relation between $\frac{c_f}{2}$ and Re_x can be obtained.

The momentum equation can be written as,

$$\frac{c_f}{2} + \frac{\rho_w v_w}{\rho_1 u_1} = \frac{d Re_0}{d Re_x} \quad (A26)$$

Substituting (A25) into (A26) gives:

(1) The derivation of this equation is described in detail in Ref. 2.

$$\frac{c_f}{2} + \frac{\rho_w v_w}{\rho_1 u_1} = \frac{d}{dRe_x} \left(\frac{y_a^+}{K} \sqrt{1 + \frac{\rho_w v_w / \rho_1 u_1}{c_f/2}} g(l) \right) \quad (A27)$$

Integrating (A27) by assuming $(\frac{c_f}{2} + \frac{\rho_w v_w}{\rho_1 u_1})$ is approximately a constant gives,

$$Re_x = \frac{\frac{y_a^+}{K} \sqrt{1 + \frac{\rho_w v_w / \rho_1 u_1}{c_f/2}} g(l)}{\frac{c_f}{2} + \rho_w v_w / \rho_1 u_1} \quad (A28)$$

or,

$$Re_x = \frac{\frac{y_a^+}{K} g(l)}{\sqrt{\frac{c_f}{2} (\frac{c_f}{2} + \frac{\rho_w v_w}{\rho_1 u_1})}} \quad (A29)$$

and finally,

$$\ln \frac{K}{y_a^+} \sqrt{\frac{c_f}{2} (\frac{c_f}{2} + \frac{\rho_w v_w}{\rho_1 u_1})} Re_x = \int_{\tilde{u}_a}^1 \frac{K(\frac{\rho}{\rho_1})^{1/2} d\tilde{u}}{\sqrt{\frac{\rho_w v_w}{\rho_1 u_1} \tilde{u} + \frac{c_f}{2}}} \quad (A30)$$

The numerical values of K and y_a^+ must be determined experimentally.

These values, in turn, depend on the type of experimental data taken; that is, whether K and y_a^+ were obtained from experiments relating c_f and Re_0 or those relating c_f and Re_x . The results obtained from each are slightly different (some incompressible results are given in Ref. 2), but the difference is neglected in this analysis.

The relation between θ and x is then easily shown to be,

$$\theta = x \left(\frac{c_f}{2} + \frac{\rho_w v_w}{\rho_1 u_1} \right) \quad (A31)$$

After integrating the right hand side of (A29), the following result is obtained which enables the computation of c_f for a given Re_x ,

$$\ln \frac{K \sqrt{\frac{c_f}{2} \left(\frac{c_f}{2} + \frac{\rho_w v_w}{\rho_1 u_1} \right) Re_x}}{y_a^+} = G \quad (A32)$$

where,

$$G = \frac{2K \left(\frac{T_1}{T_w} \right)^{1/2}}{A \sqrt{\frac{\rho_w v_w}{\rho_1 u_1}} \sqrt{\beta - \alpha}} \left\{ F \left[k_m, \phi_m(u_a) \right] - F \left[k_m, \phi_m(1) \right] \right\}$$

when,

$$k_m^2 = \frac{\beta + \sigma}{\beta - \alpha} < 1$$

$$\sin^2 \phi_m = \frac{\beta - \tilde{u}}{\beta + \sigma} \quad (A32a)$$

or,

$$G = \frac{2K \left(\frac{T_1}{T_w} \right)^{1/2}}{A \sqrt{\frac{\rho_w v_w}{\rho_1 u_1}} \sqrt{\beta + \sigma}} \left\{ F \left[k_n, \phi_n(u_a) \right] - F \left[k_n, \phi_n(1) \right] \right\}$$

when

$$k_n^2 = \frac{\beta - \alpha}{\beta + \sigma} < 1$$

$$\sin^2 \phi_n = \frac{\beta - \tilde{u}}{\beta - \alpha} \quad (A32b)$$

The term $F(k, \phi)$ is an elliptic integral of the first kind.

The definitions of α , β and σ are,

$$\alpha = \frac{B - \sqrt{B^2 + 4A^2}}{2A^2} \quad (A32c)$$

$$\beta = \frac{B + \sqrt{B^2 + 4A^2}}{2A^2} \quad (A32d)$$

$$\sigma = \frac{c_f/2}{\rho_w v_w / \rho_1 u_1} \quad (A32e)$$

APPENDIX B

Flight Conditions: $M_{\infty} = 7.0$ alt. = 100,000 ft.

$$\frac{\rho_w v_w}{\rho_1 u_1} = .01 \quad x_0 = 0.5 \text{ ft.}$$

$$T_c = 600^\circ \text{R}$$

$$T_{\infty} = 420^\circ \text{R}$$

$$\rho_{\infty} = 22.6 \frac{\text{lb}}{\text{ft}^3}$$

$$\rho_{\infty} = .00101 \frac{\text{lb}_m}{\text{ft}^3}$$

$$\frac{T_{\infty}}{T_s} = .0926$$

$$T_s = 4540^\circ \text{R}$$

From cone tables,

$$\frac{P_1 - P_{\infty}}{\frac{\gamma}{2} M_{\infty}^2 P_{\infty}} = 0.148$$

$$P_1 = 137 \frac{\text{lb}_f}{\text{ft}^2}$$

$$M_1 = 4.76$$

Thus, $\frac{T_1}{T_s} = .181$

$$T_1 = 819^\circ \text{R}$$

$$\rho_1 = \frac{P_1}{RT_1} = .00314 \frac{\text{lb}_m}{\text{ft}^3}$$

$$u_1 = M_1 \sqrt{\gamma g_c R T_1} = 6680 \text{ fps}$$

$$\mu_1 = .168 \times 10^{-4} \frac{\text{lb}_m}{\text{ft-sec.}}$$

$$Pr_1 = .685$$

} From Part E - Chapter I

$$T_{awNT} = Pr^{1/3} T_s + (1 - Pr^{1/3}) T_1$$

$$T_{awNT} = 4090^{\circ}R$$

$$Re_x = \frac{\rho_1 u_1 x_0}{\mu_1} = 6.25 \times 10^5$$

From Figure 3, Part B-a of Chapter II, T_w is calculated,

$$T_w = 804^{\circ}R$$

The following terms in Eq. (A32) can now be evaluated,

$$A = 2.15$$

$$K = .392$$

$$B = 4.64$$

$$\alpha = -0.182$$

$$\beta = 1.186$$

$$u_a^+ = 13.0$$

$$T_1/T_w = 1.02$$

Then, from Eq. (A32)

$$\frac{\ln 0.392 \sqrt{\frac{c_f}{2} \left(\frac{c_f}{2} + .01 \right)}}{y_a^+} = G$$

where

$$y_a^+ = \frac{\sqrt{\frac{c_f}{2}} \sqrt{\frac{T_w}{T_1}}}{\frac{\rho_w v_w}{\rho_1 u_1}} \ln \left(1 + \frac{\rho_w v_w}{\rho_1 u_1} \frac{u_a^+}{\sqrt{\frac{c_f}{2}}} \right)$$

$$G = \frac{2(0.392)(1.02)^{1/2}}{2.15 \sqrt{.01} \sqrt{4.64 - (-0.182)}} \left\{ F \left[k_m, \phi_m(\tilde{u}_a) \right] - F \left[k_m, \phi_m(1) \right] \right\}$$

$$k_m^2 = \frac{\beta + \sigma}{\beta + \alpha}$$

$$\sin^2 \phi_m = \frac{\beta - \alpha}{\beta + \sigma}$$

Since σ depends on $c_f/2$, this is as far as we can carry the solution before making an assumption for $c_f/2$. A trial and error solution yields a value of $c_f/2$ equal to 0.93×10^{-4} .

APPENDIX C

DETERMINATION OF K FOR $\left(\frac{c_f}{2}\right)_{F=0} = Kx^{-1/5}$

Experiments have shown that a good representation of c_f vs. θ for no injection for a flat plate is (Ref. 7),

$$\frac{c_f}{2} = \frac{A'}{\theta^{1/4}} \quad (C1)$$

$$\text{where } A' = \frac{p_r}{\rho_1} \frac{.0128}{(\frac{\rho_r u_1}{\mu_r})^{1/4}} \quad (C2)$$

Note that quantities with subscript r are to be evaluated at the reference temperature (T_r), where,

$$T_r = 0.5 T_w + 0.22 T_{B_1} + 0.28 T_1 \quad (C3)$$

Using Eqs. (C1) and (C2) to solve the momentum integral equation gives,

$$\frac{c_f}{2} = 1.125 (A')^{4/5} x^{-1/5} \quad (C4)$$

and

$$K = 1.125 (A')^{4/5} \quad (C5)$$

SKIN FRICTION IN POROUS SECTION

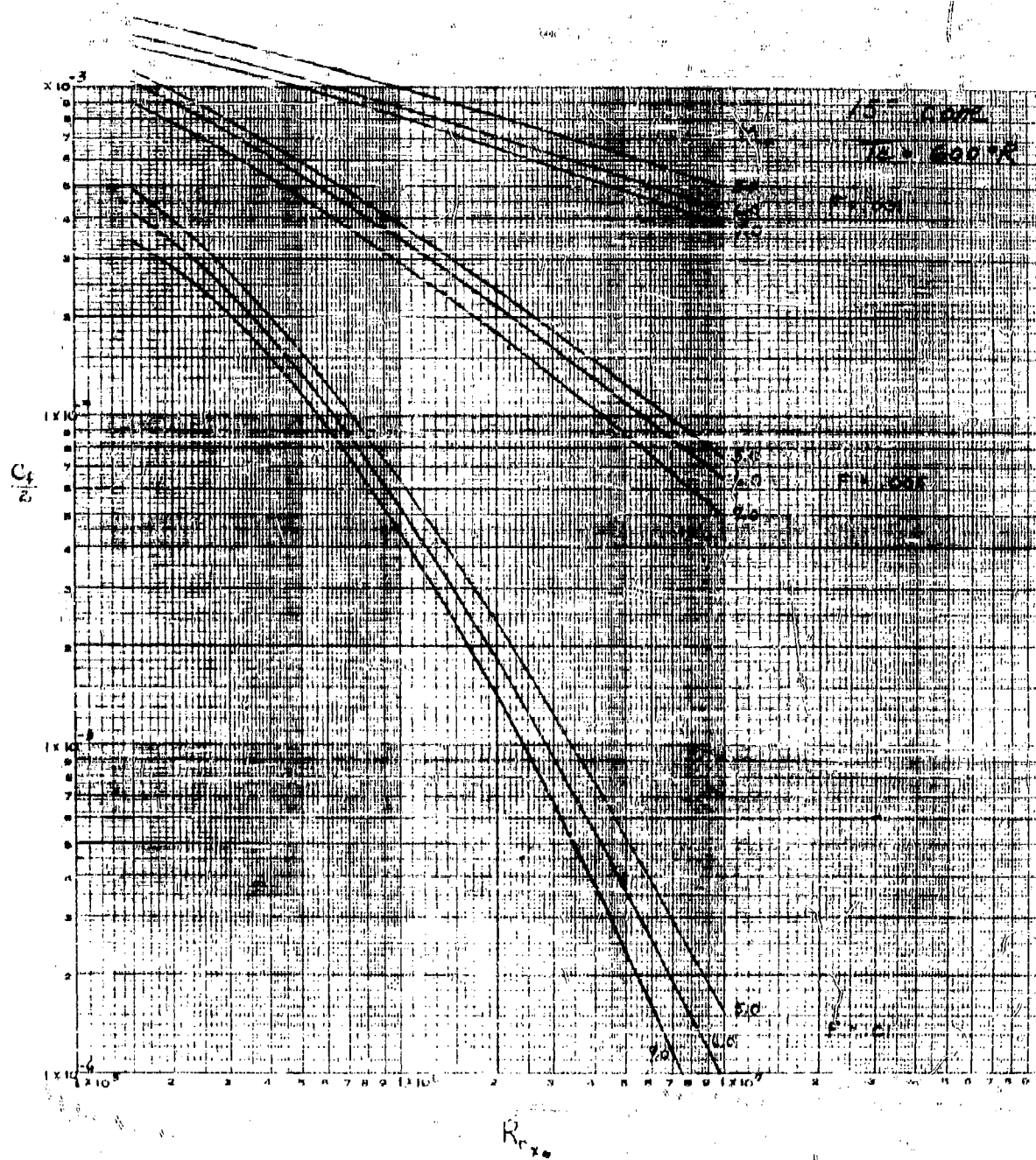
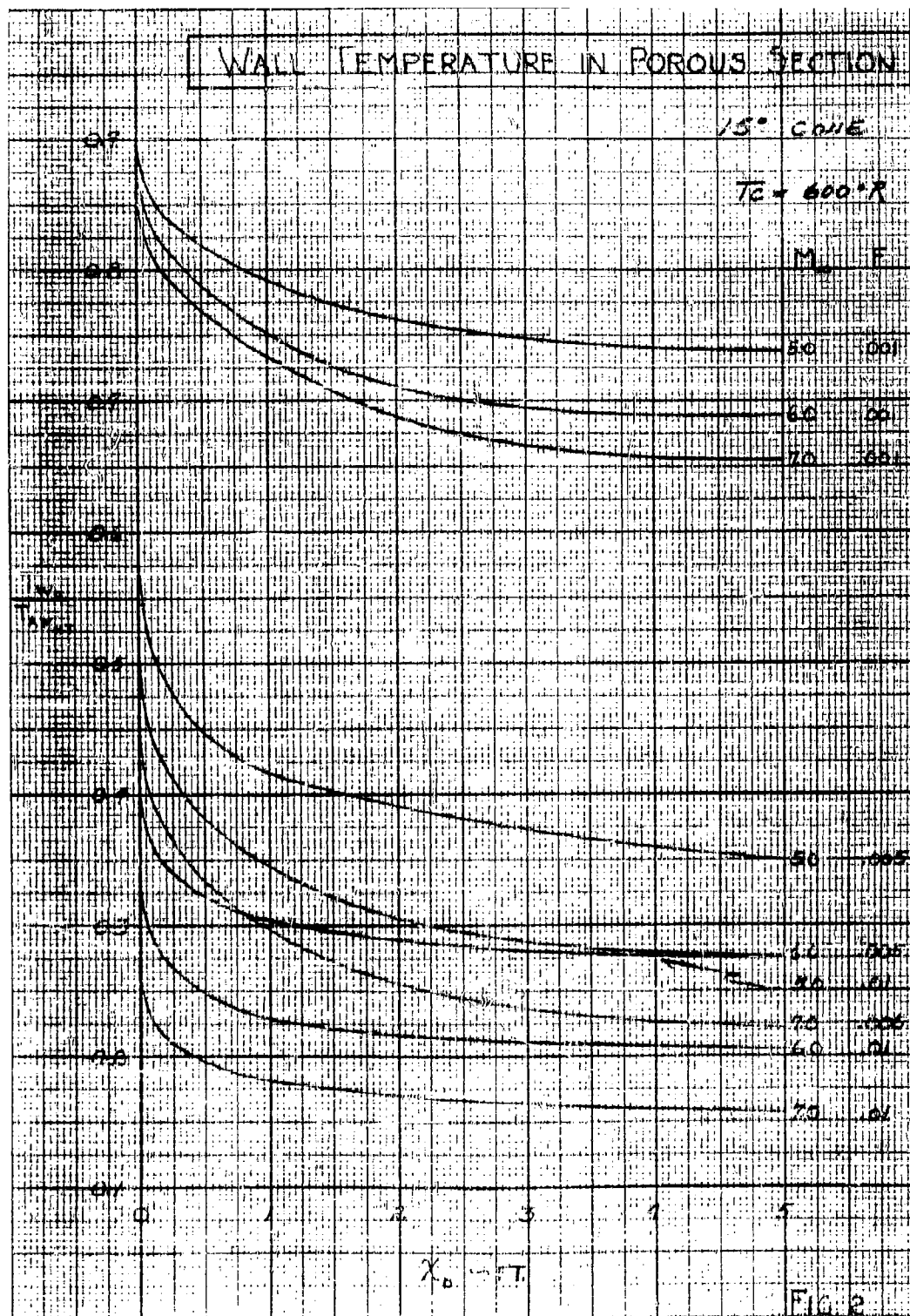
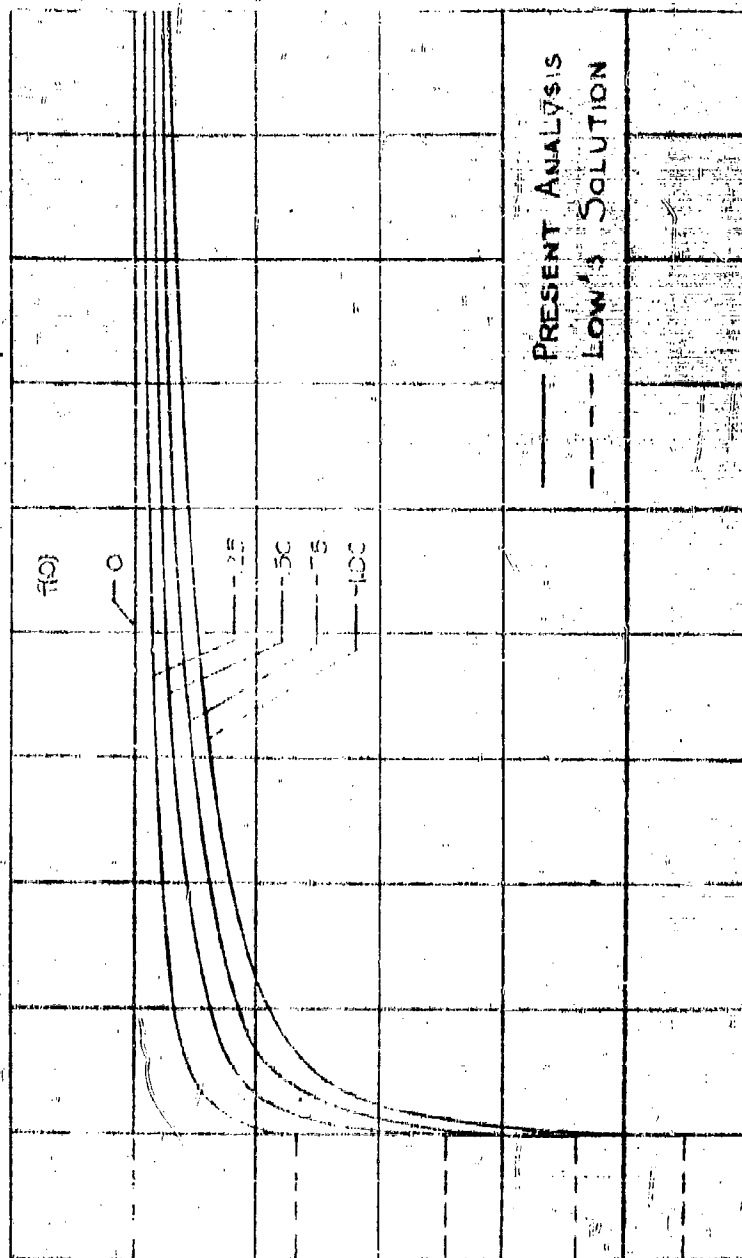


FIG. 1

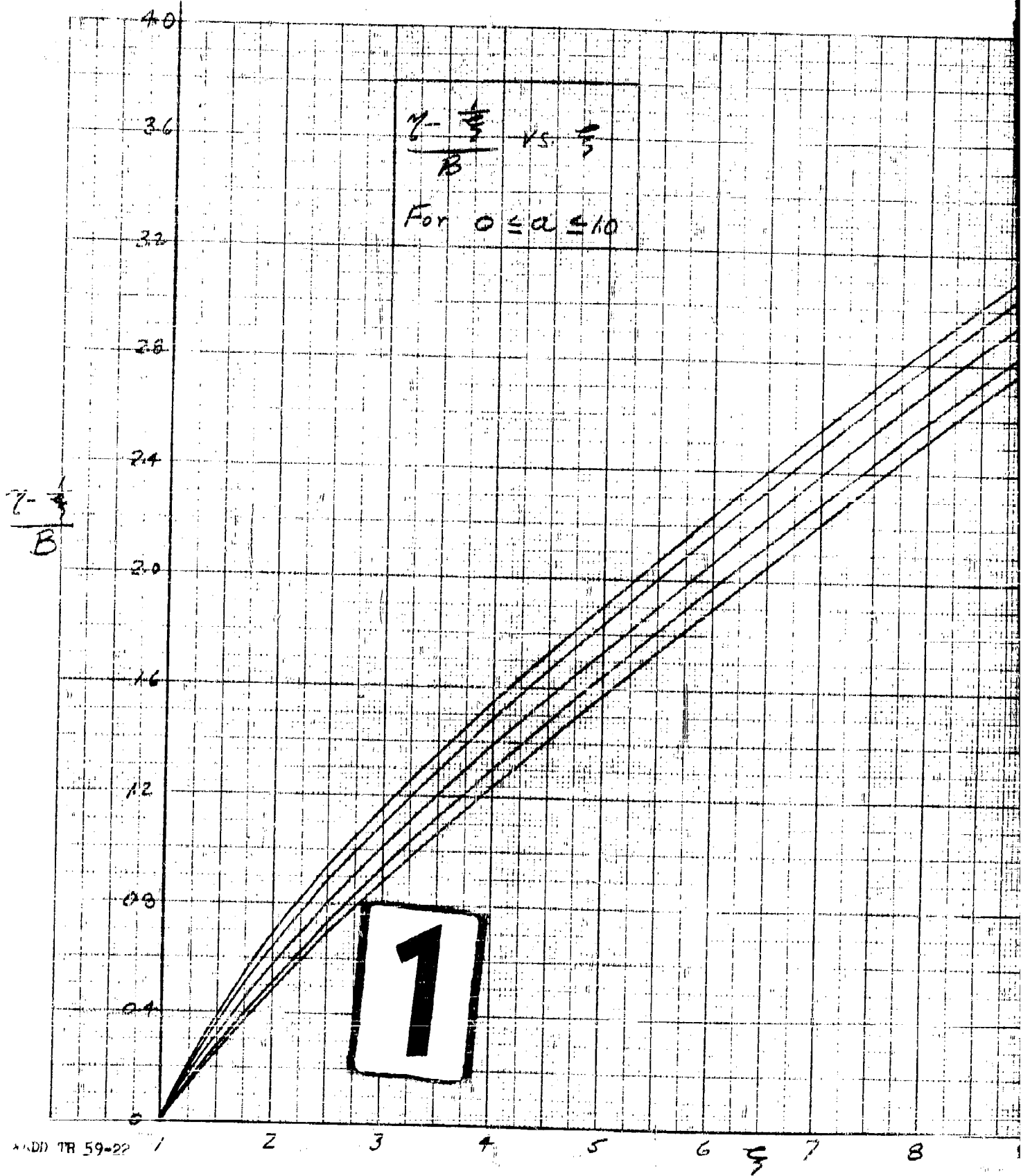


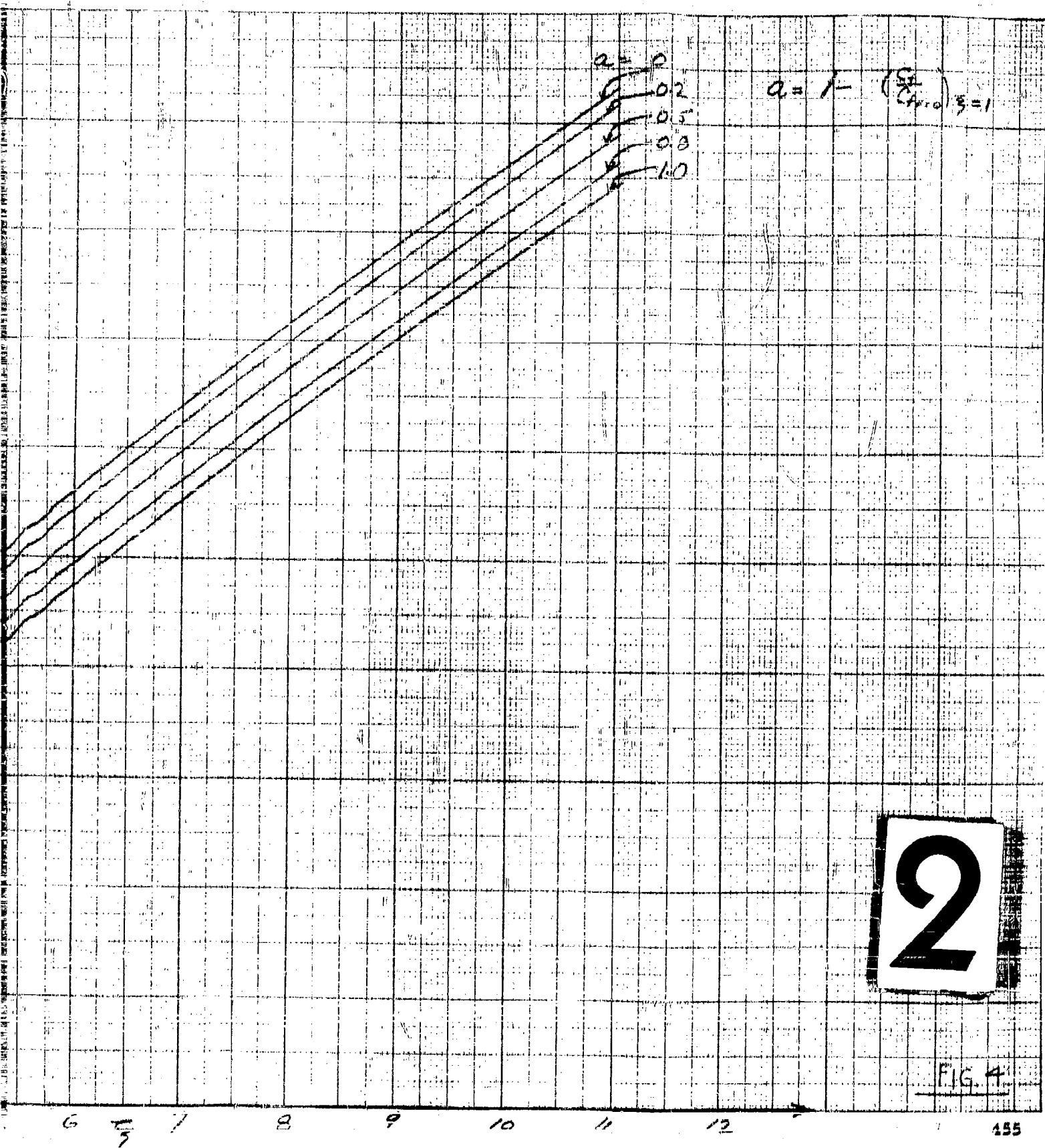
SKIN FRICTION IN NON-POROUS SECTION



$$\xi = \frac{x}{x_0}$$

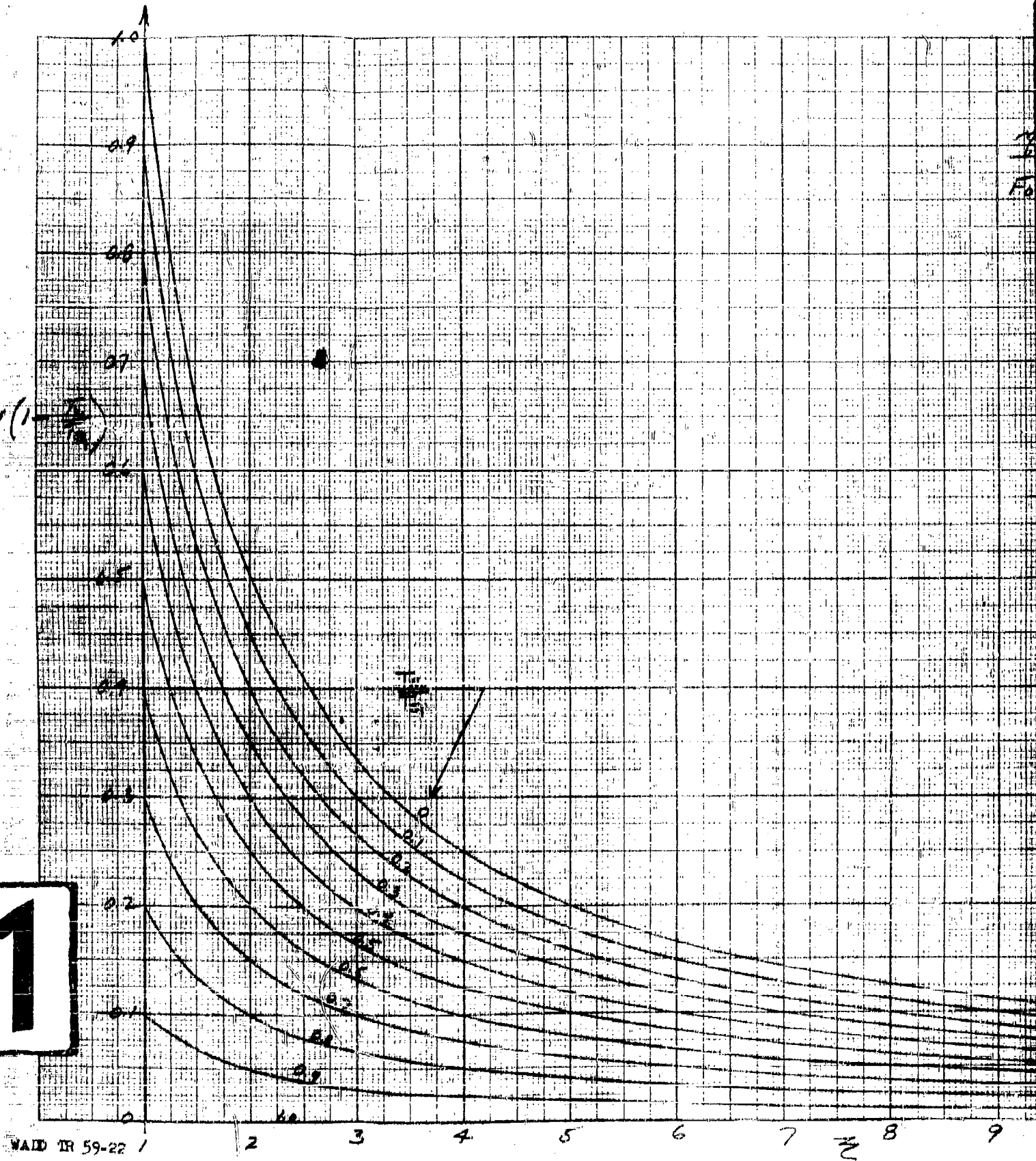
FIG. 3





$\gamma(1 - \frac{F_0}{F_0})$

1

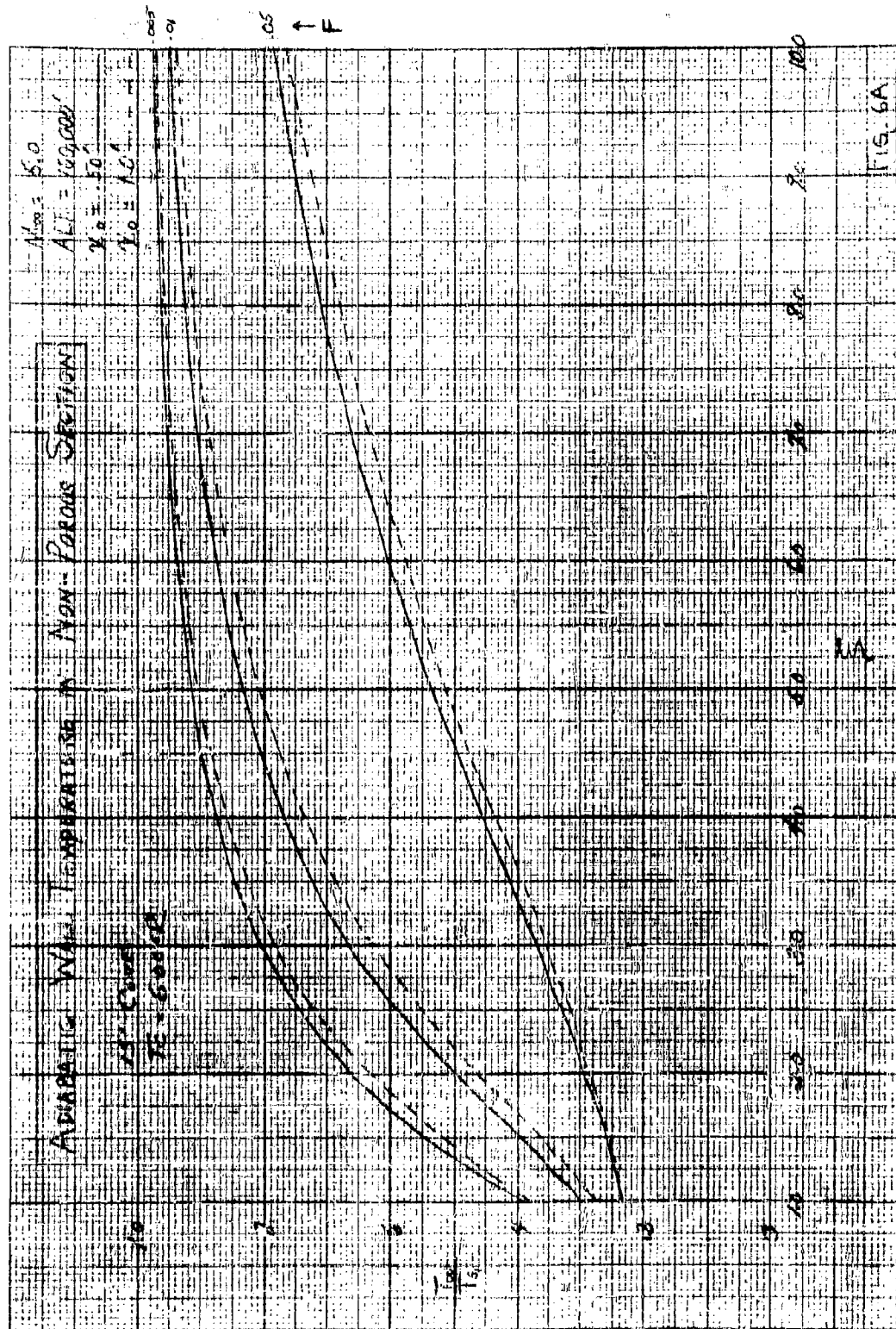


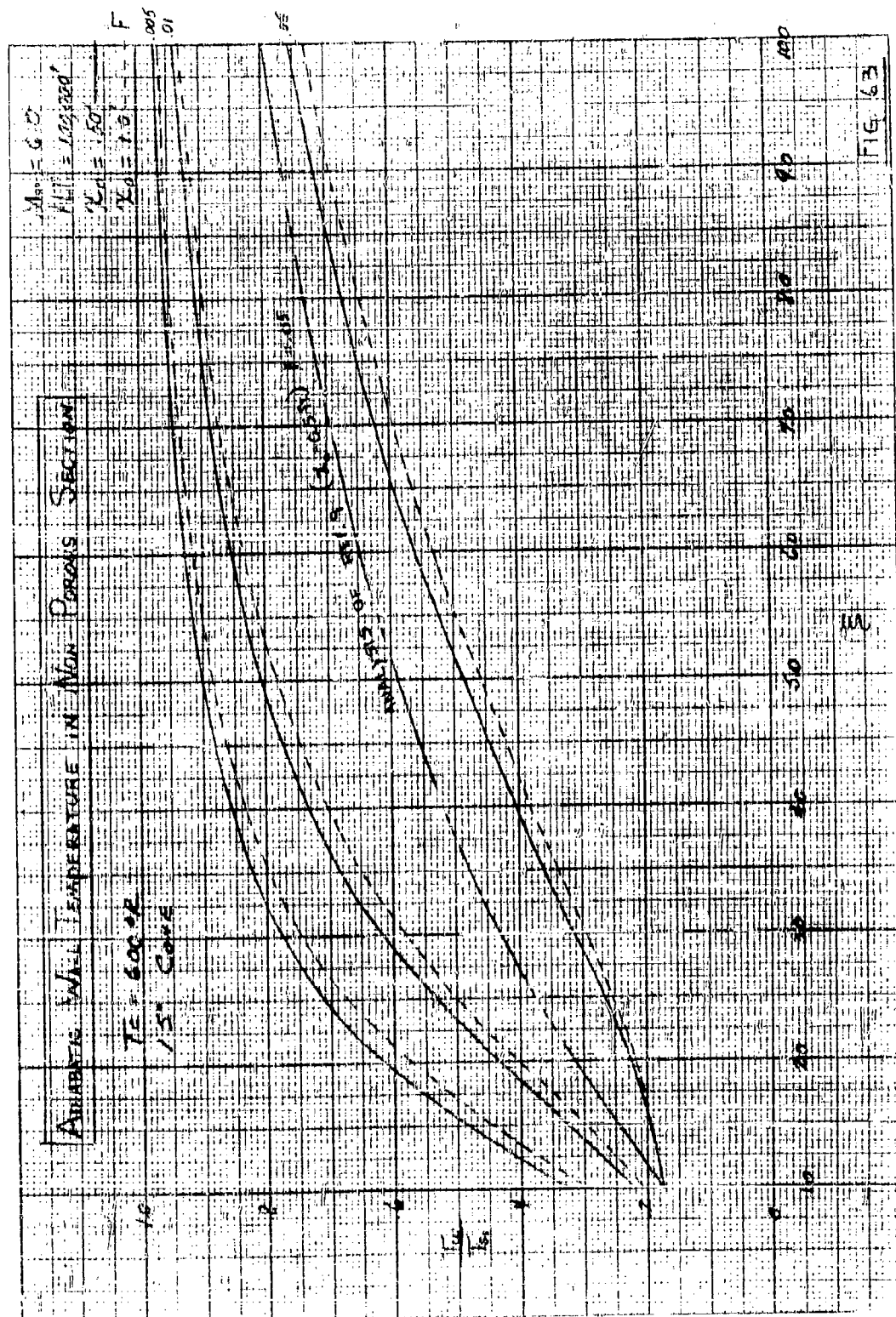
$$\frac{m}{6} \left(1 - \frac{T_{R_1}}{T_{R_2}} \right) \text{ vs. } \frac{T_{R_2}}{T_{R_1}}$$

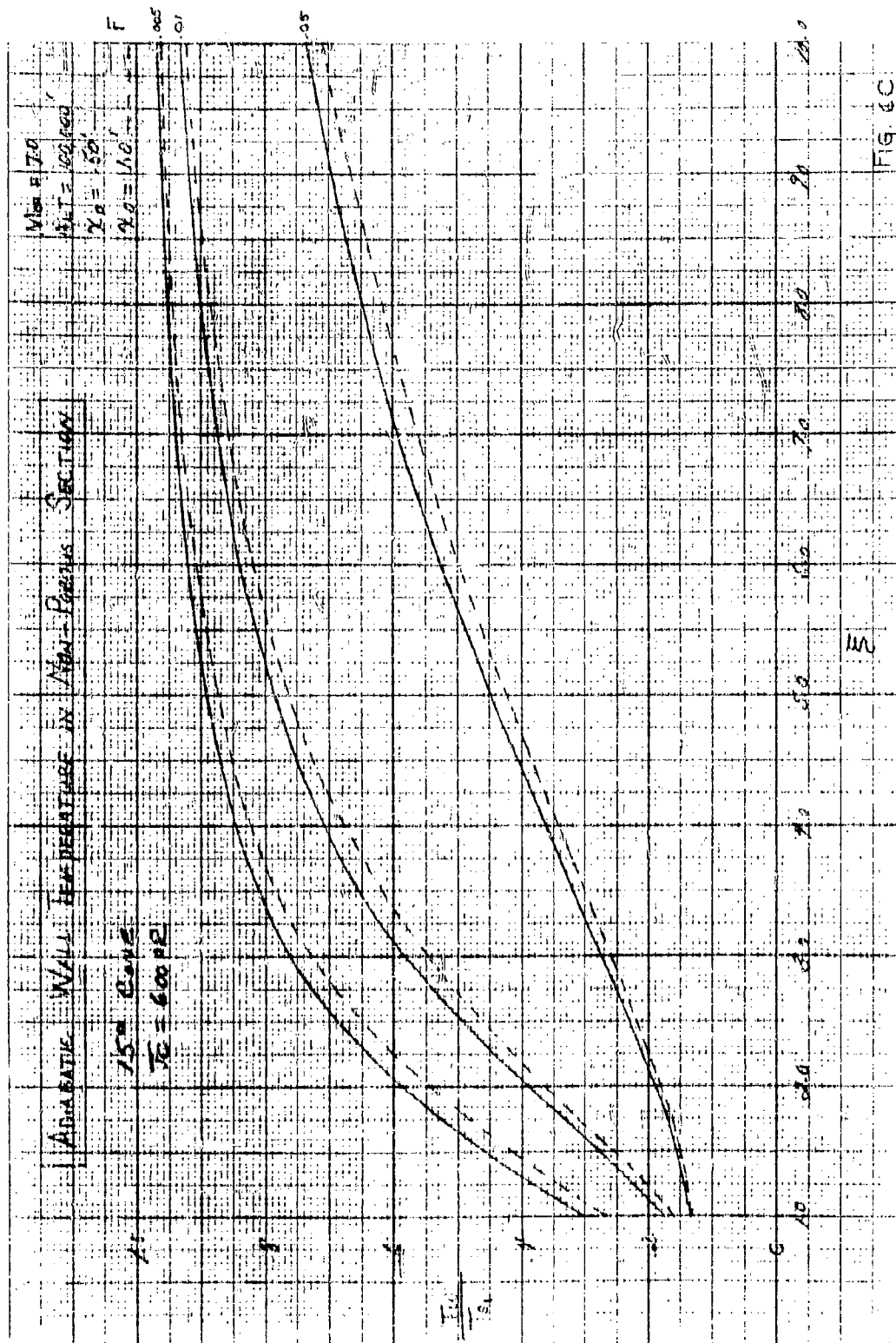
For $0 \leq \frac{T_{R_2}}{T_{R_1}} \leq 10$

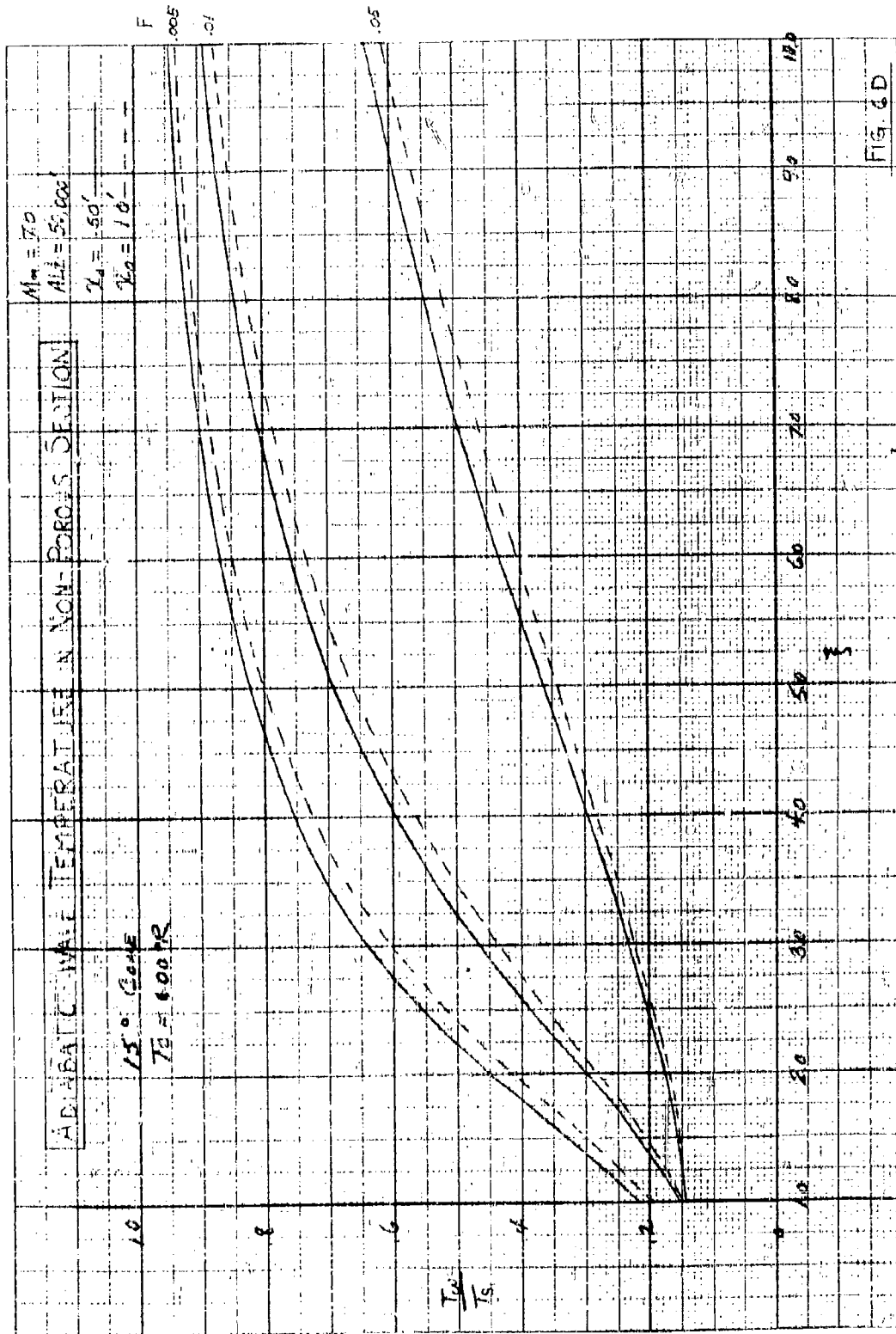
2

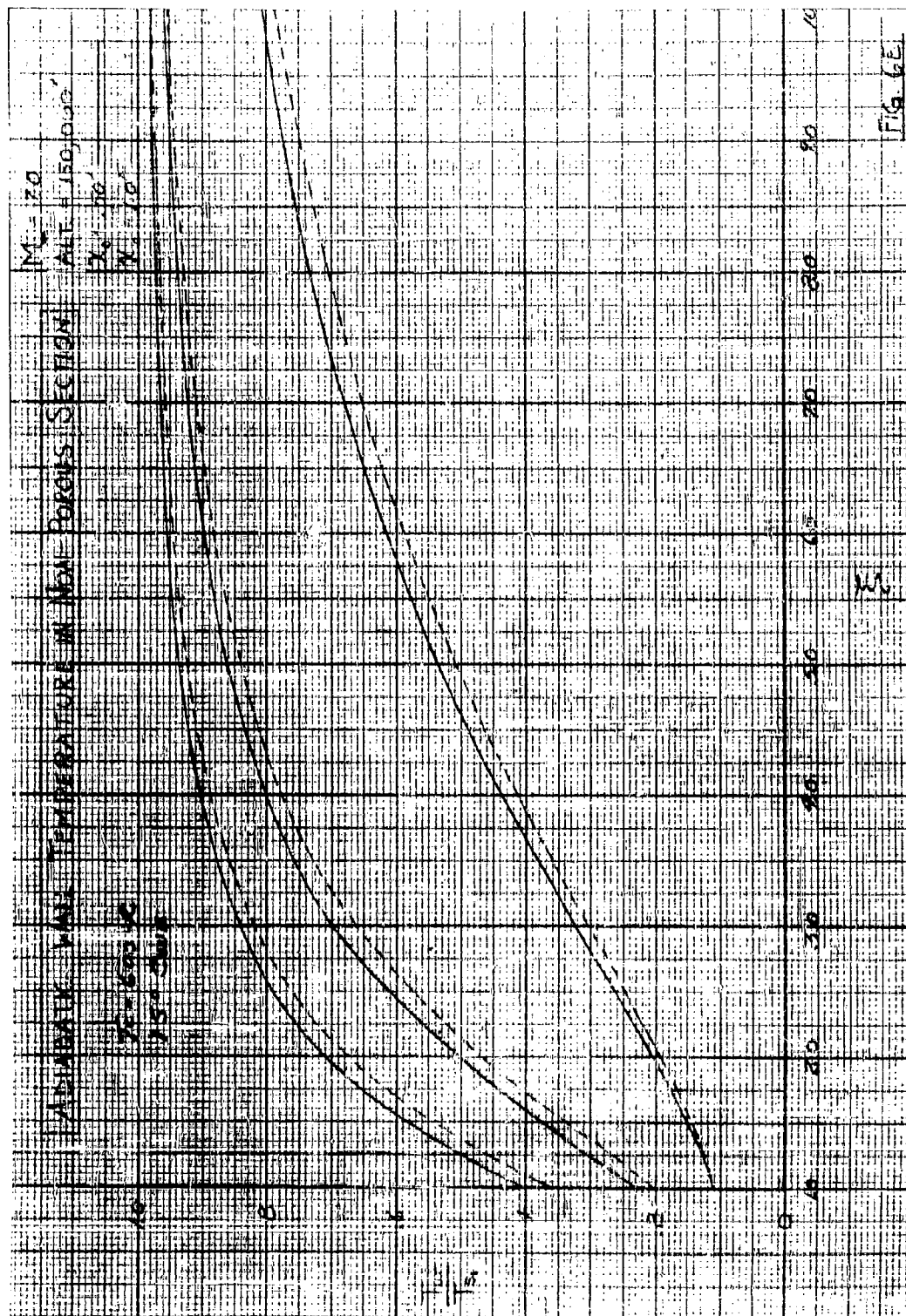
FIG. 5











CHAPTER II - PART C

THE EFFECT OF UPSTREAM TRANSPIRATION COOLING ON
THE COMPRESSIBLE, TURBULENT BOUNDARY LAYER

b. Applications of Analytical Results -
by Harold S. Pergament

TABLE OF CONTENTS

<u>Section</u>	<u>Title</u>	<u>Page</u>
	Summary	465
	Symbols	466
1	Introduction	468
2	Equilibrium Analysis	469
3	Trajectory Analysis	471
4	Results and Conclusions	473
	Figures	477

C. THE EFFECT OF UPSTREAM TRANSPIRATION
COOLING ON THE COMPRESSIBLE, TURBULENT
BOUNDARY LAYER

b. APPLICATION OF ANALYTICAL RESULTS

SUMMARY

The results of the analytical investigation of Part C-a of this chapter have been applied to a typical radome configuration for a number of flight conditions. It is shown that a (in some cases considerable) reduction in the radiation equilibrium temperature can be effected with the proper amount of mass injection.

An analysis of a typical trajectory has been made in order to determine the total coolant requirements for a given decrease in surface temperature. It is seen that for large reductions in temperature, the amount of air required may make this cooling scheme impractical. (This, of course, only refers to the trajectory considered here which has a large exposure time to severe heating.) However, it is pointed out that a weight penalty may be acceptable if a low melting point radome can be used.

SYMBOLS

a	parameter defined by Eq. (7)
h	heat transfer (film) coefficient
H	parameter defined by Eq. (9a)
k	thermal conductivity
L	thickness of radome shell
M	free stream Mach number
Pr	Prandtl number
q	heat transfer rate
t	time
T	absolute temperature
u	component of velocity parallel to surface
v	component of velocity normal to surface
w_i	total mass flow of coolant
x	distance from nose measured along surface
z	coordinate measured normal to surface
α	thermal diffusivity
ϵ	emissivity
σ	Stefan-Boltzmann constant
ρ	density
μ	viscosity
c_p	specific heat at constant pressure

Subscripts

- aw adiabatic wall value
- i value at beginning of particular time interval
- r reference value
- w wall value
- l value at edge of boundary layer

1. INTRODUCTION

In Part C-a of this Chapter, an engineering estimate of the effect of upstream transpiration cooling on the turbulent boundary layer was made, and, in particular, the reduction in adiabatic wall temperature was computed. The purpose of this part is to correlate more closely the required mass flow of coolant with the surface temperature reached (including radiation) at particular points downstream of the porous section, for a wide range of flight conditions. Then the total amount of coolant needed over a trajectory can be estimated and the feasibility of this method of cooling examined in greater detail.

Calculations were made for both equilibrium flight and flight along a trajectory. When a body flies at equilibrium conditions the surface (locally) will reach a temperature that results (for an insulated wall) from a balance of the aerodynamic heat input and the radiative heat transfer from the surface at that point. This is known as the "radiation equilibrium" temperature. Over a trajectory, however, since the flight conditions are a function of time, some heat is stored by the wall at each instant of time. Thus the surface reaches a lower temperature than it would for equilibrium flight. A typical radome configuration (shown in Figure 1) was used for this analysis.

The results presented here are based on the investigation made in Part C-a of this Chapter. The only coolant considered is air and the boundary layer fluid is assumed to act as a perfect gas.

2. EQUILIBRIUM ANALYSIS

The equation from which the radiation equilibrium temperature is calculated is determined by making a heat balance between the convective and radiative heat transfer, and can be written (for a given point on a body) as,

$$h(T_{aw} - T_w) = \sigma \epsilon T_w^4 \quad (1)$$

The heat transfer (film) coefficient, h , is assumed to remain unchanged from its value for no upstream transpiration and is computed from the following equation*,

$$h = \frac{0.00828(u_1 \rho_r)^{0.8}}{(Pr_r)^{0.667}} \left(\frac{\mu_r}{x}\right)^{0.2} \frac{\text{Btu}}{\text{sec-ft}^2 - ^\circ\text{R}} \quad (2)$$

where the subscript r indicates the property is to be evaluated at some reference temperature.

The adiabatic wall temperature (T_{aw}) is, of course, lower than the zero injection case (the amount of the decrease being dependent on the mass flow of coolant as seen in Figure 2) with the result that the equilibrium temperature is also reduced. The results of Part C-a show the variation of adiabatic wall temperature along the body for different flight conditions and injection rates ($\frac{p_w v_w}{p_1 u_1}$).

The method for calculating T_{aw} is the same as that of Part C-a except that here only two points on the body** are considered, the rear and the midpoint.

* See Part E, Chapter I.

** Note that the cone analyzed in this part has a semi-vertex angle of 20° while in Part C-a a 15° cone was used.

It is felt that the maximum value of $\frac{\rho_w v_w}{\rho_1 u_1}$ for which the analysis is still valid is about 0.10. Thus for each flight condition a curve could be obtained of adiabatic wall temperature at a specified point on the body vs. the weight flow required to get that temperature (Figure 2). Then Equation (1) is used to compute the equilibrium temperature for a given value of the emissivity (ϵ).

3. TRAJECTORY ANALYSIS

When the Mach number and altitude of the missile are considered to be functions of time, an additional term appears in the heat balance; that is, the heat stored by the body at each instant of time. Then, one must solve the heat conduction equation for the wall of the radome in order to determine the outside surface temperature. Assuming that a one-dimensional treatment is valid at each point along the body gives the following differential equation:

$$\frac{\partial^2 T}{\partial z^2} = \frac{1}{\alpha} \frac{\partial T}{\partial t} \quad (3)$$

with the boundary conditions,

$$z = 0 \quad -k \frac{\partial T}{\partial z} = q_{\text{net}} = h(T_{\text{aw}} - T) - \sigma \epsilon T^4 \quad (4)$$

$$z = L \quad \frac{\partial T}{\partial z} = 0$$

and the initial condition,

$$t = 0 \quad T = T(z) \quad (5)$$

Because of the non-linear boundary conditions, this equation is usually solved by numerical methods, and would probably have to be programmed on a high speed computer. However, if it is assumed that the wall is isothermal*, the solution is simplified considerably. The following equation may then be written,

$$h(T_{\text{aw}} - T) - \sigma \epsilon T^4 = \rho c_p L \frac{dT}{dt} \quad (6)$$

*No great generality is lost by this assumption since we are not particularly interested in the temperature distribution through the material.

This first order differential equation also contains a non-linear term, but an approximate solution can be obtained in the following manner:

$$\text{let} \quad a = \frac{1}{\rho c_p L} \quad (7)$$

$$\text{then} \quad dt = \frac{dT}{ah T_{aw} - a T (h + \sigma \epsilon T^3)} \quad (8)$$

If h and T_{aw} are assumed to be some average constant value over a small time interval, and the T^3 term is taken to be the value at the beginning of any time interval, then Equation (8) can be integrated to give,

$$T = (T_i - \frac{h}{H} T_{aw}) \exp \left[-a(h+H)(t - t_i) \right] + \frac{h}{H} T_{aw} \quad (9)$$

$$\text{where} \quad H = h + \sigma \epsilon T_i^3 \quad (9a)$$

and T_i is the temperature at the beginning of the time interval and $(t - t_i)$ is the length of the time interval. If one chooses a short time interval (for the trajectory shown in Figure 4, 5 second intervals were chosen up to $t = 100$ sec., 100 second intervals from 100 to 400 seconds, and 5 second intervals until the end of the trajectory) Equation (9) can be used with good accuracy for the transient response of the wall temperature over a trajectory.

The values of ρ , c_p and L used in the calculations are $226 \frac{\text{lb}_m}{\text{ft}^3}$, $0.2 \frac{\text{Btu}}{\text{lb}_m \cdot ^\circ\text{F}}$ and $.0167$ ft., respectively.

4. RESULTS AND CONCLUSIONS

All the results obtained in this report are specifically for the cone shown in Figure 1. It was thought that the numbers obtained for a typical radome configuration would be indicative of the effectiveness of upstream transpiration cooling. However, one must still be careful in extrapolating to other body shapes.

As mentioned before, the important parameter to be studied is the mass flow of coolant needed to keep the wall temperature below a specified maximum over an entire trajectory. This will then determine the feasibility of upstream injection as a method for cooling radomes.

Figure 2 shows the variation of adiabatic wall temperature with mass flow for a number of flight conditions. It is this quantity that actually shows the effectiveness of this method of cooling (Pt. C-a). Notice that as the altitude is increased there is a considerable reduction in the required mass flow to give a desired adiabatic wall temperature. As mentioned previously, the curves extend on the abscissa only to the point where $\frac{\rho_w v_w}{\rho_1 u_1} = 0.10$. For example, at 150,000 feet the ambient density is quite low and therefore the maximum mass flow for which the analysis is acceptable is only of the order of 0.10 lbs sec. This, of course, does not mean that more mass cannot be injected at these conditions, but rather that the results obtained by this larger mass addition cannot be predicted accurately with this analysis. Also, it should be pointed out that when $\frac{\rho_w v_w}{\rho_1 u_1}$ is approximately unity, the problem turns to one of injecting through a slot and not a porous wall.

As expected, a comparison of points at $x = 2'$ and $x = 4'$ shows the adiabatic wall temperature to be considerably reduced when the porous region is approached.

When radiation is taken into account, the temperature is less than T_{aw} , the amount depending on the magnitude of the wall temperature (since $q_r = \sigma \epsilon T_w^4$). Figure 3 shows the variation of radiation equilibrium temperature with mass flow for coolant supply temperatures of 500°R and 1000°R . (A discussion of the method of obtaining these supply temperatures may be found in Part D of this Chapter.)

In Figure 3a it can be seen that there is little difference in the resulting wall temperature for a change in the emissivity of the surface from 0.7 to 0.3. (This seems to be the range of emissivities for many radome materials.) Two additional parameters have been varied in Figure 3b; the distance at which the wall temperature is computed and the coolant temperature. It will be noticed that the curve for $x = 2'$ crosses that for $x = 4'$ near the zero weight flow condition. This occurs because the adiabatic wall temperature for no transpiration is the same at $x = 2'$ and $x = 4'$, and the value of h is higher at $x = 2'$ (since $h \sim x^{-0.2}$). Thus at $w_1 = 0$, the wall temperature is greater closer to the nose of the body. It is seen that the effect of reducing the coolant temperature to 300°R (approximately that of liquid nitrogen) is negligible at the back of this body. Of course, the smaller the distance from the porous section, the greater the effect of the coolant temperature.

The typical radome trajectory shown in Figure 4 was analyzed in order to determine the effect of injection on the wall temperature. Figure 5 gives the results of these calculations. The upper curves show that, for no cooling, the wall temperature is higher at smaller values of x . The lower curves were computed by assuming that enough mass could be injected to keep the adiabatic wall temperature to 1500°R (an arbitrary selection). The wall temperature was then found by the method described in Section 3. It will be observed that for some flight conditions, it is necessary to go beyond the range of applicability indicated previously (i.e., $\frac{\rho_w v_w}{\rho_1 u_1} \leq 0.10$) in order to reduce the adiabatic wall temperature to 1500°R . Therefore, the integrated weight flow noted on Figure 5 should only be taken as approximate. (However, it is felt that this is the correct order of magnitude of the mass requirement.)

In general, one would reject any cooling scheme that required the addition of 372 lbs. of air (not to mention the weight of the container needed to carry it) to an existing missile system. However, one must note that with this mass addition, a considerable decrease in the wall temperature has been effected (about a 50% drop in the peak temperature). So much of a decrease, in fact, that it may be possible to consider a different, lower melting point, material (e.g., fiberglass) for the radome with possibly less complications than arise in the manufacture of a high melting point ceramic. Therefore, if one were initially designing a missile system, it may be satisfactory to accept a weight penalty in order to use a radome which is easier to manufacture. This could be the most useful aspect of upstream transpiration

cooling. Naturally, the coolant requirements decrease with an increase in the allowable surface temperature.

Also, it must be pointed out that the trajectory studied here has a long exposure time to high Mach number flight, which, of course, is the reason for the relatively large amount of coolant needed. Those trajectories which either do not produce this severe aerodynamic heating condition or have a shorter exposure time will require less coolant since the necessary reduction in surface temperature will not be as great.

The possibility that the coolant can be taken aboard during the trajectory should not be overlooked. If a suitable ram air intake along with an effective refrigeration system is designed, this method of obtaining the coolant would probably result in a smaller weight penalty than if the air was stored at take-off. Some of the relative advantages of each method are discussed in Part D of this Chapter, which also considers the problem of upstream transpiration cooling for laminar flow. If the flow over the body is laminar the coolant requirements should be less than in the turbulent case for the same trajectory since the convective heat transfer is less.

In conclusion, it appears that in order to decide on the usefulness of this method of radome cooling, a particular configuration traveling a specific trajectory must be analyzed in a similar manner to the case considered in this report.

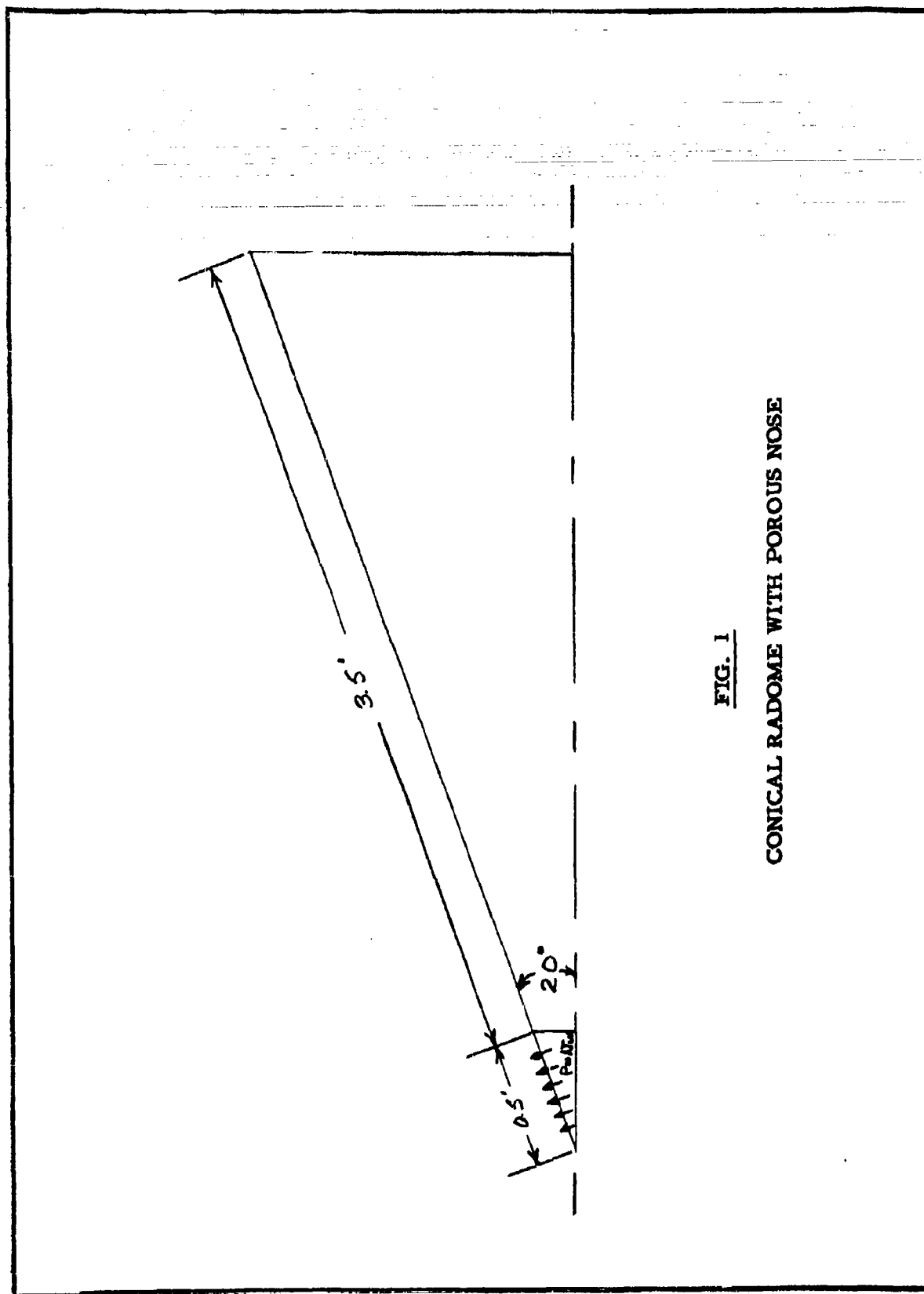
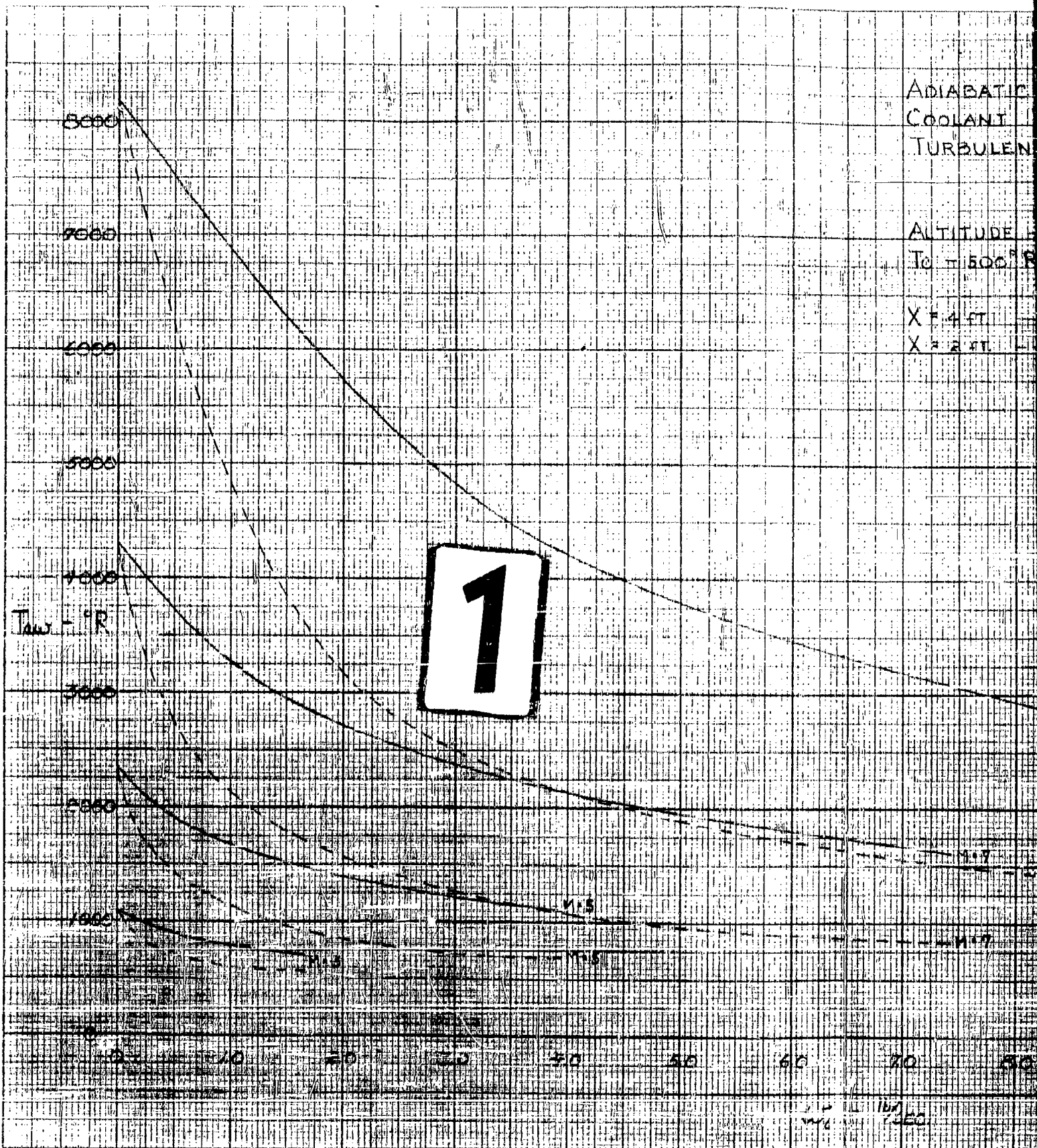


FIG. 1
CONICAL RADOME WITH POROUS NOSE



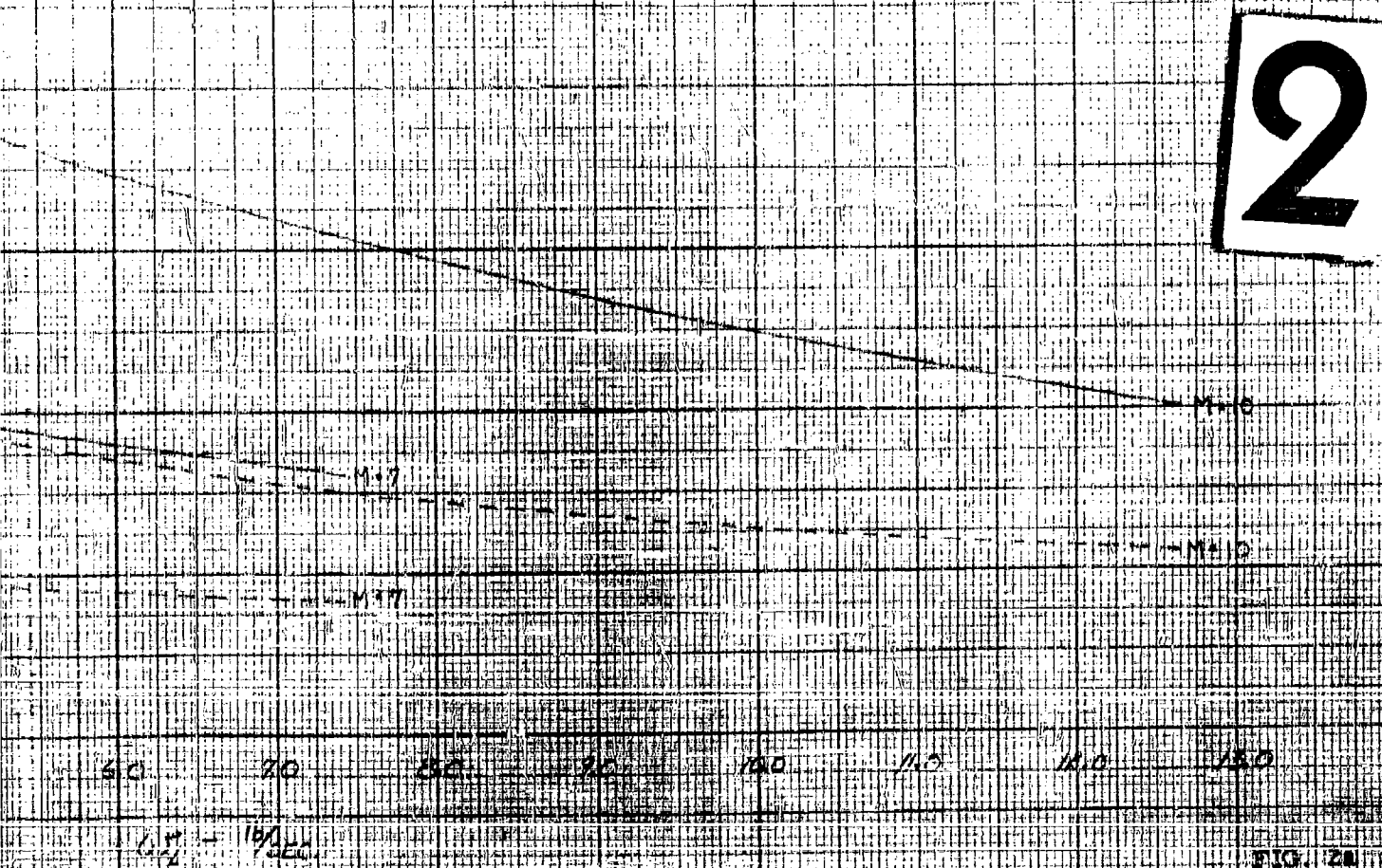
ADIABATIC WALL TEMPERATURE VS. COOLANT WEIGHT FLOW FOR TURBULENT BOUNDARY LAYER

ALTITUDE - 50,000 FT.

$T_0 = 500^\circ R$

$X = 4$ FT. ————

$X = 2$ FT. - - - - -



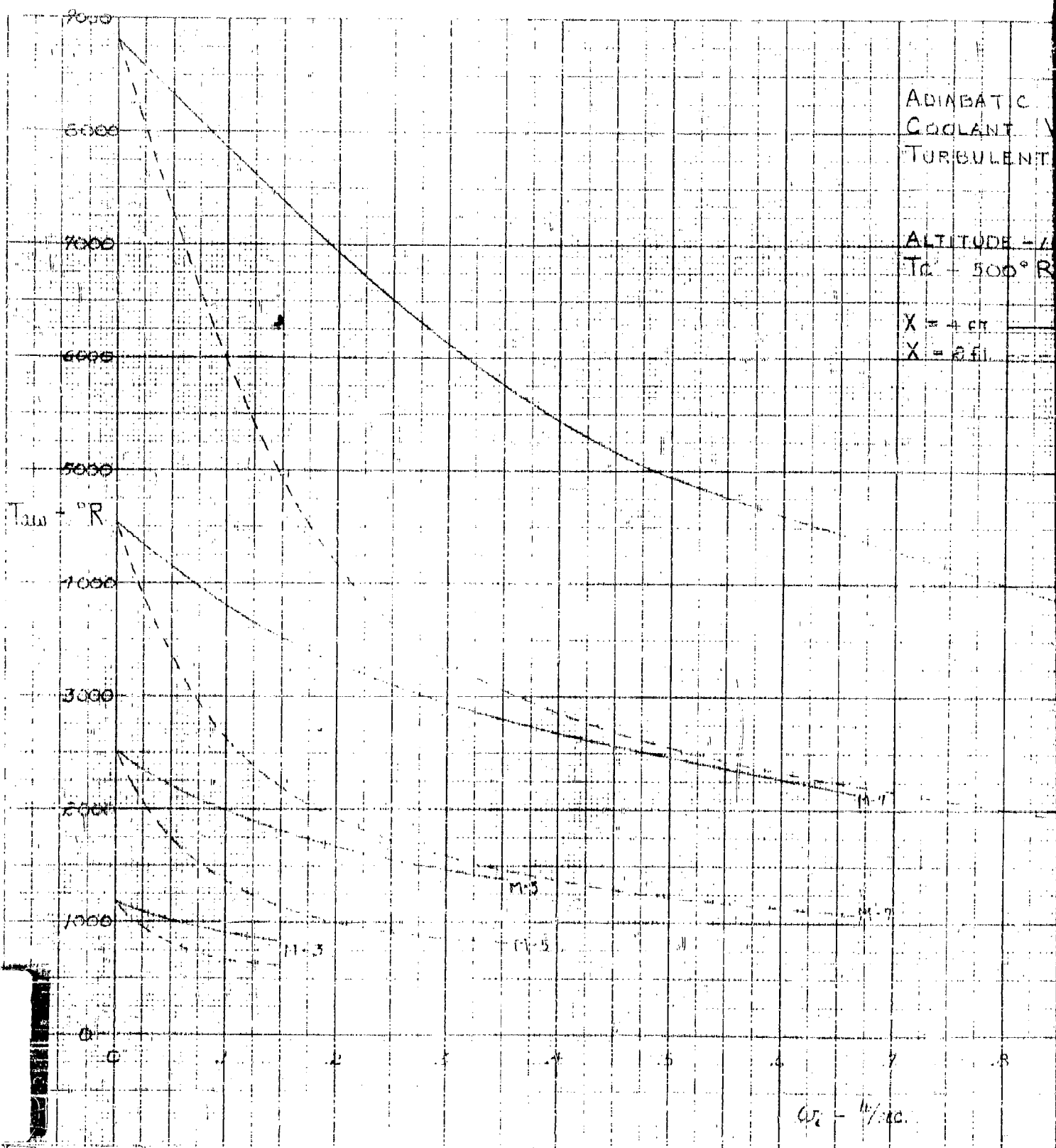
2

FIG. 2A

ADIBATIC
COOLANT
TURBULENT

ALTITUDE - 1
T_a = 500° R

X = 4 cm
X = 2 ft



$C_{p,c} = 10/30$

ADIABATIC WALL TEMPERATURE VS. COOLANT WEIGHT FLOW FOR TURBULENT BOUNDARY LAYER

ALTITUDE - 100,000 FT.

$T_c = 500^\circ R$

$X = 1 \text{ FT.}$

$X = 5 \text{ FT.}$



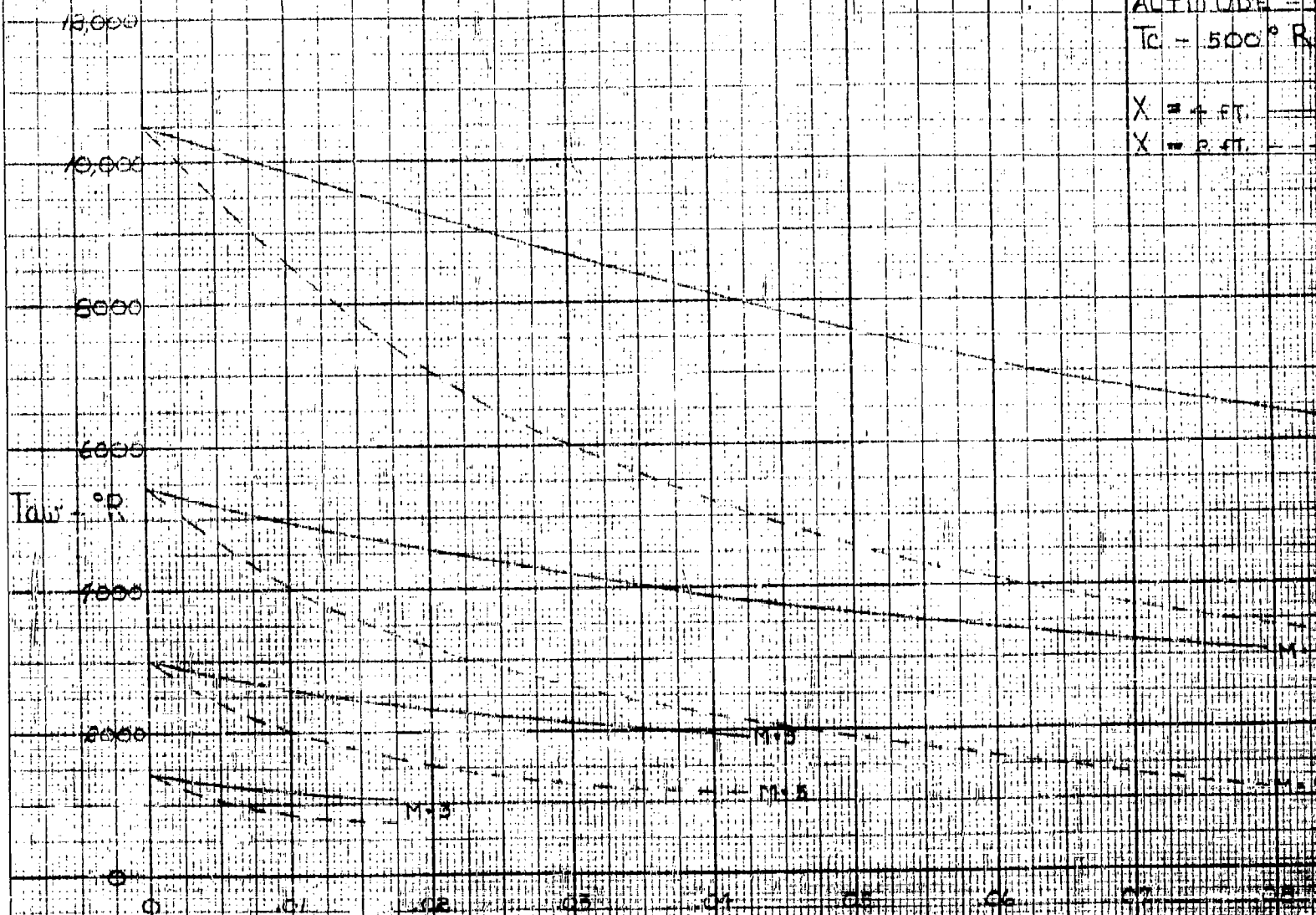
$Q_c - \text{lb/sec.}$

FIG. 2b

ADIABATIC
COOLANT W/
TURBULENCE

ALTITUDE -
 $T_c = 500^\circ R$

$X = 4$ FT. —
 $X = 8$ FT. - -



1

$Q_{in} = 10$ BTU/hr

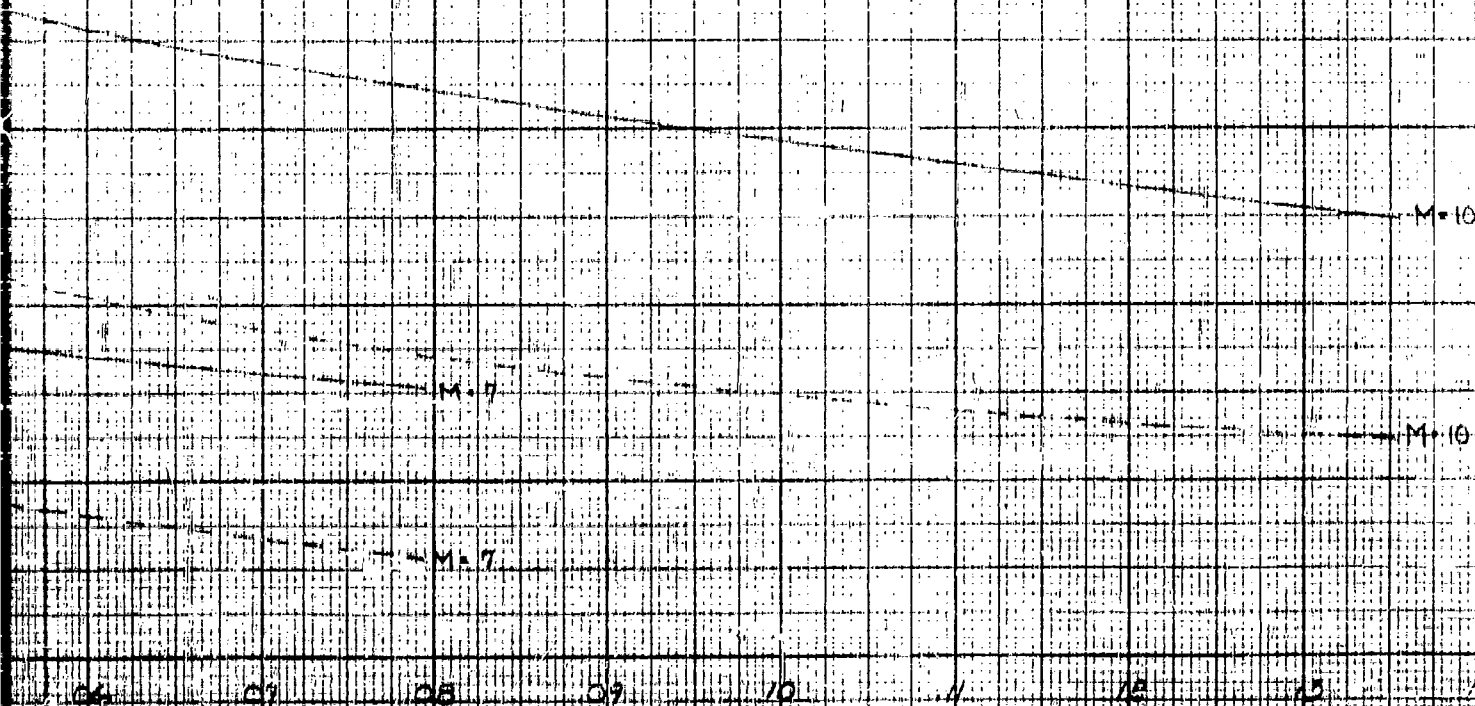
ADIABATIC WALL TEMPERATURES VS COOLANT WEIGHT FLOW FOR TURBULENT BOUNDARY LAYER

ALTITUDE - 150,000 FT

$T_c = 500^\circ R$

$X = 7$ FT

$X = 3$ FT



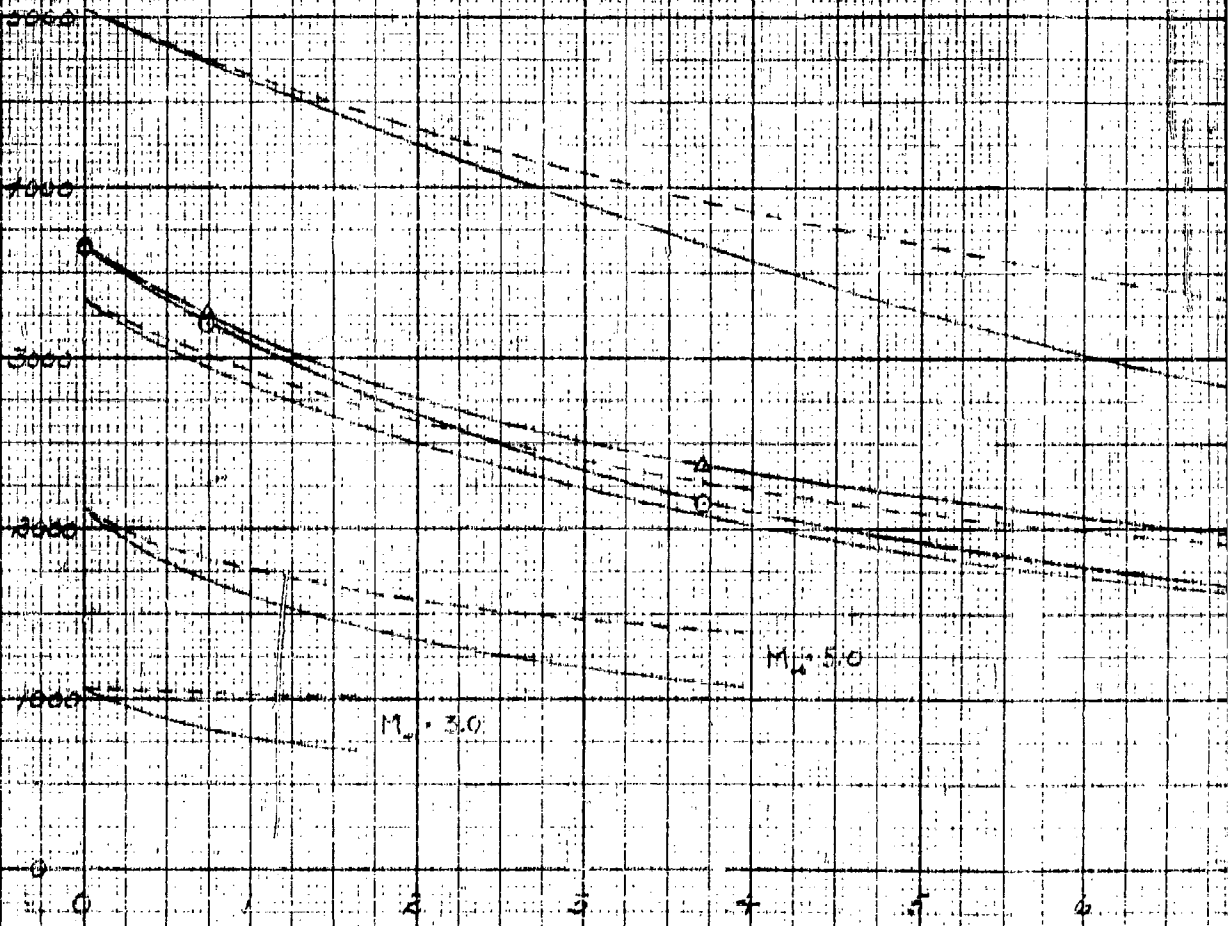
2

FIG. 2c

RADIATION EQUIL
VS. COOLANT WE
TURBULENT BOL

ALTITUDE - 50,000
X = 4.51

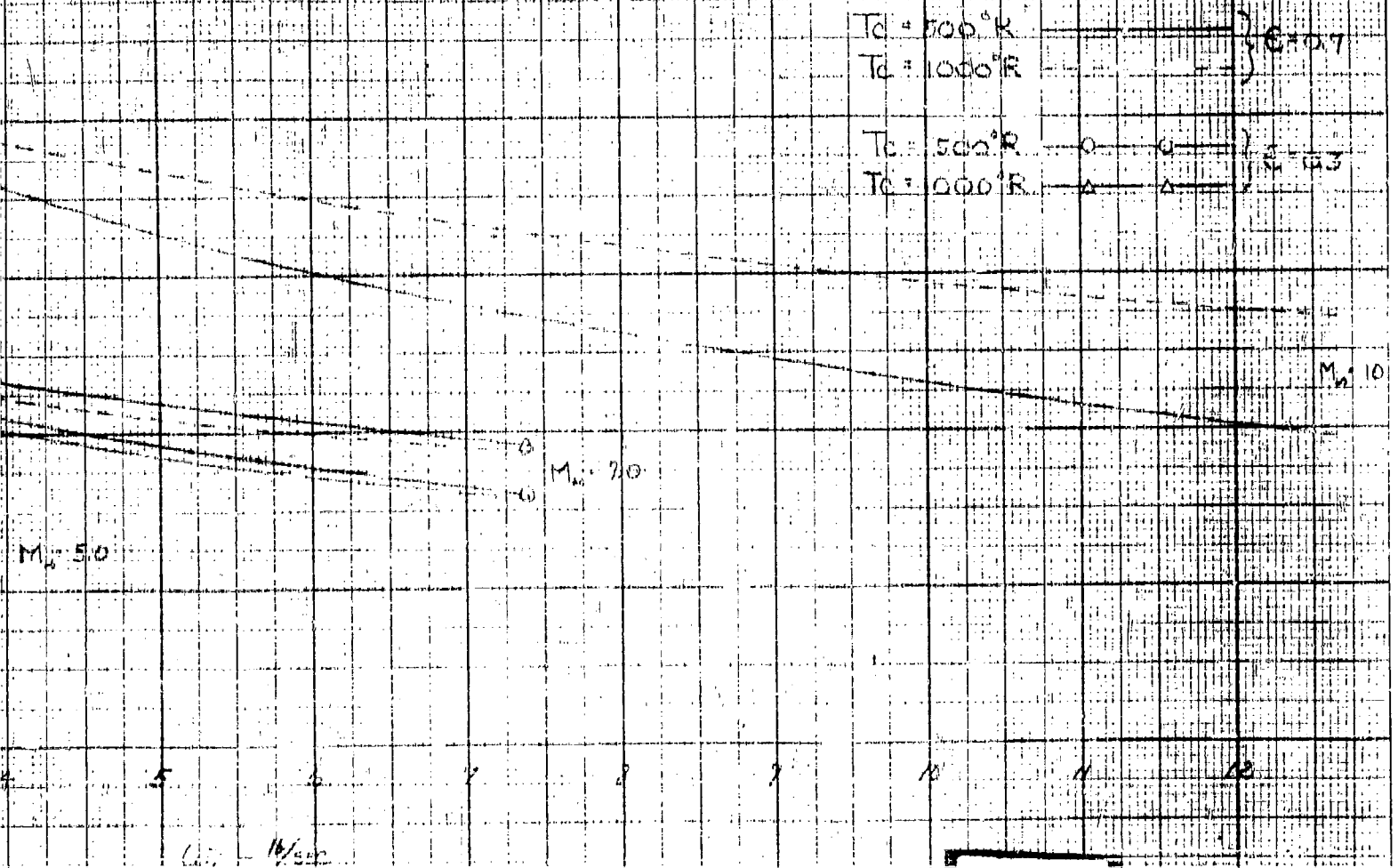
$T_w - ^\circ R$



1

RADIATION EQUILIBRIUM TEMPERATURE VS COOLANT WEIGHT FLOW FOR TURBULENT BOUNDARY LAYER

ALTITUDE - 30,000 FT
X - 10 FT

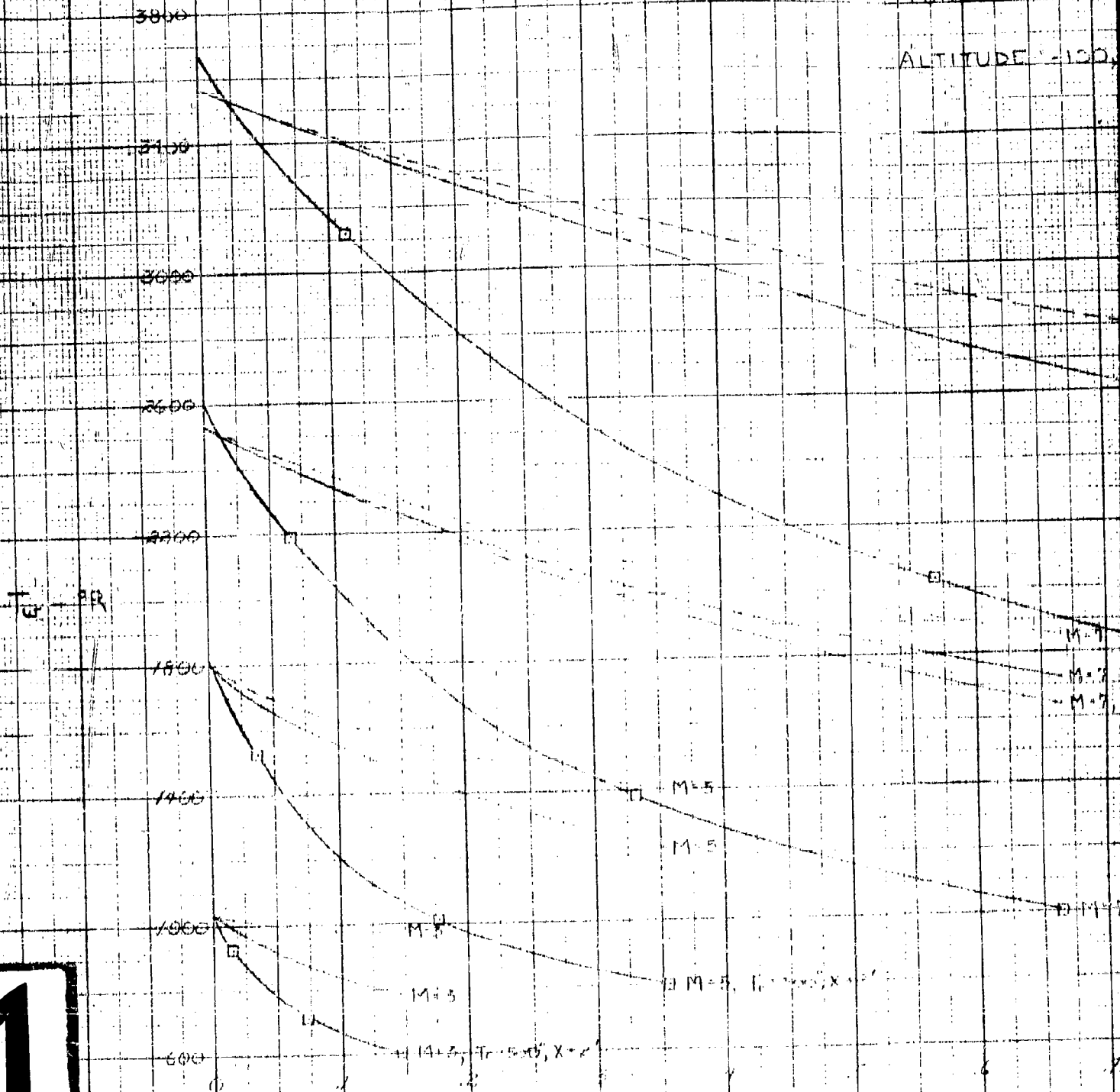


2

FIG. 3A

RADIATION EQUATION
VS. COOLANT WEIGHT
TURBULENT FLOW

ALTITUDE - 1000

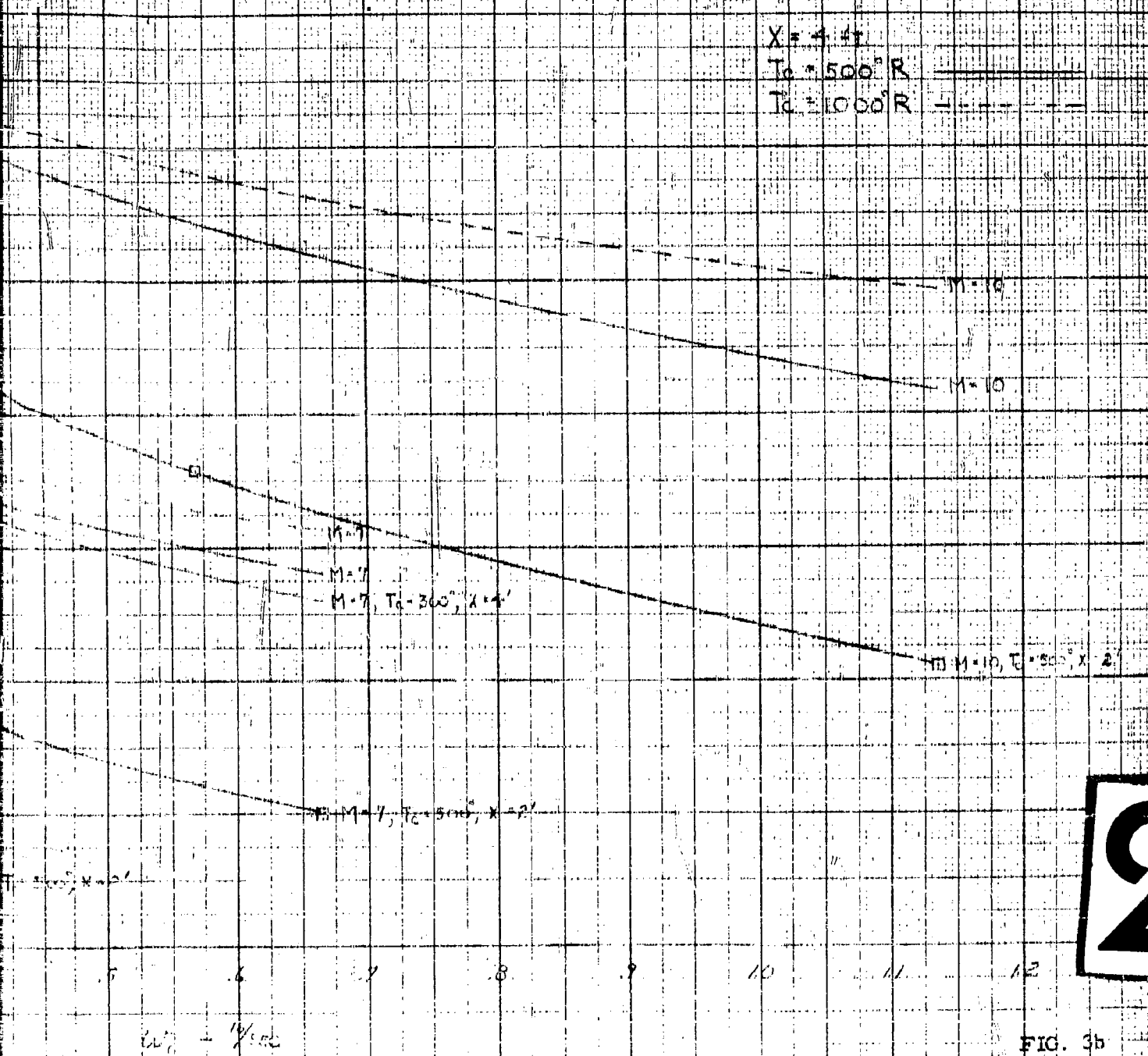


1

$G = \frac{10}{\text{cm}^2}$

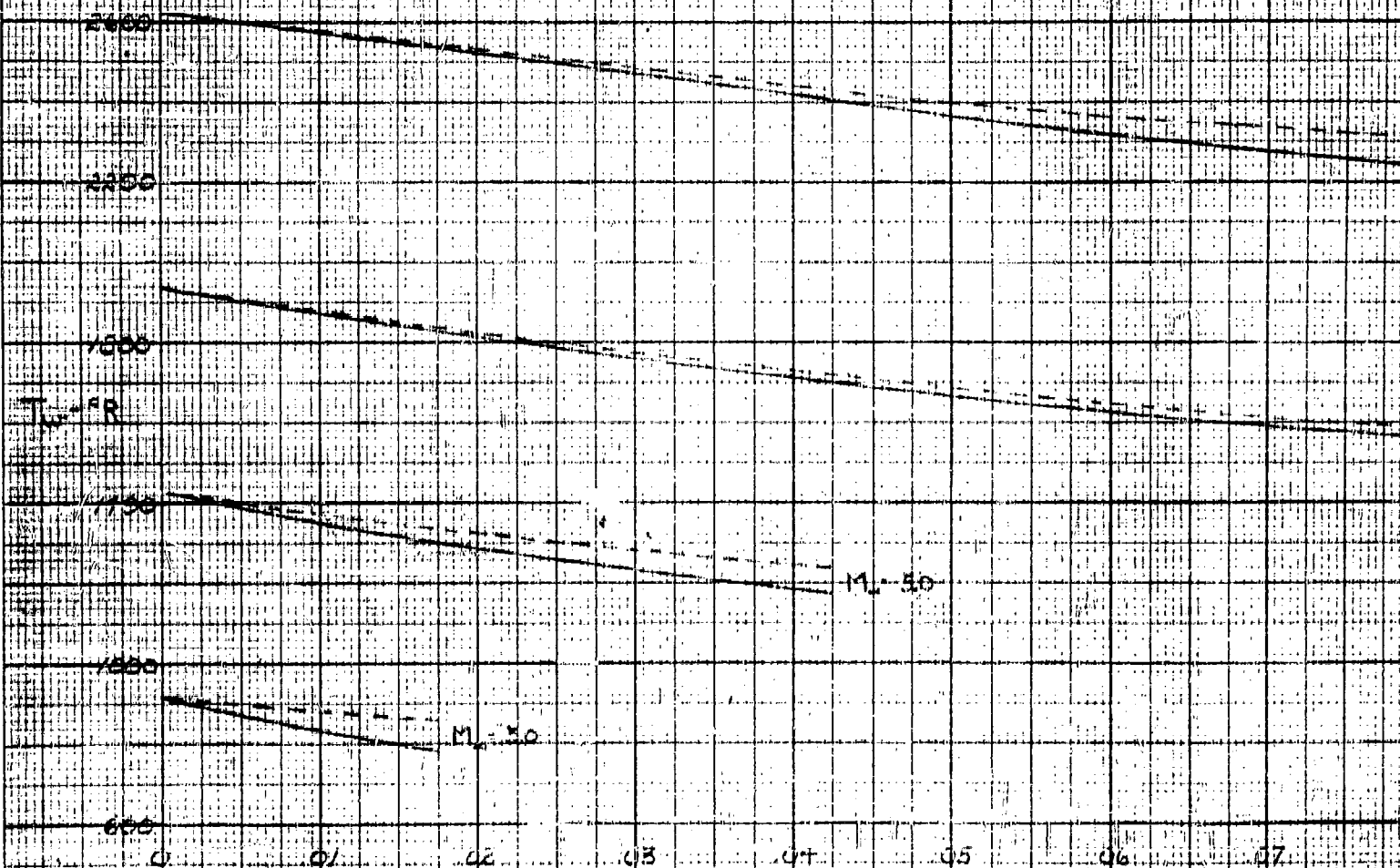
RADIATION EQUILIBRIUM TEMPERATURE VS. COOLANT WEIGHT FLOW FOR TURBULENT BOUNDARY LAYER

ALTITUDE - 100,000 FT.



RADIATION HE
 V_s 650 AM
 TURBULENT

ALTITUDE - 1



1

1.7 - 16/

RADIATION EQUILIBRIUM TEMPERATURE VS. COOLANT WEIGHT FLOW FOR TURBULENT BOUNDARY LAYER

ALTITUDE - 150,000 FT.

$X = 4.5 \text{ FT.}$

$T_a = 500^\circ \text{R.}$

$T_c = 1000^\circ \text{R.}$

$M_\infty = 7.0$

2

06

07

08

09

10

11

12

$G_c = 10^5 \text{ lb/sec.}$



TYPICAL RADOME TRAJECTORY



2

FIG. 4

WALL TEMPERATURE
OVER A TYPICAL RA

TURBULENT BOUNDAR

$T_c = 500^\circ R$

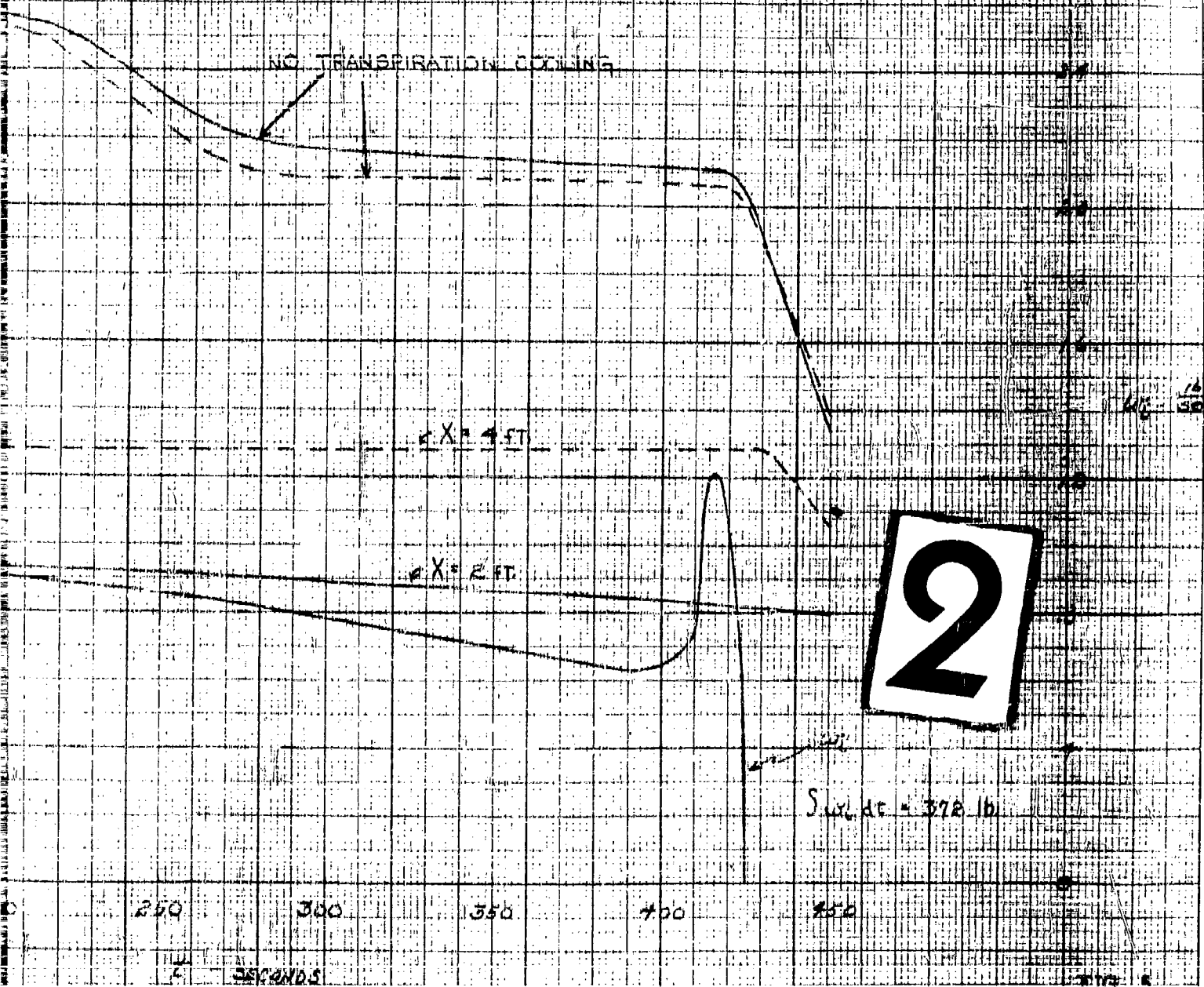


1

WALL TEMPERATURE & CORRESPONDING WEIGHT FLOW DISTRIBUTION OVER A TYPICAL RADOME TRAJECTORY

TURBULENT BOUNDARY LAYER

$T_c = 500^\circ R$



CHAPTER II - PART D

EFFECT OF UPSTREAM TRANSPIRATION COOLING IN LAMINAR
FLOW ON THE DOWNSTREAM WALL TEMPERATURE OVER THE
SURFACE OF A CONE

by L. Galowin

TABLES OF CONTENTS

<u>Section</u>	<u>Title</u>	<u>Page</u>
	Summary	488
	Symbols	489
1.	Introduction	491
2.	Analysis	494
3.	Results and Discussion	498
	References	502
	Appendix	503
	Figures	511

D. EFFECT OF UPSTREAM TRANSPIRATION COOLING IN LAMINAR
FLOW ON THE DOWNSTREAM WALL TEMPERATURE OVER THE
SURFACE OF A CONE

SUMMARY

An engineering analysis is presented for the purpose of evaluating the effect of upstream transpiration cooling on the heat transferred to a downstream impermeable wall surface in laminar flow. The solution of the problem for the flat plate in laminar flow is used for the determination of wall temperatures on a conical radome configuration. The investigation considered two cases: i) radiation equilibrium, and ii) transient trajectory conditions for application to advanced hypersonic missiles.

The appendix contains a discussion of several methods of supplying coolant mixtures for transpiration cooling at the temperatures required to cool the wall. Numerical results for several mixtures of water-air, hydrogen-air and nitrogen-air are presented.

SYMBOLS

$a = \frac{1}{\rho c_p T}$	parameter for wall material properties and thickness
c_p	specific heat at constant pressure
$f(0) = -2 \frac{\rho_s v_s}{\rho_\infty u_\infty} \sqrt{R_x}$	injection parameter
h	heat transfer coefficient
h_{a1}, h_{w1}	enthalpy of air and water at state 1
$(h_{a2})_{p_{a2}}, (h_{w2})_{p_{w2}}$	enthalpy of air and water at state 2 at their respective partial pressures
h_{fg}	heat of vaporization
$H_{av} = h_{av} + U \epsilon T_{w1}^3$	effective average heat transfer coefficient
L	length of cone
M_∞	free stream Mach number
$N_{f,x}$	ordinate of Figure 1
p_{a2}, p_{w2}	partial pressures of air and water respectively at state 2
Pr_r	Prandtl number at reference temperature
q_c	convective heat flux
q_{net}	net heat flux
Q	heat load required to cool stagnation air
R_x	Reynolds number based on length x
T_{aw}	adiabatic wall temperature
T_c	injection coolant fluid temperature
T_e	temperature at outer edge of boundary layer
T_r	reference temperature

T_t	total temperature
T_{sat}	saturation temperature
T_{stor}	storage bottle temperature
t	time
u_e	velocity at outer edge of boundary layer
u_{∞}	free stream velocity
v_s	velocity of injected coolant at surface
w	weight flow rate
w_a	weight flow rate of air
w_w	weight flow rate of water
x	coordinate along surface of cone
x_0	length of porous section along surface of cone
x_{a2}, x_{w2}	mole fractions of air and water at state 2
ϵ	emissivity of wall material
θ	half-cone angle
τ	thickness of cooled wall
μ_r	coefficient of viscosity at reference temperature
σ	Stefan-Boltzmann constant
ρ_s	density of injected coolant at surface
ρ_{∞}	free stream density
ρ_r	density at reference temperature

1. INTRODUCTION

It has been shown that the method of injecting a coolant fluid through a porous wall can reduce the extreme surface temperatures on radomes for application to missiles in high speed, high altitude flight. This technique was suggested as a method for reduction of wall temperatures on impermeable surfaces downstream of the porous section. Since the coolant injection into the boundary layer provides a source of low energy fluid which mixes with the high energy flow the resultant mixture in the boundary layer downstream of the porous section is at a reduced energy level. As a consequence, there is a significant reduction in the aerodynamic heat input over a finite length of surface downstream of the porous section. The effectiveness of the reduction is dependent upon the rate at which additional high energy air enters and mixes in the thickening boundary layer thereby eliminating the effect of the coolant fluid. This report presents the method of analysis for laminar flows and the case with turbulent flow is analyzed in Part C.

The porous material with the required manifolding and piping has the disadvantage of acting as a "blind spot" to the transmission and reception of radar waves (see Part C-c of this Chapter). Thus, it is impractical to consider an entire radome to be cooled by the method of transpiration cooling. With this method of cooling, the stagnation point can be maintained at reasonable temperature levels with large coolant flows. In order to provide sufficient additional flow of a coolant fluid such that the total effect of injected

coolant in the boundary layer over the remainder of the radome conceivably can solve the problem of reducing the high temperatures of the walls, a porous nose section can be considered. Then for this application the problem is to determine the required amount of coolant to be injected in order to maintain the downstream radome wall temperature below a prescribed (allowable) value.

In this analysis the assumption of all laminar flow appears as a possibility for an advanced hypersonic velocity missile flying along a trajectory discussed in Reference 1. Since it is not known whether the effect of porous injection on the boundary layer, for the high altitudes of interest, will result in transition from a laminar to turbulent flow this assumption requires experimental investigation.

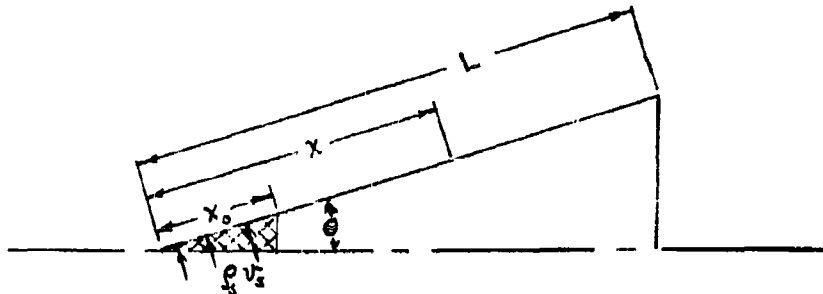
For the problem of a partially porous wall forming the apex and forward surface of a cone, it can be assumed that, for cone radii which are not small, the flat plate analysis is applicable. The solution for the porous wall temperature with various coolant flows can be obtained as described in Reference 2. Then the determination of the temperature along the downstream impermeable section can be carried out following the method described in Reference 3 for the adiabatic wall temperature.

The analysis presented in this report considers the effect of upstream transpiration cooling on the wall temperature on the downstream impermeable conical body. The coolant is considered to be air but other coolant fluids may be considered with modifications to the equations of Reference 3. The results are presented for a number of steady state flight conditions (radiation equili-

brium) and the transient wall temperature response along a typical advanced hypersonic missile trajectory.

2. ANALYSIS

The configuration considered is shown in the accompanying sketch.



The analysis presents a method for determination of the wall temperature at station x for a given amount of injected coolant per unit area, $\rho_w v_w$. The inner wall of the downstream impermeable surface is assumed to be insulated.

In steady flight, if radiation is neglected, the temperature of the wall reaches the adiabatic wall temperature. The curves presented in Figure 1 (from Ref. 3, Fig. 6) present the non-dimensionalized temperature ratio vs. non-dimensional length, $\xi = \frac{x}{x_0}$, for several injection parameters, $f(0)$. The adiabatic wall temperature can readily be determined for a given coolant temperature, flight condition (Mach number and altitude) and injection parameter from the ratio

$$T_{aw} = N_{f,x}(T_t - T_c) + T_c \quad (1)$$

where $N_{f,x}$ is the ordinate of Figure 1. For the completely impermeable cone, the adiabatic wall temperature is given by

$$T_{aw} = T_t(P_{R_r})^{1/2} + (1 - P_{R_r})^{1/2} T_c \quad (1a)$$

(See Part E of Chapter I for methods of determining heat flux for radomes.)

Note that the case for the injection parameter $f(0) = 0$ corresponds to a cooled upstream surface with the wall maintained at T_c (acting as a heat sink) without specifying the manner in which this is accomplished.

The non-dimensionalized local injection rate is defined by

$$f(0) = - \frac{2 \rho_s v_s}{\rho_\infty u_\infty} \sqrt{R_x} \quad (2)$$

Since the local injection velocity, v_s , is assumed to vary inversely with \sqrt{x} , the total weight flow rate through the porous wall surface area is obtained from

$$w = \int_0^{x_0} \rho_s v_s dA = - \frac{2}{3} \pi \frac{\rho_\infty u_\infty}{\sqrt{R_x}} f(0) x_0^2 \tan \theta \cos^2 \theta \quad (3)$$

The convective heat flux to the wall is given by

$$q_c = h (T_{aw} - T_w) \quad (4)$$

It is assumed that the relationship for the heat transfer coefficient remains unchanged with injection, so that for laminar flow

$$h = \frac{0.0796 \sqrt{3} (\rho_r u_e \mu_r)^{1/2}}{P_{R_r}^{2/3} x^{1/2}} \quad (5)$$

Fluid properties are evaluated at a reference temperature, T_r , given by

$$T_r = .5 T_w + .22 T_t + .28 T_e \quad (5a)$$

Since h is strongly dependent on conditions at the outer edge of the boundary layer, the assumption for h with injection is a good first approximation.

For the steady state condition where the local convective heat input to the wall is in balance with the local radiative heat flux away from the wall to free space, the equilibrium wall temperatures are obtained from

$$h(T_{aw} - T_w) = \sigma \epsilon T_w^4 \quad (6)$$

The adiabatic wall temperature is somewhat less than the stagnation temperature at the edge of the boundary layer for the uncooled wall. For the case under consideration here, with transpiration cooling upstream, the adiabatic wall temperature can be considerably decreased as shown in Fig.1. Hence, a reduction in heat transfer and wall temperature is obtained downstream of the porous region.

A simplified approximate method to solve the one-dimensional heat flux problem for the determination of the transient wall temperature was presented in Reference 1. The accuracy of the method has been shown to be good for walls which do not have large variations in the temperature distribution through the thickness. The calculation is carried out with average constant values of the adiabatic wall temperature and heat transfer coefficient for time intervals $\Delta t = t - t_1$. The equation for the outer wall temperature at any time is

$$T_w = (T_{w1} - \frac{h_{av}}{H_{av}} T_{aw,av}) e^{-a H_{av} \Delta t} + \frac{h_{av}}{H_{av}} T_{aw,av} \quad (7)$$

where T_{w1} is the wall temperature corresponding to the end of the previous time interval t_1 . The adiabatic wall temperature is obtained from Equation (1) or Equation (1a) and is the mean value over the time t and t_1 . Similarly, the average for h is formed from Equation (5) and then

$$H_{av} = h_{av} + \sigma \epsilon T_{wi}^3 \quad (7a)$$

Material properties of the wall and the thickness, τ , are contained in

$a = \frac{1}{\rho c_p \tau}$. From the solution of the wall temperature as a function of time, the net heat input can then be found from

$$q_{net} = h (T_{aw} - T_w) - \sigma \epsilon T_w^4 \quad (8)$$

3. RESULTS AND DISCUSSION

A representative radome configuration shown in Fig. 1, Part C-b was selected to illustrate the effect of upstream injection on wall temperatures in laminar flow. The nose cone porosity and/or pressure distribution are assumed to be combined so as to provide an injection velocity at the wall varying inversely with \sqrt{x} .

It is necessary to remove a possible ambiguity in the consideration of the limiting case of zero injection. The notation $f(0) = 0$ indicates that the wall is impermeable (in this case, the nose cone) which is cooled to the temperature of the coolant, T_c , without any consideration of the cooling mechanism for achieving this. In this case, the nose section now acts as a heat sink and provides a strongly cooled boundary layer which then affects the downstream region in a similar manner to the result with the injection of a coolant fluid. The completely impermeable radome is also considered without any cooling so that the wall reaches either the adiabatic temperature (in the absence of radiation) or is at the radiation equilibrium temperature for the steady state condition; along the trajectory, the wall attains the temperature given by the transient solution. In Table I the results of the computation of the wall temperature at $x = 2$ ft. and 4 ft. are presented. Note that for $f(0) = 0$, the wall temperatures are decreased due to the cool boundary layer formed over the heat sink. The effect of a change in T_c from 500° to 1000°R at $M = 10$ shows a small cooling effect at $x = 2$ ft. and for practical purposes has lost all effect at $x = 4$ ft.

The solution for T_w requires that a value of T_w be assumed in order to determine the reference temperature T_r to permit evaluation of flow properties. For one case $x = 4$ ft., at $M = 10$ and 100,000 ft., the insensitivity to the assumed T_w was shown by assuming $T_w = 2820^\circ\text{R}$ and finding from equation (6) a value $T_w = 2481^\circ\text{R}$. This latter value was then used to determine T_r and the resultant T_w again found from equation (6) to be 2489°R .

The reduction in adiabatic wall temperatures obtained from equation (1) for $M = 3, 5, 7, 10$ at 100,000 ft. altitude at two locations $x = 2$ ft., 4 ft. are shown in Figure 2. The further downstream location, $x = 4$ ft., experiences a lesser effect than those sections close to the porous region, while with increasing Mach number there is a greater difference between the $x = 2$ ft. and $x = 4$ ft. position. This is accounted for by the increased high energy flow mixing into the boundary layer diluting the coolant to a greater extent at higher Mach numbers.

The radiation equilibrium wall temperatures with coolant temperature $T_c = 500^\circ\text{R}$ were computed from equation (6) with equation (1) for $M = 10$ at altitudes of 50,000 ft., 100,000 ft. and 150,000 ft. and are presented in Figure 3. The reduction in temperature for the ranges of total coolant weight flow remain approximately the same since the mass flow ratios were essentially constant and limited to $f(0) = -1$, so that at the same station x , the temperature ratio from Figure 1 is the same. The effect of changing the coolant temperature T_c from 500°R to 1000°R is also shown on the figure for an altitude of 100,000 (the effect at other altitudes is similar). With

increasing length along the radome, it is seen that the coolant effects are less significant and the differences with coolant supply temperature tend to vanish.

For a constant altitude of 100,000 ft. and $T_c = 500^\circ\text{R}$, the effect of Mach number variations from 3 to 10 are shown for the case of radiation equilibrium wall temperatures in Figure 4. The results are plotted for the two stations $x = 2$ ft. and 4 ft. over a small range of w corresponding to the $f(0)$ values of Figure 1. The crossing of the curves of $x = 2$ ft. and 4 ft. for $M = 3$ and 5 results from the greater decrease in the convective heat input at $x = 2$ ft. The heat transfer coefficient decreases with length varying as $x^{-1/2}$; however, there is a stronger influence due to injection which suppresses the adiabatic wall temperature faster at $x = 2$ ft. compared to that at $x = 4$ ft. with increased coolant flow, w , which dominates the equation and reduces T_w . The required amount of coolant flow rate injected through the porous surface has been computed from equation (3). The results are summarized in Table II.

In order to illustrate the effect of the upstream injection on the transient wall temperature response, found from equation (7), a typical advanced hypersonic missile trajectory was selected as shown in Figure 4, Part C-b. Since the heat capacity of the wall provides in effect a sink for the heat input, the finite time required to absorb the heat causes a lag in the temperature response so that the equilibrium temperature is never reached.

In Figures 5a and 5b, the effect of the upstream injection on wall temperature for the uncooled cone and with cooling for values of $f(0) = 0, -0.5, -1.0$

at $x = 2$ ft. and $f(0) = 0$, -1.0 at $x = 4$ ft. is shown. Where the nose acts as a heat sink the surface is maintained at 500°R . The reduction in peak temperature due to the cooling without injection (heat sink case) is greater at $x = 2$ ft. than at $x = 4$ ft. (peak ΔT_w of 140° compared to ΔT_w of 20°). The change in heat transfer due to the mass addition in the upstream boundary layer results in further decrease in the peak wall temperature of 120° at $x = 2$ ft. and 65° at $x = 4$ ft. It is observed that there is a shift in peak wall temperature to later times as a result of the decrease in the aerodynamic heating.

The amount of coolant required to cool the wall for the trajectory considered, with the results shown in Figures 5a and 5b, was computed from equation (3) for each time instant and then integrated numerically over the total time for total coolant weight. The results of the computation are shown in Figure 6; the total coolant weight flows are 0.44 pounds for $f(0) = -.5$ and 0.89 pounds for $f(0) = -1.0$.

REFERENCES

1. Lane, F., Pergament, H. S. and Galowin, L.: Thermal Shock Testing of scaled Alumina Radomes. AMC Phase Report No. I, GASL Technical Report No. 106, May 31, 1959.
2. Low, G. M.: The Compressible Laminar Boundary Layer with Fluid Injection. NACA TN 3404, 1955.
3. Rubesin, M. W. and Inouye, M.: A Theoretical Study of the Effect of Upstream Transpiration Cooling on the Heat-Transfer and Skin-Friction Characteristics of a Compressible, Laminar Boundary Layer. NACA TN 3969, 1957.

APPENDIX

SOURCES OF COOLANT FLUIDS FOR RADOME COOLING

1. General Discussion

In order to utilize transpiration cooling as a method of cooling radomes for high speed missiles, it is necessary to consider the means of providing a source of supply for the coolant fluid. The requirements of minimum storage space and weight makes it essential to evaluate the devices for the supply of the coolant as an integral part of the complete missile. The choice between the self-contained storage supply or an external ram-air supply for the coolant is usually dependent on the propulsion system. For air-breathing engines, an air inlet is necessarily included in the missile design so that ram-air can readily be supplied for cooling purposes. The applications of rocket engines are frequently for trajectories beyond the atmosphere and protection of a radome is then necessary for short time periods with stored coolants. It is, therefore, necessary to consider the missile as a complete system. For the intended applications with porous materials, the injected coolant must be clean to prevent clogging. There should be a sufficient available internal pressure to inject the coolant through the porous wall whose external pressure is fixed by the configuration and flight condition.

There is uncertainty concerning the extent of any significant interference problem with radar transmission and reception through a wet coolant mixture flowing over the radome surface. Available information indicates that the

protected surface cannot be covered by a flow of liquid. However, a cloud-like mixture in the air-flow (so-called wet mixtures) may be permissible. For this report only dry mixtures (superheated steam, for example) are analyzed. However, one should not overlook the possibility of cooling by upstream surface evaporation, utilizing the latent of vaporization of a liquid coolant injected through a porous wall. The downstream flow will then be a mixture of air, evaporated coolant and droplets. At the low pressures on the external radome surface there will be a rapid change from the liquid to the gas phase.

For the stored coolant supply systems there is not much latitude for the designer to select any other system than the high pressure storage bottles of coolants, e. g., helium, nitrogen, hydrogen, liquid air, water, hydrogen peroxide, etc. However, in a completely integrated system, if there are cooling requirements for other components (such as electronic gear, combustion chambers and nozzles) the choice may be made of a coolant which can be vaporized during the cooling of one component and then injected through the porous wall.

For the radome cooling on a missile with an air breathing propulsion system, the ram-air supply provides the primary source of cooling air. However, for the range of Mach numbers of interest, there is need for a cooling system to reduce the stagnation temperatures of the ram-air to useable levels before it is useful as a coolant. Devices such as a turbo cooler, (described in Part B-b of Chapter II), refrigerator systems, and liquid or low-temperature gas sprays to form cool mixtures, are techniques to supply

coolants at the required temperatures. The feasibility of each system depends, of course, on the heat load to be absorbed as a result of the flight conditions.

2. Ram-Air Coolant Supply System for Application to Conical Radomes

In order to illustrate the application of several ideas previously discussed, a ram-air coolant supply system was considered. The idealized characteristics of a variable geometry inlet were utilized in order to determine the maximum available pressure at various Mach numbers and altitudes. The assumed total pressure recovery vs. M_∞ is shown in Figure 7 and was used to determine the maximum available pressure for such a coolant supply as shown in Figure 8. The external pressures which exist over the outer surface of a 15° and 20° cone into which the coolant must be injected are shown in Figure 9. The maximum pressure difference, ΔP , required to overcome the pressure drop across the porous wall and inject the coolant fluid can then readily be obtained. The pressure drop is a function of the porosity and type of porous material (sintered metal, rolled wire mesh, porous ceramics, etc.).

The simple example of determining the weight flow requirement for a coolant air supply at 1000°R was analyzed. For this purpose, a pressurized water heat exchanger was assumed with sufficient heat absorbed to cause boiling at the pressure level of the water. The assumption of a boiling system makes full utilization of the latent heat of vaporization of water, h_{fg} . The ratio of weight flow rate of water to the weight flow rate of coolant air is given by

$$\frac{w_w}{w_{air}} = \frac{Q}{\left[\bar{c}_p (T_{sat} - T_{stor}) + h_{fg} \right] w} \quad (1)$$

The heat load Q results from reduction of the stagnation temperature of the air to the air coolant supply temperature desired. The temperature rise of the water is computed from the storage temperature T_{stor} to the saturation temperature corresponding to the pressure at which the water system is pressurized.

The requirements of such a system described above are shown in Figure 10 for various Mach numbers at altitudes of 40,000 ft., 100,000 ft. and 140,000 ft. The water storage temperature was selected to be 100°F. The effect of changing the pressure of the water system on the weight ratio is small, as shown for the 100,000 ft. altitude. The increase in the weight of water required to supply coolant air at 560°R as compared to 1000°R is also shown for the three altitudes.

A more efficient utilization of water would be in a spray system where water stored under pressure would be injected into the high temperature ram-air to supply a mixture as the coolant fluid for injection through the porous material. For this study only, a resulting mixture of the superheated steam was considered. It was assumed that the water atomized from the liquid state would absorb sufficient heat from the air to change into the gas phase. The final temperature of the steam-air mixture is the coolant fluid supply temperature so that for a given temperature the weight ratio of water (steam) to air is found from an energy balance

$$\frac{w_w}{w_a} = \frac{(h_{a2})_{p_{a2}} - h_{a1}}{h_{w1} - (h_{w2})_{p_{w2}}} \quad (2)$$

The enthalpies of the air and water at the final state 2, h_{a2} , and h_{w2} , must be evaluated for the partial pressures of the mixture, p_{a2} and p_{w2} . The partial pressures are found from the mole fraction for the air and water as

$$p_{a2} = p_2 x_{a2}; \quad p_{w2} = p_2 x_{w2} \quad (3a)$$

where p_2 is the pressure of the mixture at the final state and x_{a2} , x_{w2} are the mole fractions of air and water. The mole fractions can be determined from the mass ratios of air and water m_a/m_w , and their respective molecular weights M_a , M_w , so that

$$x_w = \frac{1}{1 + \frac{m_a}{m_w} \frac{M_w}{M_a}} \quad (3b)$$

and

$$x_a = 1 - x_w \quad (3c)$$

Finally the ratio of the water flow rate per pound of mixture is formed from

$$\frac{w_w}{w_{\text{mix}}} = \frac{1}{1 + w_a/w_w} \quad (4)$$

In Figure 11, the results of the determination of the weight ratio versus Mach number is shown for coolant supply mixtures of 1000°R and 750°R for a cone half angle of 20°. Figure 9 is used to estimate the pressure on the external surface of the cone. Corresponding to this pressure, the saturation temperature is determined as a first approximation to the minimum coolant mixture supply temperature (this results in a superheated steam). The pressure drop across the porous wall was held at a constant value corresponding approximately to the maximum difference between the available pressure of the ram-air from Figure 8 and the surface pressure on the cone at

$$M_{\infty} = 3.$$

Similar calculations were carried out to illustrate the use of high pressure storage bottles of hydrogen and nitrogen which are mixed with ram-air to form a gaseous mixture and the results are shown in Figure 12. For these mixtures, a lower coolant temperature can be supplied to the porous wall section than for the steam air mixtures. The use of very low temperature gas coolants without mixing with air should not be overlooked. For such systems there are increases in weight and storage requirements. The usefulness of such applications can be determined from other studies (e.g., that reported on the preceding pages). The purpose of mixing these low temperature gases with air is that the possibility is offered of supplying a coolant mixture at a reduction in the weight of stored, pressurized gas of 50 to 90% (see Figure 12).

TABLE I
Radiation Equilibrium Wall Temperatures for
Impermeable Case - Cooled and Uncooled

	M_{∞}	$T_w(^{\circ}R)$	
		$x = 2'$	$x = 4'$
Uncooled wall (no heat sink).	3	874	839
	5	1424	1338
	7	1947	1810
	10	2680	2481
Cooled wall (heat sink at $T_c = T_w = 500^{\circ}R$)	3	847	835
	5	1369	1330
	7	1880	1805
	10	2580	2452

TABLE IICoolant Weight Flow Rate

<u>Altitude (ft.)</u>	<u>M_∞</u>	<u>f(0)</u>	<u>w(#/sec)</u>
50,000	10	0	0
"	10	-0.5	.279 x 10 ⁻²
"	10	-1.0	.531 x 10 ⁻²
100,000	All	0	0
"	3	-0.5	.192 x 10 ⁻²
"	5	-0.5	.229 x 10 ⁻²
"	7	-0.5	.255 x 10 ⁻²
"	10	-0.5	.285 x 10 ⁻²
"	3	-1.0	.385 x 10 ⁻²
"	5	-1.0	.461 x 10 ⁻²
"	7	-1.0	.525 x 10 ⁻²
"	10	-1.0	.567 x 10 ⁻²
150,000	10	0	0
"	10	-0.5	.113 x 10 ⁻²
"	10	-1.0	.226 x 10 ⁻²

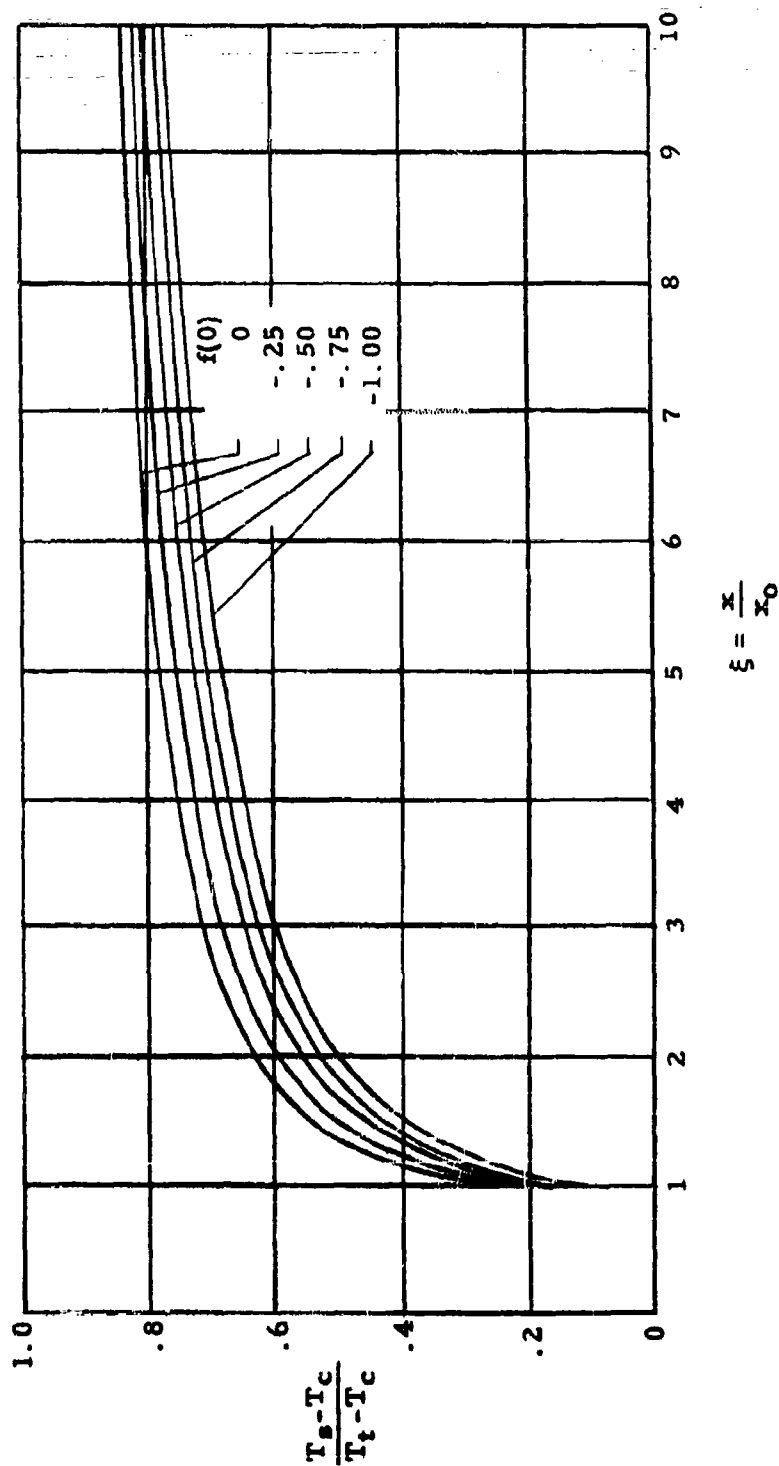
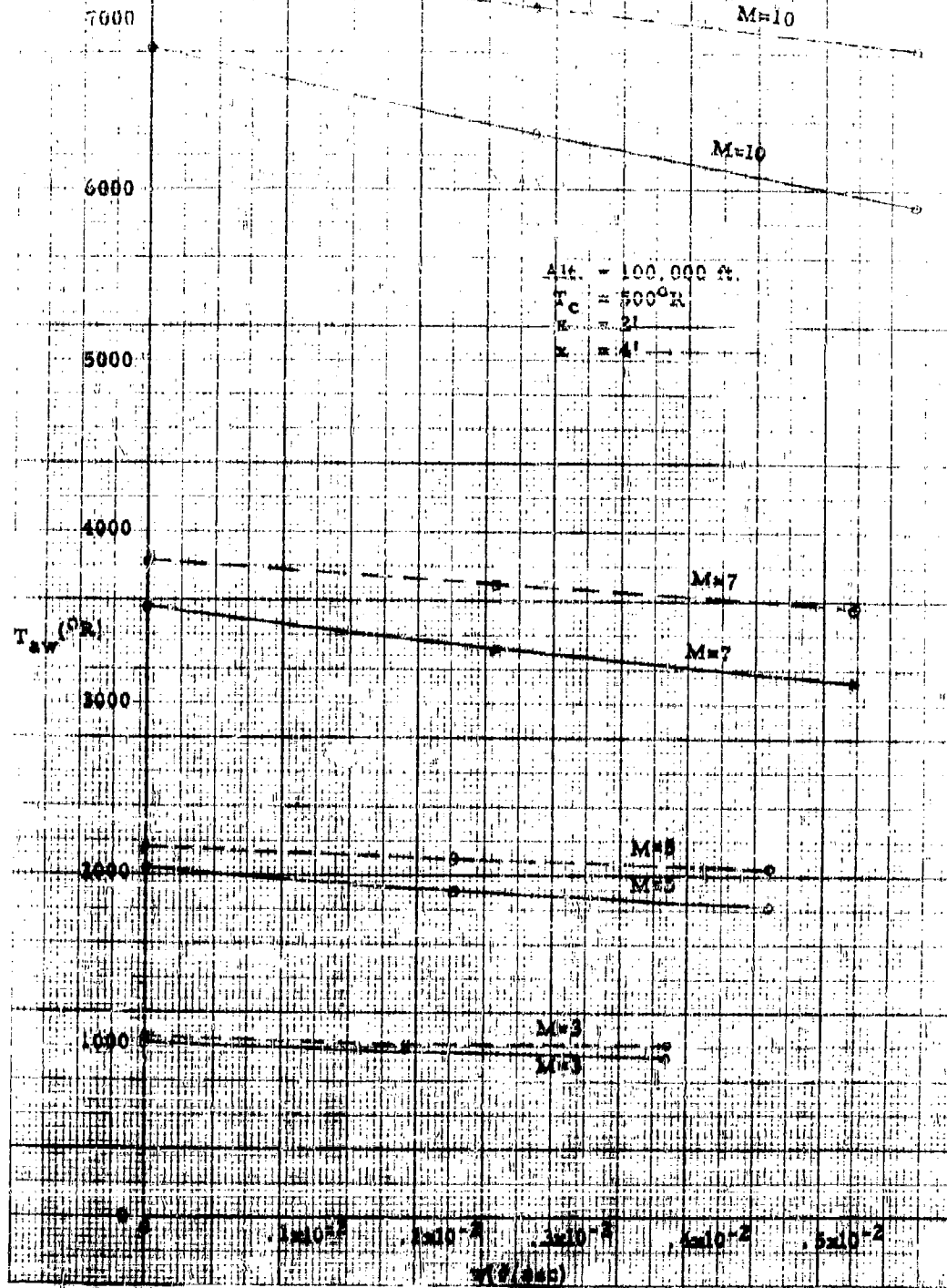
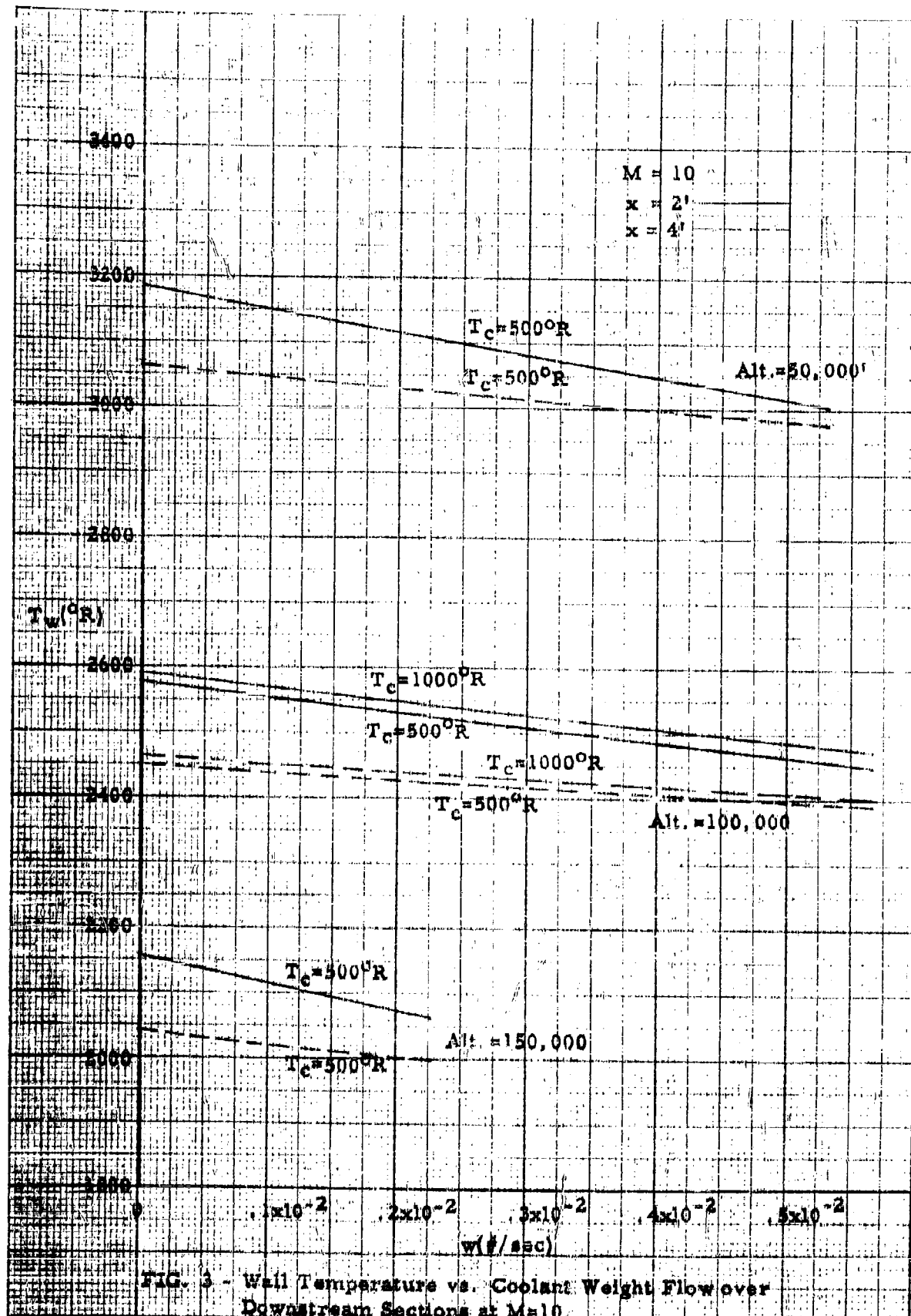


FIG. 1 - Temperature Distribution on an Insulated Nonporous Plate Behind a Region with Transpiration Cooling. (Fig. 6, Ref. 4)

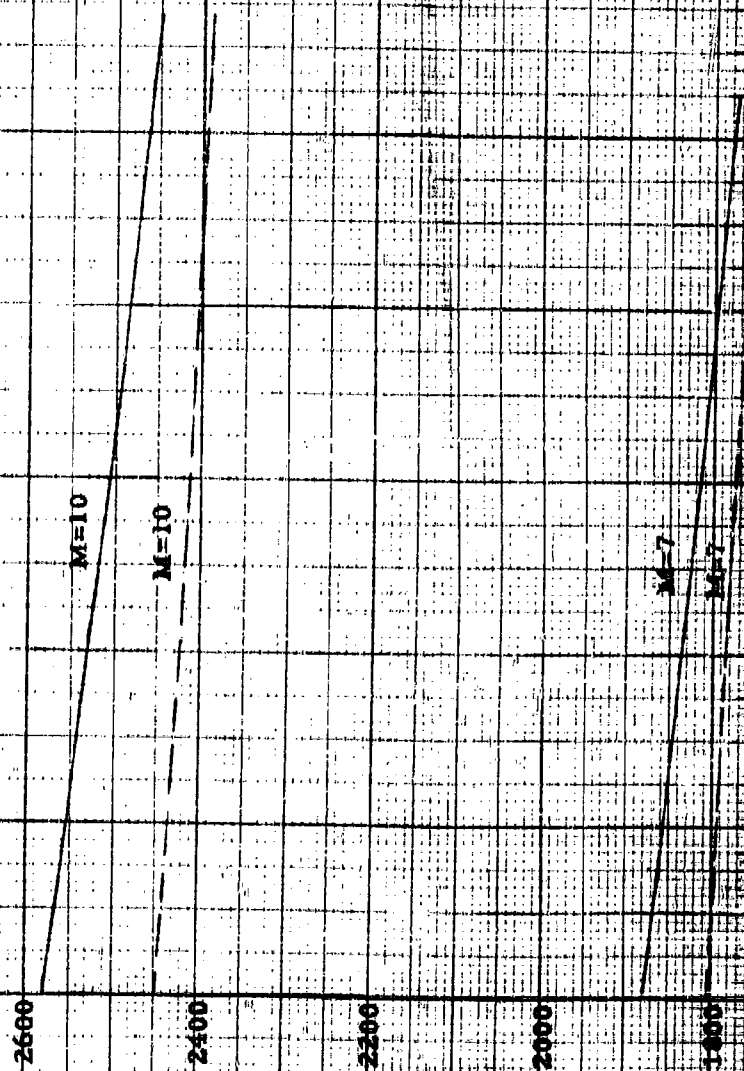
FIG. 2 - Adiabatic Wall Temperature vs.
Coolant Weight Flow over Down-
stream Sections.





1

Alt. = 100,000'
 $T_c = 500^\circ R$
 $\alpha = 2'$
 $\alpha = 4'$



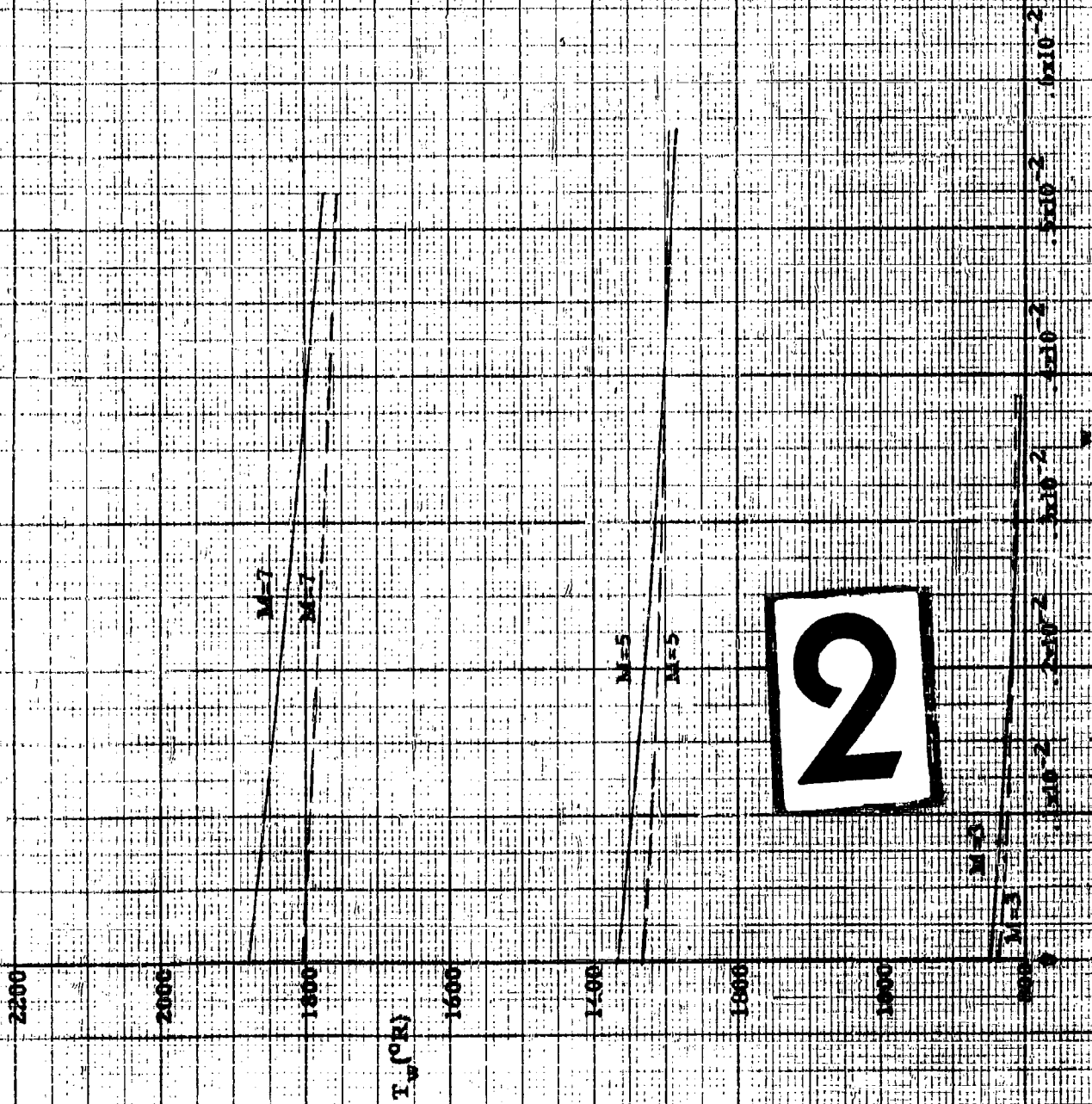
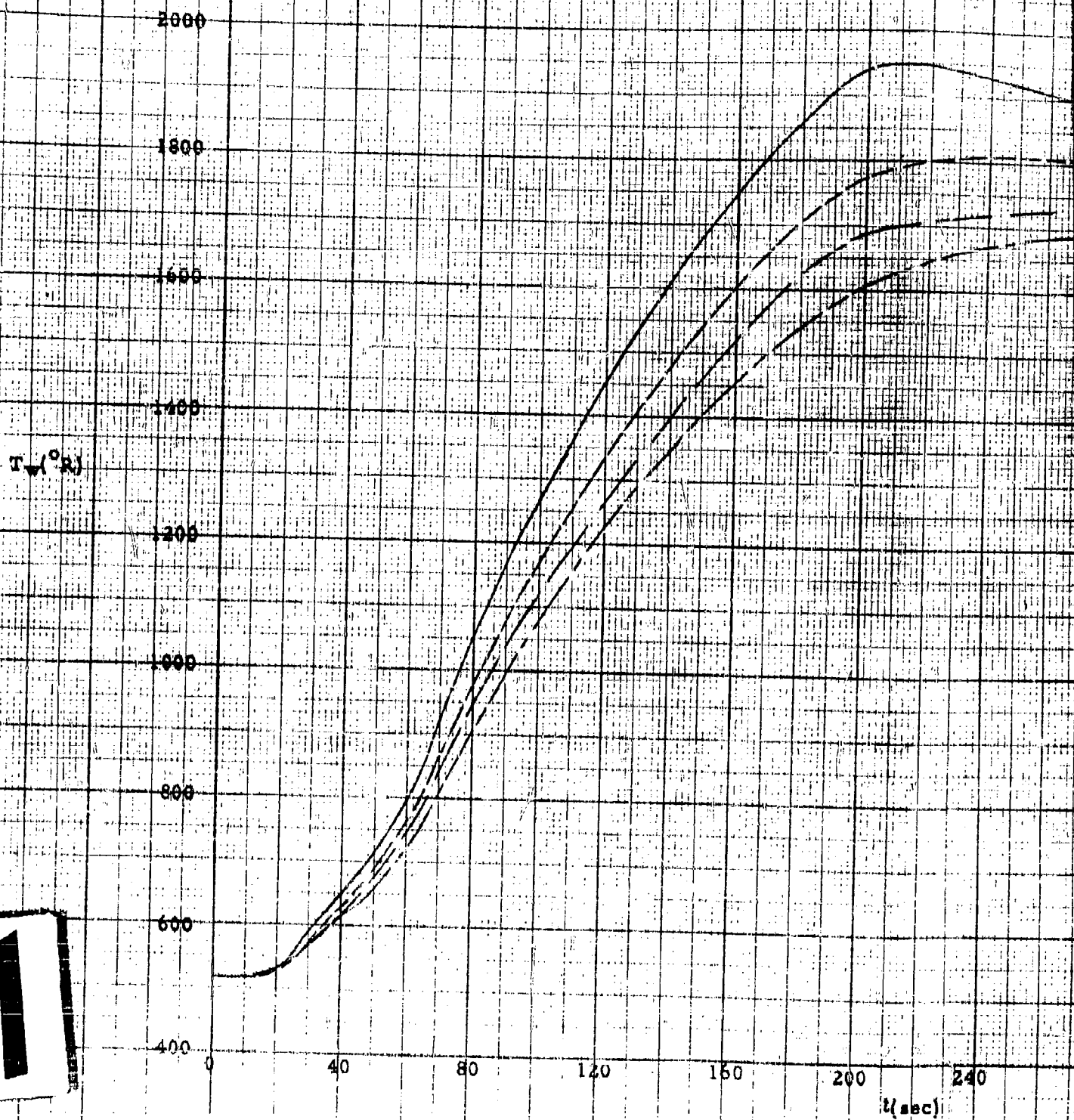


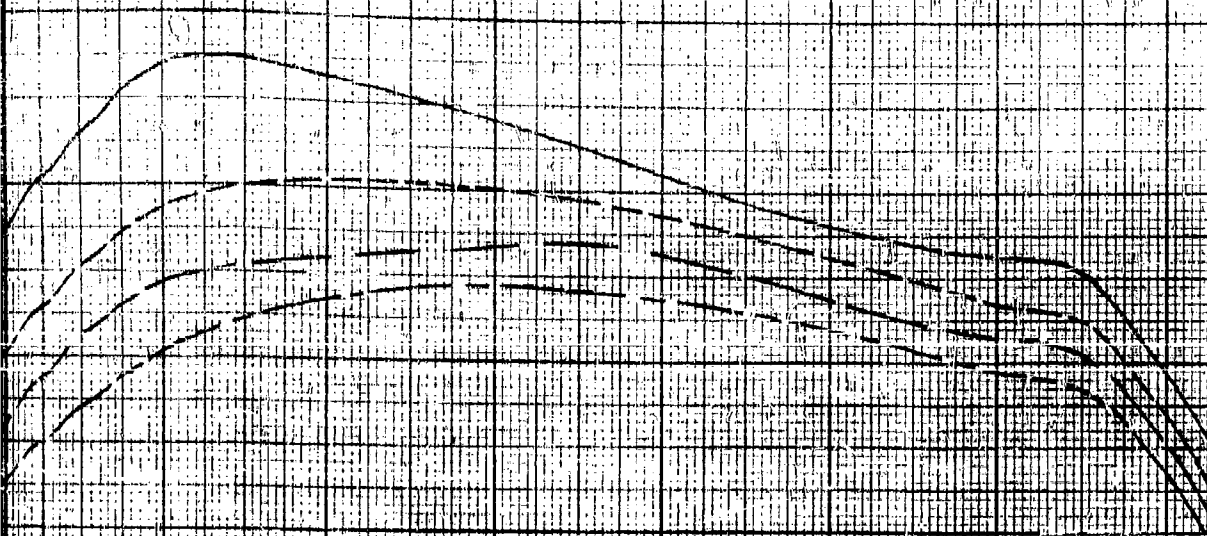
FIG. 4. Wall Temperature vs. Coolant Weight Flow over Downstream Sections for Various Mach Numbers.

FIG. 5a - Transient wall temperature T_w time at $x = 2l$



1

temperature vs. time at $x = 2'$

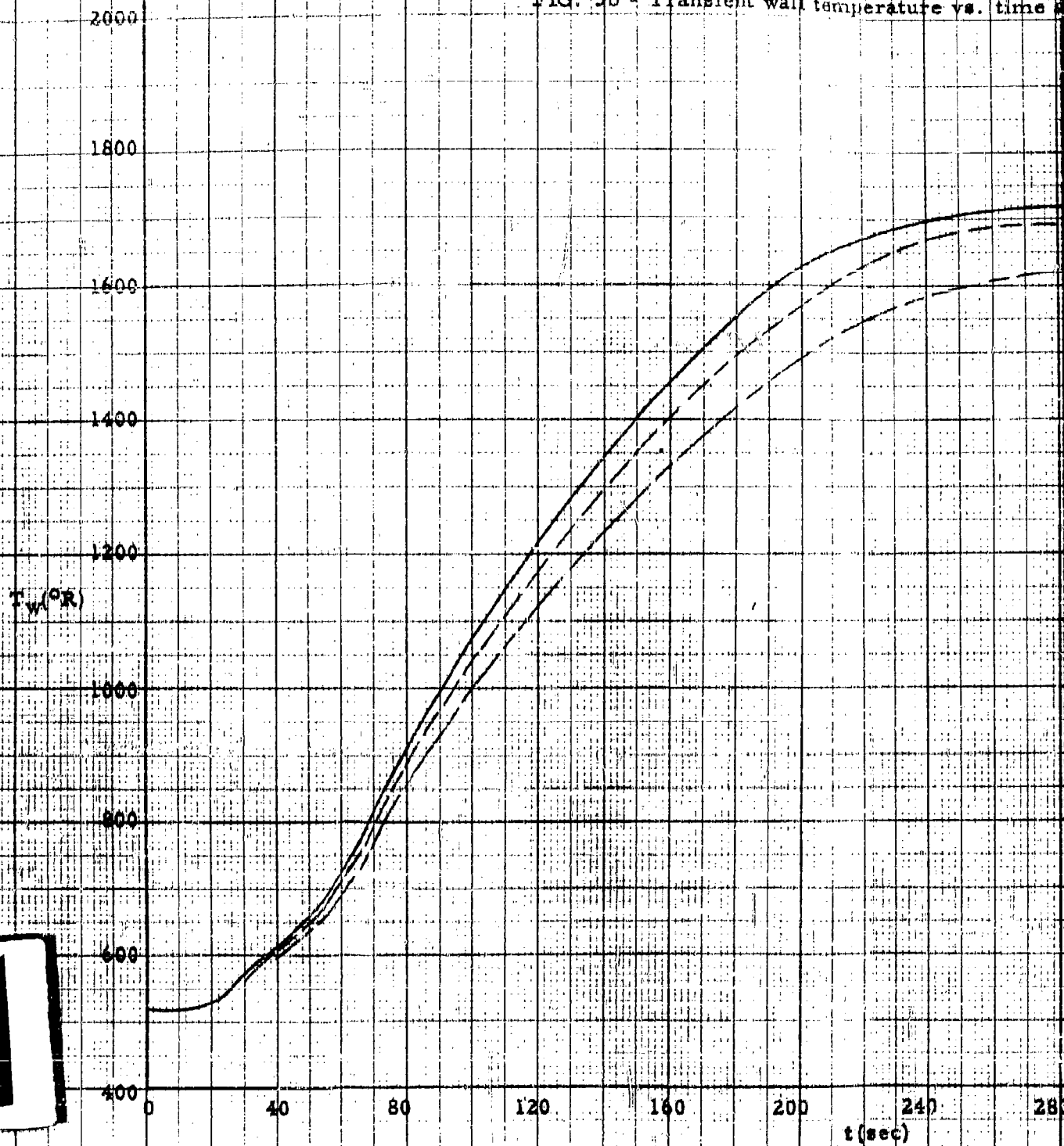


$x = 2'$
 No heat sink
 $f(0) = 0$ -----
 $f(0) = .5$ -----
 $f(0) = 1.0$ -----

2

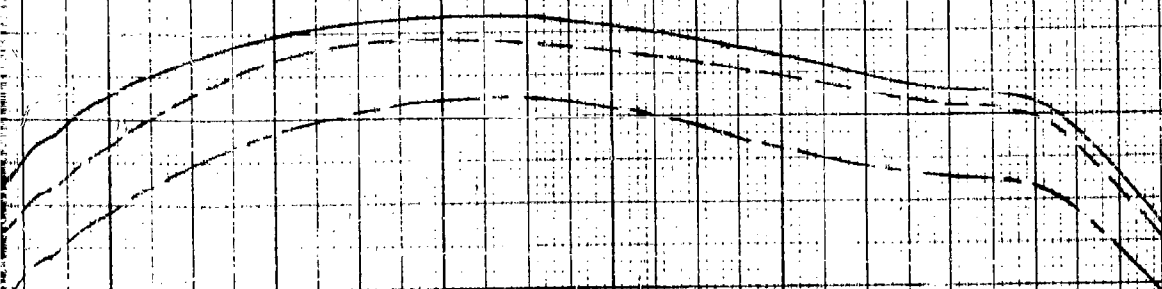
200 240 280 320 360 400 440 480
 $t(\text{sec})$

FIG. 5b - Transient wall temperature vs. time



1

ent wall temperature vs. time at $x = 4'$

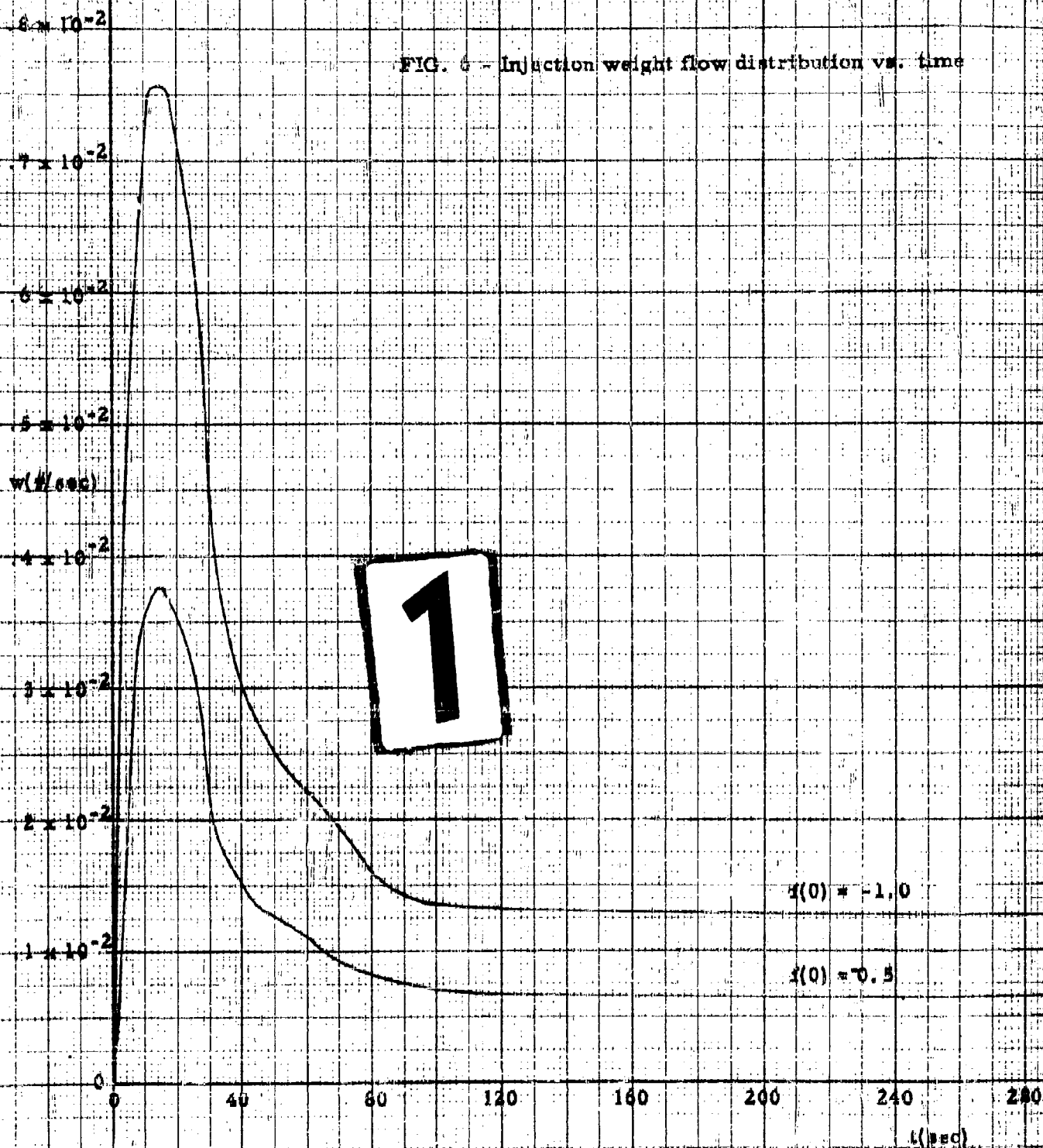


$x = 4'$
No heat sink ———
 $f(0) = 0$ - - - - -
 $f(0) = 1$ - · - · -

2

200 240 280 320 360 400 440 480
t(sec)

FIG. 6 - Injection weight flow distribution vs. time



tribution vs. time

$f(t)$	$W(\%)$
-0.5	0.44
-1.0	0.89

$f(t) = -1.0$

$f(t) = 0.5$

0 240 280 320 360 400 440 480
t(sec)

2

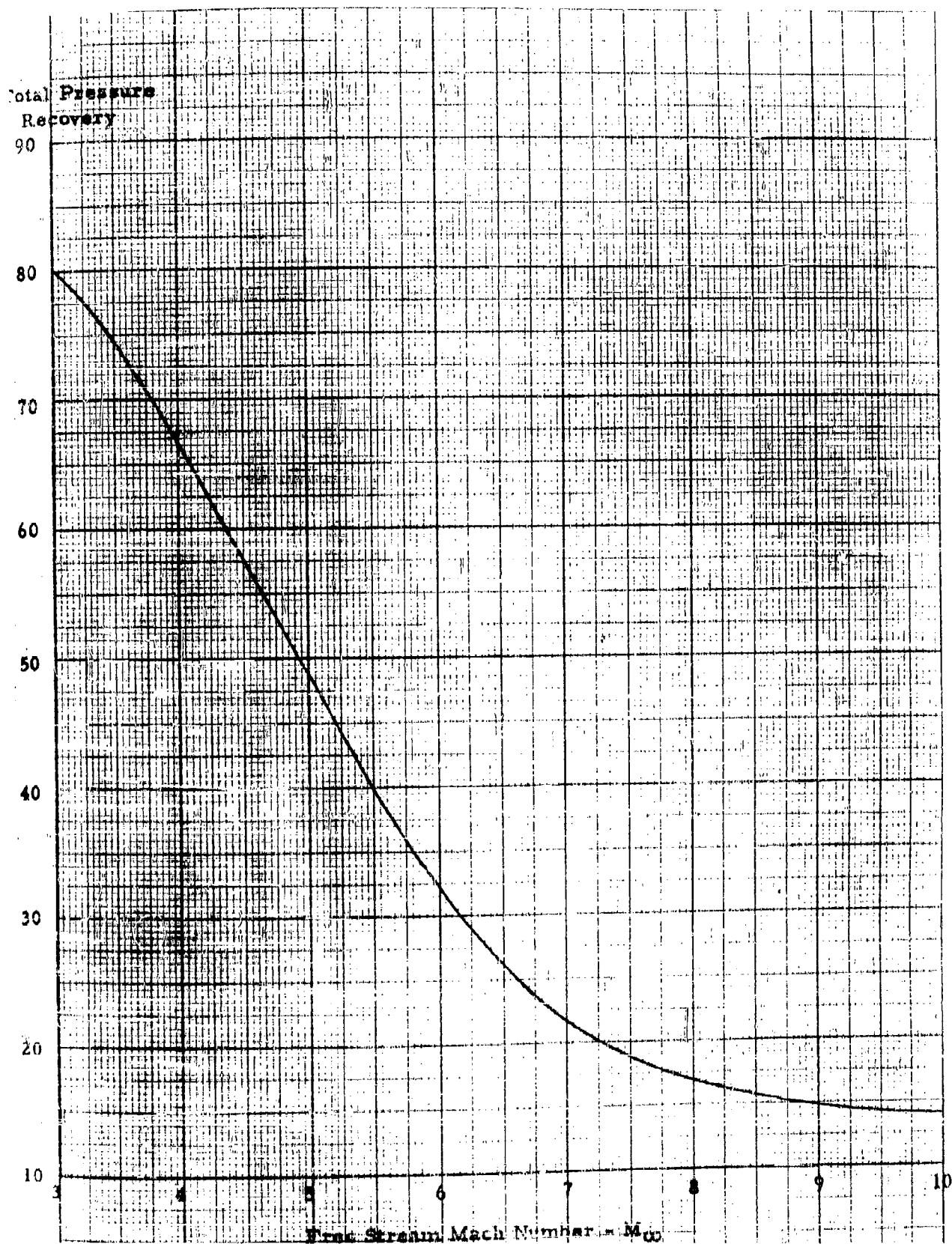
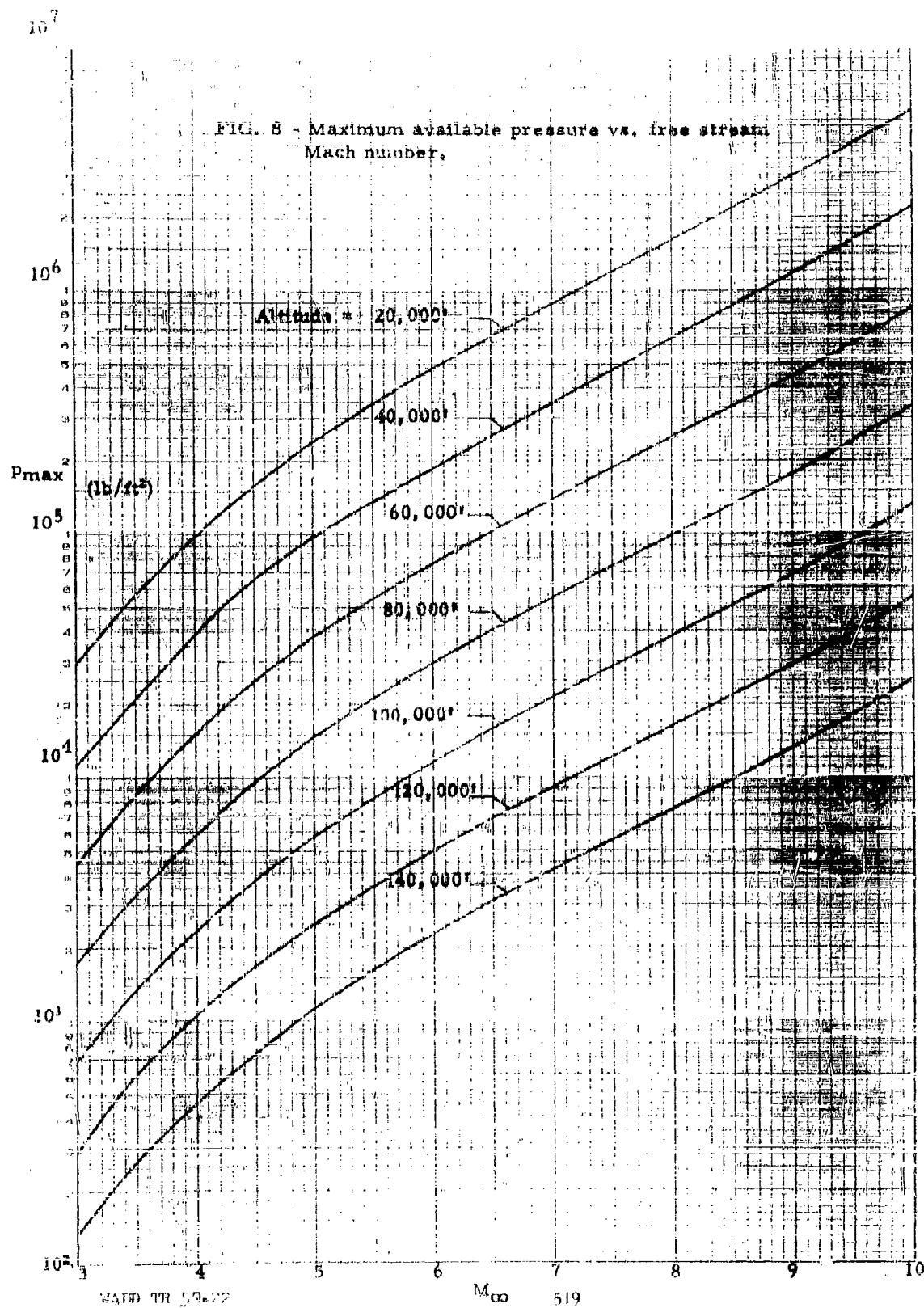


FIG. 7 - Inlet Pressure recovery vs. Mach number



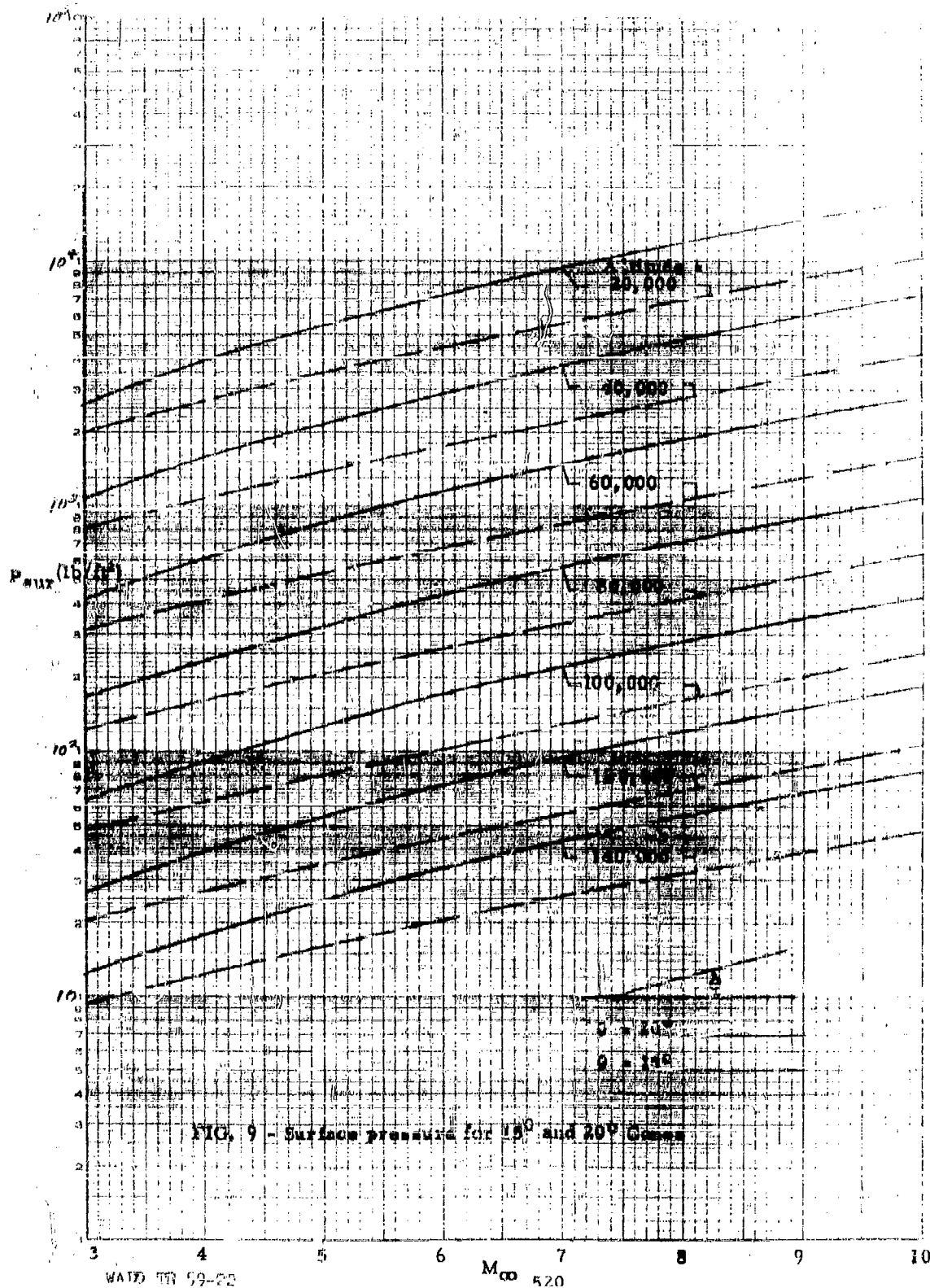


FIG. 10 - Water-air weight ratio vs. Mach number for heat exchange cooling.

$\frac{W}{a}$

1.0

.8

.6

.4

.2

.1

.05

.02

.01

.005

.002

.001

.0005

.0002

.0001

.00005

.00002

.00001

.000005

.000002

.000001

.0000005

.0000002

.0000001

WALL TR 59-22

521 M_{∞}

Coolant air supply, $T_c = 1000^{\circ}R$

Coolant air supply, $T_c = 1000^{\circ}R$

Coolant air supply, $T_c = 560^{\circ}R$

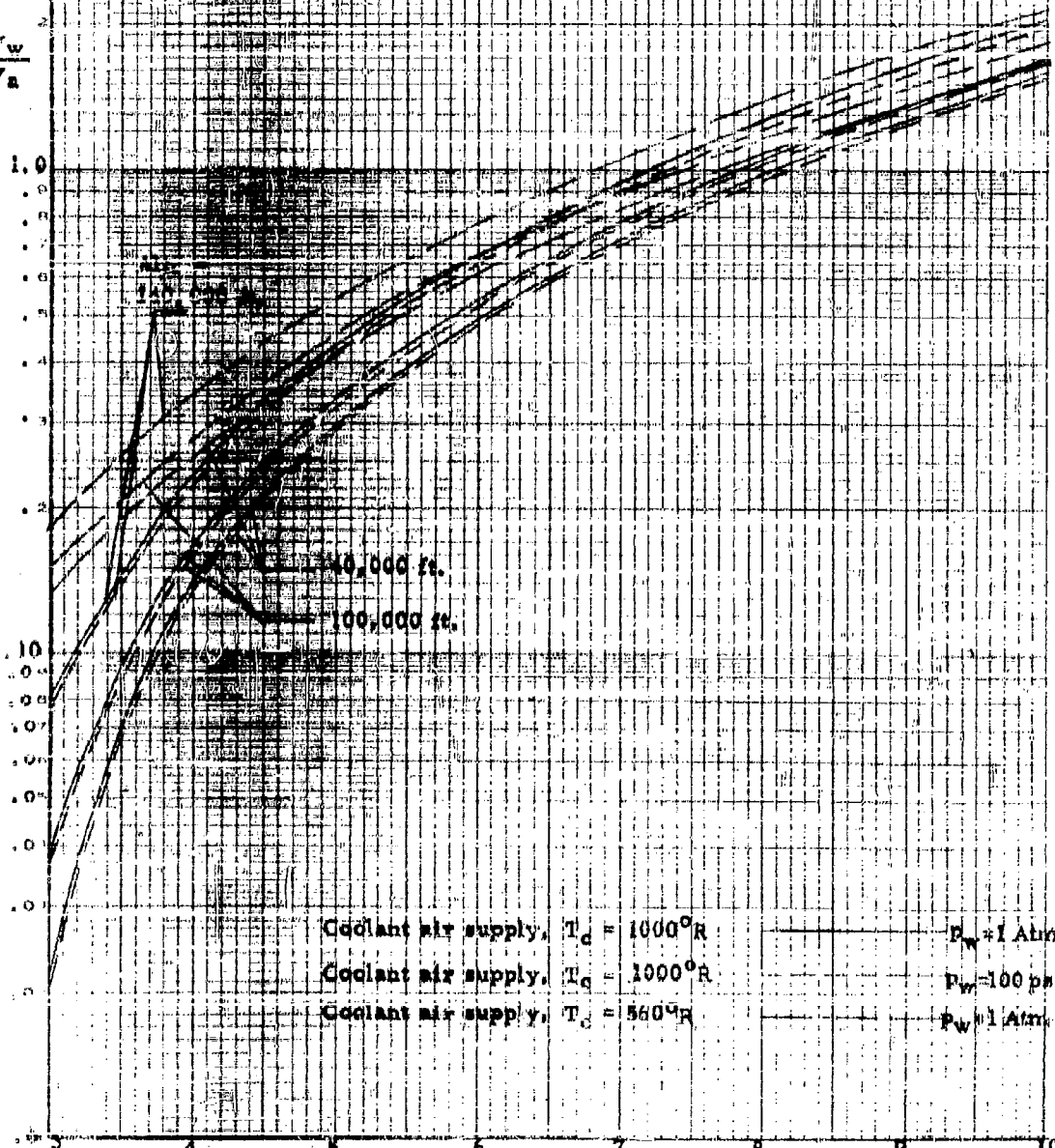
$P_w = 1 \text{ Atm}$

$P_w = 100 \text{ psi}$

$P_w = 1 \text{ Atm}$

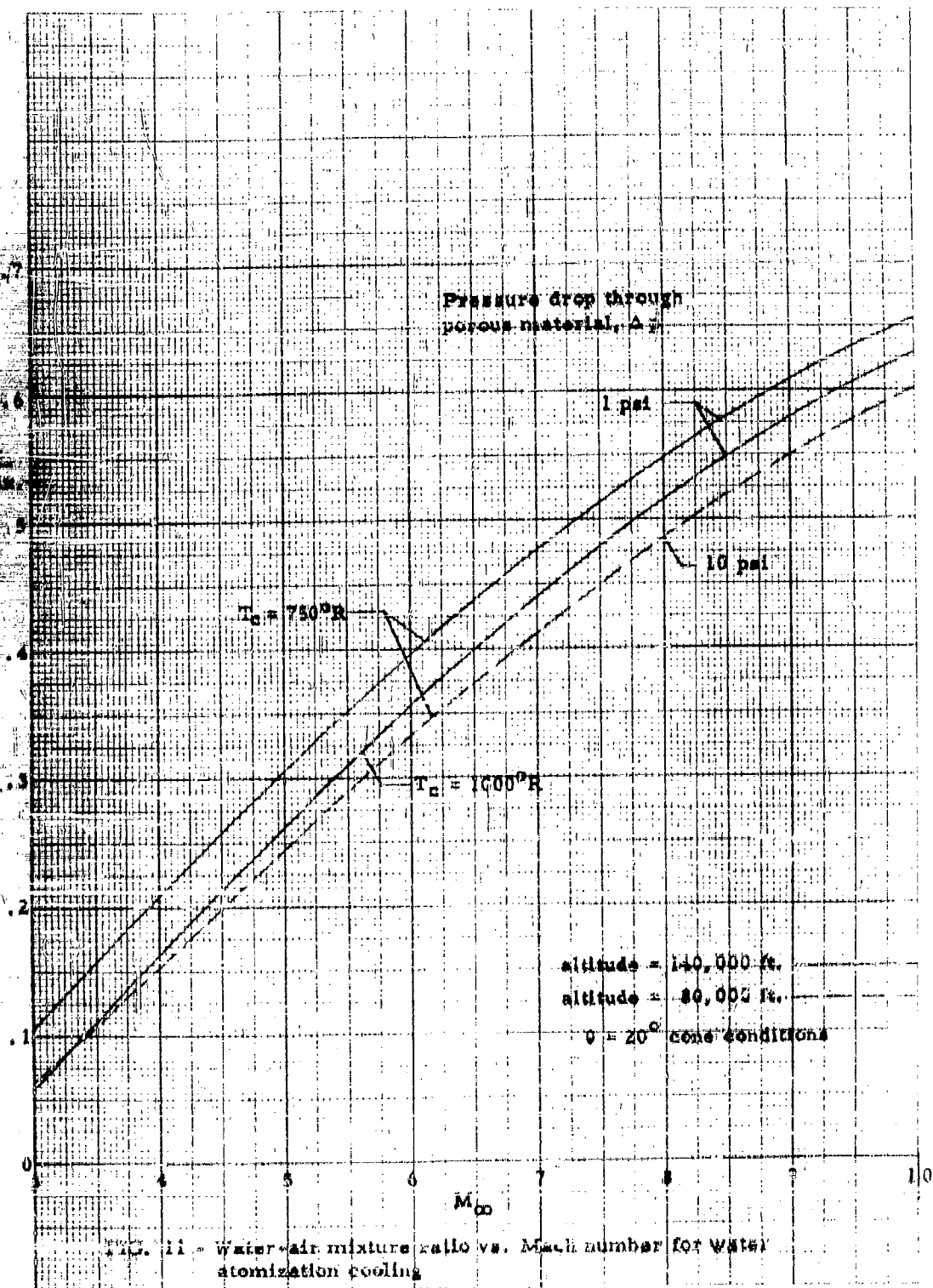
40,000 ft.

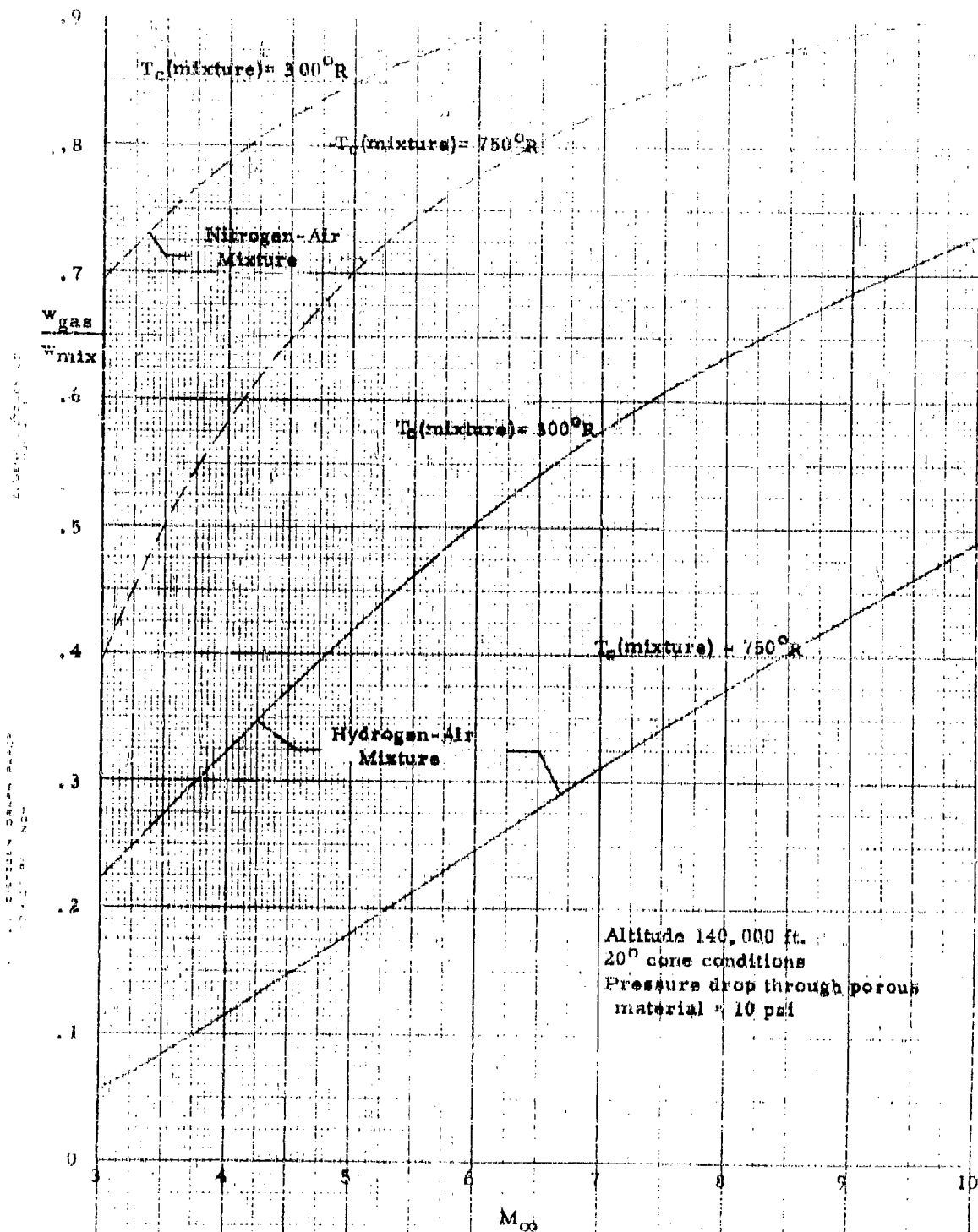
100,000 ft.



DUBOIS, BATHURST, CH.

20 X 20 PER INCH





Altitude 140,000 ft.
 20° cone conditions
 Pressure drop through porous
 material = 10 psi

FIG. 12 - Gas-air mixture ratio vs. Mach number cooling with low
 temperature altered cases

CHAPTER II - PART E

EFFECTS OF THE SEPARATED REGION ON THE HEAT TRANSFER
AND FLOW ABOUT A CHIN RADOME CONFIGURATION

by A. G. Hammitt *

* Senior Research Associate, Department of Aeronautical Engineering,
Princeton University.

TABLE OF CONTENTS

	<u>Title</u>	<u>Page</u>
	Summary	526
	Symbols	527
1.	Introduction	529
2.	Analysis	530
	a. Laminar Case	530
	b. Turbulent Case	534
3.	Conclusions	539
	References	540
	Figures	542

E. EFFECTS OF THE SEPARATED REGION OF THE HEAT TRANSFER
AND FLOW ABOUT A CHIN RADOME CONFIGURATION

SUMMARY

The effects on aerodynamic heating of the separated flow region about a chin radome installation have been investigated for both the laminar and turbulent case. The possibility of injection of cool gas into the separated region has been investigated in the laminar case and the effects of the distance of the radome from the nose considered. Injection into the separated turbulent region is shown to be ineffective, but injection into the boundary layer of the separated region would be effective.

SYMBOLS

C	Constant in linear viscosity relation
C_p	Specific heat at constant pressure
h	Height of step
K	Constant in separation pressure ratio equation
l	Length of separated region
M	Mach number
m_i	Mass injection rate
p	Pressure
Pr	Prandtl number
Re	Reynolds number
St	Stanton number
T	Temperature
u	Velocity
x	Distance from step to leading edge
x_o	Distance from separation point to leading edge
γ	Specific heat ratio
δ	Thickness of boundary layer for momentum integral
δ^*	Displacement thickness of boundary layer
ζ	Non-dimensional mass flow parameter
η	Distance from surface divided by boundary layer thickness
θ_s	Turning angle at separation point
μ	Coefficient of viscosity
ξ	Non-dimensional length of separated mixing layer
ρ	Density

Subscripts

1	Conditions ahead of separation point
l	Conditions outside boundary layer
h	Height of step
i	Conditions for injected flow
S	Separation

Superscripts

*	Non-dimensionalized by quantity at edge of boundary layer
---	---

1. INTRODUCTION

The chin radome configuration shown in Figure 1 is a possible radome location in an airplane or missile. This configuration would involve a separated flow area in front of the radome. The purpose of this study is to investigate the effects of this separated region on the aerodynamic heating of the radome in this configuration.

An important parameter in any such study is the location of transition. Separation of the flow from the body ahead of the radome would be expected and there will be important changes in this separated region depending on whether transition occurs ahead of, during, or after the separated region. In this study, the transitional case, the one with transition occurring in the separated region, will not be treated; but considerations limited to the wholly laminar and wholly turbulent cases.

In order to simplify the problem further, the chin radome configuration will be approximated by one of plane two-dimensional symmetry. The finite aspect ratio of the actual configuration will considerably alter the actual flow conditions; but the assumption of plane two-dimensionality is an important simplification which should give an initial approximation to the actual result.

2. ANALYSIS

a. Laminar Case

The laminar case can be treated in the general way outlined in Reference 1. Recent experimental work reported in Reference 2 has provided some verification of this approach. The work of Reference 1 is applied to the case of no initial boundary layer before the point of separation. This case is considered since it is the only one for which similar mixing layer profiles exist and for which good solutions are available. For the case of the chin radome, the assumption of no initial boundary layer seems unreasonable. An analysis of separated laminar mixing layers with initial boundary layer, based on a momentum integral technique, is given in References 3 and 4. The incompressible case is the only one for which a solution is given. Since the limiting conditions of $Pr = 1$ and $\mu = CT$ the boundary layer equations in terms of a mass flow coordinate or stream function are the same, the compressible solution for the mass flow in the mixing layer is the same as the incompressible result. Since the mass flow in the mixing layer is the important parameter of the analysis of Reference 1, the incompressible solution is sufficient for the present purposes.

In References 3 and 4, the parameter ξ is introduced as a measure of the length of the mixing layer. Along the mixing layer, the velocity profile changes from the initial separation profile to the final mixing profile. The profile at any station is a function of ξ alone. For the case of the wholly laminar interaction on a flat plate step configuration, the parameter ξ

at the face of the step can be predicted.

According to Reference 5, the pressure ratio for laminar separation can be expressed as

$$\frac{P_s - P_1}{P_1} = K \frac{M_1^2}{[(M_1^2 - 1) Re_h]^{1/4}}$$

where K is about 1.3. For most cases, the pressure rise at separation is small so that the associated turning is small and the two can be related by the linearized equation

$$\frac{P_s - P_1}{P_1} = \frac{\gamma M_1^2}{(M_1^2 - 1)^{1/2}} \theta_s \quad (1)$$

Assuming that the streamline near the wall can be approximated by a sharp turning at the separation point, Figure 1b, the angle θ_s by h/l .

Equation (1) gives

$$\frac{\delta}{l} = 1 + (M_1^2 - 1) \left(\frac{K}{\gamma} \right)^4 \left(\frac{l}{h} \right)^3 \frac{1}{Re_h} \quad (2)$$

A plot of x/l as a function of $\left(\frac{l}{h} \right)^3 \frac{1}{Re_h}$ and M is shown in Figure 2.

At low M , the separated distance is a larger part of the total distance to the nose than at higher M .

$$\text{By definition of References 3 and 4, } \xi = \left(\frac{l}{\delta_{10}} \right)^2 \frac{C}{Re_l}$$

Here, C is introduced in applying the definition to the compressible case.

From Reference 6

$$\frac{\delta^*}{x_0} \sqrt{\frac{Re_{x_0}}{C}} = 1.73 + 1.192 (\gamma - 1) M_1^2 \quad (3)$$

δ_{10} is the boundary layer thickness for the incompressible profile

$$\frac{u}{u_f} = \frac{1}{2} \cos \pi (1 - \eta) + \frac{1}{2}$$

The ratio $\frac{\delta^*}{\delta_{10}}$ for this profile is

$$\frac{\delta^*}{\delta_{10}} = \frac{\frac{1}{2} + \frac{\gamma - 1}{8} M_1^2}{1 + \frac{\gamma - 1}{8} M_1^2} \quad (4)$$

The cos function profile is considered the basis for a compressible profile having the same velocity mass flow characteristics in deriving the above relation.

Substituting Equations (3) and (4) into the definition of ξ gives

$$\xi = \frac{\frac{l}{x_0}}{1.73 + 1.192 (\gamma - 1) M_1^2} \left[\frac{\frac{1}{2} + \frac{\gamma - 1}{8} M_1^2}{1 + \frac{\gamma - 1}{8} M_1^2} \right]$$

The value of ξ as a function of $\frac{l}{h(Re_h)^{1/3}}$ and M_1 are given in Figure 3.

This same type of analysis can be used for any particular nose shape. The flat plate may be considered a standard and an equivalent x/h

assigned which will give a boundary layer similar to that found on the actual body.

The boundary layer velocity profiles as a function of the mass flow parameter ζ for various ξ are shown in Figure 4. Since these profiles are plotted in terms of ζ , they are good for all M . A more accurate profile, that of Reference 1, which should correspond to $\xi = \infty$ is shown over the ζ negative section to give a reference on the accuracy of the solution of References 3 and 4. A comparison of these profiles shows that the present solution can only be used to determine the trends and not the exact values.

Once the velocity is known as a function of ζ for various ξ the reattachment pressure ratio can be found as a function of ξ for various mass injections and the recovery temperature in the separated region as a function of mass injection can be determined. The details of such an analysis is presented in Part F of this chapter.

The recovery pressure ratio as a function of ξ for no mass injection is shown in Figure 5. Comparing with the more accurate result for $\xi = \infty$ shows that the relatively small velocity error introduced by the mixing layer solution leads to large errors in reattachment pressure and the results are interesting more for trends than actual values.

The effect of injection on wall recovery temperature is shown in Figure 6. At low values of ξ , the injection needed to limit the wall temperature is greatly reduced over that for $\xi = \infty$. The present

curves are for $Pr = 1$ and comparison with the more accurate result for $\xi = \infty$ and $Pr = 0.72$ shows the limitations involved.

In Figure 7, the results for different ξ have been corrected so that the $\xi = 1000$ curve agrees with the $\xi = \infty$ $Pr = 0.72$ curve. This correction has been done by scaling the r_w and ξ values linearly so that the intercepts agree. These scale factors are then applied to all other points. This correction is rather arbitrary; but, lacking better results Figure 7 is the best available for estimating purposes.

b. Turbulent Case

In Reference 1, the method which was applied to the laminar mixing layer was suggested for the turbulent layer. The predictions of heat transfer based on this assumption is that the heat transfer in the separated region be considerably more for an attached boundary layer. Experiments have not borne out this conclusion, Reference 2.

An estimate of the mixing rate for the turbulent mixing zone in the separated region in front of a step can be obtained from the data of References 8, 9 and 10, at several Mach numbers. If the heat transfer rate is assumed to be given by the total heat of the recirculating flow in the separated region, the average heat transfer rate in the separated region is about as follows:

M	$St_{\text{separated}}$	St_{attached}
2.3	$2.4 (10^{-2})$	$1.0 (10^{-3})$
2.92	$1.2 (10^{-2})$	$.9 (10^{-3})$
3.85	$2.2 (10^{-2})$	$.8 (10^{-3})$

The lower value of $M = 2.92$ is probably caused by the fact that as much detailed information is not available as at the other Mach numbers. The St for the attached boundary layer are estimated from Reference 11. Since the experiments of References 2, 12 and 13 show lower heat transfer in the separated region, this method of analysis must be in error. There are two limiting assumptions which may be made for the heat transfer in the separated region. The first assumption, that made in Reference 1, is that the limiting mechanism for heat transfer is the mixing layer and that the heat transfer between the wall and the separated region is so good that the temperature of the separated region is the wall temperature. The other possible limiting assumption is that the mixing layer does not limit the heat transfer so the separated region is at the recovery temperature and the limiting mechanism is at the wall.

The laminar separated layer seems to be approximated by the first assumption while the turbulent does not. The turbulent mixing layer seems capable of transmitting more heat than the experimental evidence shows reaches the body so this probably is not the heat transfer limiting mechanism. For the turbulent case, the wall boundary layer is probably the limiting mechanism. This reasoning leads to the assumption that the separated region is at essentially free stream temperature.

Enough data are not available on the detailed flow in the separated region to make an accurate determination of the heat transfer at the wall. A rough estimate might be made by determining the maximum mass flux of the recirculating flow in the separated region. Based on the step experiments of References 8, 9 and 10, the mass fluxes as a function of distances from the step face are shown in Figure 8, non-dimensionalized by the free stream mass flux. If the boundary layer along the wall is turbulent, Reynolds number is not a major parameter, and the relative St between the free stream and separated region would be about the same. Based on this maximum mass flux ratio at different M, the heat transfer in the separated region might be estimated to be about 0.3 or greater of free stream heat transfer for the region near the step face. Experiments (Reference 2, 12 and 13) have shown this ratio to be 0.3 to 0.5. This interpretation seems to give a result of correct order of magnitude.

There appears to be a fundamental difference between the resistance to heat flow of the mixing layer and the separated region boundary layer between the laminar and turbulent case. A reason for this difference might be that a turbulent boundary layer has a laminar sublayer which provides an important part of the resistance to heat flow of the total boundary layer. The turbulent mixing layer lacks this laminar part and, therefore, takes full advantage of the increased transport properties of the turbulent layer. The boundary layer on the wall of the separated cavity might be laminar under some conditions, but is probably turbulent with a laminar sublayer. The

laminar case, therefore, has a laminar mixing layer and boundary layer while the turbulent case has a fully turbulent mixing layer and a turbulent boundary layer with laminar sublayer. This difference shifts the principle resistance to heat flow from the mixing layer in the laminar case to the boundary layer in the turbulent case.

If the assumption that the turbulent mixing layer is not the important barrier to heat flow is correct, then it is not reasonable to attempt to limit the temperature in the separated region by mass injection. The good mixing across the turbulent layer will make it necessary to inject large quantities of mass to limit the temperature in the separated region. It would seem that mass injection for the turbulent region could be used to greater advantage, although with greater mechanical complication, if it were injected into the boundary layer of the separated region.

The advantages of injecting into the boundary layer of a separated region as opposed to that of an attached boundary layer are two-fold. The proper coordinates for evaluating mass injection, according to the theory of Reference 14 and the experiments of Reference 7 seem to be

$$\frac{m_1 C_p}{h} \quad \text{and} \quad \frac{St_1}{St}$$

A given injection rate

$$\frac{m_1 C_p}{h}$$

decreases the St in a given ratio. Therefore, the advantages of injecting in the separated region boundary layer are that less injection is required to give the same non-dimensional injection rate and the value of the Stanton number for no injection, based on free stream mass flux, is already reduced. If we assume that St , based on the local flux is the same for separated and unseparated regions, then

$$\frac{h_s}{h_\infty} = \frac{St_s}{St_\infty} \frac{\rho_s u_s}{\rho_\infty u_\infty}$$

$$\frac{m_{l_s}}{m_{l_\infty}} = \frac{\frac{m_{l_s} C_p}{h_s}}{\frac{m_{l_\infty} C_p}{h_\infty}} \frac{St_s}{St_\infty} \frac{\rho_s u_s}{\rho_\infty u_\infty}$$

$$\text{For } St_s = St_\infty \text{ and } \frac{m_{l_s} C_p}{h_s} = \frac{m_{l_\infty} C_p}{h_\infty}$$

$$\text{Then } \frac{h_s}{h_\infty} = \frac{\rho_s u_s}{\rho_\infty u_\infty} \text{ and } \frac{m_l}{m_\infty} = \frac{\rho_s u_s}{\rho_\infty u_\infty}$$

so for an injection rate reduced by the ratio of the mass fluxes, the heat transfer is also reduced by the ratio of the mass fluxes.

This condition is illustrated in Figure 9. Here the curve of reduction of heat transfer as a function of injection rate for an attached boundary layer is shown as given in Reference 7. The estimated band where the region for separated flow would fall is also shown on this same figure based on a separated region mass flux of between 0.3 and 0.5 of free stream value.

3. CONCLUSIONS

a. The aerodynamic heating of the chin radome configuration is not as severe as for a configuration which is not protected by a region of separated flow.

b. For the laminar separated region, injection of cool gas into the separated region offers an effective way to limit the recovery temperature.

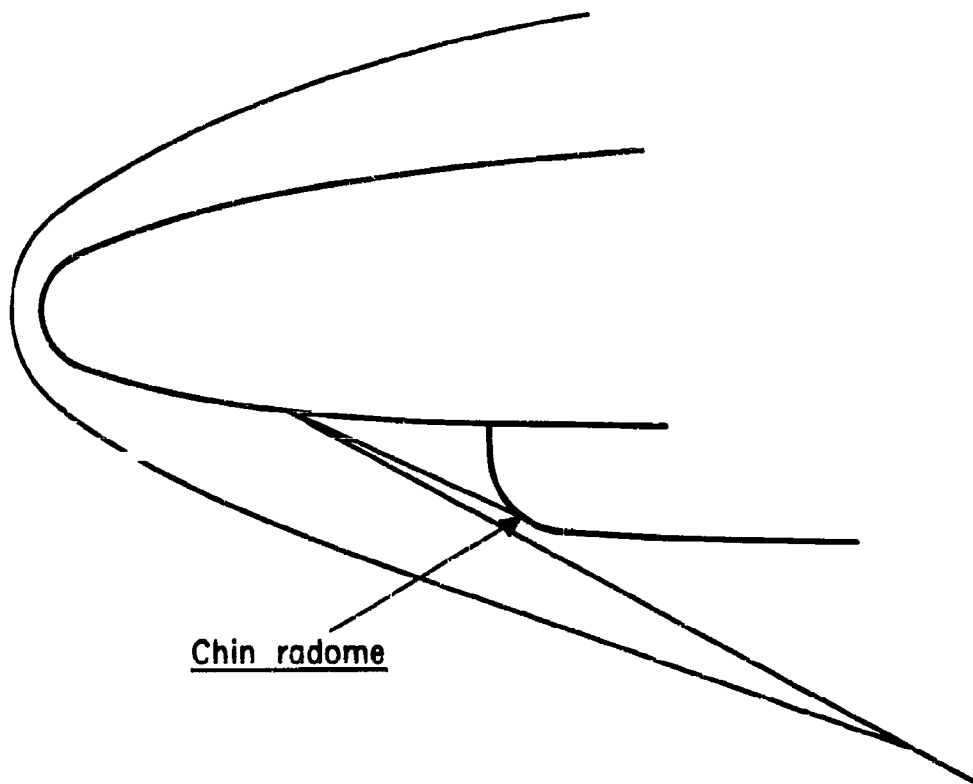
c. For turbulent separated region, injection of cool gas into the separated region is not an effective way to limit the recovery temperature.

c. Injection of cool gas into the boundary layer of the turbulent separated region would be an effective way to reduce the heat transfer rate.

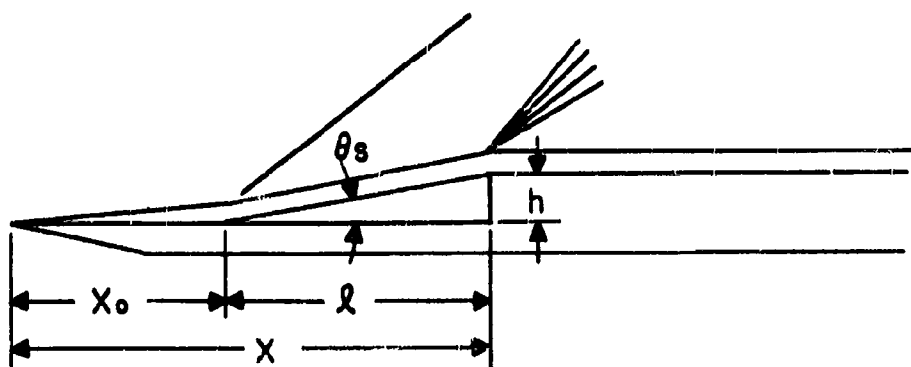
REFERENCES

1. Chapman, D. R.: A Theoretical Analysis of Heat Transfer in Regions of Separated Flow. NACA TN 3792, October 1956.
2. Larson, H. K.: Heat Transfer in Separated Flows. IAS Report 59-39, January 1959.
3. Torda, T. P. and Stillwell, H. S.: Analytical and Experimental Investigations of Incompressible and Compressible Mixing of Streams and Jets. WADC TR 55-347, March 1956.
4. Ackerman, W. O.: Laminar Incompressible Mixing of Two Streams of Different Velocities. Technical Report M-TR-4, Contract No. AF33(038)-21251, August 1952.
5. Chapman, D. R., Kuehn, D. M. and Larson, H. K.: Investigation of Separated Flows in Supersonic and Subsonic Streams with Emphasis on the Effects of Transition. NACA Report 1356, March 1957.
6. Lees, L.: The Stability of the Laminar Boundary Layer in a Compressible Fluid. NACA Report 876, 1947.
7. Pappas, C. C.: Effect on Injection of Foreign Gases on the Skin Friction and Heat Transfer of the Turbulent Boundary Layer. IAS Report 59-74.
8. Kepler, C. E. and Bogdonoff, S. M.: Interaction of a Turbulent Boundary Layer with a Step at $M = 3$. Princeton University Aero. Eng. Report No. 238, September 1953.
9. Vas, I. E. and Bogdonoff, S. M.: Interaction of a Turbulent Boundary Layer with a Step at $M = 3.85$. Princeton University Aero. Eng. Report No. 295, April 1955.
10. Wooten, G. G., Hight, S. and Vas, I. E.: Interaction of a Turbulent Boundary Layer with a Step at $M = 2.3$. Princeton University Aero. Eng. Report No. 297, April 1955.
11. Kay, J.: Survey of Friction Coefficients, Recovery Factors, and Heat Transfer Coefficients for Supersonic Flow. JAS, February 1954.
12. Hammitt, A. G.: Exploratory Study of the Heat Transfer to the Base of a Body of Revolution. General Applied Science Laboratories, Inc., TR No. 9, February 1957.

13. Powers, W. E. , Stetson, K. F. and Adams, M. C. : A Shock Tube Investigation of Heat Transfer in the Wake of a Hypersonic Cylinder with Application to Hypersonic Flight. IAS Report 59-35, January 1959.
14. Rubesin, M. W. and Pappas, C. C. : An Analysis of the Turbulent Boundary Layer Characteristics on a Flat Plate with Distributed Light Gas Injection. NACA TN 4149, February 1958.



A. Chin Radome Configuration



B. Idealized Chin Radome Model Used in Analysis

Figure 1

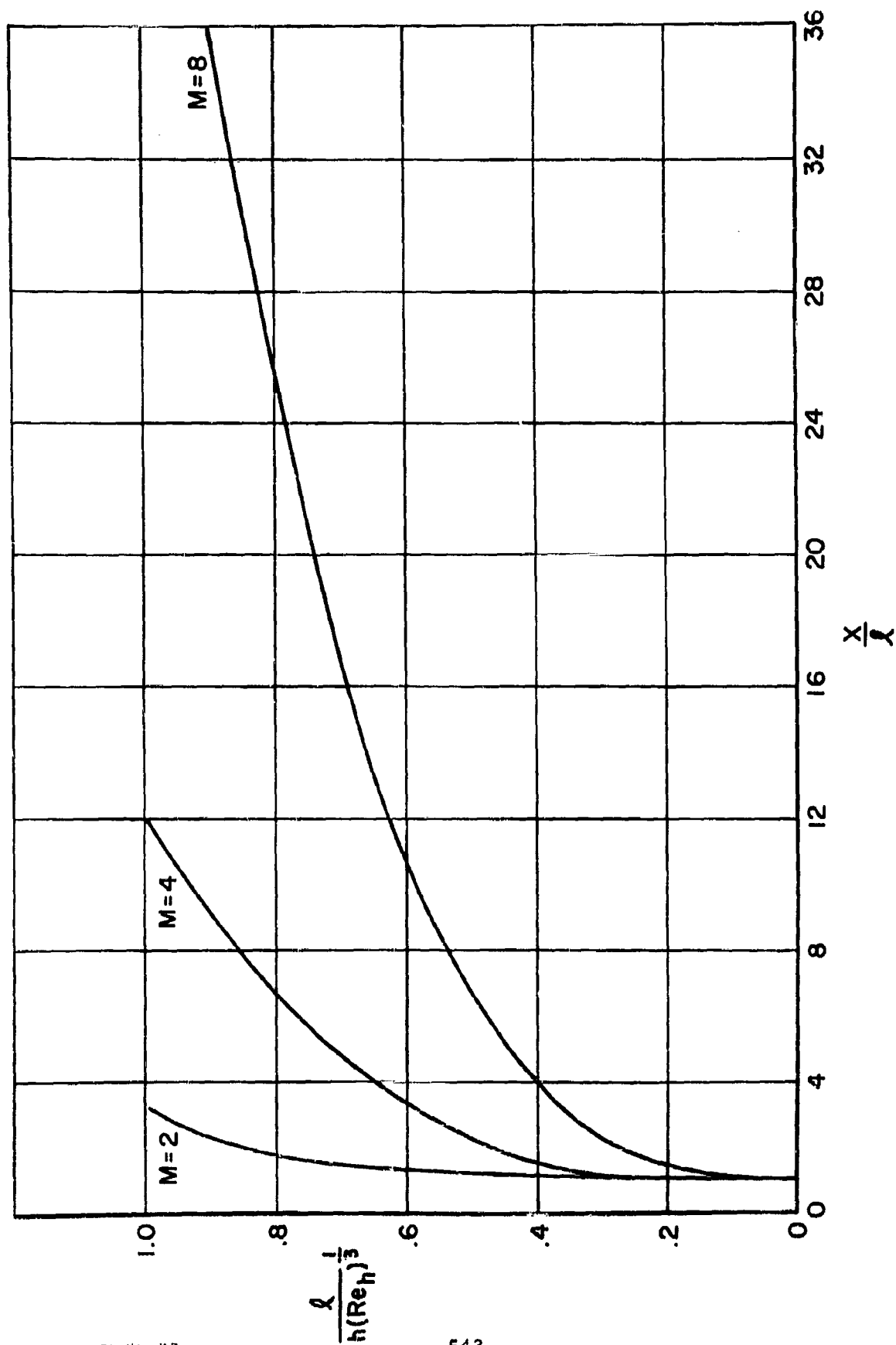


Figure 2. Length of Separated Region as a Function of M and Re .

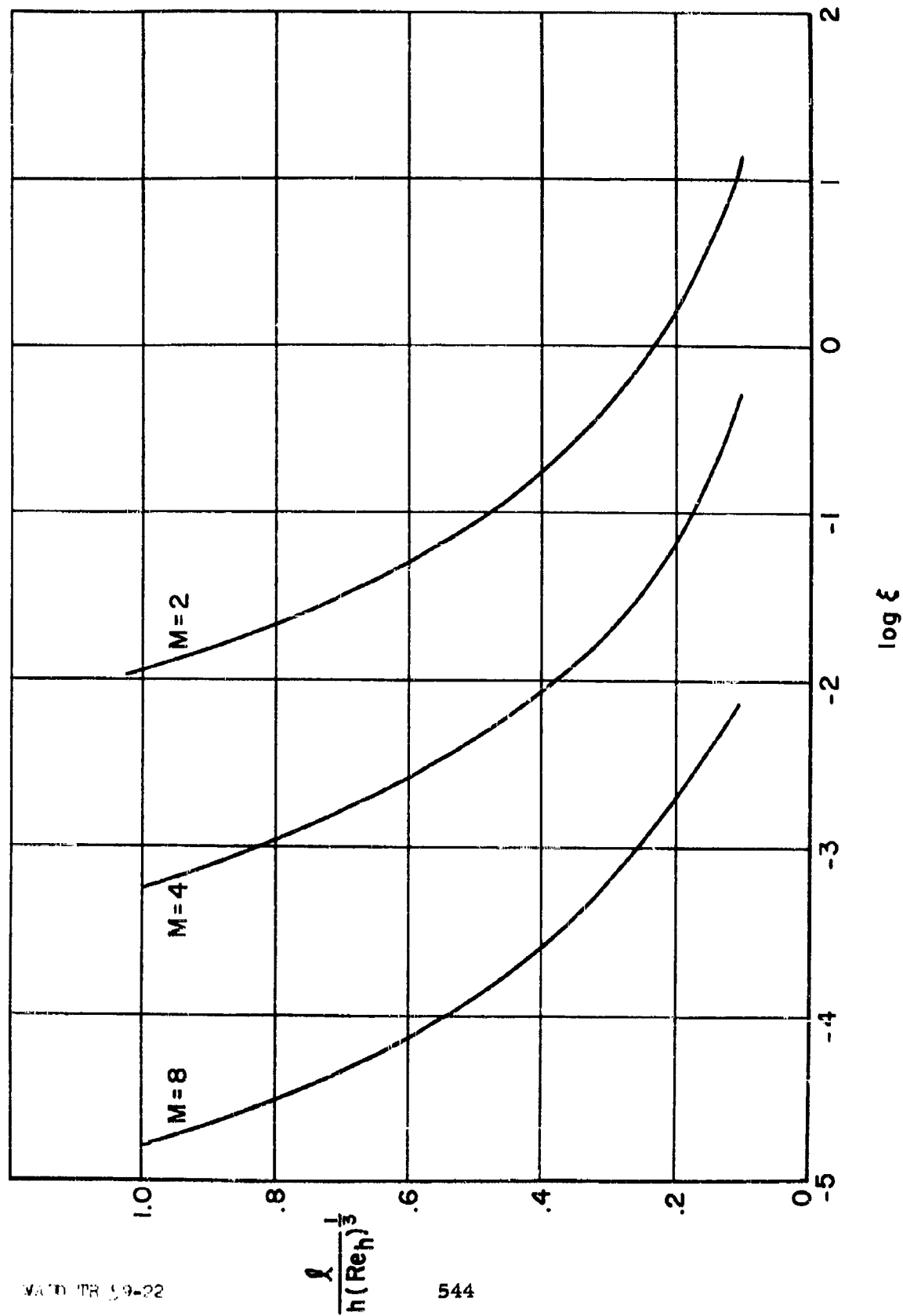


Figure 3. Non-dimensional Separated boundary layer length as a function of M and length of separated region.

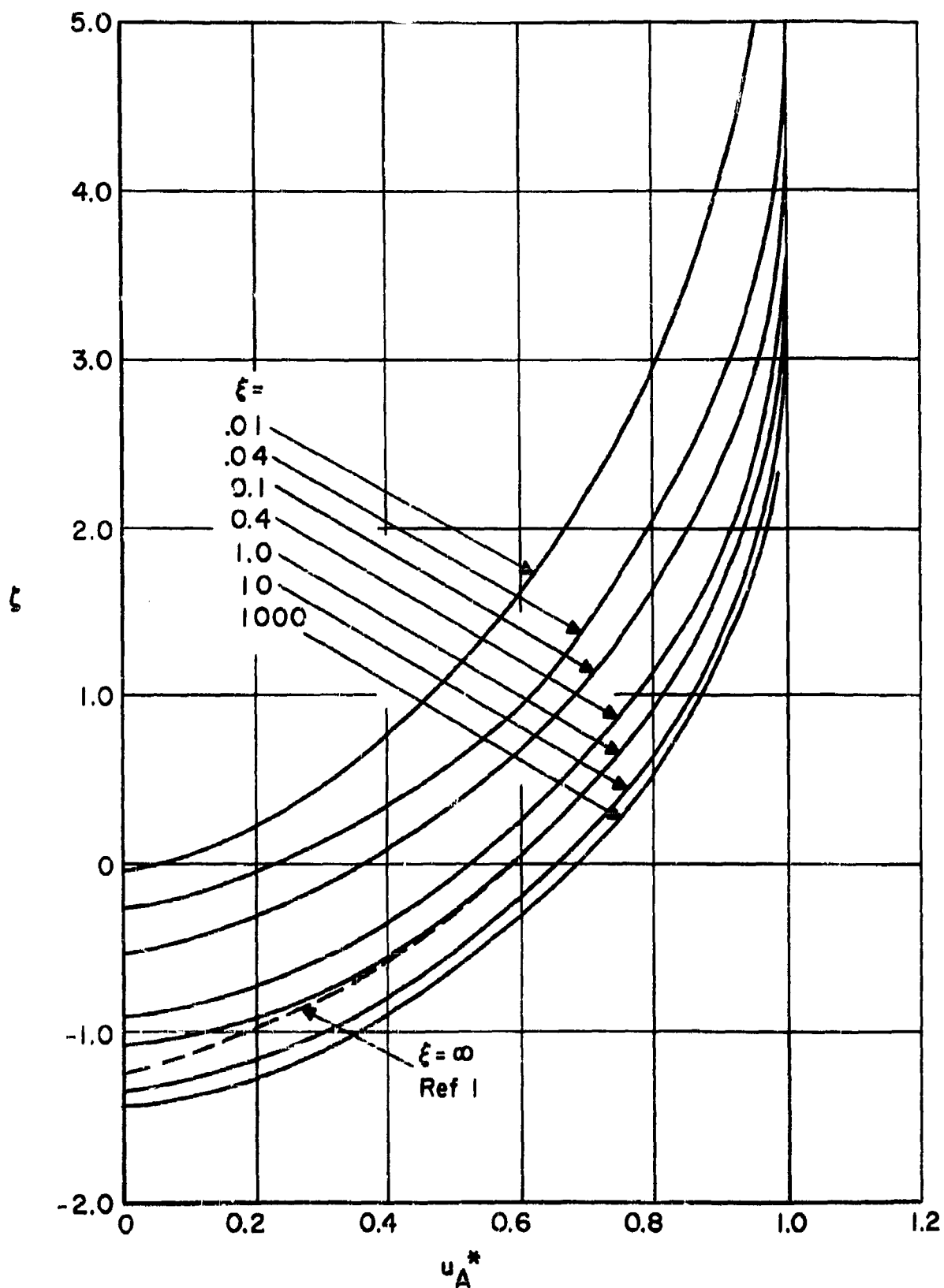
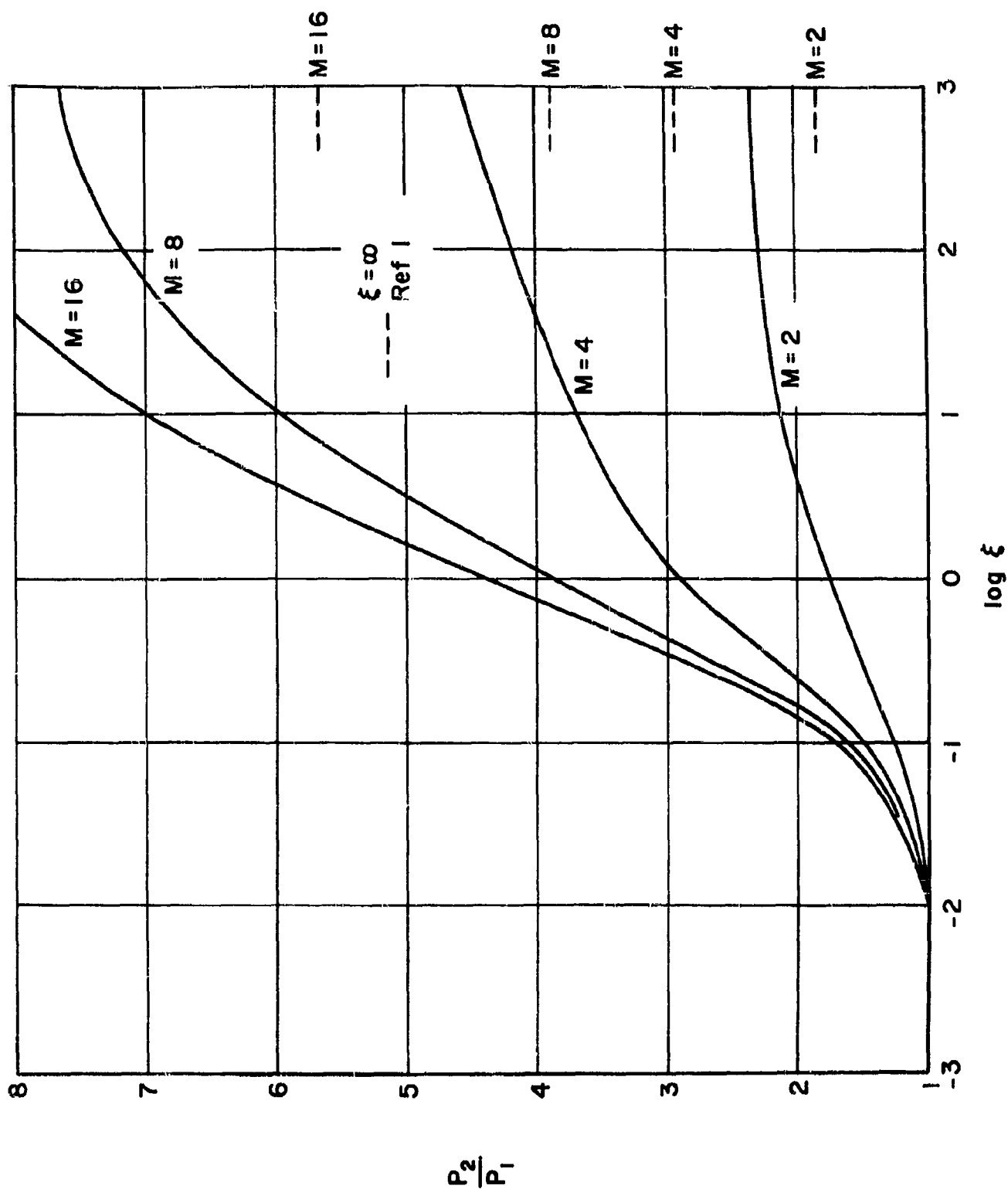


Figure 4. Mixing layer velocity as a function of mass flow parameter for different lengths of separated mixing layer.

Figure 5. Reattachment pressure ratio as a function of length of separated mixing layer for different M .



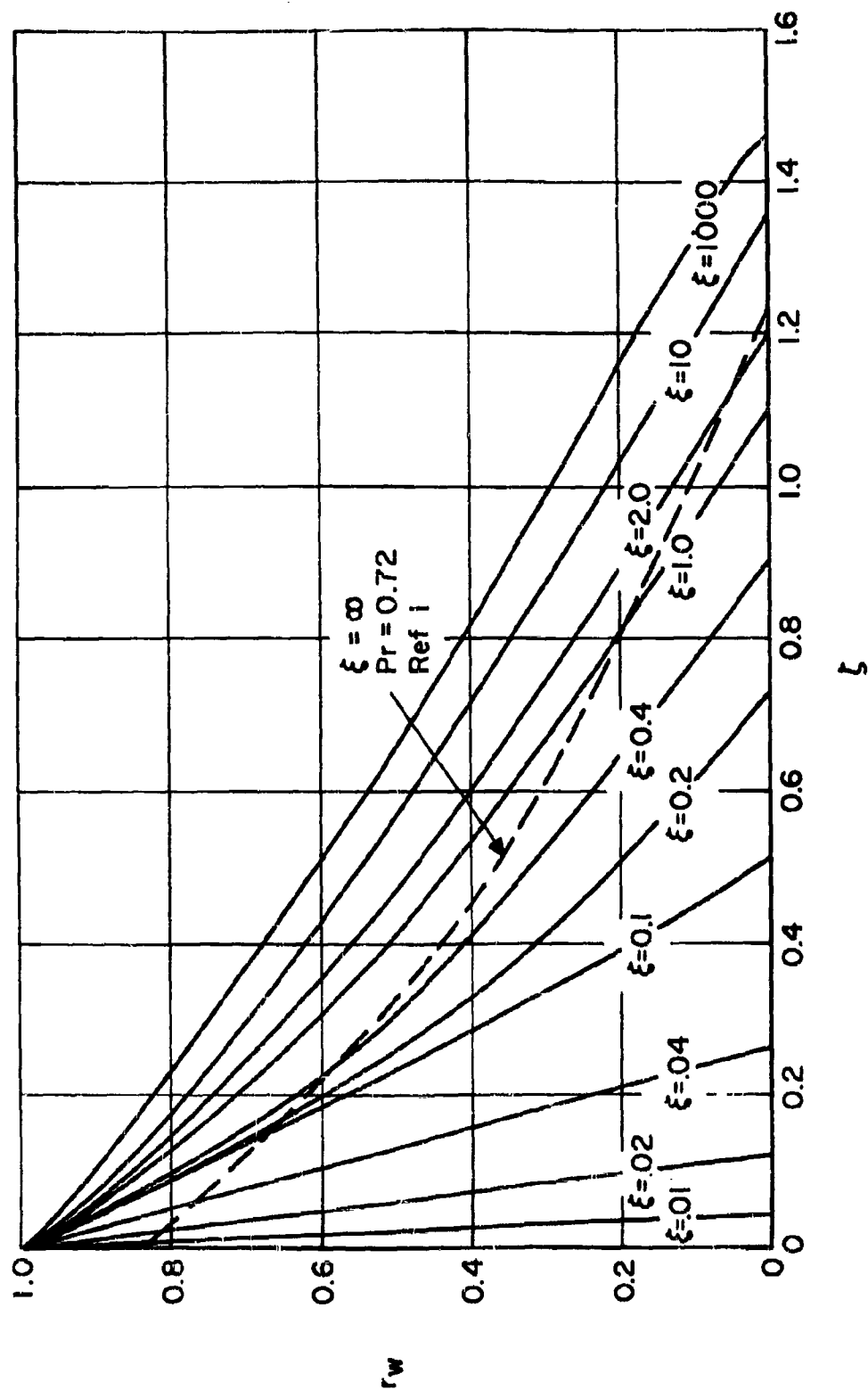


Figure 6. Wall recovery factor as a function of mass injection for different lengths of separated mixing layer.

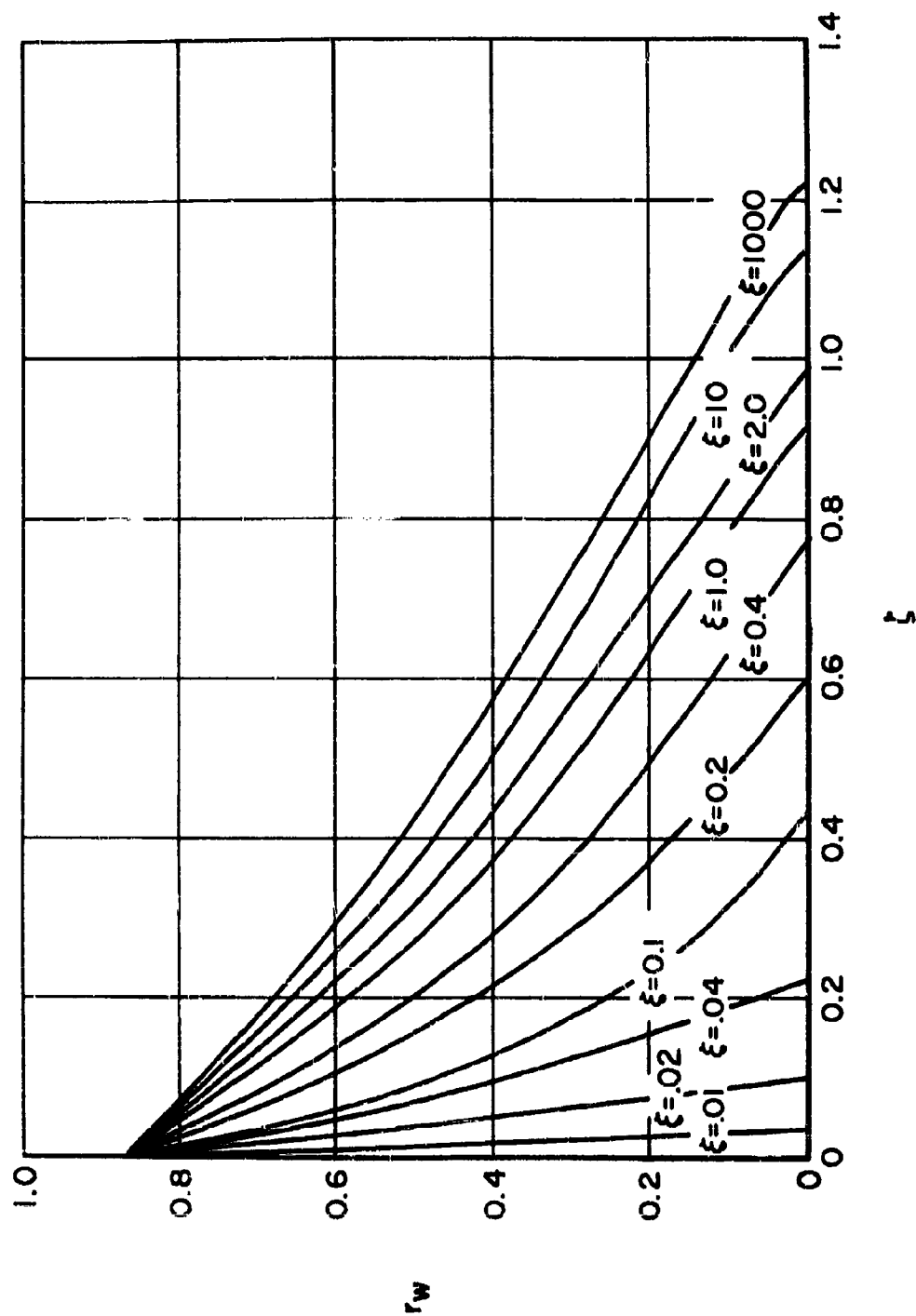


Figure 7. Wall recovery factor as a function of mass injection for different lengths of separated mixing layer corrected to be consistent with infinite length of mixing solution.

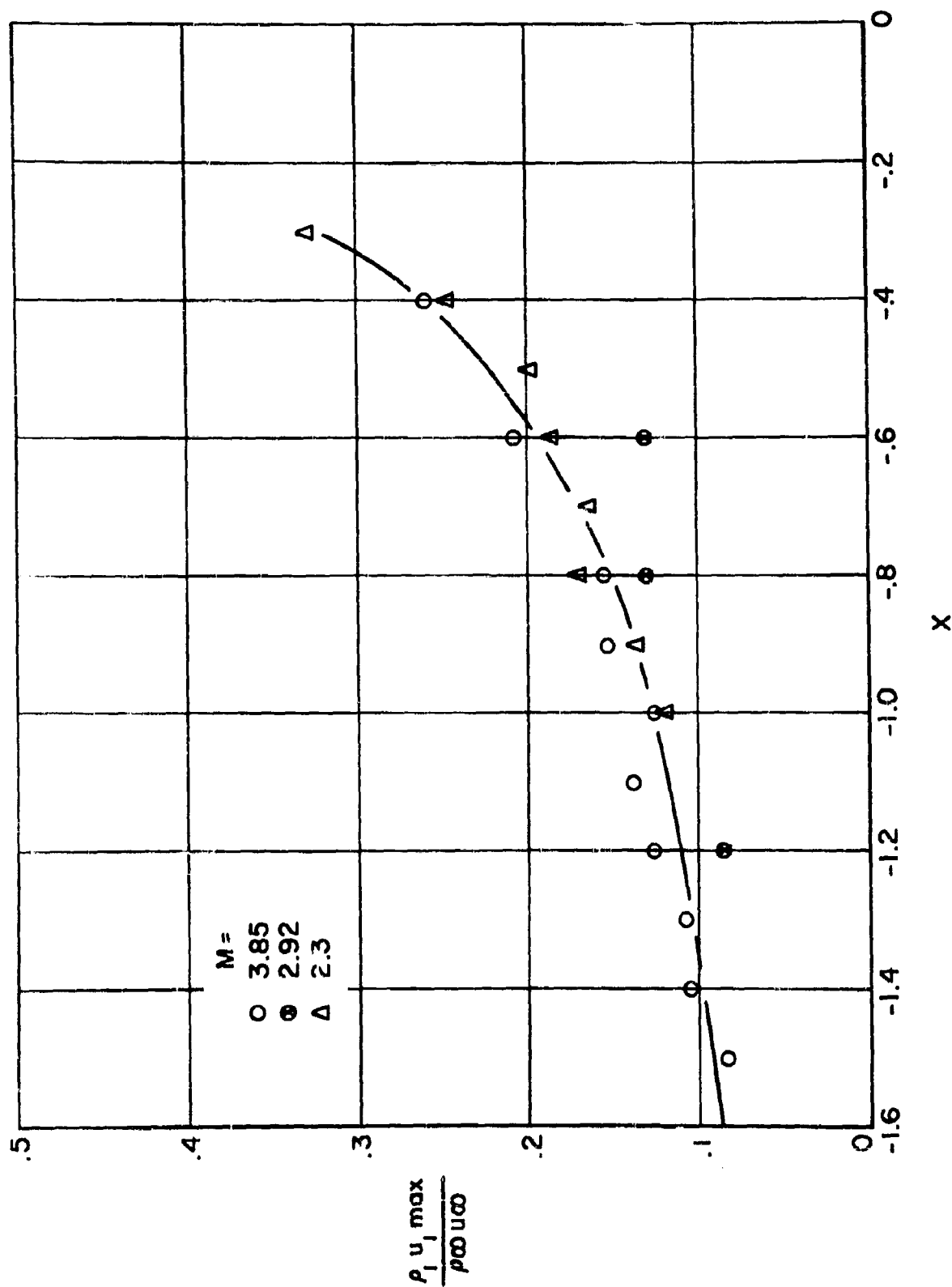
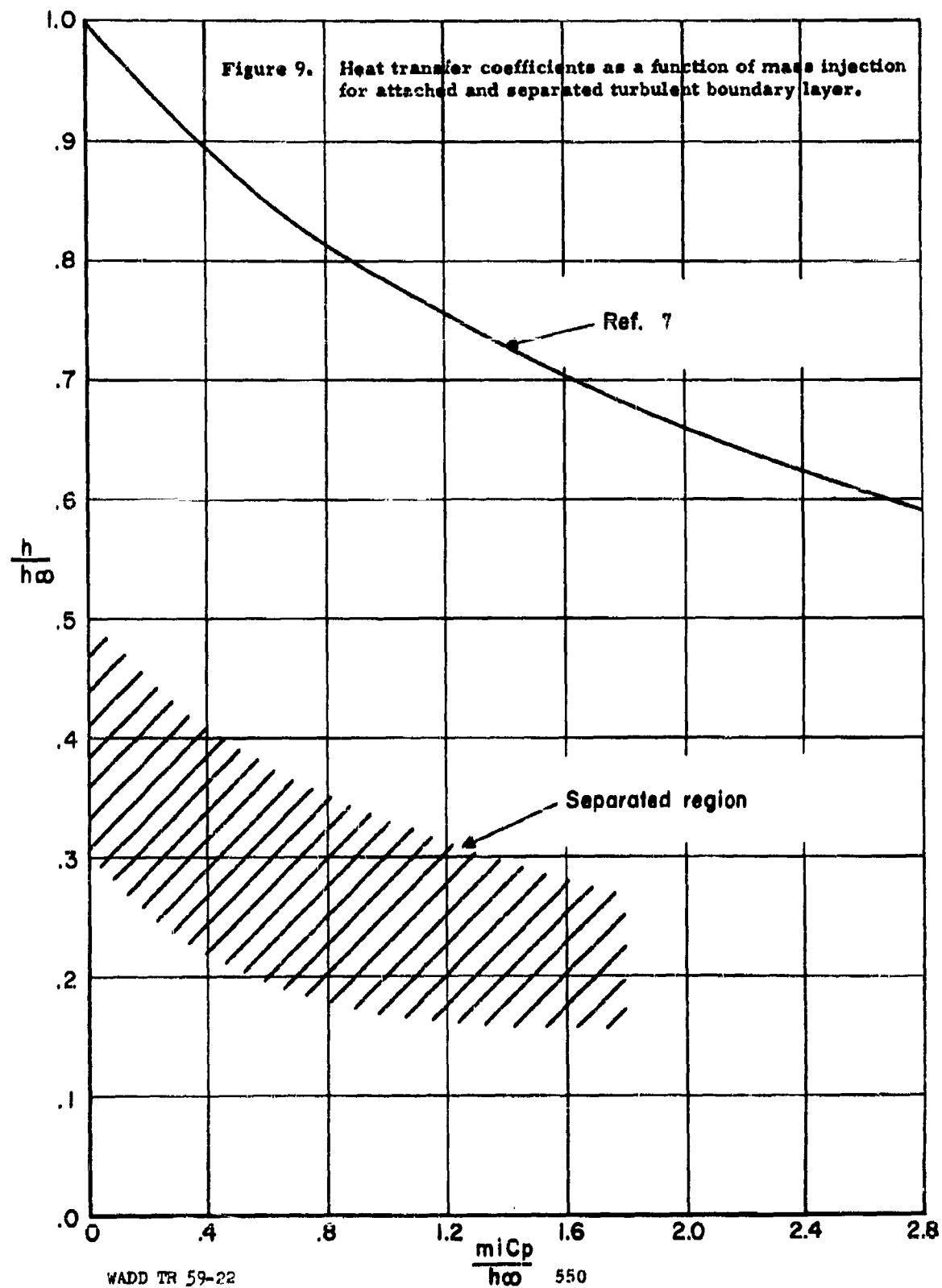


Figure 8. Mass flux in the separated region with initial turbulent boundary layer as a function of distance from face of step.



CHAPTER II - PART F

AN INVESTIGATION OF THE USE OF A SPIKE IN FRONT OF
A RADOME TO REDUCE THE TEMPERATURE

by A. G. Hammitt *

*Senior Research Associate, Department of Aeronautical Engineering,
Princeton University.

TABLE OF CONTENTS

<u>Section</u>	<u>Title</u>	<u>Page</u>
	Symbols	553
1.	Introduction	555
2.	Pressure in Separated Region	557
3.	Separation Pressure Ratios	559
4.	Reattachment Condition	560
5.	Reattachment with Mass Injection	564
6.	Wall Temperatures in Separated Region	565
7.	Comparison with Heat Transfer Experiments	570
8.	Application of Mass Injection	572
9.	Conclusions	575
	References	576
	Figures	577

SYMBOLS

a	Speed of sound
C	Constant of proportionality between viscosity and temperature
C ₁	Constant in sine function mixing layer velocity profile representation
D	Diameter of body
h	Enthalpy
L	Length of spike
m	Mass flux
M	Mach number
p	Pressure
Q	Heat flow
r	Recovery factor
R	Perfect gas constant
Re	Reynolds number
T	Temperature
u	Velocity
y	Distance from zero streamline in mixing layer
γ	Specific heat ratio
ζ	Dimensionless mass flow variable
θ	Turning angle at reattachment
λ	Velocity ratio between flow in external and separated region
μ	Viscosity
ρ	Density
Δ	Defined in text as $\frac{h - h_2}{u_2^2/2}$

Subscripts

0	Stagnation
∞	Undisturbed
2	Behind initial conical shock
3	After reattachment
4	Mixing layer below zero streamline
d	Integrated to lower edge of mixing layer
i	Injected
m	Mixing layer
s	Separated flow
w	Wall
δ	Integrated to upper edge of mixing layer

Superscripts

*	Non-dimensionalized by quantities at outer edge of mixing layer
---	---

F. AN INVESTIGATION OF THE USE OF A SPIKE

IN FRONT OF A RADOME

TO REDUCE THE TEMPERATURE

1. INTRODUCTION

A body traveling at high speed within the atmosphere is heated by friction with the air. In many cases, the nose receives the most severe heating and is the critical region. The heat transfer to the nose can be minimized by the use of a large nose radius and brought within the limits acceptable to some types of construction. However, in some special cases, the construction of the nose may be restricted by other considerations than withstanding high heat transfer rates. For these applications, some means of limiting the heat transfer rate and temperatures must be found.

A radar dome located in the nose section is such an application where the aerodynamic temperatures must be limited. There are several possible ways of accomplishing such a result, but the one investigated in this report is that of creating a region of separated flow in front of the nose and bleeding cool gas into this region.

A separated region can be created in front of a blunt body by placing a rod or spike in front of the body. Several experimental investigations of such a configuration are reported in References 1 through 8. The pressure on the

front of the body is considerably reduced by this means, and the heat transfer, if the mixing layer remains laminar, also appears to be reduced. The purpose of the present analysis is to determine some analytical method for predicting the flow in the nose region and to study the effects of bleeding cold air into the separated region as a means of limiting the temperature on the nose of the body.

2. PRESSURE IN SEPARATED REGION

In analyzing the flow in the separated region, some sort of a general flow model must be considered. A study of the various experimental work on this problem shows that it is reasonable to divide the flow into a separating region, an area of separated flow, and a reattaching region. The general configuration is shown in Figure 1. A pressure rise would be associated with the separating region and the reattachment region, while the pressure in the separated region should be relatively constant.

This general configuration should apply to either a plane two-dimensional or axially symmetric geometry. The axially symmetric case is the one which will be considered here since it is of most direct interest for a radome application and since most of the experimental data are gathered for such a configuration. With this assumption, the proposed model gives an approximately conical separated region. The experimental data contained in Reference 1, giving results for axially symmetric spiked bodies in the Princeton Hellum Hypersonic Tunnel, will be used as the chief source of data since the most complete information was available in this report and additional data could be obtained from the authors. In this case, the flow was thought to be completely laminar to beyond the reattachment point. For this reason, and in order to facilitate an analytical investigation, this study is limited to the laminar case. In Reference 1, experiments were run on bodies with different spike lengths at a nominal Mach number of 14 ahead of the model and a Reynolds number of $7(10^5)$ per inch. Much of the analysis will be carried

out for the cases tested in these experiments so that the results will be comparable.

The pressure in the separated region and the shock position are closely related. The shock wave must position itself so that certain criterion are satisfied at the separation point and at the reattachment point. For a sufficiently long spike, the pressure in the separated region is low and the flow separates from the spike well behind the tip. As the spike is shortened, the pressure in the separated region increases and the separation point approaches the tip. At some pressure, the separation point seems to arrive at the tip of the spike. The experiments are not detailed enough to determine whether separation occurs in front of the shoulder if a cone-cylinder spike is used, so this whole region will be classified as the tip. As the spike becomes shorter, the separation continues to occur from the tip of the spike. At some spike length, the flow becomes unsteady. This point depends on the configuration of the blunt body and of the tip of the spike. This unsteady flow region will not be considered in this analysis.

3. SEPARATION PRESSURE RATIOS

The pressure ratio required to cause separation based on Reference 1 is shown in Figure 2. This is a plot of pressure in the separation region to the pressure in the tunnel at the position at which the separation occurs when no model is in the tunnel. Since these tests were run in a nozzle with non-uniform flow, there is some uncertainty on how to define the separation pressure ratio, but the method used here, where p_s is the pressure on the separated region and p_1 the tunnel empty static pressure at the point of separation, would seem to be appropriate. These pressures are plotted against the Reynolds number based on distance along the spike before separation and are shown only for the cases where the distance from the tip to the separation point can be determined. The cases for which separation occurs outside of the tip region follow an approximate $1/4$ power law as found for laminar separation in Reference 9. Extrapolating the data from Mach = 3.5 in air to $M = 14.0$ in helium by the formula

$$\frac{p_s}{p_1} = 1 + K \frac{M_1^2}{[(M_1^2 - 1)Re_1 L]}^{1/4}$$

suggested in Reference 9, the dotted line shown in Figure 2 was found. The agreement is surprising considering that no correction was made for the change in γ and the large extrapolation in Mach number.

4. REATTACHMENT CONDITION

A criterion for the prediction of the reattachment pressure rise is suggested in Reference 9. This criterion is that the pressure at the reattachment point be the value required to stagnate the zero streamline which separates the recirculating from the non-recirculating flow. The calculation of this pressure ratio is performed by calculating the velocity along the zero streamline before any effect of the reattaching pressure rise is felt and then determining the pressure rise necessary to stagnate this streamline by an isentropic compression.

The value of the velocity along the zero streamline for the case of zero velocity in the separated fluid region and zero initial mixing layer thickness is given in Reference 10. If these values are applied to the cases of Reference 1, the results shown in Figure 3 for $\lambda = 0$ are found. The experimental points are uniformly above the predicted curve. There is considerable question whether the velocity in the separated region is substantially zero, especially for the axially symmetric case. If a vortex with relatively high velocity air exists in this region, the velocity along the zero streamline could be considerably larger than for the case of stagnant air in the separated region. An approximation to this case can be found by considering the mixing of two streams at different velocities.

The case of the mixing of two incompressible streams at different velocities is treated in Reference 11. The results of a numerical integration are given for several values of λ , the ratio of the velocity of the slower

stream to the faster stream, and a momentum integral system is suggested which is shown to give good results for the velocity on the zero streamline if the velocity distributions are approximated by an expression of the type

$$u_2^* = C_1 + (1 - C_1) \sin \frac{\pi}{2} \frac{y_2}{\delta_2}$$

$$u_4^* = C_1 + (1 - C_1) \sin \frac{\pi}{2} \left(-\frac{y_4}{\delta_4} \right)$$

In Reference 10, the von Mises transformation of the compressible boundary layer equations is used and the mass flow coordinate $\zeta = \frac{m}{\sqrt{\rho_2 u_2 \mu_2 x C}}$ is introduced with the result that $u^* = f(\zeta)$ is independent of compressibility effects. Therefore, if the incompressible results of Reference 11 are formulated as $u^* = f(\zeta)$, they may also be applied in the compressible case. To demonstrate the approximation involved in using the sine function representation of the velocity profile, the function $u^* = f(\zeta)$ is plotted in Figure 4 for negative values of ζ for both the sine function representation and the solution of Reference 10. The sine function representation underestimates the mass in the layer, but corresponds reasonably well and seems justified by its simplicity.

Using this sine function representation, the values of u^* at $\zeta = 0$ for different values of λ can be obtained from Reference 11. The pressure ratio necessary to stagnate the zero streamline for different values of λ can then be determined. These results are also shown in Figure 3. The line of $\lambda = 0.2$ probably represents the best approximation to the experimental

points, but there does not seem to be any reason why λ should be constant at different values of L/D . As stated before, the accuracy of the experimental results is questionable, so firm conclusions should not be drawn.

A velocity different from zero in the separated region, $\lambda \neq 0$, affects the width of the mixing layer and the amount of mass in the layer as might be expected. The width of the mixing layer decreases as the speed of the low velocity flow increases. This conclusion is reasonable since the mean velocity of the two layers only carries the phenomena along but does not affect the mixing. A plot of width of the mixing layer on both sides of the zero streamline is shown in Figure 5 based on the sine function approximation in Reference 11. Linear mixing theory, Reference 12, predicts that the mixing layer width should vary inversely as the square root of the mean velocity. The square root variation curve is also shown in Figure 5 and appears to be a reasonable mean between the two thicknesses or to represent the variation of the total mixing layer thickness.

The mass in the boundary layer on the low velocity side of the zero streamline is also shown in Figure 5. In spite of the fact that the layer becomes thinner with increasing λ , the mass increases rapidly. For $\lambda \neq 0$, this mass is not well defined since the velocity is not approaching zero at the edge of the layer and the total mass does not approach a limit. Therefore, the slope of this curve will depend on the definition of the edge of the layer.

A better way to demonstrate the variation of the mass in the boundary layer with λ is to plot the mass flow parameter ζ against y non-dimensionalized

by δ_4 for $\lambda = 0$. This has been done for the flow on the low velocity side of the zero streamline in Figure 6. For any line of constant $\frac{u - u_4}{u_2 - u_4}$, any given approach to inviscid conditions, the higher λ values give greater mass.

However, the increase in mass is largest for values of u near u_4 and increases as more of the outer edge of the boundary layer is included.

5. REATTACHMENT WITH MASS INJECTION

If mass is injected into the separated region, the effect upon reattachment pressure ratio is easily determined. Since mass is injected into the separated region, this mass will have to escape to the external stream at the reattachment point. This requirement means that the reattaching streamline will not be at $\zeta = 0$ but at some negative value of ζ . These results for the separation shock strength corresponding to the $L/D = 5$ and $\lambda = 0$ condition are shown in Figure 7. This figure shows that the reattachment pressure ratio decreases as mass injection is increased. The result of the decreased reattachment pressure would be to move the reattachment point further around the nose of the body so that more of the nose section would be immersed in the separated region.

6. WALL TEMPERATURES IN SEPARATED REGION

The heat transfer to the wall in the separated flow region might be expected to be somewhat less than to a wall with attached flow, therefore, the spiked blunt body may offer some solution to the high heat transfer encountered in the nose regions of bodies flying at high speed. By bleeding cool fluid into the separated region, the fluid temperature can be decreased, and the nose heat transfer further reduced. If cool fluid is injected into the separated region, an adiabatic wall will assume some intermediate temperature between the free stream stagnation temperature and the injection temperature. This problem has been considered in Reference 10 and the method developed therein will be applied in this analysis.

The analysis of Reference 10 is based on an energy balance in the separated region. For the case of zero mass injection and an adiabatic wall, the energy crossing the zero streamline by heat conduction and friction, must be zero. For mass injection, the temperature in the separated region will be such that energy crossing the streamline which separates the recirculating flow from the continuing flow just equals the energy needed to heat the injected fluid to the temperature of the separated region. The adiabatic wall temperature is assumed to be the same as the stagnation temperature in the separated region.

In Reference 10, the wall recovery temperature is calculated for mass injection but with the special assumption that the injected fluid is at the wall recovery temperature. This assumption leads to the conclusion that the wall

recovery temperature is hardly affected by the mass injection. The assumption of injection at wall recovery temperatures insures that all of the fluid in the separated region will have the same stagnation temperature which is desirable for the solution of the jet mixing equations; however, this assumption is very unrealistic so far as creating a practical means of reducing wall temperatures in the nose region. In this analysis, the assumption will be made that the injected fluid and the recirculating fluid completely mix with themselves to obtain an average temperature before mixing with the free stream. The wall is assumed to be at the temperature of the recirculating flow. No limitations are placed on the injection temperature. It seems very unlikely that the fluid in the separated layer will completely mix with itself before mixing with the free stream but this assumption allows an analysis to be made which should give a first approximation to the wall temperatures which might be obtainable.

The analysis is based on that of Reference 10 and only the modifications from the work in that reference will be accented here. The general flow configuration is that shown in Figure 8. The heat flow to the wall will be the energy, in excess of the energy corresponding to the wall temperature, which enters in the mixing layer. The energy associated with a unit mass of fluid is its enthalpy plus its kinetic energy. This relation is shown in a non-dimensional form in the following equation. A more detailed derivation is given in Reference 10.

$$\frac{Q_w}{\pi D h_2 \sqrt{\rho_2 u_2 \mu_2} L C} = \frac{1}{3} \int_{\zeta_d}^{\zeta_i} (h^* - h_w^* + \frac{u_2^2}{2 h_2} u^{*2}) d\zeta$$

This may be simplified and integrated to give

$$\frac{3 Q_w}{\pi D h_2 \sqrt{\rho_2 u_2 \mu_2} L C} = \frac{u_2^2}{2 h_2} \left[F_2(\zeta_d) I_1(\zeta_i) + I_2(\zeta_i) \right] - (h_i^* - h) I_1(\zeta_i) + (h_s^* - h_w^*)(\zeta_i - \zeta_d)$$

h_s^* refers to the enthalpy of the mixture of injected and recirculating fluid in the separated region and $F_2(\zeta_d)$, $I_1(\zeta_i)$ and $I_2(\zeta_i)$ represent the value of the integrals and are given in Reference 10.

Define the quantities

$$\Lambda_w = \frac{h_w - h_2}{u_2^2 / 2} \quad \Lambda_s = \frac{h_s - h_2}{u_2^2 / 2}$$

defined similarly to a recovery factor. The last equation for no heat transfer to the wall ($Q_w = 0$), becomes

$$\frac{\zeta_i - \zeta_d}{I_1(\zeta)} (\Lambda_w - \Lambda_s) + \Lambda_s = \frac{I_2(\zeta) + I_1(\zeta) F_2(\zeta_d)}{I_1(\zeta)} \equiv \Lambda_c$$

Λ_c is the quantity that was defined as the wall recovery temperature in Reference 10 under the restrictive assumption of $T_i = T_{\text{recov}}$.

By introducing a term $\Lambda_i = \frac{h_i - h_2}{u_2^2 / 2}$ to define the temperature of injected fluid, the quantity Λ_s can be found as a weighted average of Λ_i and Λ_w

$$\Lambda_s = \frac{\Lambda_i \zeta_i - \Lambda_w (\zeta_i - \zeta_d)}{\zeta_d}$$

The two equations can now be solved for Λ_w to give

$$\Lambda_w = \left[1 + \frac{\zeta_d}{\zeta_i - \zeta_d} \frac{I_1(\zeta_i)}{I_1(\zeta_i) - \zeta_i} \right] \Lambda_i + \frac{\zeta_d}{\zeta_d - \zeta_i} \frac{I_1(\zeta_i)}{I_1(\zeta_i) - \zeta_i} \Lambda_c$$

The quantities in this equation can be evaluated for $\lambda = 0$ at various Pr from the results given in Reference 10. For $\lambda \neq 0$, the integrals can be evaluated from the values of $u^* = f(\zeta)$ from the sine function profile of Reference 11. The evaluation of these integrals is considerably simplified for the case of Pr = 1, so that the computations have been made for this case only. For this case $\Lambda_c = 1$ and

$$I_1(\zeta_i) = \frac{\lambda}{1-\lambda} (\zeta_d - \zeta_i) + \frac{1}{1-\lambda} \int_{\zeta_d}^{\zeta_i} u^* d\zeta$$

The wall recovery temperature is shown in Figure 9 for $\Lambda_i = 0$, injection temperature equals free stream temperature at edge of mixing layer. Two curves for $\lambda = 0$ are shown, one curve for Pr = 0.72 based on the $u^* = f(\zeta)$ function obtained from Reference 10, and one for Pr = 1 and the sine function representation of Reference 11 for $u^* = f(\zeta)$. The difference between these two curves is representative of the errors introduced in the second curve by the simplifying assumptions. The curves at $\lambda \neq 0$ are for Pr = 1 based on the sine function representation. More mass injection is required to achieve a given reduction in recovery factor for values of $\lambda > 0$ since more mass is contained in the mixing layer. The value of Λ_w becomes equal to 0 when the injected mass is equal to the total mass in the mixing layer below the zero streamline. If the mass were injected with little momentum,

the value of λ , which is the velocity of the mixture of injected and recirculating flow, would have to be near zero for high rates of mass injection.

Therefore, high values of λ at high values of mass injection would not occur unless the mass were injected with a high velocity parallel to the recirculating flow.

7. COMPARISON WITH HEAT TRANSFER EXPERIMENTS

The results of heat transfer measurements in the separated region in front of a blunt body with a spike are also given in Reference 1. The heat transfer and recovery temperature in such a region can be calculated by the methods of Reference 10 using the equations shown here. This calculation has been carried out for three cases studied in Reference 1, the hemispherical nose case with an L/D of one and the flat-nosed case with L/D of 2 and 6. The measurements made on the hemispherical nose models were made by measuring the total heat input to a spherical segment of 45° half angle and also to the full hemispherical nose section. If the total heat input from the separated region is desired, the case of $L/D = 1$, where the reattachment is about at the 45° point, is appropriate. For the flat-nosed model, the heat transfer measuring segment covered only about one-half the area of the separated region. For these cases, the heat transfer rate was based on the area of the heat transfer segment.

The comparison between the predicted and measured results are as follows:

	Hemi- spherical $L/D=1$	Flat $L/D=2$ $L/D=6$		
Recovery factor calculated Pr = .72	.849	.849	.849	
Recovery factor measured	.870	.895	.864	
h calculated Btu/ft ² sec ⁰ R	.088	.1198	.0848	Flat nosed case based on area of heat transfer seg- ment
h measured "	.024	.0337	.0337	

The calculated heat transfer rates are 2 to 3 times the experimental ones and the calculated recovery factors are a little lower than the measured ones. This comparison at least provides an agreement on the order of magnitude of these values. The use of $Pr = 0.72$ constant throughout the large temperature range encountered is not too exact and several approximations are involved in calculating the heat transfer rates and correlating with the experimental data. Choosing the appropriate heat transfer rate in the separated region from the available experimental data cannot be done with certainty. Considering these approximations, the comparison may not be so bad as it at first seems and does give some support to the analytical analysis.

8. APPLICATION OF MASS INJECTION

The methods developed in the preceding work may be applied to a typical configuration. Figure 10 shows the mass which must be injected into the separated region at free stream temperature to limit the wall recovery temperature to 1, 2 and 4 times free stream temperature for M between 2 and 10, L/D of the separated region between 0.5 and 8.0, $\lambda = 0$ and $\gamma = 1.4$. D , in this case, is defined as the diameter of the separated region at the reattachment point so that the results are independent of nose shape. The relation for the injected mass based on ξ_i is

$$\frac{4 m_i}{\pi \rho_\infty u_\infty D^2} \sqrt{\frac{Re D_\infty}{C_\infty}} = \sqrt{\frac{3 \rho_2 u_2 T_2 L_m}{\rho_\infty u_\infty T_\infty D}} \xi_i$$

For this calculation, it is assumed that the temperature of the injected mass is free stream temperature. For $\frac{T_w}{T_\infty} = 1$, the full mass in the mixing region must be injected at all conditions so ξ_i is constant. The mass flux ratio $\frac{\rho_2 u_2}{\rho_\infty u_\infty}$ and temperature ratio T_2/T_∞ go down for larger L/D but the length of mixing layer increases.

The effect of decreasing mass flux and temperature ratio as L/D increases at first predominates but for longer spikes, the increasing mixing layer length becomes more important. These conditions result in a minimum injection for some intermediate spike length. The conical attached shock solution, on which this flow model is based, is not possible at $L/D = 5$ and $M = 2$. For the higher wall temperatures considered, not much decrease in

is possible at the higher Mach numbers since the allowable wall temperature is still low with respect to the stagnation temperature. At the lower Mach numbers, increasing the allowable wall temperature causes large decreases in the required injection.

The mass injection required for a specific configuration is shown in Figure 11. The amount of injection required to limit the temperature on a 3 foot diameter separated region traveling at $M = 6$ at 100,000 feet altitude is shown for various L/D ratios. Since the Reynolds number, based on the length of the separated region, is about $1.5(10^6)$ for the shortest spike length, $L/D = 0.5$, the separated flow would not be likely to remain laminar. The present analysis would apply better to lower Reynolds number configurations, but the case considered here was chosen to compare with data on other cooling methods.

If a spherical nose is used with a spike, the diameter of the sphere will have to be larger than the diameter of the separated region. Because of the relatively large quantities of injected air needed to limit the temperature, the reattachment pressure ratio is small corresponding to a turning angle of about 1° at reattachment. This means that the conical separated region will be almost tangent to the spherical nose. The angle between the spike and the reattachment point, and the ratio of sphere diameter to separated region diameter would be as follows:

L/D	Angle of Separated Region	Sphere diameter
		Separated region diameter
.5	44°	1.44
1.0	62°	1.13
2.0	75°	1.03

In this description, L is the length of the separated region. The actual spike would have to be longer to create separation at the appropriate pressure ratio. The Reynolds number at the separation point can be selected from the results shown in Figure.2.

9. CONCLUSIONS

1. Injection of cooled gas into a separated region caused by a spike in front of a blunt body will limit the temperature of the blunt body to any desired amount.
2. The pressure in the separated region caused by a spike in front of a blunt body may be estimated by available knowledge on separation and reattachment.
3. The velocity of the vortex flow in the separated region could be important in determining both the pressure and temperature, for the case of mass injection, in this region.

REFERENCES

1. Bogdonoff, S. M. and Vas, I. E. - Preliminary Investigation of Spiked Bodies at Hypersonic Speeds - Princeton University Report 412, March 1958.
2. Stalder, J. R. and Nielson, H. V. - Heat Transfer from a Hemisphere-Cylinder Equipped with Flow-Separating Spikes - NACA TN 3287, September 1954.
3. Mair, W. A. - Experiments on Separation of Boundary Layers on Probes in Front of Blunt-Nosed Bodies in a Supersonic Air Stream. The Phil. Mag., July 1952.
4. Beastall, D. and Turner, J. - The Effect of a Spike Protruding in Front of a Bluff Body at Supersonic Speeds - R & M No. 3007, 1957.
5. Alexander, R. - Results of Tests to Determine the Effect of a Conical Windshield on the Drag of a Bluff Body at Supersonic Speeds - NACA RM L6K08a, January 1947.
6. Alexander, S. R. and Katz, E. - Flight Tests to Determine the Effect of Length of a Conical Windshield on the Drag of a Bluff Body at Supersonic Speeds - NACA RM L6J16a, January 1947.
7. Alexander, S. R. - Flight Investigations at Low Supersonic Speeds to Determine the Effectiveness of Cones and a Wedge in Reducing the Drag of Round-Nose Bodies and Airfoils - NACA RM L8L07a, March 1949.
8. Jones, J. J. - Flow Separation from Rods Ahead of Blunt Noses at Mach Number 2.72 - NACA RM L52E05a, July 1952.
9. Chapman, D. R., Kuehn, D. M. and Larson, H. K. - Investigation of Separated Flows in Supersonic and Subsonic Streams with Emphasis on the Effect of Transition - NACA TN 3869, March 1957.
10. Chapman, D. R. - A Theoretical Analysis of Heat Transfer in Regions of Separated Flow - NACA TN 3792, October 1956.
11. Lock, R. C. - The Velocity Distribution in the Laminar Boundary Layer Between Parallel Streams - Q. Journal of Mech. and App. Math., Vol. 4, pp. 42-63, 1951.
12. Pai, S. I. - On Supersonic Flow of a Two-Dimensional Jet in Uniform Stream - JAS, Vol. 19, pp. 61-65, 1952.

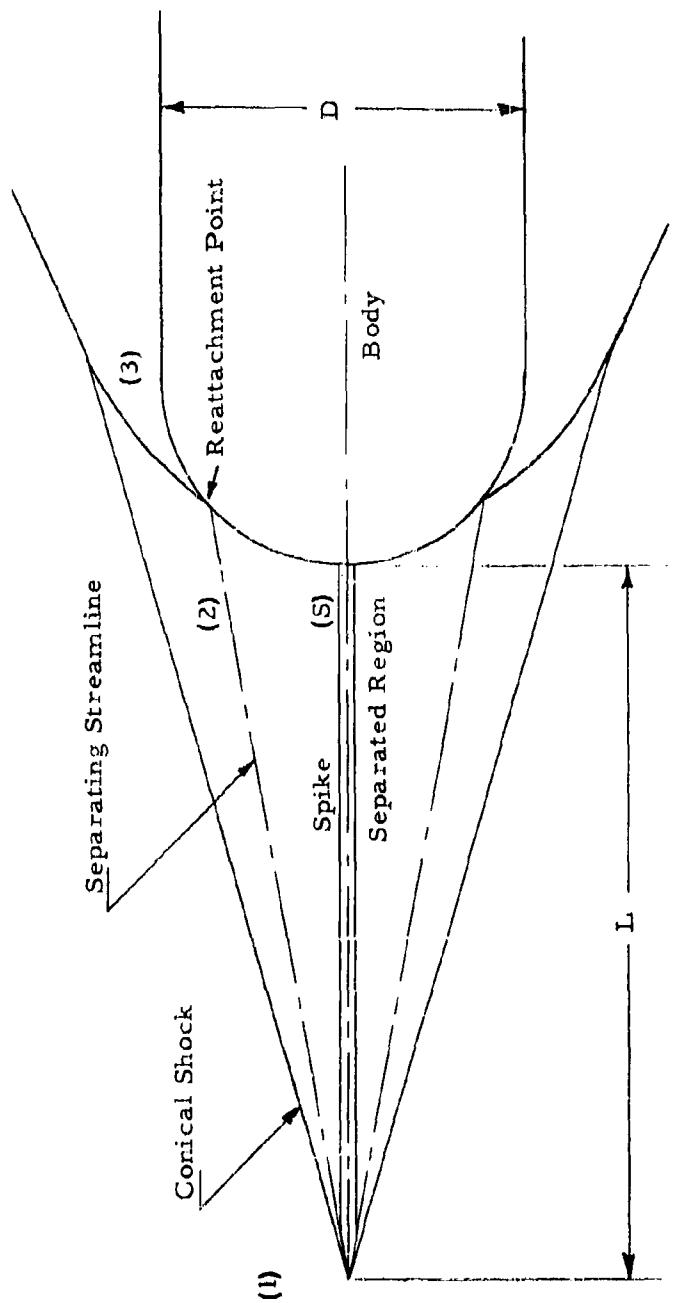


Figure 1. Sketch of General Configuration of Spike Placed in Front of Blunt Body.

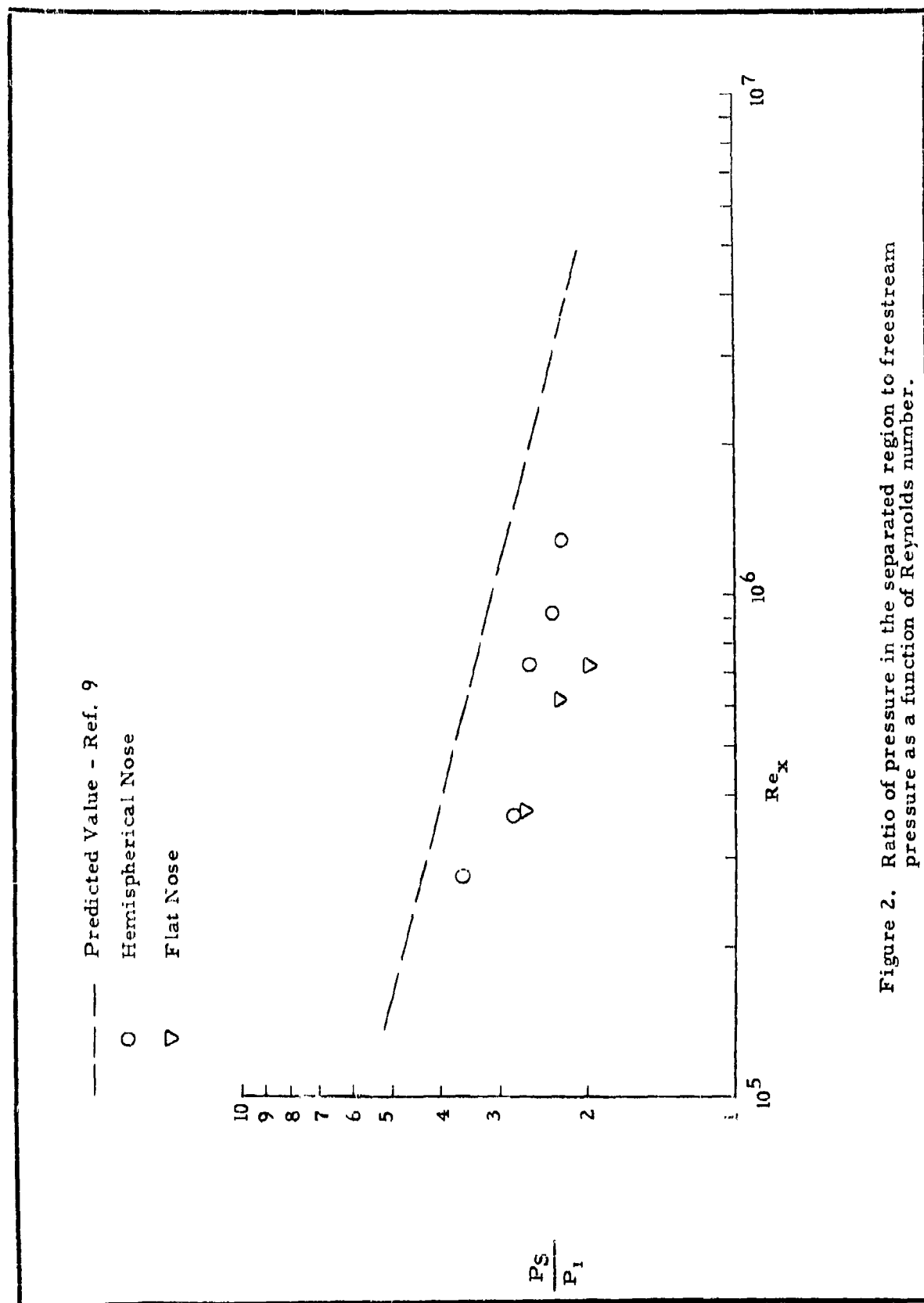


Figure 2. Ratio of pressure in the separated region to freestream pressure as a function of Reynolds number.

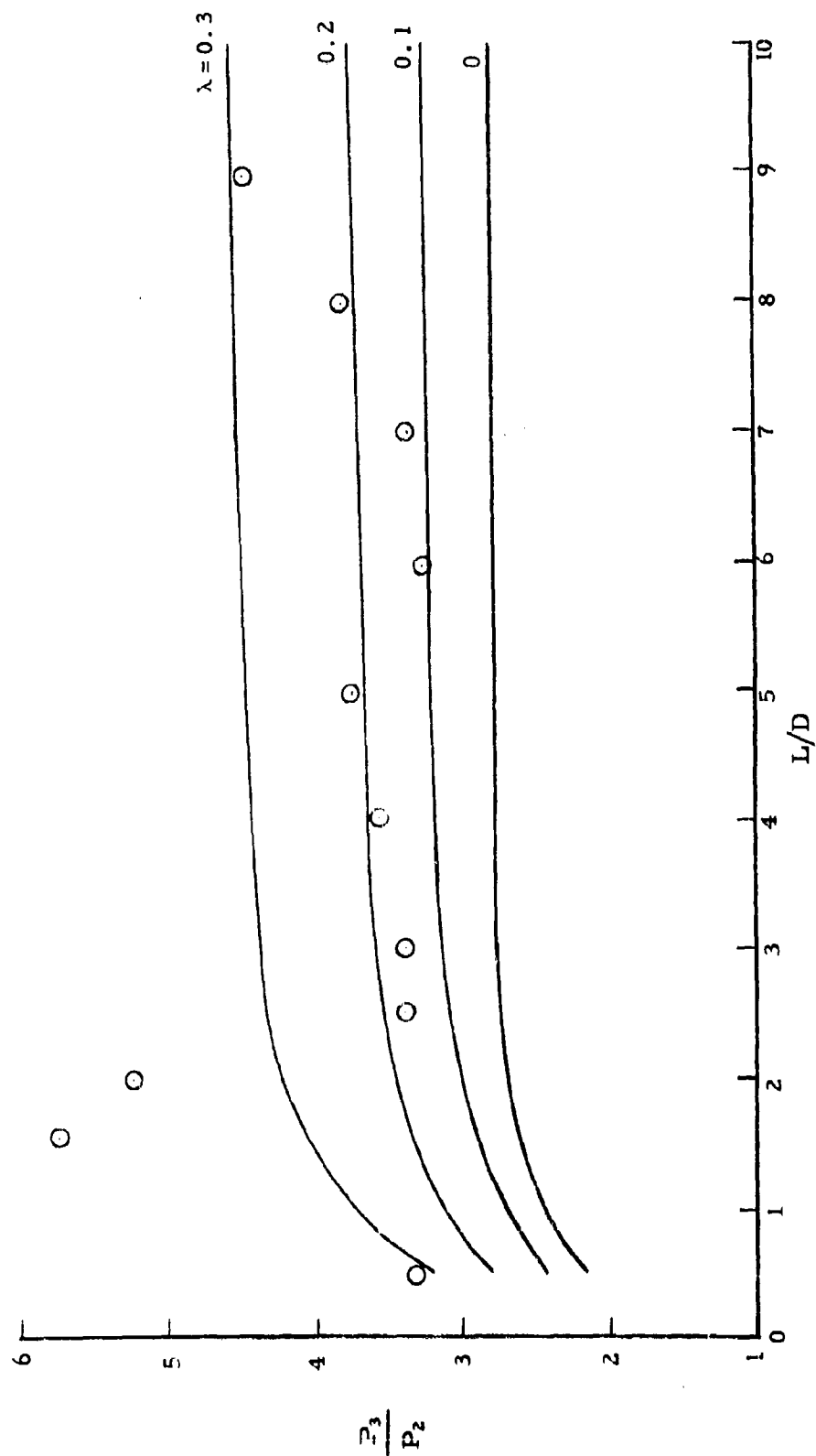


Figure 3. Comparison of the experimental reattachment pressure ratio with the values calculation for stagnation of the zero streamline for different values of separated region velocity λ .

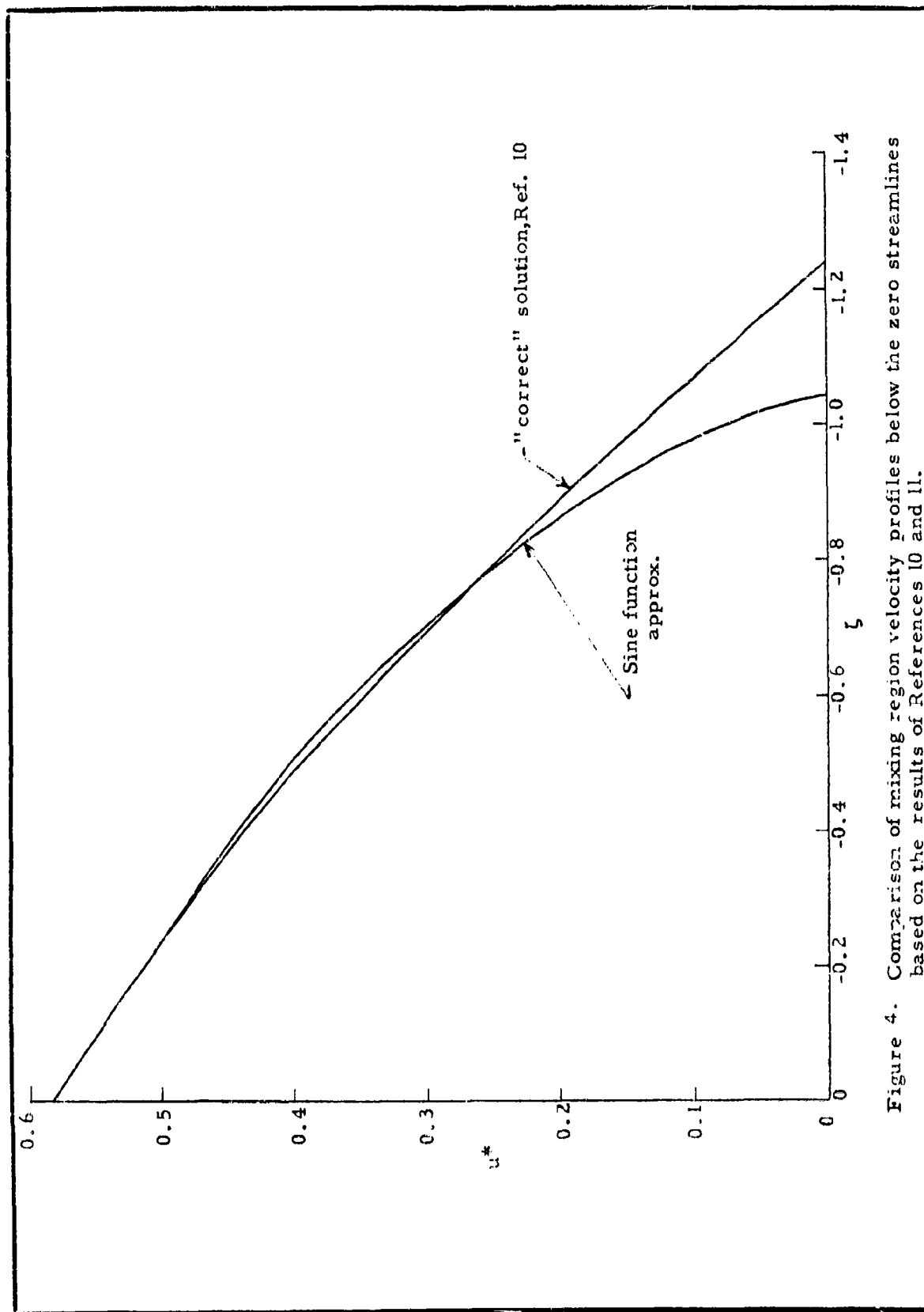


Figure 4. Comparison of mixing region velocity profiles below the zero streamlines based on the results of References 10 and 11.

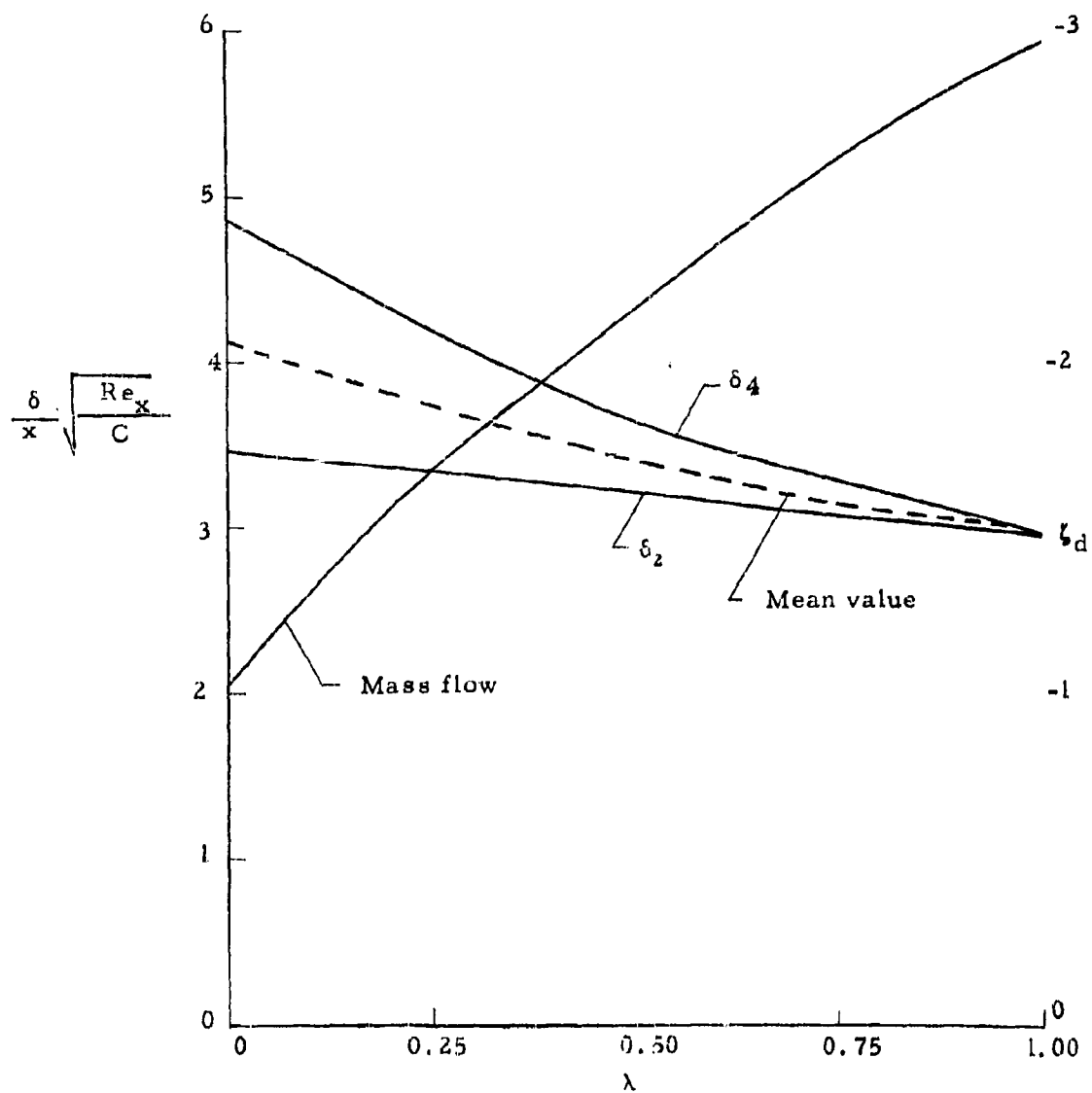


Figure 5.. The thickness of and mass contained in the mixing layer as a function of separated region velocity λ .

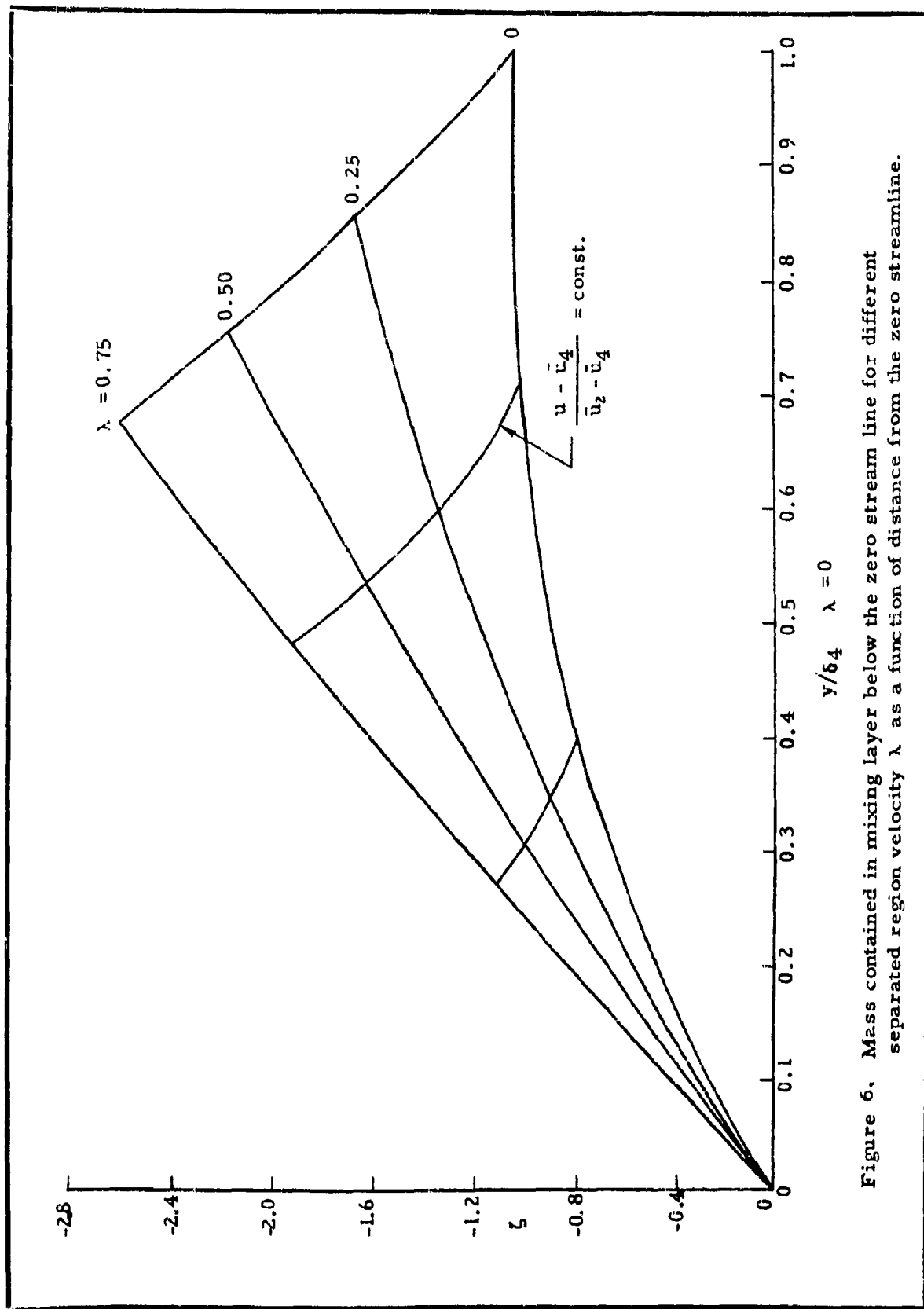


Figure 6. Mass contained in mixing layer below the zero streamline for different separated region velocity λ as a function of distance from the zero streamline.

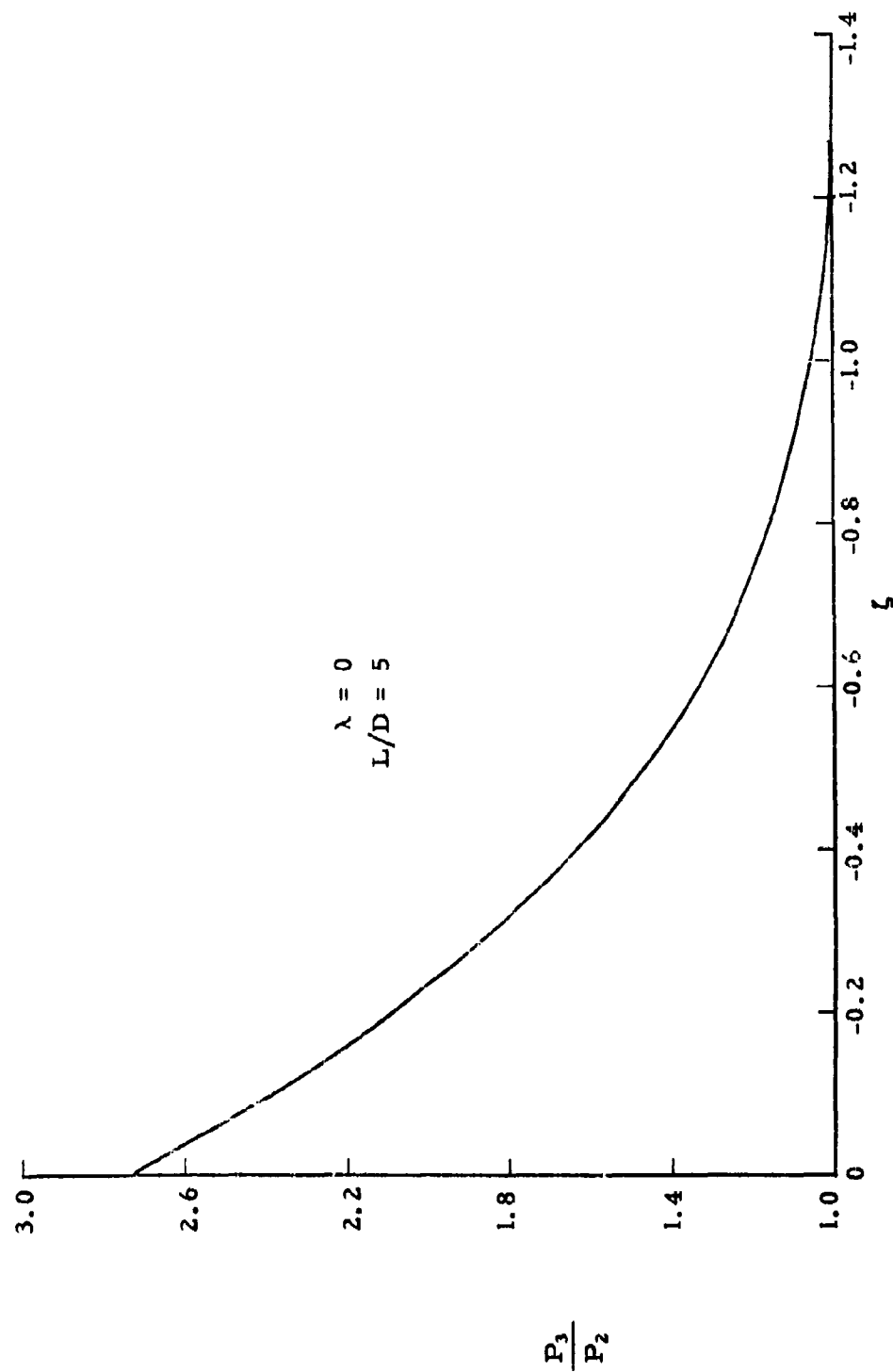


Figure 7. Reattachment pressure ratio calculated by stagnation of dividing streamline as a function of mass injection.

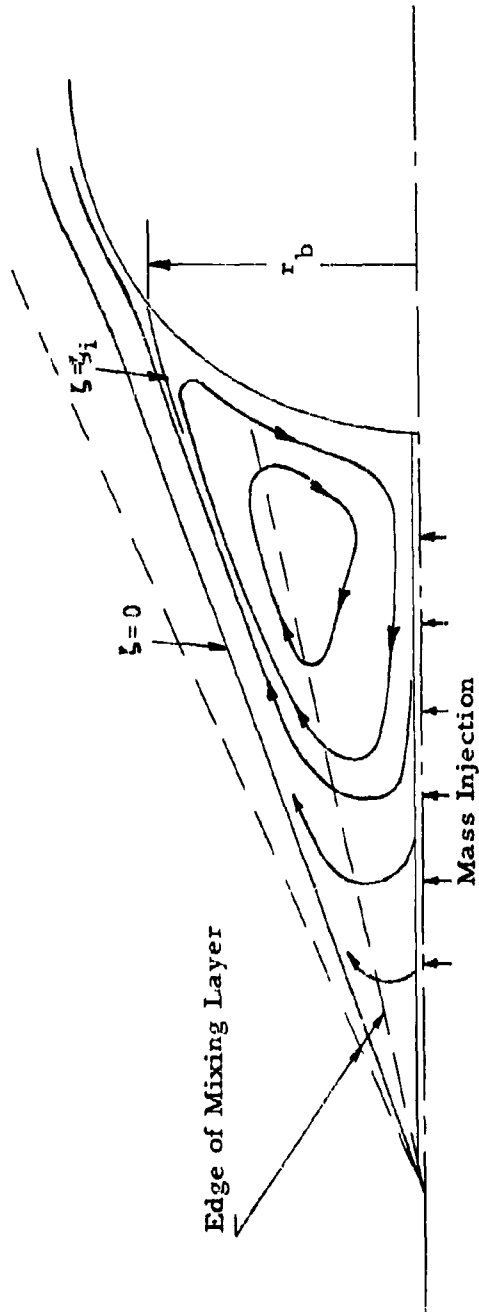


Figure 8. Sketch of Flow Model Used in the Calculation of Recovery Temperature With Mass Injection.

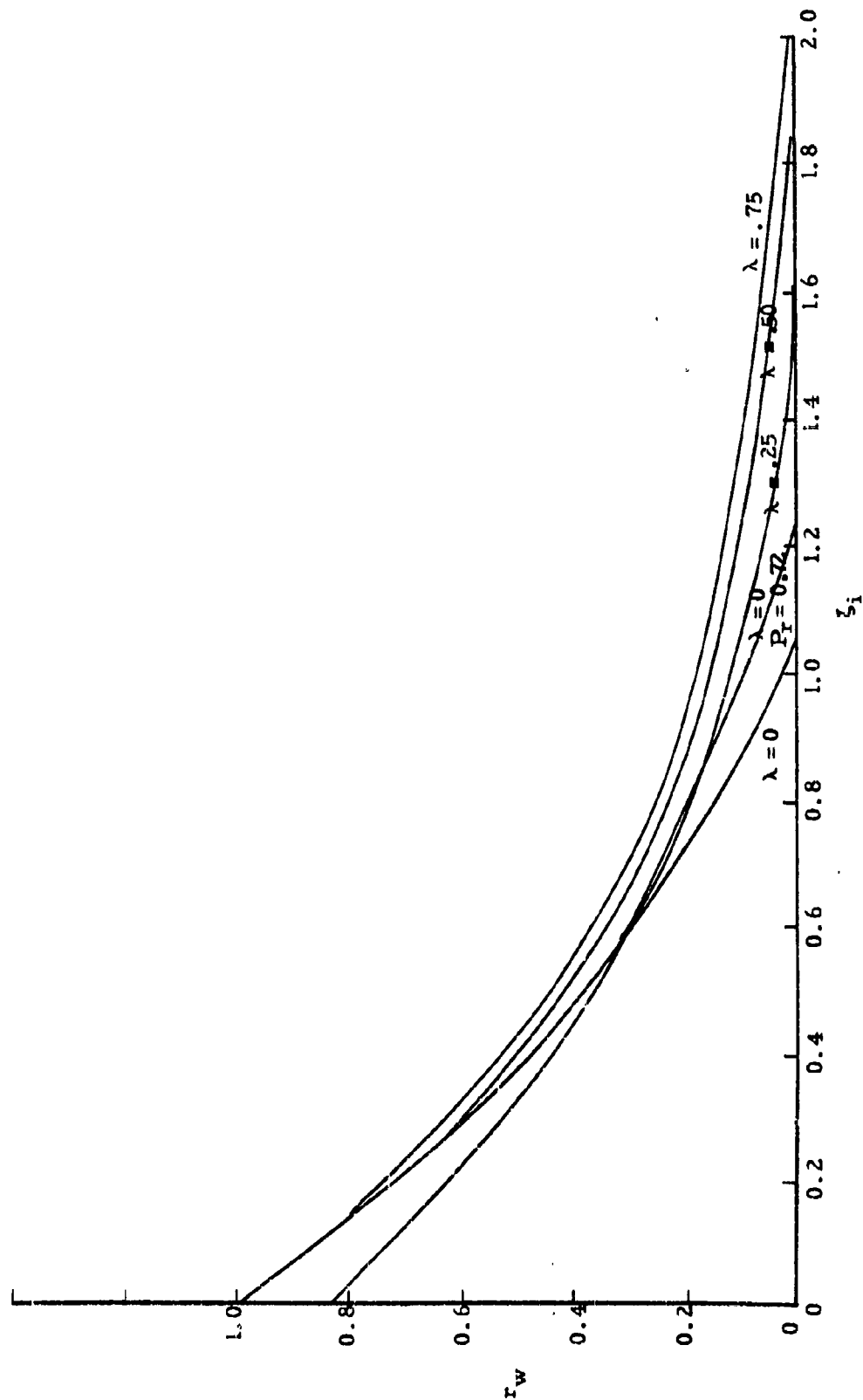


Figure 9.. Wall recovery temperatures as a function of mass injection for different separated region velocity. Mass is injected at free stream temperatures.

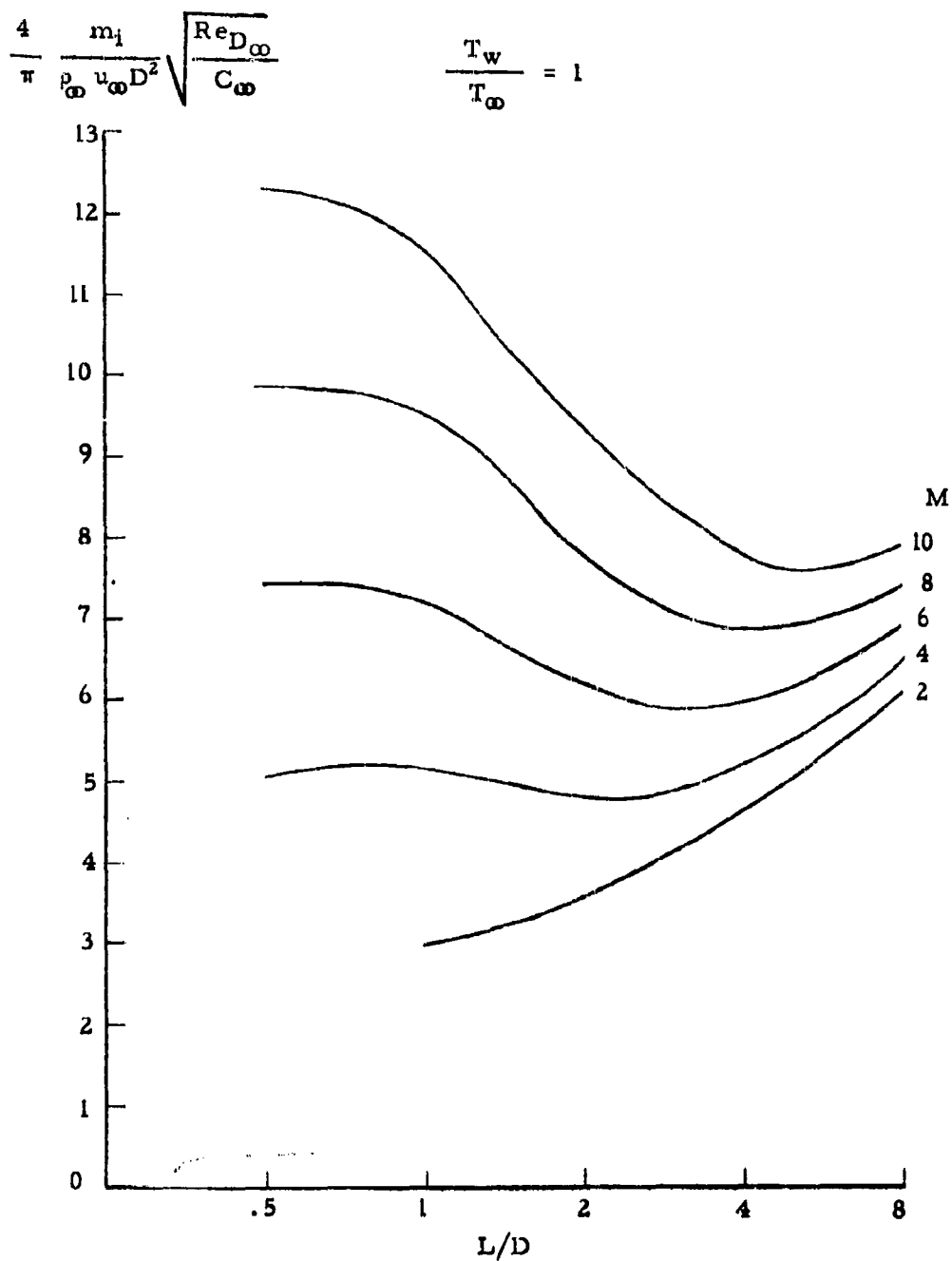


Figure 10a. Mass injection required to limit the wall temperature for various spike lengths. Injection takes place at free stream temperature.

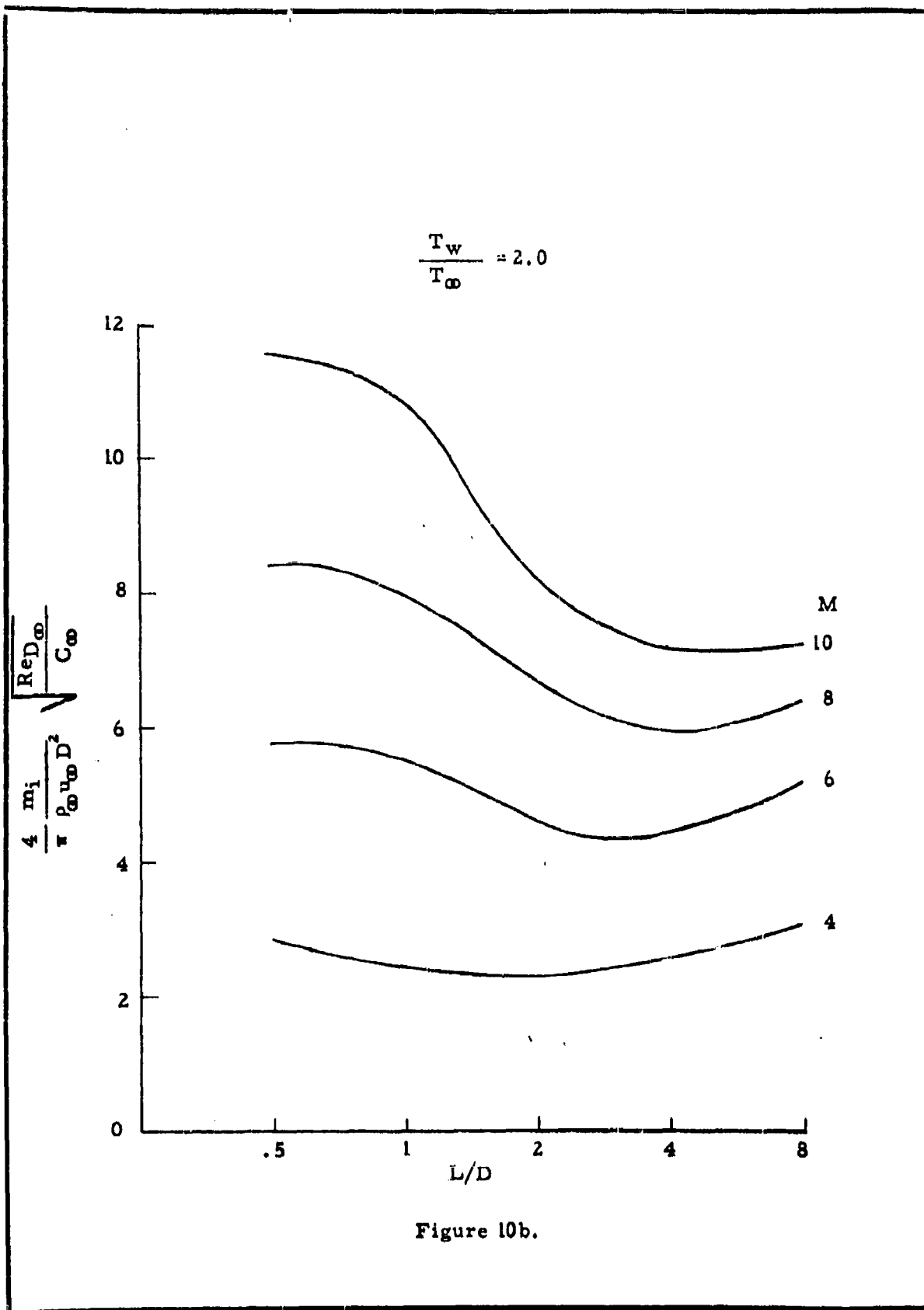


Figure 10b.

$$\frac{T_w}{T_\infty} = 4$$

$$\frac{4}{\pi} \frac{m_i}{\rho_\infty u_\infty D^2} \sqrt{\frac{Re D_\infty}{C_\infty}}$$

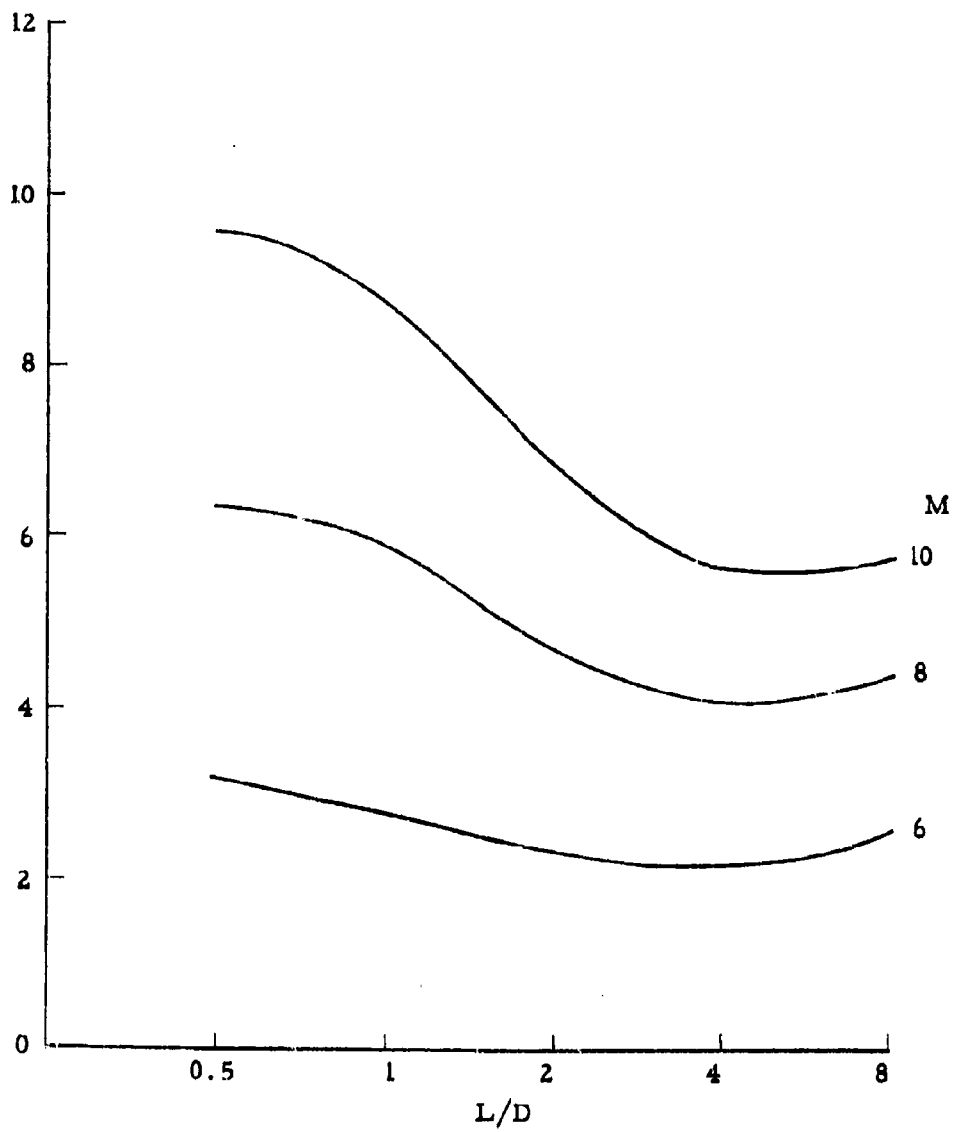


Figure 10c.

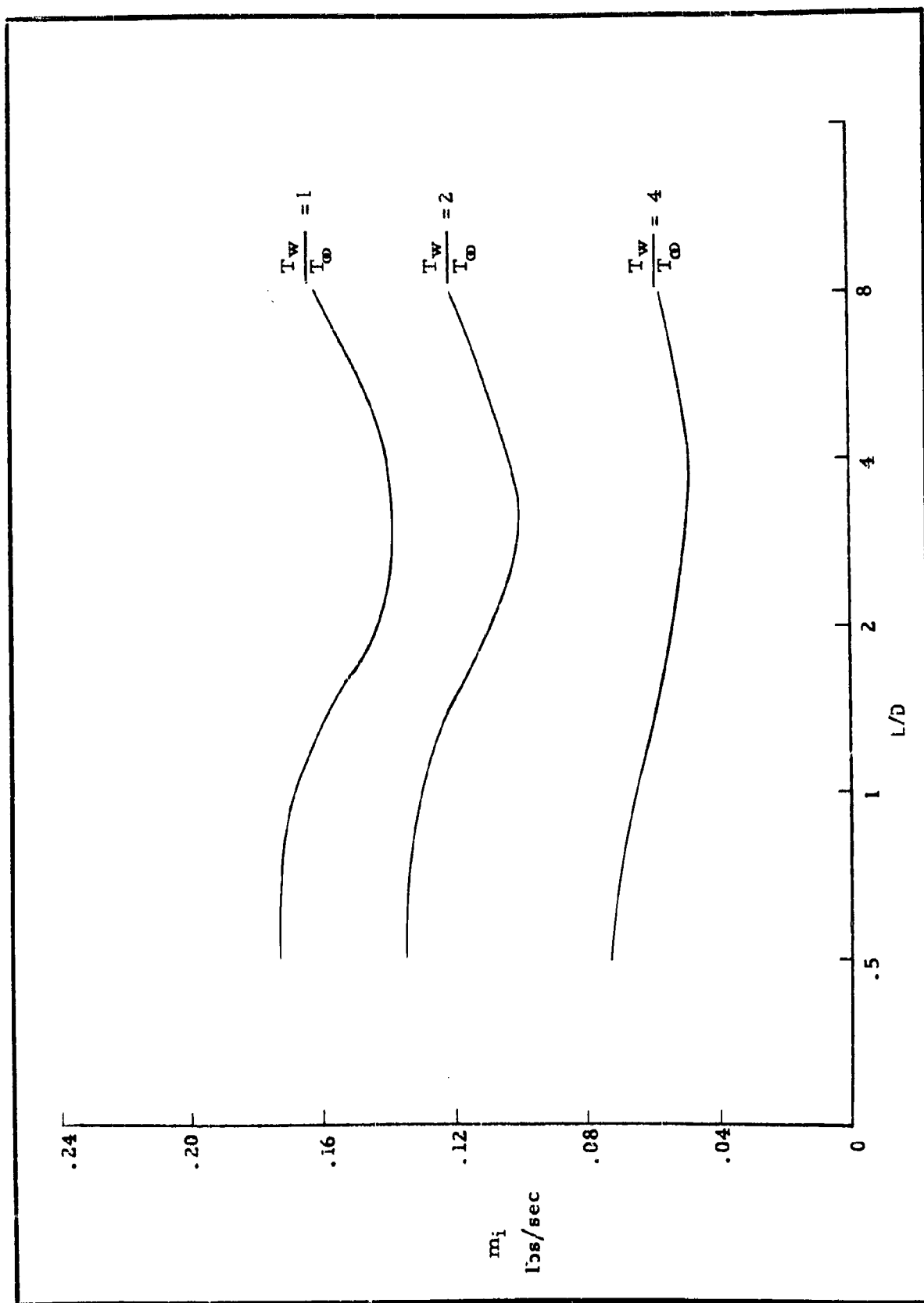


Figure 11. Mass injection required to limit the wall temperature for various spike lengths on a 3 foot diameter separated region at $M = 6$ and 100,000 foot altitude.

CHAPTER III

SHOCK LAYER IONIZATION

PART A

GENERAL DISCUSSION OF IONIZATION PROBLEMS

A. GENERAL DISCUSSION OF IONIZATION PROBLEMS

Of the many problems encountered by the designers of ballistic missile nose cones one which is of particular interest to the designer of radomes, capable of operating at hypersonic speeds, is the problem of signal attenuation caused by the presence of a plasma sheath surrounding the forward sections of a vehicle. While the interruption of signals due to the existence of the ionized layer of gas or plasma sheath can be circumvented to some extent in the development of an ICBM, signal interruption cannot be tolerated on manned reentry vehicles and hypersonic interceptor missiles. The problem of predicting the effects of the plasma sheath on electromagnetic radiation can be divided into two areas. The first area of effort is that of providing the accurate predictions of the details of the ionized flow field surrounding the vehicle. The second area of effort is concerned with the determination of the effects of a given locally ionized flow field on the transmission of electromagnetic waves through this flow field.

Many analyses have been made of the latter problem; however, they have mainly been directed toward the study of the effects of a stationary plane-uniform plasma on the transmission of a plane wave. This, of course, is not the situation in the flow surrounding a hypersonic vehicle since the plasma is moving and contains gradients in electron density. Also, the wave fronts emanating from practical antennas are not plane.

The work reported in the following part will be concerned only with the determination of the detailed characteristics of the plasma flow fields

surrounding radomes traveling at hypersonic speeds. The effects of the plasma sheath on signal transmission will not be considered here.

CHAPTER III - PART B

AN APPROXIMATE METHOD FOR THE CALCULATION OF
THE SHOCK SHAPE AND FLOW FIELD PROPERTIES ABOUT
LONG BLUNTED CONES AT HYPERSONIC SPEEDS

by Aerodynamics Department
General Applied Science Laboratories, Inc.

TABLE OF CONTENTS

<u>Section</u>	<u>Title</u>	<u>Page</u>
	Summary	595
	Symbols	596
1.	Introduction	599
2.	Description of Method	600
	a. Determination of Shock Shape	600
	b. Flow Field Properties	603
	c. Stagnation Region	608
	d. Calculation of Collision Frequency	610
3.	Applications	615
4.	Conclusions	619
	References	620
	Figures	621

B. AN APPROXIMATE METHOD FOR THE CALCULATION OF
THE SHOCK SHAPE AND FLOW FIELD PROPERTIES ABOUT
LONG BLUNTED CONES AT HYPERSONIC SPEEDS

SUMMARY

An approximate method for the determination of the shock shape and flow properties between shock and body has been developed for long blunted cones. Results are presented for a hemispherically blunted cone with half-angle of 15° , nose radius of 2.5 inches and a ratio of nose radius to base radius of $1/6$ for flight conditions corresponding to $M = 15$, $h = 150,000$ ft. and $M = 20$ at $200,000$ ft. These calculations were made assuming that the air is in thermodynamic equilibrium. Electron density distributions were also obtained for the $M = 20$, $h = 200,000$ ft. case assuming frozen equilibrium. These results are included for comparison.

The method used to compute particle collision frequency is described.

SYMBOLS

y	distance measured normal to axis of body
x	distance measured along axis of body
R	nose radius
m	mass flow
r	radial distance from axis of body
ρ	density
V	velocity
θ	angle between local flow direction and axis of body
θ_b	angle between flow direction at body surface and axis of body
l	distance measured normal to body surface
L	distance between shock and body, measured normal to the body
n	exponent in relation between density (and velocity) and distance across shock layer
δ	defined by Equation (8)
$\left. \begin{matrix} P \\ U \end{matrix} \right\}$	defined by Equation (7)
τ	coordinate defined by Equation (9)
ν_n	collision frequency of electrons with neutral particles
ν_i	collision frequency of electrons with ions

\bar{c}	thermal velocity of electrons
n_j	number of neutral particles (atoms or molecules) of the j th component
Q_j	cross section for collisions between electrons and neutral particles of j th component
T	absolute temperature
k	Boltzmann constant
m	electron mass
L	Loschmidt's number
a	number of atoms
α_j	ratio of number of particles of j th component to total number of atoms
P_0	defined by Equation (22)
e	electron charge
ϵ	dielectric constant of the vacuum

Subscripts

b	body value
L	value at $l = L$ (i. e. at shock)
s	shock value
∞	free stream value
o	value at standard conditions

1. INTRODUCTION

This report describes a method which will permit an approximate definition of shock shape and flow field properties about bodies which are typical of radome shapes. Effort has been directed toward obtaining a method which although approximate, is fairly rapid and which has associated with it a reasonable accuracy. The intention is to provide an interim solution which has sufficient merit to be useful for preliminary engineering estimates. More accurate methods, such as real gas characteristics, are available but require lengthy machine calculations. The approximate method which has been developed makes use of some results obtained using the real gas characteristics method as have been applied to other problems. Until such time as the real gas characteristics calculations can be reduced to routine machine operation, the following method is proposed.

2. DESCRIPTION OF METHOD

The approximate method considers two problems: (1) the determination of the shock shape about the body, and (2) the determination of the flow field properties across the shock layer at various stations located normal to the body surface.

a. Determination of Shock Shape

For long, spherically blunted, cones of the type under consideration, it has been found that the shock shape can be reasonably approximated by the following method. These results will yield gross properties of the shock system. Exact details of shock shape such as the overexpansion at the sphere-cone junction are not predicted by this method. For the 15° half angle cone considered here, the magnitude of the overexpansion is, in any case, relatively small. For the given body shape, the effect can be neglected for considerations relating to overall engineering design estimates.

The shock ahead of the spherical body surface corresponding to approximately one radian of body arc length measured from the body centerline can be described by a parabola

$$\left(\frac{y}{R}\right)^2 = K\left(\frac{x}{R}\right)$$

where the arbitrary constant K is determined by requiring that the radius of curvature of the shock at $y = 0$ match the radius of curvature of the body at $x = 0, y = 0$. This approximation is well known and has been found to be adequate as checked by real gas characteristics calculations.

For this class of bodies, the effect of blunting (shock curvature) is felt only over a relatively small part of the whole shock. For given flight conditions, the inclination of the conical shock is known; however, its location is not known a priori. From previous calculations on similar blunt bodies, it develops that the effect of blunting is no longer present beyond the vicinity of about one radius length from the juncture of sphere and cone. This means that the origin of the conical portion of the shock may be located somewhere along a station approximately one radius from the juncture of the sphere and the body. A station is defined as a line normal to the body surface. For long slender bodies, it will become evident from the following development that the error introduced by the improper selection of the station where the shock becomes conical is not critical. It is suggested that the station for the origin of the conical flow may be reasonably assumed to be one radius downstream from the sphere-cone junction.

The point along this station where the origin of the conical shock is located remains to be determined. Because of the cone blunting, it is known that the conical shock must be located further from the body than the conical shock which would result from a pointed cone with the same half angle at the same flight conditions. The procedure for locating the origin of the conical shock consists of arbitrarily selecting several possible locations for the conical shock along the station located at one radius from the sphere-cone juncture and from mass flow considerations, applied at the rear of the body, selecting which origin location is appropriate. The

application of continuity considerations at the rear of the body requires some knowledge of the density and velocity profiles at the rearmost stations. Fortunately, for this type of body, the density and velocity profiles far back on the body are essentially those corresponding to the conical flow field with a correction for the high entropy layer near the body surface due to the blunting of the cone. In first approximation, this may be accomplished by assuming that the pressure is constant across the layer at the rear of the body, there approximating the entropy profile as a step function comprised of two entropy layers; the layer close to the body at the entropy level behind the normal shock, and the layer behind the shock, at the entropy level corresponding to the conical shock. The thickness of these two layers is then determined by finding the location of the streamline which separates the two layers and satisfies overall continuity.

Knowing the inclination, and now, the location of the conical shock, there remains to connect the parabolic shock over the nose with the conical shock over the aft portion of the body. The shock shape in this region has been found to be reasonably well approximated by the following cubic:

$$\frac{x}{R} = a \left| \frac{y}{R} \right|^3 + b \left| \frac{y}{R} \right|^2 + c \left| \frac{y}{R} \right| + d$$

where the four arbitrary constants are determined by matching coordinates and slopes of the parabolic and conical shocks.

From this development, it is clear that any reasonable error in the determination of the location of the station where the conical shock originates

does not result in large changes in the shock shape. The portion of the shock given by the cubic is only weakly dependent on the x-coordinate of the cubic-conical juncture. Consequently, the shock shape does not change significantly when this boundary condition varies while the other three boundary conditions remain fixed.

b. Flow Field Properties

With the shock shape approximated, all the properties immediately behind the shock can be determined. On the body, the pressure distribution is approximated using Newtonian theory applied over the forward portion of the nose combined with a Prandtl-Meyer expansion. The two theories are joined where the pressure and the derivative of the pressure match. The Prandtl-Meyer expansion is then faired into the value of pressure corresponding to the cone surface pressure. With the pressure distribution, the entropy on the body surface, and the total enthalpy of the flow field known, all other properties and quantities on the body surface are determinable.

The analysis of the flow field is divided into two regions - the region where the profiles across the layer are influenced only by the curved shock and the region where the flow field is influenced by the conical shock.

In the region where the shock is curved with the shape of the shock, and the pressure distribution known, appropriate functional forms are assumed for several of the quantities defining the flow field. A mass flow balance is set up across the shock layer from which the constant appearing in the functional forms is determined. It must be emphasized that the results of this

calculation are necessarily approximate. The analysis yields a flow field which satisfies conservation of mass on the average across the layer. Momentum and energy are not conserved. However, by choosing functional forms appropriately (i.e., by physical considerations) for the various quantities appearing in the mass balance, the solution obtained cannot deviate far from physical reality.

Consider each station to be a line normal to the body surface between the body and the shock. Let l denote distance along this line, measured from the body. Then the mass flow across this control surface is (see Figure 1)

$$m = 2 \pi \int_0^L r \rho V \cos (\theta - \theta_b) dl \quad (1)$$

where θ and θ_b are the local and body values of flow direction with respect to the axis, respectively. The quantity r may be expressed in terms of l by

$$r = r_b + (r_L - r_b) \frac{l}{L} \quad (2)$$

The following assumptions are made with respect to the remaining quantities of Equation (1).

At hypersonic speeds the shock wave wraps itself closely around the body. Except in the vicinity of the stagnation point, the flow direction at the shock wave is not very different from the flow direction at the body. The value of $\cos (\theta - \theta_b)$ is then very close to unity. No significant error will be made, therefore, if one uses a linear variation of this function between the

body and the shock wave.

$$\cos(\theta - \theta_b) = 1 - \left[1 - \cos(\theta_L - \theta_b) \right] \frac{l}{L} \quad (3)$$

This approximation is not valid in the nose region very close to the axis,

An alternative approach for the streamline passing through the stagnation point is discussed later.

Inspection of known solutions for other bodies of similar shape indicates that the density and velocity profiles vary very slowly near the body surface and have increasing value of slope as the shock wave is approached. Hence, the following forms are assumed for the density and velocity profiles:

$$\begin{aligned} \rho &= \rho_0 + \rho_1 \left(\frac{l}{L} \right)^n \\ V &= V_0 + V_1 \left(\frac{l}{L} \right)^n \end{aligned} \quad (4)$$

The values of the constants, ρ_0 , ρ_1 , V_0 and V_1 , can be determined by requiring that the density and velocity at the body and at the shock wave have the values consistent with the flight condition and the assumed pressure distribution and shock shape. Thus, one obtains

$$\begin{aligned} \rho &= \rho_b + (\rho_s - \rho_b) \left(\frac{l}{L} \right)^n \\ V &= V_b + (V_s - V_b) \left(\frac{l}{L} \right)^n \end{aligned} \quad (5)$$

where L = total distance between shock and body normal to the body.

l = distance to any point in the field measured from the body in the distance of L

and the subscripts

b - referring to the body values

s - referring to shock values

The value of n may be determined by inserting Equations (5) in Equation (1), noting that $m = \pi r_s^2 \rho_\infty V_\infty$, and solving the resulting algebraic equation for n . Here, r_s is the value of r at $l = L$.

It is pointed out that because of the approximation scheme used, not only does this method give approximate solutions, but the results are not necessarily thermodynamically consistent. Thus, one can determine the streamlines by calculating the position on the control surface at which the stream tube to be determined intersects the control surface. The streamlines should be lines of constant entropy. However, if one used the calculated values of density and velocity together with the total enthalpy appropriate to the problem at hand, a slightly different value of entropy is generally obtained. The difference in the two values of entropy depends essentially on how good the approximations are that are used to represent the various quantities entering into Equation 1. For the calculated results presented in this report, the entropy profile calculated from the locally determined flow field properties were found to be in close agreement with the entropy profiles determined from the entropy behind the shock and traced back to the particular station in question along the flow field streamlines.

It is noted that better results might be expected if the functional forms were chosen with additional unknown constants to be determined by requiring

conservation of momentum and energy across the shock layer. Such a calculation would be straightforward for a perfect gas. In the case of a chemically reacting gas, the equation of state is not known analytically and one would have to resort to trial-and-error methods of calculation.

In the region where the flow field is influenced by the conical shock, a slightly different procedure is employed to determine the flow field properties. The functional form suitable for the density and velocity is still the exponential variation, Equation (5); however, it is employed only in the region between the body and the point in the field where the field properties become constant, corresponding to the portion of the flow field influenced by the conical shock. The previously described method of comparing the entropy profiles at a station is employed in the same manner to check for thermodynamic consistency of the results.

Where the conical flow field is a significant portion of the flow field, i. e., far back on the body, the procedure for obtaining properties at downstream stations, once the properties at an upstream station (in the region of influence of the conical shock) have been determined, may be simplified further. Assume that the entropy profile across the layer at an upstream station has been calculated to a satisfactory approximation by the previously described method. At other downstream stations, far back on the body, the pressure across the layer is for all practical purposes constant, and equal to the value behind the shock. The entropy profile at the downstream station may be approximated by applying an affine transformation to the entropy

profile of the upstream station such that the resulting profile has the correct distribution of entropy corresponding to the constant entropy thickness of the layer at the downstream station. The thickness of the constant entropy layer can be estimated by mass flow considerations. Using the transformed entropy profile and the assumption of constant pressure across the layer the remaining properties can be determined.

c. Stagnation Region

In the vicinity of the stagnation point the following method for determining flow field properties may be employed.

In the region of the stagnation point the local Mach number is quite low and hence there is very little variation in the state properties from point-to-point. A reasonable approximation is therefore to consider the fluid to be of constant composition. The idea of using an assumed form for some of the physical quantities may then be coupled with some of the analytical results of Ferri and Vaglio-Laurin (Reference 1) which was developed for the purpose of determining the flow field about blunt bodies at supersonic speeds. The latter method allows an exact numerical integration of the differential equations to be performed, but must be carried out on a high speed computer.

All of the thermodynamic quantities of interest vary very little on the axis between the shock and the body. The quantity which undergoes the largest change is the velocity. Hence, if the variation of the velocity is closely approximated, all other quantities will be determined to a still better degree of approximation. Since both the velocity and velocity gradient vary

monotonically along the axis, a reasonable approximation to the form of the velocity is

$$V = V_s \left(\frac{L}{L} \right)^n \quad (6)$$

where V_s is the value of the velocity just behind the shock wave. The value of the exponent n can be determined by requiring that the velocity gradient at the shock wave have the correct value. Since the assumed velocity distribution will then have the correct value and slope at the shock wave, Equation (6) can be expected to give a good representation of the velocity variation along the axis.

If one makes the usual hypersonic approximations regarding strong shock waves (i. e., ambient pressure and enthalpy can be neglected when compared with $\rho_\infty V_\infty^2$ and $\frac{V_\infty^2}{2}$, respectively) then one obtains, for the velocity and density on the axis immediately behind the shock wave

$$\bar{U} = \frac{u}{V_\infty} = \delta \text{ and } P = \frac{\rho \delta}{\rho_\infty} = 1 \quad (7)$$

where

$$\delta = \frac{\gamma - 1}{\gamma + 1} \quad (8)$$

Here γ is evaluated behind the shock wave.

It is shown in Reference 1 that if one makes the transformation from a cylindrical coordinate system x, r to the coordinate system τ, y defined by

$$\begin{aligned} \frac{\partial}{\partial x} &= -\frac{2P\bar{V}}{y\delta} \frac{\partial}{\partial \tau} \\ \frac{\partial}{\partial r} &= \frac{2}{y} \left[\frac{P\bar{U}}{\delta} - \tau \right] \frac{\partial}{\partial \tau} + \frac{\partial}{\partial y} \end{aligned} \quad (9)$$

Then, the velocity along the axis can be determined from

$$\bar{U} \left[\frac{1 - \bar{U}^2}{1 - \delta^2} \right] \frac{1 - \delta}{2\delta} = \tau \delta \quad (10)$$

The velocity gradient at the shock wave ($\tau = 1$) is therefore

$$\frac{\partial u}{\partial x} = -\frac{2PV_\infty}{\delta} \frac{\partial \bar{V}}{\partial y} \frac{\partial \bar{U}}{\partial \tau} \quad (11)$$

If the equation of the shock wave is expressed in the form $x = F(y)$, then using the strong shock approximation, it can be seen from Reference 1 that

$$\frac{\partial \bar{V}}{\partial y} = (1 - \delta) \frac{\partial^2 F}{\partial y^2} \quad (12)$$

and, from Equation (10)

$$\frac{\partial \bar{U}}{\partial \tau} = \frac{\delta \bar{U}(1 - \bar{U}^2)}{\delta - \bar{U}^2} \quad (13)$$

Combining Equations (6), (11), (12) and (13), one finally obtains

$$\left(\frac{\partial u}{\partial x} \right)_L = -\frac{n\delta V_\infty}{L} = -\frac{2V_\infty(1 - \delta) \bar{U}(1 - \bar{U}^2)}{\delta - \bar{U}^2} \frac{\partial^2 F}{\partial y^2} \quad (14)$$

from which n can be determined. Once n is known, the velocity can be combined with the known values of the total enthalpy and the entropy behind the shock wave to determine the state of the gas at every point on the axis.

d. Calculation of Collision Frequency

The method used in computing collision frequency is as follows:

In order to handle the problem more easily, we compute the collision

frequency of the electrons by splitting it into two parts:

$$\nu = \nu_n + \nu_i \quad (15)$$

where:

ν_n = collision frequency of electrons with neutral particles

ν_i = collision frequency of electrons with ions.

The first term is given by the formula:

$$\nu_n = \bar{c} \sum n_j Q_j \quad (16)$$

where: \bar{c} is the thermal velocity of the electrons (in m/s)

n_j is the number of neutral particles (atoms or molecules) of the
j-th component of air per cubic meter

Q_j is the cross-section for collisions between electrons and neutral
particles of the j-th component (in square meters).

The velocity is computed by the formula:

$$\bar{c} = \left(\frac{8kT}{\pi m} \right)^{1/2} \cdot 10^3 \quad (\text{MKSQ units}) \quad (17)$$

where k is the Boltzmann constant:

$$k = 1.38 \times 10^{-23} \text{ joule/}^\circ\text{K}$$

and m is the electron mass:

$$m = 9 \times 10^{-31} \text{ Kg}$$

Thus, we can write, instead of Equation (1.7):

$$\bar{c} = 6240 T^{1/2} \quad (\text{m/s}) \quad (18)$$

In computing the n_j 's, we made use of References 5 and 6. There are some discrepancies between the numerical results of these papers, but

they are of an order of magnitude which do not affect our conclusions. In fact, all we are interested in (and, on the other hand, all we can pretend to get) is the order of magnitude of the collision frequency. Now, this order of magnitude is not affected by the small differences between the results of References 5 and 6. The same argument applies to other simplifications which we adopted.

We assumed as standard density the value:

$$\rho_0 = 8.04 \times 10^{-2} \text{ lb/ft}^3$$

The number of molecules contained in a cubic meter of air (Loschmidt's number in MKSQ units) at standard conditions is:

$$L_0 = 2.687 \times 10^{25}$$

according to Reference 7. The corresponding number of atoms, a_0 , is

$$a_0 = 1.991 \times 2.687 \times 10^{25} = 5.35 \times 10^{25}$$

assuming that 99% of the air is biatomic and 1% is monatomic.

Nevertheless, Reference 6 used a value of L_0 :

$$L_0 = 2.568 \times 10^{25}$$

which gives a value for a_0 :

$$a_0 = 5.12 \times 10^{25}$$

We rounded a_0 to the value:

$$a_0 = 5.2 \times 10^{25} \text{ m}^{-3}$$

Figures 2 and 7, drawn using the results of Reference 5, give, for the principal components of air, the ratio a_j :

$$a_j = \frac{\text{number of particles of the } j\text{-th component}}{\text{total number of atoms}}$$

as a function of T and ρ/ρ_0 .

We may assume that the composition of the air does not change when passing from the standard conditions to the non-perturbed conditions at the flight height. In the "hot" layer behind the shock wave, the molecular composition is changed, but the atomic composition remains the same, in thermodynamic equilibrium. So, we may express every n_j as the product of the corresponding a_j by a , the number of atoms contained in a cubic meter of air at the considered temperature and density, where in turn a , according to the previous argument, is obviously given by:

$$a = a_0 \rho/\rho_0 = 5.2 \times 10^{25} \rho/\rho_0 \quad (\text{m}^{-3}) \quad (19)$$

Thus, from Equations (16), (18) and (19), we get

$$\nu_n = 3.24 \times 10^{29} T^{1/2} \frac{\rho}{\rho_0} \sum a_j Q_j \quad (\text{sec}^{-1}) \quad (20)$$

provided that the cross-section Q_j be given in m^2 .

Figure 8, taken from Reference (8), gives the cross-sections as functions of the temperature.

The second term in Equation (15) is computed following Reference 9:

$$\nu_i = 8\pi \log \Lambda \cdot \bar{c} n_i p_0^2 \quad (21)$$

where $\log \Lambda$ is evaluated from the Table 5.1 of Reference 9, and \bar{c} again is given by Equation (18). In Equation (21), n_i is the number of ions per cubic meter, which again may be written as the product of a by the number of ions per number of air atoms. Figure 7, taken from Reference 6, gives the ratio a_i between the number of ions and the total number of atoms as a function of the temperature.

The length p_0 (Reference 9, page 67) is given, in MKSQ units by:

$$p_0 = e^2 / 4 \pi \epsilon m c^{-2} \quad (m) \quad (22)$$

where:

$$e = \text{electron charge} = 1.6 \times 10^{-19} \text{ coulombs}$$

$$m = \text{electron mass} = 9 \times 10^{-31} \text{ Kg}$$

$$\epsilon = \text{dielectric constant of the vacuum} = \frac{1}{36\pi} 10^{-9} \text{ farad m}$$

Here we assumed that the whole of the ions are simply ionized. So we have using Equation (18)

$$p_0 = \frac{6.58 \times 10^{-6}}{T} \text{ meters} \quad (23)$$

and from Equations (21), (18), (19) and (23), we have

$$v_1 = 3.4 \times 10^{20} \log \frac{T^{1/2}}{T^2} a_1 \frac{\rho}{\rho_0} (\text{sec}^{-1}) \quad (24)$$

3. APPLICATIONS

Results of the application of this approximate method to several cases are presented in the following section.

Figure 9 shows the shock shape as developed for $M = 2.0$, $h = 200,000$ ft. The equations of the shock shape are given on Figure 9. The locations of the ten stations where the flow field properties were determined are also indicated. The calculated pressure distribution for this flight condition is given in Figure 10. Figures 11, 12, 13 and 14 show the calculated density, temperature and entropy profiles at the various stations along the body. These calculations are based on argon-free air in thermodynamic equilibrium using the results of Reference 2 and the atmosphere detailed in Reference 3.

Using the density and temperature profiles at each station, the electron density distribution was obtained. These profiles are shown in Figure 15. For electron densities below 10^{10} particles/c.c., the data of Reference 4 was used, while for densities greater than 10^{10} particles/c.c., the data of Reference 5 was employed.

Collision frequency has been computed using the above results by the method described previously. Figure 16 shows the results of this calculation.

The flow field about this same body has been examined at a different flight condition using the same approximate method. The flight condition selected was $M = 15$, $h = 150,000$ ft. again, assuming the gas in the shock layer to be in thermodynamic equilibrium. For this case, the equations

of the shock were found to be

$$\frac{y^2}{R} = 2.118 \frac{x}{R} \quad (0 \leq \frac{x}{R} \leq .280) \quad (25)$$

$$\frac{x}{R} = -.125 \left| \frac{y}{R} \right|^3 + 2.22 \left| \frac{y}{R} \right|^2 - 2.48 \left| \frac{y}{R} \right| + 0.93 \quad (26)$$

$$0.280 \leq \frac{x}{R} \leq 1.7036$$

$$\frac{dy}{dx} = \tan 17.1^\circ \quad \frac{x}{R} \geq 1.7036 \quad (27)$$

Surface pressure is given by Figure 17.

The density and temperature profiles calculated for the same stations as the previous case are presented in Figure 18. The corresponding electron density and collision frequency profiles are shown in Figures 19 and 20, respectively.

To obtain an approximation of the difference in results depending upon the assumption of frozen or equilibrium flow, a third case was investigated. The case considered was $M = 20$, $h = 200,000$ ft. However, frozen flow was assumed in the calculation.

The calculation procedure employed involves assuming the shock shape is, in first approximation, the same as the shock shape determined for the $M = 20$, $h = 200,000$ ft. equilibrium flow calculation. With this shock shape it is possible to determine enthalpy, pressure and density locally behind the shock. The internal energy is given by

$$e = h - \frac{p}{\rho} \quad (28)$$

from this the speed of sound can be obtained using

$$a^2 = (h - e) \frac{h}{e} = \gamma \frac{p}{\rho} \quad (29)$$

and subsequently the local value of γ can be determined.

The flow behind the shock is divided into stream tubes using the average values of γ and average initial properties as determined above. Assuming that the downstream pressure at any station is the average value between shock and body, and that isentropic flow at the constant average gamma exists in each stream tube, it is possible to compute average downstream properties. From the average properties, the location of the streamlines within the shock layer can be obtained. At any particular station, the summing of the stream tube locations eventually locates the shock position at that station. In our case, when this was done, it was found that little change occurred in shock location so the problem was not iterated using the new shock shape.

The electron density profiles determined using this method of calculation were obtained for several stations along the body and are shown in Figure 21. Comparing these results with the calculation at the same flight condition but assuming equilibrium flow, it is seen that the electron density computed on a frozen flow basis is generally lower near the body surface for the forward stations and generally lower across the whole layer for stations far back on the body. These results should not be generalized, however, since the comparison was made at a single flight condition.

The analysis which has been described neglects viscous effects. The effects of the boundary layer have been considered for the $M = 20$, $h = 200,000$ ft. flight condition. Results of this calculation show that the

region within the boundary layer where significant reductions in temperature occur is confined to a thin layer. At the rear of the body, for assumed wall temperatures of 1000 and 4000°R, this lower temperature layer has a thickness which is less than 10% of the distance between the shock and the body. With the inherent approximation of the method considered, neglecting viscous effects appears justifiable.

4. CONCLUSIONS

An approximate procedure for predicting shock shape about a blunted body similar to a radome shape and for predicting gross effects within the shock layer surrounding the body has been developed. The method is rapid and suitable for engineering estimates. For a detailed understanding of the blunt body problem, more accurate methods such as real gas characteristics must be employed.

REFERENCES

1. Vaglio-Laurin, R. and Ferri, A.: Theoretical Investigations of the Flow about Blunt-Nosed Bodies in Supersonic Flight. Journal of Aero/Space Sciences, Vol. 25, No. 12, Dec. 1958, pp. 761-770.
2. Hilsenrath, J. and Beckett, C.W.: Tables of Thermodynamic Properties of Argon-Free Air to 15,000°K. AEDC Report TN-56-12, Sept. 1956.
3. U. S. Government, Dept. of Navy, Bureau of Ordnance: Handbook of Supersonic Aerodynamics. NAVORD Report No. 1488, Vol. I, Washington, D.C., G.P.O., 1950.
4. Hochstien, A.R.: Gas Properties Behind Shocks at Hypersonic Velocities. Convair, San Diego, Calif.
5. Gilmore, F.R.: Equilibrium Composition and Thermodynamic Properties of Air to 24,000°K. Rand Corp. Report RM-1543, August 1955.
6. Logan, J. and Treanor, C.: Table of Thermodynamic Properties of Air from 3000 - 10,000°K at Intervals of 100°K. Cornell Aeronautical Laboratory Report No. BE-1007-A-3, January 1957.
7. American Institute of Physics Handbook, 1957.
8. Lamb, L., Lin, S.C.: Electrical Conductivity of Thermally Ionized Air Produced in a Shock Tube. Journal of Applied Physics, 28, 754, 1957.
9. Spitzer, L.: Physics of Fully Ionized Gases, 1956.

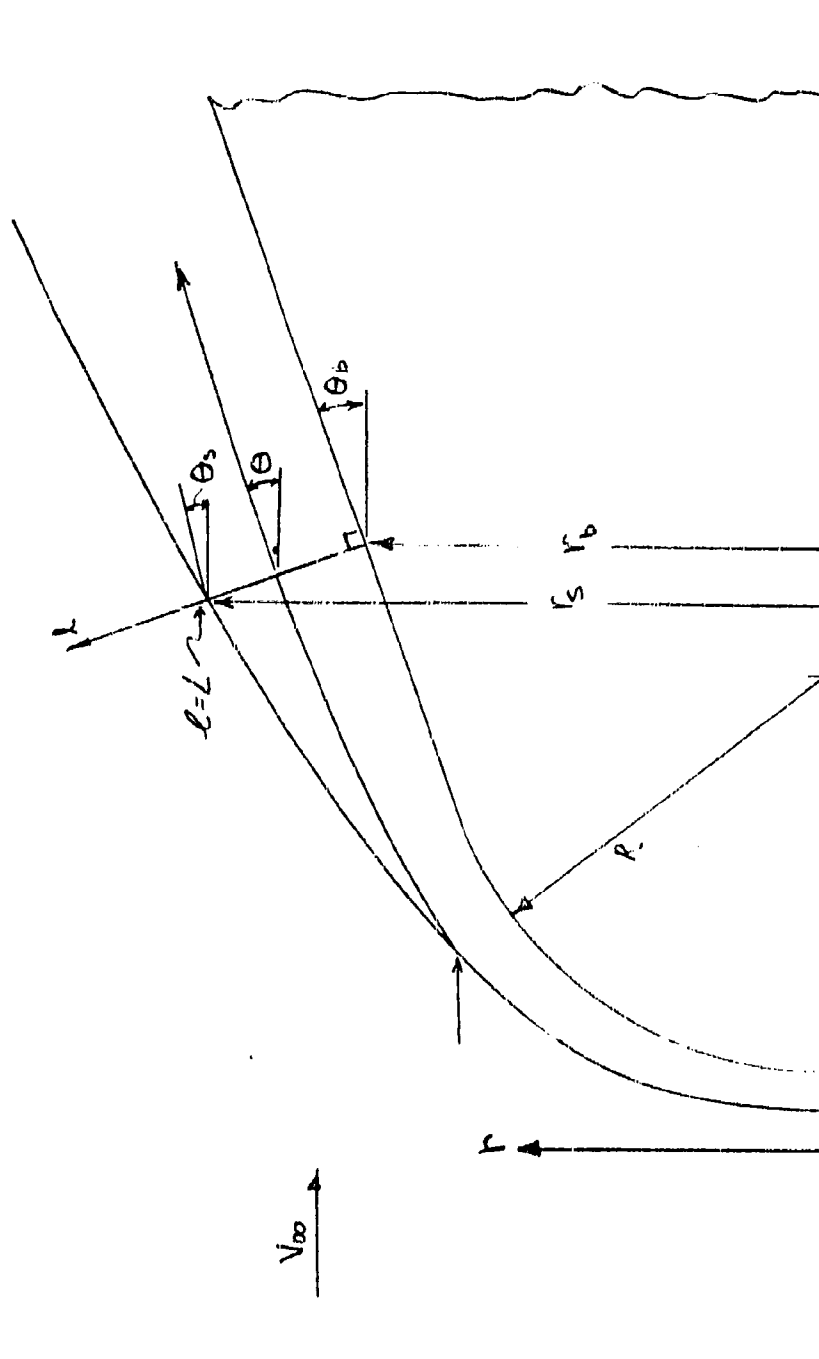
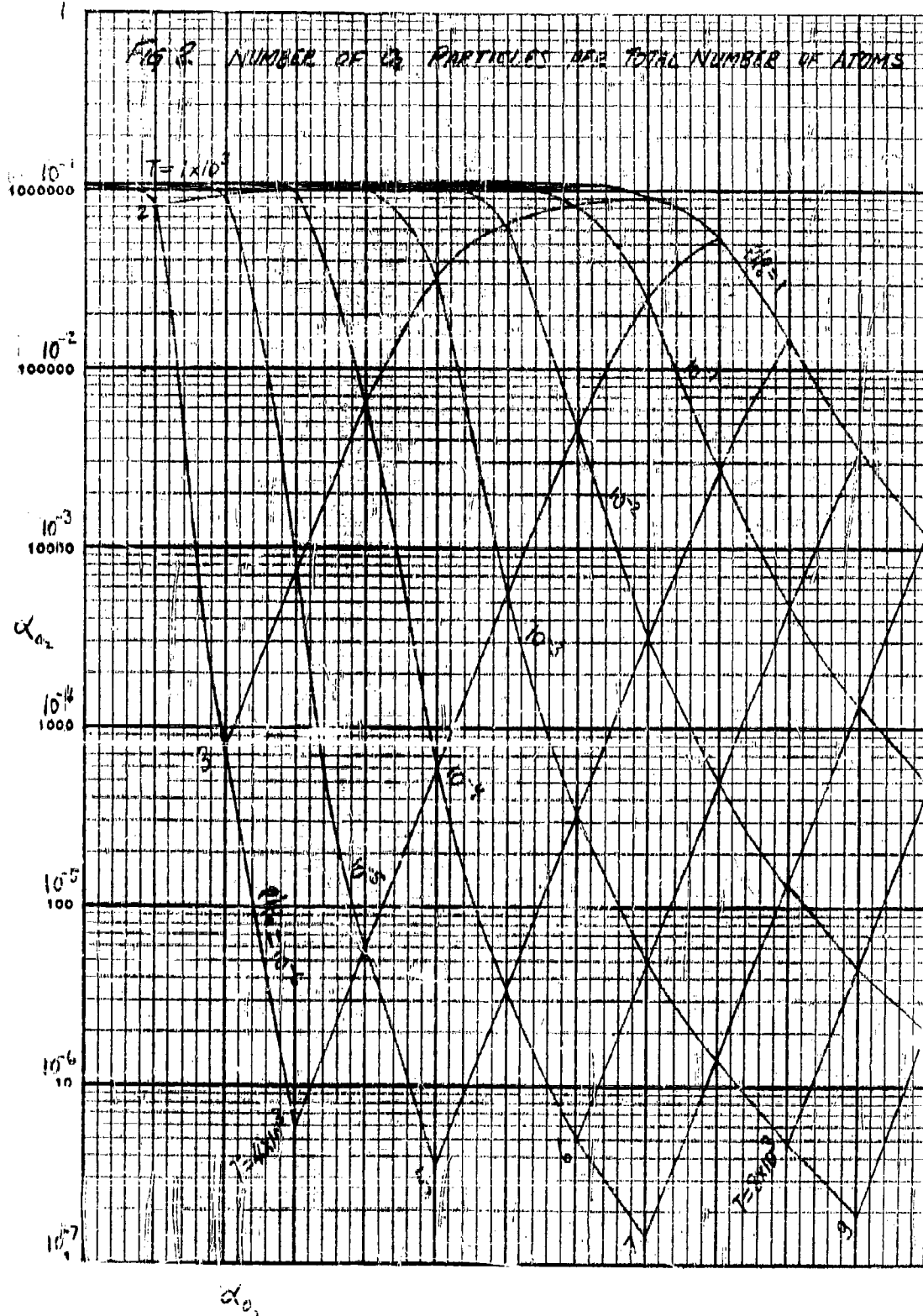
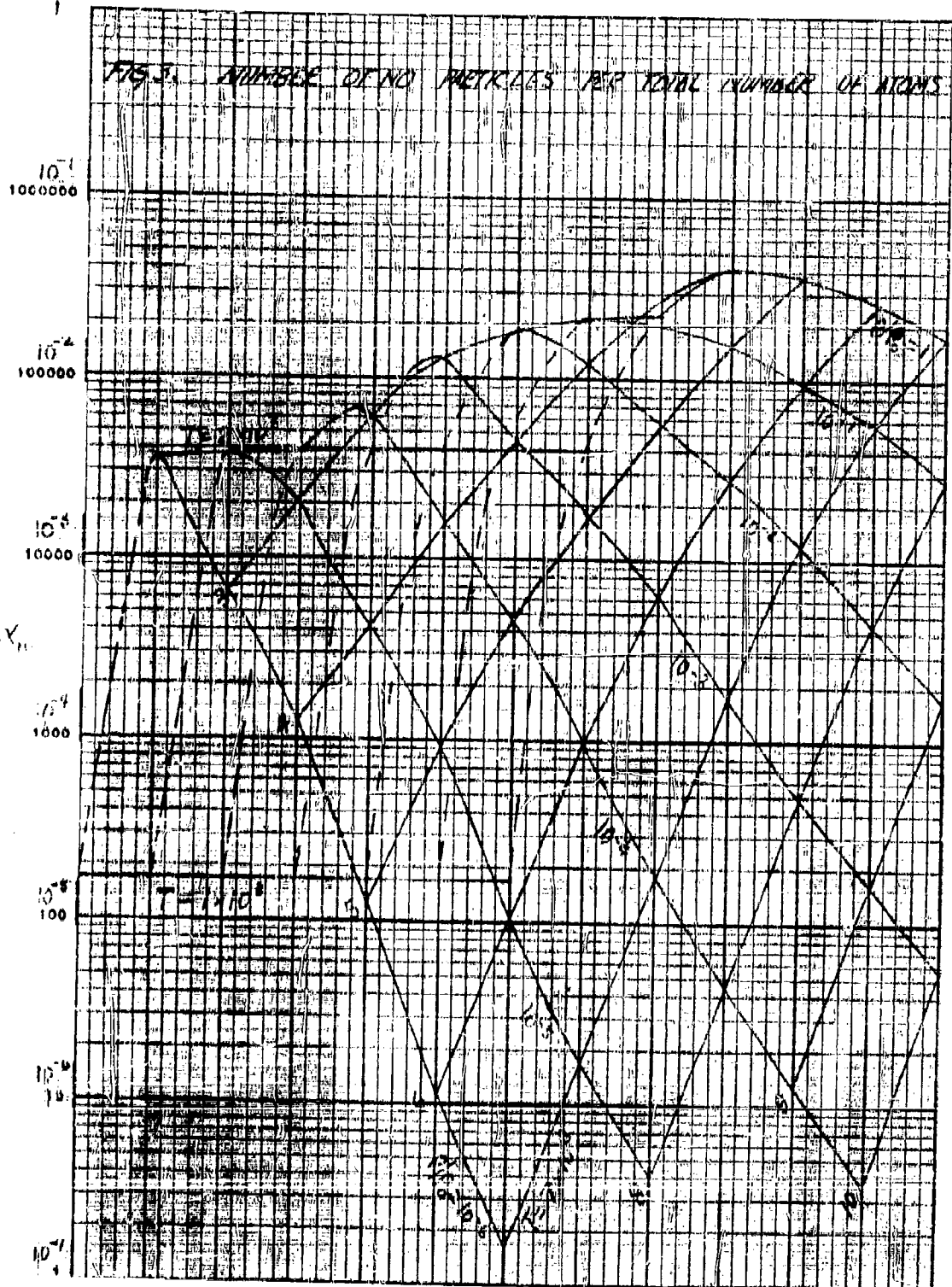
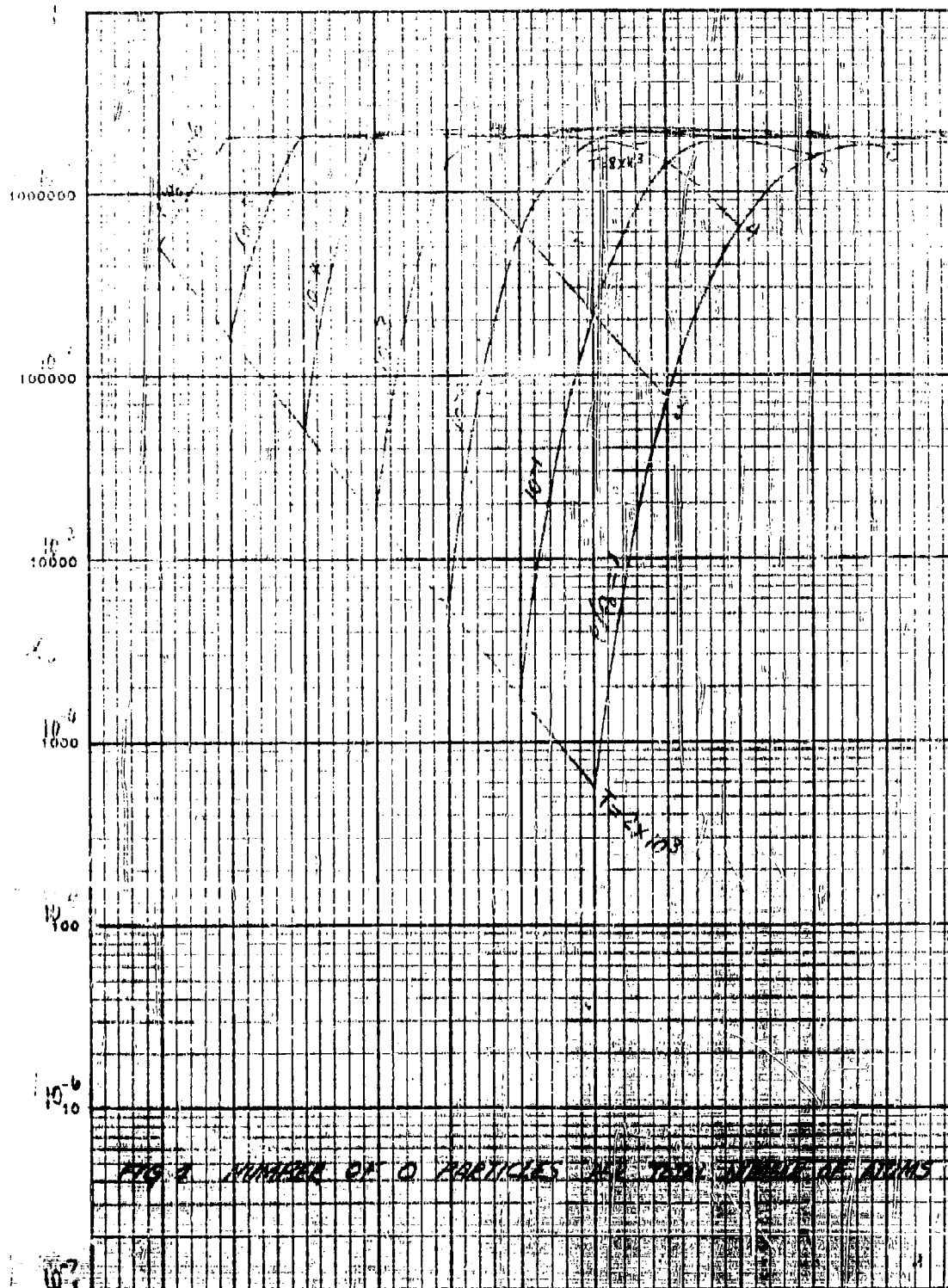


FIG 1 NOMENCLATURE

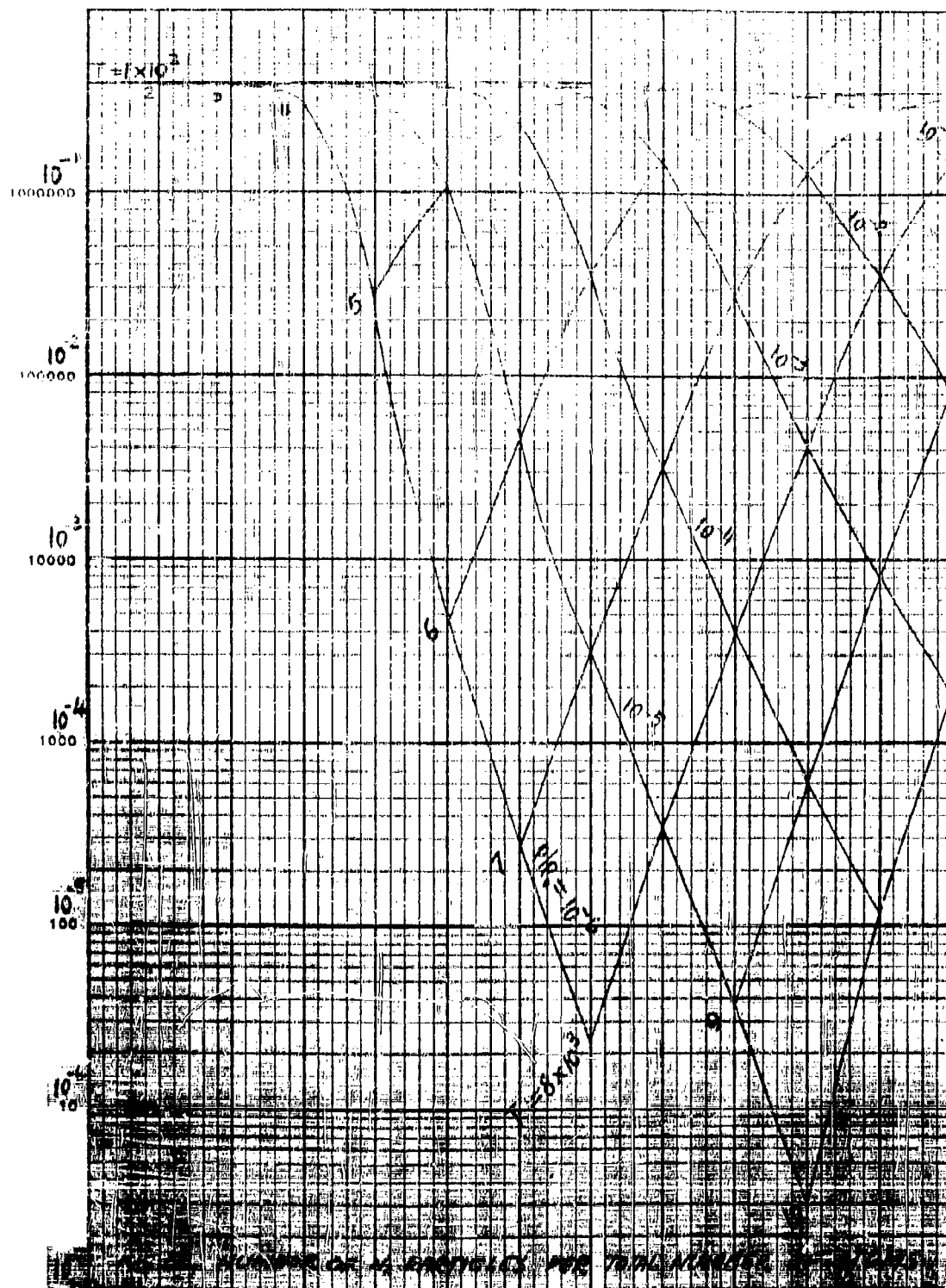






MODEL

DATE



MODEL

DATE

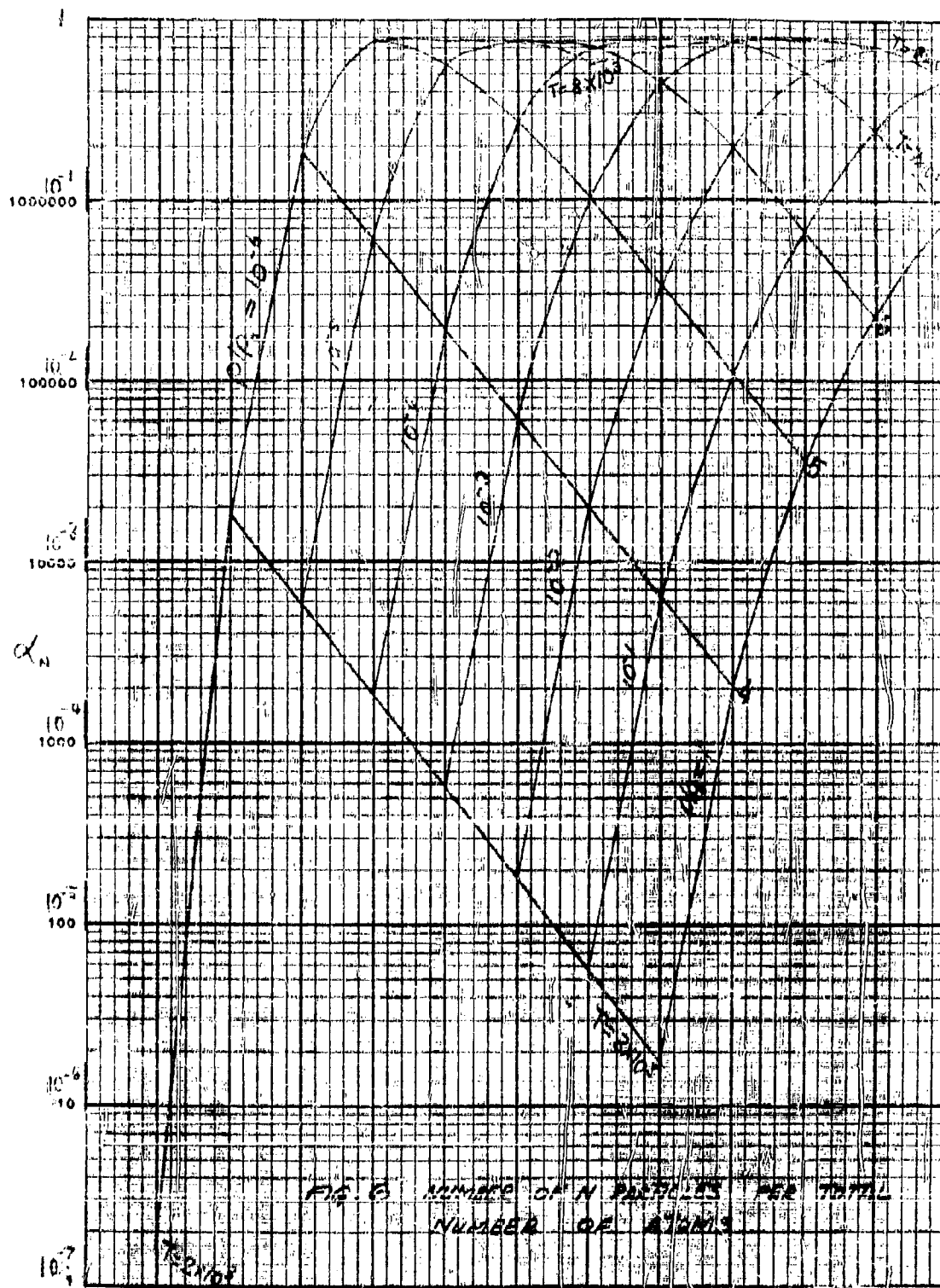
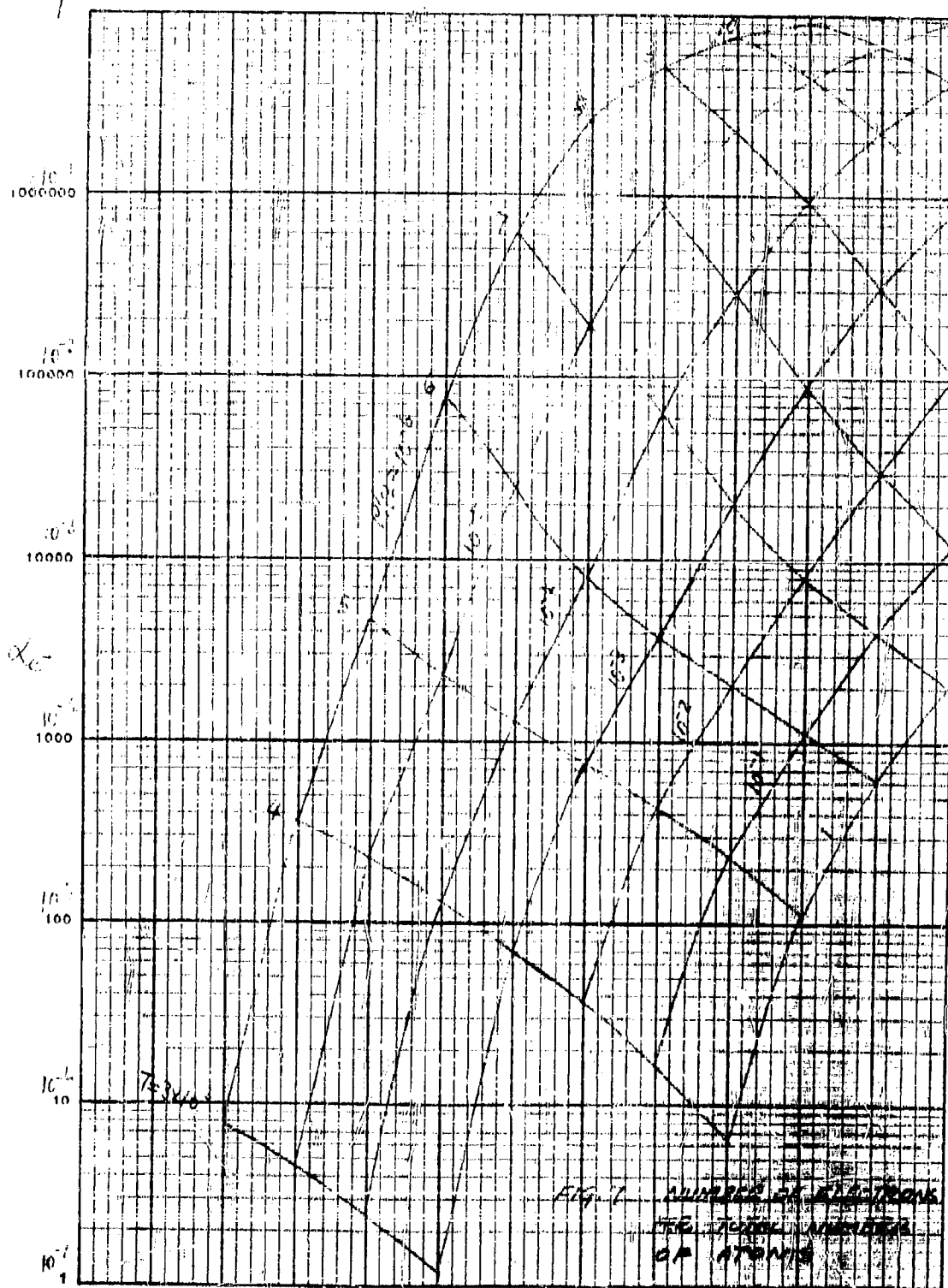


FIG. 6 NUMBER OF N PARTICLES PER TOTAL NUMBER OF ATOMS

α_N

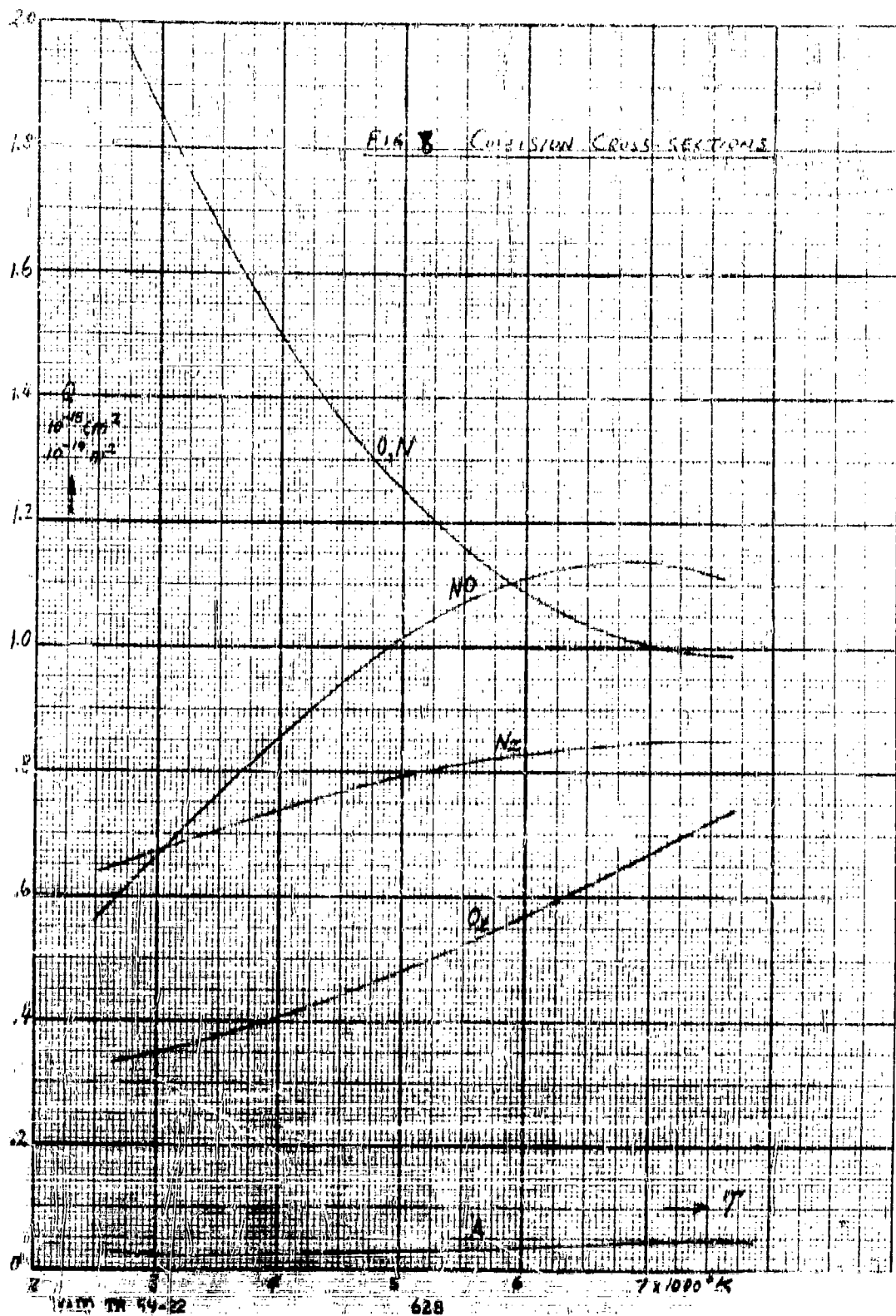
MODEL

DATE



WADD TR 59-22

627



1

FIG. 9
SHOCK PATTERN ABOUT BAUNTED WIRE

$M = 10$, $h = 200,000$ FT.

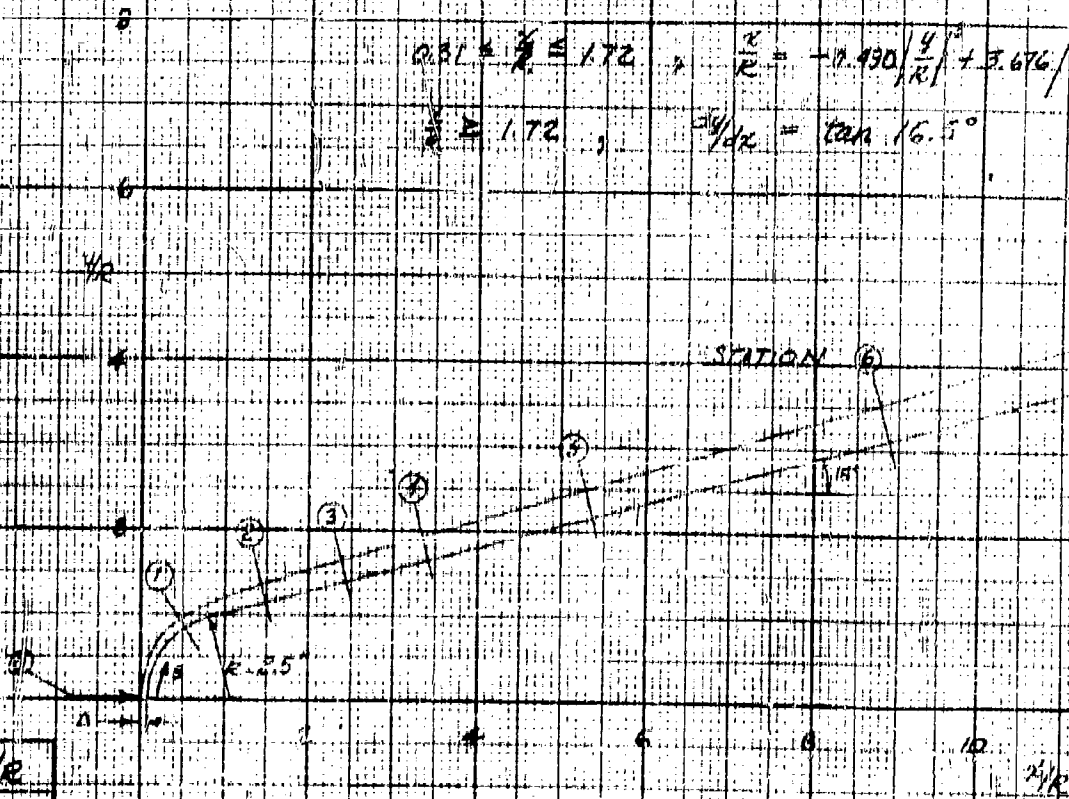
$\Delta = .0425R$

EQUATION OF THE SHOCK

$0 \leq \frac{x}{R} \leq 0.31$, $\left(\frac{y}{R}\right)^2 = 2.085\left(\frac{x}{R}\right)$

$0.31 \leq \frac{x}{R} \leq 1.72$, $\frac{y}{R} = -0.430\left(\frac{x}{R}\right)^2 + 3.676\left(\frac{x}{R}\right)$

$\frac{x}{R} \geq 1.72$, $\frac{dy}{dx} = \tan 16.5^\circ$



STATION	x/R
0	0
1	1.0
2	2.0
3	3.0
4	4.0
5	5.0
6	6.0
7	7.0
8	8.0
9	9.0

FIG 9
 POINT BLUNTED CONE
 20,000 FT

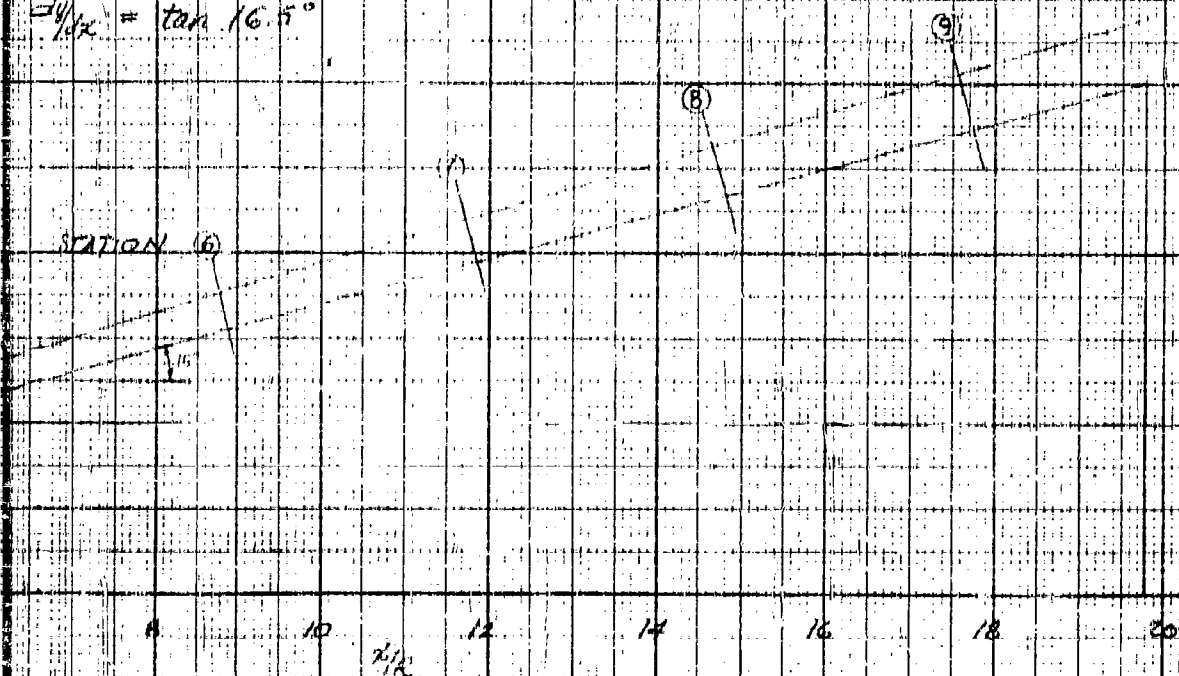
THE SHOCK

$$\left(\frac{y}{x}\right)^3 = 2.085 \left(\frac{x}{R}\right)$$

$$\frac{y}{R} = -0.490 \left(\frac{x}{R}\right)^3 + 3.676 \left(\frac{x}{R}\right)^2 - 4.177 \left(\frac{x}{R}\right) + 1.551$$

$$dy/dx = \tan 16.5^\circ$$

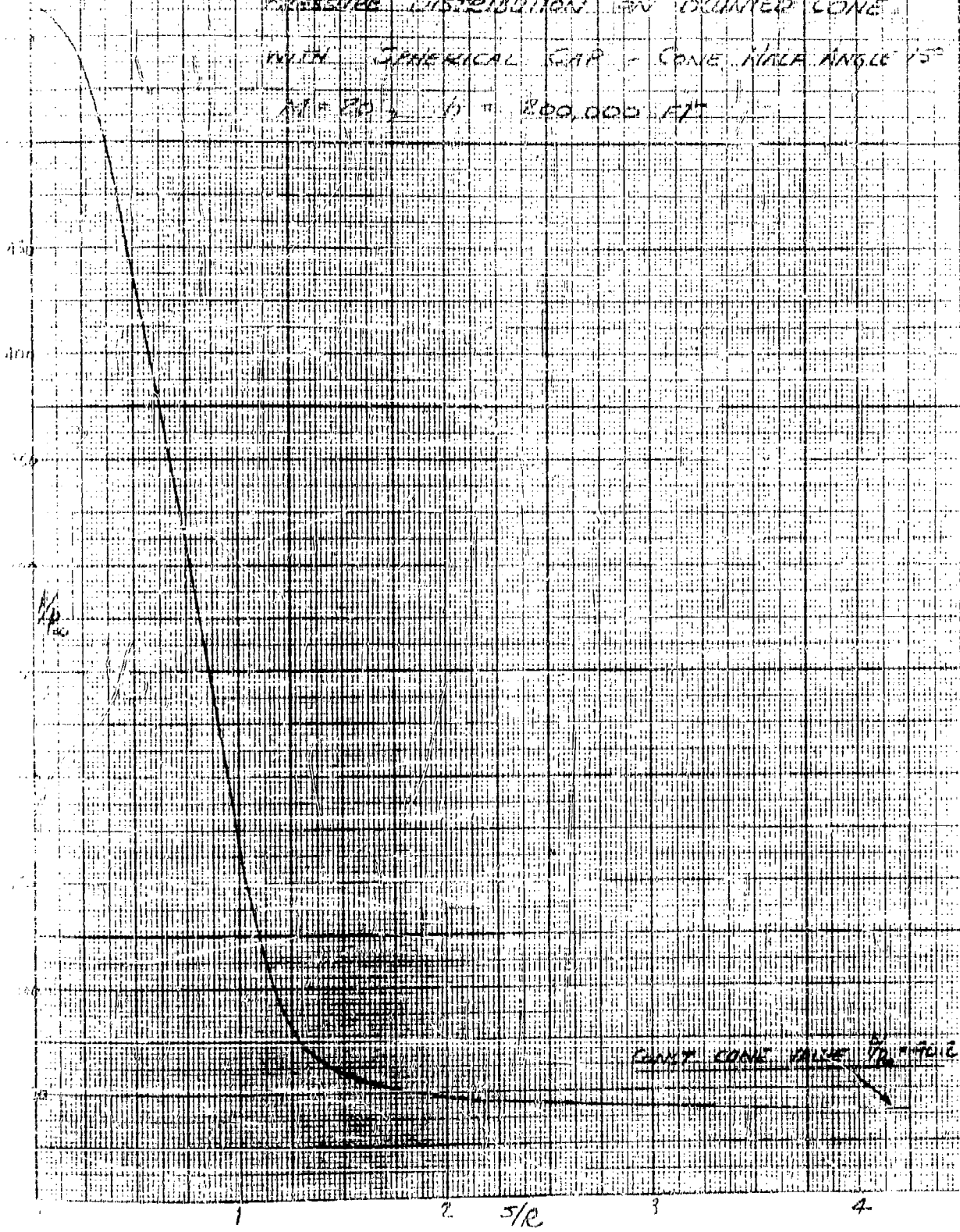
STATION (6)



2

FIG. 10

PRESSURE DISTRIBUTION ON BLUNTED CONE
WITH SPHERICAL GAP - CONE HALF ANGLE 15°
 $M = 20$, $\rho = 200,000 \text{ FT}$



SECTION 2

Fig 11

EQUILIBRIUM FLOW $M=20$, $M=200$ AND 100

$T = \frac{1}{L}$, $L = 0.00896$ FT

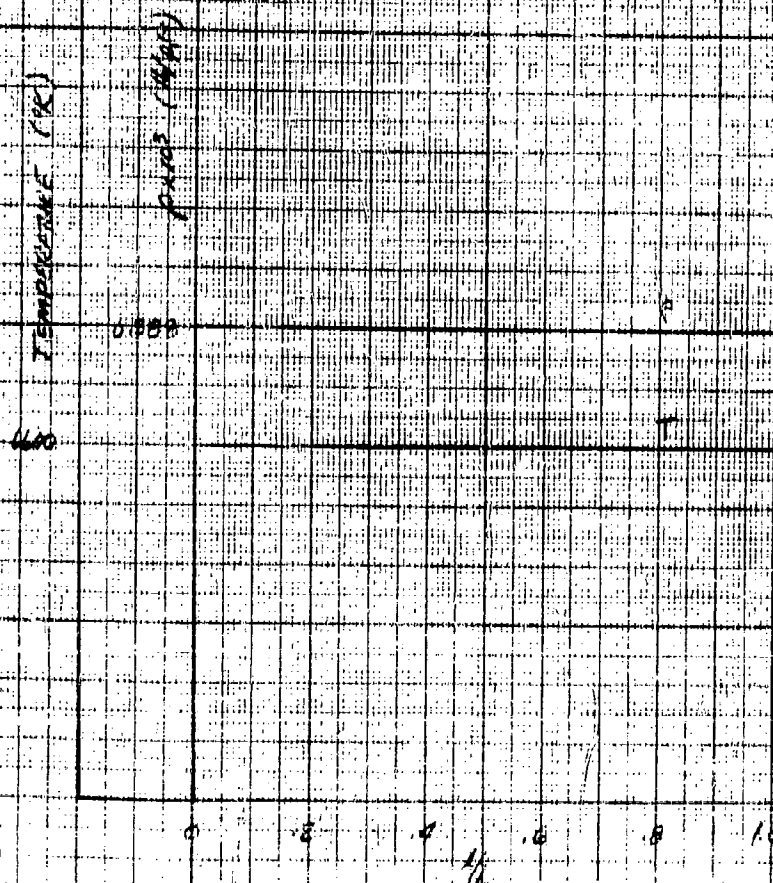


Fig. 12.10

DENSITY PROFILE FOR STATION ①

EQUILIBRIUM FLOW MA 30, $A = 200,000 \text{ FT}^2$

$L = 2200 \text{ FT}$

$X = \frac{1}{2} L$

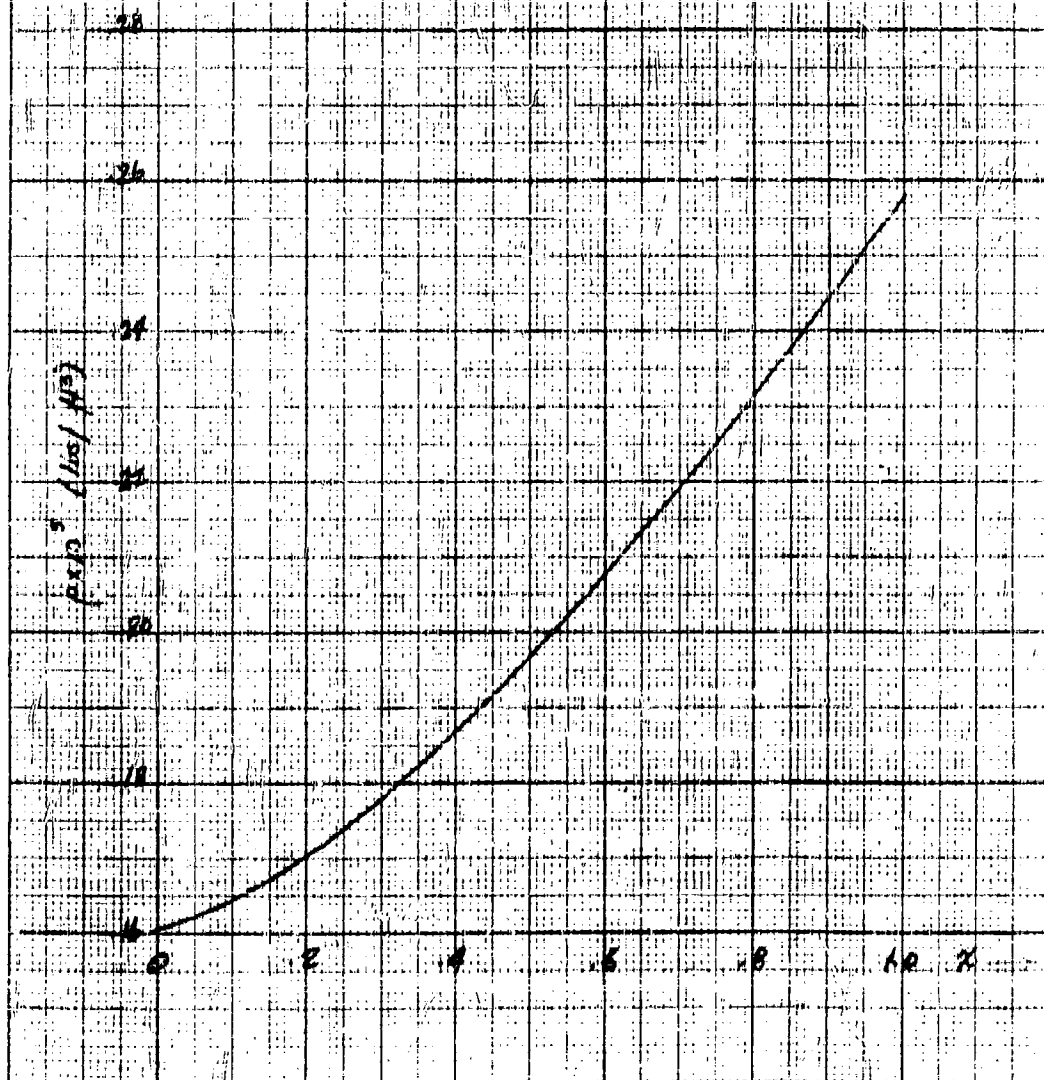


FIG. 126

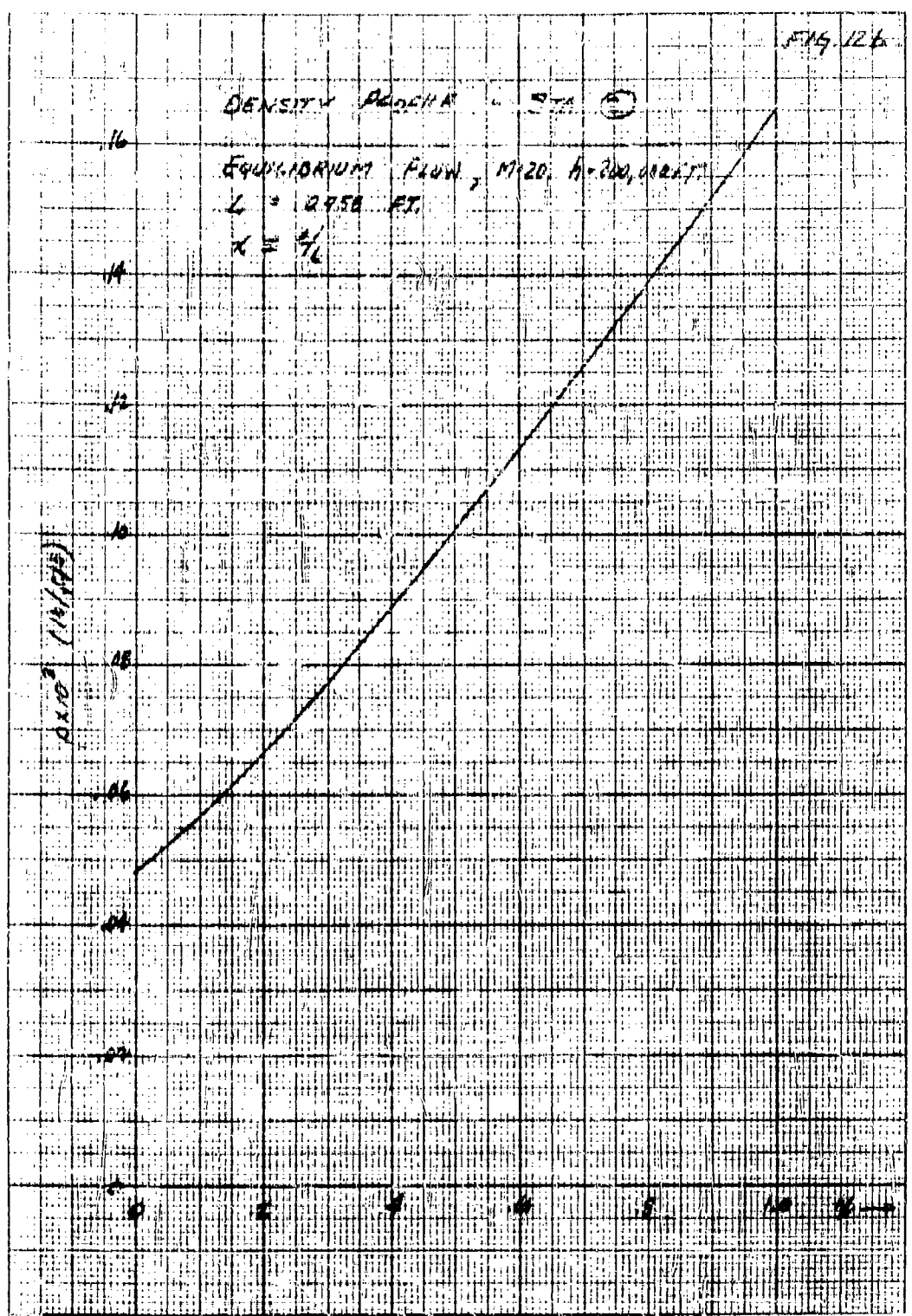
DENSITY PROFILE - STA. 6

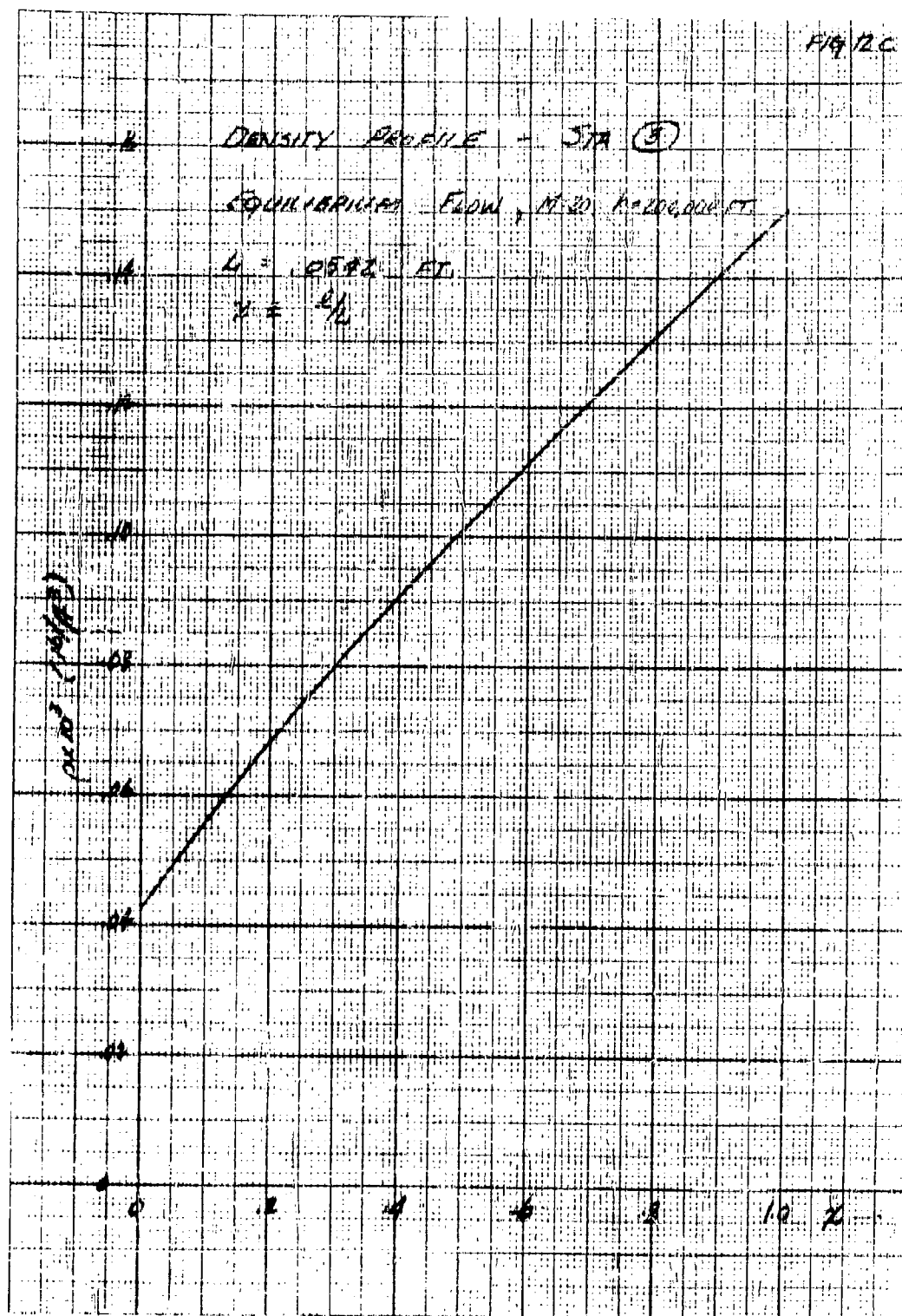
EQUILIBRIUM FLOW, $M=20$, $H=200$, $Q=2.5$

$L = 29.50$ FT.

$\alpha = 1/6$

$\rho \times 10^3$ (lb./ft.³)



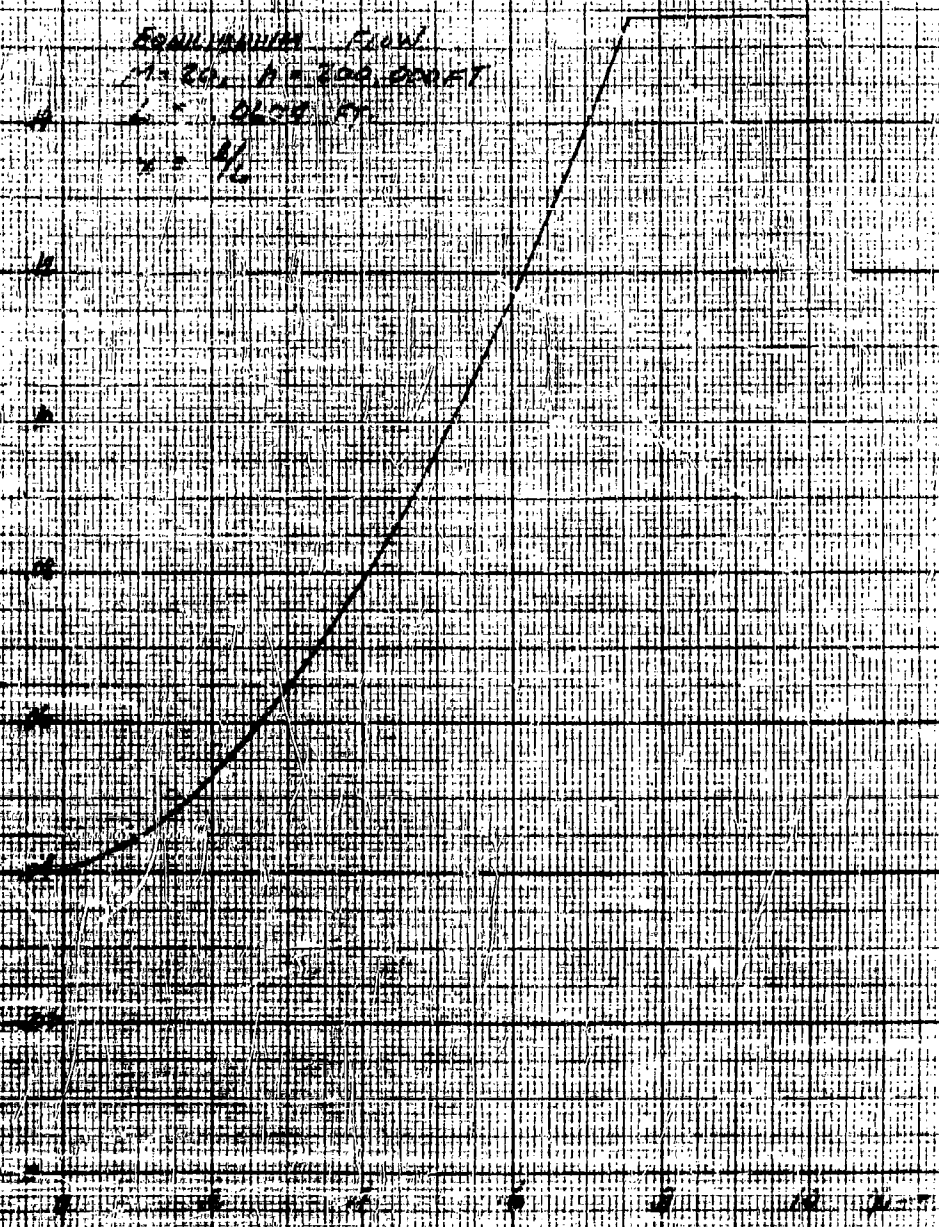


Aug 12 1954

16 DENSITY PROFILE 5713 (4)

EQUILIBRIUM FLOW
 $M = 20$, $P = 200$ DMMET
 $L = 0.009$ FT
 $\mu = 4/L$

(CH₄)
 2.0000



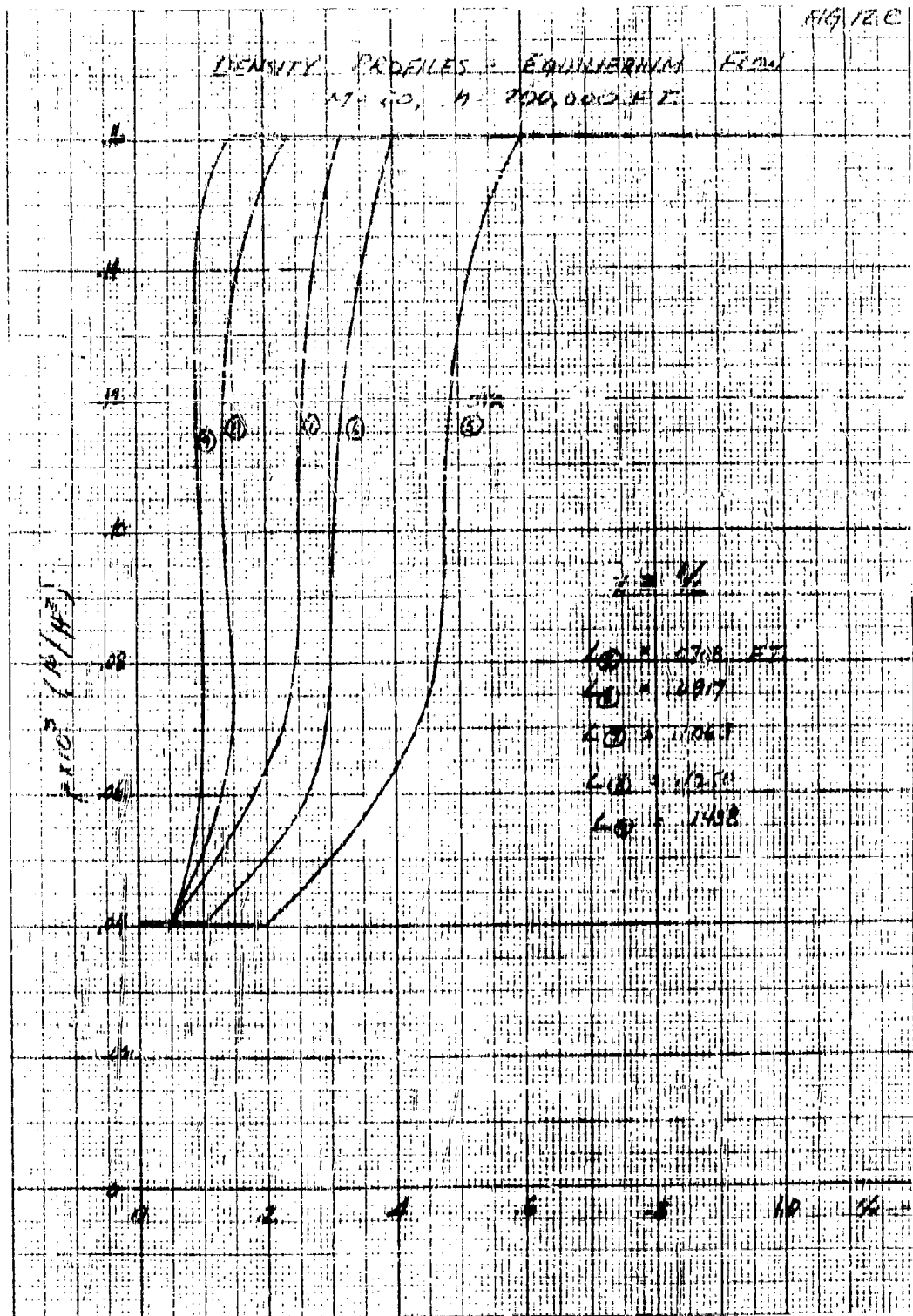
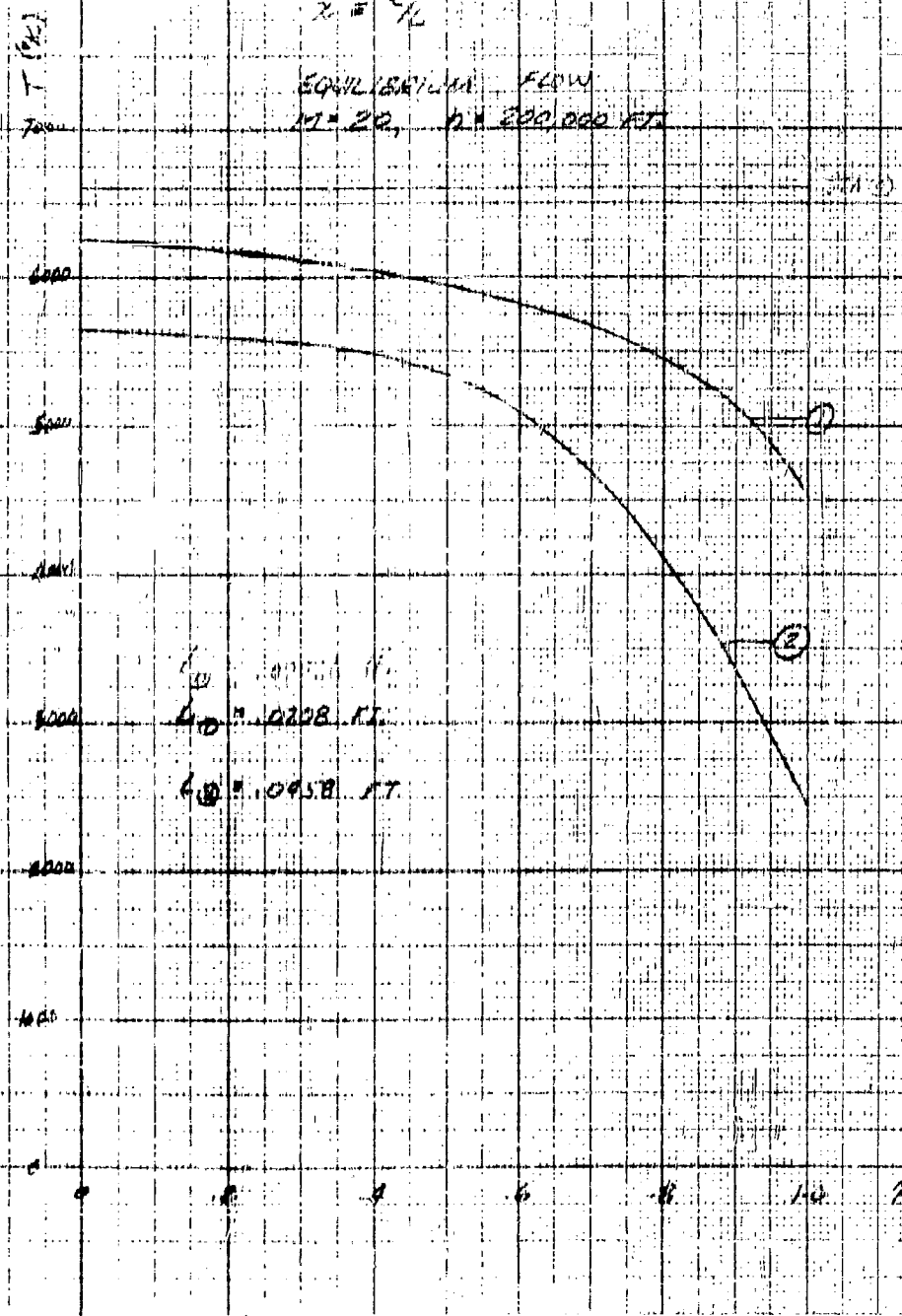


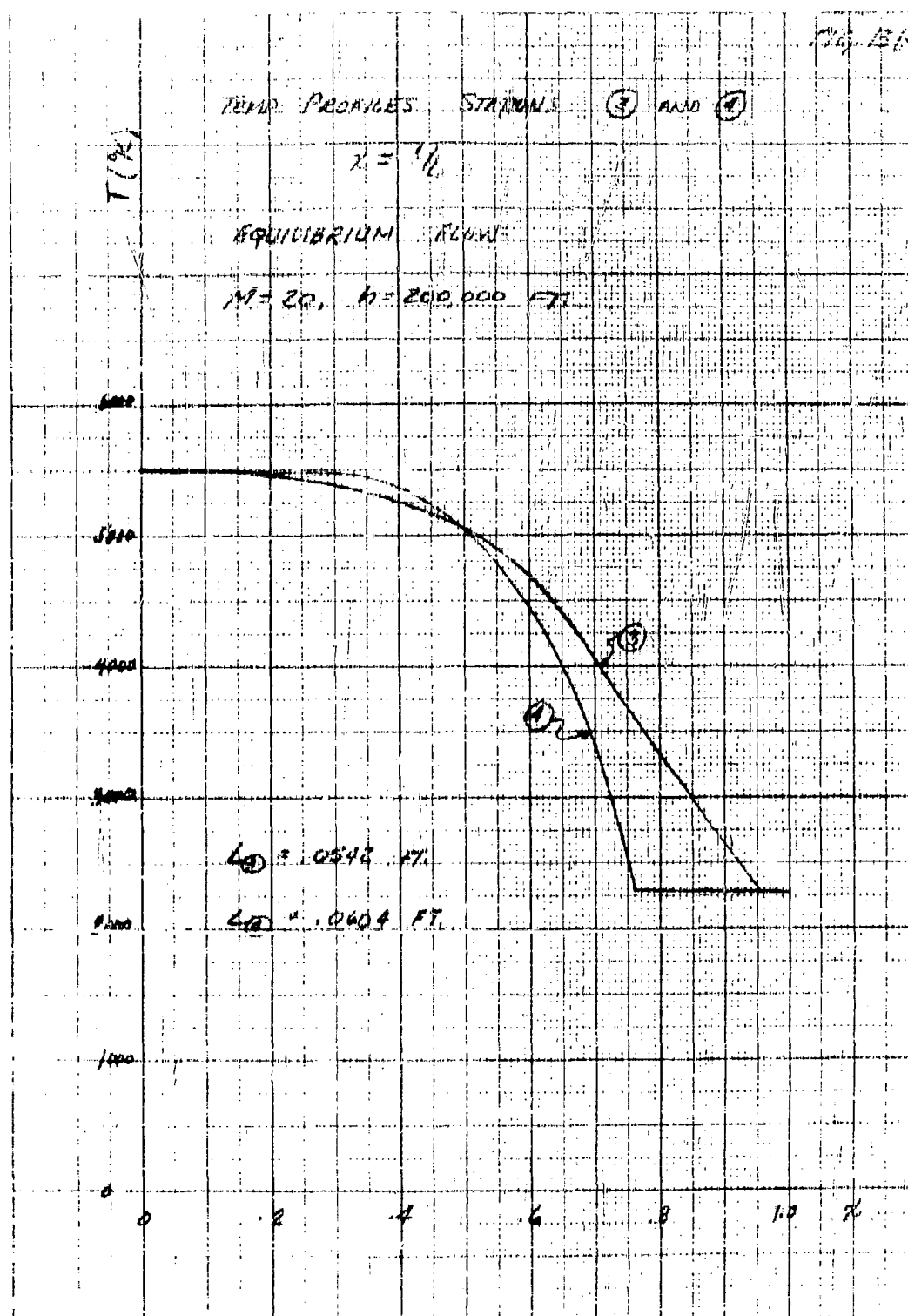
Fig. 130

TEMPERATURE PROFILES (1) AND (2)

$$x = \frac{L}{L}$$

EQUILIBRIUM FLOW
 $M = 20, \quad n = 200,000 \text{ FT}$





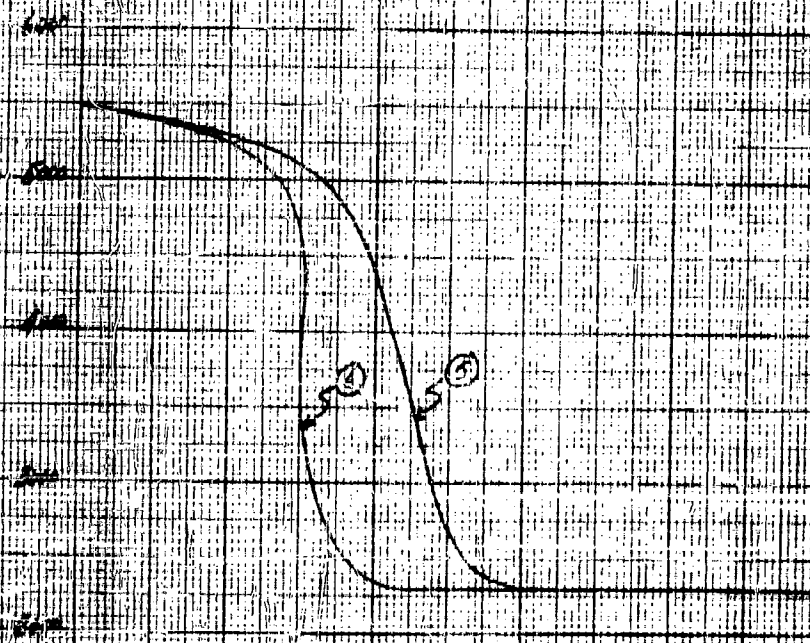
TEMP. PROFILES

STATION ③ AND ④

$x = 1/2$

EQUILIBRIUM TEMPERATURE

APPROX. $T = 300,000$ F.



③ = 0.0712 F.

④ = 0.0917 F.

TEMP. PROFILES STATIONS ①, ② AND ③

$$\alpha = 1/4$$

EQUILIBRIUM FLOW

$$M = 29, \quad h = 200,000 \text{ F.T.}$$

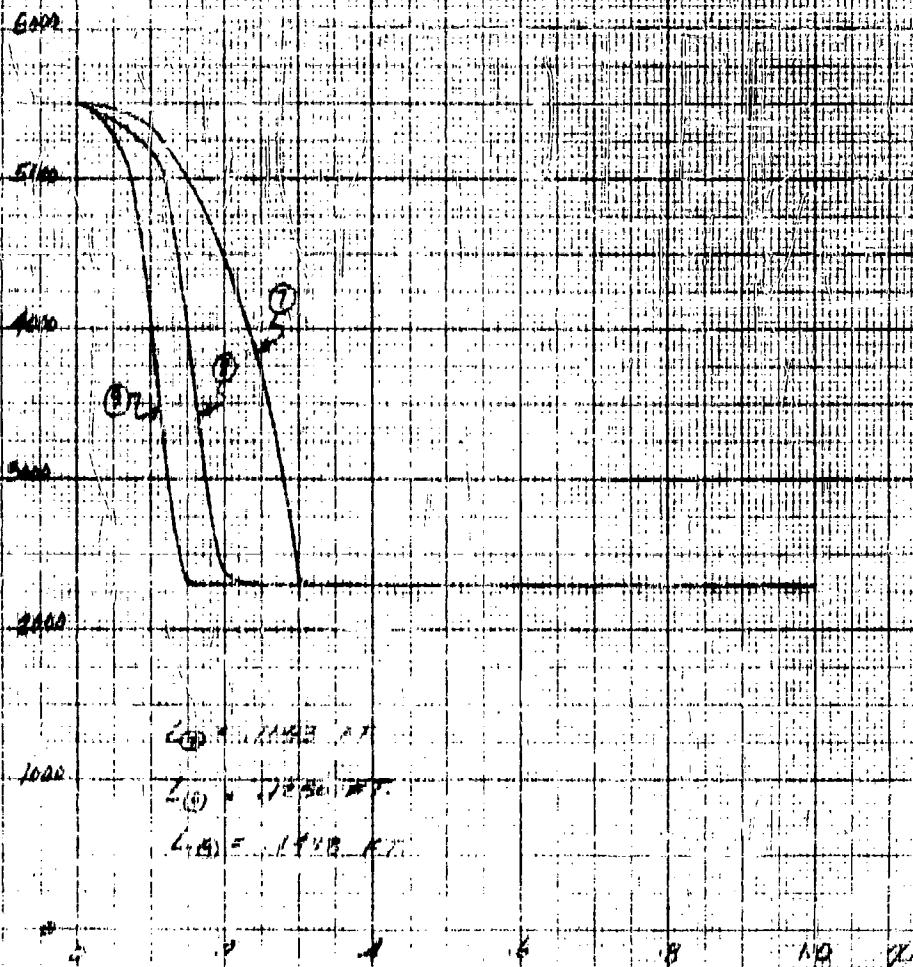


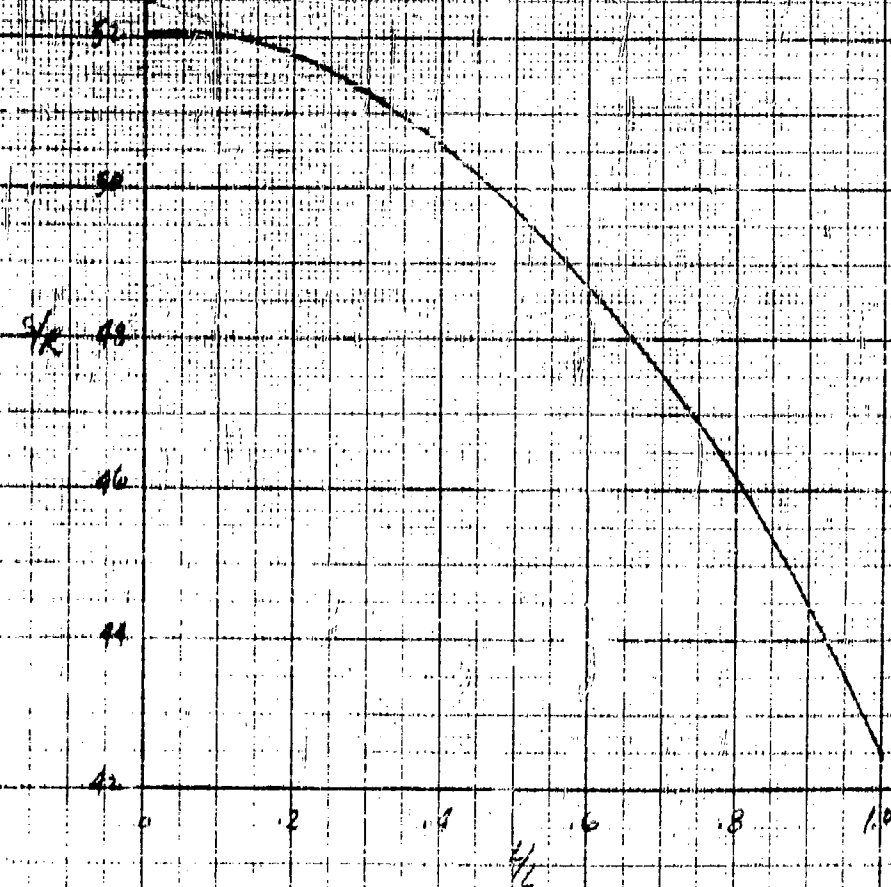
FIG. 14A.

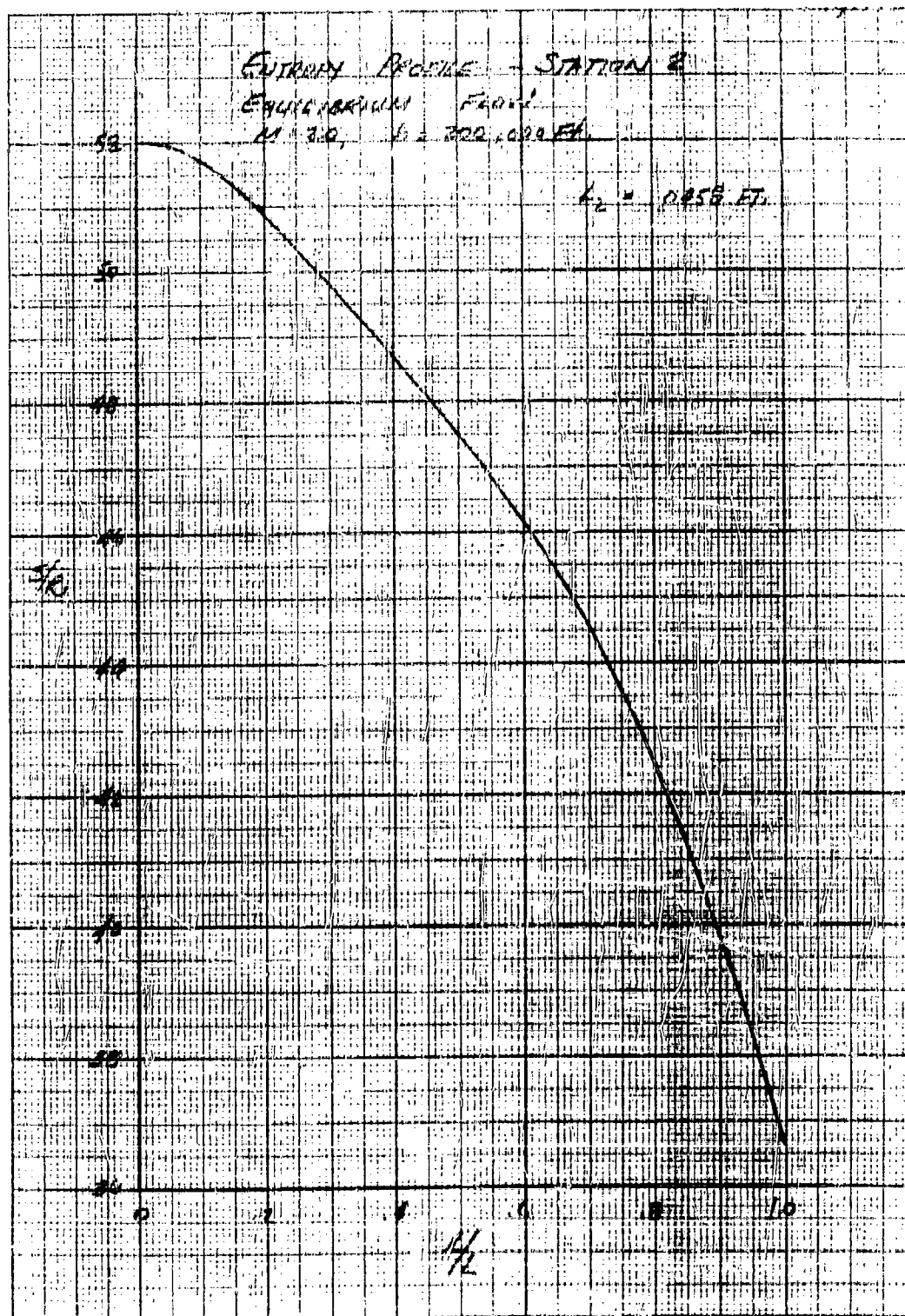
ENTRAN PROFILES - STATION 1

EQUILIBRIUM FLOW

$h = 20$, $h = 200,000$ ft

$L_1 = 0.809$ ft





FRANK P. DEWEY Senator

44-38861-1012A-170W

1947 F 241 1947 F 241 1947 F 241 1947 F 241

4-97 FA



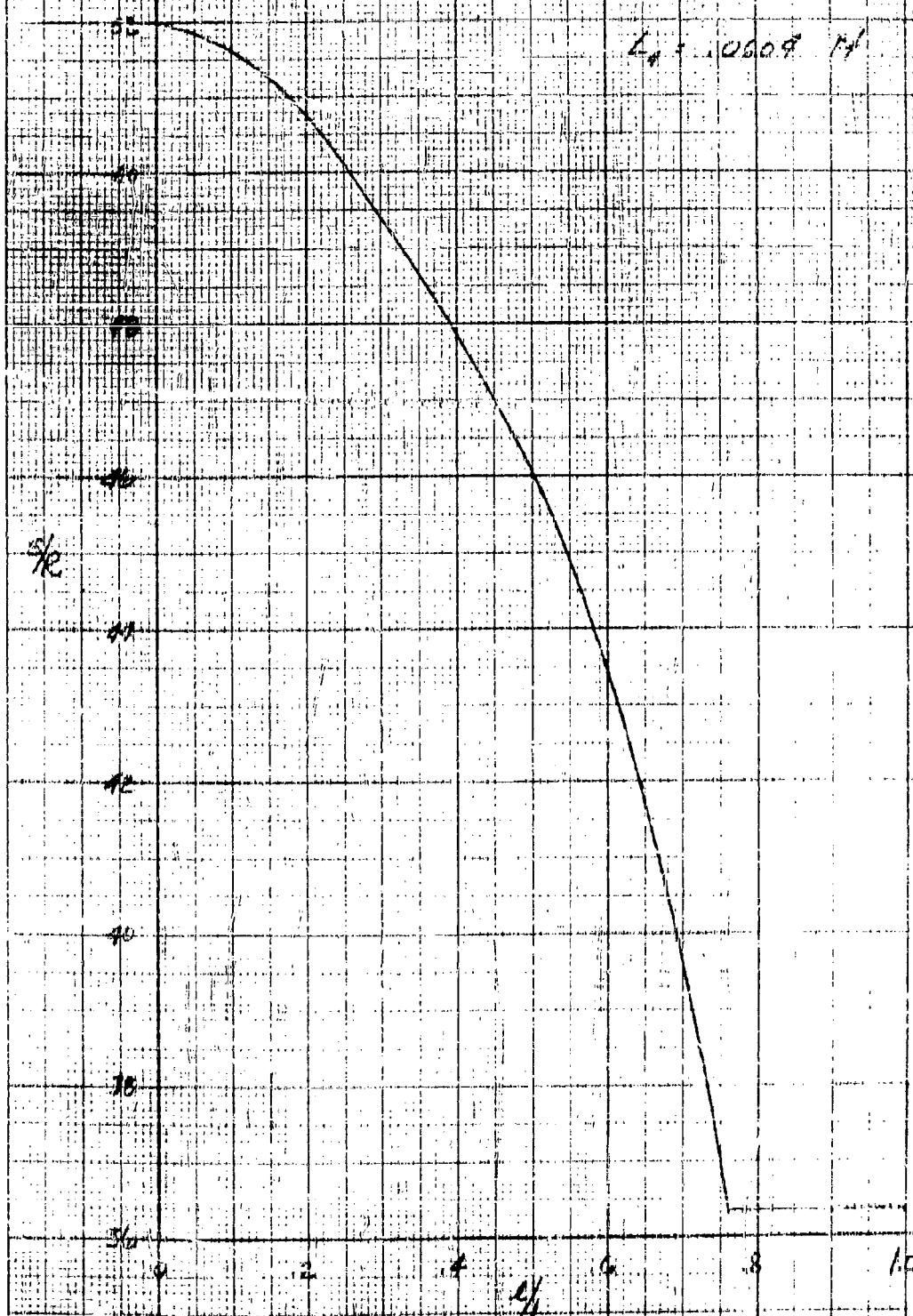
10

ENTROPY PROFILE - STATION 4 EQUILIBRIUM FLOW

FIG 14d

$M = 20$, $h = 200,000 \text{ ft}$

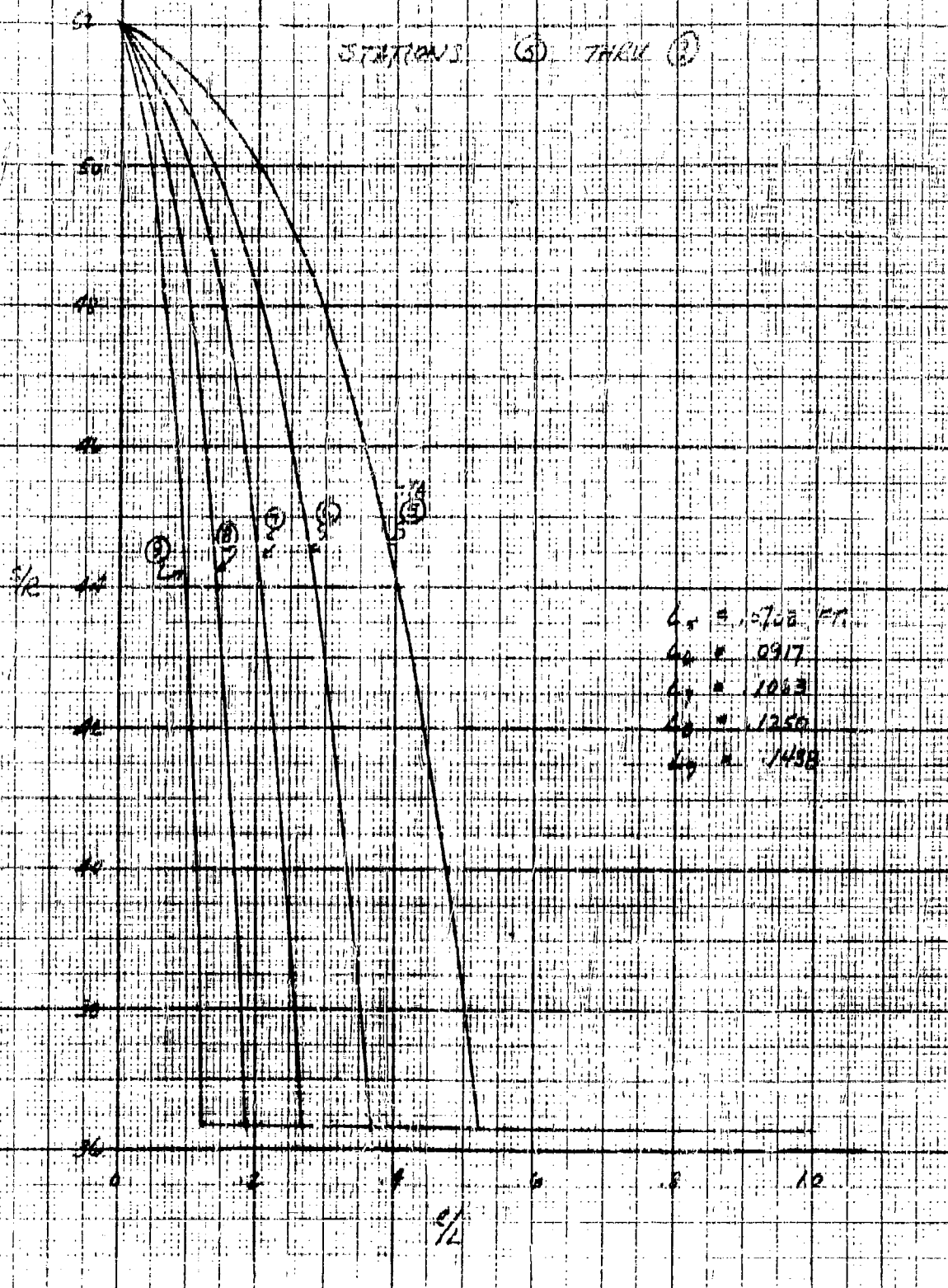
$L_0 = .0609 \text{ M}$



ENTROPY PROFILES - EQUILIBRIUM FLOW

$M = 2.0$ $h = 200,000$ FT.

STATIONS ⑤ TANK ③



ELECTRON DENSITY (per/100)

Fig. 15
J. L. A.

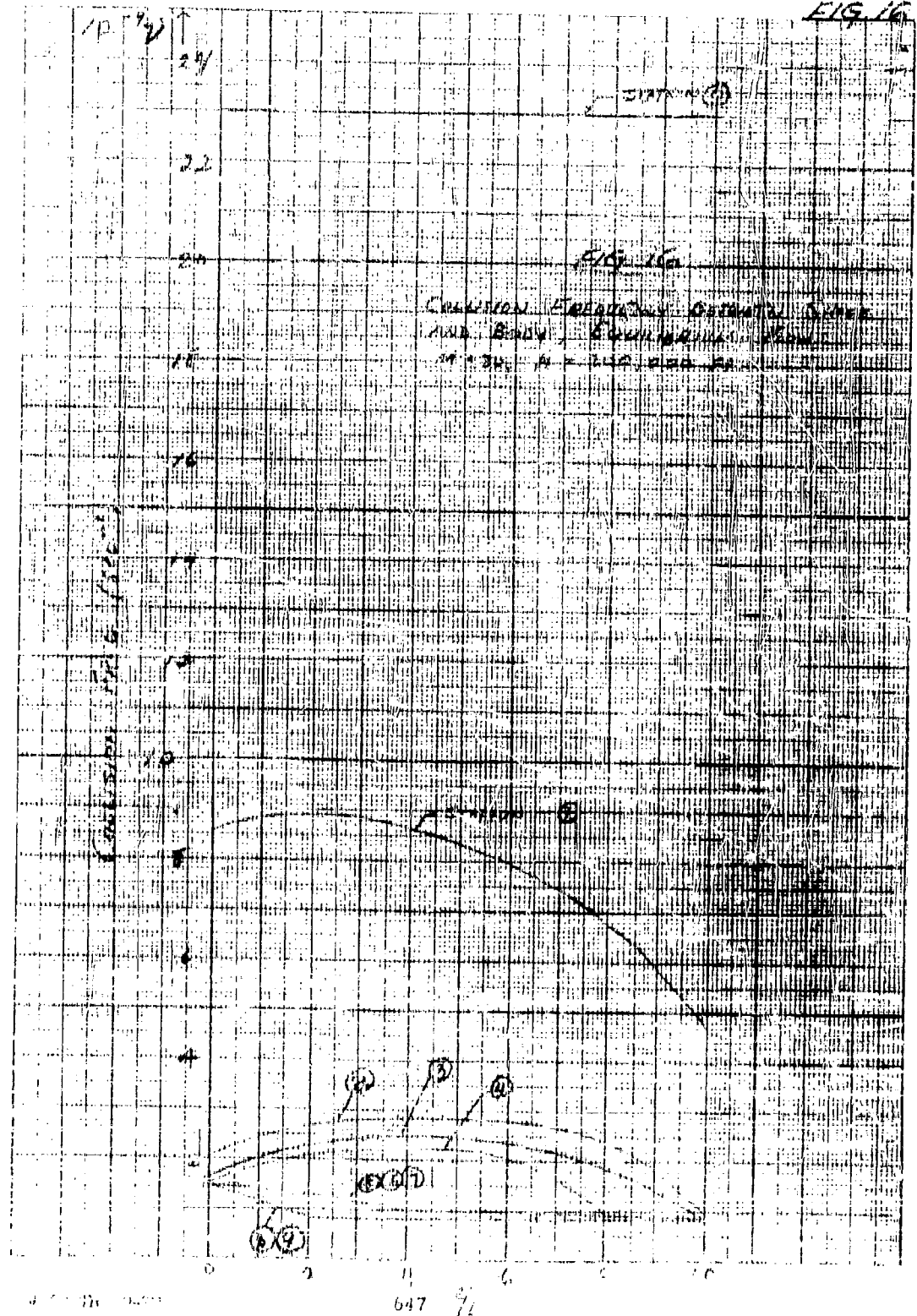
1

Fig. 15

ELECTRON DENSITY DISTRIBUTIONS BETWEEN SHIP AND BODY
EQUILIBRIUM STATE 11.20, 11.20, 0.00 FT.

2

FIG. 16



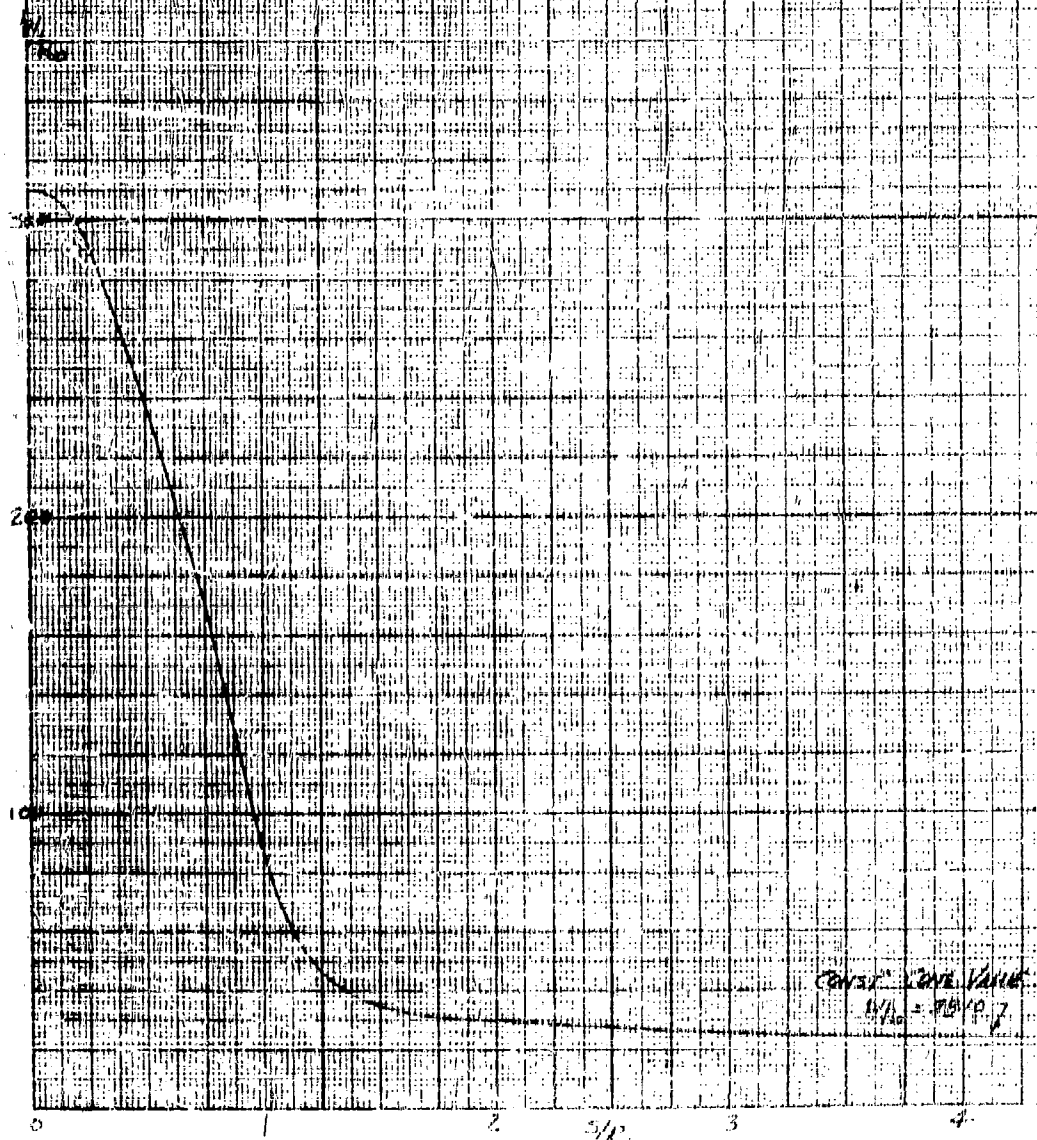
647

647

FIG 17

PRESSURE DISTRIBUTION ON BLUNTED CONE
WITH SPHERICAL CAP 15° CONE HALF ANGLE

$M = 1.4$ $\gamma = 1.4$

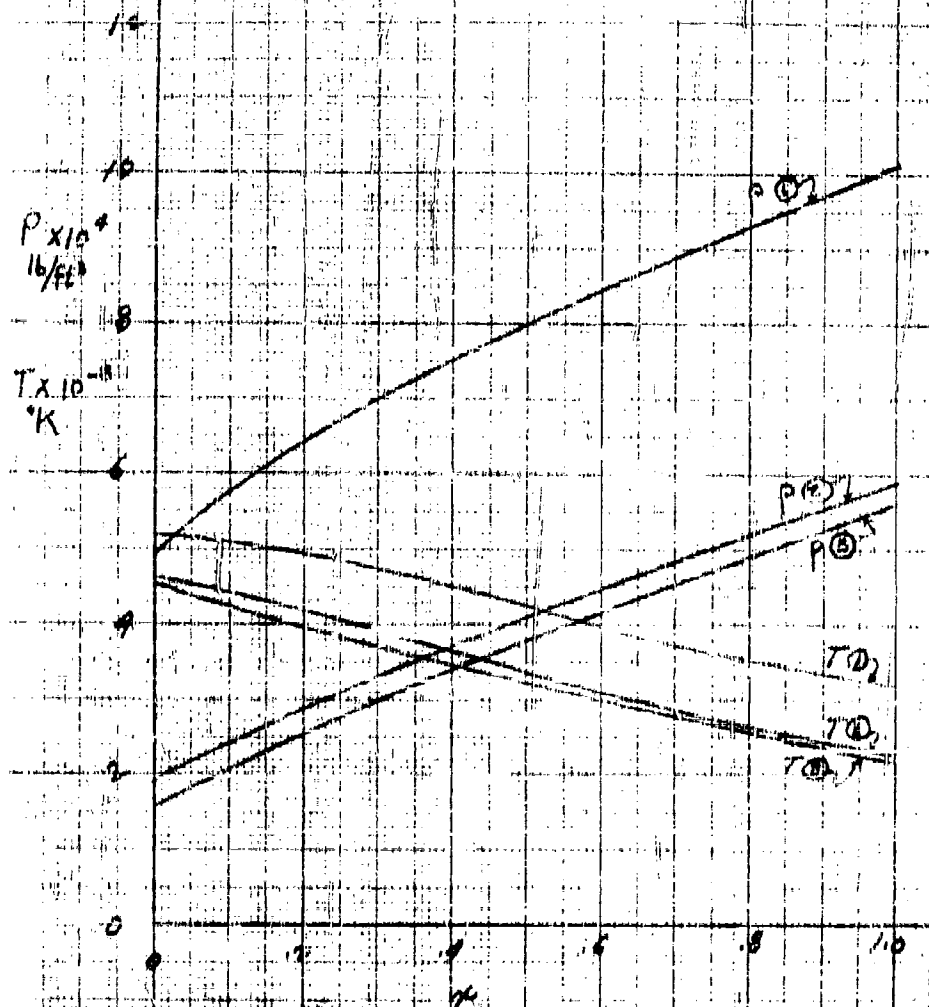


CONST. CONE VALUE
 $W/P_0 = 7.0/P_0$

FIG. 180.

DENSITY AND TEMP. PROFILES STATIONS 1, 2, AND 3

$M = 15$, $LH = 150,000$ FT.
EQUILIBRIUM FLOW ASSUMED



$M = 15$

$L_1 = 1000$ FT.

$L_2 = 0510$

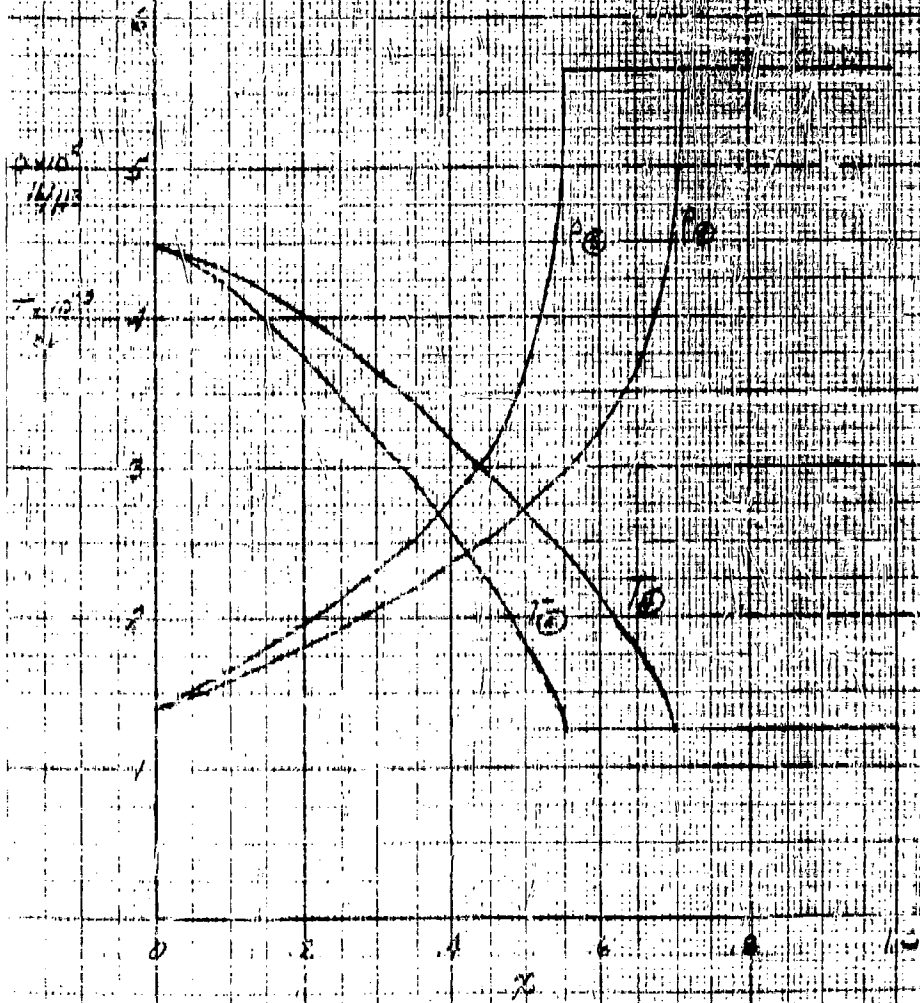
$L_3 = 0605$

DENSITY AND TEMP PROFILES
 FOR STATIONS 2 AND 5
 M = 15, H = 150, 600 KTS
 EQUILIBRIUM FLOW ASSUMED

$\lambda = 1/2$

$L_1 = 2570$ KTS

$L_2 = 2031$



419 186

DENSITY AND TEMPERATURE PROFILES FOR STATIONS 6 AND 7

$M = 15$, $H = 150,000$ FT.

EQUILIBRIUM FLOW ASSUMED

$K = 9/2$

$L_1 = 1000$ FT.

$L_2 = 1000$ FT.

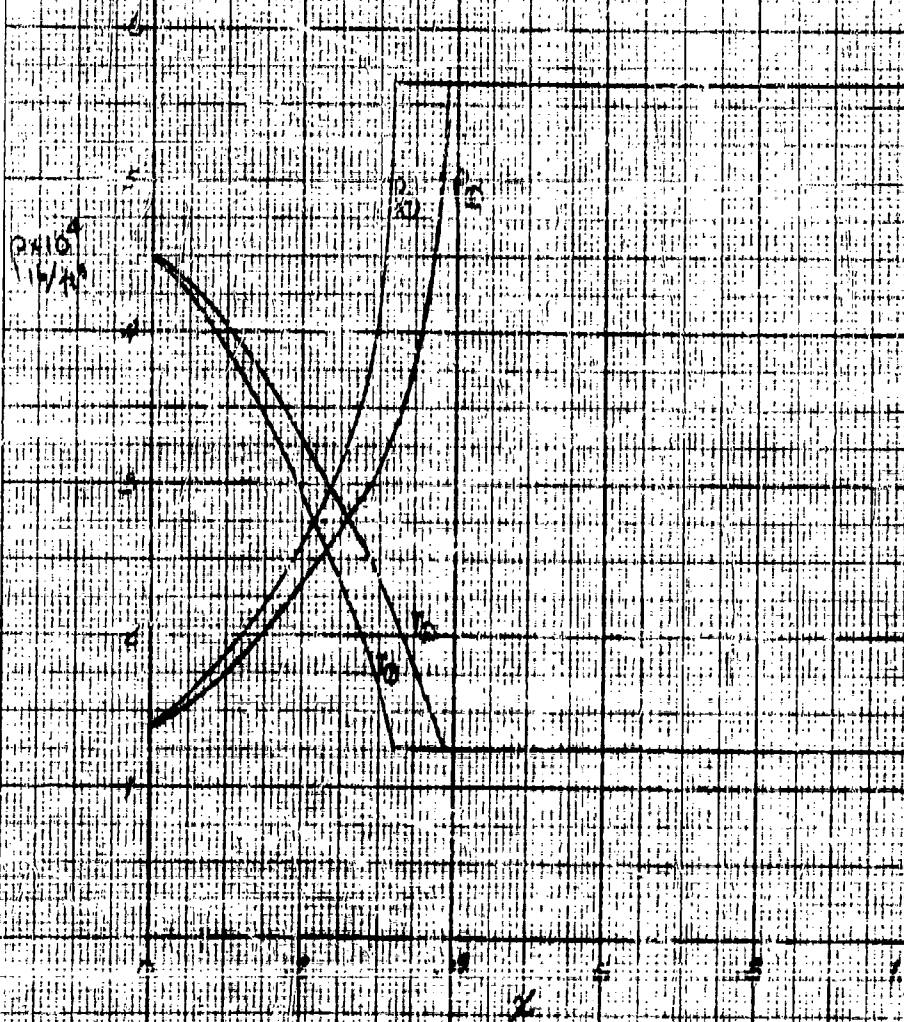


Fig. 13d

DENSITY AND TEMP PROFILES
FOR SYNDIOM 8 AND 9

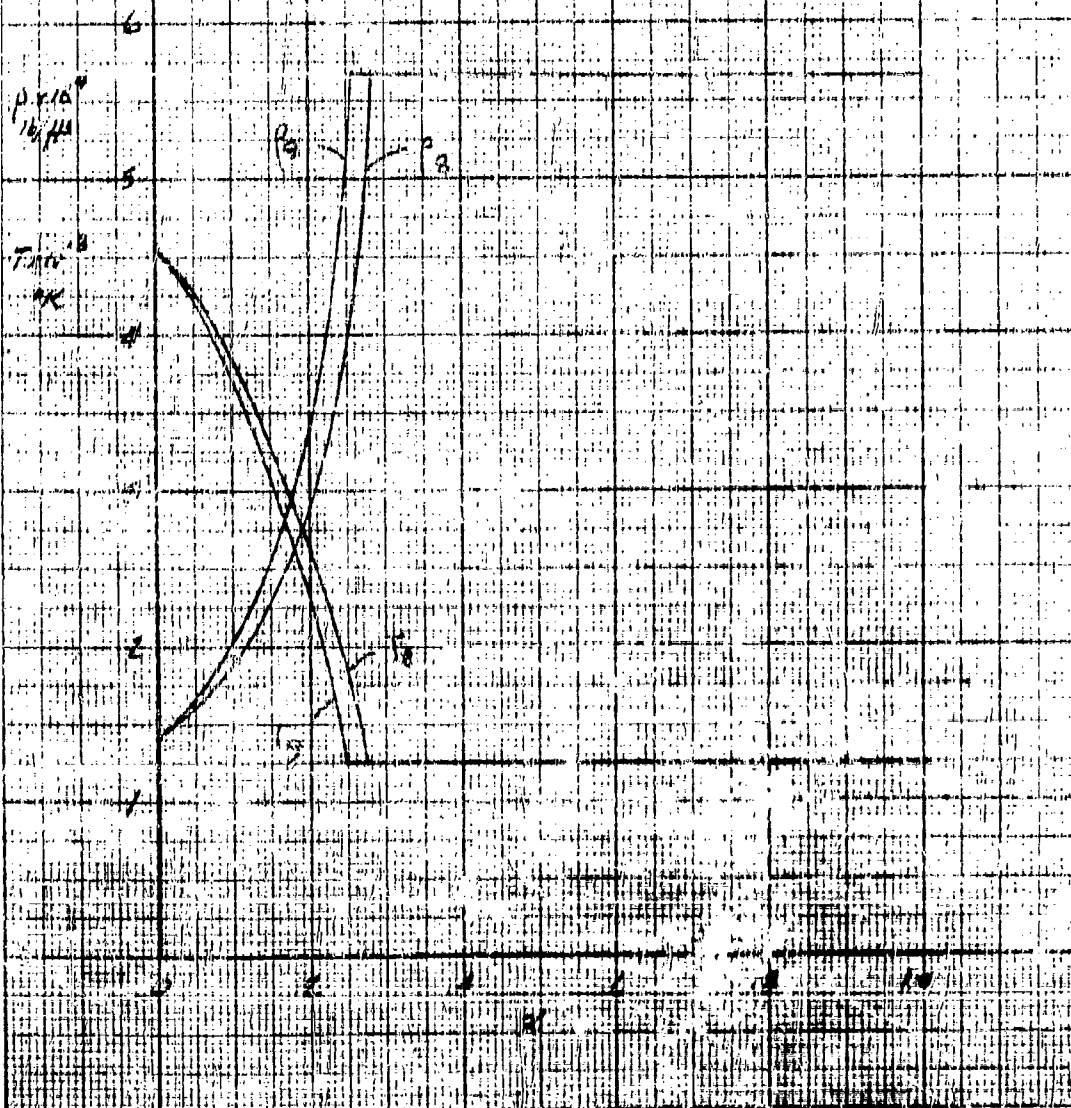
MIS, h = 150,000 FT

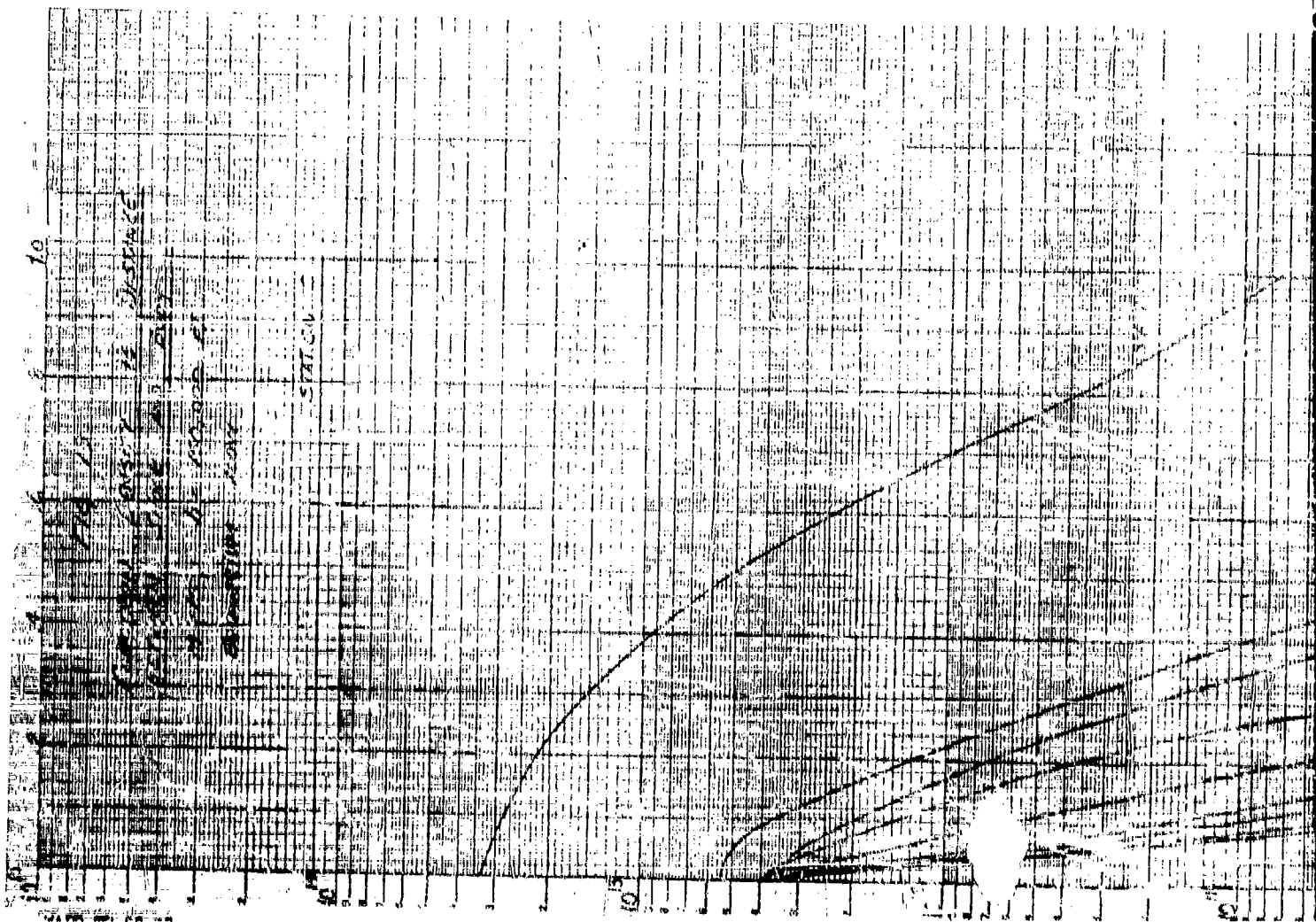
EQUILIBRIUM FLOWS

$X = 4\%$

$L_8 = 1.89 \text{ ft}$

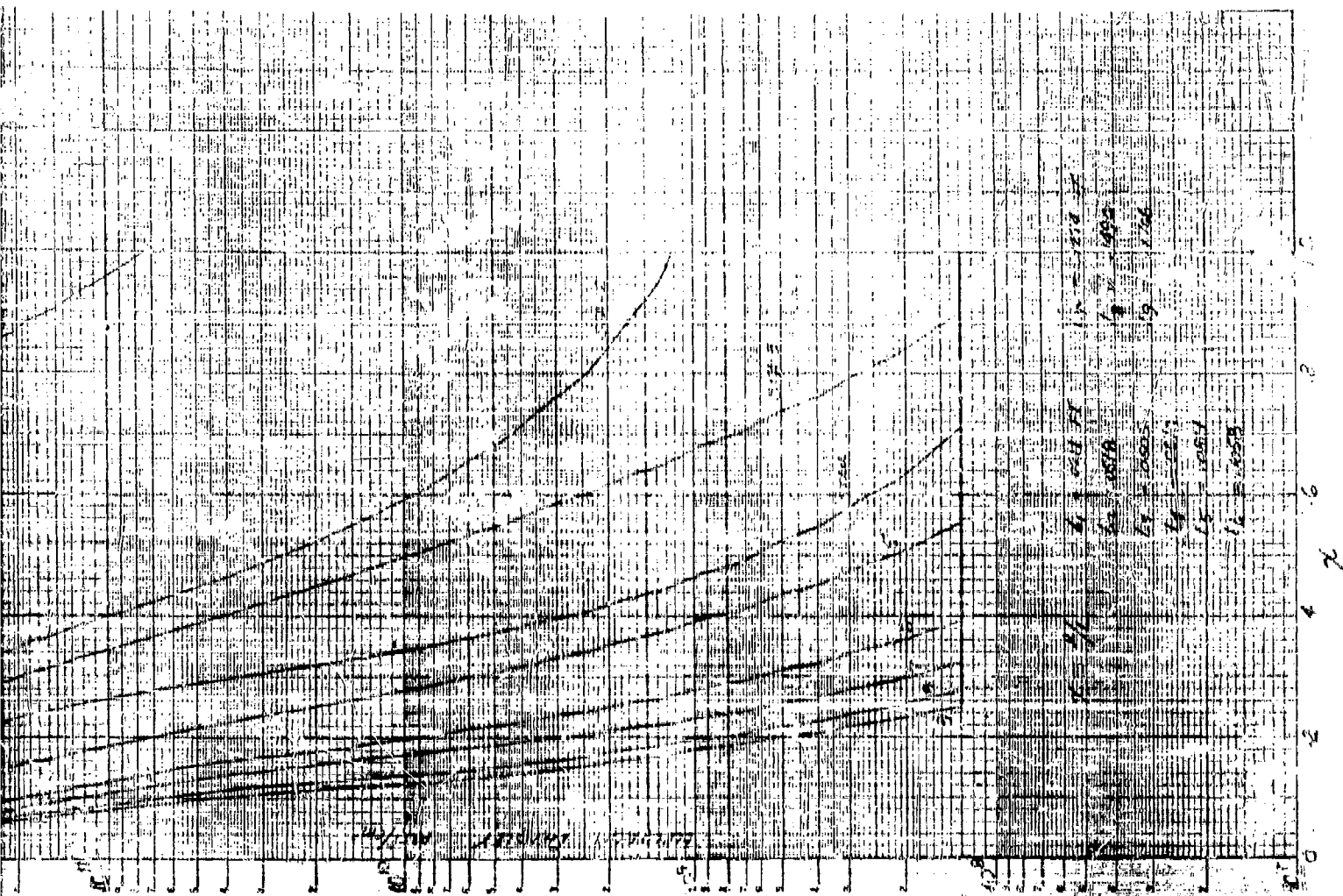
$L_9 = 1.71 \text{ ft}$





MADE IN U.S.A.

1



175 20
 COLLISION & FLOW OF WATER
 BETWEEN 5000 AND 15000 FT
 CONSIDERABLE FLOW

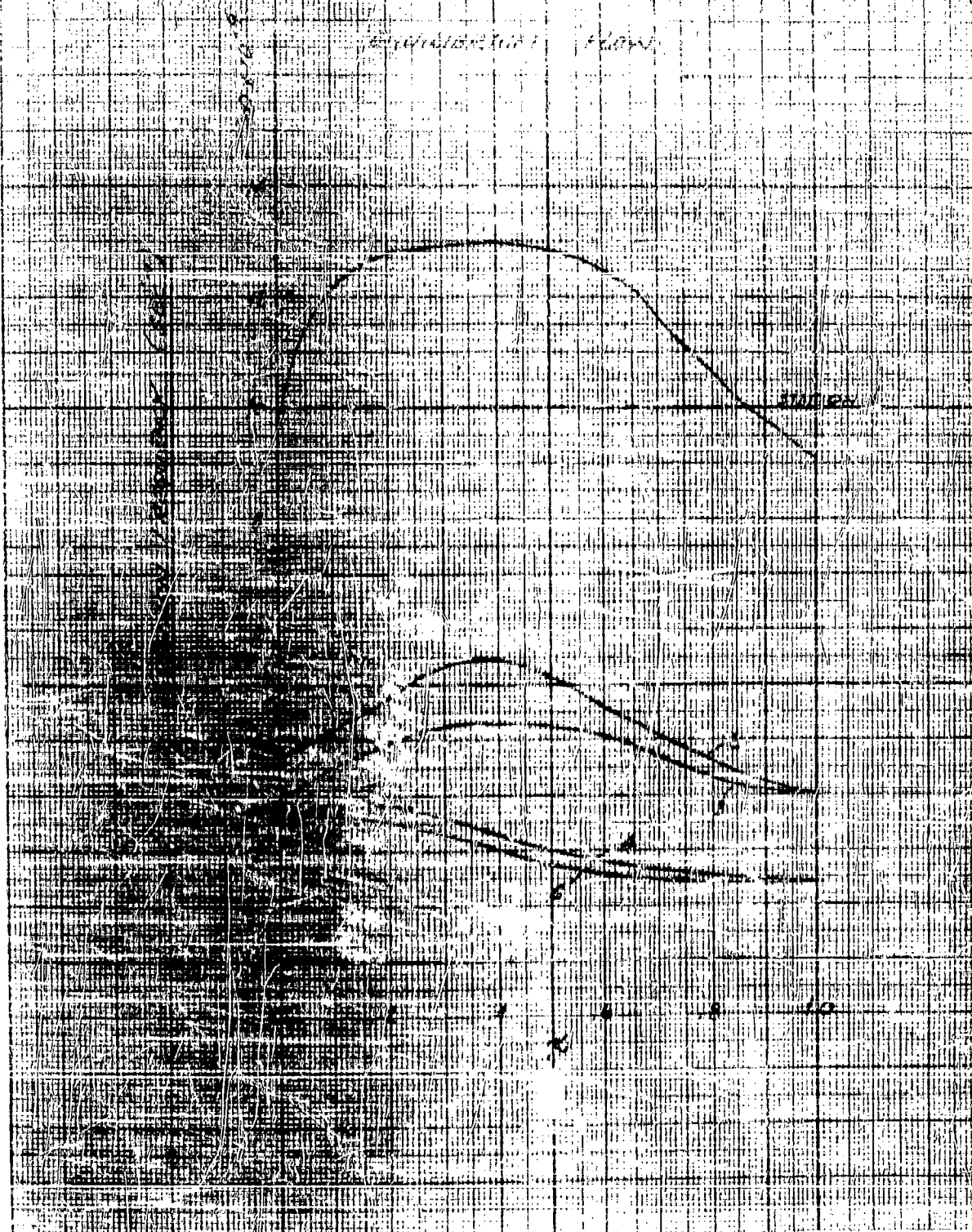


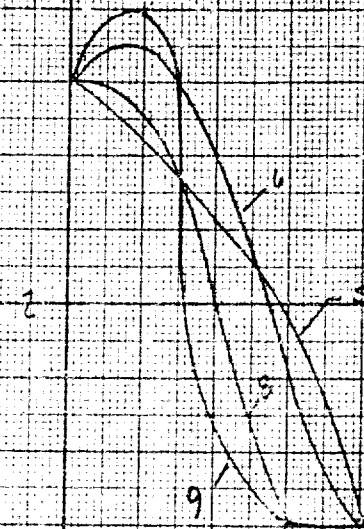
FIG 20 CONT.

COLLISION FREQUENCY VS
DISTANCE BETWEEN SHOCK
AND BODY

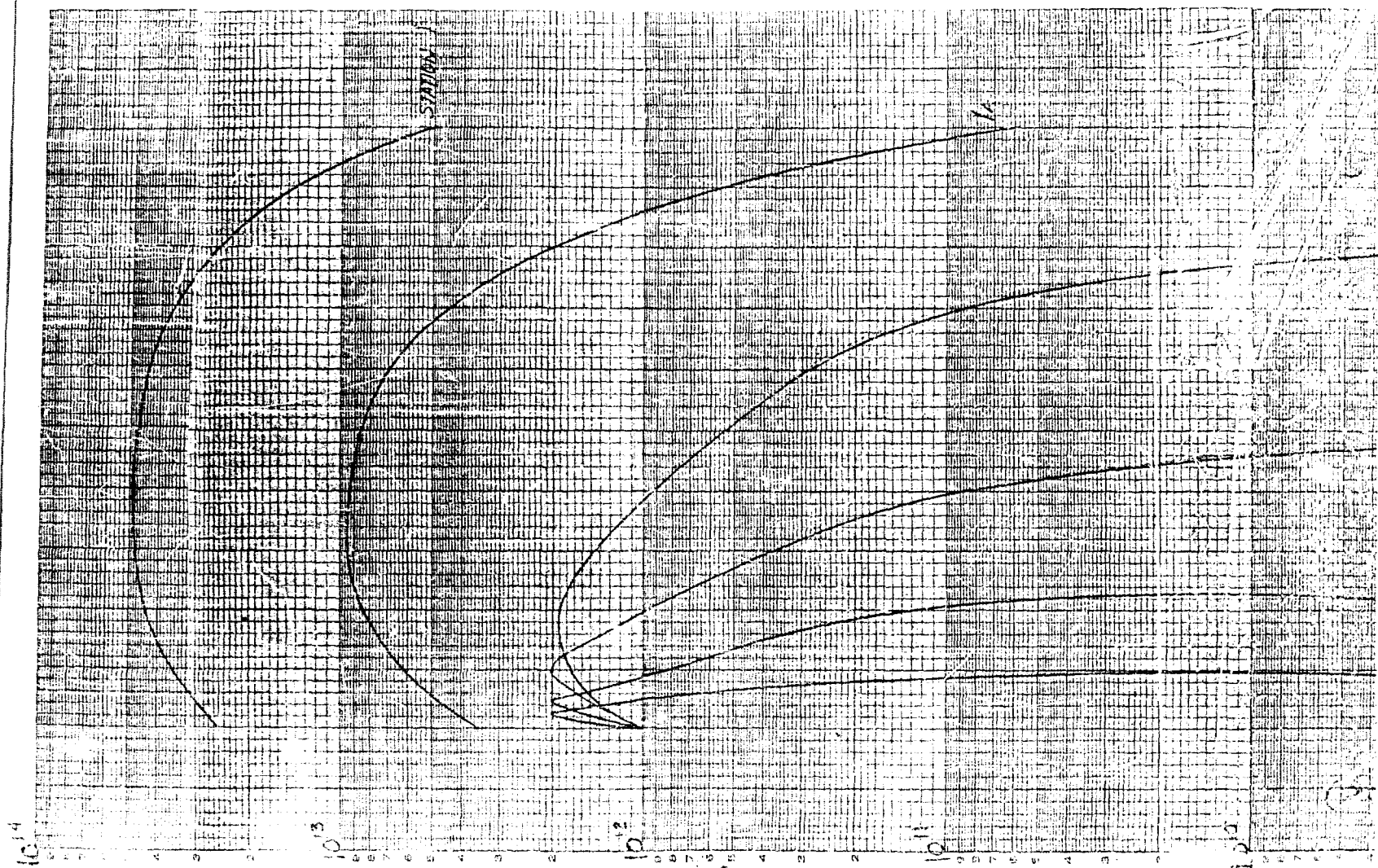
$M = 15$, $h = 150,000$ FT.

EQUILIBRIUM FLOW

COLLISION FREQUENCY (SEC⁻¹)



X



WADD TR 59-22



UNCLASSIFIED

UNCLASSIFIED